**Designing Novel Molecular Catalyst Systems for Electrochemical CO$_2$ Reduction
with High Activity at Low Effective Overpotentials**

by

Weixuan Nie

A dissertation submitted in partial fulfillment
of the requirements for the degree of
Doctor of Philosophy
(Chemistry)
in the University of Michigan
2021

Doctoral Committee:

      Assistant Professor Charles C. L. McCrory, Chair
      Professor Nicolai Lehnert
      Professor James E. Penner-Hahn
      Associate Professor Nathaniel Szymczak

Weixuan Nie

niewx@umich.edu

ORCID iD: 0000-0003-2094-6840

Acknowledgements

First and foremost, I want to thank my thesis advisor, Prof. Charles C. L. McCrory, for his patient training and guidance and kind help and support during my Ph.D. study. Most of my achievements throughout these 6 years in McCrory Lab could not be made without his mentorship. I was lucky that I studied electrochemistry and conducted research with such a wonderful scientist together during these years. Prof. McCrory not only helped me grow up to a quantified Ph.D. student but also shaped me as a professional chemist researcher and led me into the academia career.

I also appreciate the guide and help from my thesis committee members: Prof. Nathaniel Szymczak, Prof. Nicolai Lehnert and Prof. James E. Penner-Hahn. Especially I thank Prof. Nathaniel Szymczak for providing a lot of inspiring suggestions and ideas in our frequent discussions. I also thank Prof. Levi T. Thompson for initially serving on my thesis committee who moved to University of Delaware two years ago. I also thank my lovely current and former McCrory lab members who I worked with, played jokes with, and enjoyed beers with, in Ann Arbor during these 5~6 years: Dr. Chia-Cheng Lin, Dr. Yingshou Liu, Dr. Kwan Leung, Jeremy Kallick, Robert Bonsall, William Dean, Samuel Michaud, Taylor Soucy, Kevin Riverva-Cruz, Jukai Zhou, Drew Tarnopol, Ammar Ibrahim, Ziqiao Xu, Weijie Feng and Michael Riehs. The McCrory Group has been an integral part of my memory in Ann Arbor.

In addition, I would like to thank the Chemistry Department staff at University of Michigan who provided great service and helpful support for my graduate study. I thank Mr. Roy Wentz for making and modifying my glassware and electrochemical cells perfectly which saved me a lot of

time and pushed forward my research efficiently. I also thank Mr. James Windak for training and helping me at any time when I had problems with the instruments in the department.

Besides my advisor, thesis committee, lab members and friends in Ann Arbor, I deeply appreciate the love and sacrifices from my family to support me to successfully accomplish my Ph.D. study in a foreign country. Especially I want to thank my mom and dad for their contribution to the family and taking good care of my grandparents for me so that I could focus on my research abroad and pursue my career goal more confidently. I also dedicate this thesis to the memory of my grandparents who passed away during these years when I was studying abroad. I feel so regret that I was not able to go back to see them in the last moment! I believe they forgive me and are also proud of me and I promise my grandparents I will not disappoint them in the future as well.

There is one Chinese saying that there is usually a wonderful woman standing behind a successful man. In the end, I want to express my gratitude and love to this lovely woman, Yaqi Zhang, standing behind me during these years. Your patience and love are the warm sunshine waking me up every morning across the ocean and encouraging me to face anything in the unknown future.

Table of Contents

List of Tables

data point of FeTDHPP and circled numbers represent (TOF, η) data points of cited catalysts from preparative-scale experiments. Adapted with permission from *Science* **2012**, *338*, 90-94 [66], Copyright © 2012, American Association for the Advancement of Science

Figure 1.12 a) The structure of HPDFe-3SA, HPDFe-Gnd and HPDFe-PhOH with their corresponding catalytic current for the CO_2RR, adapted with permission from *Organometallics* **2019**, 38, 6, 1219–1223 [58], Copyright © 2019, American Chemical Society; b) Schematic comparison of catalytic performance between $MnBr(F-HOPh-bpy)(CO)_3$ with more acidic pendant proton and $MnBr(2.2'-bipyridine)(CO)_3$ with less acidic pendant proton, adapted with permission from *Organometallics* **2020**, 39, 13, 2425–2437 [82], Copyright © 2020, American Chemical Society.

Figure 1.13 a) *fac*-$Mn^I([(MeO)_2Ph]_2bpy)(CO)_3(CH_3CN)(OTf)$ with four pendant methoxy groups establishes an allosteric H-bonding network among pendant -OMe groups, external Brønsted acid and $Mn-CO_2$ adduct, leading to the *protonation-first* pathway of reducing CO_2 at lower overpotentials, adapted with permission from *J. Am. Chem. Soc.* **2017**, 139, 7, 2604–2618 [84], Copyright © 2017, American Chemical Society; b) a series of $[CpCo(P^R_2N^{R'}_2)I]^+$ complexes containing two pendant amine residues in $P^R_2N^{R'}_2$ ligand show increased activity for selective CO_2 reduction to formic acid by facilitating the hydride transfer from the Co site to the CO_2 molecule through H-bonding interactions with the proton source H_2O, adapted with permission from *J. Am. Chem. Soc.* **2017**, 139, 10, 3685–3696 [63], Copyright © 2017, American Chemical Society; c) The ligand-controlled product selectivity for the CO_2RR by a series of Mn complexes with modified bipyridine or phenanthroline ligands with different pendant proton relay groups in the secondary coordination sphere; adapted with permission from *J. Am. Chem. Soc.* **2020**, 142, 9, 4265–4275 [85], Copyright © 2020, American Chemical Society; d) A family of polypyridyl-iron $[(bpy^RPY2Me)Fe^{II}]$ complexes show varying selection for CO_2RR or HER with different pendant proton relay groups with varying acidities (-H, -OH, -OMe AND -NHEt), adapted with permission from *Inorg. Chem.* **2020**, 59, 7, 5206–5217 [88], Copyright © 2020, American Chemical Society.

Figure 1.14 a) The structure of Co aminopyridine macrocycle complexes with varying number of NH and NMe groups in the ligand scaffold; b) the correlation between catalytic rate and number of pendant NH group in the secondary coordination sphere; 3) the correlation between catalytic

MeCN with 0.1 M nBu$_4$NPF$_6$. The right chamber held the counter electrode in 15 mL of a 5 mM ferrocene solution in MeCN. These two chambers were separated by a fine-porosity glass frit. The working electrode was a 3.2 cm × 1.6 cm × 0.1 cm glassy carbon plate (HTW Hochtemperatur-Werkstoff GmbH) which was half immersed in the solution. The reference electrode was a Ag/AgNO$_3$ (1.0 mM)/MeCN nonaqueous reference electrode (also containing 0.1 M nBu$_4$NPF$_6$) separated from the solution by a Vycor frit (Bioanalytical Systems, Inc.). The counter electrode was nichrome wire (ARCOR). 275

Abstract

The electrocatalytic CO_2 reduction reaction (CO_2RR) is a promising strategy of converting CO_2 to fuels and value-added chemicals by renewable energy sources. However, designing active catalysts for selective CO_2 reduction at low effective overpotentials remains a challenge. Compared to most state-of-the-art solid-state catalysts such as Cu, which reduce CO_2 with high activity but usually suffer from poor selectivity, molecular catalysts show promise for the selective conversion of CO_2 to single products with intrinsic catalytic ability that can be tuned through synthetic structure modifications.

For most traditional molecular catalysts, beneficial decreases in overpotentials are usually correlated with detrimental decreases in catalytic activity, which is referred to as the "*molecular scaling relationship*". The main reason for the "*molecular scaling relationship*" is that the catalytic reaction is initiated by the redox activation of the metal center where the substrate is coordinated and reduced, so that both the kinetic reactivity and the effective overpotential scale with the nucleophilicity of metal sites, which correlates to the redox potential of the metal center. The goal of this thesis is to design novel and efficient molecular catalyst systems to break the typical "*molecular scaling relationship*", showing high activity at low effective overpotentials for electrocatalytic CO_2 reduction.

In this thesis, two series of transition metal complexes with redox-active ligands have been designed and investigated as promising molecular catalysts for the CO_2RR—cobalt bis(pyridylmonoimine) complexes ([Co(BPMI)]) and cobalt pyridyldiimine complexes ([Co(PDI-R)]). For both molecular catalyst systems, catalytic onset is preceded by the formation of a ligand

radical through a ligand-based redox process instead of a metal-based process. This unique redox feature provides an opportunity to break "*molecular scaling relationships*" by modulating the kinetic reactivity and the effective overpotential of the catalyst independently through rational ligand design and modification.

In Chapter 2, a planar Co-bis(pyridylmonoimine) [Co(L-L)] was prepared and studied, which shows catalytic activity for the CO_2RR in acetonitrile. Addition of a proton source such as water or trifluoroethanol dramatically improves the activity and stability of the catalyst. The further electrochemical kinetic studies of [Co(L-L)] in Chapter 3 reveal that [Co(L-L)] undergoes a reductive dimerization upon reduction to the Co^I complex, delaying the catalytic onset for the CO_2RR. To facilitate the CO_2RR, a series of [Co(L-R-L)] complexes were designed and prepared by modulating ligand flexibility and changing the complex's planarity. This not only prevents catalyst dimerization but also leads to both a positive shift in catalyst onset and an increase in initial catalytic activity for CO_2RR, thus breaking the typical "*scaling relationship."* In Chapter 4, for [Co(PDI-R)] complexes, three substituent effects are sequentially integrated into the structure to facilitate the ligand reduction, which leads to the inverse "*molecular scaling relationship"* achieved in Chapter 3. The resulting [Co(PDI-PyCH$_3^+$I$^-$)] catalyst shows one of the highest TOF$_{cat}$ ($\sim 4.1 \times 10^4$ s^{-1}) reported for CO_2RR. In Chapter 5, a binuclear bi-[MCo(PDI)] complex (M = Co and/or Zn) represents another efficient system which breaks the "*molecular scaling relationship*," operating with ~4 orders of magnitude higher activity at 0.15 V lower magnitude overpotential for the CO_2RR compared to the mononuclear [Co(PDI)] analog.

The work in this thesis highlights several molecular catalyst designs, where a ligand-based redox event precedes catalytic onset, to break the "*scaling relationship*" for the CO_2RR. As discussed in Chapters, these designs are believed applicable for other catalytic reactions as well.

Chapter 1 Introduction: Challenges and Strategies for Breaking the Scaling Relationship to Design and Make Efficient Molecular Catalysts for the Electrochemical CO₂ Reduction

1.1 Preface

This chapter presents some background information and fundamental concepts necessary on the electrochemical CO_2 reduction reaction (CO_2RR) by molecular catalysts. This is followed by an overview of some of the existing challenges and reported strategies for designing and making efficient molecular catalysts for the CO_2RR. Included at the end of this chapter is an overview of the strategies undertaken in this thesis to address these existing challenges, and in particular to break molecular scaling relationships. An outline of the work presented in each chapter of this thesis is also included at the end of this chapter.

1.2 The Electrochemical CO₂ Reduction Reaction (CO₂RR)

In the last few decades, the electrocatalytic CO_2 reduction reaction (CO₂RR) by renewable electricity generated from intermittent energy sources (e.g. solar and wind energy) has attracted increasing attention as a promising strategy for converting CO_2, an industrial waste product and environmental contaminant, into solar fuels and other value-added products.[1-5] Based on the studies and reports published in literatures so far, CO_2 can be reduced to variable products via different multi-electron proton-coupled pathways. Several selected electrochemical CO_2 reduction processes are listed in Table 1.1 with the corresponding standard redox potential E^0 and standard Gibbs free energy change ΔG^0 for the reaction in aqueous solutions.[6-10] These slightly negative E^0 values (some of them are even positive) of these processes indicate that such multi-electron proton-coupled CO_2 reduction pathways are relatively thermodynamically favorable under the standard condition because the standard Gibbs free energy of these products are similar to that of the reagent CO_2 molecular and some of products are even more thermodynamically stable than CO_2 (Table 1.1).

However, it is important to emphasize here that the E^0 and ΔG^0 values in Table 1.1 only indicate the thermodynamic driving force necessary for these processes to occur at the standard conditions (Figure 1.1). In real practical cases, additional driving force is required to reach a reasonable reaction rate for the direct CO_2 reduction, in another words, more negative potentials than those thermodynamic values listed in Table 1.1 need to be applied to obtain a reasonable catalytic current for the direct electrochemical CO₂RR. This is due to a high kinetic energy barrier for the direct and uncatalyzed CO_2 reduction through the out-sphere (non-bonded) electron transfer (Figure 1.1, $\Delta G_1^{\ddagger}$ for the red curve).[7-9, 11] For example, the direct and uncatalyzed one-electron reduction of CO_2 to $CO_2^{\bullet-}$ occurs at the very negative thermodynamic potential of -1.48 V, as a

result of the large structural reorganization energy between the linear CO_2 molecule and the bent $CO_2^{\bullet-}$ radical anion.[8, 10, 12] Although the radical anion intermediate can be sequentially protonated and/or dimerized a little more favorably to form the final products ($C_2O_4^{2-}$ or $H_2C_2O_4$), the high energy barrier for forming this high-energy intermediate requires a very negative potential to initiate the whole reaction process. In order to avoid the formation of such high-energy intermediates and decrease the kinetic activation energy barrier for the CO_2RR, designing and developing efficient catalysts, which stabilize high-energy intermediate by forming CO_2-adducts and catalyze the CO_2RR through inner-sphere electron transfer with lower kinetic energy barrier (Figure 1.1, $\Delta G_2^{\ddagger}$ for the green curve), is therefore very crucial for realizing the efficient electrochemical CO_2 reduction in practical applications.

Table 1.1 Selected CO_2RR processes with corresponding standard thermodynamic potential E^0 (V, vs. SHE) and standard Gibbs energy change ΔG^0 for the reaction in aqueous solutions in the standard condition.

reaction processes	E^0 / V		ΔG^0 / kJ
CO_2 (g) + $2H^+$ + $2e^-$ = HCOOH (l)	-0.25		48.2
CO_2 (g) + $2H^+$ + $2e^-$ = CO (g) + H_2O (l)	-0.11		21.2
CO_2 (g) + $4H^+$ + $4e^-$ = CH_2O (l) + H_2O (l)	-0.07		27.0
CO_2 (g) + $6H^+$ + $6e^-$ = CH_3OH (l) + H_2O (l)	$+0.02$	$\Delta G^0 = -nE^0F$	-11.6
CO_2 (g) + $8H^+$ + $8e^-$ = CH_4 (g) + $2H_2O$ (l)	$+0.17$		-131.2
CO_2 (g) + $12H^+$ + $12e^-$ = CH_3CH_2OH (l) + $3H_2O$ (l)	$+0.08$		-92.6
CO_2 (g) + $12H^+$ + $12e^-$ = CH_2CH_2 (g) + $4H_2O$ (l)	$+0.06$		-69.5
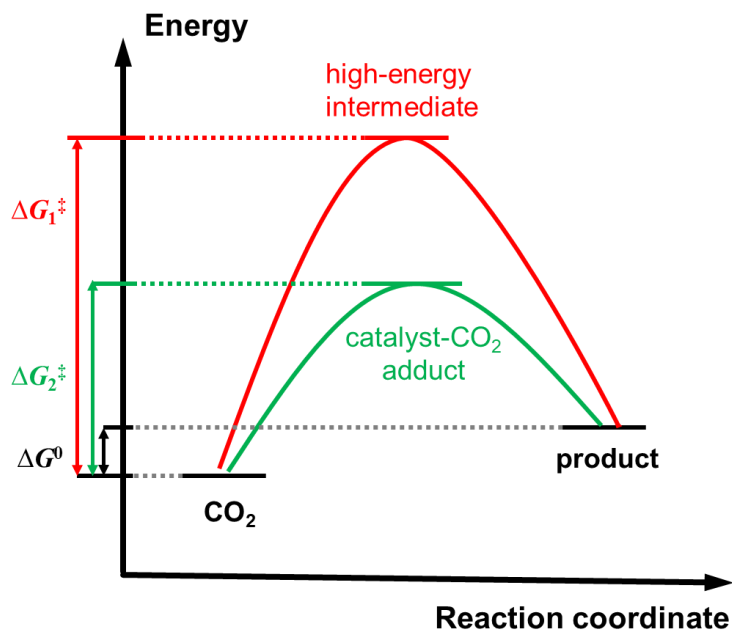
Figure 1.1 The Gibbs free energy diagrams for the electrochemical CO2 reduction processes. Red curve: a direct and uncatalyzed process through the out-sphere electron transfer; Green: a catalyzed process by forming catalyst-CO2 adduct through the inner-sphere electron transfer

1.3 The Electrocatalytic CO₂ Reduction

1.3.1 CO₂ Reduction by Heterogenous Solid-State Catalysts

In contrast to the direct and uncatalyzed CO_2 reduction process through the out-sphere electron transfer on inert electrode surfaces, some solid-state materials, in particular some metal electrodes, can bind CO_2 molecules on the surface to form the adsorbed CO_2 adducts, which is followed or coupled by the inner-sphere electron transfer at certain applied potentials to form different metastable reductive intermediates according to different reaction pathways (Figure 1.2a). [13-17] These processes effectively lower the kinetic energy barrier for the CO_2 reduction (Figure 1.1) and these electrode surfaces are referred as heterogenous solid-state CO₂RR catalysts. On these metal electrode surfaces, a reasonable catalytic current i_c for the CO₂RR can be achieved at a comparatively low overpotential η, which is defined as the difference between the applied potential on the electrode surface $E_{electrode}$ and the thermodynamic potential for the CO_2 reduction E_{CO2RR} (Figure 1.3a and b). In addition, more negative applied potential $E'_{electrode}$ leads to higher overpotential η' (larger driving force) and lower kinetic energy barrier $\Delta G'^{\ddagger}$ for the CO_2 reduction, so that the catalytic current i_c keeps increasing as the applied $E_{electrode}$ moves more negative (cf. Tafel plot[18]) in the catalytic cyclic voltammetry (CV) for solid-state catalysts (Figure 1.3b).

In the last decade, a lot of efforts have been devoted to improving the mechanistic understanding of the catalytic processes on the solid-state catalysts for the CO₂RR. [13-17, 19-25] Many experimental and computational studies show that the lack of product selectivity in the CO₂RR remains a challenge for the solid-state catalysts despite good activity achieved at low overpotentials. [13-17, 26] This is because the ability of adsorbing different reductive intermediates, including CO_2 and product molecules, varies greatly on different solid-state electrode surfaces. The competition among these binding species on the catalytic electrode surface is a key factor

governing the final distribution of reduction products.[26] For example, Au and Ag catalysts mainly reduce CO_2 to CO but still suffer from competitive H_2 formation in protic solutions,[15-17] while Cu electrode generates up to 16 C-based products including multi-carbon products as well in aqueous solutions.[13-15] In addition to the chemical composition of electrodes, the different surface morphology of the same material also shows a significant effect on the product distribution for the CO_2 reduction.[8] The low-coordination sites such as edges, steps, defects, and specific exposed crystal facets exhibit more excellent activity and selectivity for a certain product.[27-30] Based on these experimental discoveries, recent advances in solid-state catalyst design, including the use of nanostructured and mesoporous catalyst surfaces and composite electrode materials, show increased selectivity for specific products.[19-25] However unpredictable structural changes of these materials at varying applied electrode potentials raise another issue of potential dependent selectivity for the solid-state catalysts in recent years.
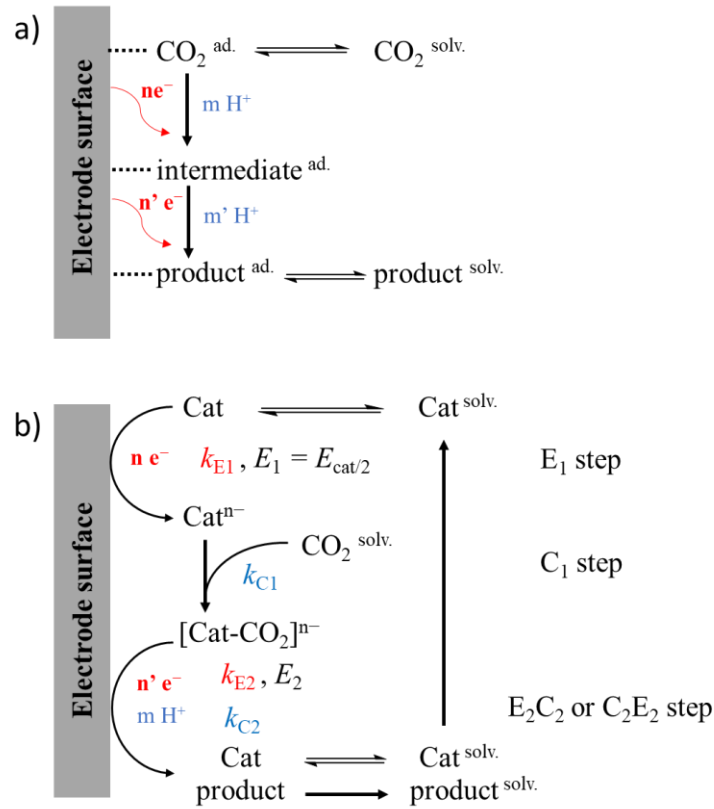
Figure 1.2 a) Electrochemical CO_2 reduction by heterogenous solid-state catalysts; b) Electrochemical CO_2 reduction by homogenous molecular catalysts.
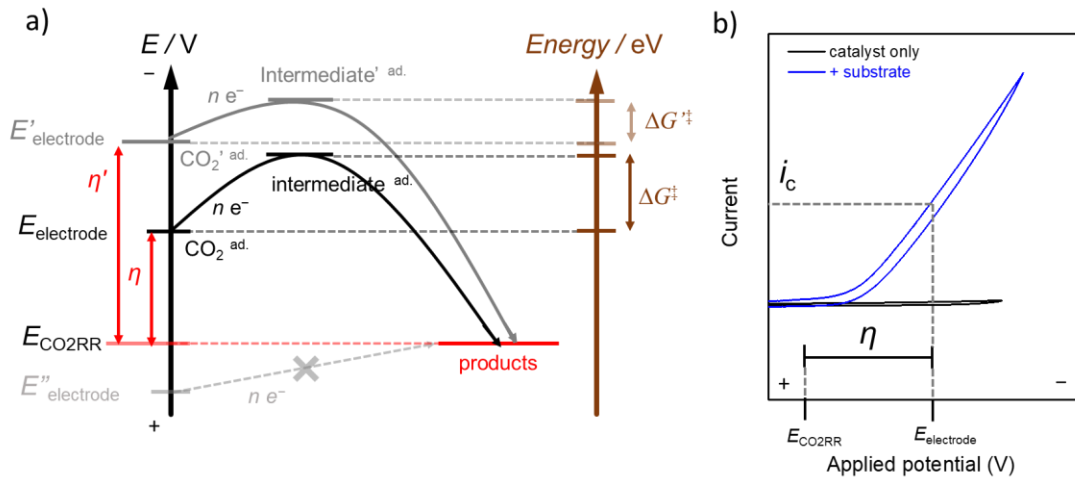
Figure 1.3 a) Schematic representation of electron transfer in the process of electrocatalytic CO_2RR by heterogenous solid-state catalysts; b) Cyclic voltammograms of electrocatalytic CO_2RR by heterogenous solid-state catalysts in the presence (blue curve) and absence (black curve) of the substrate CO_2.

1.3.2 CO$_2$ Reduction by Homogenous Molecular Catalysts

In parallel to the heterogenous solid-state catalysts, homogenous molecular catalysts, in particular transition metal complexes, show significant promise for the selective conversion of CO$_2$ to single products. Instead of transferring electrons directly from the electrode surface to the adsorbed CO$_2$ molecules, the homogenous molecular catalysts act as electron shuttles between the electrode and CO$_2$ molecules (Figure 1.2b). [7, 10, 31] In this case, the molecular catalyst Cat is first reduced to the active species Cat^{n-} on the electrode surface at the redox potential $E_{cat/2}$ of itself, which is the first electronic step (E$_1$ step, Figure 1.2b) to initiate the whole catalytic cycle. Then the active species Cat^{n-} diffuses and coordinates CO$_2$ to form a CO$_2$-adduct intermediate [Cat-CO$_2$]$^{n-}$, which is equivalent to a chemical step (C$_1$) and requires a favorable kinetic rate k_{C1} for the efficient coordination (Figure 1.2b). The metastable intermediate [Cat-CO$_2$]$^{n-}$ can be further reduced (E$_2$) on the electrode surface and/or protonated (C$_2$) by the proton source in the solution to generate the final product and release the re-oxidized molecular catalysts Cat, completing the catalytic cycle for the homogenous CO$_2$RR. In order to render the whole efficient catalysis, both electronic and chemical steps should exhibit feasible kinetics.

In the process of the homogenous catalysis discussed above, the redox potential $E_{cat/2}$ of the molecular catalyst should be more negative than the thermodynamic CO$_2$RR potential E_{CO2RR}, providing a thermodynamic driving force for the electron transfer from the molecular catalyst to the CO$_2$ molecule (Figure 1.4a and b), which is referred as the effective overpotential η_{eff} for the catalytic reaction. [7, 10, 31-32] In contrast to the scenario of heterogenous solid-state catalysts (Figure 1.3), the effective overpotential η_{eff} for the CO$_2$RR by molecular catalysts does not change as the applied electrode potential $E_{electrode}$ varies, because η_{eff} is defined as the potential difference between thermodynamic CO$_2$RR potential E_{CO2RR} and the redox potential $E_{cat/2}$ of the catalyst, both

of which are fixed during the catalytic process.[7, 10, 31] More negative $E'_{electrode}$ can facilitate the redox activation/conversion of the molecular catalyst and the intermediate (E_1 and E_2 step) but has no influence on the CO_2 bonding and protonation steps (C_1 and C_2 steps) in the catalytic cycle, because these chemical steps are only related to the intrinsic electronic features of the molecular catalysts, which is independent of the electrode potential. Therefore, in most cases where chemical steps are the rate-determine step for the whole catalytic process, the catalytic current will reach a maximum plateau instead of keeping increasing as the electrode potential moves more negative (Figure 1.4b).[11, 33] The maximum catalytic turnover frequency (TOF_{max}) can be estimated from the plateaued catalytic current. This unique character of the catalytic CV of molecular catalysts indicates that the maximum catalytic activity for the CO_2RR is modulated by the intrinsic catalytic ability of the molecular catalyst rather than the electron transfer through the electrode interface.[11, 33]

Compared to the solid-state catalyst surface with variable types of binding sites, the molecular catalyst only provides a single type of coordination environment to bind CO_2 at the metal center to form a CO_2-adduct intermediate with a specific coordination mode. This intermediate employing a certain coordination structure can be further reduced and/or protonated to generate a single product selectively (usually CO or formic acid).[9-11] Besides improved selectivity for the CO_2RR, the tunability of electronic properties of metal complexes and the coordination sphere environment of ligand scaffolds provides us with opportunities of designing and developing efficient catalytic systems with both high activity and excellent selectivity for the CO_2RR through rational design and modification of the complex structure.[34-39]
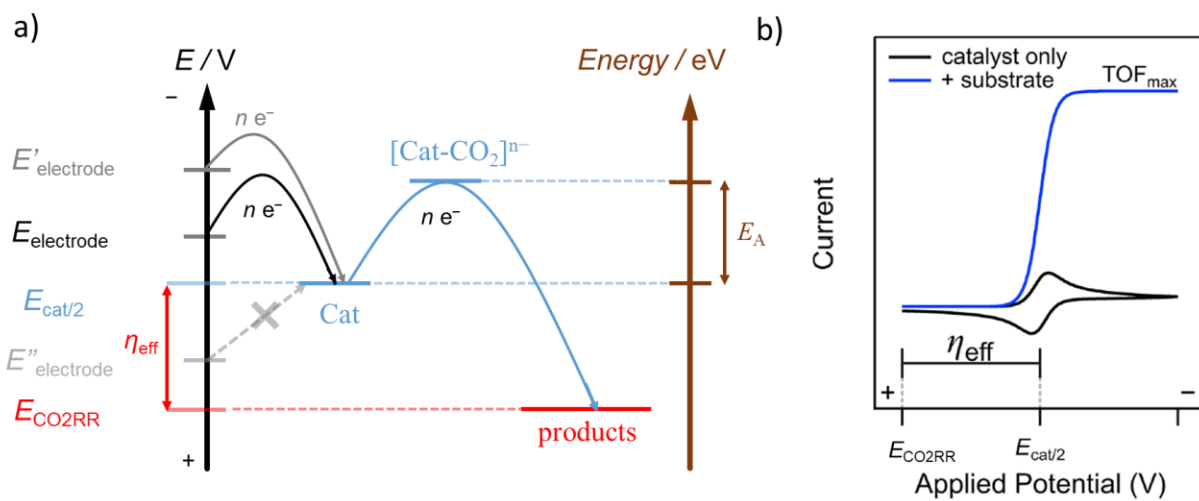
Figure 1.4 a) Schematic representation of electron transfer in the process of electrocatalytic CO_2RR by homogenous molecular catalysts; b) Cyclic voltammograms of electrocatalytic CO_2RR by homogenous molecular catalysts in the presence (blue curve) and absence (black curve) of the substrate CO_2, adapted with permission from *Acc. Chem. Res.* **2020**, 53, 5, 1056–1065.[32] Copyright © 2020, American Chemical Society.

1.3.3 The Typical Scaling Relationship for Molecular Catalysts

Based on the definition and discussion of the homogenous CO_2RR by molecular catalysts above, the kinetic reactivity (TOF_{max}) and the effective overpotential (η_{eff}) for the CO_2RR can be determined from electrochemical measurements for different molecular catalysts. Analyzing the correlations between TOF_{max} and η_{eff} for variable molecular catalysts with different structural features allows us to derive structure/activity relationships of molecular catalysts for the CO_2RR. Understanding such relationships is essential for developing more efficient next-generation molecular catalysts.

Ideally, the most efficient molecular catalyst refers to the one that can reduce CO_2 with the highest TOF_{max} but at the lowest η_{eff} (Figure 1.5a).[32, 40] However, in most practical cases of electrocatalytic reactions by molecular catalysts, such as H_2 evolution,[41-43] O_2 reduction,[44] and CO_2 reduction,[45-47] beneficial decreases in η_{eff} is typically correlated to detrimental decreases in TOF_{max}. This general trend is referred to as the "*molecular scaling relationship*" (Figure 1.5a).[32] The main reason for the "*molecular scaling relationship*" is that both the kinetic reactivity (TOF_{max}) and the effective overpotential (η_{eff}) scale with a catalyst's metal site nucleophilicity (Figure 1.5b). [48-49] For typical molecular catalysts, CO_2 coordination and reduction immediately follows a metal reduction event. Therefore, the activity of the catalyst is correlated to the ability of the reduced metal center to coordinate and activate CO_2.[48-49] Modifying the molecular catalyst's structure can shift the redox potential $E_{cat/2}$ of the metal center positive to $E_{cat/2}$', decreasing the effective overpotential (η_{eff}') for the CO_2RR (Figure 1.6a), however, the more positive $E_{cat/2}$' leads to a decrease in the nucleophilicity of the metal site, thus limiting the complex's ability to coordinate and activate CO_2 with higher kinetic activation energy E_A' for the catalytic process (Figure 1.6a). [50-52] As a result, although the corresponding catalytic onset is observed at the lower

effective overpotential η_{eff}', the maximum plateau current and activity (TOF_{max}') is decreased in the catalytic CV (Figure 1.6b), showing the typical "*molecular scaling relationship*".

Nevertheless, elucidating the correlation between thermodynamic η_{eff} and kinetic TOF_{max} for molecular catalysts is complicated because many experimental factors in practical scenarios influence these two catalytic metrics[32]. For instance, η_{eff} varies with the change of either $E_{cat/2}$ or E_{CO2RR}. E_{CO2RR} varies greatly in different solvents with different buffer pK_a of added electrolyte and proton sources.[53-54] In addition, molecular catalysts made of different metal centers (early or late transition metals)[37] and different ligand scaffolds (porphyrin, phthalocyanine, bi-pyridine, pyridyldiimine, etc.)[35, 39, 55-56] also show dramatically varying electronic structure and catalytic ability, leading to a large change in the kinetic parameter TOF_{max}. Despite of these issues, several emerging studies have been reported in the last few years, attempting to identify multiple effects on the scaling relationship for molecular catalysts[40, 44, 57] and figure out useful strategies of breaking the typical scaling relationship to design more efficient molecular catalysts.[40-41, 44, 58-67]
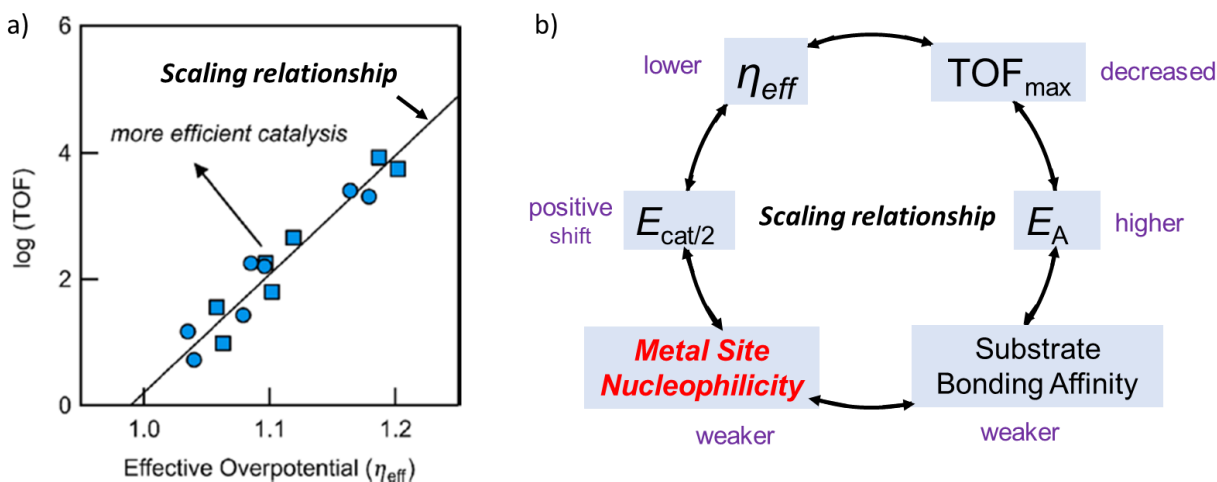
Figure 1.5 a) The "scaling relationship" between TOF and η_{eff} for molecular catalysts, adapted with permission from *J. Am. Chem. Soc.* **2017**, *139*, 11000-11003. http://dx.doi.org/10.1021/jacs.7b05642;[40] Copyright © 2017 American Chemical Society, further permissions related to the material excerpted should be directed to the ACS. b) thermodynamic parameters (η_{eff} and $E_{cat/2}$) and kinetic parameters (E_A and TOF_{max}) scale up with the metal site nucleophilicity to bond and activate CO_2 molecules.
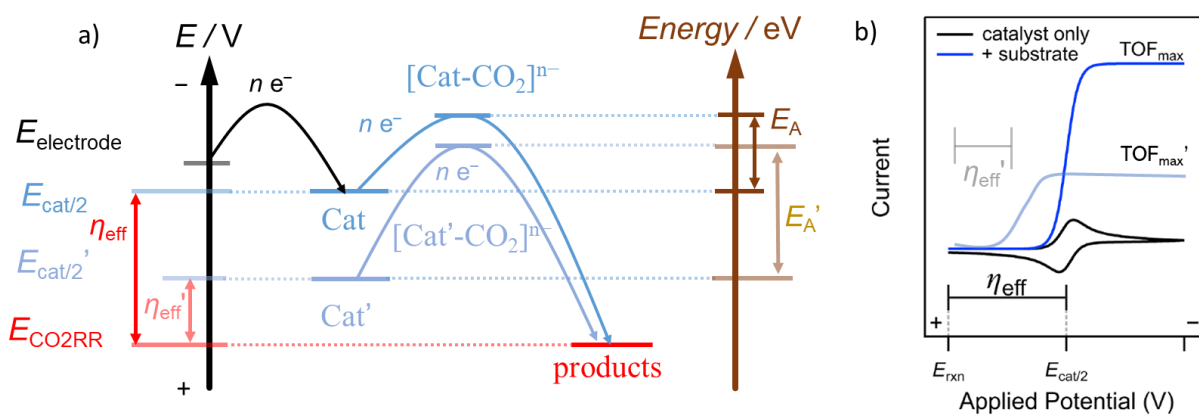
Figure 1.6 a) Positive shift of $E_{cat/2}$ leads to the decrease in η_{eff} but the increase in E_A; b) Positive shift of $E_{cat/2}$ results in the smaller η_{eff}' but lower plateaued TOF_{max}' corresponding to the "scaling relationship" for molecular catalysts, adapted with permission from *Acc. Chem. Res.* **2020**, 53, 5, 1056–1065.[32] Copyright © 2020, American Chemical Society.

13

1.4 Strategies for Breaking the Scaling Relationship for Molecular Catalysts

Due to several sophisticated benchmarking theories and electrochemical analytic methods for the homogenous electrocatalysis proposed and developed in the last few years,[11, 68-73] there have been more and more investigations and discussions regarding the structure-and-activity relationships for the reported molecular catalysts.[32, 47-48, 56-57, 74] People have recognized that the typical scaling relationship for molecular catalysts—the trade-off between η_{eff} and TOF_{max}—becomes one of the main obstacles for designing and developing more efficient molecular catalysts for futural practical applications. For typical molecular catalysts where catalytic onset for the CO_2RR is preceded by the reduction of the metal center, the activity of the catalyst is correlated with the ability of the metal center to coordinate CO_2 to form the intermediate (Figure 1.5b).[48-49] The metal center's ability of binding CO_2 is weakened as a result of shifting the redox potential of the molecular catalyst ($E_{cat/2}$) positive (thus lower η_{eff}).[48-49] However, if the CO_2-adduct intermediate can be effectively stabilized through some substituent effects introduced into the catalysts structure, it could be possible to maintain or even enhance the catalytic activity for the CO_2RR at lower overpotentials, overcoming the detrimental effect of decreased nucleophilicity of the metal center on the catalytic activity. Over the past several years, three strategies have been applied frequently to help stabilize CO_2-adduct intermediates and facilitate catalytic reaction for molecular catalysts (Figure 1.7), which provide great opportunity to break the typical scaling relationship and develop more efficient molecular catalysts for the CO_2RR.[40-41, 44, 58-67] In the following sections, more details will be introduced and discussed for each of these three strategies reported in the recent literatures.
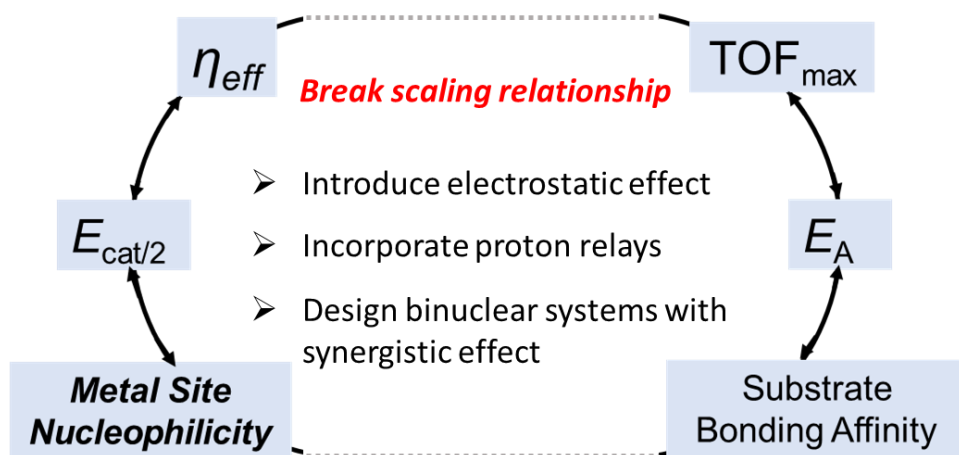
Figure 1.7 Three strategies for breaking the scaling relationship for molecular catalysts.

1.4.1 Introduce the Intramolecular Electrostatic Effect into the Structure of Metal Complexes

Modifying structures of molecular catalysts by incorporating inductive effects into the ligand scaffold does not generally break molecular scaling relationships between η_{eff} and TOF_{max}. This is because for most molecular catalysts, incorporating electron withdrawing functional groups into the structure, which leads to positive shifts in the redox potential and decreased η_{eff}, decreases the nucleophilicity of the metal and thus decreases TOF_{max}. For example, in the case of the CO_2RR by a series of Fe(TPP) complexes modified with pentaflurophenyl groups (Figure 1.8, FeTPP, FeF5TPP, FeF10TPP and FeF20TPP), incorporating more electron-withdrawing pentaflurophenyl groups into the structure leads to a beneficial decrease in E^0_{cat} (thus lower η_{eff}) but a detrimental decrease in TOF_{max}.[47] However, when charged trimethylanilinium (TMA) groups are incorporated into the FeTPP structure, notable deviations from the typical molecular scaling relationships are observed for Fe-*p*-TMA and Fe-*o*-TMA (Figure 1.8).[65] Fe-*p*-TMA with four positively charged TMA groups at the *para* positions of TPP phenyl rings shows more than one order of magnitude higher activity (log(TOF)) for the CO_2RR compared to FeF10TPP at the same overpotential η (Figure 1.8).[65] This increase in CO_2RR activity of Fe-*p*-TMA is attributed to the through-space Coulombic stabilization of the reduced Fe-CO_2 adduct structure by the positively-charged TMA groups.[65] We refer to this stabilization as an *intramolecular electrostatic effect.* In contrast, for Fe-*p*-PSULF with four sulfonate groups at the *para* positions of TPP phenyl rings, a negative deviation from the molecular scaling relationship is exhibited, due to the Coloumbic destabilization of the CO_2-adduct intermediate by the negative charge of sulfonate groups.[65] Moreover, moving the four positively charged trimethylanilinuim groups to the *ortho* position of TPP phenyl rings results in the most efficient catalyst, Fe-*o*-TMA (Figure 1.8). The additional

increased CO₂RR activity of Fe-*o*-TMA compared to Fe-*p*-TMA is most likely due to the closer

proximity of positive charge to the Fe center, enhancing the stabilization of Fe-CO₂ adduct via the

intramolecular electrostatic effect.[65]
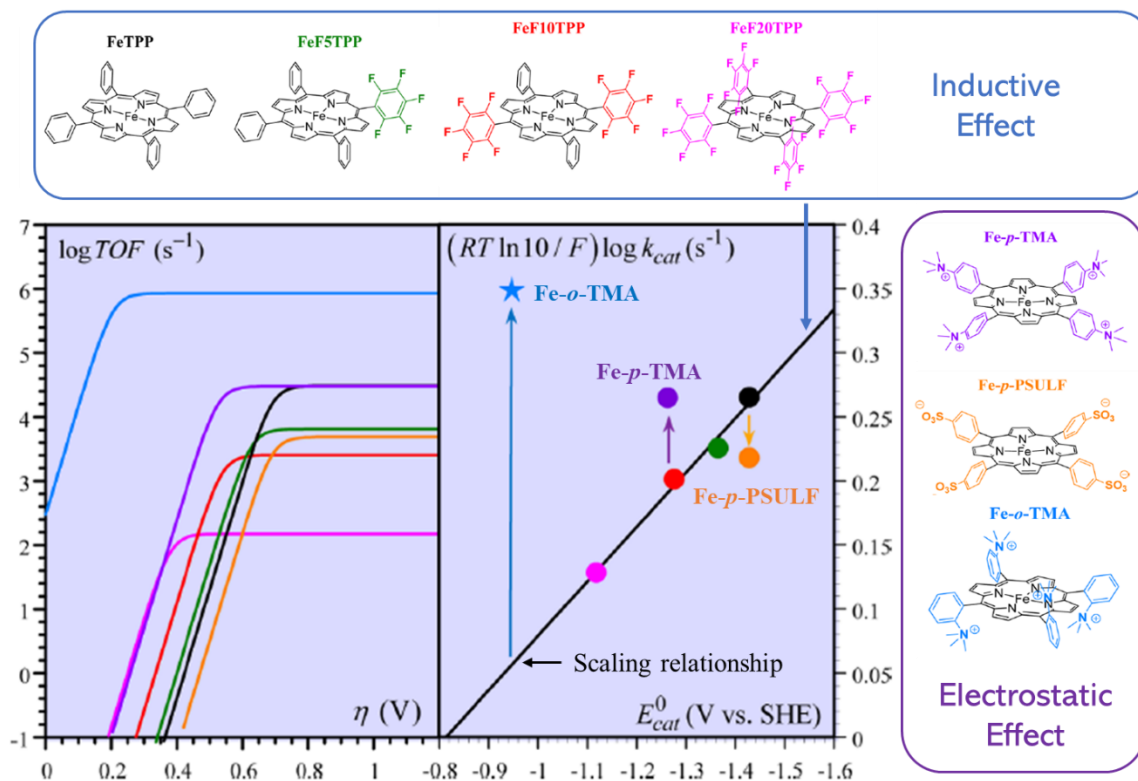
Figure 1.8 (Left) Tafel plots of log TOF vs. *η* and (Right) correlation between TOF_max = *k*_cat and redox potentials of the catalysts *E*_cat⁰ for iron tetraphenylporphyrin (TPP) complexes: FeTPP (black), FeF5TPP (green), FeF10TPP (red) and FeF20TPP (magenta) modified through inductive effect showing typical scaling relationship; Fe-*p*-TMA (purple), Fe-*p*-PSULF (oringe), Fe-*o*-TMA (blue) modified through electrostatic effect showing deviation from the typical scaling relationship. Adapted with permission from *J. Am. Chem. Soc.* **2016**, 138, 51, 16639–16644.[65] Copyright © 2016, American Chemical Society.

Different from the approach of integrating charged functional groups into the catalyst structure, the intramolecular electrostatic effect can also be installed by incorporating a series of alkali and alkaline cations (Figure 1.9a, $M_2 = Na^+$, K^+, Ca^{2+}, Sr^{2+} and Ba^{2+}) into a crown-like cavity appended to the transition metal ($M_1 = Co^{2+}$, Ni^{2+}, Fe^{2+} and Mn^{2+}) Schiff base complexes (Figure 1.9a).[75-78] These redox inactive cations M_2 can tune the redox potential of redox active M_1 sites effectively. In the case of Co(salen) derivatives (salen = N,N'-bis(salicylidene)ethylenediamine), the $Co^{2+/+}$ redox potential positively shifts in such dicationic $[M_1M_2]^{n+}$ structures with the extent of potential shift correlated with the ionic size and Lewis acidity of M_2 (Figure 1.9a).[78] Similar correlations are observed for Ni, Fe and Mn-salen-M_2 complexes.[75-77] According to the results of electronic absorption, infrared spectra and DFT calculations of these complexes, it is found that the incorporated redox inactive cations M_2 have a negligible influence on the molecular orbitals' order of transition metal centers M_1 in the structure, suggesting that the shift of redox potential of M_1 is primarily due to the effect of the electrostatic field exerted by the redox inactive M_2 cations rather than the inductive effect of M_2 cations on the electronic structure of metal complexes.[75-78]

Although these dicationic complexes above was not reported for the catalytic CO_2RR, the applications of M_1-salen-M_2 structures for other molecular catalytic reactions confirm the validity of the strategy of introducing intramolecular electrostatic effect to break the scaling relationship for molecular catalysts[76-77]. For instance, in the case of a Mn^VN Schiff-base complex A where one electron oxidation of the structure leads to bimolecular coupling to generate N_2 (Figure 1.9b), incorporating redox inactive alkali and alkaline cations into the structures (Figure 1.9b 1Na, 1K, 1Ba and 1Sr) shows an inverse linear scaling relationship between reaction rate (k_2) and the redox potential of Mn sites ($E_{1/2}$ ($Mn^{VI/V}$)) (Figure 1.9b), which diametrically opposed to the result observed when Mn^VN Schiff-base complexes were modulated by ligand modification through

inductive effects.[77] In addition, Fe(salen) complexes with redox-inactive cations incorporated also show the promotion in catalytic activity for aerobic C-H oxidation at mild potentials, overcoming the typical scaling relationship for molecular catalysts.[76]
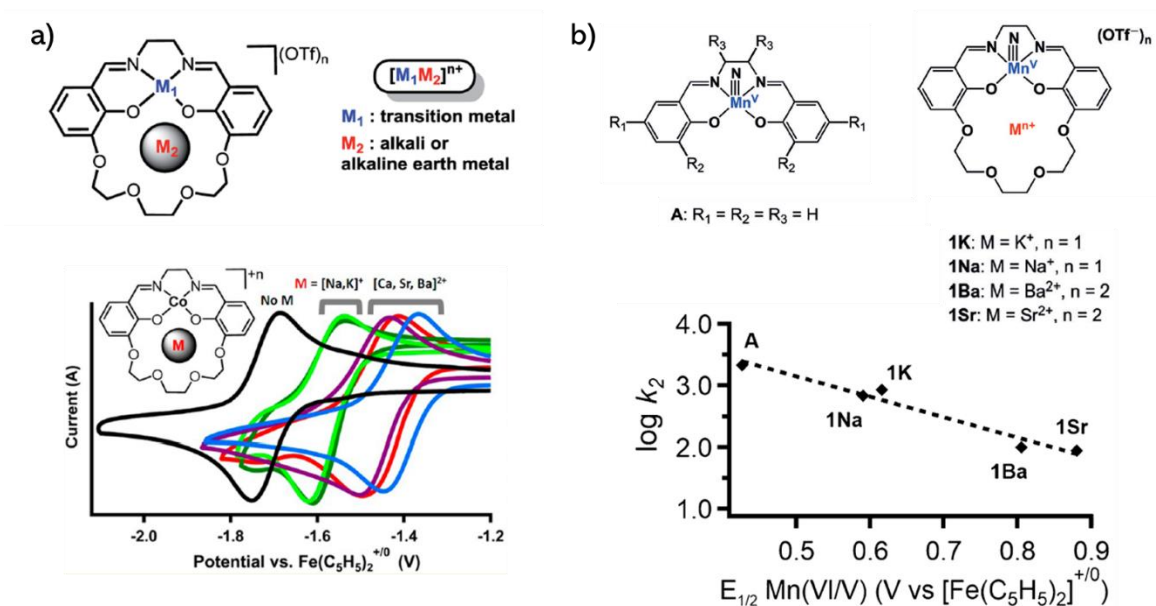
Figure 1.9 a) Top: the structures of a series of transition metal Schiff-base complexes with alkali and alkaline cations incorporated in the crown-like cavity appended to the ligand, Adapted with permission from *Chem. Sci.*, **2019**, 10, 10135,[75] Published by The Royal Society of Chemistry and *Inorg. Chem.* **2017**, 56, 6, 3713–3718[78], Copyright © 2017, American Chemical Society; Bottom: schematic CVs showing the potential shift of $Co^{2+/+}$ redox potential correlated with the ionic size and Lewis acidity of M_2 for Co(salen) complexes; b) Top: the structures of Mn^VN Schiff-base complex **A** and modified dicationic complexes with redox inactive cations incorporated **1Na**, **1K**, **1Ba** and **1Sr**; Bottom: an inverse linear scaling relationship between reaction rate (k_2) and the redox potential of Mn sites ($E_{1/2}$ ($Mn^{VI/V}$)) for **A**, **1Na**, **1K**, **1Ba** and **1Sr**. Adapted with permission from *Angew.Chem.Int.Ed.* **2018**, 57,14037 –14042 [77], © 2018 Wiley-VCH Verlag GmbH & Co. KGaA, Weinheim.

1.4.2 Incorporate Proton Relays into the Secondary Coordination Sphere of Metal Complexes

Compared to the artificial molecular catalysts, biological structures designed by the nature, such as carbon monoxide dehydrogenase (Ni, Fe-CODHases, Figure 1.10), show greater capability of interconverting CO_2 to CO with higher activity but near the thermodynamic CO_2RR potential.[79] Detailed analysis of Ni, Fe-CODHases structure reveals that the secondary coordination environment around the active Ni-Fe cluster plays a crucial role in its catalytic CO_2 reduction.[79] The protonated imidazolium and amine groups from histidine and lysine protein residues not only stabilize CO_2-adduct intermediates through the H-bonding network, but also facilitate protonation and C-O bond cleavage of CO_2-adduct via proton transfer by proton relays in the structure (Figure 1.10).[79] This consequently leads to the lower energy barrier E_A of converting CO_2-adduct intermediates to the final products, and thus the increased activity at lower overpotentials for the CO_2RR. Inspired by the delicate design of nature-made Ni, Fe-CODHases, decorating the secondary coordination sphere of metal complexes by incorporating proton relays have been thought as a promising strategy for breaking the scaling relationship for molecular catalysts.
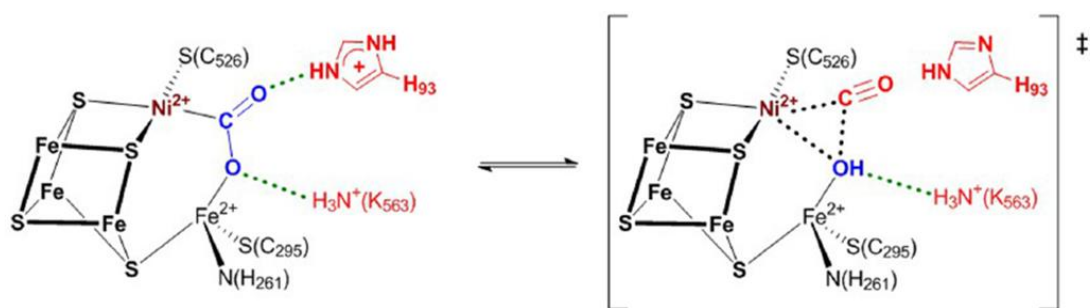
Figure 1.10 Schematic representation of CO_2 activation in the active site of Ni, Fe-CODHases. Adapted with permission from *J. Am. Chem. Soc.* **2019**, 141, 16, 6569–6582,[80] Copyright © 2019, American Chemical Society.

1.4.2.1 Incorporate Acidic Proton Donors to Increase the Local Proton Concentration Proximate to the Catalytic Active Site.

To mimic the protonic secondary coordination environment in Ni, Fe-CODHases, acidic phenolic hydroxyl groups were incorporated in *ortho* and *ortho'* sites of TPP phenyl groups of the FeTPP complex, which considerably accelerates the catalytic CO_2 reduction to CO at a lower overpotential by the FeTDHPP complex compared to FeTPP (Figure 1.11).[66] According to the comparison with a series of reported molecular catalysts for the CO_2RR (in the table in Figure 1.11), it is found that FeTDHPP is the most efficient one, showing the highest TOF value at the lowest overpotential (the star sign in the plot of log(TOF) vs. η in Figure 1.11).[66] Compared to the analog FeTDMPP complex with less acidic -OMe group instead of the -OH group in the TPP phenyl rings, FeTDHPP reaches the equivalent activity but at > 0.5 V lower overpotential for the CO_2RR (Figure 1.11).[66] Considering the intrinsic catalytic turnover frequency TOF_0 at $\eta = 0$ V, FeTDHPP shows ~1 billion times higher intrinsic activity than FeTDMPP, which highlights the crucial role of the phenolic protons in the FeTDHPP structure in boosting the catalytic ability for the CO_2RR.[66] It is proposed that the enhanced catalytic activity of FeTDHPP is probably due to the increased local proton concentration associated with the proximate phenolic hydroxyl moieties, which is supported by the control experiment of the FeTPP complex showing the equivalent activity but with estimated much higher phenol concentration (150 M) in DMF.[66]
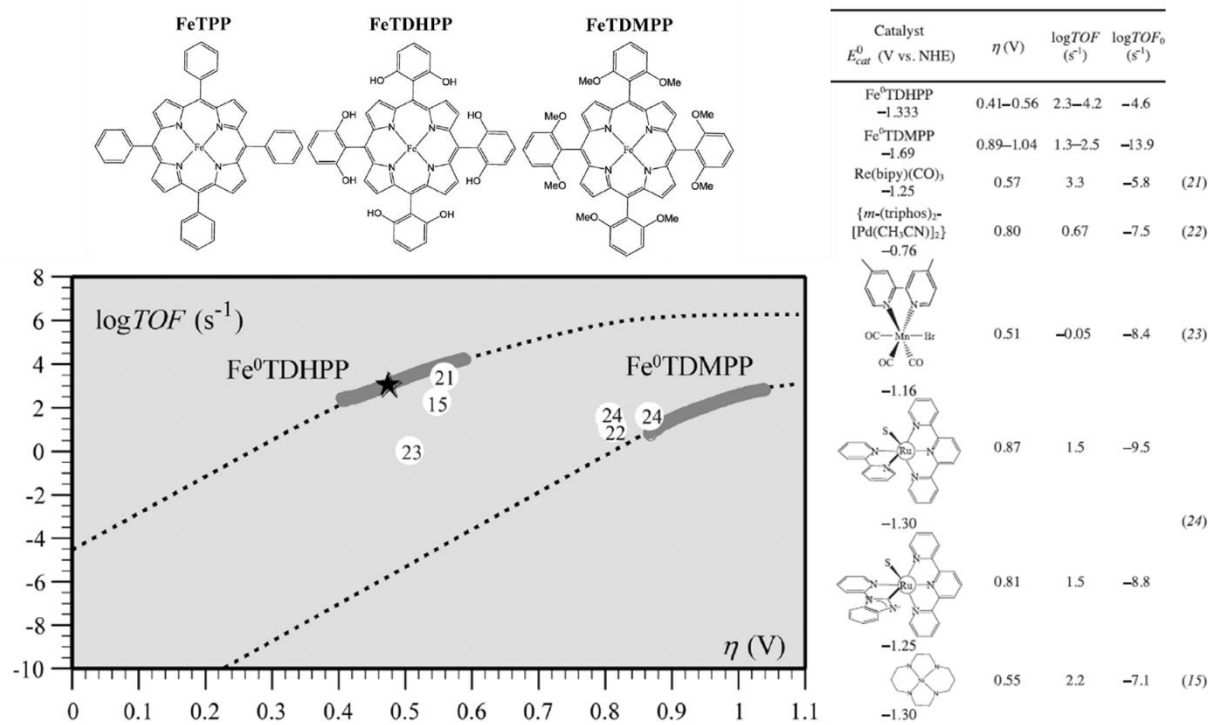
Figure 1.11 Correlation between turnover frequency logTOF and overpotential η for FeTPP, FeTDHPP, FeTDMPP and a series of cited catalysts for comparison listed in the table. Thick gray segments represent TOF values calculated from Foot-of-the-wave analysis of catalytic CVs of FeTDHPP and FeTDMPP in DMF with 2.0 M H_2O. Dashed lines show the Tafel plots for FeTDHPP and FeTDMPP in DMF with 2.0 M H_2O respectively. The star represents the (TOF, η) data point of FeTDHPP and circled numbers represent (TOF, η) data points of cited catalysts from preparative-scale experiments. Adapted with permission from *Science* **2012**, *338*, 90-94 [66], Copyright © 2012, American Association for the Advancement of Science

The similar optimization of catalytic ability was observed in the study of the CO_2RR by a series of iron hangman porphyrin complexes bearing arenesulfonic acid (HPDFe-3SA), guanidyl (HPDFe-Gnd) and phenolic (HPDFe-PhOH) hanging groups in the secondary coordination sphere (Figure 1.12a).[58] HPDFe-PhOH shows both higher activity and lower overpotential for the CO_2RR compared to HPDFe-Gnd, which is due to the lower pK_a of the hydroxyl group with better intramolecular hydrogen-bonding and proton-donating capability to increase the proton concentration proximate to the active Fe site. However, HPDFe-3SA with more acidic arenesulfonic acid ($pK_a = \sim 3$ in DMF) displays lower activity than HPDFe-PhOH ($pK_a = \sim 18$ in DMF) (Figure 1.12a). This is because arenesulfonic acid group is deprotonated in DMF electrolyte and the Coulombic repulsion between the negatively charged porphyrin ring and the deprotonated sulfonate group hinders the effective H-bonding interaction in the secondary coordination sphere to facilitate CO_2 reduction.[58] In another example, MnBr(6-(2-hydroxyphenol)-2.2'-bipyridine)$(CO)_3$ ((MnBr(HOPh-bpy)$(CO)_3$) with an acidic phenolic group in close proximity to the Mn center shows seven times higher activity and lower overpotential for the CO_2RR compared to MnBr(2.2'-bipyridine)$(CO)_3$ ((MnBr(bpy)$(CO)_3$). The enhancement of catalytic ability is due to the facilitated proton-assisted C-O bond cleavage of the CO_2-adduct intermediate by the increased acidic phenolic proton concentration proximate to the Mn center.[81] However, increasing the acidity of proton donors in the secondary coordination sphere does not always lead to more efficient catalysts for the CO_2RR. MnBr(F-HOPh-bpy)$(CO)_3$ with more acidic fluoro-phenolic groups in the structure (Figure 1.12b) exhibits decreased partial catalytic current and worse selectivity for the CO_2 reduction compared to (MnBr(HOPh-bpy)$(CO)_3$ discussed before.[82] Spectro-electrochemistry and DFT studies suggest that Mn(I) hydride is generated more easily for MnBr(F-

HOPh-bpy)(CO)$_3$ with more acidic phenolic proton proximate to the Mn center compared to (MnBr(HOPh-bpy)(CO)$_3$, leading to competing H$_2$ production at the expense of CO$_2$ reduction.[82]
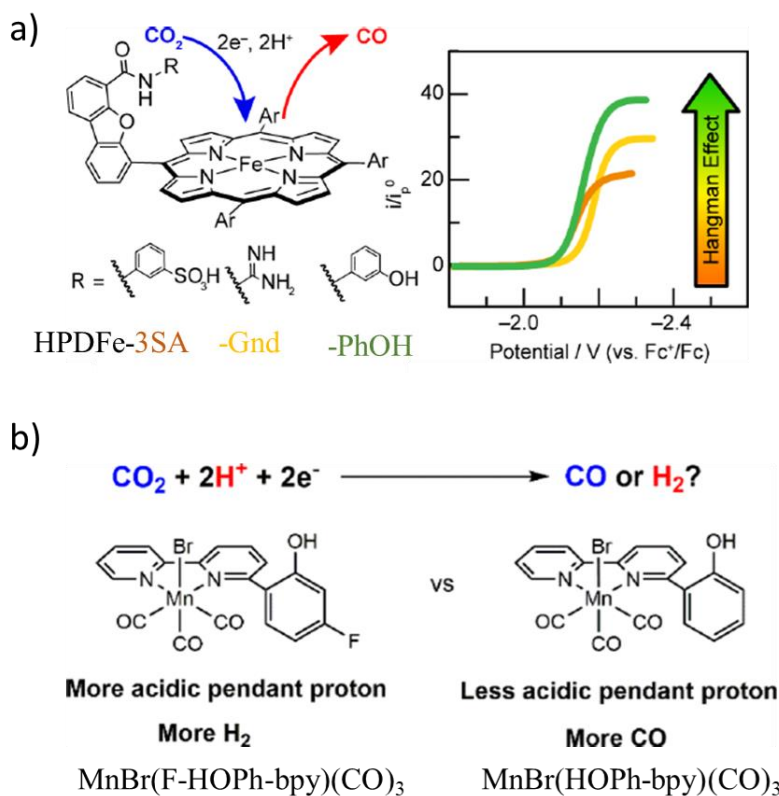
Figure 1.12 a) The structure of HPDFe-3SA, HPDFe-Gnd and HPDFe-PhOH with their corresponding catalytic current for the CO$_2$RR, adapted with permission from *Organometallics* **2019**, 38, 6, 1219–1223 [58], Copyright © 2019, American Chemical Society; b) Schematic comparison of catalytic performance between MnBr(F-HOPh-bpy)(CO)$_3$ with more acidic pendant proton and MnBr(2.2'-bipyridine)(CO)$_3$ with less acidic pendant proton, adapted with permission from *Organometallics* **2020**, 39, 13, 2425–2437 [82], Copyright © 2020, American Chemical Society.

1.4.2.2 Incorporate Less Acidic Proton Relay Groups to Enhance H-bonding Interaction In the Secondary Coordination Sphere.

Besides phenolic hydroxyl groups, less acidic proton relays such as methoxy[83-84], amine[59, 61, 63-64, 85-86], amide[59-60], imidazolium[62, 80], urea[59] and thiourea[87] groups have been used as well to decorate the secondary coordination sphere to tune the catalytic activity for the CO_2RR. Instead of protonating the CO_2-adduct directly, these less acidic proton relay groups stabilize the intermediate through the H-bonding network established among CO_2-adduct, external proton sources and the proton relays in ligand scaffolds, facilitating protonation and C-O bond cleavage via proton transfer from external proton sources to the CO_2 adduct.[59-61, 63-64, 83-88]

For example, the Mn bipyridyl tricarbonyl complex *fac*-$Mn^I([(MeO)_2Ph]_2bpy)(CO)_3(CH_3CN)(OTf)$ with four pendant methoxy groups in the ligand 6,6′-bis(2,6-dimethoxyphenyl)-2,2′-bipyridine ($[(MeO)_2Ph]_2bpy$) (Figure 1.13a) shows a respectable catalytic activity with high product selectivity for CO production through a *protonation-first* pathway, which is at > 0.55 V lower overpotential compared to the thermodynamically demanding *reductive-first* pathway (Figure 1.13a).[84] The electro-spectroscopic studies and DFT analysis suggest that H-bonding interactions among pendant -OMe groups, external Brønsted acid and Mn-CO_2 adduct dramatically decrease the energy barrier for protonation and C-O bond cleavage of the Mn-carboxylic intermediate, leading to the *protonation-first* pathway at the lower overpotential.[84] Another example of enhancing catalytic activity by introducing proton relays in the secondary coordination sphere was observed for a series of $[CpCo(P^R_2N^{R'}_2)I]^+$ complexes containing two pendant amine residues in $P^R_2N^{R'}_2$ ligand (Figure 1.13b).[63] In particular, the complex **4** (Figure 1.13b) with the most electronic-donating phosphine ligand and the most basic amine moieties shows the highest activity with TOF >1000 s^{-1} for the selective CO_2 reduction to formic acid,

ranking itself among the most active CO_2-to-formic acid reducing molecular catalysts to date. Subsequent mechanistic studies and DFT calculations confirm that the pendant amine groups in the secondary coordination sphere of these $[CpCo(P^R_2N^{R'}_2)I]^+$ complexes play a crucial role in stabilizing CO_2-adduct intermediates through H-bonding interactions with the proton source H_2O and facilitating the hydride transfer from the Co site to the CO_2 molecule to generate the final product (Figure 1.13b).[63]

Furthermore, decorating secondary coordination sphere of molecular catalysts with proton relays can not only enhance the catalytic activity for the CO_2RR, but also modulate the selectivity for different products according to variable types of pendant groups. For example, ligand-controlled product selectivity for the CO_2RR was observed for a series of Mn complexes with modified bipyridine or phenanthroline ligands (Figure 1.13c).[85-86] It is found that Mn complexes with -OH and -Me as pendant proton relay groups in the secondary coordination sphere only reduce CO_2 to CO with lower $TOF_{max} \sim 860$ s^{-1} while Mn complexes with tertiary amines -NEt_2 positioned proximate to the metal center reduce CO_2 to formic acid with higher $TOF_{max} \sim 5500$ s^{-1} at even 300 mV lower overpotential than -OH and -Me analogs.[85] Such increased activity and altered selectivity of the CO_2 reduction to formic acid was found to arise from *in situ* protonated amine groups in the secondary coordination sphere, aiding in the formation of Mn-hydride intermediates for the selective production of formic acid.[85-86] This is supported by the infrared spectroelectrochemistry and DFT analysis of these complexes.[85-86] The similar phenomenon was also observed for a family of polypyridyl-iron $[(bpy^RPY2Me)Fe^{II}]$ complexes which can achieve varying selectivity for CO_2RR or HER by changing different pendant proton relay groups with varying acidities (-H, -OH, -OMe AND -NHEt) proximate to the active Fe center (Figure 1.13d).[88]

Figure 1.13 a) *fac*-Mn^I([(MeO)$_2$Ph]$_2$bpy)(CO)$_3$(CH$_3$CN)(OTf) with four pendant methoxy groups establishes an allosteric H-bonding network among pendant -OMe groups, external Brønsted acid and Mn-CO$_2$ adduct, leading to the *protonation-first* pathway of reducing CO$_2$ at lower overpotentials, adapted with permission from *J. Am. Chem. Soc.* **2017**, 139, 7, 2604–2618 [84], Copyright © 2017, American Chemical Society; b) a series of [CpCo(P$^R_2$N$^{R'}_2$)I]$^+$ complexes containing two pendant amine residues in P$^R_2$N$^{R'}_2$ ligand show increased activity for selective CO$_2$ reduction to formic acid by facilitating the hydride transfer from the Co site to the CO$_2$ molecule through H-bonding interactions with the proton source H$_2$O, adapted with permission from *J. Am. Chem. Soc.* **2017**, 139, 10, 3685–3696 [63], Copyright © 2017, American Chemical Society; c) The ligand-controlled product selectivity for the CO$_2$RR by a series of Mn complexes with modified bipyridine or phenanthroline ligands with different pendant proton relay groups in the secondary coordination sphere; adapted with permission from *J. Am. Chem. Soc.* **2020**, 142, 9, 4265–4275 [85], Copyright © 2020, American Chemical Society; d) A family of polypyridyl-iron [(bpy^{R}PY2Me)Fe^{II}] complexes show varying selection for CO$_2$RR or HER with different pendant proton relay groups with varying acidities (-H, -OH, -OMe AND -NHEt), adapted with permission from *Inorg. Chem.* **2020**, 59, 7, 5206–5217 [88], Copyright © 2020, American Chemical Society.

Moreover, the correlation between the catalytic activity of molecular catalysts and the number of proton relay groups in the secondary coordination scaffold was ascertained based on the study of a series of Co aminopyridine macrocycle complexes with varying number of secondary (-NH) and tertiary (-NMe) amines in the ligand scaffold (Figure 1.14).[61] The electrochemical and kinetic studies of these Co complexes revealed a linear dependence of catalytic rate on the number of pendant -NH groups in the secondary coordination sphere—higher catalytic rate was observed with more -NH groups in the structure (Figure 1.14b), which is consistent with the DFT results showing more negative CO_2 binding free energy correlated with larger number of -NH groups in the secondary coordination sphere (Figure1.14c). This is because the pendant NH groups facilitate the proton transfer from external proton sources to the CO_2-adduct through a H-bonding network built in the secondary coordination sphere based on their DFT calculations,[64] which is consistent with the previous report showing that the presence of pendant -NH groups in Co aminopyridine macrocycle structures leads to at least two orders of magnitude higher activity and lower overpotentials for the CO_2RR compared to the structure with pendant N-alkyl groups[64].
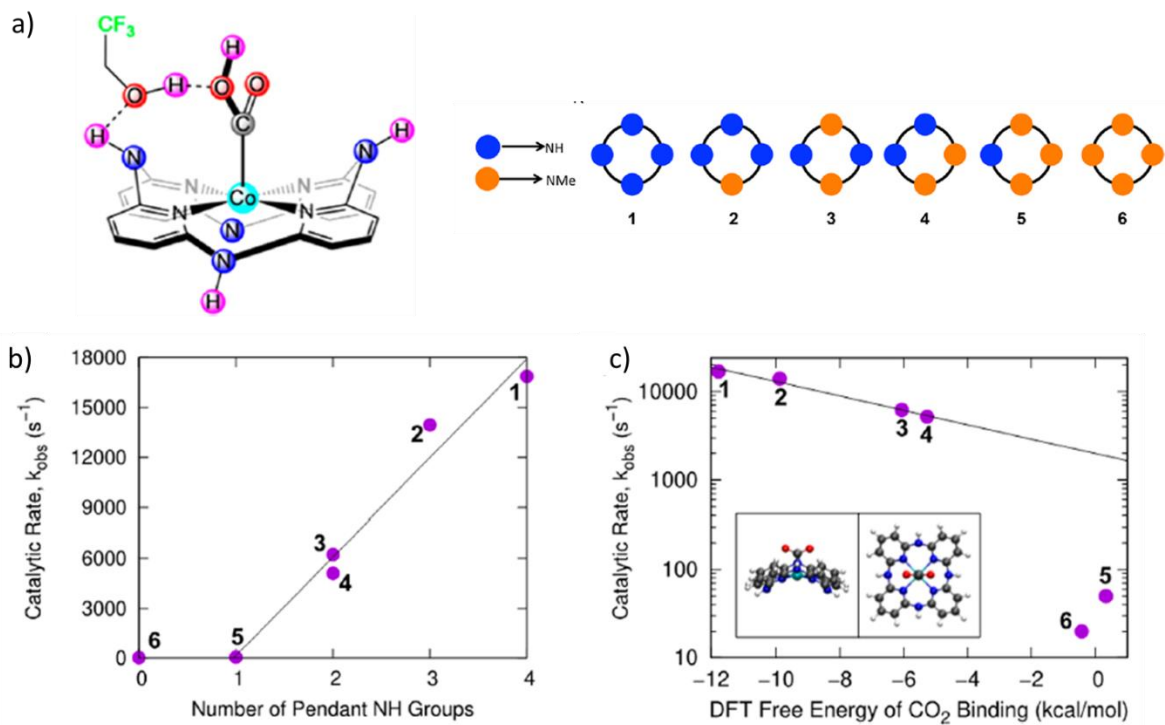
Figure 1.14 a) The structure of Co aminopyridine macrocycle complexes with varying number of NH and NMe groups in the ligand scaffold; b) the correlation between catalytic rate and number of pendant NH group in the secondary coordination sphere; 3) the correlation between catalytic rate and DFT free energy of CO2 binding. Adapted with permission from *ACS Cent. Sci.* 2018, 4, 3, 397–404 https://pubs.acs.org/doi/10.1021/acscentsci.7b00607 [61], Copyright © 2018 American Chemical Society, further permissions related to the material excerpted should be directed to the ACS.

Aimed at increasing proton relay moieties in the secondary coordination sphere, urea groups were incorporated as multipoint H-bonding pillars to decorate the periphery of porphyrin ligand of the iron complex FeTPP, resulting in an iron porphyrin complex FeTPP-Ur (Figure 1.15a) showing incredibly increased TOF for the CO_2RR at a significantly lower overpotential (Figure 1.15b).[59] Compared to the analog FeTPP-Am with amido groups as single-point H-bonding pillars in the structure (Figure 1.15a), FeTPP-Ur is more efficient, showing the equivalently high TOF_{max} but with a remarkable drop in the overpotential, despite that both FeTPP-Ur and FeTPP-Am deviate from the typical scaling relationship built by FeTPP, FeTPPF8 and FeTPPF20 (Figure 1.15b).[59] Besides controlling the number of H-bonding moieties in the secondary coordination sphere, properly positioning the pendant proton relay groups proximate to the active meter center in the structure can also significantly modulate the catalytic ability of molecular catalysts for the CO_2RR. Four Fe-TPP complex derivatives bearing proximal and distal pendant amide groups on the *ortho* and *para* position of the phenyl ring in the core TPP scaffold (Figure 1.15c) were reported to show the departure from the typical scaling relationship between TOF and η built by FeTPP analogs only with electronic inductive effects (Figure 1.15d).[60] Although adjusting the position of proton relays in these Fe complexes does not affect the overpotential for the CO_2RR, Fe-*ortho*-1-amide and Fe-*ortho*-2-amide shows higher turnover frequency than their *para*-amide analogs Fe-*pare*-1-amide and Fe-*pare*-2-amide, due to the more effective through-space H-bonding interactions between the CO_2-adduct and amide groups more proximate to the metal center in the secondary coordination sphere (Figure 1.15c and d). In particular, Fe-*ortho*-2-amide even shows more than two orders of magnitudes higher TOF value than its proximal-amide analog Fe-*ortho*-1-amide (Figure 1.8d), which suggests again the fine

position tuning of second-sphere proton relays as another effective approach of designing more efficient molecular catalysts to break the scaling relationship.[60]
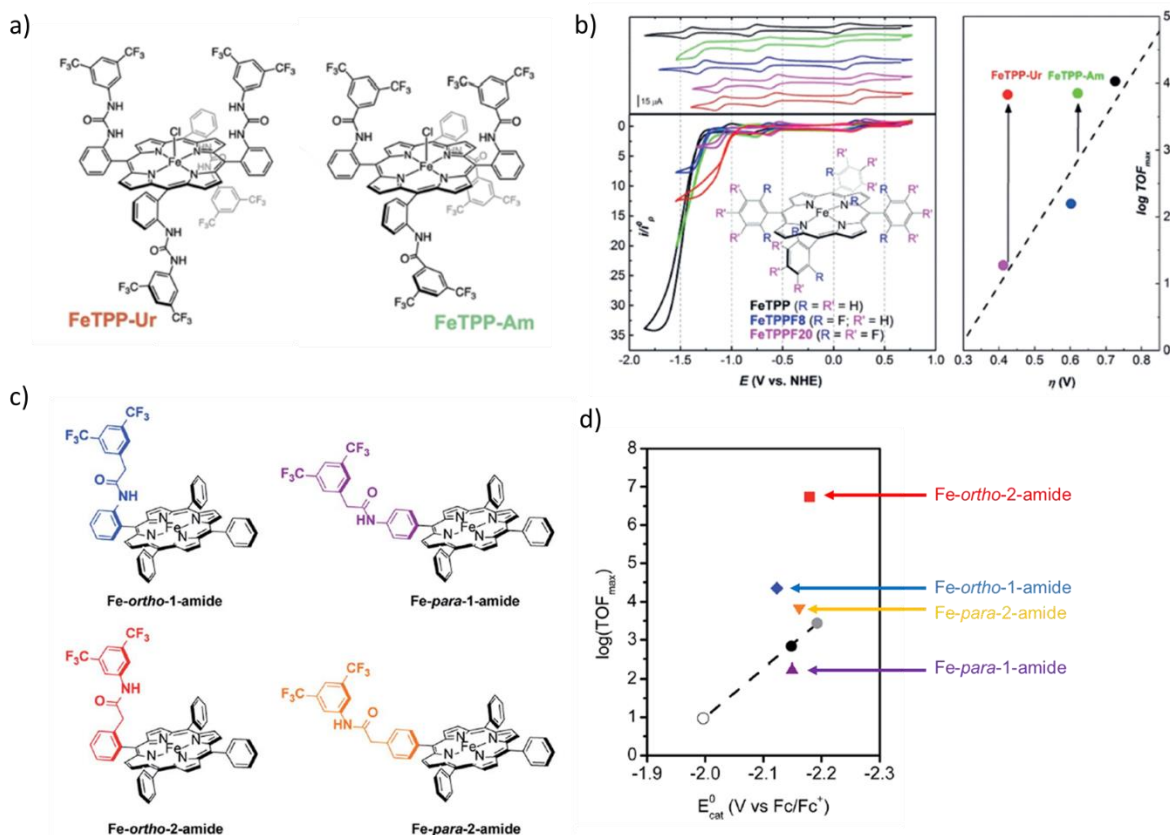
Figure 1.15 a) The structures of FeTPP-Ur and FeTPP-Am; b) Left: CVs of FeTPP-Ur (red) and FeTPP-Am (green) with other FeTPP derivatives in DMF solution with 0.1 M Bu4NPF6 under argon (top left) and under CO2 with 5.5 M water as proton source (bottom left); Right: correlations between logTOF$_{max}$ (from FOWA analysis) and catalytic overpotential η for different FeTPP derivatives, the dash line represents the scaling relationship built by FeTPP derivatives without secondary coordination effects. Adapted with permission from *Angew. Chem. Int. Ed*. **2019**, 58, 4504 –4509[59], © 2019 Wiley-VCH Verlag GmbH & Co. KGaA, Weinheim; c) The structures of positional isomers of amide-functionalized FeTPP complexes; d) Correlations between log(TOFmax) and redox potentials of complexes for Fe-*ortho*-1-amide, Fe-*ortho*-2-amide, Fe-*pare*-1-amide and Fe-*pare*-2-amide, the dash line represents the scaling relationship built by FeTPP derivatives without secondary coordination effects, Adapted with permission from *Chem. Sci.*, **2018**, 9, 2952 [60] - Published by The Royal Society of Chemistry.

1.4.3 Design Binuclear Metal Complexes with Synergistic Coordination Effect

Another important structural feature of Ni, Fe-CODHases leading to the excellent catalytic ability for the CO_2RR is the active binuclear Ni-Fe cluster where the Ni center coordinates with the C atom of CO_2 as an active reducing site while the Fe center interacts with one O atom of CO_2 as a Lewis acid site to assist the protonation and C-O bond cleavage of the intermediate (Figure 1.10)[79]. The structural feature of Ni-Fe cluster offers a promising strategy of designing binuclear molecular catalysts with suitable M-M separation, which can activate CO_2 via synergistic coordination mode to boost catalytic activity for the CO_2RR. Despite rare examples of such binuclear metal complexes reported for this purpose, probably due to the synthetic difficulty, there are a few emerging attempts of designing and studying binuclear metallic complexes with synergistic catalytic effect for the CO_2 reduction.[89-92]

In 2017, a binuclear cobalt cryptate complexes $[Co_2(OH)L^1](ClO_4)_3$ ($CoCoL^1$, L^1 = cryptate ligand) (Figure 1.16a) was reported to display incredibly increased turnover number (TON = 16896) and improved selectivity (Faradaic efficiency, FE = 98%) for the photocatalytic CO_2 reduction to CO, compared to its mononuclear Co analog (CoL^2, TON = 1600 and 85% selectivity) (Figure 1.16a).[89] The boosted activity of $CoCoL^1$ is attributed to the synergistic coordination effect where one Co site binds and reduces CO_2 while the other serves as an assistant Lewis acid site to facilitate protonation and C-O bond cleavage at meantime,[89] mimicking the function of the Ni-Fe cluster for CO_2RR. The synergistic catalysis between two Co sites of $CoCoL^1$ is supported by the kinetic study showing a first-order dependence of CO evolution rate on the concentration of $CoCoL^1$ catalysts, suggesting that only one Co site acts as a reducing site. The further DFT calculation also confirms the formation of the intermediate with one CO_2 molecular trapped by two Co sites in a single $CoCoL^1$ structure.[89]

Given that only one Co site in CoCoL[1] acts as the active site for the reduction with the other as a Lewis acid site, the catalyst is optimized by replacing one of Co sites with a more Lewis acidic Zn, resulting in a heterometallic binuclear CoZnL[1] complex (Figure 1.16a).[90] As expected, although Zn is less photocatalytic active than Co, it shows stronger binding affinity to the O atom, which strengthens the synergistic catalytic cooperation between Co and Zn in the CoZnL[1] complex. As a result, CoZnL[1] complex shows 4 times higher activity than the previous CoCoL[1] complex and 45 times higher activity than the mononuclear CoL[2] analog.[90] The improvement in the activity of CoZnL[1] due to the optimized synergistic catalytic effect is further confirmed by the control experiments of merely adding Zn^{2+} as a Lewis acid to the solution of mononuclear CoL[2] and binuclear CoCoL[1] complexes, none of which shows increased activity for the CO_2 reduction.[90]

Following the same design idea for CoCoL[1] and CoZnL[1] catalysts above, another two examples of binuclear Ni complex $[Ni_2L](ClO_4)_4$ (L = 1,2-bis((5,7-dimethyl-1,4,8,11-tetraazacyclotetradecan-6-yl)methyl)benzene)[91] (Figure 1.16b) and binuclear Co complex $[Co_2biqpy]^{4+}$ (biqpy = 4,4''''-(2,7-di-*tert*-butyl-9,9-dimethyl-9*H*-xanthene-4,5-diyl)[92] (Figure 1.16c) have been reported to show a dramatic increase in the catalyst ability compared to their mononuclear analogs. Despite that there are only a small number of binuclear complexes reported for the CO_2RR so far, most applied for the photocatalysis, which is likely due to the stability issues of binuclear structures on electrode surfaces with potential bias. However, the aforementioned studies provide us with a promising strategy of optimizing catalytic ability of molecular catalysts and breaking the typical scaling relationship by designing binuclear metal complexes with synergistic coordination effect.
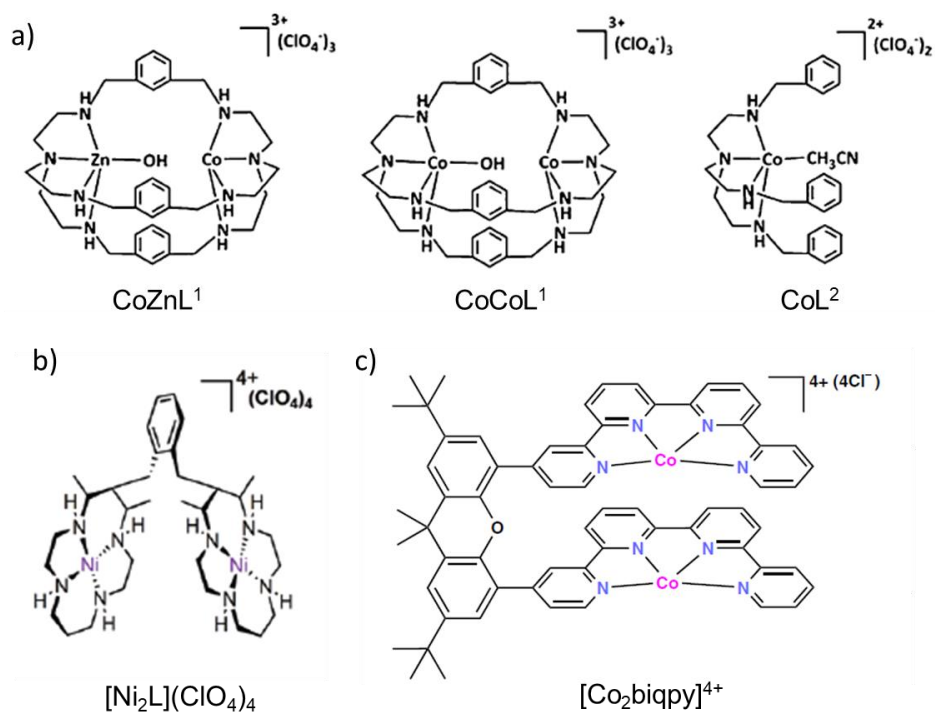
Figure 1.16 a) The structures of CoZnL[1], CoCoL[1] and CoL[2] (L[1], L[2] = cryptate ligands), adapted with permission from *Angew.Chem.Int.Ed*. **2018**, 57 ,16480 –16485 [90], © 2018 Wiley-VCH Verlag GmbH & Co. KGaA, Weinheim; b) The structure of [Ni₂L](ClO₄)₄ (L = 1,2-bis((5,7-dimethyl-1,4,8,11-tetraazacyclotetradecan-6-yl)methyl)benzene), adapted with permission from *Green Chem.*, **2018**, 20, 798-803 [91] with permission from The Royal Society of Chemistry; c) The structure of [Co₂biqpy][4+] (biqpy = 4,4''''-(2,7-di-*tert*-butyl-9,9-dimethyl-9*H*-xanthene-4,5-diyl), adapted with permission from *Nature Catalysis* **2019**, *2*, 801-808 [92], Copyright © 2019, The Author(s), under exclusive licence to Springer Nature Limited.

1.5 Strategies of Breaking the Scaling Relationship for Molecular Catalysts in This Thesis

By carefully analyzing and comparing the reported strategies of breaking the scaling relationship for molecular catalysts in literatures, it is revealed that all designs and optimizations of metal complexes above aspire to the same goal—stabilizing CO_2-adduct intermediates and lowering the kinetic activation energy barrier E_A of converting the intermediate to the final product, which thus results in the increased overall catalytic rate for the CO_2RR (Figure 1.17a). Alternatively, there are rare examples of breaking the scaling relationship through modulating the redox potential of metal centers (Figure 1.17a), because it is very difficult, if not impossible, to disconnect the thermodynamic correlation between the redox potential $E_{cat/2}$ and the nucleophilicity of metal centers. Positively shifting redox potential of the metal center has been theoretically proved to cause its decreased nucleophilicity and thus result in the lower bonding affinity to the substrate.[32, 40, 44, 48-49] Therefore, the only effective way to break the scaling relationship is to minimize the kinetic reaction energy barrier by stabilizing the CO_2-adduct intermediate and facilitating the protonation and bond cleavage through three strategies discussed above. However, all the analysis and strategies are based on one prerequisite that the catalytic onset for the CO_2RR is preceded by a metal-based redox event (Figure 1.17a). What if we were to break this prerequisite?

To answer this question, my work in this thesis focuses on designing molecular catalysts with redox active ligands, in which the catalytic onset is preceded by the formation of ligand radical structure—a ligand-based redox process rather than a metal-based redox event (Figure 1.17b). In this scenario, the affinity of CO_2 bonding is not related to either $E_{cat/2}$ or nucleophilicity of the metal center, instead the initial catalysis onset can be modulated by the redox potential of ligand/ligand-radical couple without changing the oxidation state of the metal center. Tuning the

electronic structure of the ligand can not only shift the ligand-based redox process but also modulate the ability of the ligand to store charge equivalents upon reduction through stabilization of the resulting ligand radical. We postulate that the increased ability to store charge equivalents on the ligand can result in the more positive redox potential for the ligand-based reduction but has a beneficial influence on catalytic activity of molecular catalysts. This unique electronic feature provides us with possibility to break the scaling relationship for molecular catalysts through both thermodynamic and kinetic approaches individually (Figure 1.17b). Therefore, in this thesis, I would present several strategies of adjusting the thermodynamic overpotentials for the CO_2RR by modifying the structural planarity, flexibility and coordination geometry of ligand scaffolds, as well as optimizing the kinetic catalytic activity of catalysts by incorporating variable substitution effects in ligand frameworks to modulate the electronic structure of metal complexes (Figure 1.17b), both of which are aimed to effectively break the scaling relationship and design more efficient molecular catalysts for the CO_2RR.
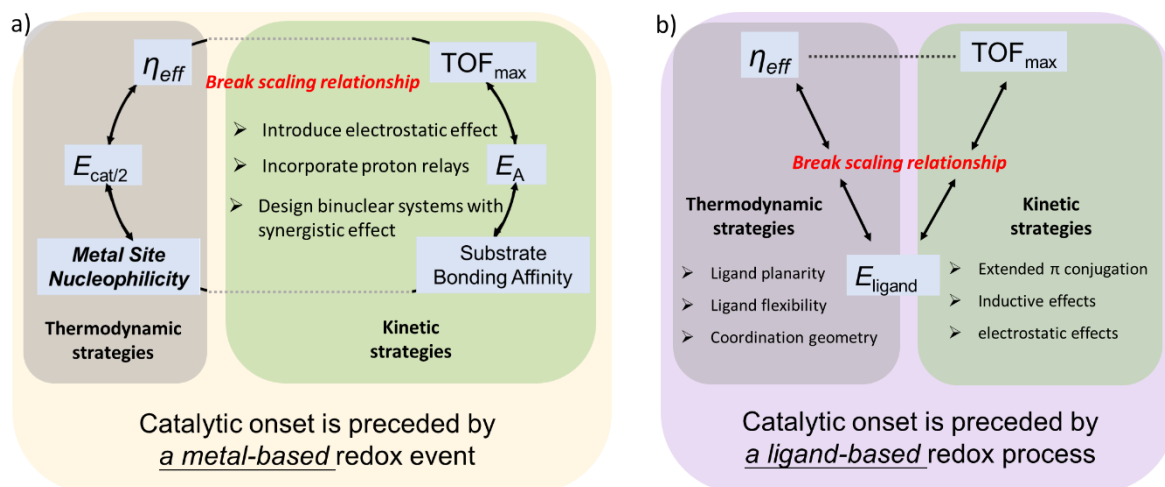
Figure 1.17 a) The reported strategies of breaking the scaling relationship for the molecular catalysts where the catalytic onset is preceded by the metal-based redox event; b) The strategies of breaking the scaling relationship for the molecular catalysts with redox active ligands in this thesis, where the catalytic onset is preceded by the ligand-based redox process.

1.6 Reference

1.   De Luna, P.; Hahn, C.; Higgins, D.; Jaffer, S. A.; Jaramillo, T. F.; Sargent, E. H. "What would it take for renewably powered electrosynthesis to displace petrochemical processes?," *Science* **2019**, *364*, eaav3506. http://dx.doi.org/10.1126/science.aav3506

2.   Birdja, Y. Y.; Pérez-Gallent, E.; Figueiredo, M. C.; Göttle, A. J.; Calle-Vallejo, F.; Koper, M. T. M. "Advances and challenges in understanding the electrocatalytic conversion of carbon dioxide to fuels," *Nature Energy* **2019**, *4*, 732-745. http://dx.doi.org/10.1038/s41560-019-0450-y

3.   Nielsen, D. U.; Hu, X.-M.; Daasbjerg, K.; Skrydstrup, T. "Chemically and electrochemically catalysed conversion of CO2 to CO with follow-up utilization to value-added chemicals," *Nature Catalysis* **2018**, *1*, 244-254. http://dx.doi.org/10.1038/s41929-018-0051-3

4.   Chen, C.; Khosrowabadi Kotyk, J. F.; Sheehan, S. W. "Progress toward Commercial Application of Electrochemical Carbon Dioxide Reduction," *Chem* **2018**, *4*, 2571-2586. http://dx.doi.org/https://doi.org/10.1016/j.chempr.2018.08.019

5.   Appel, A. M.; Bercaw, J. E.; Bocarsly, A. B.; Dobbek, H.; DuBois, D. L.; Dupuis, M.; Ferry, J. G.; Fujita, E.; Hille, R.; Kenis, P. J. A.; Kerfeld, C. A.; Morris, R. H.; Peden, C. H. F.; Portis, A. R.; Ragsdale, S. W.; Rauchfuss, T. B.; Reek, J. N. H.; Seefeldt, L. C.; Thauer, R. K.; Waldrop, G. L. "Frontiers, Opportunities, and Challenges in Biochemical and Chemical Catalysis of CO2 Fixation," *Chemical Reviews* **2013**, *113*, 6621-6658. http://dx.doi.org/10.1021/cr300463y

6.   Leung, C.-F.; Ho, P.-Y. "Molecular Catalysis for Utilizing CO2 in Fuel Electro-Generation and in Chemical Feedstock," *Catalysts* **2019**, *9*, 760. http://dx.doi.org/10.3390/catal9090760

7.   Francke, R.; Schille, B.; Roemelt, M. "Homogeneously Catalyzed Electroreduction of Carbon Dioxide—Methods, Mechanisms, and Catalysts," *Chemical Reviews* **2018**, *118*, 4631-4701. http://dx.doi.org/10.1021/acs.chemrev.7b00459

8.   Qiao, J.; Liu, Y.; Hong, F.; Zhang, J. "A review of catalysts for the electroreduction of carbon dioxide to produce low-carbon fuels," *Chemical Society Reviews* **2014**, *43*, 631-675. http://dx.doi.org/10.1039/C3CS60323G

9.   Schneider, J.; Jia, H.; Muckerman, J. T.; Fujita, E. "Thermodynamics and kinetics of CO2, CO, and H+ binding to the metal centre of CO2reductioncatalysts," *Chemical Society Reviews* **2012**, *41*, 2036-2051. http://dx.doi.org/10.1039/c1cs15278e

10.   Benson, E. E.; Kubiak, C. P.; Sathrum, A. J.; Smieja, J. M. "Electrocatalytic and homogeneous approaches to conversion of CO2 to liquid fuels," *Chemical Society Reviews* **2009**, *38*, 89-99. http://dx.doi.org/10.1039/b804323j

11.   Costentin, C.; Robert, M.; Saveant, J.-M. "Catalysis of the electrochemical reduction of carbon dioxide," *Chemical Society Reviews* **2013**, *42*, 2423-2436. http://dx.doi.org/10.1039/c2cs35360a

12.   Sutin, N.; Creutz, C.; Fujita, E. "Photo-Induced Generation of Dihydrogen and Reduction of Carbon Dioxide Using Transition Metal Complexes," *Comments on Inorganic Chemistry* **1997**, *19*, 67-92. http://dx.doi.org/10.1080/02603599708032729

13.   Li, C. W.; Kanan, M. W. "CO2 Reduction at Low Overpotential on Cu Electrodes Resulting from the Reduction of Thick Cu2O Films," *Journal of the American Chemical Society* **2012**, *134*, 7231-7234. http://dx.doi.org/10.1021/ja3010978

14.   Kuhl, K. P.; Cave, E. R.; Abram, D. N.; Jaramillo, T. F. "New insights into the electrochemical reduction of carbon dioxide on metallic copper surfaces," *Energy & Environmental Science* **2012**, *5*, 7050-7059. http://dx.doi.org/10.1039/C2EE21234J

15.   Hori, Y. "Electrochemical CO2 Reduction on Metal Electrodes," In *Modern Aspects of Electrochemistry*; Vayenas, C. G.; White, R. E.; Gamboa-Aldeco, M. E., Eds.; Springer New York: New York, NY, 2008, p 89-189.

16.   Hatsukade, T.; Kuhl, K. P.; Cave, E. R.; Abram, D. N.; Jaramillo, T. F. "Insights into the electrocatalytic reduction of CO2 on metallic silver surfaces," *Physical Chemistry Chemical Physics* **2014**, *16*, 13814-13819. http://dx.doi.org/10.1039/C4CP00692E

17.   Yoshio, H.; Katsuhei, K.; Shin, S. "PRODUCTION OF CO AND CH4 IN ELECTROCHEMICAL REDUCTION OF CO2 AT METAL ELECTRODES IN AQUEOUS HYDROGENCARBONATE SOLUTION," *Chemistry Letters* **1985**, *14*, 1695-1698. http://dx.doi.org/10.1246/cl.1985.1695

18.   Tafel, J. "Über die Polarisation bei kathodischer Wasserstoffentwicklung," *Zeitschrift für Physikalische Chemie* **1905**, *50U*, 641-712. http://dx.doi.org/https://doi.org/10.1515/zpch-1905-5043

19.   Tang, W.; Peterson, A. A.; Varela, A. S.; Jovanov, Z. P.; Bech, L.; Durand, W. J.; Dahl, S.; Nørskov, J. K.; Chorkendorff, I. "The importance of surface morphology in controlling the selectivity of polycrystalline copper for CO2 electroreduction," *Physical Chemistry Chemical Physics* **2012**, *14*, 76-81. http://dx.doi.org/10.1039/C1CP22700A

20.   Reske, R.; Mistry, H.; Behafarid, F.; Roldan Cuenya, B.; Strasser, P. "Particle Size Effects in the Catalytic Electroreduction of CO2 on Cu Nanoparticles," *Journal of the American Chemical Society* **2014**, *136*, 6978-6986. http://dx.doi.org/10.1021/ja500328k

21.   Kas, R.; Kortlever, R.; Milbrat, A.; Koper, M. T. M.; Mul, G.; Baltrusaitis, J. "Electrochemical CO2 reduction on Cu2O-derived copper nanoparticles: controlling the catalytic

selectivity of hydrocarbons," *Physical Chemistry Chemical Physics* **2014**, *16*, 12194-12201. http://dx.doi.org/10.1039/C4CP01520G

22.   Hall, A. S.; Yoon, Y.; Wuttig, A.; Surendranath, Y. "Mesostructure-Induced Selectivity in CO2 Reduction Catalysis," *Journal of the American Chemical Society* **2015**, *137*, 14834-14837. http://dx.doi.org/10.1021/jacs.5b08259

23.   Ren, D.; Deng, Y.; Handoko, A. D.; Chen, C. S.; Malkhandi, S.; Yeo, B. S. "Selective Electrochemical Reduction of Carbon Dioxide to Ethylene and Ethanol on Copper(I) Oxide Catalysts," *ACS Catalysis* **2015**, *5*, 2814-2821. http://dx.doi.org/10.1021/cs502128q

24.   Yoon, Y.; Hall, A. S.; Surendranath, Y. "Tuning of Silver Catalyst Mesostructure Promotes Selective Carbon Dioxide Conversion into Fuels," *Angewandte Chemie International Edition* **2016**, *55*, 15282-15286. http://dx.doi.org/https://doi.org/10.1002/anie.201607942

25.   Feng, X.; Jiang, K.; Fan, S.; Kanan, M. W. "A Direct Grain-Boundary-Activity Correlation for CO Electroreduction on Cu Nanoparticles," *ACS Central Science* **2016**, *2*, 169-174. http://dx.doi.org/10.1021/acscentsci.6b00022

26.   Li, Y.; Chan, S. H.; Sun, Q. "Heterogeneous catalytic conversion of CO2: a comprehensive theoretical review," *Nanoscale* **2015**, *7*, 8663-8683. http://dx.doi.org/10.1039/C5NR00092K

27.   Wang, Y.; Han, P.; Lv, X.; Zhang, L.; Zheng, G. "Defect and Interface Engineering for Aqueous Electrocatalytic CO2 Reduction," *Joule* **2018**, *2*, 2551-2582. http://dx.doi.org/https://doi.org/10.1016/j.joule.2018.09.021

28.   Kas, R.; Yang, K.; Bohra, D.; Kortlever, R.; Burdyny, T.; Smith, W. A. "Electrochemical CO2 reduction on nanostructured metal electrodes: fact or defect?," *Chemical Science* **2020**, *11*, 1738-1749. http://dx.doi.org/10.1039/C9SC05375A

29.   Clark, E. L.; Ringe, S.; Tang, M.; Walton, A.; Hahn, C.; Jaramillo, T. F.; Chan, K.; Bell, A. T. "Influence of Atomic Surface Structure on the Activity of Ag for the Electrochemical Reduction of CO2 to CO," *ACS Catalysis* **2019**, *9*, 4006-4014. http://dx.doi.org/10.1021/acscatal.9b00260

30.   Hagman, B.; Posada-Borbón, A.; Schaefer, A.; Shipilin, M.; Zhang, C.; Merte, L. R.; Hellman, A.; Lundgren, E.; Grönbeck, H.; Gustafson, J. "Steps Control the Dissociation of CO2 on Cu(100)," *Journal of the American Chemical Society* **2018**, *140*, 12974-12979. http://dx.doi.org/10.1021/jacs.8b07906

31.   Dalle, K. E.; Warnan, J.; Leung, J. J.; Reuillard, B.; Karmel, I. S.; Reisner, E. "Electro- and Solar-Driven Fuel Synthesis with First Row Transition Metal Complexes," *Chemical Reviews* **2019**, *119*, 2752-2875. http://dx.doi.org/10.1021/acs.chemrev.8b00392

32.   Martin, D. J.; Wise, C. F.; Pegis, M. L.; Mayer, J. M. "Developing Scaling Relationships for Molecular Electrocatalysis through Studies of Fe-Porphyrin-Catalyzed O2 Reduction," *Accounts of Chemical Research* **2020**, *53*, 1056-1065. http://dx.doi.org/10.1021/acs.accounts.0c00044

33.   Costentin, C.; Passard, G.; Savéant, J.-M. "Benchmarking of Homogeneous Electrocatalysts: Overpotential, Turnover Frequency, Limiting Turnover Number," *Journal of the American Chemical Society* **2015**, *137*, 5461-5467. http://dx.doi.org/10.1021/jacs.5b00914

34.   Smith, P. T.; Nichols, E. M.; Cao, Z.; Chang, C. J. "Hybrid Catalysts for Artificial Photosynthesis: Merging Approaches from Molecular, Materials, and Biological Catalysis," *Accounts of Chemical Research* **2020**, *53*, 575-587. http://dx.doi.org/10.1021/acs.accounts.9b00619

35.   Chen, L.; Chen, G.; Leung, C.-F.; Cometto, C.; Robert, M.; Lau, T.-C. "Molecular quaterpyridine-based metal complexes for small molecule activation: water splitting and CO2 reduction," *Chemical Society Reviews* **2020**, *49*, 7271-7283. http://dx.doi.org/10.1039/D0CS00927J

36.   Luo, Y.-H.; Dong, L.-Z.; Liu, J.; Li, S.-L.; Lan, Y.-Q. "From molecular metal complex to metal-organic framework: The CO2 reduction photocatalysts with clear and tunable structure," *Coordination Chemistry Reviews* **2019**, *390*, 86-126. http://dx.doi.org/https://doi.org/10.1016/j.ccr.2019.03.019

37.   Jiang, C.; Nichols, A. W.; Machan, C. W. "A look at periodic trends in d-block molecular electrocatalysts for CO2 reduction," *Dalton Transactions* **2019**, *48*, 9454-9468. http://dx.doi.org/10.1039/C9DT00491B

38.   Corbin, N.; Zeng, J.; Williams, K.; Manthiram, K. "Heterogeneous molecular catalysts for electrocatalytic CO2 reduction," *Nano Research* **2019**, *12*, 2093-2125. http://dx.doi.org/10.1007/s12274-019-2403-y

39.   Fukuzumi, S.; Lee, Y.-M.; Ahn, H. S.; Nam, W. "Mechanisms of catalytic reduction of CO2 with heme and nonheme metal complexes," *Chemical Science* **2018**, *9*, 6017-6034. http://dx.doi.org/10.1039/c8sc02220h

40.   Pegis, M. L.; Wise, C. F.; Koronkiewicz, B.; Mayer, J. M. "Identifying and Breaking Scaling Relations in Molecular Catalysis of Electrochemical Reactions," *Journal of the American Chemical Society* **2017**, *139*, 11000-11003. http://dx.doi.org/10.1021/jacs.7b05642

41.   Raugei, S.; Helm, M. L.; Hammes-Schiffer, S.; Appel, A. M.; O'Hagan, M.; Wiedner, E. S.; Bullock, R. M. "Experimental and Computational Mechanistic Studies Guiding the Rational

Design of Molecular Electrocatalysts for Production and Oxidation of Hydrogen," *Inorganic Chemistry* **2016**, *55*, 445-460. http://dx.doi.org/10.1021/acs.inorgchem.5b02262

42.   Dutta, A.; Ginovska, B.; Raugei, S.; Roberts, J. A. S.; Shaw, W. J. "Optimizing conditions for utilization of an H2 oxidation catalyst with outer coordination sphere functionalities," *Dalton Transactions* **2016**, *45*, 9786-9793. http://dx.doi.org/10.1039/C6DT00280C

43.   Cardenas, A. J. P.; Ginovska, B.; Kumar, N.; Hou, J.; Raugei, S.; Helm, M. L.; Appel, A. M.; Bullock, R. M.; O'Hagan, M. "Controlling Proton Delivery through Catalyst Structural Dynamics," *Angewandte Chemie International Edition* **2016**, *55*, 13509-13513. http://dx.doi.org/https://doi.org/10.1002/anie.201607460

44.   Pegis, M. L.; McKeown, B. A.; Kumar, N.; Lang, K.; Wasylenko, D. J.; Zhang, X. P.; Raugei, S.; Mayer, J. M. "Homogenous Electrocatalytic Oxygen Reduction Rates Correlate with Reaction Overpotential in Acidic Organic Solutions," *ACS Central Science* **2016**, *2*, 850-856. http://dx.doi.org/10.1021/acscentsci.6b00261

45.   Tignor, S. E.; Kuo, H.-Y.; Lee, T. S.; Scholes, G. D.; Bocarsly, A. B. "Manganese-Based Catalysts with Varying Ligand Substituents for the Electrochemical Reduction of CO2 to CO," *Organometallics* **2019**, *38*, 1292-1299. http://dx.doi.org/10.1021/acs.organomet.8b00554

46.   Clark, M. L.; Cheung, P. L.; Lessio, M.; Carter, E. A.; Kubiak, C. P. "Kinetic and Mechanistic Effects of Bipyridine (bpy) Substituent, Labile Ligand, and Brønsted Acid on Electrocatalytic CO2 Reduction by Re(bpy) Complexes," *ACS Catalysis* **2018**, *8*, 2021-2029. http://dx.doi.org/10.1021/acscatal.7b03971

47.   Azcarate, I.; Costentin, C.; Robert, M.; Savéant, J.-M. "Dissection of Electronic Substituent Effects in Multielectron–Multistep Molecular Catalysis. Electrochemical CO2-to-CO Conversion

Catalyzed by Iron Porphyrins," *The Journal of Physical Chemistry C* **2016**, *120*, 28951-28960. http://dx.doi.org/10.1021/acs.jpcc.6b09947

48.   Barlow, J. M.; Yang, J. Y. "Thermodynamic Considerations for Optimizing Selective CO2 Reduction by Molecular Catalysts," *ACS Central Science* **2019**, *5*, 580-588. http://dx.doi.org/10.1021/acscentsci.9b00095

49.   Ceballos, B. M.; Yang, J. Y. "Directing the reactivity of metal hydrides for selective CO$_2$ reduction," *Proceedings of the National Academy of Sciences* **2018**, *115*, 12686-12691. http://dx.doi.org/10.1073/pnas.1811396115

50.   Ogata, T.; Yanagida, S.; Brunschwig, B. S.; Fujita, E. "Mechanistic and Kinetic Studies of Cobalt Macrocycles in a Photochemical CO2 Reduction System: Evidence of Co-CO2 Adducts as Intermediates," *Journal of the American Chemical Society* **1995**, *117*, 6708-6716. http://dx.doi.org/10.1021/ja00130a009

51.   Schmidt, M. H.; Miskelly, G. M.; Lewis, N. S. "Effects of redox potential, steric configuration, solvent, and alkali metal cations on the binding of carbon dioxide to cobalt(I) and nickel(I) macrocycles," *Journal of the American Chemical Society* **1990**, *112*, 3420-3426. http://dx.doi.org/10.1021/ja00165a027

52.   Fujita, E.; Creutz, C.; Sutin, N.; Szalda, D. J. "Carbon dioxide activation by cobalt(I) macrocycles: factors affecting carbon dioxide and carbon monoxide binding," *Journal of the American Chemical Society* **1991**, *113*, 343-353. http://dx.doi.org/10.1021/ja00001a048

53.   Matsubara, Y. "Standard Electrode Potentials for the Reduction of CO2 to CO in Acetonitrile–Water Mixtures Determined Using a Generalized Method for Proton-Coupled Electron-Transfer Reactions," *ACS Energy Letters* **2017**, *2*, 1886-1891. http://dx.doi.org/10.1021/acsenergylett.7b00548

54.   Pegis, M. L.; Roberts, J. A. S.; Wasylenko, D. J.; Mader, E. A.; Appel, A. M.; Mayer, J. M. "Standard Reduction Potentials for Oxygen and Carbon Dioxide Couples in Acetonitrile and N,N-Dimethylformamide," *Inorganic Chemistry* **2015**, *54*, 11883-11888. http://dx.doi.org/10.1021/acs.inorgchem.5b02136

55.   Elgrishi, N.; Chambers, M. B.; Wang, X.; Fontecave, M. "Molecular polypyridine-based metal complexes as catalysts for the reduction of CO2," *Chemical Society Reviews* **2017**, *46*, 761-796. http://dx.doi.org/10.1039/c5cs00391a

56.   Sawatlon, B.; Wodrich, M. D.; Corminboeuf, C. "Unraveling Metal/Pincer Ligand Effects in the Catalytic Hydrogenation of Carbon Dioxide to Formate," *Organometallics* **2018**, *37*, 4568-4575. http://dx.doi.org/10.1021/acs.organomet.8b00490

57.   Wang, Y.-H.; Schneider, P. E.; Goldsmith, Z. K.; Mondal, B.; Hammes-Schiffer, S.; Stahl, S. S. "Brønsted Acid Scaling Relationships Enable Control Over Product Selectivity from O2 Reduction with a Mononuclear Cobalt Porphyrin Catalyst," *ACS Central Science* **2019**, *5*, 1024-1034. http://dx.doi.org/10.1021/acscentsci.9b00194

58.   Margarit, C. G.; Schnedermann, C.; Asimow, N. G.; Nocera, D. G. "Carbon Dioxide Reduction by Iron Hangman Porphyrins," *Organometallics* **2019**, *38*, 1219-1223. http://dx.doi.org/10.1021/acs.organomet.8b00334

59.   Gotico, P.; Boitrel, B.; Guillot, R.; Sircoglou, M.; Quaranta, A.; Halime, Z.; Leibl, W.; Aukauloo, A. "Second-Sphere Biomimetic Multipoint Hydrogen-Bonding Patterns to Boost CO2 Reduction of Iron Porphyrins," *Angewandte Chemie International Edition* **2019**, *58*, 4504-4509. http://dx.doi.org/10.1002/anie.201814339

60.   Nichols, Eva M.; Derrick, J. S.; Nistanaki, S. K.; Smith, P. T.; Chang, C. J. "Positional effects of second-sphere amide pendants on electrochemical CO2 reduction catalyzed by iron porphyrins," *Chemical Science* **2018**, *9*, 2952-2960. http://dx.doi.org/10.1039/C7SC04682K

61.   Chapovetsky, A.; Welborn, M.; Luna, J. M.; Haiges, R.; Miller, T. F.; Marinescu, S. C. "Pendant Hydrogen-Bond Donors in Cobalt Catalysts Independently Enhance CO2 Reduction," *ACS Central Science* **2018**, *4*, 397-404. http://dx.doi.org/10.1021/acscentsci.7b00607

62.   Sung, S.; Kumar, D.; Gil-Sepulcre, M.; Nippe, M. "Electrocatalytic CO2 Reduction by Imidazolium-Functionalized Molecular Catalysts," *Journal of the American Chemical Society* **2017**, *139*, 13993-13996. http://dx.doi.org/10.1021/jacs.7b07709

63.   Roy, S.; Sharma, B.; Pécaut, J.; Simon, P.; Fontecave, M.; Tran, P. D.; Derat, E.; Artero, V. "Molecular Cobalt Complexes with Pendant Amines for Selective Electrocatalytic Reduction of Carbon Dioxide to Formic Acid," *Journal of the American Chemical Society* **2017**, *139*, 3685-3696. http://dx.doi.org/10.1021/jacs.6b11474

64.   Chapovetsky, A.; Do, T. H.; Haiges, R.; Takase, M. K.; Marinescu, S. C. "Proton-Assisted Reduction of CO2 by Cobalt Aminopyridine Macrocycles," *Journal of the American Chemical Society* **2016**, *138*, 5765-5768. http://dx.doi.org/10.1021/jacs.6b01980

65.   Azcarate, I.; Costentin, C.; Robert, M.; Savéant, J.-M. "Through-Space Charge Interaction Substituent Effects in Molecular Catalysis Leading to the Design of the Most Efficient Catalyst of CO2-to-CO Electrochemical Conversion," *Journal of the American Chemical Society* **2016**, *138*, 16639-16644. http://dx.doi.org/10.1021/jacs.6b07014

66.   Costentin, C.; Drouet, S.; Robert, M.; Savéant, J.-M. "A Local Proton Source Enhances CO2 Electroreduction to CO by a Molecular Fe Catalyst," *Science* **2012**, *338*, 90-94. http://dx.doi.org/10.1126/science.1224581

67.   Helm, M. L.; Stewart, M. P.; Bullock, R. M.; DuBois, M. R.; DuBois, D. L. "A Synthetic Nickel Electrocatalyst with a Turnover Frequency Above 100,000 s^{-1} for H$_2$ Production," *Science* **2011**, *333*, 863-866. http://dx.doi.org/10.1126/science.1205864

68.   Wang, V. C. C.; Johnson, B. A. "Interpreting the Electrocatalytic Voltammetry of Homogeneous Catalysts by the Foot of the Wave Analysis and Its Wider Implications," *ACS Catalysis* **2019**, 7109-7123. http://dx.doi.org/10.1021/acscatal.9b00850

69.   Lee, K. J.; McCarthy, B. D.; Dempsey, J. L. "On decomposition, degradation, and voltammetric deviation: the electrochemist's field guide to identifying precatalyst transformation," *Chemical Society Reviews* **2019**, *48*, 2927-2945. http://dx.doi.org/10.1039/C8CS00851E

70.   Lee, K. J.; Elgrishi, N.; Kandemir, B.; Dempsey, J. L. "Electrochemical and spectroscopic methods for evaluating molecular electrocatalysts," *Nature Reviews Chemistry* **2017**, *1*, 0039. http://dx.doi.org/10.1038/s41570-017-0039

71.   Rountree, E. S.; McCarthy, B. D.; Eisenhart, T. T.; Dempsey, J. L. "Evaluation of Homogeneous Electrocatalysts by Cyclic Voltammetry," *Inorganic Chemistry* **2014**, *53*, 9983-10002. http://dx.doi.org/10.1021/ic500658x

72.   Roberts, J. A. S.; Bullock, R. M. "Direct Determination of Equilibrium Potentials for Hydrogen Oxidation/Production by Open Circuit Potential Measurements in Acetonitrile," *Inorganic Chemistry* **2013**, *52*, 3823-3835. http://dx.doi.org/10.1021/ic302461q

73.   Costentin, C.; Drouet, S.; Robert, M.; Savéant, J.-M. "Turnover Numbers, Turnover Frequencies, and Overpotential in Molecular Catalysis of Electrochemical Reactions. Cyclic Voltammetry and Preparative-Scale Electrolysis," *Journal of the American Chemical Society* **2012**, *134*, 11235-11242. http://dx.doi.org/10.1021/ja303560c

74.   Hansen, H. A.; Varley, J. B.; Peterson, A. A.; Nørskov, J. K. "Understanding Trends in the Electrocatalytic Activity of Metals and Enzymes for CO2 Reduction to CO," *The Journal of Physical Chemistry Letters* **2013**, *4*, 388-392. http://dx.doi.org/10.1021/jz3021155

75.   Kang, K.; Fuller, J.; Reath, A. H.; Ziller, J. W.; Alexandrova, A. N.; Yang, J. Y. "Installation of internal electric fields by non-redox active cations in transition metal complexes," *Chemical Science* **2019**, *10*, 10135-10142. http://dx.doi.org/10.1039/C9SC02870F

76.   Chantarojsiri, T.; Ziller, J. W.; Yang, J. Y. "Incorporation of redox-inactive cations promotes iron catalyzed aerobic C–H oxidation at mild potentials," *Chemical Science* **2018**, *9*, 2567-2574. http://dx.doi.org/10.1039/C7SC04486K

77.   Chantarojsiri, T.; Reath, A. H.; Yang, J. Y. "Cationic Charges Leading to an Inverse Free-Energy Relationship for N−N Bond Formation by MnVI Nitrides," *Angewandte Chemie International Edition* **2018**, *57*, 14037-14042. http://dx.doi.org/10.1002/anie.201805832

78.   Reath, A. H.; Ziller, J. W.; Tsay, C.; Ryan, A. J.; Yang, J. Y. "Redox Potential and Electronic Structure Effects of Proximal Nonredox Active Cations in Cobalt Schiff Base Complexes," *Inorganic Chemistry* **2017**, *56*, 3713-3718. http://dx.doi.org/10.1021/acs.inorgchem.6b03098

79.   Jeoung, J.-H.; Dobbek, H. "Carbon Dioxide Activation at the Ni,Fe-Cluster of Anaerobic Carbon Monoxide Dehydrogenase," *Science* **2007**, *318*, 1461-1464. http://dx.doi.org/10.1126/science.1148481

80.   Sung, S.; Li, X.; Wolf, L. M.; Meeder, J. R.; Bhuvanesh, N. S.; Grice, K. A.; Panetier, J. A.; Nippe, M. "Synergistic Effects of Imidazolium-Functionalization on fac-Mn(CO)3 Bipyridine Catalyst Platforms for Electrocatalytic Carbon Dioxide Reduction," *Journal of the American Chemical Society* **2019**, *141*, 6569-6582. http://dx.doi.org/10.1021/jacs.8b13657

81.   Agarwal, J.; Shaw, T. W.; Schaefer, H. F.; Bocarsly, A. B. "Design of a Catalytic Active Site for Electrochemical CO2 Reduction with Mn(I)-Tricarbonyl Species," *Inorganic Chemistry* **2015**, *54*, 5285-5294. http://dx.doi.org/10.1021/acs.inorgchem.5b00233

82.   Lense, S.; Grice, K. A.; Gillette, K.; Wolf, L. M.; Robertson, G.; McKeon, D.; Saucedo, C.; Carroll, P. J.; Gau, M. "Effects of Tuning Intramolecular Proton Acidity on CO2 Reduction by Mn Bipyridyl Species," *Organometallics* **2020**, *39*, 2425-2437. http://dx.doi.org/10.1021/acs.organomet.0c00230

83.   Nichols, A. W.; Hooe, S. L.; Kuehner, J. S.; Dickie, D. A.; Machan, C. W. "Electrocatalytic CO2 Reduction to Formate with Molecular Fe(III) Complexes Containing Pendent Proton Relays," *Inorganic Chemistry* **2020**, *59*, 5854-5864. http://dx.doi.org/10.1021/acs.inorgchem.9b03341

84.   Ngo, K. T.; McKinnon, M.; Mahanti, B.; Narayanan, R.; Grills, D. C.; Ertem, M. Z.; Rochford, J. "Turning on the Protonation-First Pathway for Electrocatalytic CO2 Reduction by Manganese Bipyridyl Tricarbonyl Complexes," *Journal of the American Chemical Society* **2017**, *139*, 2604-2618. http://dx.doi.org/10.1021/jacs.6b08776

85.   Rønne, M. H.; Cho, D.; Madsen, M. R.; Jakobsen, J. B.; Eom, S.; Escoudé, É.; Hammershøj, H. C. D.; Nielsen, D. U.; Pedersen, S. U.; Baik, M.-H.; Skrydstrup, T.; Daasbjerg, K. "Ligand-Controlled Product Selectivity in Electrochemical Carbon Dioxide Reduction Using Manganese Bipyridine Catalysts," *Journal of the American Chemical Society* **2020**, *142*, 4265-4275. http://dx.doi.org/10.1021/jacs.9b11806

86.   Madsen, M. R.; Jakobsen, J. B.; Rønne, M. H.; Liang, H.; Hammershøj, H. C. D.; Nørby, P.; Pedersen, S. U.; Skrydstrup, T.; Daasbjerg, K. "Evaluation of the Electrocatalytic Reduction of Carbon Dioxide using Rhenium and Ruthenium Bipyridine Catalysts Bearing Pendant Amines in

the Secondary Coordination Sphere," *Organometallics* **2020**, *39*, 1480-1490. http://dx.doi.org/10.1021/acs.organomet.9b00815

87.   Haviv, E.; Azaiza-Dabbah, D.; Carmieli, R.; Avram, L.; Martin, J. M. L.; Neumann, R. "A Thiourea Tether in the Second Coordination Sphere as a Binding Site for CO2 and a Proton Donor Promotes the Electrochemical Reduction of CO2 to CO Catalyzed by a Rhenium Bipyridine-Type Complex," *Journal of the American Chemical Society* **2018**, *140*, 12451-12456. http://dx.doi.org/10.1021/jacs.8b05658

88.   Zee, D. Z.; Nippe, M.; King, A. E.; Chang, C. J.; Long, J. R. "Tuning Second Coordination Sphere Interactions in Polypyridyl–Iron Complexes to Achieve Selective Electrocatalytic Reduction of Carbon Dioxide to Carbon Monoxide," *Inorganic Chemistry* **2020**, *59*, 5206-5217. http://dx.doi.org/10.1021/acs.inorgchem.0c00455

89.   Ouyang, T.; Huang, H.-H.; Wang, J.-W.; Zhong, D.-C.; Lu, T.-B. "A Dinuclear Cobalt Cryptate as a Homogeneous Photocatalyst for Highly Selective and Efficient Visible-Light Driven CO2 Reduction to CO in CH3CN/H2O Solution," *Angewandte Chemie International Edition* **2017**, *56*, 738-743. http://dx.doi.org/10.1002/anie.201610607

90.   Ouyang, T.; Wang, H.-J.; Huang, H.-H.; Wang, J.-W.; Guo, S.; Liu, W.-J.; Zhong, D.-C.; Lu, T.-B. "Dinuclear Metal Synergistic Catalysis Boosts Photochemical CO2-to-CO Conversion," *Angewandte Chemie International Edition* **2018**, *57*, 16480-16485. http://dx.doi.org/10.1002/anie.201811010

91.   Cao, L.-M.; Huang, H.-H.; Wang, J.-W.; Zhong, D.-C.; Lu, T.-B. "The synergistic catalysis effect within a dinuclear nickel complex for efficient and selective electrocatalytic reduction of CO2 to CO," *Green Chemistry* **2018**, *20*, 798-803. http://dx.doi.org/10.1039/C7GC03451B

92.   Guo, Z.; Chen, G.; Cometto, C.; Ma, B.; Zhao, H.; Groizard, T.; Chen, L.; Fan, H.; Man, W.-L.; Yiu, S.-M.; Lau, K.-C.; Lau, T.-C.; Robert, M. "Selectivity control of CO versus HCOO− production in the visible-light-driven catalytic reduction of CO2 with two cooperative metal sites," *Nature Catalysis* **2019**, *2*, 801-808. http://dx.doi.org/10.1038/s41929-019-0331-6

Chapter 2 Electrocatalytic CO$_2$ Reduction by a Cobalt Bis(pyridylmonoimine) Complex: Effect of Acid Concentration on Catalyst Activity and Stability

2.1 Preface

This chapter presents the study of the electrocatalytic CO$_2$ reduction by a cobalt complex with a redox active bis(pyridylmonoimine) based ligand in acetonitrile solution. In particular, this work found that addition of a proton source, such as water or trifluoroethanol, dramatically improves the activity and stability of the molecular catalyst to reduce CO$_2$ to CO selectively. This chapter of my dissertation is derived from the manuscript which was published in *Chemical Communication.*[1] I was the primary author on the manuscript, responsible for all catalyst synthesis and characterization, electrochemical measurements, data analysis, as well as the manuscript writing and preparation. My advisor, Dr. Charles C. L. McCrory, contributed significant insight and expertise in electroanalytic instruction and discussion, and provided help with writing and revising the manuscript.

2.2 Abstract

A Co complex with a redox-active bis(pyridylmonoimine) ligand has been prepared and shows catalytic activity for the electrochemical CO_2 reduction in acetonitrile. Addition of a proton source such as water or trifluoroethanol dramatically improves the activity and stability of the molecular catalyst. The Co complex reduces CO_2 to CO selectively at -1.95 V vs Fc$^{+/0}$ in the presence of high concentrations of water. Base on the electrochemical study of the activity and stability of the Co complex for the CO_2 reduction, a proposed mechanism has been discussed to show the switch of catalytic pathways as the concentration of a proton source is increased. Overall, the activity of the Co complex for CO_2 reduction compares favorably to other molecular Co-based catalysts in acetonitrile solutions.

2.3 Introduction

The electrochemical CO_2 reduction reaction (CO_2RR) is a promising strategy for the conversion of waste CO_2 into value added products.[1-3] State-of-the-art solid-state CO_2 reduction catalysts such as Cu reduce CO_2 to highly-reduced products, but suffer from poor selectivity and generate multiple gaseous and liquid products.[4-5] In contrast, several molecular electrocatalysts reduce CO_2 selectively to single products, making them an important class of CO_2RR catalysts.[6-7] Moreover, the activity and selectivity of molecular catalysts can be tuned by altering their ligand structure.[8-9]

Redox-active ligands have been shown to play an important role in CO_2RR by molecular electrocatalysts.[9-16] Redox-active ligands are able to store electrons in the ligand structure, facilitating the multi-electron reduction of CO_2. Previous reports have shown that cobalt complexes with pyridylimine-based ligands efficiently reduce CO_2 to CO in the presence of H_2O[14, 17-19] and propose that the redox-active properties of the ligand contribute to the preferential reduction of CO_2 over competitive proton reduction. However, inactivation and decomposition of the catalyst is also prevalent in these systems. The decomposition mechanism may involve the formation of a catalyst-CO_2 adduct via CO_2-ligand bonding with the redox active ligands.[9, 20-21]

In this work, a Co complex with a bis(pyridylmonoimine) ligand [Co(L-L)Br$_2$]Br has been prepared (Figure 2.1) and shows catalytic activity for CO_2 reduction in acetonitrile (CH_3CN). The addition of the proton sources H_2O and 2,2,2-trifluoroethanol (TFE) accelerates the rate of electrocatalytic CO_2 reduction and also improves catalyst stability and Faradaic efficiency. In the presence of high concentrations of H_2O and TFE, the [Co(L-L)Br$_2$] catalyst reduces CO_2 selectively to CO with high Faradaic efficiency and high turnover frequency (TOF) compared to other reported Co complexes with similar ligands.[14, 17-19]
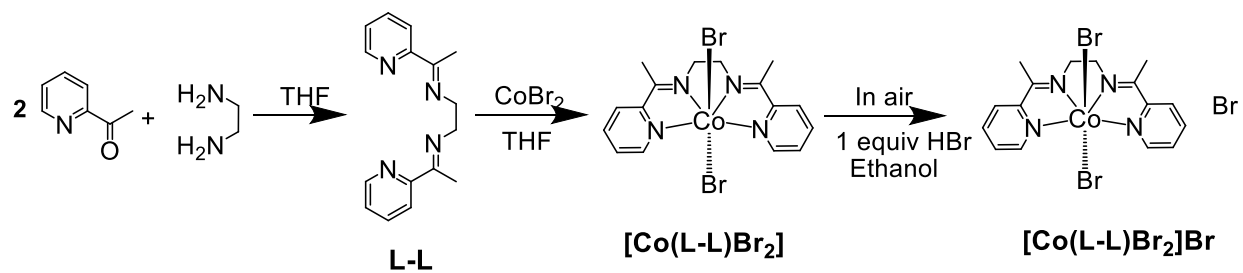
Figure 2.1 Synthesis of the ligand L-L, complex catalyst [Co(L-L)Br$_2$], and [Co(L-L]Br$_2$]Br.

2.4 Experimental

2.4.1 Materials

Ultrapure water (18.2 MΩ cm resistivity) was purified with a Thermo Scientific Barnstead Nanopure water purification system. Nitrogen (N_2) was boil-off gas from a liquid nitrogen source. Carbon dioxide (CO_2, medical grade, >99.0%) was purchased from Cryogenic gases. Tetrabutylammonium hexaflurophosphate (nBu$_4$NPF$_6$, >98.0%) was purchased from TCI America and recrystallized from Methonal/H_2O (v/v = 8/1). 2,2,2-trifluoroethanol (TFE, ReagentPlus grade, ≥99.0%) was purchased from Sigma Aldrich. Acetonitrile (MeCN, HPLC plus, ≥99.9%) was purchased from Sigma Aldrich and used without additional purification. The typical water concentration in MeCN as received has been previously measured to be $[H_2O] \approx 0.040$ M.[22] Nitric acid (HNO_3, 67-70% w/w, TraceMetal Grade with <1 ppb metal concentration) was purchased from Fisher Scientific. All other chemicals were purchased from commercial sources, and all chemicals were used as received unless otherwise noted.

2.4.2 General Methods

NMR spectra were recorded on Varian MR400 (400 MHz) spectrometers, and chemical shifts are reported in ppm relative to TMS standards. Elemental analyses were performed by Midwest Microlab, Inc. Gas chromatography measurements were conducted on a custom-designed 2-channel Thermo Scientific Trace 1310 gas chromatograph with dual TCD detectors. HPLC measurements were collected using a Thermo Scientific Dionex Ultimate 3000 series HPLC. Electrochemical experiments were conducted using a Bio-Logic/Science Instruments SP-200 potentiostat using the EC-Lab V10.44 software package. UV-Vis spectra were collected with Perkin Elmer PDA UV-Vis Lambda 265 equipment. IR spectra were collected with Thermo Scientific NICOLET iS50 FT-IR. ICP-MS data were collected using PerkinElmer NexION 2000.

X-ray diffraction data was collected on a CrystalClear-SM Expert 2.0 r16 (Rigaku, 2014) with a Rigaku Saturn944+ CCD detector using Cu Kα (wavelength is 1.54 Å). The structure was solved by direct methods and refined on F2 full-matrix least-squares using SHELXL-2013 (Sheldrick, 2013).[23]

2.4.3 Synthesis

Preparation of Ligand L-L. The Ligand L-L was synthesized according to literature methods.[24] A solution of 2-acetylpyridine (1.00 g, 8.04 mmol) in 20 mL *i*-PrOH was added into a solution of ethylenediamine (0.24 g, 4.00 mmol) in 20 mL *i*-PrOH. The mixture was stirred at room temperature for 24 hours. After removing the solvent, the yellow oil residue was put into a - 4 ℃ refrigerator to get a semi-solid crude product. The crude ligand was re-crystallized from 5 mL hexane to give white needles which were dried in vacuum overnight (0.70 g, 65% yield). ^{1}H NMR (CD$_3$Cl-d_3, 400 MHz, Figure A.1 in Appendix A.1): δ 8.59 (2H, d, *Ar*-H), δ 8.07 (2H, d, *Ar*-H), δ 7.69 (2H, m, *Ar*-H), δ 7.28 (2H, m, *Ar*-H), δ 3.98 (4H, s, CH$_2$), δ 2.44 (6H, s, CH$_3$).

Preparation of [Co(L-L)Br$_2$]. A 5 mL THF solution of CoBr$_2$ (87.50 mg, 0.40 mmol) was added into a 3 mL THF solution of ligand L-L (106.50 mg, 0.40 mmol) with a 1:1 metal salt : ligand molar ratio. The mixture was stirred at room temperature for 24 hours. The dark purple precipitate was collected by filtration and then washed with THF and ether three times. The product was obtained after drying in vacuum overnight (183.40 mg, 95% yield). Anal. Calcd (found) for [Co(L-L)Br$_2$], (C$_{16}$H$_{18}$N$_4$CoBr$_2$): %C 39.62, (38.92); %H 3.74, (3.80); %N 11.55, (11.22).

Preparation of [Co(L-L)Br$_2$]Br. Aerobic oxidation of in situ prepared [Co(L-L)Br$_2$] in the presence of 1 equiv HBr(aq) in ethanol overnight (18 hours) resulted a green solid (179.78 mg, 80% yield). Recrystallization was accomplished by diffusion of Et$_2$O into a MeOH solution of the green solid. Dark green crystals were obtained after a few days and kept in dark to avoid

photochemical degradation. ^{1}H NMR (Trifluoroacetic acid-d_1, 400 MHz, Figure A.2): δ 9.44 (2H, d, Ar-H), δ 8.28 (2H, t, Ar-H), δ 8.14 (2H, d, Ar-H), δ 7.94 (2H, t, Ar-H), δ 4.81 (4H, s, CH$_2$), δ 2.92 (6H, s, CH$_3$). Anal. Calcd (found) for [Co(L-L)Br$_2$]Br (C16H18N4CoBr3): %C 34.01, (34.07); %H 3.21, (3.30); %N 9.92, (9.89).

2.4.4 Electrochemical Methods and Product Analysis

Cyclic Voltammetry. The working electrode was a 0.071 cm^2 glassy carbon disk electrode (CH instruments), and the counter electrode was carbon rod (99.999% Strem). The reference electrode was a Ag/AgNO$_3$ (1.0 mM)/MeCN nonaqueous reference electrode (also containing 0.1 M nBu$_4$NPF$_6$), separated from the solution by a Vycor frit (Bioanalytical Systems, Inc.) and externally referenced to ferrocene. The scan rate was 50 mV/s. Prior to each set of measurements, the uncompensated solution resistance (R$_u$) in the cell was measured using a single-point impedance measurement at 100 kH$_z$ with a 20 mV amplitude about the open-circuit potential. Cyclic voltammograms were automatically corrected for IR drop at 85% through positive feedback using the Bio-Logic ECLab software.

Controlled-Potential Electrolysis. The controlled-potential electrolysis experiments were conducted in a two-chamber H-cell shown in Figure A.3. The left chamber held the working and reference electrodes and was filled with 20 mL of 0.3 mM catalyst solution in MeCN with 0.1 M nBu$_4$NPF$_6$. The right chamber held the counter electrode in 15 mL of a 5 mM ferrocene solution in MeCN. These two chambers were separated by a fine-porosity glass frit. The working electrode was a 3.2 cm $\times$ 1.6 cm $\times$ 0.1 cm glassy carbon plate (HTW Hochtemperatur-Werkstoff GmbH) which was half immersed in the solution. Prior to each experiment, the working electrode was first polished on 600-grit SiC polishing paper (Buehler, Ltd) and sonicated for 5 min in *i*-PrOH. The reference electrode was a Ag/AgNO$_3$ (1.0 mM)/MeCN nonaqueous reference electrode (also

containing 0.1 M nBu$_4$NPF$_6$) separated from the solution by a Vycor frit (Bioanalytical Systems, Inc.). The counter electrode was nichrome wire (ARCOR). Prior to each electrolysis experiment, the cell was purged with CO_2 or N_2 for 30 minutes and then sealed under an atmosphere of CO or N_2. The CPE experiments were conducted with no IR compensation for solution resistance (~60 Ω), and the reported electrolysis potentials are the actual applied potentials. After each electrolysis, the headspace was sampled using a Thermo Scientific 10 mL Syringe, and the CO and H_2 concentration were measured by gas chromatography. The post-electrolysis solution was analyzed using HPLC to determine HCOOH concentration. The Faradaic efficiency of every product was calculated by dividing the measured product concentrations by the amount expected on the basis of charge passed during the CPE measurement.

Product Analysis. Gaseous products (*i.e.* CO and H_2) in the headspace were measured using a Thermo Scientific Trace 1310 with two analyzer systems. Using a valve system, column configuration, and method developed by Thermo Scientific and Custom Solutions Group LLC., gases were separated so that H_2 was detected on one channel using an Ar carrier, and all other gases were detected on a second channel using a He carrier gas. 5.0 mL aliquots of the working-electrode headspace were collected using a Thermo Scientific 10 mL Syringe. The headspace sample was injected directly into the 5 mL sample loop. Gases were detected on both channels using thermal conductivity detectors (TCDs), and chromatographs were analyzed using Thermo Scientific Dionex Chromeleon^{TM} 7.2.2.6686 Chromatography Data System software.

Liquid products (*i.e.* HCOOH) were analyzed using high-performance liquid chromatography (HPLC). HPLC measurements were collected using a Thermo Scientific Dionex Ultimate 3000 series HPLC equipped with a UV-Vis detector and refractive index detector (RID). Liquid aliquots were collected from the working-electrode chamber post-electrolysis and placed

in an autosampler from which 10 μL aliquots of each liquid sample was injected into a HyperREZ XP Carbohydrate H+ column. The eluent was 0.05 M H_2SO_4 aqueous solution at a flow rate of 0.6 mL min^{-1}. The temperature of the column was maintained at 50 °C. Products were detected using the RID detector and chromatographs were analyzed using Thermo Scientific Dionex Chromeleon^{TM} 7.2.2.6686 Chromatography Data System software.

Faradaic efficiencies were calculated by dividing the total number of moles of each product by the moles of electrons calculated from the amount of charge passed during the electrolyses normalized for the number of electrons required to produce each product.

SEM-EDS tests. All electrodes tested by SEM-EDS (JEOL-7800FLV FE) were not rinsed post electrolysis. The SEM images showing the morphology of the electrode surface were recorded with a field emission gun scanning electron microscope at 18 kV, equipped with an energy dispersive X-ray (EDS) detector. The EDS analyses were conducted using an SEM acceleration voltage of 18 kV.

2.5 Results and discussion

2.5.1 Synthesis and characterization of the complex

The ligand L-L was synthesized via a classic Schiff base condensation reaction of ethylenediamine with 2-acetylpyridine. [Co(L-L)Br$_2$] was prepared by allowing L-L to react with 1 equivalent of CoBr$_2$ in THF. Aerobic oxidation of [Co(L-L)Br$_2$] in the presence of 1 equiv HBr(aq) for 18 hours afforded green [Co(L-L)Br$_2$]Br (Figure 2.1), which was characterized by ^{1}H-NMR (Figure A.2) and elemental analysis. The infrared (IR) spectra of [Co(L-L)Br$_2$] and [Co(L-L)Br$_2$]Br solid samples show the characteristic C=N stretching adsorptions at 1690~1650 cm^{-1}, indicating the formation of imine bonds of the Schiff base ligand structure in these two Co complexes (Figure A.4). Dark green crystals of [Co(L-L)Br$_2$]Br suitable for the X-ray crystallography were successfully obtained by diffusion of Et$_2$O into a MeOH solution of the complex. The X-ray single crystal structure of [Co(L-L)Br$_2$]Br shows that the central cobalt metal adopts a bipyramidal six-coordinated configuration. The tetradentate ligand L-L coordinates to Co with four N atoms in a slightly distorted square planar mode. Two Br atoms occupy the axial coordination sites, and a third Br atom exists outside the coordination sphere as a counter anion (Figure 2.2). In addition, the spin state and electronic configuration of [Co(L-L)Br$_2$] at room temperature was also estimated by Evans method through paramagnetic susceptibility measurements (see section A.1.3 for detailed discussion of Evans method). Note that in this study [Co(L-L)Br$_2$] (the Co^{2+} complex) was used for all electrochemical measurements and [Co(L-L)Br$_2$]Br (the Co^{3+} complex) was used only for characterization of the complex.
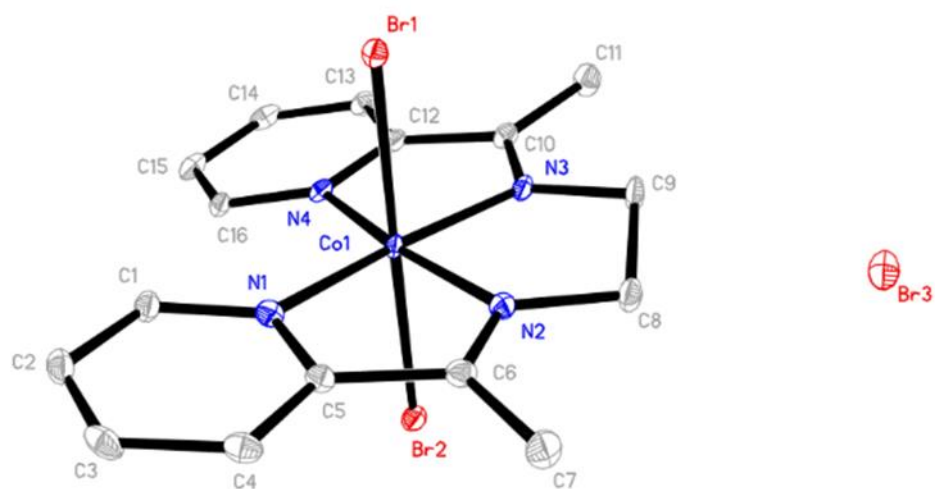
Figure 2.2 X-ray single crystal structure of [Co(L-L)Br₂]Br with ellipsoids shown at 50 % probability (H atoms are omitted for clarity).

2.5.2 Cyclic voltammograms (CVs) of complex [Co(L-L)Br$_2$] under N$_2$ and CO$_2$

Cyclic voltammograms (CVs) of complex [Co(L-L)Br$_2$] were recorded in a nitrogen-saturated CH$_3$CN solution with 0.1 M nBu$_4$NPF$_6$ (Figure 2.3). Note that all CVs have been IR compensated. Two reversible peaks are observed at -0.42 V vs Fc$^{+/0}$ and -1.00 V vs Fc$^{+/0}$ and are assigned as the Co$^{3+/2+}$ and Co$^{2+/1+}$ redox couples, respectively. The broad quasi-reversible redox feature observed at ~-1.6 V vs Fc$^{+/0}$ is assigned to a ligand-based redox process. This assignment is consistent with that of metal complexes with other redox-active pyridylmonimine[9] and bipyridyl[8] ligands. The most-negative reversible peak at -2.16 V vs Fc$^{+/0}$ is assigned to the Co$^{1+/0}$ couple.

The cyclic voltammogram (CV) of complex [Co(L-L)Br$_2$] in a CO$_2$-saturated CH$_3$CN solution shows a large increase in the reductive current consistent with an electrocatalytic process (Figure 2.3). The onset potential of the electrocatalytic current is ~-1.65 V vs Fc$^{+/0}$, the approximate potential of the ligand reduction. Adding the proton source H$_2$O to the electrolyte solution increases the magnitude of the catalytic current (Figure 2.4a for 0.82 M and 11.1 M H$_2$O, other concentrations shown in Figure A.5 and A.6). Increasing the concentration of H$_2$O also slightly shifts the catalytic peak potential, from -2.0 V vs Fc$^{+/0}$ at 0.82 M H$_2$O to -1.95 V vs Fc$^{+/0}$ at 11.1 M. A similar phenomenon was observed when adding 2,2,2-trifluoroethanol (TFE) as a proton source (Figure 2.4b and Figure A.7 and A.8). Since TFE is more acidic than H$_2$O in CH$_3$CN,[25-27] a lower concentration of TFE is necessary to reach a comparable catalytic current under CO$_2$. To confirm that the catalytic peak is due to CO$_2$ reduction and not competitive H$_2$ evolution, CVs were also measured in the absence of CO$_2$ (Figure 2.4c for H$_2$O, Figure A.9 for TFE). The onset of H$_2$ evolution occurs only at much more negative potentials than the CO$_2$ reduction peak. Note that the catalytic peak shape in the presence of proton source resembles an

"inverted peak" (the inverted return wave when potential is scanned back).[28] We attribute this peak shape to the overlap of the catalytic current response for CO_2 reduction with the more negative, reversible $Co^{1+/0}$ redox feature (Figure A.10 and A.11). A similar behavior has been observed in the case of CO_2 reduction by $[Mn(mesbpy)(CO)_3(MeCN)]^+$.[27]
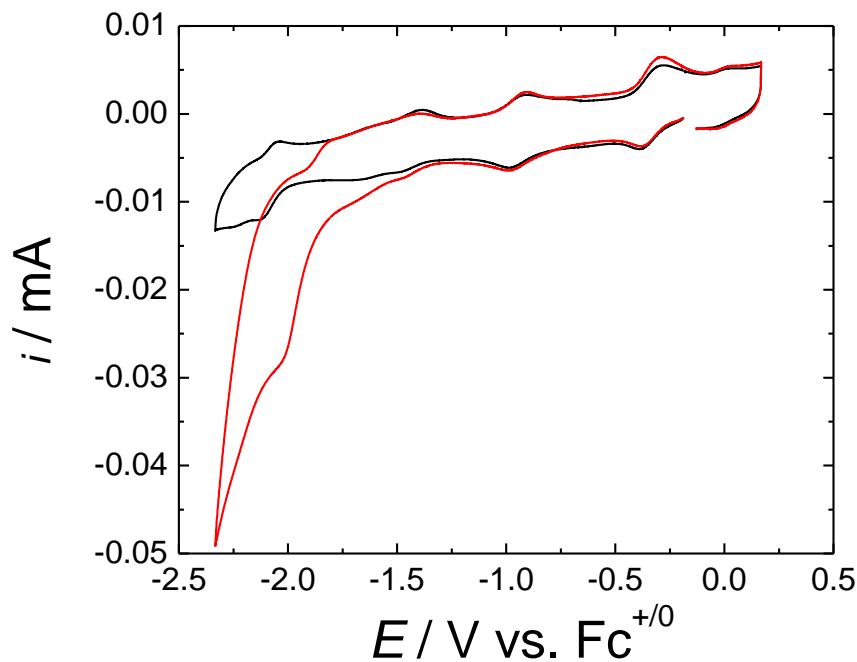
Figure 2.3 The CVs of 1.2 mM **[Co(L-L)Br₂]** in CH_3CN with 0.1 M nBu_4NPF_6 (Black: under N_2; Red: under CO_2; Conditions: scan rate: 50 mV/s; working electrode: glassy carbon working electrode; reference electrode: Ag/AgNO₃(1 mM); counter electrode: carbon rod.)
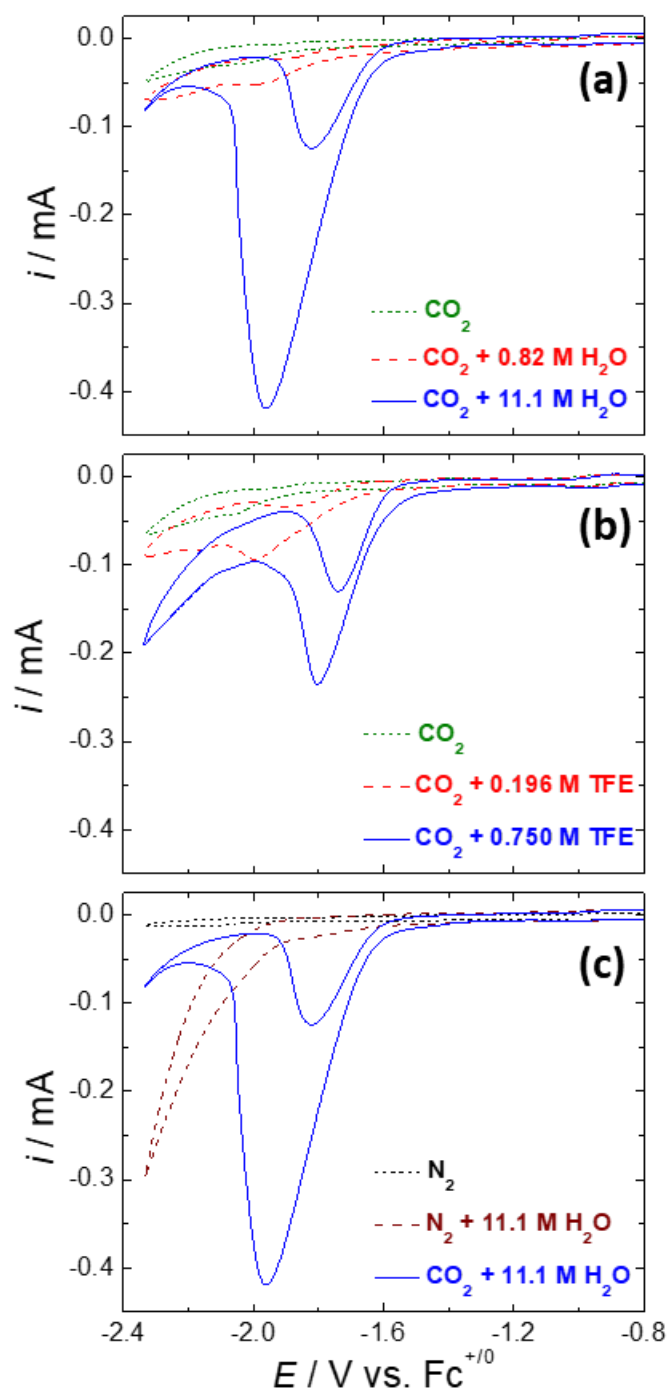
Figure 2.4 CVs of 0.3 mM **[Co(L-L)Br₂]** in CH₃CN with 0.1 M nBu₄NPF₆ a) under CO_2 in the presence of H_2O of different concentrations; b) under CO_2 in the presence of TFE of different concentrations; c) under N_2 and CO_2 with 11.1 M H_2O.

2.5.3 Controlled potential electrolysis (CPE) experiments for the CO₂RR

To further confirm the catalytic ability of [Co(L-L)Br$_2$] for CO$_2$ reduction, we conducted a series of 30-minute controlled potential electrolysis (CPE) experiments in CH$_3$CN (Table 2.1 and Table A.3). The CPE experiments were conducted with no IR compensation for solution resistance, and the reported electrolysis potentials are the actual applied potentials. Note that the electrolyte solutions as prepared contain up to ~0.04 M H$_2$O even when no additional proton source is added.[22] Gas and liquid phases were analyzed by GC and HPLC, respectively, and the Faradaic efficiency of each product (FE$_{product}$) was determined. Turnover frequencies (TOFs) were calculated using two methods: 1) by dividing the total amount of CO generated by the catalyst amount in solution and 2) calculated from CPE data with the equations described by Savéant et al.[29-30] (see section A.1.3 for further discussion of TOF). The electrolysis potentials were chosen based on the peak potential of CO$_2$ reduction in Figure 2.4. After each electrolysis, the un-rinsed electrode surface was investigated with both scanning electron microscopy-energy dispersion spectroscopy (SEM-EDS) and inductively coupled plasma-mass spectrometry (ICP-MS) to detect the formation of solid-state deposits (Figure A.12~A.19, Table A.6 and section A.1.3).[31] Control experiments consisting of 30 min CPE with the glassy carbon electrode and clean electrolyte, only CoBr$_2$ in solution, and only the ligand L-L in solution all showed no activity for CO$_2$ reduction (Table A.4).

Table 2.1 Conditions and Product Analysis of the Controlled Potential Electrolysis for the CO_2 reduction

E / V vs. Fc$^{+/0\ a}$	[Proton source] / M	Charge / C	TOF$_A$ / s$^{-1\ b}$	TOF$_B$ / s$^{-1\ c}$	Faradaic Efficiency / %			Co weight% on the electrode surface from EDS^d
					CO	H$_2$	HCOOH	
−1.95	-	2.2 ±0.3	$(2.9 \pm 2.1)\times 10^{-5}$	0.053	2.8 ±2.6	0	6.3 ±2.6	0.52 %
−2.15	-	4.3 ±1.4	$(8.1 \pm 2.5)\times 10^{-5}$	0.453	4.2 ±1.7	0	2.7 ±0.9	0.52 %
−1.95	1.1 M H$_2$O	3.4 ±0.4	$(2.7 \pm 0.9)\times 10^{-4}$	4.26	16.3 ±5.1	0	4.5 ±1.1	-^{e}
−1.95	5.5 M H$_2$O	7.9 ±0.7	$(2.3 \pm 0.5)\times 10^{-3}$	393	67.4 ±11.0	0.3 ±0.1	1.9 ±0.5	-^{e}
−1.95	11.0 M H$_2$O	8.3 ±0.9	$(3.2 \pm 0.4)\times 10^{-3}$	620	80.5 ±4.7	1.1 ±0.5	0.7 ±0.2	0.35 %
−2.15	11.0 M H$_2$O	16.2 ±2.5	$(8.1 \pm 1.3)\times 10^{-3}$	3961	104.3 ±5.5	0.6±0.4	0	0.18 %
−1.85	5.5 M TFE	10.1 ±2.3	$(4.2 \pm 0.5)\times 10^{-3}$	1089	87.7 ±8.2	1.7 ±0.7	0	0.01 %
−2.05	5.5 M TFE	16.8 ±2.5	$(8.2 \pm 0.9)\times 10^{-3}$	4131	102.7 ±3.1	1.0 ±0.4	0	0.007 %

^{a}Applied potential without IR compensation; ^{b}TOF$_A$ is calculated based on total concentration of catalyst in solution, and therefore is a significant underestimate of catalytic activity (section A.1.3); ^{c}TOF$_B$ is derived from CPE data as described by Savéant et al. (section A.1.3)[29-30]; ^{d}"Co weight%" means the weight% of Co in the total surface atoms; ^{e}Not measured.

For electrolyte solutions containing [Co(L-L)Br$_2$] in the absence of any added proton source, the solution became turbid after 30 mins of CPE at -1.95 V vs Fc$^{+/0}$ and -2.15 V vs Fc$^{+/0}$. Only a small amount of CO (FE$_{CO}$ = 2.8 % @-1.95 V, 4.2 % @-2.15 V) and formic acid HCOOH (FE$_{HCOOH}$ = 6.3 % @-1.95 V, 2.7 % @-2.15 V) were detected after the electrolyses (Table 2.1 and Table A.5). SEM-EDS measurements of the electrodes post electrolysis show Co-based particles deposited on the surface with a weight percent of 0.52 % of total atoms measured (Figire A.12). ICP-MS measurements were used to better quantify the amount of Co deposited and indicate the amount of Co on the electrode surface corresponds to 5.92 % of initial Co complex loading in the electrolysis solution (Table A.6). These measurements suggest that the catalyst decomposes during electrolysis in the absence of added proton source.

Upon addition of a proton source, significantly more charge was passed in 30 min CPE and the Faradaic efficiency for CO increased while the Faradaic efficiency for HCOOH decreased. A summary of the product distribution after 30 min CPE at -1.95 V vs Fc$^{+/0}$ for selected concentrations of H$_2$O is shown in Table 2.1 (and all concentrations in Table A.3). At the highest concentration of H$_2$O investigated (11.0 M), CO$_2$ was reduced to CO with 80.5 % efficiency at -1.95 V vs Fc$^{+/0}$.

Similarly, CPE conducted in 5.50 M TFE showed selective CO$_2$ reduction to CO with 87.7 % Faradaic efficiency at -1.85 V vs Fc$^{+/0}$. In both cases, the TOF values for CO increase dramatically. During the electrolysis, the solution remained transparent and the UV-vis spectra of the solution before and after 30 min CPE remained nearly identical (Figure. A.24). Both SEM-EDS and ICP-MS measurements of the electrode surfaces post-electrolysis showed less catalyst decomposition to adsorbed solid-state materials (Table 2.1, Figure A.14 and A.15, Table A.6). When the CPE experiments were conducted at 0.2 V more negative applied potentials (to manually

account for IR drop due to ~60 Ω solution resistance in our electrolysis cell), higher Faradaic efficiencies and TOF values were observed for CO production and even less decomposition to surface Co species was observed by SEM-EDS (Table 2.1). Compared to other Co-based CO_2RR catalysts, [Co(L-L)Br$_2$] reduces CO_2 to CO with high Faradaic efficiency and fast TOF at less negative applied potentials (Table A.8).

Note that when CPE experiments were conducted in 11.1 M H_2O at potentials which are more positive (-1.75 V vs Fc$^{+/0}$) and more negative (-2.35 V vs Fc$^{+/0}$) than the catalytic peak potential in Figure 2.4, Faradaic efficiency for CO production decreased and an increase in Co decomposition/deposition was observed (Table A.5). Longer time CPE measurements were also conducted in 11.1 M H_2O at -1.95 V vs Fc$^{+/0}$, and similar catalyst activity and Faradaic Efficiencies for CO were observed after 60 min and 90 min electrolysis when compared to the results from the 30 min electrolyses (Table A.7). However, significant loss of CO_2 activity and increased catalyst decomposition was observed after 120 min CPE in both 11.1 M H_2O and 5.5 M TFE (Table A.7, Figure A.27 and A.28). These results indicate that the stability of the catalyst under CO_2 reduction conditions is both potential and time dependent.

2.5.4 The proposed mechanism for the CO2RR by [Co(L-L)Br2]

The results of our CPE experiments suggest that adding a proton source not only accelerates the catalysis but also increases the catalyst's stability. We propose a mechanism to explain our results in Figure 2.5. Here, $[Co(L-L)]^{2+}$ is reduced sequentially by 2 e$^-$ to form $[Co(L-L)]$, the active species for CO_2 reduction. $[Co(L-L)]$ coordinates CO_2 to form a $[Co(L-L)CO_2]$ adduct. At high proton concentration, $[Co(L-L)CO_2]$ undergoes a 1 e$^-$ reduction and 2 H$^+$ protonation by the proton source to generate CO and H_2O and regenerate the $[Co(L-L)]^+$ complex (Figure 2.5, Path (a)). However, at low proton concentration, the $[Co(L-L)CO_2]$ abstracts a proton from the ligand to generate HCOO$^-$, leading to decomposition of the complex (Figure 2.5, path (b), Figure 2.6). This latter step is supported by recent reports of catalyst inactivation and decomposition of Re, Mo and Mn complexes with pyridylimine ligands due to the formation of catalyst-CO_2 adducts involving CO_2-ligand bonding.[9, 20-21, 32] Thus, we postulate that the increased stability for the catalyst at higher proton source concentrations is because the rate of protonation by the external proton source is sufficiently large to prevent intramolecular H$^+$-abstraction. However, we note that the decomposition could also be due to a purely electrochemical step at the electrode.
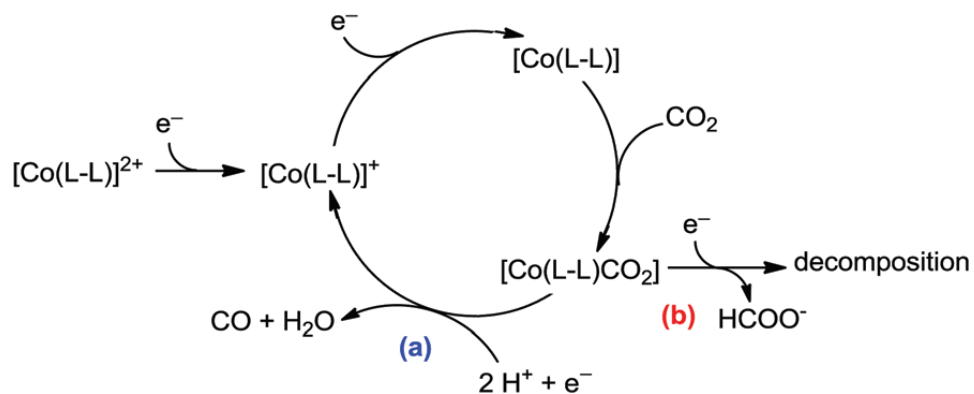
Figure 2.5 Proposed catalytic mechanism of CO_2 reduction with [Co(L-L)]. In the presence of an added proton source, the mechanism proceeds via path (a) forming CO as the final C-containing product. In the absence of added proton source, the mechanism proceeds via path (b) to catalyst decomposition with stoichiometric $HCOO^-$ production.
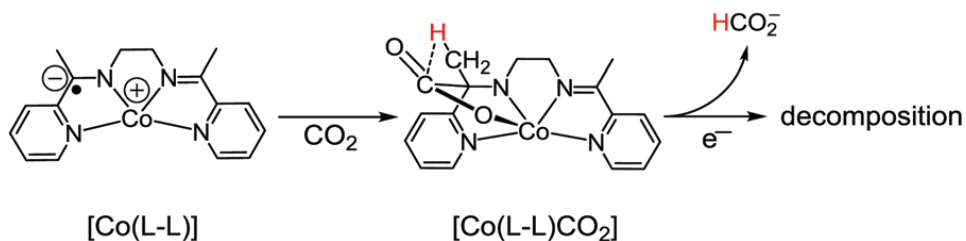
Figure 2.6 Proposed mechanism of the catalyst decomposition.

71

2.6 Conclusion

In conclusion, we have prepared a Co complex with a redox-active bis(pyridylmonoimine) ligand L-L and studied its CO_2 reduction activity in CH_3CN. We have shown that adding a proton source not only accelerates the electrocatalytic rate of CO_2 reduction by [Co(L-L)Br$_2$], but also improves the stability of the catalyst by promoting intermolecular protonation of the CO_2-catalyst intermediate and preventing intramolecular H^+-abstraction. The [Co(L-L)Br$_2$] system reduces CO_2 selectively to CO in the presence of added proton source with high TOF at less negative potentials compared to previously reported Co-based catalysts.

2.7 Reference

1. Appel, A. M.; Bercaw, J. E.; Bocarsly, A. B.; Dobbek, H.; DuBois, D. L.; Dupuis, M.; Ferry, J. G.; Fujita, E.; Hille, R.; Kenis, P. J. A.; Kerfeld, C. A.; Morris, R. H.; Peden, C. H. F.; Portis, A. R.; Ragsdale, S. W.; Rauchfuss, T. B.; Reek, J. N. H.; Seefeldt, L. C.; Thauer, R. K.; Waldrop, G. L. "Frontiers, Opportunities, and Challenges in Biochemical and Chemical Catalysis of CO2 Fixation," *Chemical Reviews* **2013**, *113*, 6621-6658. http://dx.doi.org/10.1021/cr300463y

2. Berardi, S.; Drouet, S.; Francas, L.; Gimbert-Surinach, C.; Guttentag, M.; Richmond, C.; Stoll, T.; Llobet, A. "Molecular artificial photosynthesis," *Chemical Society Reviews* **2014**, *43*, 7501-7519. http://dx.doi.org/10.1039/c3cs60405e

3. Qiao, J.; Liu, Y.; Hong, F.; Zhang, J. "A review of catalysts for the electroreduction of carbon dioxide to produce low-carbon fuels," *Chemical Society Reviews* **2014**, *43*, 631-675. http://dx.doi.org/10.1039/c3cs60323g

4. Hori, Y.; Wakebe, H.; Tsukamoto, T.; Koga, O. "Electrocatalytic process of CO selectivity in electrochemical reduction of CO2 at metal electrodes in aqueous media," *Electrochimica Acta* **1994**, *39*, 1833-1839. http://dx.doi.org/http://dx.doi.org/10.1016/0013-4686(94)85172-7

5. Kuhl, K. P.; Cave, E. R.; Abram, D. N.; Jaramillo, T. F. "New insights into the electrochemical reduction of carbon dioxide on metallic copper surfaces," *Energy & Environmental Science* **2012**, *5*, 7050-7059. http://dx.doi.org/10.1039/c2ee21234j

6. Benson, E. E.; Kubiak, C. P.; Sathrum, A. J.; Smieja, J. M. "Electrocatalytic and homogeneous approaches to conversion of CO2 to liquid fuels," *Chemical Society Reviews* **2009**, *38*, 89-99. http://dx.doi.org/10.1039/b804323j

7.   Takeda, H.; Cometto, C.; Ishitani, O.; Robert, M. "Electrons, Photons, Protons and Earth-Abundant Metal Complexes for Molecular Catalysis of CO2 Reduction," *ACS Catalysis* **2017**, *7*, 70-88. http://dx.doi.org/10.1021/acscatal.6b02181

8.   Clark, M. L.; Grice, K. A.; Moore, C. E.; Rheingold, A. L.; Kubiak, C. P. "Electrocatalytic CO2 reduction by M(bpy-R)(CO)4 (M = Mo, W; R = H, tBu) complexes. Electrochemical, spectroscopic, and computational studies and comparison with group 7 catalysts," *Chemical Science* **2014**, *5*, 1894-1900. http://dx.doi.org/10.1039/c3sc53470g

9.   Machan, C. W.; Chabolla, S. A.; Kubiak, C. P. "Reductive Disproportionation of Carbon Dioxide by an Alkyl-Functionalized Pyridine Monoimine Re(I) fac-Tricarbonyl Electrocatalyst," *Organometallics* **2015**, *34*, 4678-4683. http://dx.doi.org/10.1021/acs.organomet.5b00406

10.   Benson, E. E.; Sampson, M. D.; Grice, K. A.; Smieja, J. M.; Froehlich, J. D.; Friebel, D.; Keith, J. A.; Carter, E. A.; Nilsson, A.; Kubiak, C. P. "The Electronic States of Rhenium Bipyridyl Electrocatalysts for CO2 Reduction as Revealed by X-ray Absorption Spectroscopy and Computational Quantum Chemistry," *Angewandte Chemie International Edition* **2013**, *52*, 4841-4844. http://dx.doi.org/10.1002/anie.201209911

11.   Chen, Z.; Chen, C.; Weinberg, D. R.; Kang, P.; Concepcion, J. J.; Harrison, D. P.; Brookhart, M. S.; Meyer, T. J. "Electrocatalytic reduction of CO2 to CO by polypyridyl ruthenium complexes," *Chemical Communications* **2011**, *47*, 12607-12609. http://dx.doi.org/10.1039/c1cc15071e

12.   Simpson, T. C.; Durand, R. R. "Ligand participation in the reduction of CO2 catalyzed by complexes of 1,10 o-phenanthroline," *Electrochimica Acta* **1988**, *33*, 581-583. http://dx.doi.org/http://dx.doi.org/10.1016/0013-4686(88)80181-6

13.   Fujita, E.; Muckerman, J. T. "Why Is Re−Re Bond Formation/Cleavage in [Re(bpy)(CO)3]2 Different from That in [Re(CO)5]2? Experimental and Theoretical Studies on the Dimers and Fragments," *Inorganic Chemistry* **2004**, *43*, 7636-7647. http://dx.doi.org/10.1021/ic048910v

14.   Lacy, D. C.; McCrory, C. C. L.; Peters, J. C. "Studies of Cobalt-Mediated Electrocatalytic CO2 Reduction Using a Redox-Active Ligand," *Inorganic Chemistry* **2014**, *53*, 4980-4988. http://dx.doi.org/10.1021/ic403122j

15.   Smieja, J. M.; Kubiak, C. P. "Re(bipy-tBu)(CO)3Cl−improved Catalytic Activity for Reduction of Carbon Dioxide: IR-Spectroelectrochemical and Mechanistic Studies," *Inorganic Chemistry* **2010**, *49*, 9283-9289. http://dx.doi.org/10.1021/ic1008363

16.   Keith, J. A.; Grice, K. A.; Kubiak, C. P.; Carter, E. A. "Elucidation of the Selectivity of Proton-Dependent Electrocatalytic CO2 Reduction by fac-Re(bpy)(CO)3Cl," *Journal of the American Chemical Society* **2013**, *135*, 15823-15829. http://dx.doi.org/10.1021/ja406456g

17.   Lieber, C. M.; Lewis, N. S. "Catalytic reduction of carbon dioxide at carbon electrodes modified with cobalt phthalocyanine," *Journal of the American Chemical Society* **1984**, *106*, 5033-5034. http://dx.doi.org/10.1021/ja00329a082

18.   Tinnemans, A. H. A.; Koster, T. P. M.; Thewissen, D. H. M. W.; Mackor, A. "Tetraaza-macrocyclic cobalt(II) and nickel(II) complexes as electron-transfer agents in the photo(electro)chemical and electrochemical reduction of carbon dioxide," *Recueil des Travaux Chimiques des Pays-Bas* **1984**, *103*, 288-295. http://dx.doi.org/10.1002/recl.19841031004

19.   Chen, L.; Guo, Z.; Wei, X.-G.; Gallenkamp, C.; Bonin, J.; Anxolabéhère-Mallart, E.; Lau, K.-C.; Lau, T.-C.; Robert, M. "Molecular Catalysis of the Electrochemical and Photochemical Reduction of CO2 with Earth-Abundant Metal Complexes. Selective Production of CO vs

HCOOH by Switching of the Metal Center," *Journal of the American Chemical Society* **2015**, *137*, 10918-10921. http://dx.doi.org/10.1021/jacs.5b06535

20.   Sieh, D.; Lacy, D. C.; Peters, J. C.; Kubiak, C. P. "Reduction of CO2 by Pyridine Monoimine Molybdenum Carbonyl Complexes: Cooperative Metal–Ligand Binding of CO2," *Chemistry – A European Journal* **2015**, *21*, 8497-8503. http://dx.doi.org/10.1002/chem.201500463

21.   Sieh, D.; Kubiak, C. P. "A Series of Diamagnetic Pyridine Monoimine Rhenium Complexes with Different Degrees of Metal-to-Ligand Charge Transfer: Correlating 13C NMR Chemical Shifts with Bond Lengths in Redox-Active Ligands," *Chemistry – A European Journal* **2016**, *22*, 10638-10650. http://dx.doi.org/10.1002/chem.201600679

22.   McCrory, C. C. L.; Szymczak, N. K.; Peters, J. C. "Evaluating Activity for Hydrogen-Evolving Cobalt and Nickel Complexes at Elevated Pressures of Hydrogen and Carbon Monoxide," *Electrocatalysis* **2016**, *7*, 87-96. http://dx.doi.org/10.1007/s12678-015-0281-y

23.   Sheldrick, G. "Crystal structure refinement with SHELXL," *Acta Crystallographica Section C* **2015**, *71*, 3-8. http://dx.doi.org/doi:10.1107/S2053229614024218

24.   Gourbatsis, S.; Perlepes, S. P.; Hadjiliadis, N.; Kalkanis, G. "The coordination chemistry ofN, N′-ethylenebis(2-acetylpyridine imine) andN, N′-ethylenebis(2-benzoylpyridine imine); two potentially tetradentate ligands containing four nitrogen atoms," *Transition Metal Chemistry* **1990**, *15*, 300-308. http://dx.doi.org/10.1007/BF01061939

25.   Ngo, K. T.; McKinnon, M.; Mahanti, B.; Narayanan, R.; Grills, D. C.; Ertem, M. Z.; Rochford, J. "Turning on the Protonation-First Pathway for Electrocatalytic CO2 Reduction by Manganese Bipyridyl Tricarbonyl Complexes," *Journal of the American Chemical Society* **2017**, *139*, 2604-2618. http://dx.doi.org/10.1021/jacs.6b08776

26.   Liyanage, N. P.; Dulaney, H. A.; Huckaba, A. J.; Jurss, J. W.; Delcamp, J. H. "Electrocatalytic Reduction of CO2 to CO With Re-Pyridyl-NHCs: Proton Source Influence on Rates and Product Selectivities," *Inorg. Chem.* **2016**, *55*, 6085-6094. http://dx.doi.org/10.1021/acs.inorgchem.6b00626

27.   Sampson, M. D.; Nguyen, A. D.; Grice, K. A.; Moore, C. E.; Rheingold, A. L.; Kubiak, C. P. "Manganese Catalysts with Bulky Bipyridine Ligands for the Electrocatalytic Reduction of Carbon Dioxide: Eliminating Dimerization and Altering Catalysis," *Journal of the American Chemical Society* **2014**, *136*, 5460-5471. http://dx.doi.org/10.1021/ja501252f

28.   Limoges, B. t.; Savéant, J.-M. "Catalysis by immobilized redox enzymes. Diagnosis of inactivation and reactivation effects through odd cyclic voltammetric responses," *Journal of Electroanalytical Chemistry* **2004**, *562*, 43-52. http://dx.doi.org/https://doi.org/10.1016/j.jelechem.2003.07.035

29.   Costentin, C.; Robert, M.; Saveant, J.-M. "Catalysis of the electrochemical reduction of carbon dioxide," *Chem. Soc. Rev.* **2013**, *42*, 2423-2436. http://dx.doi.org/10.1039/C2CS35360A

30.   Costentin, C.; Drouet, S.; Robert, M.; Savéant, J.-M. "A Local Proton Source Enhances CO_2 Electroreduction to CO by a Molecular Fe Catalyst," *Science* **2012**, *338*, 90-94. http://dx.doi.org/10.1126/science.1224581

31.   Kaeffer, N.; Morozan, A.; Fize, J.; Martinez, E.; Guetaz, L.; Artero, V. "The Dark Side of Molecular Catalysis: Diimine–Dioxime Cobalt Complexes Are Not the Actual Hydrogen Evolution Electrocatalyst in Acidic Aqueous Solutions," *ACS Catalysis* **2016**, *6*, 3727-3737. http://dx.doi.org/10.1021/acscatal.6b00378

32.   Stichauer, R.; Helmers, A.; Bremer, J.; Rohdenburg, M.; Wark, A.; Lork, E.; Vogt, M. "Rhenium(I) Triscarbonyl Complexes with Redox-Active Amino- and Iminopyridine Ligands:

Metal–Ligand Cooperation as Trigger for the Reversible Binding of CO2 via a Dearmomatization/Rearomatization Reaction Sequence," *Organometallics* **2017**, *36*, 839-848.

Chapter 3 Electrocatalytic CO₂ Reduction by Cobalt Bis(pyridylmonoimine) Complexes: Effect of Ligand Flexibility on Catalytic Activity

3.1 Preface

This chapter presents the study of the electrocatalytic CO_2 reduction by a series of cobalt complexes with bis(pyridylmonoimine) ligands with different degrees of structural planarity and highlights the nuanced, and somewhat contradictory, effects of ligand flexibility on CO_2 reduction activity. In particular, increasing ligand flexibility leads to a beneficial shift of catalytic onset to more positive potentials, but a detrimental decrease in overall activity in the presence of added proton sources. This work highlights the importance of careful mechanistic studies to inform and understand catalyst design parameters for complicated multi-step and multi-electron reactions like CO_2 reduction, even if the catalysts studied are not the "best" or "most active" systems. This chapter of my dissertation is derived from the manuscript originally published in the journal of *ACS Catalysis*.[2] I was the first author of the manuscript and I was responsible for all the compound synthesis and characterization, electrochemical experiment measurements and data analysis, as well as the manuscript writing and revision. Dr. Yanming Wang provided the DFT calculations in support of this work. Dr. Tao Zheng provided help with interpreting X-ray crystallographic data for synthesized complexes in this work. Ammar Ibrahim and Ziqiao Xu helped with sample

preparation and synthesis. Dr. Charles C. L. McCrory provided significant insight and expertise in electroanalytic instruction and discussion, and provided help with writing and revising the manuscript.

3.2 Abstract

A series of Co complexes with bis(pyridylmonoimine)-based ligands with different degrees of structural flexibility have been prepared and studied for the electrocatalytic CO_2 reduction reaction to CO. First, electrochemical kinetic studies of the structurally-rigid [Co(L-L)] complex show that it undergoes a reductive dimerization upon reduction to the Co^I complex. This dimerization is facilitated by the planar geometry of the [Co(L-L)] complex. The dimer structure dissociates after reduction of the ligand, forming a monomer species that is active for CO_2 reduction. The reductive dimerization can be sterically prevented by either adding the strong axially-coordinating ligand such as triphenylphosphine (PPh_3), or by distorting the square planarity of the Co geometry by modulating the flexibility of the ligand scaffold. The more-flexible [Co(L-R-L)] complexes prevent catalyst dimerization and operate with more positive catalytic onset potentials for CO_2 reduction compared to the more rigid [Co(L-L)] complex, but operate with lower overall activity in the presence of a proton source. CO-binding and inhibition studies provide evidence that the lower activity for CO_2 reduction of the more flexible [Co(L-R-L)] complexes compared to [Co(L-L)] is due to CO poisoning because of the stronger binding affinity of the CO product to the flexible [Co(L-R-L)] complexes. This highlights an important trade-off in catalyst design for this class of molecular electrocatalysts: Co bis(pyridylmonoimine) complexes with higher degrees of structural flexibility prevent dimerization and shift the onset of CO_2 reduction catalysis to more positive potentials, but decrease the maximum activity due to CO product inhibition.

3.3 Introduction

The electrocatalytic CO_2 reduction reaction (CO_2RR) is a promising strategy for converting CO_2, an industrial waste product and environmental contaminant, into solar fuels and other value-added products.[1-8] Significant efforts have been devoted to the development of efficient catalysts for the CO_2RR. In particular, molecular electrocatalysts with redox-active ligands show promise for the selective conversion of CO_2 to single products,[9-18] and the activity and selectivity of these molecular catalysts can be tuned through synthetic modification of the ligand structure.[2, 13, 19-23] In particular, we have recently shown that a Co complex of bis(pyridylmonoimine) ligand, [Co(L-L)], is an efficient electrocatalyst for the reduction of CO_2 to CO with high activity in MeCN using high concentrations of H_2O or trifluoroethanol (TFE) as a proton source.[18] However, in the absence of a strong proton source, the [Co(L-L)] catalyzes the reduction of CO_2 to HCOOH with concurrent degradation of the complex. Based on previous studies of CO_2 interactions of a related Mo complex with a pyridylmonoimine ligand,[24] we propose that this catalyst degradation is due to an intramolecular H-abstraction from a $-CH_3$ group adjacent to the CO_2 adduct in the absence of sufficient proton source (Scheme 3.1).[18] Decomposition was evidenced by deposition of Co deposits on the electrode measured using SEM-EDX according to previously-reported protocols.[25]
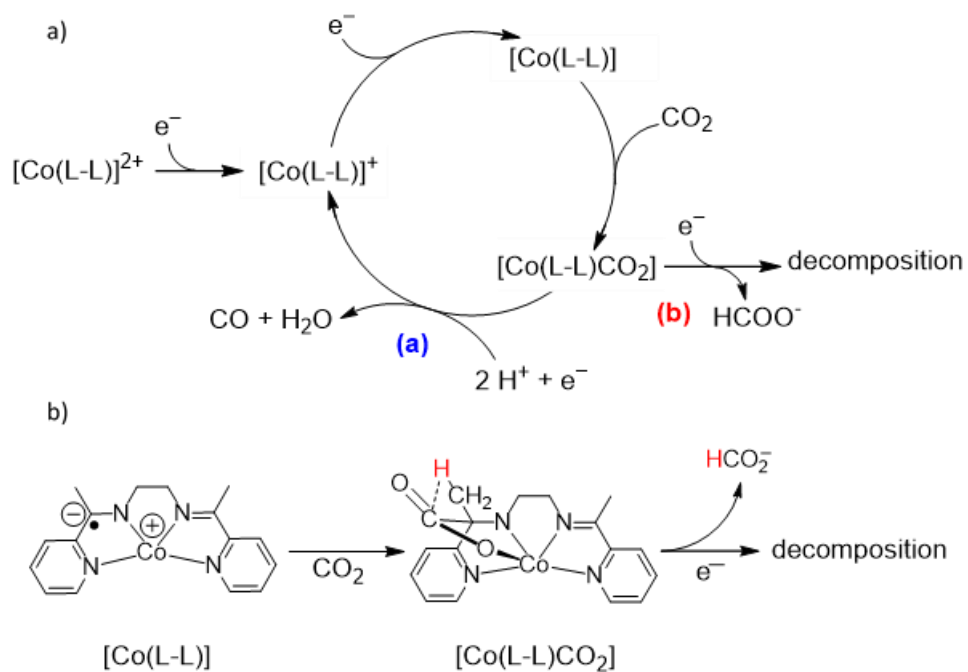
Scheme 3.1 a) Proposed catalytic mechanism of CO$_2$RR with [Co(L-L)]. b) Proposed decomposition process of the catalyst via intramolecular H-abstraction. [Nie, W. X.; McCrory, C. C. L. *Chem. Commun.*, **2018**, *54*, 1579-1582] – Adapted by permission of The Royal Society of Chemistry.

In this report, we use a combination of kinetic studies and systematic ligand modifications to further elucidate the mechanism of the CO_2RR by [Co(L-L)] and related complexes. First, we show that the [Co(L-L)] undergoes a reductive dimerization event upon reduction to the Co^I state ([Co^I(L-L)]$_2$), as evidenced by a decrease in the diffusion coefficient in two stepwise reduction processes of each ligand L-L to L-L$^{\bullet-}$ in [Co^I(L-L)]$_2$. After the reduction of both ligands, the dimer structure dissociates into two [Co^I(L-L$^{\bullet-}$)] monomer species which are the active species for the CO_2RR in the presence of water. We show that addition of the strongly-coordinating ligand triphenylphosphine (PPh$_3$) to the electrolyte solution prevents dimerization of [Co(L-L)], presumably due to axial coordination of the PPh$_3$ to the Co center, with negligible change to the observed activity for the CO_2RR. This suggests that even though dimerization occurs, the monomer [Co^I(L-L$^{\bullet-}$)] species is the active species for the CO_2RR.

To better determine the effect of [Co(L-L)] dimerization on CO_2RR activity, we systematically altered the flexibility of the ligand scaffold (Scheme 3.2a) based on the hypothesis that increased ligand flexibility will distort the square-planar geometry of the CoN$_4$ active site and prevent dimerization. In all complexes studied, the redox-active pyridylmonoimine subunits, which have been proposed to stabilize radical anions upon reduction (Scheme 3.2b) that facilitate multi-electron reduction of CO_2,[17-18, 24, 26] are connected by an aliphatic bridge forming [Co(L-R-L)] structures. Using a combination of electrochemical measurements, single crystal X-ray structures and DFT calculations, we show that increased ligand flexibility does distort the catalysts' planarity in a way that prevents reductive dimerization but does not affect the redox-active properties of the pyridylmonoimine moieties nor obviously influence the onset potentials for their non-catalytic redox couples. That makes this series of complexes effective models to study the effect of the complexes' planarity on catalyst dimerization and CO_2RR activity.

We demonstrate that the more flexible [Co(L-R-L)] complexes show no evidence of reductive dimerization as compared to the more rigid [Co(L-L)] structure. Moreover, we demonstrate that the more flexible [Co(L-R-L)] complexes show a more positive electrocatalytic onset potential for the CO_2RR compared to the more rigid [Co(L-L)], but operate with lower Faradaic efficiencies for CO in the presence of water without appreciable decomposition to Co deposits. We postulate that although the more flexible [Co(L-R-L)] catalysts seem to activate CO_2 more efficiently than [Co(L-L)], they are more likely to be poisoned by the CO generated during electrolysis which makes them less efficient for overall CO_2 reduction. This postulate is supported by experimental CO poisoning studies that show both stronger binding affinities for CO and increased CO inhibition of the CO_2RR by the more flexible [Co(L-R-L)] catalysts compared to the more rigid [Co(L-L)] system.

This work highlights an important trade-off between structure flexibility and catalytic activity for this class of square-planar Co complexes. More rigid square-planar complexes such as [Co(L-L)] are efficient for CO production, but show more negative catalytic onset compared to more flexible [Co(L-R-L)] complexes. Although the more-flexible [Co(L-R-L)] complexes prevent catalyst dimerization and show more positive catalytic onsets compared to the more rigid structures, they result in lower measured overall conversion due to CO poisoning. These studies highlight important design considerations regarding structure planarity for future CO_2RR catalysts based on putatively square-planar transition metal complexes with imine-based ligands.

a) [Co(L-R-L)]:

[Co(L-L)]

[Co(L-cyc-L)]

[Co(L-CH$_2$-L)]
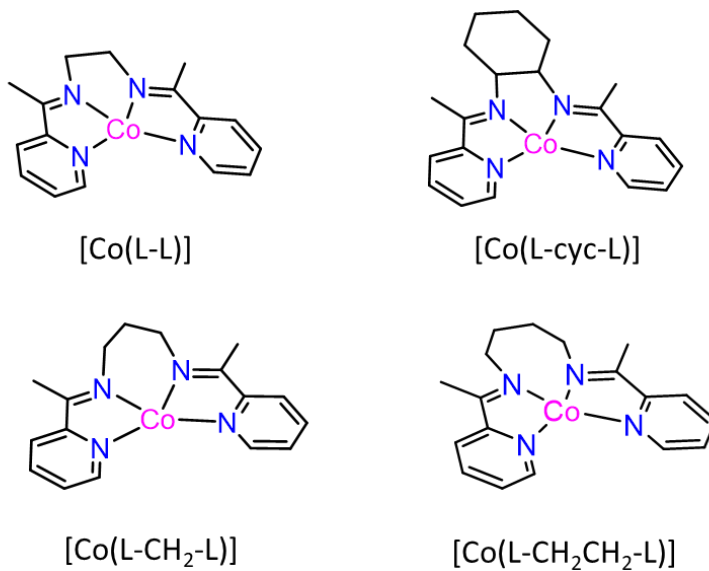
[Co(L-CH$_2$CH$_2$-L)]

b) Redox-active property of BPMI
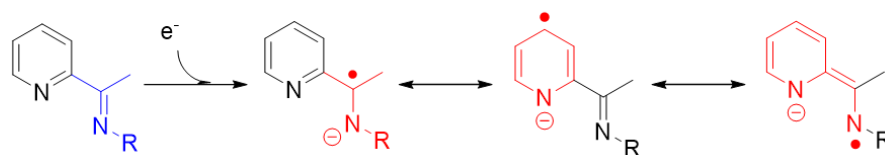
Scheme 3.2 a) Structure of [Co(L-R-L)] catalysts: [Co(L-L)], [Co(L-cyc-L)], [Co(L-CH2-L)] and [Co(L-CH2CH2-L)]; b) redox-active property of pyridylmonoimine moiety of L-R-L ligands

3.4 Experimental

3.4.1 Materials

Tetrabutylammonium hexafluorophosphate (nBu$_4$NPF$_6$, >98.0%) was purchased from TCI America and recrystallized from methanol/H$_2$O (v/v = 8/1) before use. Acetonitrile (MeCN, HPLC plus, $\geq$ 99.9%), and methanol (HPLC grade, $\geq$ 99.9%) were purchased from Sigma Aldrich and used without further purification. The typical water concentration in MeCN as received has been previously measured to be [H$_2$O] $\approx$ 0.04 M.[27] Ethanol (EtOH, 200 proof, anhydrous) was purchased from Decon Labs, Inc., and used without further purification. Cobalt bromide (CoBr$_2$, 99%), hydrogen bromide aqueous solutions (HBr(aq), ACS reagent, 48%), 2-propanol (i-PrOH, 99.9% for HPLC) and ethylenediamine ($\geq$ 99.5% GC) were purchased from Sigma Aldrich and used without further purification. 1,3-diaminopropane (98%) was purchased from Alfa Aesar and used without further purification. 2-acetylpyridine (99%) was purchased from Oakwood Chemical and used without further purification. Glacial acetic acid (HPLC grade, 99.7%) was purchased from Fisher scientific and used without further purification. All water used in this study was purified to 18.2 MΩ cm resistivity using a Thermo Scientific Barnstead^{TM} GenPure^{TM} UV-TOC/UF xCAD-plus water purification system. Nitrogen (N$_2$) was boil-off gas from a liquid nitrogen source. Carbon dioxide (CO$_2$, medical grade, > 99.0%) and Carbon Monoxide (CO, 99.5%) were purchased from Cryogenic Gases. All other chemicals were purchased from commercial sources, and all chemicals were used as received unless otherwise noted.

3.4.2 General Methods

NMR spectra were recorded on Varian MR-400 (400 MHz) spectrometers, and chemical shifts are reported in ppm relative to TMS standards. Elemental analyses were performed by Midwest Microlab, Inc. X-ray diffraction data was collected on a Rigaku AFC10K Saturn 944+ CCD-based X-ray diffractometer equipped with a low temperature device and Micromax-007HF Cu-target micro-focus rotating anode (l = 1.54187 A) operated at 1.2 kW power (40 kV, 30 mA). The X-ray intensities were measured at 85(1) K with the detector placed at a distance 42.00 mm from the crystal. The structure was solved by direct methods and refined on F^2 full-matrix least-squares using SHELXL-2018/1 (Sheldrick, 2018).[28] The hydrogen atoms positions are calculated. All atoms are refined anisotropically, except hydrogen atoms.

Geometry optimizations and single point energy evaluations were calculated by density functional theory (DFT) with BP86 functional using the Gaussian 16 package.[29] The 6-31G** basis sets were used for light atoms (C, H, O, N) and the LANL2DZ basis sets with pseudopotential were used for heavy atoms (Co, Br). All species were calculated with the lowest possible spin multiplicities.

3.4.3 Synthesis

Preparation of [Co(L-L)Br₂]Br. [Co(L-L)Br₂]Br was prepared as previously reported[18] according to the synthesis scheme shown in Scheme 3.3. ^{1}H NMR (Trifluoroacetic acid-d_1, 400 MHz): δ 9.44 (2H, d, *Ar*-H), δ 8.28 (2H, t, *Ar*-H), δ 8.14 (2H, d, *Ar*-H), δ 7.94 (2H, t, *Ar*-H), δ 4.81 (4H, s, CH₂), δ 2.92 (6H, s, CH₃). Anal. Calcd (found) for [Co(L-L)Br₂]Br ($C_{16}H_{18}N_4CoBr_3$): %C 34.01, (34.07); %H 3.21, (3.30); %N 9.92, (9.89).

Preparation of [Co(L-cyc-L)Br₂]Br. A scheme for the synthesis of [Co(L-cyc-L)Br₂]Br is shown in Scheme 3.4. A solution of 2-acetylpyridine (484.6 mg, 4.00 mmol) and ($\pm$)-*trans*-1,2-cyclohexanediamine (228.4 mg, 2.00 mmol) in 15 mL toluene with 20.0 *u*L acetic acid was stirred and refluxed with molecular sieves for 24 hours. After the mixture was allowed to cool to room temperature, the molecular sieves were separated by filtration and the organic solvent was removed by rotary-evaporation. The yellow residue was placed into a −4 ℃ refrigerator to yield a semi-solid crude product. The crude ligand L-cyc-L was recrystallized from 5 mL hexane to give light yellow crystals that were used for the next synthesis step without further purification.

A 5 mL ethanol solution of CoBr₂ (109.4 mg, 0.5 mmol) was added into a 5 mL ethanol solution of ligand L-cyc-L (160.2 mg, 0.5 mmol) with a 1:1 molar ratio under N₂ atmosphere. The mixture was stirred at 55 ℃ for 24 hours. After the mixture was allowed to cool to room temperature, the dark purple precipitate [Co(L-cyc-L)Br₂] was collected by filtration and then washed with cold ethanol three times. The [Co(L-cyc-L)Br₂] product was aerobically oxidized by suspending in ethanol with 1 equiv HBr(*aq*) and stirring overnight (18 h) under air, resulting in the green solid product [Co(L-cyc-L)Br₂]Br (126.5mg, 40.86% yield). ^{1}H NMR (CD₃OD-d_4, 400 MHz, Figure A.33): δ 9.65 (2H, d, *Py*-H), δ 8.41 (4H, d, *Py*-H), δ 8.05 (2H, m, *Py*-H), δ 3.09 (6H, s, CH₃), δ 2.19~1.78 (10H, m, CH₂). Anal. Calcd (found) for [Co(L-cyc-L)Br₂]Br,

($C_{20}H_{24}N_4CoBr_3$): %C 38.80, (39.02); %H 3.91, (3.89); %N 9.05, (8.97). The crystals suitable for X-ray single crystal diffraction measurement were obtained by the slow evaporation of the solvent of a [Co(L-cyc-L)Br$_2$]Br methanol solution in the air.

Preparation of [Co(L-CH₂-L)Br₂]Br. A scheme for the synthesis of [Co(L-CH$_2$-L)Br$_2$]Br is shown in Scheme 3.5. An 8.00 mL ethanol solution of CoBr$_2$ (218.8 mg, 1.0 mmol) was added into an 8 mL ethanol solution of 2-acetylpyridine (242.3 mg, 2.00 mmol) and 1,3-propylenediamine (74.1 mg, 1.0 mmol). The mixture was stirred at 55 ℃ for 24 hours. After the mixture was allowed to cool to room temperature, the brown precipitate [Co(L-CH$_2$-L)Br$_2$] was collected by filtration and then washed with cold ethanol three times. The [Co(L-CH$_2$-L)Br$_2$] product was aerobically oxidized by suspending in ethanol with 1 equiv HBr(*aq*) and stirring overnight (18 h) under air, resulting in the green solid product [Co(L-CH$_2$-L)Br$_2$]Br (253.0 mg, 43.70% yield). ^{1}H NMR (CD$_3$OD-d_4, 400 MHz, Figure A.34): δ 9.54 (2H, d, *Py*-H), δ 8.45~8.36 (4H, m, *Py*-H), δ 7.96 (2H, t, *Py*-H), δ 4.21 (4H, t, -N*CH₂*CH₂*CH₂*N-), δ 2.97 (6H, s, CH$_3$), δ 2.74 (2H, m, -NCH$_2$*CH₂*CH$_2$N-). Anal. Calcd (found) for [Co(L-CH$_2$-L)Br$_2$]Br, ($C_{17}H_{20}N_4CoBr_3$): %C 35.26, (35.08); %H 3.48, (3.54); %N 9.68, (9.76). The crystals suitable for X-ray single crystal diffraction measurement were obtained by the slow evaporation of the solvent of a [Co(L-CH$_2$-L)Br$_2$]Br- methanol solution in the air.

Preparation of [Co(L-CH₂CH₂-L)Br₂]Br. A scheme for the synthesis of [Co(L-CH$_2$CH$_2$-L)Br$_2$]Br is shown in Scheme 3.6. An 8.00 mL ethanol solution of CoBr$_2$ (218.8 mg, 1.0 mmol) was added into an 8 mL ethanol solution of 2-acetylpyridine (242.3 mg, 2.00 mmol) and 1,4-butanediamine (88.2 mg, 1.0 mmol). The mixture was stirred at 55 ℃ for 24 hours. After the mixture was allowed to cool to room temperature, the light brown precipitate [Co(L-CH$_2$CH$_2$-L)Br$_2$] was collected by filtration and then washed with cold ethanol three times. The [Co(L-

CH$_2$CH$_2$-L)Br$_2$] product was aerobically oxidized by suspending in ethanol with 1 equiv HBr(*aq*) and stirring overnight (18 h) under air, resulting in the dark solid product [Co(L-CH$_2$CH$_2$-L)Br$_2$]Br (320.2mg, 54.4% yield). ^{1}H NMR (CD$_3$OD-d_4, 400 MHz, Figure A.35): δ 10.10 (1H, m, *Py*-H), δ 8.51 (2H, m, *Py*-H), δ 8.36 (1H, m, *Py*-H), δ 8.25 (1H, m, *Py*-H), δ 8.06 (1H, m, *Py*-H), δ 7.57 (1H, m, *Py*-H), δ 7.18 (1H, m, *Py*-H), δ 5.87 (1H, m, -CH$_2$-), δ 4.56 (1H, m, -CH$_2$-), δ 4.16 (1H, m, -CH$_2$-), δ 3.09 (1H, s, CH$_3$), δ 3.02 (1H, m, -CH$_2$-), δ 2.83 (1H, s, CH$_3$), δ 2.72 (1H, m, -CH$_2$-), δ 2.15~2.11 (3H, m, -CH$_2$-). Anal. Calcd (found) for [Co(L-CH$_2$CH$_2$-L)Br$_2$]Br, (C$_{18}$H$_{22}$N$_4$CoBr$_3$): %C 36.46, (36.29); %H 3.74, (3.57); %N 9.45, (9.18).
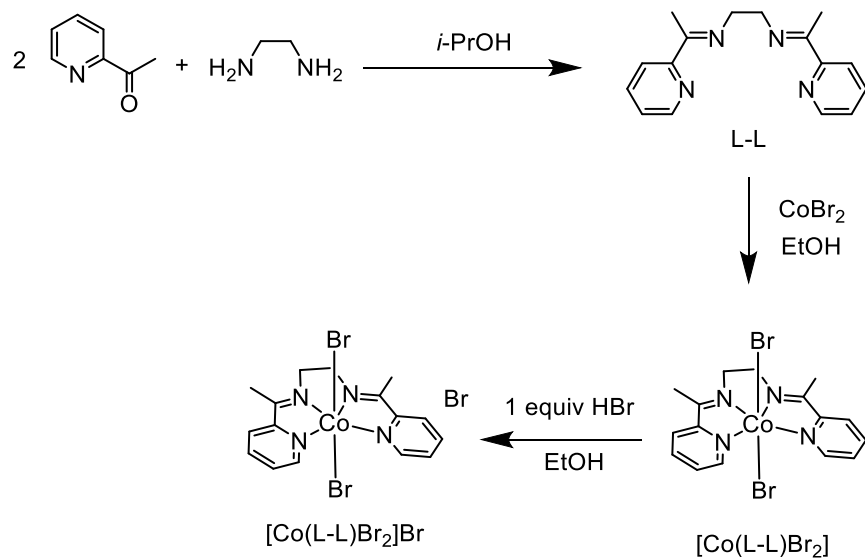
Scheme 3.3 Synthetic route for [Co(L-L)Br$_2$]Br
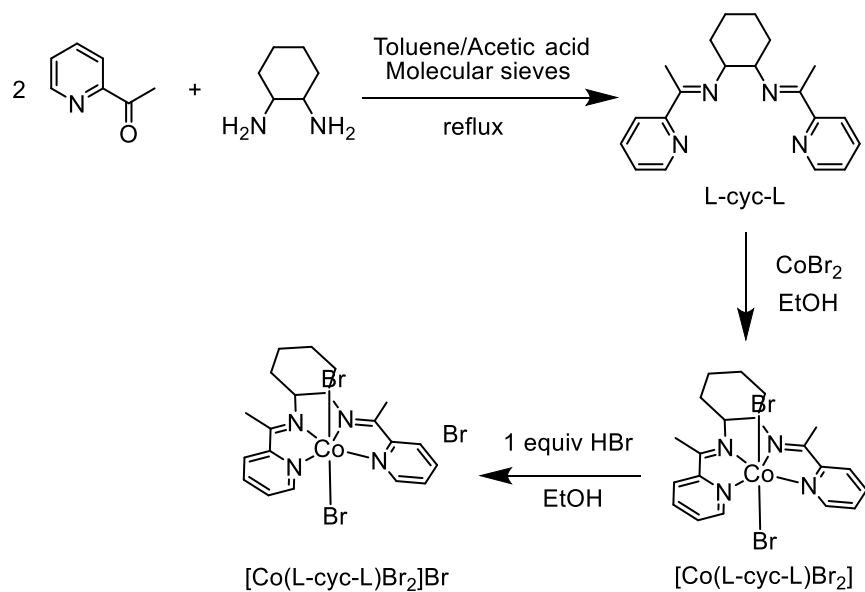
Scheme 3.4 Synthetic route for [Co(L-cyc-L)Br$_2$]Br
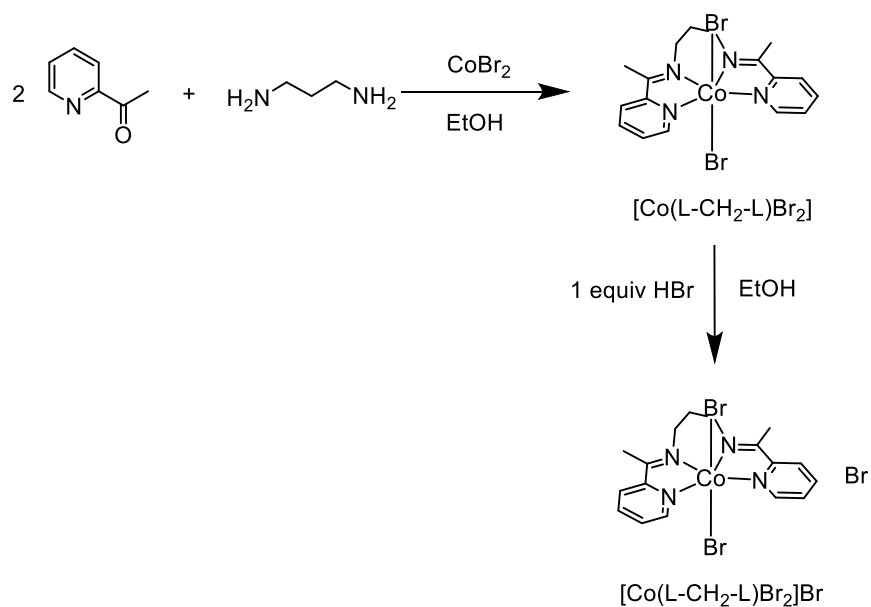
Scheme 3.5 Synthetic route for [Co(L-CH$_2$-L)Br$_2$]Br
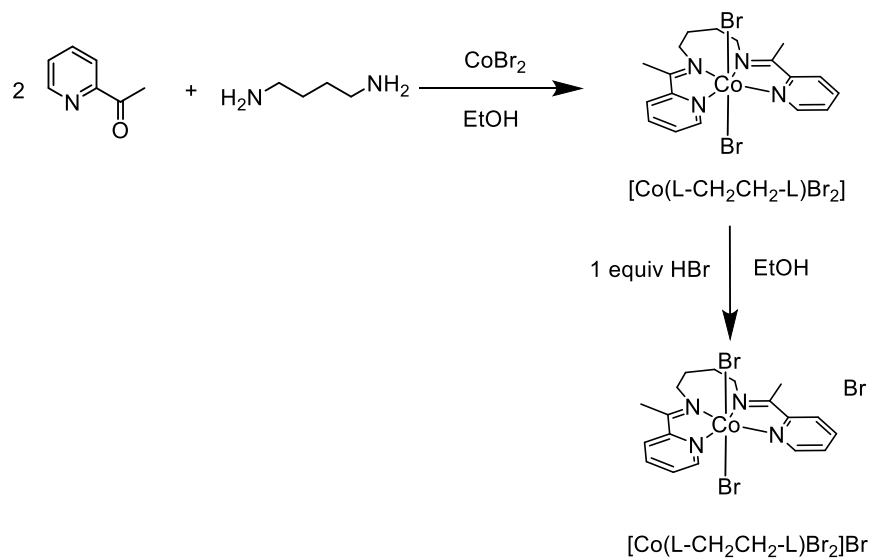
Scheme 3.6 Synthetic route for [Co(L-CH$_2$CH$_2$-L)Br$_2$]Br

3.4.4 Electrochemical Methods and Product Analysis

Electrochemical experiments were conducted using a Bio-Logic SP-200 potentiostat/galvanostat and data were recorded using the Bio-Logic EC-Lab V10.44 software package. In all measurements, the reference electrode was a Ag/AgNO$_3$ (1.0 mM)/MeCN (0.1 M nBu$_4$NPF$_6$) nonaqueous reference electrode separated from the solution by a CoralPor$^®$ glass frit (Bioanalytical Systems, Inc.) and externally referenced to the ferrocenium/ferrocene redox couple (Fc$^{+/0}$).

Cyclic Voltammetry (CV) under N$_2$, CO$_2$, and CO. Cyclic voltammograms were conducted using a 0.071 cm^2 glassy carbon disk working electrode (CH instruments) and carbon rod auxiliary electrode (99.999%, Strem Chemicals) in quiescent solution. Electrolyte solutions contained 0.1 M nBu$_4$NPF$_6$ in MeCN and added H$_2$O concentrations as reported in the results and discussion section. The typical scan rate for reported CVs was 0.050 V/s unless otherwise noted. Prior to each voltammogram, the electrolyte solution was sparged for at least 10 min with either N$_2$, CO$_2$, or CO as indicated, and the headspace was then blanketed with the same gas during the measurement. To prevent electrolyte evaporation, all gases were saturated with MeCN before use by first bubbling them through a gas-washing bottle filled with MeCN. Prior to each set of measurements, the uncompensated solution resistance (R$_u$) in the cell was measured using a single-point impedance measurement at 100 kH$_z$ with a 20 mV amplitude about the open-circuit potential. For a typical CV measurement, R$_u$ ≈ 120 Ω. CVs were automatically corrected for iR drop at 85% through positive feedback using the Bio-Logic EC-Lab software.

Rotating Disk Voltammetry (RDV) Measurements. Rotating Disk Voltammetries (RDVs) were conducted using a 0.1963 cm^2 glassy carbon disk working electrode (Sigradur-G grade, HTW Hochtemperatur-Werkstoffe GmbH) and carbon rod auxiliary electrode (99.999%, Strem

Chemicals) in MeCN solution under N_2. Working electrodes were used in combination with a Pine Research Instrumentation E6-series change-disk rotating disk electrode (RDE) assembly attached to a Pine Research Instrumentation MSR rotator. Other experimental conditions for RDVs are the same as those for cyclic voltammetry described above.

Cyclic Voltammetry (CV) under CO/N₂ and CO/CO₂ Gas Mixtures. In order to measure CO binding constants, dissociation constants and CO-inhibition of CO_2RR, cyclic voltammograms were conducted in electrolyte solutions sparged and then blanketed with CO/CO_2 and CO/N_2 gas mixtures. The electrodes, electrochemical cells, electrolyte solutions, scan rates, and iR-correction were identical to those reported above for CVs under single gases. The CO/N_2 gas mixtures were formed by bubbling CO and N_2 gases through a 500 mL gas-washing three-neck round-bottom flask filled with 200 mL MeCN. CO and N_2 gases flowed into the flask through two of the three necks and mixed in MeCN, and the well-mixed gas mixture in the headspace flowed out through the third neck. The partial pressure of CO in the gas mixture was modulated by changing the flow rate ratio of CO and N_2 via gas flow meters. In order to determine the accurate partial pressure of CO in CO/N_2 gas mixtures, the gas mixtures flowed through a second 500 mL empty three-neck round-bottom flask as a temporary gas storage tank where the gas could be sampled by a Pressure-Lok gas-tight syringe (10 mL, Valco VICI Precision Sampling, Inc.) and injected into a gas chromatography system to determine CO partial pressure (the total pressure of the gas mixtures was fixed at 1 atm). CO/CO_2 gas mixtures were prepared in an analogous fashion.

Controlled-Potential Electrolysis (CPE). The controlled-potential electrolysis experiments were conducted in the two-chamber H-cell shown in Figure A.36. The first, larger chamber held the working and reference electrodes and was filled with 20 mL solution of MeCN containing 0.3 mM catalyst, 0.1 M nBu₄NPF₆ and the concentrations of H_2O reported in the results

and discussion sections. The second chamber held the counter electrode in 15 mL solution of MeCN containing 5 mM Fc, 0.1 M nBu$_4$NPF$_6$, and the same concentration of H_2O as the first chamber. The two chambers were separated by a fine-porosity glass frit. The total volume of cell (149.56 mL) was determined by measuring the mass of H_2O necessary to completely fill the cell when the cell was fully assembled with the working and reference electrodes, and the headspace volume of 114.56 mL for the CPE was calculated by subtracting the electrolyte solution volume 35.00 mL from the total cell volume.

The working electrode was a 3.2 cm × 1.6 cm × 0.1 cm glassy carbon plate (HTW Hochtemperatur-Werkstoff GmbH) which was half immersed in the electrolyte solution. Prior to each experiment, the working electrode was first manually polished on 600-grit SiC polishing paper (Buehler, Ltd) and sonicated for 5 min in i-PrOH. The counter electrode was Nichrome wire (0.2595 Ω ft^{-1}, Arcor Electronics). Prior to each electrolysis experiment, the cell was purged with CO_2 or N_2 for 30 minutes and then sealed under an atmosphere of CO_2 or N_2. To prevent electrolyte evaporation, all gases were saturated with MeCN before use by first bubbling them through a gas-washing bottle filled with MeCN.

The CPE experiments were conducted with no iR compensation for solution resistance (Ru $\approx$ 60 Ω), and the reported electrolysis potentials are the actual applied potentials. After each electrolysis, a Pressure-Lok gas-tight syringe (10 mL, Valco VICI Precision Sampling, Inc.) was used to collect 5 mL aliquots of the headspace of the electrolysis cell, and the aliquots were injected into a 3 mL sample loop on a gas chromatography system to determine CO and H_2 concentrations. The post-electrolysis solution was analyzed using high performance liquid chromatography to determine the concentrations of C_1-C_3 liquid products including HCOOH. The Faradaic efficiency of every product was calculated by dividing the measured product concentrations by the amount

expected on the basis of charge passed during the CPE measurement. In general, the only products observed in measurable quantities (> 0.02 % v/v for GC and > 0.025 mM for HPLC) from our experiments were CO, H_2, and HCOOH.

To confirm the electrolysis cell was gastight, we conducted electrolysis experiments in N_2-sparged MeCN solutions of 1 M acetic acid for the hydrogen evolution reaction (HER). The working electrodes for these HER control experiments were either a Pt foil (0.1 mm thick, Premion^{TM}, 99.99% metals basis), or a 3.2 cm $\times$ 1.6 cm $\times$ 0.1 cm glassy carbon plate (HTW Hochtemperatur-Werkstoff GmbH) which was half immersed in the electrolyte solution. The Faradaic Efficiency for H_2 production as measured from the post-electrolysis headspace was ~100% (Table A.12), confirming that the electrolysis cell is gastight.

Product Analysis. Gaseous products (*i.e.* CO and H_2) in the headspace were measured using a Thermo Scientific Trace 1310 Gas Chromatograph (GC) with a single 3 mL sample loop leading to two analyzer channels. Using a valve system, column configuration, and method developed by Thermo Scientific and Custom Solutions Group LLC., gases were separated so that H_2 was detected on one channel using an Ar carrier gas, and all other gases were detected on a second channel using a He carrier gas. Gases were detected on both channels using thermal conductivity detectors (TCDs), and chromatographs were analyzed using Thermo Scientific Dionex Chromeleon^{TM} 7.2.2.6686 Chromatography Data System software.

Liquid samples of post-electrolysis solutions were analyzed for dissolved products such as formic acid using a Thermo Scientific Dionex Ultimate 3000 series HPLC equipped with a 5 cm Thermo Scientific HyperREZ XP Carbohydrate H$^+$ LC guard column and a 30 cm Thermo Scientific HyperREZ XP Carbohydrate H$^+$ 8µm LC analytical column in series. ~1 mL liquid samples were collected from the working-electrode chamber post electrolysis and placed in an

autosampler from which 10 μL aliquots of each liquid sample were injected into the columns. The eluent was 0.005 M H_2SO_4 aqueous solution at a flow rate of 0.6 mL·min^{-1}. The temperature of the column was maintained at 50 °C. Products were detected using a refractive index detector (RID) and a UV-Vis detector, and chromatographs were analyzed using Thermo Scientific Dionex Chromeleon^{TM} 7.2.2.6686 Chromatography Data System software.

Faradaic efficiencies were calculated by dividing the total number of moles of each product by the moles of electrons calculated from the amount of charge passed during the electrolysis normalized for the number of electrons required to produce each product.

3.4.5 Scanning Electron Microscopy/Energy Dispersive X-Ray Spectroscopy (SEM-EDS).

SEM-EDS measurements were used to look for evidence of metal nanoparticle deposits associated with catalyst decomposition. All electrodes tested by SEM-EDS (JEOL-7800FLV FE) were <u>not</u> rinsed post electrolysis as per established best practices.[25] SEM images showing the morphology of the electrode surface were recorded with a field emission gun scanning electron microscope at 20 kV acceleration voltage equipped with an energy dispersive X-ray (EDS) detector. For each electrode, SEM-EDS measurements were conducted at 3 random sites on the electrode surface, and the values were then averaged to give the Co weight % for that specific electrode. Each measurement in the manuscript was reproduced for electrodes after 3 independent electrolysis experiments. Therefore, each EDS measurement reported is an average of at least 9 measurements: 3 measurements each on 3 electrodes after independent electrolysis. Reported errors are standard deviations of all 9 EDS measurements for each electrolysis condition.

3.5 Results and Discussion

3.5.1 Synthesis and Structural Characterization of [Co(L-R-L)] complexes.

The [Co(L-R-L)] complexes investigated in this study (Scheme 3.2a) were synthesized by two methods depending on ligand flexibility. 1) The complexes [Co(L-L)Br$_2$]Br and [Co(L-cyc-L)Br$_2$]Br with comparatively rigid ligand scaffolds were prepared by first independently synthesizing the L-L and L-cyc-L ligands via a classic Schiff base condensation reaction of 2-acetylpyridine and the appropriate diamine reagents. This was followed by metalation with CoBr$_2$ in EtOH to precipitate [Co(L-L)Br$_2$] and [Co(L-cyc-L)Br$_2$]. The precipitates were stirred in HBr(aq) in EtOH under air for 18 h to afford the diamagnetic [Co(L-L)Br$_2$]Br and [Co(L-cyc-L)Br$_2$]Br structures (Schemes 3.3 and 3.4). 2) For the complexes [Co(L-CH$_2$-L)Br$_2$]Br and [Co(L-CH$_2$CH$_2$-L)Br$_2$]Br, the comparative ligand flexibility made it difficult to independently synthesize and purify the ligand. Instead, [Co(L-CH$_2$-L)Br$_2$] and [Co(L-CH$_2$CH$_2$-L)Br$_2$] were prepared by a one-pot synthesis in an EtOH solution of 2-acetylpyridine and related diamine reagents with CoBr$_2$ added as a templating agent. The resulting precipitates were stirred in HBr(aq) in EtOH in air for 18 h to afford the diamagnetic [Co(L-CH$_2$-L)Br$_2$]Br and [Co(L-CH$_2$CH$_2$-L)Br$_2$]Br structures (Schemes 3.5 and 3.6). [Co(L-L)Br$_2$]Br has been reported in our previous work[18] and all the other three [Co(L-R-L)Br$_2$]Br complexes were characterized by NMR (Figure A.33-A.35) and elemental analysis.

Single crystals of [Co(L-L)Br$_2$]Br, [Co(L-cyc-L)Br$_2$]Br and [Co(L-CH$_2$-L)Br$_2$]Br suitable for X-ray diffraction experiments were obtained from MeOH solutions via slow solvent evaporation. Note, the structure of [Co(L-L)Br$_2$]Br has been previously reported by our group.[18] All three complexes crystallized with a distorted square-bipyramidal configuration about the central Co atom (Figure 3.1, Table A.13) with the L-R-L ligands occupying the equatorial positions

in a slightly distorted square-planar geometry and the axial positions occupied by Br anions. The third Br counter anion sits outside the primary coordination sphere. Despite repeated attempts, a high-quality single crystal of $[Co(L-CH_2CH_2-L)Br_2]Br$ suitable for X-ray diffraction experiment was not collected. However, the optimized structure of $[Co(L-CH_2CH_2-L)Br_2]Br$ from DFT calculation shows the same general coordination geometry about Co (Figure A.37). Comparison of structural parameters of $[Co(L-R-L)Br_2]Br$ complexes from X-ray diffraction experimental data with those from DFT geometry optimizations of these structures show close correlation (Table A.14), suggesting that the DFT calculations in this study are accurate predictors of $[Co(L-R-L)]$ structure.

One key difference between the four Co(L-R-L) complexes is the square-planarity of the Co(L-R-L) unit as defined by the twist angle between the two pyridine planes. Of the $[Co(L-R-L)Br_2]Br$ complexes, $[Co(L-L)Br_2]Br$ has the most planar Co(L-R-L) unit with a twist angle of ~16.3º based on the XRD single crystal structure and ~10.6º based on the DFT calculations, whereas the Co(L-R-L) units from $[Co(L-cyc-L)Br_2]Br$, $[Co(L-CH_2-L)Br_2]Br$, and $[Co(L-CH_2CH_2-L)Br_2]Br$ show increasing twist angle (decreasing planarity) as the ligand flexibility increases across the series (Table 3.1). Because the active species for CO_2 reduction is thought to be the triply-reduced $[Co^+(L-R-L^{\bullet-})]$ species, we used DFT calculations to predict the twist angle of the triply-reduced $[Co^+(L-L^{\bullet-})]$, $[Co^+(L-cyc-L^{\bullet-})]$, $[Co^+(L-CH_2-L^{\bullet-})]$ and $[Co^+(L-CH_2CH_2-L^{\bullet-})]$ complexes (Figure A.38). The trends in twist angle are similar to those for the $[Co(L-R-L)Br_2]Br$ parent complexes, with the $[Co^+(L-L^{\bullet-})]$ having the most planar structure with the smallest twist angle of 24.8º, and $[Co^+(L-CH_2CH_2-L^{\bullet-})]$ having the least planar structure with the largest twist angle of 47.2º.
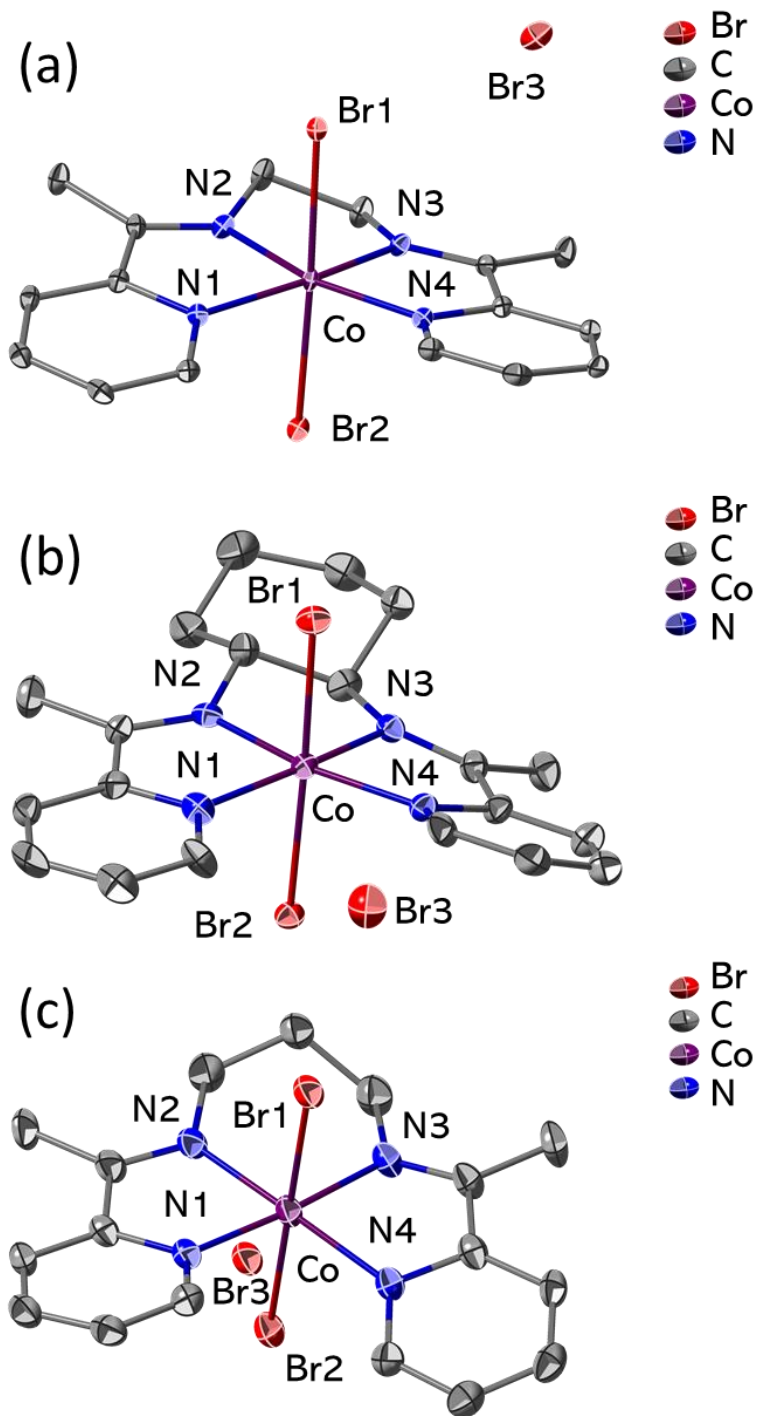
Figure 3.1 X-ray single crystal structures of (a) [Co(L-L)Br$_2$]Br, (b) [Co(L-cyc-L)Br$_2$]Br and (c) [Co(L-CH$_2$-L)Br$_2$]Br. Hydrogen atoms and co-crystallized solvent molecules are omitted for clarity.

Table 3.1 Twist angles between pyridyl planes of [Co(L-R-L)] complexes

Measurement Method	Twist angle between two pyridyl planes /°			
	[Co(L-L)Br$_2$]Br	[Co(L-cyc-L)Br$_2$]Br	[Co(L-CH$_2$-L)Br$_2$]Br	[Co(L-CH$_2$CH$_2$-L)Br$_2$]Br
X-ray	16.3	19.7	21.2	-[a]
DFT	10.6	24.4	30.2	31.5
	[Co$^+$(L-L$^{•-}$)]	[Co$^+$(L-cyc-L$^{•-}$)]	[Co$^+$(L-CH$_2$-L$^{•-}$)]	[Co$^+$(L-CH$_2$CH$_2$-L$^{•-}$)]
DFT	24.8	31.7	40.1	47.2

[a]We were unable to collect X-ray single crystal structure data for [Co(L-CH$_2$CH$_2$-L)Br$_2$]Br

3.5.2 Cyclic Voltammetry in N$_2$-saturated Solutions

CVs of [Co(L-L)Br$_2$]Br, [Co(L-cyc-L)Br$_2$]Br, [Co(L-CH$_2$-L)Br$_2$]Br and [Co(L-CH$_2$CH$_2$-L)Br$_2$]Br recorded in N$_2$-saturated MeCN solution with 0.1 M nBu$_4$NPF$_6$ as supporting electrolyte are shown in Figure 3.2. Note that all CVs have been *iR* compensated as discussed in the experimental section and all potentials are referenced versus Fc$^{+/0}$. [Co(L-cyc-L)Br$_2$]Br, [Co(L-CH$_2$-L)Br$_2$]Br and [Co(L-CH$_2$CH$_2$-L)Br$_2$]Br display four distinct redox couples which we assign, from the most positive to negative potential, to the Co$^{3+/2+}$, Co$^{2+/+}$, L-R-L/L-R-L$^{\bullet-}$ and Co$^{+/0}$ redox processes with the $E_{1/2}$ values summarized in Table 3.2.

The potential of the Co$^{3+/2+}$ redox couples shift positive with increasing ligand flexibility from −0.34 V vs Fc$^{+/0}$ for [Co(L-L)] to −0.12 V vs Fc$^{+/0}$ for [Co(L-CH$_2$CH$_2$-L)], while the potential of the Co$^{2+/+}$ couple shows the opposite trend and shifts negative from −0.94 V vs Fc$^{+/0}$ for [Co(L-L)] to −1.19 V vs Fc$^{+/0}$ for [Co(L-CH$_2$CH$_2$-L)]. This suggests that the changes in the coordination geometry observed with increasing ligand flexibility influence the electronic structure of the Co center and modulate the associated Co redox potentials. However, the potential associated with the ligand-based reduction at ca. −1.60 V vs Fc$^{+/0}$ does not change appreciably with increasing ligand flexibility for [Co(L-cyc-L)], [Co(L-CH$_2$-L)], and [Co(L-CH$_2$CH$_2$-L)], suggesting that the aliphatic bridge has very small effect on the electronic structure of the redox-active pyridylmonoimine moieties.

Unlike [Co(L-cyc-L)Br$_2$]Br, [Co(L-CH$_2$-L)Br$_2$]Br and [Co(L-CH$_2$CH$_2$-L)Br$_2$]Br which display one reversible redox peak associated with ligand reduction, [Co(L-L)Br$_2$]Br displays two stepwise reduction peaks. The more-positive ligand reduction peak (−1.42 V vs Fc$^{+/0}$) has an associated oxidation peak at −1.36 V vs Fc$^{+/0}$ and the more-negative reduction peak (−1.66 V vs Fc$^{+/0}$) has a much smaller associated oxidation feature at *ca.* −1.60 V vs Fc$^{+/0}$. Note that the sum

of the peak areas of the ligand reduction peaks is approximately equal to the sum of the peak areas

of the ligand oxidation peaks, suggesting that the reduction and oxidation features are associated

with each other.
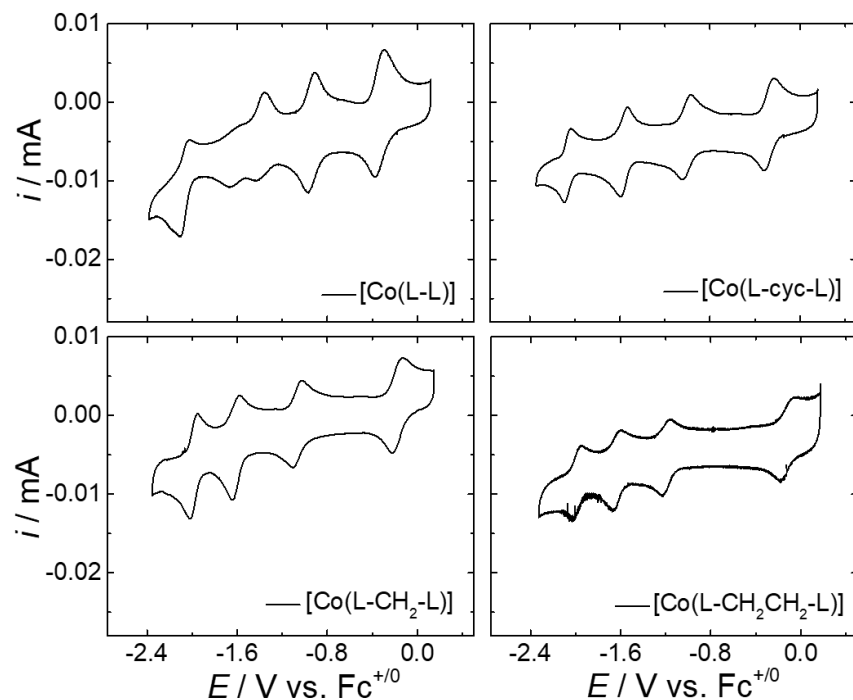
Figure 3.2 CVs of 0.3 mM [Co(L-L)Br$_2$]Br, [Co(L-cyc-L)Br$_2$]Br, [Co(L-CH$_2$-L)Br$_2$]Br and [Co(L-CH$_2$CH$_2$-L)Br$_2$]Br in MeCN with 0.1 M nBu$_4$NPF$_6$ under N$_2$.

Table 3.2 $E_{1/2}$ of redox processes for [Co(L-R-L)Br$_2$]Br catalysts.

Catalyst	$E_{1/2}(\text{Co}^{3+}/\text{Co}^{2+})^a$	$E_{1/2}(\text{Co}^{2+}/\text{Co}^+)^a$	$E_{1/2}(\text{L-R-L}/\text{L-R-L}^{\bullet-})$	$E_{1/2}(\text{Co}^+/\text{Co}^0)^a$
[Co(L-L)]^b	−0.34 V	−0.94 V	Ox^b: −1.36 V, ~ −1.60 V Red^b: −1.42 V, −1.66 V	−2.07 V
[Co(L-cyc-L)]	−0.27 V	−1.00 V	−1.56 V	−2.04 V
[Co(L-CH$_2$-L)]	−0.18 V	−1.06 V	−1.61 V	−1.99 V
[Co(L-CH$_2$CH$_2$-L)]	−0.12 V	−1.19 V	−1.64 V	−1.99 V

^{a} All potentials reported vs vs Fc$^{+/0}$. ^{b}The potentials of two oxidation features (Ox) and associated reduction peaks (Red) are listed

for L-R-L/L-R-L$^{\bullet-}$ process of [Co(L-L)] instead of $E_{1/2}$ values. This is because the relatively small size of the second oxidation

feature makes it difficult to accurately measure the peak potential, complicating determination of $E_{1/2}$ values.

Previous studies have suggested that redox peak splitting similar to that observed for the ligand-centered redox features in [Co(L-L)] may be evidence of catalyst dimerization.[30-31] We hypothesize that such a dimerization is occuring in our system, and each of the sequential reductions in the ligand-centered redox features corresponds to reduction of ½ of each dimer as shown in Scheme 3.7a. If this hypothesis is correct, then there are two important electrochemical implications. First, because each ligand-based reduction only effects ½ of each dimer, the effective concentration of [Co(L-L)] units participating in each ligand-based reduction step is ½ of the total bulk concentration. Second, the diffusion coefficient of the electrochemically-generated dimer species will have a smaller diffusion coefficient due to its larger hydrodynamic radius. To experimentally test for dimerization, we determined the observed diffusion coefficeint, D_{obs}, of the electroactive species associated with each redox couple based on the assumption that the concentration of electroactive species is equal to the bulk concentration of [Co(L-R-L)Br$_2$]Br in solution. Note that the D_{obs} reported in this study are not necessarily *actual* diffusion coefficients of the electroactive species, but rather an electrochemically-derived parameter that is a suitable indicator of change of effective concentration and/or diffusion coefficient. A smaller measured D_{obs} is consistent with a combination of both decreased effective concentration and decreased diffusion coefficient, and thus is consistent with a dimerization event. We measured D_{obs} of [Co(L-L)Br$_2$]Br and the other [Co(L-R-L)Br$_2$]Br complexes at each redox potential using two complimentary but distinct electrochemical methods.
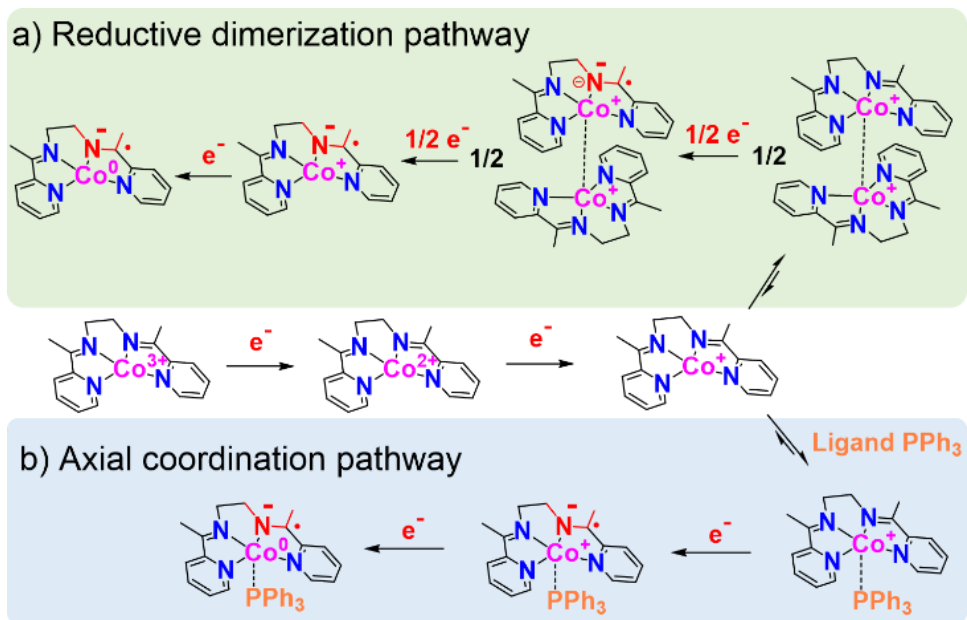
Scheme 3.7 The proposed structures of [Co(L-L)] species at each redox potential for (a) reductive dimerization pathway and (b) axial coordination pathway. Note that in (a) the dashed line between the Co centers is not meant to invoke Co-Co bonding in the dimer species, but rather is meant to illustrate only intermolecular interaction between the two complexes which could occur at the Co sites, the ligands, or some combination of Co and ligand.

First, we determined D_{obs} from non-catalytic CVs by measuring the peak current for each redox couple as a function of scan rate. Representative CVs at different scan rates for [Co(L-L)Br$_2$]Br are shown in Figure 3.3 and for the other [Co(L-R-L)Br$_2$]Br complexes in Figures A.39-A.41. For reversible redox processes for diffusing species, the scan-rate dependent cathodic peak current, i_p, is related to the diffusion coefficient by the Randles-Sevcik equation (Equation 1):[32-33]

$$i_p = 0.446 n^{3/2} AC \left(\frac{\upsilon F^3 D_{obs}}{RT} \right)^{1/2} \qquad \text{Eq. 1}$$

Here, diffusion coefficient is expressed as D_{obs} based on the assumption that the effective concentration of electroactive species at each redox potential, C, is equal to the bulk concentration of [Co(L-R-L)Br$_2$]Br in solution. $n = 1$ is the number of electrons transferred for each redox event, $A = 0.0707$ cm^2 is the surface area of the electrode, $C = 3 \times 10^{-7}$ mol/cm^3 is the bulk concentration of [Co(L-R-L)Br$_2$]Br in solution, $T = 298$ K is the temperature, R is the ideal gas constant, F is Faraday's constant, and υ is the scan rate in units of V·s^{-1}. Representative plots of i_p as a function of $\upsilon^{1/2}$ for the Co$^{3+/2+}$, Co$^{2+/+}$, L-L$^{0/-}$, and Co$^{+/0}$ reduction peaks for [Co(L-L)Br$_2$]Br are shown in Figure 3.4 and for the other [Co(L-R-L)Br$_2$]Br complexes in Figures A.42-A.44. The D_{obs} values of the complexes at each redox couple were determined from the slope of the linear plots using Equation 1, and the results are summarized in Table 3.3.
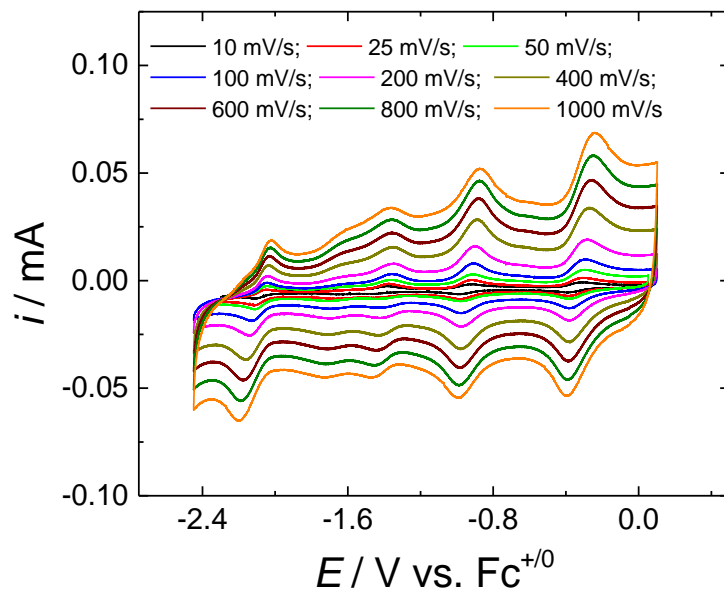
Figure 3.3 CVs of 0.3 mM [Co(L-L)Br$_2$]Br at different scan rates in MeCN with 0.1 M nBu$_4$NPF$_6$ under N$_2$
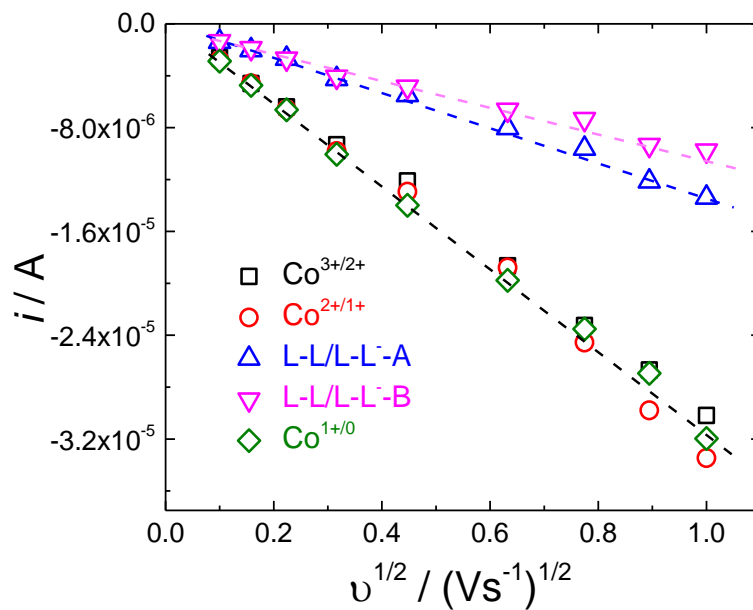
Figure 3.4 Representative plots of i_p as a function of $v^{1/2}$ for the Co$^{3+/2+}$, Co$^{2+/+}$, L-L$^{0/-}$, and Co$^{+/0}$ reduction peaks for [Co(L-L)Br$_2$]Br based on the Randles-Sevcik equation.

110

Table 3.3 D_{obs} values measured at different redox peak potentials of [Co(L-R-L)] catalysts.

Catalyst	$D_{obs(Co^{3+/2+})}$ 10^{-5} cm^2 s^{-1}	$D_{obs(Co^{2+/+})}$ 10^{-5} cm^2 s^{-1}	$D_{obs(L-R-L^{0/-})}$ 10^{-5} cm^2 s^{-1}		$D_{obs(Co^{+/0})}$ 10^{-5} cm^2 s^{-1}
[Co(L-L)]	2.01 ± 0.61^a	2.16 ± 0.98^a	0.34 ± 0.15^a	0.22 ± 0.05^a	1.83 ± 0.84^a
	1.61 ± 0.56 ^{b}	1.74 ± 0.54^b	0.99 ± 0.30^b	0.72 ± 0.20^b	1.49 ± 0.56^b
[Co(L-cyc-L)]	0.76 ± 0.17^a	0.39 ± 0.10^a	0.52 ± 0.03^a		0.48 ± 0.10^a
	1.23 ± 0.26^b	1.27 ± 0.22^b	1.25 ± 0.36^b		1.08 ± 0.36^b
[Co(L-CH$_2$-L)]	1.17 ± 0.18^a	0.87 ± 0.19^a	1.13 ± 0.12^a		1.35 ± 0.13^a
	1.62 ± 0.27 ^{b}	1.59 ± 0.22 ^{b}	1.67 ± 0.44 ^{b}		1.76 ± 0.30^b
[Co(L-CH$_2$CH$_2$-L)]	0.86 ± 0.07^a	0.64 ± 0.04 ^{a}	0.91 ± 0.11^a		0.89 ± 0.13^a
	1.29 ± 0.11 ^{b}	1.34 ± 0.21 ^{b}	1.36 ± 0.31 ^{b}		1.69 ± 0.29^b
[Co(L-L)] with 2 equiv. PPh$_3$	1.68 ± 0.29^a	1.65 ± 0.35^a	1.76 ± 0.32^a		1.78 ± 0.42^a
	1.33 ± 0.25 ^{b}	1.39 ± 0.79^b	1.68 ± 0.41^b		2.05 ± 0.15^b

D_{obs} values are averages from at least three independent sets of measurements and are reported with standard deviations.

[a]Determined from cyclic voltammetry measurements. [b]Determined from rotating disk voltammetry measurements

We also determined D_{obs} using rotating disk voltammetry (RDV) by measuring the rotation-rate dependence of the reduction plateau currents near each potential of interest. Representative RDVs at different rotation rates for [Co(L-L)Br$_2$]Br are shown in Figure 3.5 and for the other [Co(L-R-L)Br$_2$]Br complexes in Figures A.45-A.47. The plateau currents, i_L, are related to the diffusion coefficient by the Levich equation (Equation 2):[34-35]

$$i_L = 0.62nFAD_{obs}^{2/3}v^{-1/6}C\omega^{1/2} \qquad \text{Eq. 2}$$

Here, diffusion coefficient is expressed as D_{obs} based on the assumption that the effective concentration of electroactive species at each redox potential, C, is equal to the bulk concentration of [Co(L-R-L)Br$_2$]Br in solution. $n = 1$ is the number of electrons transferred for each redox event, $A = 0.1963$ cm^2 is the surface area of the electrode, F is Faraday's constant, $v = 0.00448$ cm^2/s is the kinematic viscosity of the electrolyte solution, $C = 3 \times 10^{-7}$ mol/cm^3 is the bulk concentration of [Co(L-R-L)Br$_2$]Br in solution, and ω is the angular momentum in units of s^{-1} calculated from the rotation rate (in rotations per minute, rpm) according to Equation 3:

$$\omega = \frac{2\pi \times rpm}{60} \quad \text{Eq. 3.}$$

Representative Levich plots of i_L as a function of $\omega^{1/2}$ at potentials just negative of the Co$^{3+/2+}$, Co$^{2+/+}$, L-L$^{0/-}$, and Co$^{+/0}$ couple for [Co(L-L)Br$_2$]Br are shown in Figure 3.6 and for the other [Co(L-R-L)Br$_2$]Br complexes in Figures A.48-A.50. The diffusion coefficients of the complexes at each redox couple were determined from the slope of the linear Levich plots using Equation 2, and the results are summarized in Table 3.3.
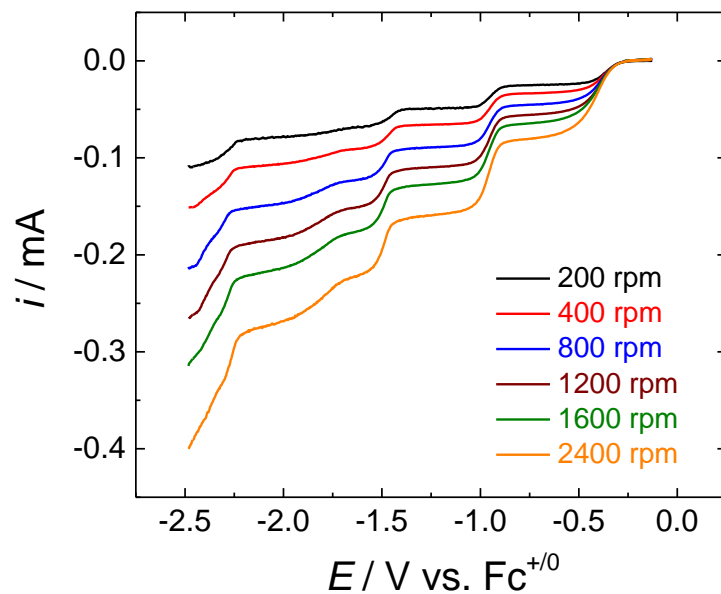
Figure 3.5 Rotating disk voltammograms (RDVs) of 0.3 mM [Co(L-L)Br$_2$]Br at different rotation rates in MeCN with 0.1 M *n*Bu$_4$NPF$_6$ under N$_2$.
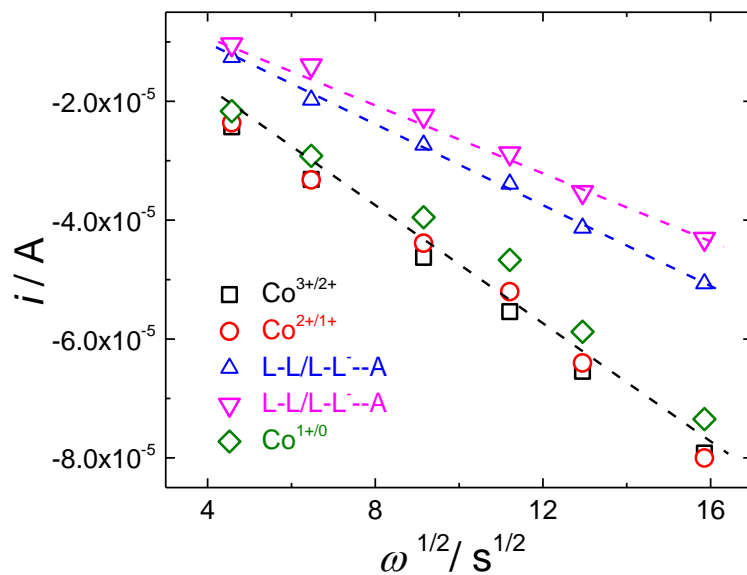
Figure 3.6 Representative plots of i_L as a function of $\omega^{1/2}$ at potentials just negative of the Co$^{3+/2+}$, Co$^{2+/+}$, L-L$^{0/-}$, and Co$^{+/0}$ couple for [Co(L-L)Br$_2$]Br based on the Levich equation.

The D_{obs} values of the complexes determined by the two different methods show consistent trends which lends credibility to the qualitative validity of these measurements. In the case of [Co(L-L)], both cyclic voltammetry measurements and rotating disk voltammetry measurements show a significant decrease in D_{obs} values associated with L-L/L-L$^{\bullet-}$ couples compared to $Co^{3+/2+}$, $Co^{2+/+}$ and $Co^{+/0}$ couples. This observed decrease of D_{obs} at stepwise ligand-based redox couples supports our hypothesis of a reductive dimerization event upon reduction to the Co^+ state as shown in Scheme 3.7a. The larger D_{obs} associated with the $Co^{+/0}$ couple compared to the L-L/L-L$^{\bullet-}$ suggests that upon full reduction of the ligands in the dimer, the resulting $[Co^+(L-L^{\bullet-})]_2$ dissociates back into two monomer species.

Note that due to the complexity of the dimerization process and the necessary convolution of concentration, mass transport, and electron transfer in the Randles-Sevcik and Levich equation, there are alternative choices for electrochemically-determined parameters that could be chosen to reflect potential-dependent changes in mass transport and effective concentration. In particular, the combination ($n^{3/2}CD^{1/2}$) in Randles-Sevcik equation and ($nCD^{2/3}$) in Levich equation are alternative parameters to D_{obs} that should reflect the same trends without the necessity of making assumptions regarding effective concentration. Based on this consideration, ($n^{3/2}CD^{1/2}$) and ($nCD^{2/3}$) of [Co(L-L)] at each redox couple are calculated and summarized in Table A.15. Both parameters have decreased values at the ligand-based redox couples, consistent with the dimerization mechanism proposed in Scheme 3.7a.

To provide additional support for our proposed dimerization pathway, we added a strongly-coordinating ligand, triphenylphosphine (PPh$_3$), to the system. Our hypothesis was that a strongly-coordinating ligand like PPh$_3$ would axially coordinate to the Co center in [Co(L-L)] and sterically prevent dimerization. Upon addition of sufficient concentrations of PPh$_3$ to the electrolyte solution,

114

we see a gradual merging of the two stepwise ligand-based redox features into one reversible redox process (Figure A.51). In the presence of 2 equivalent of PPh$_3$, the ligand-based redox feature is fully merged into one reversible couple with $E_{1/2}$(L-L/L-L$^{\bullet-}$) = −1.62 V vs Fc$^{+/0}$ which is more negative than the first ligand-based redox couple potential (~−1.42 V vs Fc$^{+/0}$) in the dimer structure (Figure 3.7). There is also a positive shift in the Co$^{2+/+}$ redox couple to $E_{1/2}$(Co$^{2+/+}$) = −0.82 V vs Fc$^{+/0}$ compared to $E_{1/2}$(Co$^{2+/+}$) = −0.94 V vs Fc$^{+/0}$ in the case of no PPh$_3$ added (Figure 7). Both the changes of ligand-based redox features and the potential shift of Co$^{2+/+}$ couple support that adding PPh$_3$ results in axial coordination of PPh$_3$ to the Co center, and this axial coordination prevents dimerization. Moreover, when 2 equivalents of PPh$_3$ are present in the electrolyte solution, the *D* values determined from both scan rate dependence cyclic voltammetry measurements (Figure A.52, A.53) and rotating disk voltammetry measurements (Figure A.54, A.55) for each redox couple are similar (Table 3.3). These results measured in the presence of PPh$_3$ are consistent with the prevention of [Co(L-L)] reductive dimerization due to the putative coordination of PPh$_3$ to the metal center (Scheme 3.7b), which in turn supports the proposed dimerization pathway of [Co$^+$(L-L)] in the absence of an axial coordination ligand (Scheme 3.7a).

Note that the other [Co(L-R-L)Br$_2$]Br complexes besides [Co(L-L)Br$_2$]Br show no evidence of reductive dimerization based on their electrochemically-determined diffusion coefficients as seen in Table 3.3. This suggests that the more-flexible L-R-L ligands also prevent dimerization, presumably due to the decreased square-planarity of the [Co(L-R-L)] units in their structures.
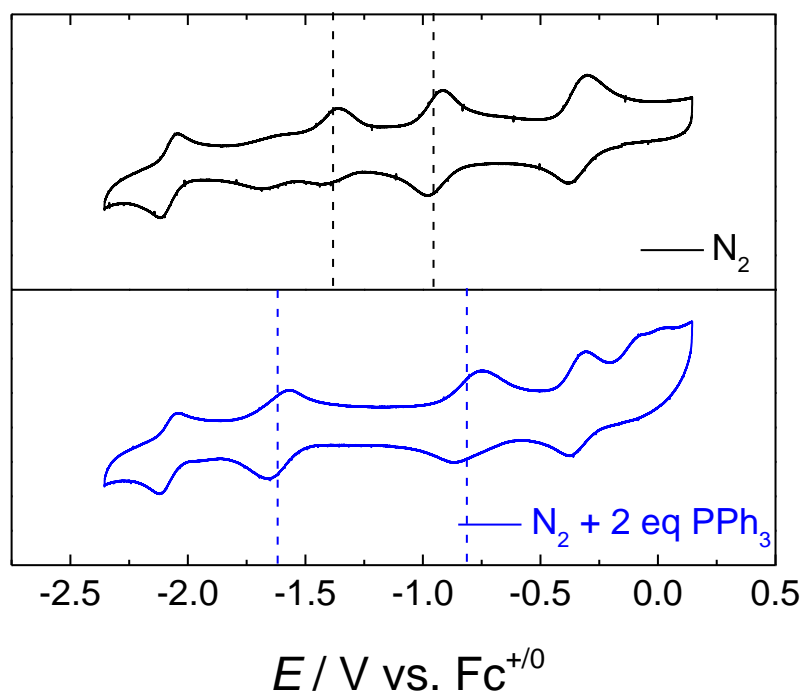
Figure 3.7 The comparison of CVs of 0.3 mM [Co(L-L)Br$_2$]Br with and without 2 equivalent of PPh$_3$ in MeCN with 0.1 M nBu$_4$NPF$_6$ under N$_2$

3.5.3 Electrocatalytic Activity in CO_2-containing Solutions.

CVs of all [Co(L-R-L)] complexes in CO_2-saturated MeCN solutions are shown in Figure 3.8. For all complexes, there is an increase in the magnitude of the reductive current near the L-R-L/L-R-L$^{•-}$ couple consistent with catalytic turnover, suggesting that the [Co$^+$(L-R-L)$^{•-}$] species are the active species for CO_2 reduction. Although [Co(L-L)] exists as a dimer structure at L-L/L-L$^{•-}$ redox couple, the catalytic current under CO_2 is of the same intensity as that in the presence of 2 equivalents of PPh$_3$ under CO_2 (Figure A.56, A.57), indicating that the active species for CO_2 reduction is likely the monomer [Co$^+$(L-L)$^{•-}$] rather than the dimer species. Based on the CVs, we define the catalytic peak current, i_p, as the maximum current in the catalytic peak at the peak potential E_p, and the catalytic onset potential, E_{onset} as the intersection point between the linear extrapolations of the rising portion of the catalytic current and the baseline current (see Figure A.58). For each [Co(L-R-L)] complex, i_p for CO_2 reduction are all roughly the same magnitude, although E_{onset} and E_p occur at more positive potentials for the [Co(L-R-L)] complexes with more flexible ligands (Table 3.4). Note that there is a ~0.3 V shift in E_{onset} to more negative potentials as a function of scan rate for [Co(L-L)], and the extent of this shift is appreciably larger than that observed for the other [Co(L-R-L)] complexes (Figure A.59, A.60 and Table A.16). This is qualitatively consistent with the proposed existence of a slow dimer dissociation event preceding catalytic onset of CO_2 reduction in the case of [Co(L-L)] that is not observed for the [Co(L-R-L)] complexes with more flexible ligands.
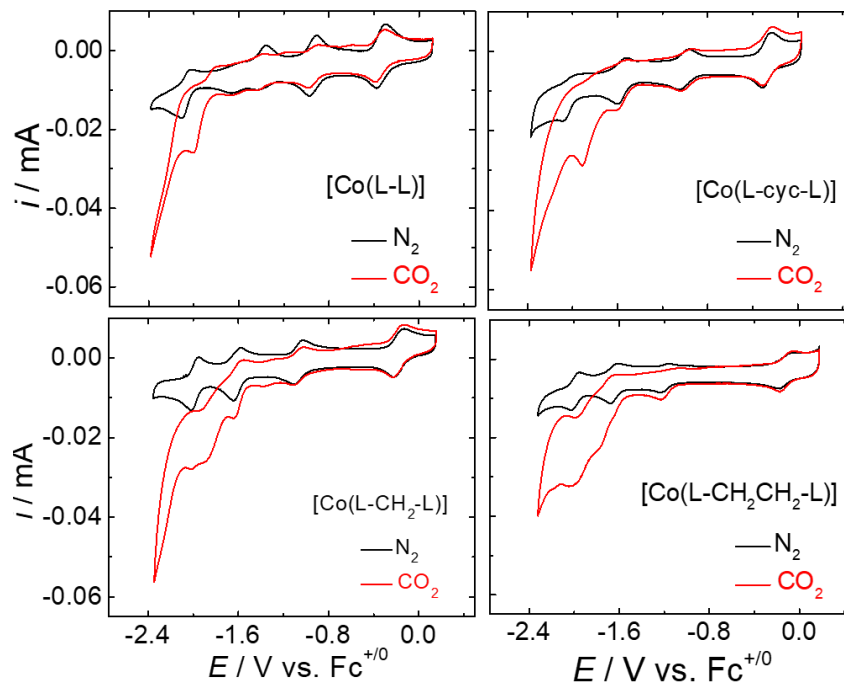
Figure 3.8 CVs for 0.3 mM [Co(L-R-L)] in MeCN solutions with 0.1 M nBu$_4$NPF$_6$ under N$_2$ and CO$_2$ at 0.05 V/s scan rate.

Table 3.4 E_{onset}, E_p, and i_p for [Co(L-R-L)] complexes based on the CVs in Figure 3.8.

Catalysts	E_{onset}^a / V	E_p / V	i_p / mA
[Co(L-L)]	−1.86	−2.00	−0.026
[Co(L-cyc-L)]	−1.63	−1.91	−0.029
[Co(L-CH$_2$-L)]	−1.59	−1.90	−0.027
[Co(L-CH$_2$CH$_2$-L)]	−1.53	−1.96	−0.032

^{a} E_{onset} is determined based on the definition and method in Figure A.58.

We have previously reported that electrocatalytic activity and stability of $[Co(L\text{-}L)Br_2]Br$ for the CO_2RR is significantly enhanced in the presence of large concentrations of H_2O which acts as a proton source.[18] Adding H_2O into the CO_2-saturated electrolyte solutions for each $[Co(L\text{-}R\text{-}L)]$ complex leads to a measurable increase in the magnitude of the catalytic current (Figure 3.9 for 5.5 M H_2O, Figures A.61-A.63 for other H_2O concentrations). However, the extent of the increase in the magnitude of catalytic peak current is significantly larger for $[Co(L\text{-}L)]$ compared to the other $[Co(L\text{-}R\text{-}L)]$ complexes with more-flexible ligands, and the total magnitude catalytic current for $[Co(L\text{-}L)]$ is significantly larger than those of the other $[Co(L\text{-}R\text{-}L)]$ complexes. Kinetic isotope effect (KIE) studies of the CO_2RR showed no appreciable attenuation of catalytic activity upon replacing 5.5 M H_2O with 5.5 M D_2O for any of the catalyst investigated as shown in Figure 3.9, suggesting that the rate determining step of the catalytic mechanism does not involve a formal proton-transfer event.[36-39]
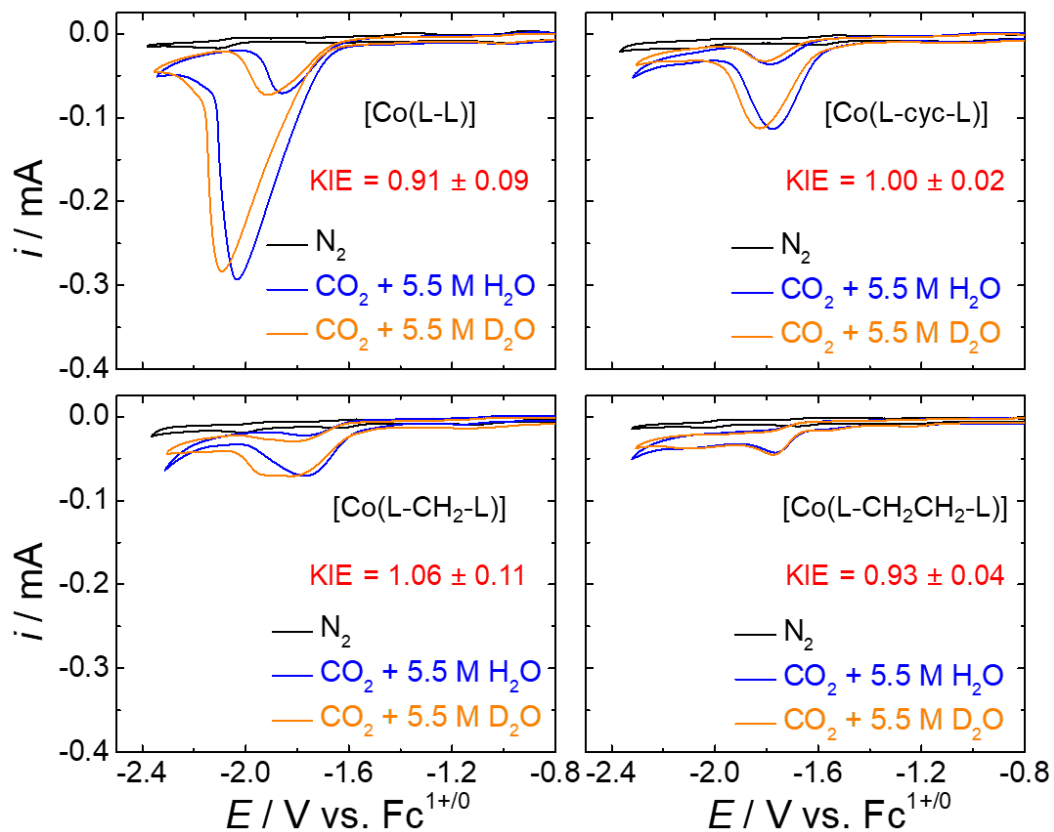
Figure 3.9 CVs and KIE studies of all [Co(L-R-L)] complexes in MeCN solutions (with 0.1 M nBu$_4$NPF$_6$) in the presence of 5.5 M H$_2$O and D$_2$O under CO$_2$.

Product distributions from the electrocatalytic CO_2RR by [Co(L-cyc-L)], [Co(L-CH_2-L)] and [Co(L-CH_2CH_2-L)] were determined from 30-min controlled-potential electrolysis (CPEs) experiments. CPEs were conducted in electrolyte solutions with varying concentrations of added H_2O up to 11.0 M at an applied potential (E_{app}) of -1.95 V vs $Fc^{+/0}$, the approximate E_p for CO_2 reduction by [Co(L-L)] in a solution containing 5.5 M H_2O as shown in Figure 3.9.[18] Note that CPE experiments for the [Co(L-R-L)] complexes in solutions containing 11.0 M H_2O were conducted at two additional applied potentials: 1) E_p for the specific [Co(L-R-L)] catalyst as shown in Figure 3.9; and 2) an *iR*-corrected potential ($E_p - iR$) where R is estimated at 60 Ω and *i* was estimated from the average current measured during the electrolysis at E_p. The headspace and liquid electrolyte were sampled post-electrolysis and analyzed by GC and HPLC, respectively. Faradaic efficiencies were calculated based on the amount of products measured in the samples. After each electrolysis, the working electrode was removed from the solution without rinsing and investigated for solid-state metal deposits using SEM-EDS according to established best practices.[25] Turnover frequencies (TOFs) for CO_2RR products were calculated based on CPE results by two methods: dividing the total amount of CO_2RR products (CO and HCOOH) (1) by the catalyst amount in bulk solution in 30 minutes (TOF-A) and (2) by the catalyst amount in the reaction-diffusion layer near the electrode surface (TOF-B)[40-41] (see Section A.2.3 for further discussion of TOFs). Results from these CPE experiments and determined TOF-B values for [Co(L-cyc-L)], [Co(L-CH_2-L)] and [Co(L-CH_2CH_2-L)] are shown in Table 3.5 and Table 3.6, respectively, along with previously-reported data of [Co(L-L)] for comparison.[18]

Note that although we determine TOF-A for each catalyst investigated in this study because such measurements are historically included in electrocatalytic studies, it is a less useful measure of catalytic activity than TOF-B. This is because it does not estimate the rate of catalyst transport

to the electrode surface and therefore significantly underestimates catalytic activity.[40-42] This also means that TOF-A depends on the configuration of the electrolysis cell, and so while it can be used for comparisons within a research lab, it is not as accurate for activity comparisons between groups. Therefore, for the purpose of discussion we will refer only to TOF-B as our primary metric of comparison, although we do report TOF-A in the Table S6 in the supporting information. Note that the same qualitative trends observed for TOF-B are consistent with those observed for TOF-A as expected.

Table 3.5 Conditions and product analysis of the controlled potential electrolysis for CO_2 reduction

Catalyst	E_{app} / V vs Fc$^{+/0}$	[H_2O] / M	Q / C	Faradaic efficiency / %			Co weight% on electrode from EDS [g]
				CO	H_2	HCOOH	
[Co(L-L)][a]	-1.95 (E_p)[e]	~0.04[b]	2.2 ± 0.3	2.8 ± 2.6	−[c]	6.3 ± 2.6	0.52 ± 0.46%
		1.10	3.4 ± 0.4	16.3 ± 5.1	−[c]	4.5 ± 1.1	−[d]
		5.50	7.9 ± 0.7	67.0 ± 11.0	0.3 ± 0.1	1.9 ± 0.5	−[d]
		11.0	8.3 ± 0.9	80.5 ± 4.7	1.1 ± 0.5	0.7 ± 0.2	0.35 ± 0.26%
	-2.15 ($E_p − iR$)[f]	11.0	16.2 ± 2.5	104.3 ± 5.5	0.6 ± 0.4	−[c]	0.18 ± 0.16%
[Co(L-cyc-L)]	-1.95	~0.04[b]	4.3 ± 0.4	1.6 ± 0.5	−[c]	22.6 ± 6.0	0.09 ± 0.01%
		1.10	3.4 ± 0.3	21.0 ± 0.4	−[c]	5.9 ± 1.7	0.28 ± 0.12%
		5.50	4.3 ± 0.4	21.8 ± 2.0	6.9 ± 3.8	1.7 ± 1.2	0.34 + 0.01%
		11.0	6.0 ± 0.2	11.1 ± 2.6	34.3 ± 4.7	−[c]	1.14 ± 0.40%
	-1.77 (E_p)[e]	11.0	5.0 ± 1.1	4.9 ± 4.5	4.9 ± 2.8	0.2 ± 0.1	1.06 ± 0.92%
	-1.93 ($E_p − iR$)[f]	11.0	6.4 ± 0.4	5.6 ± 1.0	19.6 ± 3.6	0.4 ± 0.3	0.99± 0.59%
[Co(L-CH$_2$-L)]	-1.95	~0.04[b]	3.0 ± 0.9	5.1 ± 1.1	−[c]	13.9 ± 1.6	0.08 ± 0.01%
		1.10	5.2 ± 0.8	20.4 ± 12.8	−[c]	7.1 ± 1.4	0.10 ± 0.02%
		5.50	7.5 ± 0.9	41.9 ± 3.1	0.6 ± 0.1	5.4 ± 0.9	0.06 ± 0.01%
		11.0	6.1 ± 0.5	51.5 ± 8.4	1.6 ± 1.8	1.8 ± 1.4	0.05 ± 0.05%
	-1.77 (E_p)[e]	11.0	4.9 ± 0.5	31.5 ± 9.0	−[c]	2.2 ± 1.0	0.08 ± 0.07%
	-1.93 ($E_p − iR$)[f]	11.0	5.5 ± 0.2	51.2 ± 8.6	1.0 ± 0.7	1.1 ± 1.0	0.05 ± 0.05%
[Co(L-CH$_2$CH$_2$-L)]	-1.95	~0.04[b]	3.1 ± 0.7	3.5 ± 2.4	−[c]	8.0 ± 2.4	0.19 ± 0.08%
		1.10	4.2 ± 0.2	17.4 ± 3.9	−[c]	5.8 ± 2.2	0.10 ± 0.04%
		5.50	6.5 ± 0.8	25.5 ± 6.7	0.7 ± 1.0	3.5 ± 1.9	0.21 ± 0.07%
		11.0	6.1 ± 0.9	31.2 ± 2.5	27.9 ± 13.4	1.8 ± 0.9	0.33 ± 0.01%
	-1.75 (E_p)[e]	11.0	4.4 ± 1.0	12.5 ± 2.0	1.6 ± 1.1	0.5 ± 0.4	0.56 ± 0.34%
	-1.89 ($E_p − iR$)[f]	11.0	5.6 ± 0.6	28.6 ± 9.2	9.1 ± 4.6	1.1 ± 0.9	0.31± 0.23%

All values for Q and Faradaic efficiencies are averages from at least three independent electrolysis using freshly prepared electrolytes, catalyst solutions and freshly-polished working electrodes. Reported errors are standard deviations from at least three independent measurements. [a]Data from Reference 18. [b]These solutions contained no added H_2O. The estimated ~0.04 M water is based on Karl-Fischer titrations of similar grade MeCN as previously reported.[27] [c] "–" means that no product was detected within the detection limit of the GC (> 0.02 % v/v) or HPLC (> 0.025 mM). [d] "–" means no measurement was conducted. [e]E_p is the catalytic peak potential from CV measurements. [f](E_p - iR) is the Ohmic drop corrected catalytic peak potential. [g]Each Co weight % is an average of 9 EDS measurements: 3 measurements each on 3 electrodes from independent electrolysis experiments. Reported errors are standard deviations of all 9 EDS measurements for each electrolysis experiment.

Table 3.6 TOFs of Co catalysts for CO_2RR calculated based on CPE results

Catalyst	E_{app} / V vs. $Fc^{+/0}$	$[H_2O]$ / M	TOF-B[b] / s^{-1}
[Co(L-L)][c]	−1.95	~0.04[a]	0.13 ± 0.08
		1.10	1.7 ± 0.8
		5.50	78.4 ± 31.6
		11.0	142.0 ± 35.2
	−2.15 ($E_p − iR$)	11.0	903.5 ± 297.6
[Co(L-cyc-L)]	−1.95	~0.04[a]	12.7 ± 4.8
		1.10	10.3 ± 2.7
		5.50	12.0 ± 3.3
		11.0	5.6 ± 2.7
	−1.93 ($E_p − iR$)	11.0	1.7 ± 0.6
[Co(L-CH$_2$-L)]	−1.95	~0.04[a]	1.5 ± 0.8
		1.10	12.7 ± 3.2
		5.50	52.7 ± 9.3
		11.0	43.7 ± 8.8
	−1.93 ($E_p − iR$)	11.0	36.6 ± 9.5
[Co(L-CH$_2$CH$_2$-L)]	−1.95	~0.04[a]	0.8 ± 0.4
		1.10	6.0 ± 1.5
		5.50	21.5 ± 4.6
		11.0	25.8 ± 6.2
	−1.89 ($E_p − iR$)	11.0	17.1 ± 6.9

[a]These solutions contained no added H_2O. The estimated ~0.04 M water is based on Karl-Fischer titrations of similar grade MeCN as previously reported.[27] [b]Calculated by dividing the total amount of CO_2RR products by the estimated catalyst amount in the reaction-diffusion layer near the electrode surface.[40, 43]

For CPEs conducted with no added proton source (~0.04 M H_2O), we previously reported that solutions containing [Co(L-L)Br$_2$]Br turned turbid after 30 mins electrolysis and produced small amounts (FE < 10 %) of CO and HCOOH.[18] This observed turbidity and low Faradaic efficiency was attributed to catalyst decomposition as demonstrated by the relatively large amount of Co deposited on the electrode surface post-electrolysis determined by SEM-EDS (Figure A.64). However, in the cases of [Co(L-cyc-L)], [Co(L-CH$_2$-L)], and [Co(L-CH$_2$CH$_2$-L)], we see increased production of CO and HCOOH (FE > 10% combined) in the absence of added proton source with higher TOF values for CO$_2$RR products compared to [Co(L-L)], though the total Faradaic efficiency is significantly below 100%. In addition, there is significantly less Co deposited onto the post-electrolysis electrode surface under these conditions with no added proton source for the [Co(L-cyc-L)], [Co(L-CH$_2$-L)], and [Co(L-CH$_2$CH$_2$-L)] complexes than [Co(L-L)] (Figure A.65-A.67). This suggests that catalysts with more flexible ligands show both improved catalytic activity and increased stability under CO$_2$RR conditions at low concentrations of proton-source. Note that no deposited Co is observed when the catalysts are dissolved in electrolyte solutions at open-circuit (with no applied bias), further supporting that any observed Co deposits are due to an electrochemical Co degradation (Table A.17, Figures A.68-A.71).

At high concentrations of H_2O = 11.0 M and an applied potential of −1.95 V vs Fc$^{+/0}$, [Co(L-L)] shows significantly improved electrocatalytic activity to produced CO as the predominant product compared to low concentrations of H_2O,[18] as evidenced by both a ~4-fold increase in charge passed and ~1000-fold increase in TOF-B for CO$_2$RR production (Table 3.6) compared to the activity in presence of no added proton source. In the cases of [Co(L-cyc-L)], [Co(L-CH$_2$-L)], and [Co(L-CH$_2$CH$_2$-L)], there is a smaller ~2-fold increase of charge passed during the CPE experiments for CO$_2$RR in the presence of 11.0 M H_2O at an applied potential of

−1.95 V vs Fc$^{+/0}$, along with a general decrease in the Faradaic efficiency for HCOOH and an increase for CO as a function of increasing H_2O concentration. However, the catalytic activity of all these three complexes for CO_2RR at high concentration of H_2O (11.0 M) is unexpectedly much lower than that of [Co(L-L)] based on TOF-B values for CO_2RR (Table 3.6). Note that CPE experiments conducted at (E_p−iR) for [Co(L-cyc-L)], [Co(L-CH$_2$-L)], and [Co(L-CH$_2$CH$_2$-L)] show qualitatively similar activity and Faradaic Efficiency compared to those conducted at −1.95 V vs Fc$^{+/0}$.

For [Co(L-cyc-L)], no increase of TOF values are observed as more H_2O is added. Instead, the TOF values in the case of 11.0 M H_2O (TOF-B: 5.6 s^{-1}) are even smaller than those at ~0.04 M H_2O (TOF-B: 12.7 s^{-1}). This suggests the catalyst [Co(L-cyc-L)] may be decomposing during electrocatalytic turnover in the presence of significant concentrations of H_2O, which is also supported by significant increase of Co deposition on the electrode surface (Figure A.73).

For [Co(L-CH$_2$CH$_2$-L)], the result of CPEs shows slightly increased TOF values as a function of increasing H_2O concentration (Table 3.6). However, an slight increase in the amount of deposited Co on the surface (Table 3.5) indicates that the catalyst [Co(L-CH$_2$CH$_2$-L)] may be decomposing during the electrolysis as more H_2O is added. Note that, in both CPEs of [Co(L-cyc-L)] and [Co(L-CH$_2$CH$_2$-L)], appreciable H_2 production is observed in solutions containing 11.0 M H_2O (Table 3.5). Control experiments conducted with the post-electrolysis electrode and the bare glassy carbon electrode in fresh CO_2-saturated electrolyte in the presence of 11.0 M H_2O but with no Co complex present (Table A.18) shows the similar Faradaic efficiency for H_2 evolution, suggesting that H_2 production is due to the activity of the glassy carbon electrode rather than the deposited Co on the surface.

In the case of [Co(L-CH$_2$-L)], CPEs conducted at 11.0 M H$_2$O show ~50% Faradaic efficiency for CO with no appreciable H$_2$ or HCOOH formed. The comparatively small amount of Co deposited on the electrode suggests that there is not significant decomposition of the catalyst to electrodeposited Co during the electrolysis measurements. Nevertheless, the measured TOF values do not significantly increase with increasing H$_2$O as expected, and the total Faradaic efficiency of all products by [Co(L-CH$_2$-L)] remains below 100%. We take these results to suggest that an alternative deactivation process not associated with catalyst degradation may be responsible for the lower activity and Faradaic efficiency for CO$_2$RR. We suggest one such process to explain catalyst deactivation may be poisoning of the catalyst by electrogenerated CO. This postulated CO poisoning is consistent with time-dependent CPE measurements (Table A.19) that show larger Faradaic efficiencies for CO for shorter-time electrolyses (15-30 min) and significantly decreased Faradaic efficiencies for longer-time electrolyses (90 min) where this is more electrogenerated CO that can inhibit the CO$_2$RR. However, increased catalyst degradation during longer-time electrolyses also influences the observed Faradaic efficiencies, and so additional CO-inhibition studies were conducted as described below.

3.5.4 CO-inhibition of the CO₂RR

Previous studies have suggested that CoN_4 macrocyclic complexes tend to coordinate CO strongly, and this strong coordination can lead to inhibition of electrocatalytic processes.[15, 27] This is important to consider in the case of CO_2 reduction by [Co(L-R-L)] complexes in the presence of the proton source H_2O because CO is the primary product. Moreover, we observe a low overall Faradaic efficiency for the CO₂RR of [Co(L-cyc-L)], [Co(L-CH₂-L)], and [Co(L-CH₂CH₂-L)] even at high concentrations of H_2O, but no observable degradation in the case of [Co(L-CH₂-L)] and relatively little degradation in the case of [Co(L-CH₂CH₂-L)]. One possible explanation for this loss of activity could be catalyst deactivation due to CO coordination and inhibition. For this reason, we explored the electrochemistry of [Co(L-R-L)] catalysts in the presence of CO under both non-catalytic and catalytic conditions.

The non-catalytic CVs of all [Co(L-R-L)] catalysts in the CO saturated MeCN solutions are shown in Figure 3.10. The catalysts' respective non-catalytic CVs under N_2 are included in the figure for comparison. For all four [Co(L-R-L)] catalysts, the potential of the $Co^{3+/2+}$ couple is constant under both CO and N_2, indicating CO does not coordinate to the Co center in the Co^{3+} or Co^{2+} complexes (Scheme 3.8a). However, there is a positive shift of the $Co^{2+/1+}$ redox potential of all [Co(L-R-L)] catalysts under CO which is consistent with a Nernstian shift due to CO coordination upon reduction of the Co^{2+} complexes to the Co^+ complexes as shown in Scheme 3.8b.[27, 44-46] Note that there is very little shift in the L-R-L/L-R-L·⁻ redox potential for any of the [Co(L-R-L)] catalysts which strongly suggests that 1) CO coordination to the metal center has only a slight effect on the electronic structure of the L-R-L ligand, and 2) there is no CO coordination/association step coupled to this ligand-based redox process (Scheme 3.8c). In addition, the extent of electrochemical reversibility decreases for all of the redox couples of [Co(L-

cyc-L)], [Co(L-CH$_2$-L)] and [Co(L-CH$_2$CH$_2$-L)] negative of the Co$^{2+/+}$ couples, and a new oxidation feature for [Co(L-CH$_2$-L)] and [Co(L-CH$_2$CH$_2$-L)] appears at ca. -0.35 V vs. Fc$^{+/0}$. All of these observations are consistent with the coordination of CO to [Co(L-cyc-L)], [Co(L-CH$_2$-L)] and [Co(L-CH$_2$CH$_2$-L)] upon reduction to the Co$^+$ oxidation state to form a stable [Co$^+$(CO)(L-R-L)] complex as shown in Scheme 3.8b. In contrast, no new oxidative feature is observed in the CV of [Co(L-L)] under CO and all redox couples of [Co(L-L)] remain reversible except the Co$^{1+/0}$ couple which shows a broad reduction peak with a slightly smaller oxidation speak. This provides qualitative evidence that CO coordination to [Co(L-L)] is comparably weaker than the other three Co complexes. Note that for [Co(L-L)] under CO, only one L-L/L-L$^{\bullet-}$ redox feature is present, as opposed to two measured under N$_2$, suggesting that reductive coordination of CO to the [Co$^+$(L-L)] prevents dimerization analogous to the PPh$_3$ case.
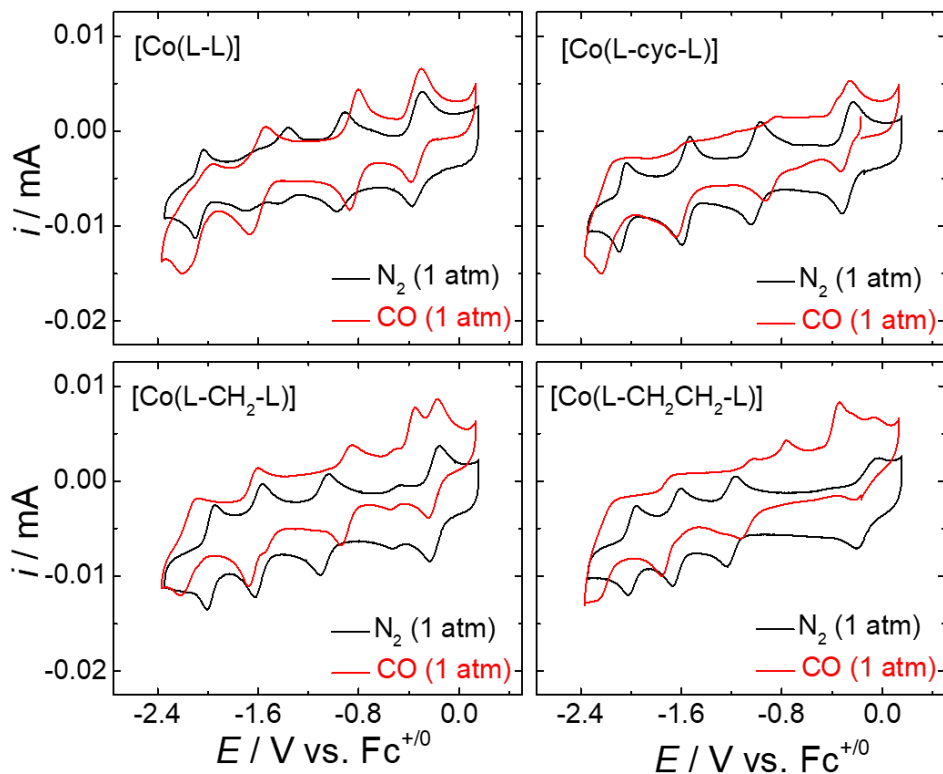
Figure 3.10 The non-catalytic CVs of all [Co(L-R-L)] catalysts in the CO saturated MeCN solutions along with non-catalytic CVs under N_2 for comparison.
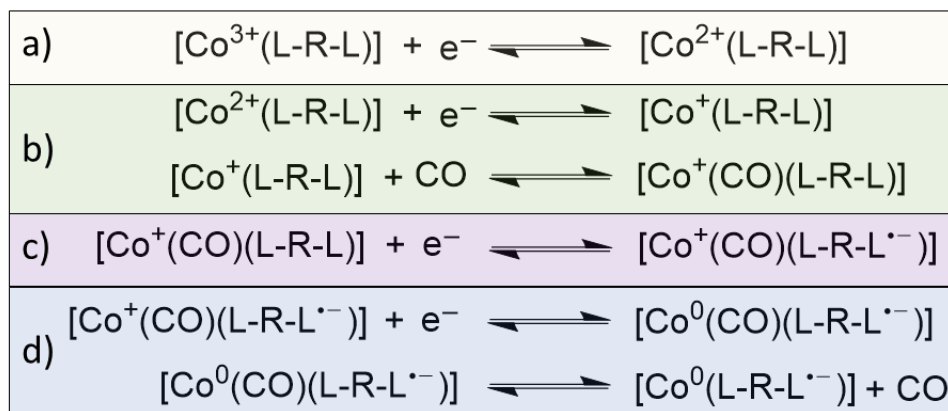
Scheme 3.8 Proposed steps in the electrochemical reduction of [Co^{3+}(L-R-L)] in the presence of CO based on the non-catalytic CVs showing a) the initial reduction of the Co^{3+} to Co^{2+} complex, b) the reductive CO coordination event, c) the ligand reduction event, and d) the reductive CO dissociation steps.

Our qualitative assessments of Figure 3.10 discussed above suggest that the all four [Co(L-R-L)] complexes reductively coordinate CO upon reduction to the Co^+ oxidation state, but that [Co(L-L)] does so with a lower CO-binding affinity compared to the other three [Co(L-R-L)] catalysts with more flexible structures. To quantitatively address these trends, we determined the CO-binding equilibrium constant, K_{CO}, for each [Co(L-R-L)] catalyst (Equation 3) by measuring the extent of the Nernstian potential shift in $E_{1/2}(Co^{2+/+})$ as a function of CO concentration in the electrolyte solution as shown in Equation 4.[27]

$$K_{CO} = \frac{c([Co^+(CO)(L-R-L)])}{c([Co^+(L-R-L)]) \times c(CO)} \qquad \text{Eq 3}$$

$$E_{1/2}^{CO}(Co^{2+/+}) - E_{1/2}^{N_2}(Co^{2+/+}) = \frac{RT}{nF}\ln(1 + c(CO)K_{CO}) \quad \text{Eq 4}$$

Here K_{CO} is the CO binding equilibrium constant; $c([Co^+(CO)(L-R-L)])$ and $c([Co^+(L-R-L)])$ are the concentrations of Co-CO adduct species and [Co$^+$(L-R-L)] in Scheme 3.8; $c(CO)$ is the concentration of CO in electrolyte solutions calculated from Henry's law using the Henry's law constant $k_H = 8.3 \times 10^{-3}$ M·atm^{-1};[46] $E_{1/2}^{CO}(Co^{2+/+})$ and $E_{1/2}^{N_2}((Co^{2+/+})$ are redox potentials of $Co^{2+/+}$ couple under CO and N$_2$, respectively; $R = 8.314$ J·mol^{-1}·K^{-1} is the ideal gas constant; $T = 298$ K is the solution temperature; $n = 1$ is the number of electrons transferred during the redox process; and $F = 96485$ C·mol^{-1} is Faraday's constant.

CVs of each complex at different CO concentrations are shown in Figures A.76-A.79, and a plot of potential shift of $Co^{2+/+}$ redox couple ($\Delta E_{1/2}(Co^{2+/+}) = E^{CO}_{1/2}(Co^{2+/+}) - E^{N2}_{1/2}(Co^{2+/+})$) as the function of $c(CO)$ in the electrolyte solution for each catalyst is shown in Figure 3.11. Fitting the data points of each catalyst based on Eq 4 yields their corresponding K_{CO} also reported in Figure 3.11. The determined K_{CO} for each complex roughly increases with increasing ligand flexibility: $K_{CO}[Co(L-L)] \ll K_{CO}[Co(L-cyc-L)] < K_{CO}[Co(L-CH_2CH_2-L)] < K_{CO}[Co(L-CH_2-L)]$. This suggests that the Co complexes with more flexible ligand structures may facilitate CO

coordination during catalytic turnover. Moreover, the values of K_{CO} for the [Co(L-cyc-L)], [Co(L-CH$_2$-L)] and [Co(L-CH$_2$CH$_2$-L)] complexes are similar to the measured K_{CO} values of other reported Co complexes whose electrocatalytic activity is inhibited by strong CO-binding.[15, 27] In contrast, the smaller K_{CO} value of the more rigid [Co(L-L)] and its reversible redox features maintained under CO suggest that its catalytic activity for CO$_2$RR is less likely to be inhibited by CO compared to the other three [Co(L-R-L)] catalysts with more flexible ligands.
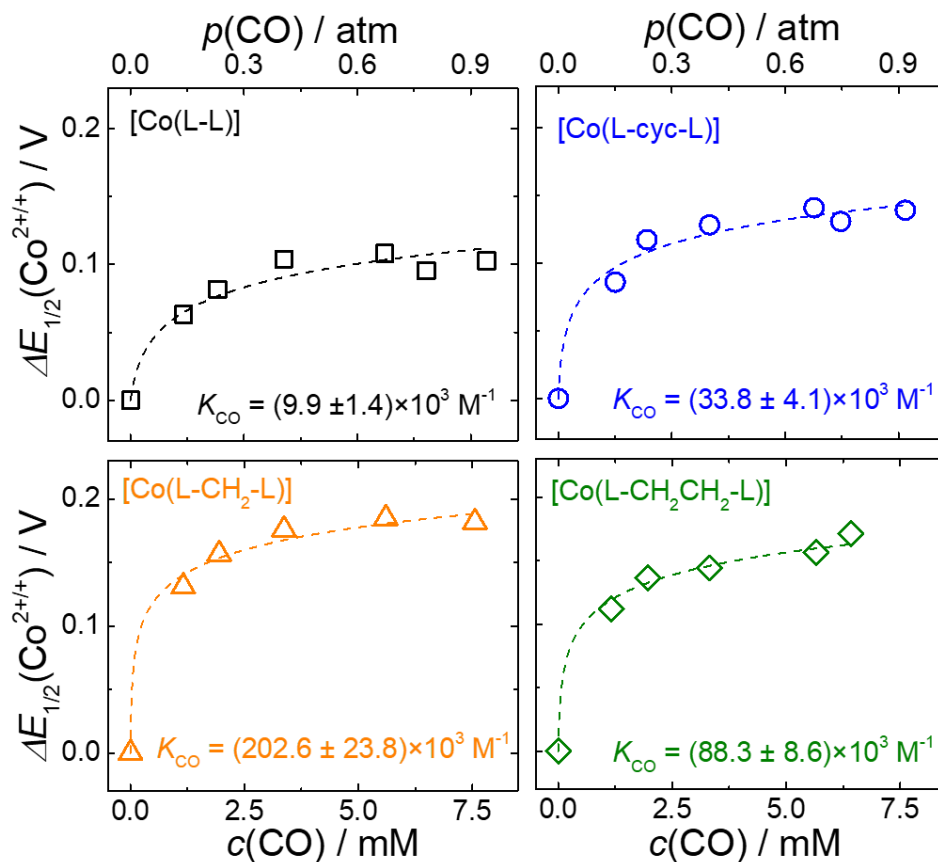
Figure 3.11 The plot of potential shift of $Co^{2+/+}$ redox couple for each [Co(L-R-L)] as the function of $c(CO)$ in the electrolyte solution (or equivalently, the pressure $p(CO)$ in the CO/N_2 mixture as shown on the top x-axis). The dashed lines show the fits of the data to Equation 4, and the resulting K_{CO} values are listed in each panel. Cyclic voltammograms of each [Co(L-R-L)] complex measured in a series of CO/N_2 mixtures investigated are shown in Figures A.76-A.79.

Note that the increased CO binding equilibrium constants of the flexible [Co(L-R-L)] structures may be due to their more negative $E_{1/2}(Co^{2+}/Co^{+})$ compared to [Co(L-L)] (Table 3.2). In the more flexible [Co(L-R-L)] structures, the [Co^{+}(L-R-L)] complex will be more reducing compared to [Co^{+}(L-L)] and therefore result in stronger Co^{+} to CO back bonding, leading to larger CO binding equilibrium constants. Similar arguments have been used to describe the trends in the CO binding constants of Co tetrazamacrocycles and their derivatives.[46]

An additional feature of each complex is the negative shift in the Co$^{1+/0}$ couple under CO which is indicative of reductive CO dissociation (Scheme 3.8d). We determined the CO-dissociation equilibrium constant, K_d, for each [Co(L-R-L)] catalyst (Equation 5) by measuring the extent of the Nernstian potential shift in $E_{1/2}(Co^{+/0})$ as a function of CO concentration in the electrolyte solution as shown in Equation 6. This is conceptually equivalent to our measurements for CO-binding equilibrium constants K_{CO} described above. A plot of potential shift of Co$^{+/0}$ redox couple ($\Delta E_{1/2}(Co^{+/0}) = E^{CO}_{1/2}(Co^{+/0}) - E^{N2}_{1/2}(Co^{+/0})$) as the function of $c(CO)$ in the electrolyte solution for each catalyst is shown in Figure 3.12. The determined K_d for each complex decreases with increasing ligand flexibility, with $K_d([Co(L-L)]) \gg K_d([Co(L-cyc-L)]) > K_d([Co(L-CH_2-L)]) > K_d([Co(L-CH_2CH_2-L)])$. This suggests that not only do the more flexible ligand scaffolds facilitate CO binding at the Co^{+} state as determined by the K_{CO} values, but they also stabilize the CO adduct against reductive dissociation compared to [Co(L-L)]. The difference of K_{CO} and K_d of these [Co(L-R-L)] catalysts further suggests that the Co complexes with more flexible ligands may be product inhibited by CO generated during the CO$_2$RR reaction.

$$K_d = \frac{c([Co^0(L-R-L)^{\bullet-}]) \times c(CO)}{c([Co^0(CO)(L-R-L^{\bullet-})])} \qquad \text{Eq 5}$$

$$E^{CO}_{1/2}(Co^{+/0}) - E^{N_2}_{1/2}(Co^{+/0}) = -\frac{RT}{nF}\ln\left(1 + \frac{c(CO)}{K_{dis}}\right) \qquad \text{Eq 6}$$

134
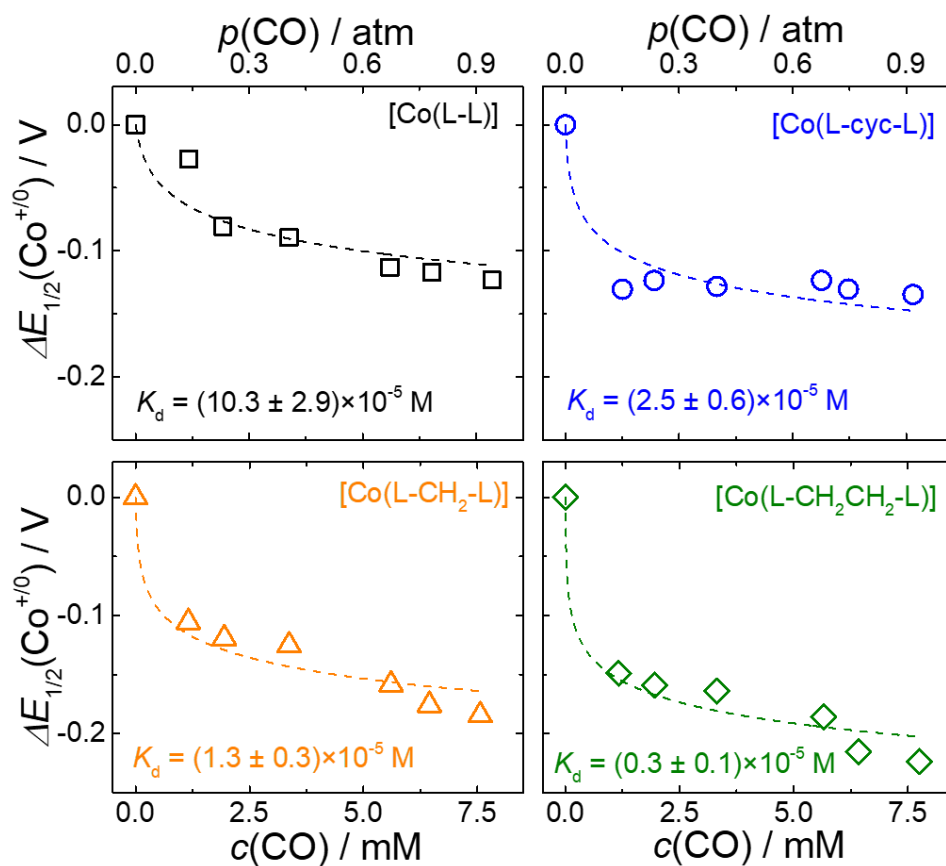
Figure 3.12 The plot of potential shift of $Co^{+/0}$ redox couple for each [Co(L-R-L)] as the function of $c(CO)$ in the electrolyte solution (or equivalently, the pressure $p(CO)$ in the CO/N_2 mixture as shown on the top x-axis). The dashed lines show the fits of the data to Equation 6, and the resulting K_d values are listed in each panel. Cyclic voltammograms of each [Co(L-R-L)] complex measured in a series of CO/N_2 mixtures investigated are shown in Figures A.76-A.79.

To directly demonstrate CO-inhibition of CO_2RR for each $[Co(L-R-L)]$ catalyst, the catalytic CVs of all $[Co(L-R-L)]$ catalysts in MeCN solutions saturated by CO_2/CO (1:1) in the presence of 5.5 M H_2O were conducted and compared to their corresponding catalytic CVs in the case of CO_2/N_2 (1:1) as shown in Figure 3.13. The qualitative extent of inhibition was determined by dividing the peak current under CO_2/CO mixed gas, $i_p(CO_2/CO)$, by the peak current under CO_2/N_2 mixed gas, $i_p(CO_2/N_2)$, as summarized in Table 3.7. For $[Co(L-L)]$, which has the smallest determined K_{CO} and largest K_d, the intensity of catalytic current peak is only slightly attenuated in the presence of CO, indicating small effect of CO-inhibition on its CO_2RR activity. However, for other three $[Co(L-R-L)]$ catalysts, the activity for CO_2RR is suppressed significantly in the presence of CO, as evidenced by the dramatic decrease of catalytic current (Table 3.7). This distinction of CO-inhibition effect on the catalytic activity of $[Co(L-R-L)]$ catalysts matches very well with the trend of their different K_{CO} and K_d values (summarized in Table 3.7): larger K_{CO} values and smaller K_d values of $[Co(L-cyc-L)]$, $[Co(L-CH_2-L)]$ and $[Co(L-CH_2CH_2-L)]$ reflect comparably stronger CO-binding affinity which inhibits the regeneration of active species during catalytic turnover and suppresses CO_2RR activity. In contrast, $[Co(L-L)]$ remains the most of catalytic activity for CO_2RR in the presence of CO due to its comparably weak CO binding reflected by its smaller K_{CO} and larger K_d. The stronger effect of CO-inhibition on the catalytic activity of $[Co(L-cyc-L)]$, $[Co(L-CH_2-L)]$ and $[Co(L-CH_2CH_2-L)]$ complexes for CO_2RR also explains why they show higher initial CO_2RR activity with low concentration of H_2O, but lower overall conversion with high concentration of H_2O as a proton source in the CPE experiments.
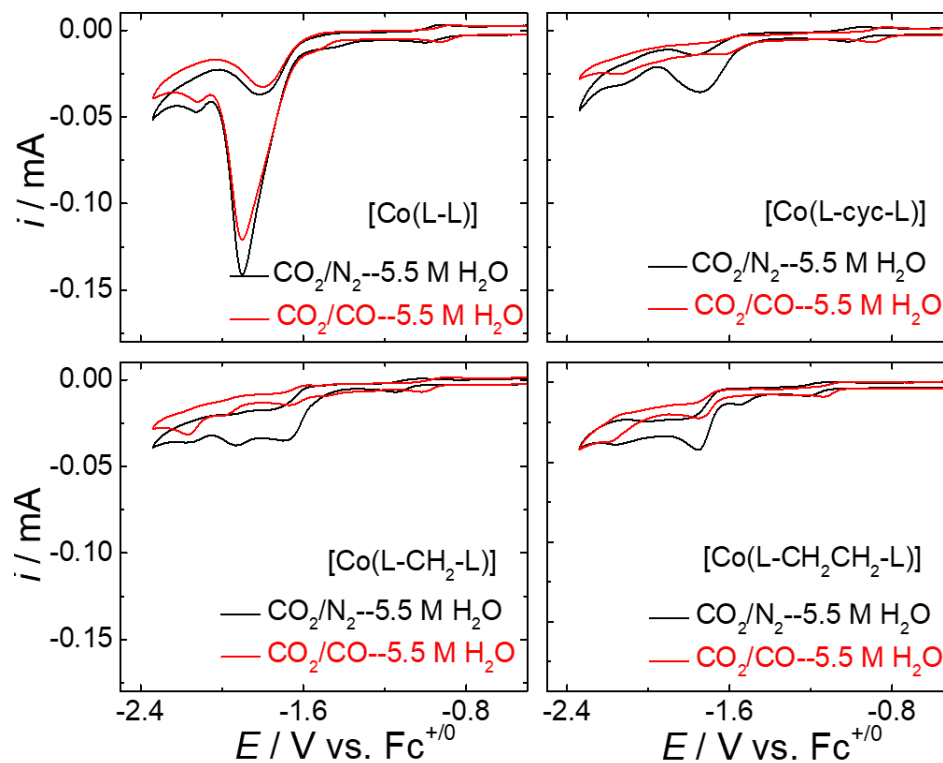
Figure 3.13 The catalytic CVs of all [Co(L-R-L)] catalysts in MeCN solutions saturated by CO_2/CO (1:1) and CO_2/N_2 (1:1) in the presence of 5.5 M H_2O.

Table 3.7 Extent of CO-inhibition of catalytic peaks in CO_2RR reduction ($i_p(CO_2/CO)/i_p(CO_2/N_2)$)

Catalyst	[Co(L-L)]	[Co(L-cyc-L)]	[Co(L-CH2-L)]	[Co(L-CH2CH2-L)]
$i_p(CO_2/CO)/i_p(CO_2/N_2)$	0.85	0.23	0.20	0.38
K_{CO} / M^{-1}	$(9.9 \pm 1.4) \times 10^3$	$(33.8 \pm 4.1) \times 10^3$	$(202.6 \pm 23.8) \times 10^3$	$(88.3 \pm 8.6) \times 10^3$
K_d / M	$(10.3 \pm 2.9) \times 10^{-5}$	$(2.5 \pm 0.6) \times 10^{-5}$	$(1.3 \pm 0.3) \times 10^{-5}$	$(0.3 \pm 0.1) \times 10^{-5}$

3.5.5 Proposed mechanism and the effect of structure flexibility on CO$_2$RR

Based on the results and discussion above, the proposed mechanism of CO$_2$RR for [Co(L-L)] and [Co(L-R-L)] is shown in Scheme 3.9. Although the CO$_2$RR mechanism of [Co(L-L)] has been discussed in our previous paper,[18] we update it here based on our recent studies. For [Co(L-L)], a reductive dimerization occurs upon the formation of Co$^+$ state (Scheme 3.9a) while the more flexible [Co(L-R-L)] complexes exist as monomer Co$^+$ species (Scheme 3.9b) due to their decreased planarity compared to [Co(L-L)]. However, for all [Co(L-R-L)] catalysts, the active species to initiate CO$_2$RR is the monomer species [Co$^+$(L-R-L$^{\bullet-}$)] which coordinates CO$_2$ to form the [Co(L-R-L)CO$_2$] adduct. At low proton concentration (pathway (i) in Scheme 3.9a and 3.9b), [Co(L-R-L)CO$_2$] adducts abstract a hydrogen from the ligand to generate HCOO$^-$, resulting in the decomposition of the catalysts as reported in our previous work.[18] At high proton concentration (pathway (ii) in Scheme 3.9a and 3.9b), [Co(L-R-L)CO$_2$] adducts undergo a 1 e$^-$ reduction and 2 H$^+$ protonation by the proton source to generate CO and H$_2$O. In the case of [Co(L-L)], the protonation of the reduced CO$_2$ adduct by the proton source outcompetes hydrogen abstraction from the ligand scaffold and results in increased stability (pathway (ii) in Scheme 3.9b). However, for [Co(L-R-L)], CO poisoning of Co$^+$ species leads to the deactivation of [Co(L-R-L)] catalysts (pathway (ii) in Scheme 3.9b).
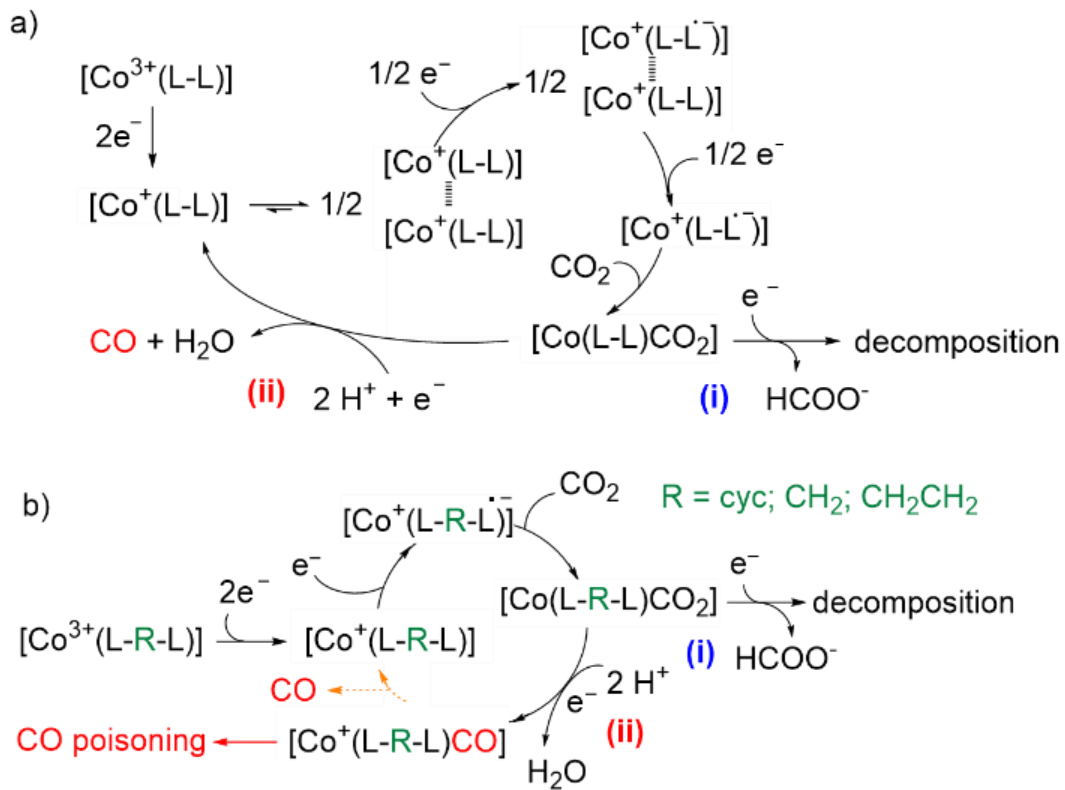
Scheme 3.9 The proposed mechanism of CO$_2$RR for [Co(L-L)] (a) and [Co(L-R-L)] (b).

Besides further elucidating the mechanism of the CO_2RR for [Co(L-R-L)] catalysts, our studies highlight an important trade-off with structure flexibility and catalytic activity for this class of square-planar Co complexes. On one hand, the more-flexible [Co(L-R-L)] complexes prevent catalyst dimerization and show more positive catalytic onsets (more positive E_{onset}) with higher initial activity (larger TOF values in the case of low concentration of H_2O) for CO_2RR compared to the more rigid [Co(L-L)]. This may be because the monomer active species $[Co^+(L\text{-}R\text{-}L^{\bullet-})]$ can initiate CO_2RR immediately once generated, without undergoing dimerization which can contribute to sluggish kinetics and the delay of the onset of observable catalysis. On the other hand, the more flexible [Co(L-R-L)] catalysts show stronger binding affinities for CO (larger K_{CO} values and smaller K_d values) and increased CO inhibition of CO_2RR (smaller $i_p(CO_2/CO)/i_p(CO_2/N_2)$), which makes them less efficient for overall CO_2 reduction compared to more rigid [Co(L-L)].

Note that in our studies, we have attempted to distinguish the effects of ligand flexibility on CO_2RR activity and CO-inhibition from other ligand effects by comparing complexes in which the ligands all have aliphatic bridging units and in which the other parts of the L-R-L ligands are kept nearly identical. However, it is important to acknowledge that other ligand effects such as inductive effects, H-bonding propensity, nucleophilicity, etc., also influence the CO_2RR activity and CO-inhibition of the Co complexes in this report.[23, 43, 47-49]

3.6 Conclusion

   We have elucidated the mechanism of the CO_2RR by a series of Co-bis(pyridylmonoimine) based complexes and demonstrated the trade-offs between structural flexibility and catalytic activity for these systems. First, we demonstrated that the structurally-rigid [Co(L-L)] undergoes a reductive dimerization upon reduction to the Co^+ complex, but that this dimerization can be sterically prevented by either adding the strong axially-coordinating ligand triphenylphosphine (PPh_3) or distorting the square planarity of the CoN_4 structure by modulating the flexibility of the L-R-L ligand scaffold. The more-flexible [Co(L-R-L)] complexes prevent catalyst dimerization and show more positive catalytic onsets with higher initial activity at low concentrations of proton source for CO_2RR compared to the more rigid [Co(L-L)]. However, at high concentrations of proton source, the [Co(L-R-L)] complexes with flexible ligands operated with lower activity and Faradaic efficiency for CO compared to [Co(L-L)]. This lower overall activity for the [Co(L-R-L)] complexes with more flexible ligands compared to [Co(L-L)] was attributed to CO product inhibition based on the [Co(L-R-L)] complexes' higher experimentally-measured CO binding equilibrium constants, lower measured CO dissociation constants, and decreased activity in CO inhibition studies under CO_2/CO gas mixtures. The stronger CO binding affinity of the [Co(L-R-L)] complexes with flexible ligands may be because the [Co^+(L-R-L)] complexes are more reducing than the more structurally-rigid [Co^+(L-L)] analogue, leading to increased stabilization of CO adducts. Future studies will explore designing ligands that retain ligand flexibility to increase CO_2 binding and activity, but that modulate the redox potential of the $Co^{2+/+}$ couple to more positive potentials, resulting in less reducing Co^+ complexes that will less strongly coordinate CO. These studies provide important design considerations regarding structure

flexibility for future CO_2RR catalysts based on putatively square-planar transition metal complexes with imine-based ligands.

3.7 Reference

1.   De Luna, P.; Hahn, C.; Higgins, D.; Jaffer, S. A.; Jaramillo, T. F.; Sargent, E. H. "What would it take for renewably powered electrosynthesis to displace petrochemical processes?," *Science* **2019**, *364*, eaav3506. http://dx.doi.org/10.1126/science.aav3506

2.   Dalle, K. E.; Warnan, J.; Leung, J. J.; Reuillard, B.; Karmel, I. S.; Reisner, E. "Electro- and Solar-Driven Fuel Synthesis with First Row Transition Metal Complexes," *Chem. Rev.* **2019**, *119*, 2752-2875. http://dx.doi.org/10.1021/acs.chemrev.8b00392

3.   Birdja, Y. Y.; Pérez-Gallent, E.; Figueiredo, M. C.; Göttle, A. J.; Calle-Vallejo, F.; Koper, M. T. M. "Advances and challenges in understanding the electrocatalytic conversion of carbon dioxide to fuels," *Nature Energy* **2019**, *4*, 732-745. http://dx.doi.org/10.1038/s41560-019-0450-y

4.   Nielsen, D. U.; Hu, X.-M.; Daasbjerg, K.; Skrydstrup, T. "Chemically and electrochemically catalysed conversion of CO2 to CO with follow-up utilization to value-added chemicals," *Nature Catalysis* **2018**, *1*, 244-254. http://dx.doi.org/10.1038/s41929-018-0051-3

5.   Chen, C.; Khosrowabadi Kotyk, J. F.; Sheehan, S. W. "Progress toward Commercial Application of Electrochemical Carbon Dioxide Reduction," *Chem* **2018**, *4*, 2571-2586. http://dx.doi.org/https://doi.org/10.1016/j.chempr.2018.08.019

6.   Qiao, J.; Liu, Y.; Hong, F.; Zhang, J. "A review of catalysts for the electroreduction of carbon dioxide to produce low-carbon fuels," *Chemical Society Reviews* **2014**, *43*, 631-675. http://dx.doi.org/10.1039/c3cs60323g

7.   Appel, A. M.; Bercaw, J. E.; Bocarsly, A. B.; Dobbek, H.; DuBois, D. L.; Dupuis, M.; Ferry, J. G.; Fujita, E.; Hille, R.; Kenis, P. J. A.; Kerfeld, C. A.; Morris, R. H.; Peden, C. H. F.; Portis, A. R.; Ragsdale, S. W.; Rauchfuss, T. B.; Reek, J. N. H.; Seefeldt, L. C.; Thauer, R. K.;

Waldrop, G. L. "Frontiers, Opportunities, and Challenges in Biochemical and Chemical Catalysis of CO2 Fixation," *Chemical Reviews* **2013**, *113*, 6621-6658. http://dx.doi.org/10.1021/cr300463y

8.   Berardi, S.; Drouet, S.; Francas, L.; Gimbert-Surinach, C.; Guttentag, M.; Richmond, C.; Stoll, T.; Llobet, A. "Molecular artificial photosynthesis," *Chemical Society Reviews* **2014**, *43*, 7501-7519. http://dx.doi.org/10.1039/c3cs60405e

9.   Sung, S.; Li, X.; Wolf, L. M.; Meeder, J. R.; Bhuvanesh, N. S.; Grice, K. A.; Panetier, J. A.; Nippe, M. "Synergistic Effects of Imidazolium-Functionalization on fac-Mn(CO)3 Bipyridine Catalyst Platforms for Electrocatalytic Carbon Dioxide Reduction," *Journal of the American Chemical Society* **2019**, *141*, 6569-6582. http://dx.doi.org/10.1021/jacs.8b13657

10.   Steinlechner, C.; Roesel, A. F.; Oberem, E.; Päpcke, A.; Rockstroh, N.; Gloaguen, F.; Lochbrunner, S.; Ludwig, R.; Spannenberg, A.; Junge, H.; Francke, R.; Beller, M. "Selective Earth-Abundant System for CO2 Reduction: Comparing Photo- and Electrocatalytic Processes," *ACS Catalysis* **2019**, *9*, 2091-2100. http://dx.doi.org/10.1021/acscatal.8b03548

11.   Gonell, S.; Massey, M. D.; Moseley, I. P.; Schauer, C. K.; Muckerman, J. T.; Miller, A. J. M. "The Trans Effect in Electrocatalytic CO2 Reduction: Mechanistic Studies of Asymmetric Ruthenium Pyridyl-Carbene Catalysts," *Journal of the American Chemical Society* **2019**, *141*, 6658-6671. http://dx.doi.org/10.1021/jacs.9b01735

12.   Haviv, E.; Azaiza-Dabbah, D.; Carmieli, R.; Avram, L.; Martin, J. M. L.; Neumann, R. "A Thiourea Tether in the Second Coordination Sphere as a Binding Site for CO2 and a Proton Donor Promotes the Electrochemical Reduction of CO2 to CO Catalyzed by a Rhenium Bipyridine-Type Complex," *J. Am. Chem. Soc.* **2018**, *140*, 12451-12456. http://dx.doi.org/10.1021/jacs.8b05658

13.   Clark, M. L.; Cheung, P. L.; Lessio, M.; Carter, E. A.; Kubiak, C. P. "Kinetic and Mechanistic Effects of Bipyridine (bpy) Substituent, Labile Ligand, and Brønsted Acid on

Electrocatalytic CO2 Reduction by Re(bpy) Complexes," *ACS Catalysis* **2018**, *8*, 2021-2029. http://dx.doi.org/10.1021/acscatal.7b03971

14.   Sampson, M. D.; Kubiak, C. P. "Manganese Electrocatalysts with Bulky Bipyridine Ligands: Utilizing Lewis Acids To Promote Carbon Dioxide Reduction at Low Overpotentials," *J. Am. Chem. Soc.* **2016**, *138*, 1386-1393. http://dx.doi.org/10.1021/jacs.5b12215

15.   Froehlich, J. D.; Kubiak, C. P. "The Homogeneous Reduction of CO2 by [Ni(cyclam)]+: Increased Catalytic Rates with the Addition of a CO Scavenger," *Journal of the American Chemical Society* **2015**, *137*, 3565-3573. http://dx.doi.org/10.1021/ja512575v

16.   Arana, C.; Yan, S.; Keshavarz-K, M.; Potts, K. T.; Abruna, H. D. "Electrocatalytic reduction of carbon dioxide with iron, cobalt, and nickel complexes of terdentate ligands," *Inorganic Chemistry* **1992**, *31*, 3680-3682. http://dx.doi.org/10.1021/ic00043a034

17.   Lacy, D. C.; McCrory, C. C. L.; Peters, J. C. "Studies of Cobalt-Mediated Electrocatalytic CO2 Reduction Using a Redox-Active Ligand," *Inorganic Chemistry* **2014**, *53*, 4980-4988. http://dx.doi.org/10.1021/ic403122j

18.   Nie, W.; McCrory, C. C. L. "Electrocatalytic CO2 reduction by a cobalt bis(pyridylmonoimine) complex: effect of acid concentration on catalyst activity and stability," *Chemical Communications* **2018**, *54*, 1579-1582. http://dx.doi.org/10.1039/C7CC08546J

19.   Chapovetsky, A.; Welborn, M.; Luna, J. M.; Haiges, R.; Miller, T. F.; Marinescu, S. C. "Pendant Hydrogen-Bond Donors in Cobalt Catalysts Independently Enhance CO2 Reduction," *ACS Central Science* **2018**, *4*, 397-404. http://dx.doi.org/10.1021/acscentsci.7b00607

20.   Takeda, H.; Cometto, C.; Ishitani, O.; Robert, M. "Electrons, Photons, Protons and Earth-Abundant Metal Complexes for Molecular Catalysis of CO2 Reduction," *ACS Catalysis* **2017**, *7*, 70-88. http://dx.doi.org/10.1021/acscatal.6b02181

21.   Rao, H.; Schmidt, L. C.; Bonin, J.; Robert, M. "Visible-light-driven methane formation from CO_2 with a molecular iron catalyst," *Nature* **2017**, *548*, 74-77. http://dx.doi.org/10.1038/nature23016

22.   Bonin, J.; Maurin, A.; Robert, M. "Molecular catalysis of the electrochemical and photochemical reduction of CO_2 with Fe and Co metal based complexes. Recent advances," *Coordination Chemistry Reviews* **2017**, *334*, 184-198. http://dx.doi.org/http://dx.doi.org/10.1016/j.ccr.2016.09.005

23.   Azcarate, I.; Costentin, C.; Robert, M.; Savéant, J.-M. "Through-Space Charge Interaction Substituent Effects in Molecular Catalysis Leading to the Design of the Most Efficient Catalyst of CO_2-to-CO Electrochemical Conversion," *Journal of the American Chemical Society* **2016**, *138*, 16639-16644. http://dx.doi.org/10.1021/jacs.6b07014

24.   Sieh, D.; Lacy, D. C.; Peters, J. C.; Kubiak, C. P. "Reduction of CO_2 by Pyridine Monoimine Molybdenum Carbonyl Complexes: Cooperative Metal–Ligand Binding of CO_2," *Chem. Eur. J.* **2015**, *21*, 8497-8503. http://dx.doi.org/10.1002/chem.201500463

25.   Kaeffer, N.; Morozan, A.; Fize, J.; Martinez, E.; Guetaz, L.; Artero, V. "The Dark Side of Molecular Catalysis: Diimine–Dioxime Cobalt Complexes Are Not the Actual Hydrogen Evolution Electrocatalyst in Acidic Aqueous Solutions," *ACS Catal.* **2016**, *6*, 3727-3737. http://dx.doi.org/10.1021/acscatal.6b00378

26.   Zhang, M.; El-Roz, M.; Frei, H.; Mendoza-Cortes, J. L.; Head-Gordon, M.; Lacy, D. C.; Peters, J. C. "Visible Light Sensitized CO_2 Activation by the Tetraaza [CoIIN4H(MeCN)]2+ Complex Investigated by FT-IR Spectroscopy and DFT Calculations," *J. Phys. Chem. C* **2015**, *119*, 4645-4654. http://dx.doi.org/10.1021/jp5127738

27.   McCrory, C. C. L.; Szymczak, N. K.; Peters, J. C. "Evaluating Activity for Hydrogen-Evolving Cobalt and Nickel Complexes at Elevated Pressures of Hydrogen and Carbon Monoxide," *Electrocatalysis* **2016**, *7*, 87-96. http://dx.doi.org/10.1007/s12678-015-0281-y

28.   Sheldrick, G. "Crystal structure refinement with SHELXL," *Acta Crystallographica Section C* **2015**, *71*, 3-8. http://dx.doi.org/doi:10.1107/S2053229614024218

29.   Frisch, M. J.; Trucks, G. W.; Schlegel, H. B.; Scuseria, G. E.; Robb, M. A.; Cheeseman, J. R.; Scalmani, G.; Barone, V.; Petersson, G. A.; Nakatsuji, H.; Li, X.; Caricato, M.; Marenich, A. V.; Bloino, J.; Janesko, B. G.; Gomperts, R.; Mennucci, B.; Hratchian, H. P.; Ortiz, J. V.; Izmaylov, A. F.; Sonnenberg, J. L.; Williams; Ding, F.; Lipparini, F.; Egidi, F.; Goings, J.; Peng, B.; Petrone, A.; Henderson, T.; Ranasinghe, D.; Zakrzewski, V. G.; Gao, J.; Rega, N.; Zheng, G.; Liang, W.; Hada, M.; Ehara, M.; Toyota, K.; Fukuda, R.; Hasegawa, J.; Ishida, M.; Nakajima, T.; Honda, Y.; Kitao, O.; Nakai, H.; Vreven, T.; Throssell, K.; Montgomery Jr., J. A.; Peralta, J. E.; Ogliaro, F.; Bearpark, M. J.; Heyd, J. J.; Brothers, E. N.; Kudin, K. N.; Staroverov, V. N.; Keith, T. A.; Kobayashi, R.; Normand, J.; Raghavachari, K.; Rendell, A. P.; Burant, J. C.; Iyengar, S. S.; Tomasi, J.; Cossi, M.; Millam, J. M.; Klene, M.; Adamo, C.; Cammi, R.; Ochterski, J. W.; Martin, R. L.; Morokuma, K.; Farkas, O.; Foresman, J. B.; Fox, D. J. *Gaussian 16 Rev. C.01*, Wallingford, CT, 2016.

30.   Smieja, J. M.; Sampson, M. D.; Grice, K. A.; Benson, E. E.; Froehlich, J. D.; Kubiak, C. P. "Manganese as a Substitute for Rhenium in CO2 Reduction Catalysts: The Importance of Acids," *Inorganic Chemistry* **2013**, *52*, 2484-2491. http://dx.doi.org/10.1021/ic302391u

31.   Smieja, J. M.; Kubiak, C. P. "Re(bipy-tBu)(CO)3Cl−improved Catalytic Activity for Reduction of Carbon Dioxide: IR-Spectroelectrochemical and Mechanistic Studies," *Inorganic Chemistry* **2010**, *49*, 9283-9289. http://dx.doi.org/10.1021/ic1008363

32.   Bard, A. J.; Faulkner, L. R. *Electrochemical Methods: Fundamentals and Applications*; John Wiley & Sons, Inc.: Hoboken, NJ, 2001, p 228-232.

33.   Costentin, C.; Drouet, S.; Robert, M.; Savéant, J.-M. "Turnover Numbers, Turnover Frequencies, and Overpotential in Molecular Catalysis of Electrochemical Reactions. Cyclic Voltammetry and Preparative-Scale Electrolysis," *Journal of the American Chemical Society* **2012**, *134*, 11235-11242. http://dx.doi.org/10.1021/ja303560c

34.   Levich, V. G. *Physicochemical Hydrodynamics*; Prentice Hall, Inc.: Englewood Cliffs, 1962, p 60-72.

35.   Bard, A. J.; Faulkner, L. R. *Electrochemical Methods: Fundamentals and Applications, 2nd ed.*; John Wiley & Sons, Inc.: Hoboken, NJ, 2001, p 335-348.

36.   Northrop, D. B. "Steady-state analysis of kinetic isotope effects in enzymic reactions," *Biochemistry* **1975**, *14*, 2644-2651. http://dx.doi.org/10.1021/bi00683a013

37.   Sawata, S.; Komiyama, M.; Taira, K. "Kinetic evidence based on solvent isotope effects for the nonexistence of a proton-transfer process in reactions catalyzed by a hammerhead ribozyme: Implication to the double-metal-ion mechanism of catalysis," *Journal of the American Chemical Society* **1995**, *117*, 2357-2358. http://dx.doi.org/10.1021/ja00113a028

38.   Liu, Y.; McCrory, C. C. L. "Modulating the mechanism of electrocatalytic CO_2 reduction by cobalt phthalocyanine through polymer coordination and encapsulation," *Nature Communications* **2019**, *10*, 1683. http://dx.doi.org/10.1038/s41467-019-09626-8

39.   Tignor, S. E.; Shaw, T. W.; Bocarsly, A. B. "Elucidating the origins of enhanced CO_2 reduction in manganese electrocatalysts bearing pendant hydrogen-bond donors," *Dalton Transactions* **2019**, *48*, 12730-12737. http://dx.doi.org/10.1039/C9DT02060H

40.   Costentin, C.; Robert, M.; Savéant, J.-M. "Catalysis of the electrochemical reduction of carbon dioxide," *Chemical Society Reviews* **2013**, *42*, 2423-2436. http://dx.doi.org/10.1039/C2CS35360A

41.   Costentin, C.; Drouet, S.; Robert, M.; Savéant, J.-M. "A Local Proton Source Enhances CO2 Electroreduction to CO by a Molecular Fe Catalyst," *Science* **2012**, *338*, 90-94. http://dx.doi.org/10.1126/science.1224581

42.   Sawyer, D. T.; Sobkowiak, A.; Roberts Jr., J. L. *Electrochemistry for Chemists*; 2nd ed.; John Wiley & Sons, Inc: New York, 1995, p 86-97.

43.   Costentin, C.; Drouet, S.; Robert, M.; Savéant, J.-M. "A Local Proton Source Enhances CO₂ Electroreduction to CO by a Molecular Fe Catalyst," *Science* **2012**, *338*, 90-94. http://dx.doi.org/10.1126/science.1224581

44.   Gangi, D. A.; Durand, R. R. "Binding of carbon dioxide to cobalt and nickel tetra-aza macrocycles," *J. Chem. Soc., Chem. Commun.* **1986**, 697-699. http://dx.doi.org/10.1039/C39860000697

45.   Schmidt, M. H.; Miskelly, G. M.; Lewis, N. S. "Effects of redox potential, steric configuration, solvent, and alkali metal cations on the binding of carbon dioxide to cobalt(I) and nickel(I) macrocycles," *J. Am. Chem. Soc.* **1990**, *112*, 3420-3426. http://dx.doi.org/10.1021/ja00165a027

46.   Fujita, E.; Creutz, C.; Sutin, N.; Szalda, D. J. "Carbon dioxide activation by cobalt(I) macrocycles: factors affecting carbon dioxide and carbon monoxide binding," *Journal of the American Chemical Society* **1991**, *113*, 343-353. http://dx.doi.org/10.1021/ja00001a048

47.   Azcarate, I.; Costentin, C.; Robert, M.; Savéant, J.-M. "Dissection of Electronic Substituent Effects in Multielectron–Multistep Molecular Catalysis. Electrochemical CO_2-to-CO Conversion

Catalyzed by Iron Porphyrins," *J. Phys. Chem. C* **2016**, *120*, 28951-28960. http://dx.doi.org/10.1021/acs.jpcc.6b09947

48.   Göttle, A. J.; Koper, M. T. M. "Determinant Role of Electrogenerated Reactive Nucleophilic Species on Selectivity during Reduction of CO2 Catalyzed by Metalloporphyrins," *J. Am. Chem. Soc.* **2018**, *140*, 4826-4834. http://dx.doi.org/10.1021/jacs.7b11267

49.   De Riccardis, A.; Lee, M.; Kazantsev, R. V.; Garza, A. J.; Zeng, G.; Larson, D. M.; Clark, E. L.; Lobaccaro, P.; Burroughs, P. W. W.; Bloise, E.; Ager, J. W.; Bell, A. T.; Head-Gordon, M.; Mele, G.; Toma, F. M. "Heterogenized Pyridine-Substituted Cobalt(II) Phthalocyanine Yields Reduction of CO2 by Tuning the Electron Affinity of the Co Center," *ACS Appl. Mater. Interfaces* **2020**, *12*, 5251-5258. http://dx.doi.org/10.1021/acsami.9b18924

Chapter 4 Three-in-One Catalyst Design: Dramatically Enhancing Electrocatalytic Activity for CO₂ Reduction by Simultaneously Modulating Three Substituent Effects in a Single Molecular Catalyst Structure

4.1 Preface

This chapter presents a novel "three-in-one" catalyst design, where three substituent effects—extended π-conjugation effect, electron-withdrawing inductive effect, and intramolecular electrostatic effect—are sequentially integrated into a cobalt pyridyldiimine complex ([Co(PDI)]) leading to the greatly enhanced electrocatalytic activity for CO_2 reduction. The stepwise incorporation of these effects into the catalyst structure results in a series of complexes that show an atypical *inverse scaling relationship* for CO_2 reduction—the maximum activity of the resulting catalysts increases as the onset potentials are driven positive due to the ligand electronic substituent effects. In particular, [Co(PDI-PyCH$_3^+$I$^-$)] with all three effects incorporated simultaneously into the catalyst structure shows dramatically enhanced activity for CO_2 reduction, operating with over an order of magnitude higher activity ($TOF_{cat} = 4.1 \times 10^4$ s^{-1}) and ~0.2 V more positive catalytic onset ($E_{onset} = -1.52$ V vs Fc$^{+/0}$) compared to the parent complex, an intrinsic activity parameter $TOF_0 = 6.3 \times 10^{-3}$ s^{-1}, and > 95% Faradaic efficiency for CO production in acetonitrile with 11 M water. This chapter of my dissertation is derived from the manuscript originally published in the journal of *Journal of the American Chemical Society*.[3] I was the first author of the manuscript and

I was responsible for all the compound synthesis and characterization, electrochemical experiment measurements and data analysis, as well as the manuscript writing and revision. Drew E. Tarnopol provided help with sample synthesis and manuscript proofreading. Dr. Charles C. L. McCrory provided significant insight and expertise in electroanalytic instruction and discussion and provided help with writing and revising the manuscript.

4.2 Abstract

The electrocatalytic activity for CO_2 reduction is greatly enhanced for Co complexes with pyridyldiimine-based ligands through the stepwise integration of three synergistic substituent effects: extended π-conjugation, electron-withdrawing ability, and intramolecular electrostatic effects. The stepwise incorporation of these effects into the catalyst structures results in a series of complexes that show an atypical inverse scaling relationship for CO_2 reduction—the maximum activity of the resulting catalysts increases as the onset potentials are driven positive due to the ligand electronic substituent effects. Incorporating all three effects simultaneously into the catalyst structure results in a Co complex [Co(PDI-PyCH$_3^+$I$^-$)] with dramatically enhanced activity for CO_2 reduction, operating with over an order of magnitude higher activity (TOF$_{cat}$ = 4.1×10^4 s^{-1}) and ~0.2 V more positive catalytic onset (E_{onset} = -1.52 V vs Fc$^{+/0}$) compared to the parent complex, an intrinsic activity parameter TOF$_0$ = 6.3×10^{-3} s^{-1}, and > 95% Faradaic efficiency for CO production in acetonitrile with 11 M water. This makes [Co(PDI-PyCH$_3^+$I$^-$)] among the most active molecular catalysts reported for the CO_2 reduction reaction. In this chapter, our work highlights a three-in-one catalyst design strategy for molecular CO_2RR catalysts—enhancing catalytic ability by tuning three synergistic substituent effects simultaneously in a single catalyst structure.

4.3 Introduction

The electrochemical CO_2 reduction reaction (CO_2RR) is a promising strategy for converting CO_2 into fuels and value-added chemicals by renewable electricity generated from intermittent energy sources (e.g. solar and wind energy).[1-6] However, designing efficient catalysts for selective CO_2 reduction at low overpotential remains a challenge. Molecular catalysts—in particular, transition metal complexes with redox-active ligands—show promise for the selective conversion of CO_2 to single products with activity that can be tuned through synthetic ligand modifications.[7-13]

Over the past several years, three ligand modification strategies have been used frequently to enhance the activity and/or decrease the effective operating overpotential of molecular catalysts for the CO_2RR: 1) extending ligand π-conjugation to stabilize reduced metal centers at more positive redox potentials and facilitate the storage of electron equivalents in the larger charge-delocalized ligand structure, thus lowering the magnitude of overpotential needed to initiate CO_2 reduction;[14-23] 2) introducing electron-withdrawing groups to shift the redox potential of the active metal centers positive and thus decrease the magnitude of the operating overpotential, albeit typically at the cost of maximum catalytic activity due to the decreased electron density at metal centers;[24-28] and 3) introducing an intramolecular electrostatic effect by incorporating cationic species in the ligand scaffold that stabilize reduced CO_2 intermediates by through-space Coulombic interactions, thus increasing catalytic activity and decreasing magnitude operating overpotentials.[29-35] There has been considerable effort and progress exploring how each of these catalyst modification strategies individually influences electrocatalytic activity for CO_2 reduction. Our approach is to combine these three effects in a single Co complex and demonstrate how they work synergistically to dramatically enhance the catalyst's activity for the CO_2RR.

We sequentially integrated extended π-conjugation effects, electron withdrawing effects, and intramolecular electrostatic effects into a cobalt pyridyldiimine complex ([Co(PDI)]) by modifying the PDI ligand with phenyl, pyridyl, and *N*-methylpyridinium groups, respectively, to form [Co(PDI-Ph)], [Co(PDI-Py)] and [Co(PDI-PyCH$_3^+$I$^-$)] (Figure 4.1). As each substituent effect is sequentially introduced into the system, there is a corresponding positive shift in the catalytic onset potential and an increase in the catalyst's intrinsic activity parameter (TOF$_0$) and Faradaic efficiency for CO_2 reduction to CO in acetonitrile (MeCN) with 11 M H_2O as the proton source. Simultaneously incorporating all three substituent effects into a single catalyst structure results in the [Co(PDI-PyCH$_3^+$I$^-$)] complex which operates with a 0.18 V more positive onset potential and nearly 4 orders of magnitude higher TOF$_0$ for the CO_2RR compared to the parent [Co(PDI)] and > 95% FE for CO. This makes [Co(PDI-PyCH$_3^+$I$^-$)] among the most active molecular catalysts reported for the CO_2 reduction reaction.

Moreover, our studies show evidence of an atypical *inverse* molecular scaling relationship as electronic substituent effects are added to the [Co(PDI-R)] system. General molecular scaling relationships show that beneficial decreases in effective overpotential are typically correlated with detrimental decreases in catalyst activity.[13, 27, 32, 36-38] In contrast, our results show that as the onset potential for the CO_2RR by [Co(PDI-R)] is driven to more positive potentials (decreased effective overpotentials) through incorporation of substituent effects, there is a corresponding increase in catalytic activity: an *inverse* scaling relationship. Overall, our study highlights a "three-in-one" catalyst design strategy in which the catalytic performance for the CO_2RR is dramatically improved through the simultaneous incorporation of three synergistic substituent effects.
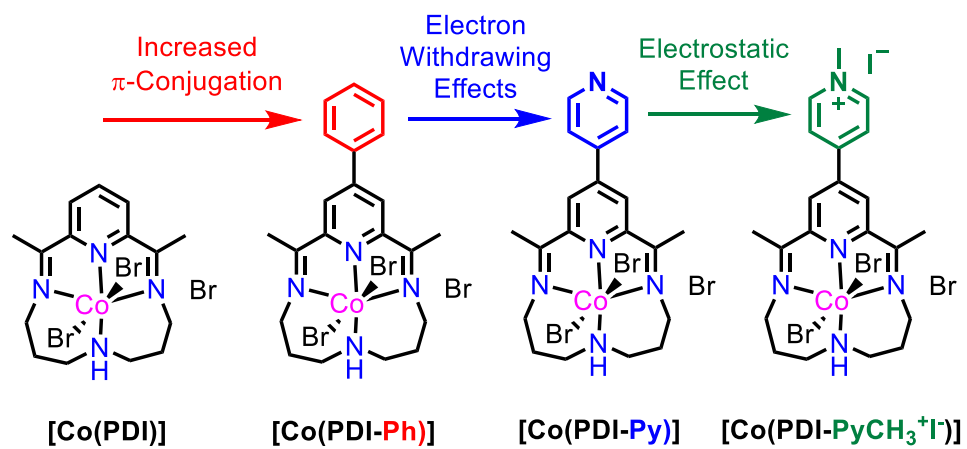
Figure 4.1 Stepwise integration of extended π-conjugation, electron withdrawing effects, and intramolecular electrostatic effects into cobalt pyridyldiimine complexes increases activity. This general class of complexes is referred to as [Co(PDI-R)] in this manuscript.

4.4 Experimental

4.4.1 Materials and General Methods

Tetrabutylammonium hexafluorophosphate (nBu$_4$NPF$_6$, >98.0%) was purchased from TCI America and recrystallized from Ethanol/H$_2$O (v/v = 8/1) before use. Acetonitrile (MeCN, HPLC plus, ≥ 99.9%), and methanol (HPLC grade, ≥ 99.9%) were purchased from Sigma Aldrich and used without further purification. The typical water concentration in MeCN as received has been previously measured to be [H$_2$O] ≈ 0.04 M.[39] Ethanol (EtOH, 200 proof, anhydrous) was purchased from Decon Labs, Inc., and used without further purification. Dichloromethane (DCM, Certified ACS), Hexane (Certified ACS, Various Methylpentanes, 4.2%) and Ethyl acetate (Certified ACS) were purchased from Fisher Chemical and used without further purification. Anhydrous dimethylformamide (DMF, 99.8%) was purchased from Sigma Aldrich and used without further purification. p-Dioxane, 4-Bromopyridine hydrochloride, Phenylboronic acid, 4-4-Pyridylboronic acid, Pyruvic acid, Bis(pinacolato)diboron, Potassium acetate, Pd(dppf)Cl$_2$, Zinc bromide (ZnBr2, 98%), Potassium iodide (KI, 98%) and CsF were purchased from Oakwood Chemical and used without further purification. Cobalt bromide (CoBr$_2$, 99%), hydrogen bromide aqueous solutions (HBr(aq), ACS reagent, 48%) were purchased from Sigma Aldrich and used without further purification. H$_2$SO$_4$ (Certified ACS Plus) was purchased from Fisher Chemical and used without further purification. 2,6-Diacetylpyridine (**DAP**, 99%) and iodomethane CH$_3$I (ReagentPlus®, 99.5%) were purchased from Aldrich and used without further purification. Na$_2$CO$_3$ (99.6%, ACS reagent, anhydrous) was purchased from ACROS ORGANIC and used without further purification. AgNO$_3$ (99.7%) was purchased from Sigma and used without further purification. (NH$_4$)$_2$S$_2$O$_8$ (98%), Anhydrous MgSO$_4$, Silica gel 60 (0.032-0.063mm, 230-450 mesh) and NH$_4$Cl (98+%) were purchased from Alfa Aesar and used without further purification.

3,3'-Diaminodipropylamine (>98%) was purchased from TCI America and used without further purification. Glacial acetic acid (HPLC grade, 99.7%) was purchased from Fisher scientific and used without further purification. All water used in this study was purified to 18.2 MΩ cm resistivity using a Thermo Scientific Barnstead^{TM} GenPure^{TM} UV-TOC/UF xCAD-plus water purification system. Nitrogen (N_2) was boil-off gas from a liquid nitrogen source. Carbon dioxide (CO_2, medical grade, > 99.0%) was purchased from Cryogenic Gases. All other chemicals were purchased from commercial sources, and all chemicals were used as received unless otherwise noted.

NMR spectra were recorded on Varian MR-400 (400 MHz) spectrometers, and chemical shifts are reported in ppm relative to TMS standards. Elemental analyses were performed by Midwest Microlab, Inc.

4.4.2 Synthesis

Preparation of 4-Bromo-2,6-diacetylpyridine (1). A scheme for the synthesis of 4-Bromo-2,6-diacetylpyridine (**1**) is shown in Scheme 4.1. 4-Bromopyridine hydrochloride (2.92 g, 15.0 mmol) was dissolved in water under N_2 atmosphere and basified by saturated Na_2CO_3 aqueous solution to pH 10. Then the mixture was extracted by dichloromethane (DCM, 3×40 mL) and the organic fractions were collected. After removing the organic solvent, 4-bromopyridine was obtained as orange oil and was used without purification. The fresh 4-bromopyridine was dissolved in 100 mL 0.4 M H_2SO_4 aqueous solution while stirring under N_2. Pyruvic acid (2.32 g, 1.83 mL, 26.4 mmol) and $AgNO_3$ solution (0.123g, 0.726 mmol in 0.3 mL H_2O) were added. Additionally $(NH_4)_2S_2O_8$ (9.10 g, 40.0 mmol) was added into the solution slowly, followed by the evolution of CO_2 gas. The solution was stirred at the room temperature for 24 hours. The precipitate was collected and washed with DCM (3×20 mL). The aqueous part was extracted by DCM (3×40 mL). The combined DCM fraction was dried by anhydrous $MgSO_4$. After removing the solvent, crude **1** was obtained as yellow oil and purified via column chromatography (SiO_2, hexane/ethyl acetate, 3/1). Compound **1** (1.12 g, yield: 31.1%) was obtained as white solid. ^{1}H NMR ($CDCl_3$-d, 400 MHz, Figure A.80): δ 8.35 (2H, s, *Py*-H), δ 2.78 (6H, s, CH_3)
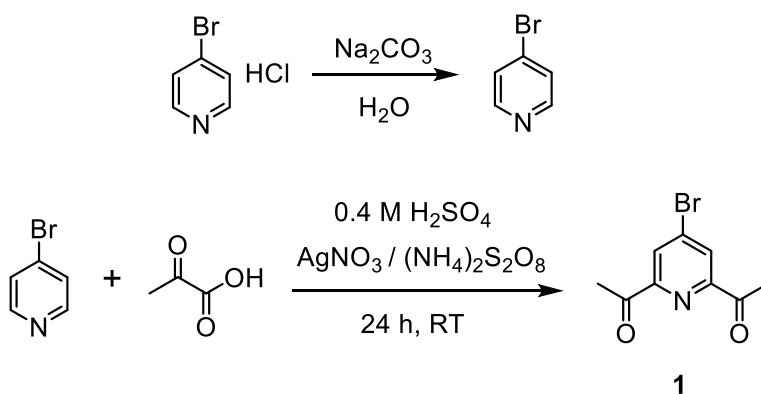
Scheme 4.1 Synthetic route for 4-Bromo-2,6-diacetylpyridine (**1**)

Preparation of 4-Phenyl-2,6-diacetylpyridine (DAP-Ph). A scheme for the synthesis of 4-Phenyl-2,6-diacetylpyridine is shown in Scheme 4.2. Compound **1** (361.5 mg, 1.50 mmol) and Phenylboronic acid **2** (183.2 mg, 1.50 mmol) were dissolved in 20 mL mixed solvent of *p*-dioxane/H_2O (16 mL/4 mL), which was deoxygenated by three freeze-pump-thaw cycles and protected by N_2. After adding CsF (584.2 mg, 3.85 mmol) and Pd(dppf)Cl_2 (28.2 mg, 0.038 mmol), the suspension was stirred and heated at 90 ℃ for 24 hours. After cooling down to the room temperature, 100 mL of 20 wt.% NH_4Cl aqueous solution was added. The mixture was extracted by EtOAc (3 × 50 mL). The organic fractions were combined and washed with saturated brine, dried with anhydrous $MgSO_4$. After removing the solvent, 4-Phenyl-2,6-diacetylpyridine (357.1 mg, yield: 99.2%) was obtained by column chromatography (silica gel, hexane/EtOAc, 3/1). ^{1}H NMR (CCl$_3$D-*d*, 400 MHz, Figure A.81): δ 8.46 (2H, s, *Py*-H), δ 7.74~7.76 (2H, m, *Phenyl*-H), δ 7.50~7.53 (3H, m, *Phenyl*-H), δ 2.84 (6H, s, CH$_3$).
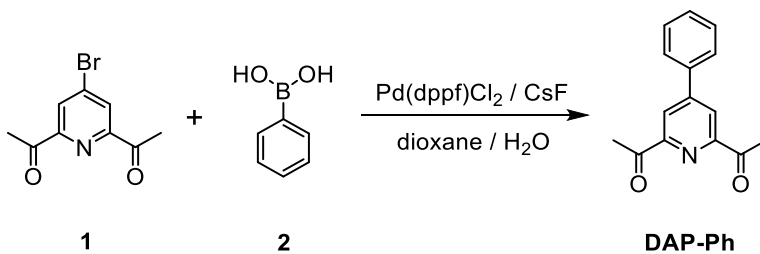
Scheme 4.2 Synthesis route for 4-Phenyl-2,6-diacetylpyridine (**DAP-Ph**)

Preparation of 4-4-Pyridyl-2,6-diacetylpyridine (DAP-Py). A scheme for the synthesis of 4-4-Pyridyl-2,6-diacetylpyridine is shown in Scheme 4.3. Compound **1** (361 mg, 1.5 mmol) and 4-4-Pyridylboronic acid **3** (184 mg, 1.5 mmol) were dissolved in 20 mL mixed solvent of *p*-dioxane/H_2O (16 mL/4 mL), which was deoxygenated by three freeze-pump-thaw cycles and protected by N_2. After adding CsF (701 mg, 4.63 mmol) and Pd(dppf)Cl_2 (33.8 mg, 0.046 mmol), the suspension was stirred and heated at 90 ℃ for 24 hours. After cooling down to the room temperature, 100 mL of 20 wt.% NH_4Cl aqueous solution was added. The mixture was extracted by EtOAc (3 × 50 mL). The organic fractions were combined and washed with saturated brine, dried with anhydrous $MgSO_4$. After removing the solvent, 4-4-Pyridyl-2,6-diacetylpyridine (322 mg, yield: 89.4%) was obtained by column chromatography (silica gel, DCM/EtOAc, 2/1). ^{1}H NMR (CCl$_3$D-*d*, 400 MHz, Figure A.82): *δ* 8.80 (2H, d, *Py*-H), *δ* 8.49 (2H, s, *Py*-H), *δ* 7.65 (2H, d, *Py*-H), *δ* 2.85 (6H, s, CH$_3$).
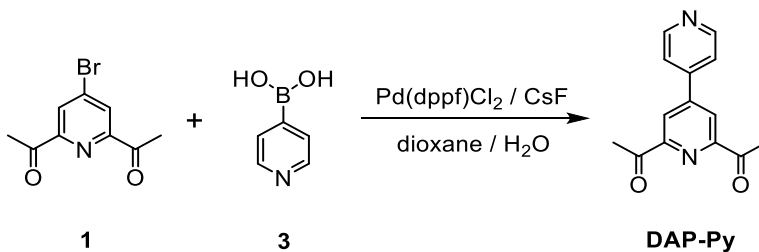
Scheme 4.3 Synthesis route for 4-4-Pyridyl-2,6-diacetylpyridine (**DAP-Py**).

Preparation of 4-(N-methyl-4-pyridyl)-2,6-diacetylpyridine (DAP-PyCH₃⁺I⁻). A scheme

for the synthesis of 4-(N-methyl-4-Pyridyl)-2,6-diacetylpyridine is shown in Scheme 4.4. 4-4-

Pyridyl-2,6-diacetylpyridine (313 mg, 1.3 mmol) and iodomethane CH_3I (80.9 µL, 1.3 mmol) were

refluxed in 15 mL MeCN under N2 for 24 hours. After cooling down to the room temperature, the

volume was reduced to 5.0 mL and 20 mL ethyl acetate was added. The orange precipitate was

filtered out and washed with ethyl acetate three times. The product 4-(N-methyl-4-Pyridyl)-2,6-

diacetylpyridine (373 mg, yield: 75.2%) was obtained after dried in vacuum overnight. ^{1}H NMR

(DMSO-d_6, 400 MHz, Figure A.83): δ 9.16~9.17 (2H, d, *Py*-H), δ 8.78~8.80 (2H, d, *Py*-H), δ 8.70

(2H, s, *Py*-H), δ 4.40 (3H, s, N-CH_3^+), δ 2.82 (6H, s, CH_3).
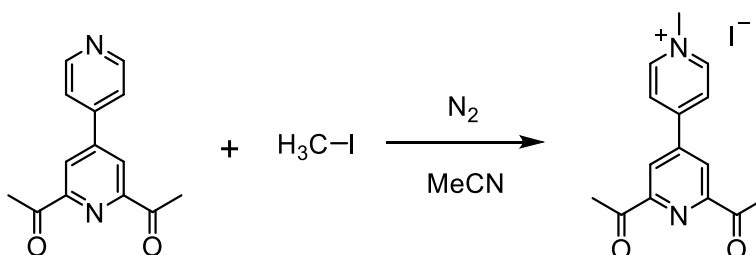
Scheme 4.4 Synthesis route for 4-(N-methyl-4-Pyridyl)-2,6-diacetylpyridine (**DAP-PyCH₃⁺I⁻**).

Preparation of [Co(PDI)]Br₃. [Co(PDI)]Br$_3$ was prepared as previously reported,[40] according to the synthesis scheme shown in Scheme 4.5. ^{1}H NMR (DMSO-d_6, 400 MHz, Figure A.84): δ 8.69 (3H, s, *Py*-H), δ 6.66 (H, t, -CH$_2$*NH*CH$_2$-), δ 4.17~4.21 (2H, d, -*CH$_2$*NHCH$_2$-), δ 3.38~3.51 (2H, t, -C=N-*CH$_2$*-), δ 3.25~3.28 (2H, m, -CH$_2$*CH$_2$*CH$_2$-), δ 3.02~3.05 (2H, d, -CH$_2$NH*CH$_2$*-), δ 2.96 (6H, s, CH$_3$), δ 2.24~2.28 (2H, m, -CH$_2$*CH$_2$*CH$_2$-), δ 2.02~2.12 (2H, m, -C=N-*CH$_2$*-). Anal. Calcd (found) for [Co(PDI)]Br$_3$ (C$_{15}$H$_{22}$N$_4$CoBr$_3$): %C 32.34, (32.18); %H 3.98, (4.08); %N 10.06, (9.61).
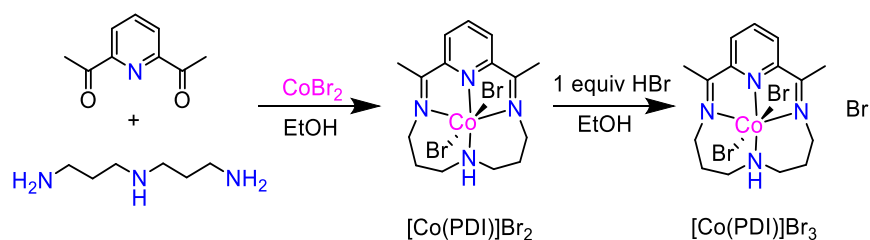
Scheme 4.5 Synthesis route for [Co(PDI)]Br$_3$.

Preparation of [Co(PDI-Ph)]Br₃. A scheme for the synthesis of [Co(PDI-Ph)]Br$_3$ is shown in Scheme 4.6. 4-Phenyl-2,6-diacetylpyridine (**DAP-Ph**, 288.1 mg, 1.2 mmol) was dissolved in 6.00 mL ethanol. A 4.00 mL ethanol solution of CoBr$_2$ (262.5 mg, 1.2 mmol) was added into this mixture with stirring under N$_2$. Then 3,3'-diaminodipropylamine (167.2 μL, 1.2 mmol) was slowly dropped in. The mixture was stirred and refluxed at 55℃ for 24 hours. After the mixture was allowed to cool to room temperature, the dark purple precipitate [Co(PDI-Ph)]Br$_2$ was collected by filtration and then washed with cold ethanol three times. [Co(PDI-Ph)]Br$_2$ was aerobically oxidized by suspending and stirring in ethanol with 1 equiv HBr(aq) overnight (18 h) in air, resulting in the green solid product [Co(PDI-Ph)]Br$_3$ (292.7 mg, yield: 38.5%). ^{1}H NMR (DMSO-d_6, 400 MHz, Figure A.85): δ 8.98 (2H, s, *Py*-H), δ 8.25~8.28 (2H, d, *Phenyl*-H), δ 7.65~7.72 (3H, m, *Phenyl*-H), δ 6.66~6.71 (H, t, -CH$_2$*NH*CH$_2$-), δ 4.20~4.24 (2H, d, -*CH$_2$*NHCH$_2$-), δ 3.53~3.60 (2H, t, -C=N-*CH$_2$*-), δ 3.24~3.30 (4H, m, -CH$_2$*CH$_2$*CH$_2$- and -CH$_2$NH*CH$_2$*-), δ 3.05 (6H, s, CH$_3$), δ 2.25~2.29 (2H, m, -CH$_2$*CH$_2$*CH$_2$-), δ 2.04~2.15 (2H, m, -C=N-*CH$_2$*-). Anal. Calcd (found) for [Co(PDI-Ph)]Br$_3$ (C$_{21}$H$_{26}$N$_4$CoBr$_3$): %C 39.84, (40.44); %H 4.14, (4.48); %N 8.85, (8.32).
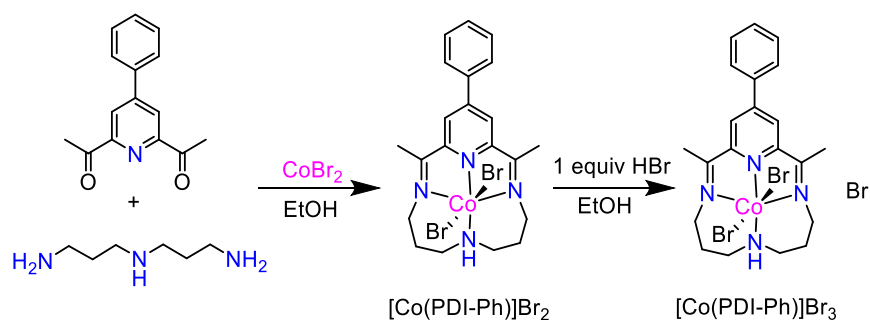
Scheme 4.6 Synthesis route for [Co(PDI-Ph)]Br$_3$.

Preparation of [Co(PDI-Py)]Br₃. A scheme for the synthesis of [Co(PDI-Py)]Br₃ is shown in Scheme 4.7. 4-4-Pyridyl-2,6-diacetylpyridine (**DAP-Py**, 334.0 mg, 1.4 mmol) was dissolved in 6.00 mL ethanol. A 4.00 mL ethanol solution of $CoBr_2$ (306.2 mg, 1.4 mmol) was added into this mixture with stirring under N_2. Then 3,3'-diaminodipropylamine (195.9 µL, 1.4 mmol) was slowly dropped in. The mixture was stirred and refluxed at 55℃ for 24 hours. After the mixture was allowed to cool to room temperature, the dark purple precipitate [Co(PDI-Py)]Br₂ was collected by filtration and then washed with cold ethanol three times. [Co(PDI-Py)]Br₂ was aerobically oxidized by suspending and stirring in ethanol with 1 equiv HBr(aq) overnight (18 h) in air, resulting in the green solid product [Co(PDI-Py)]Br₃ (488.2 mg, yield: 55.0%). ¹H NMR (DMSO-d_6, 400 MHz, Figure A.86): δ 8.96~9.08 (4H, s,s, *Py*-H), δ 8.30 (2H, s, *Py*-H), δ 6.69~6.74 (H, t, -CH₂*NH*CH₂-), δ 4.20~4.24 (2H, d, -*CH₂*NHCH₂-), δ 3.54~3.61 (2H, t, -C=N-*CH₂*-), δ 3.20~3.33 (4H, m, -CH₂*CH₂*CH₂- and -CH₂NH*CH₂*-), δ 3.06 (6H, s, CH₃), δ 2.25~2.30 (2H, m, -CH₂*CH₂*CH₂-), δ 2.04~2.15 (2H, m, -C=N-*CH₂*-). Anal. Calcd (found) for [Co(PDI-Ph)]Br₃ ($C_{20}H_{25}N_5CoBr_3$): %C 37.88, (37.37); %H 3.97, (4.08); %N 11.04, (10.84).
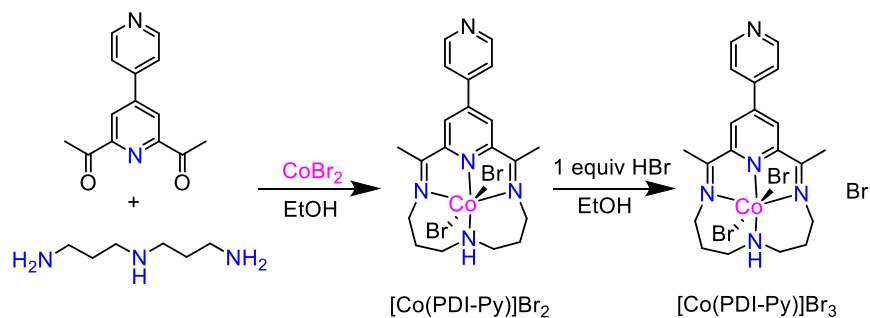
Scheme 4.7 Synthesis route for [Co(PDI-Py)]Br₃.

Preparation of [Co(PDI-Py-CH₃⁺I⁻)]Br₃. A scheme for the synthesis of [Co(PDI-Py-CH$_3^+$I⁻)]Br$_3$ is shown in Scheme 4.8. 4-(N-methyl-4-Pyridyl)-2,6-diacetylpyridine (***DAP-Py-CH₃⁺I⁻***, 352 mg, 0.92 mmol) was dissolved in 8 mL MeCN and 1 mL ethanol. A 4.00 mL ethanol solution of CoBr$_2$ (201 mg, 0.92 mmol) was added into this mixture with stirring under N$_2$. Then 3,3'-diaminodipropylamine (128.18 µL, 0.92 mmol) was slowly dropped in. The mixture was stirred and refluxed at 55℃ for 24 hours. After the mixture was allowed to cool to room temperature, the dark precipitate [Co(PDI-Py-CH$_3^+$I⁻)]Br$_2$ was collected by filtration and then washed with cold ethanol three times. [Co(PDI-Py-CH$_3^+$I⁻)]Br$_2$ was aerobically oxidized by suspending and stirring in ethanol with 1 equiv HBr(aq) overnight (18 h) in air, resulting in the brown solid product [Co(PDI-Py-CH$_3^+$I⁻)]Br$_3$ (202 mg, yield: 28.3%). ^{1}H NMR (DMSO-d_6, 400 MHz, Figure A.87): δ 9.37~9.39 (2H, d, *Py*-H), δ 9.27 (2H, s, *Py*-H), δ 9.00~9.02 (2H, d, *Py*-H), δ 6.74~6.79 (H, t, -CH$_2$*NH*CH$_2$-), δ 4.48 (3H, s, N-*CH$_3^+$*), δ 4.21~4.25 (2H, d, -*CH$_2$*NHCH$_2$-), δ 3.55~3.62 (2H, t, -C=N-*CH$_2$*-), δ 3.24~3.31 (4H, m, -CH$_2$*CH$_2$*CH$_2$- and -CH$_2$NH*CH$_2$*-), δ 3.08 (6H, s, CH$_3$), δ 2.27~2.32 (2H, m, -CH$_2$*CH$_2$*CH$_2$-), δ 2.04~2.14 (2H, m, -C=N-*CH$_2$*-). Anal. Calcd (found) for [Co(PDI-Py-CH$_3^+$I⁻)]Br$_3$ (C$_{21}$H$_{28}$N$_5$CoIBr$_3$): %C 32.50, (33.02); %H 3.64, (3.40); %N 9.02, (9.16).
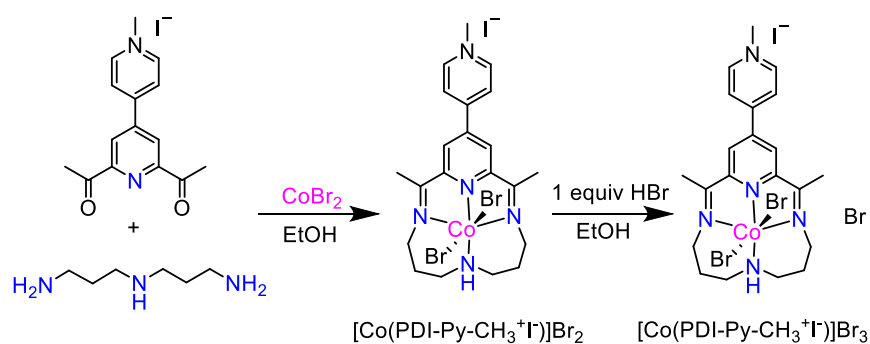
Scheme 4.8 Synthesis route for [Co(PDI-Py-CH$_3^+$I⁻)]Br$_3$.

Preparation of [Zn(PDI-R)]Br₂. The general synthesis methods for the [Zn(PDI-R)]Br$_2$ complexes are analogous to those for the [Co(PDI-R)]Br$_2$ complexes. Briefly, the relevant DAP-R compound (0.92 mmol) was dissolved in 8 mL MeCN and 1 mL ethanol. A 4.00 mL ethanol solution of ZnBr$_2$ (207 mg, 0.92 mmol) was added into this mixture with stirring under N$_2$. Then 3,3'-diaminodipropylamine (128.18 µL, 0.92 mmol) was slowly dropped in. The mixture was stirred and refluxed at 70 ℃ for 24 hours. After the mixture was allowed to cool to room temperature, diethyl ether was added and the light precipitate [Zn(PDI-R)]Br$_2$ (yield: 25.0% ~45.0 %) was collected by filtration and then washed with cold ethanol and diethyl ether three times.

[Zn(PDI)]Br₂. ^{1}H NMR (DMSO-d_6, 400 MHz, Figure A.88): δ 8.61~8.65 (H, t, *Py*-H), δ 8.50~8.52 (2H, d, *Py*-H), δ 4.49~4.55 (H, t, -CH$_2$*NH*CH$_2$-), δ 4.13~4.18 (2H, d, -*CH$_2$*NHCH$_2$-), δ 3.73~3.79 (2H, t, -C=N-*CH$_2$*-), δ 3.13~3.19 (2H, m, -CH$_2$*CH$_2$*CH$_2$-), δ 2.93~2.96 (2H, d, -CH$_2$NH*CH$_2$*-), *δ* 2.60 (6H, s, CH$_3$), δ 2.10~2.16 (2H, d, -CH$_2$*CH$_2$*CH$_2$-), δ 1.61~1.71 (2H, m, -C=N-*CH$_2$*-). Anal. Calcd (found) for [Zn(PDI)]Br$_2$ (C$_{15}$H$_{22}$N$_4$ZnBr$_2$): %C 37.26, (37.17); %H 4.59, (4.51); %N 11.59, (10.89).

[Zn(PDI-Ph)]Br₂. ^{1}H NMR (DMSO-d_6, 400 MHz, Figure A.89): *δ* 8.74 (2H, s, *Py*-H), *δ* 8.14~8.17 (2H, d, *Phenyl*-H), *δ* 7.65~7.67 (3H, m, *Phenyl*-H), *δ* 4.50~4.56 (H, t, -CH$_2$*NH*CH$_2$-), *δ* 4.16~4.20 (2H, d, -*CH$_2$*NHCH$_2$-), *δ* 3.75~3.81 (2H, t, -C=N-*CH$_2$*-), *δ* 3.12~3.21 (2H, m, -CH$_2$*CH$_2$*CH$_2$-), *δ* 2.94~2.98 (2H, d, -CH$_2$NH*CH$_2$*-), *δ* 2.69 (6H, s, CH$_3$), *δ* 2.13~2.17 (2H, d, -C=N-*CH$_2$*-), δ 1.62~1.72 (2H, m, -CH$_2$*CH$_2$*CH$_2$-). Anal. Calcd (found) for [Zn(PDI-Ph)]Br$_2$ (C$_{21}$H$_{26}$N$_4$ZnBr$_2$): %C 45.07, (45.78); %H 4.68, (4.86); %N 10.01, (10.43).

[Zn(PDI-Py)]Br₂. ^{1}H NMR (DMSO-d_6, 400 MHz, Figure A.90): *δ* 8.88~8.90 (2H, d, *Py*-H), *δ* 8.84 (2H, s, *Py*-H), *δ* 8.15~8.17 (2H, d, *Py*-H), *δ* 4.49~4.55 (H, t, -CH$_2$*NH*CH$_2$-), *δ* 4.17~4.20 (2H, d, -*CH$_2$*NHCH$_2$-), *δ* 3.76~3.82 (2H, t, -C=N-*CH$_2$*-), *δ* 3.11~3.20 (2H, m, -CH$_2$*CH$_2$*CH$_2$-), *δ*

2.95~2.98 (2H, d, -CH$_2$NH*CH$_2$*-), δ 2.69 (6H, s, CH$_3$), δ 2.14~2.17 (2H, d, -C=N-*CH$_2$*-), δ 1.62~1.72 (2H, m, -CH$_2$*CH$_2$*CH$_2$-). Anal. Calcd (found) for [Zn(PDI-Py)]Br$_2$ (C$_{20}$H$_{25}$N$_5$ZnBr$_2$): %C 42.85, (43.02); %H 4.49, (4.50); %N 12.49, (13.08).

[Zn(PDI-Py-CH$_3$$^+I^-$)]Br$_2$. ^{1}H NMR (DMSO-$d_6$, 400 MHz, Figure A.91): δ 9.33~9.35 (2H, d, *Py*-H), δ 9.03 (2H, s, *Py*-H), δ 8.94~8.95 (2H, d, *Py*-H), δ 4.51~4.57 (H, t, -CH$_2$*NH*CH$_2$-), δ 4.47 (3H, s, N-*CH$_3$*$^+$), δ 4.19~4.22 (2H, d, -*CH$_2$*NHCH$_2$-), δ 3.77~3.84 (2H, t, -C=N-*CH$_2$*-), δ 3.12~3.20 (2H, m, -CH$_2$*CH$_2$*CH$_2$-), δ 2.97~3.00 (2H, d, -CH$_2$NH*CH$_2$*-), δ 2.72 (6H, s, CH$_3$), δ 2.15~2.19 (2H, d, -C=N-*CH$_2$*-), δ 1.65~1.75 (2H, m, -CH$_2$*CH$_2$*CH$_2$-). Anal. Calcd (found) for [Zn(PDI-Py-CH$_3$$^+I^-$)]Br$_2$ (C$_{21}$H$_{28}$N$_5$ZnIBr$_2$): %C 35.90, (36.04); %H 4.02, (4.08); %N 9.97, (10.16).

4.4.3 Electrochemical Methods and Product Analysis

Electrochemical experiments were conducted using a Bio-Logic SP-200 potentiostat/galvanostat with data recorded using the Bio-Logic EC-Lab V10.44 software package. In all measurements, the reference electrode was a Ag/AgNO$_3$ (1.0 mM in MeCN with 0.1 M nBu$_4$NPF$_6$) nonaqueous reference electrode separated from the solution by a CoralPor® glass frit (Bioanalytical Systems, Inc.) and externally referenced to the ferrocenium/ferrocene redox couple (Fc$^{+/0}$).

Cyclic Voltammetry (CV) under N$_2$ and CO$_2$. Cyclic voltammograms were conducted in quiescent solution, using a 0.071 cm^2 glassy carbon disk working electrode (CH instruments), a Ag/AgNO$_3$ (1.0 mM in MeCN with 0.1 M nBu$_4$NPF$_6$) nonaqueous reference electrode and a carbon rod auxiliary electrode (99.999%, Strem Chemicals). Electrolyte solutions contained 0.1 M nBu$_4$NPF$_6$ in MeCN with reported concentrations of H$_2$O. The typical scan rate for reported CVs was 0.050 V/s unless otherwise noted. Prior to each measurement, the electrolyte solution was sparged with either N$_2$ or CO$_2$ as indicated for at least 10 min, and the headspace was then blanketed with the same gas during the measurement. To avoid electrolyte evaporation, all gases were saturated with MeCN before use by first bubbling them through a gas-washing bottle filled with MeCN. The uncompensated solution resistance (R$_u$ $\approx$ 120 Ω) in the cell was measured using a single-point impedance measurement at 100 kH$_z$ with a 20 mV amplitude about the open-circuit potential before each set of measurements. CVs were automatically corrected for *iR* drop at 85% through positive feedback using the Bio-Logic EC-Lab software.

For all the calculations of kinetic parameters in our study, $E^0_{CO_2} = -1.36$ V vs Fc$^{+/0}$ (-0.72 V vs SHE) is used as the thermodynamic potential for the CO$_2$ reduction in MeCN in the presence of H$_2$O. This thermodynamic potential takes into consideration that the true proton source is

dissolved CO_2 (i.e. carbonic acid, H_2CO_3) instead of H_2O.[27, 31] More recently, some reports have shown that apparent acidity of the CO_2-saturated acetonitrile/water system is also dependent on the concentration of H_2O, and that $E^0_{CO_2}$ can vary greatly from -1.63 V vs $Fc^{+/0}$ in 0.01 M H_2O to -1.25 V vs $Fc^{+/0}$ in the presence of 11 M H_2O.[41-42]

Controlled-Potential Electrolysis (CPE). All controlled-potential electrolysis experiments in this study were conducted in the H-cell shown in Figure A.92. We have previously shown this electrolysis cell design is gas-tight through electrolysis experiments in N_2-sparged MeCN solutions with 1 M acetic acid for the hydrogen evolution reaction (HER) at Pt foil (0.1 mm thick, Premion™, 99.99% metals basis) and glassy carbon plate (HTW Hochtemperatur-Werkstoff GmbH) working electrodes.[43] The Faradaic Efficiency for H_2 production as measured from the post-electrolysis headspace was ~100% in these previous studies (Table A.20),[43] confirming that the electrolysis cell is gastight.

The left chamber held the glassy carbon working electrode and $Ag/AgNO_3$ reference electrode, and was filled with 20 mL MeCN solution of 0.3 mM catalyst with 0.1 M nBu₄NPF₆ and the reported concentrations of H_2O in the manuscript. The right chamber held the Nichrome wire counter electrode, filled with 15 mL MeCN solution of 5 mM Fc with 0.1 M nBu₄NPF₆ and the same concentration of H_2O as the left chamber. The two chambers were separated by a fine-porosity glass frit. The total volume of cell (149.56 mL) was determined by measuring the mass of H_2O necessary to fill the cell completely when the cell was fully assembled with the working and reference electrode, and the headspace volume of 114.56 mL for the CPE was calculated by subtracting the electrolyte solution volume 35.00 mL from the total cell volume.

The working electrode was a glassy carbon plate (3.2 cm × 1.6 cm × 0.1 cm, HTW Hochtemperatur-Werkstoff GmbH) with half immersed in the electrolyte solution. Before each

experiment, the working electrode was manually polished on 600-grit SiC polishing paper (Buehler, Ltd) and sonicated for 5 min in *i*-PrOH. The counter electrode was Nichrome wire (0.2595 Ω ft^{-1}, Arcor Electronics). Prior to each CPE experiment, the electrolyte solution was purged with CO_2 or N_2 for 30 minutes and then sealed under an atmosphere of CO_2 or N_2. To prevent electrolyte evaporation, all gases were saturated with MeCN before use by first bubbling them through a gas-washing bottle filled with MeCN.

The CPE experiments were conducted without *iR* compensation for solution resistance (Ru $\approx 60 \ \Omega$), and the reported electrolysis potentials are the actual applied potentials. After each electrolysis, 5 mL aliquots of the headspace of the electrolysis cell was collected by a Pressure-Lok gas-tight syringe (10 mL, Valco VICI Precision Sampling, Inc.), and injected into a 3 mL sample loop on a gas chromatography system to determine CO and H_2 concentrations. The post-electrolysis solution was analyzed using high performance liquid chromatography to determine the concentrations of other possible liquid products including HCOOH. The Faradaic efficiency of every product was calculated by dividing the measured product amount by the amount expected on the basis of charge passed during the CPE measurement. In general, the only products observed in measurable quantities (> 0.02 % v/v for GC and > 0.025 mM for HPLC) from our experiments were CO and H_2.

Product Analysis. Gaseous products (*i.e.* CO and H_2) in the headspace after electrolysis were tested by a Thermo Scientific Trace 1310 Gas Chromatograph (GC) with a single 3 mL sample loop leading to two analyzer channels. Using a valve system, column configuration, and method developed by Thermo Scientific and Custom Solutions Group LLC., gases were separated so that H_2 was detected on one channel using an Argon carrier gas, and all other gases were detected on a second channel using a Helium carrier gas. Gases were detected on both channels

using thermal conductivity detectors (TCDs), and chromatographs were analyzed using Thermo Scientific Dionex Chromeleon^{TM} 7.2.2.6686 Chromatography Data System software.

Liquid samples were analyzed for possible dissolved products such as formic acid using a Thermo Scientific Dionex Ultimate 3000 series HPLC equipped with a 5 cm Thermo Scientific HyperREZ XP Carbohydrate H$^+$ LC guard column and a 30 cm Thermo Scientific HyperREZ XP Carbohydrate H$^+$ 8µm LC analytical column in series. ~1 mL liquid samples were collected from the working-electrode chamber post electrolysis and placed in an autosampler from which 10 µL aliquots of each liquid sample were injected into the columns. The eluent was 0.005 M H$_2$SO$_4$ aqueous solution with a flow rate of 0.6 mL·min^{-1}. The temperature of the column was maintained at 50 ℃. Products were detected using a UV-Vis detector, and chromatographs were analyzed using Thermo Scientific Dionex Chromeleon^{TM} 7.2.2.6686 Chromatography Data System software.

4.4.4 Scanning Electron Microscopy/Energy Dispersive X-Ray Spectroscopy (SEM-EDS)

SEM-EDS measurements were used to detect metal deposits associated with catalyst decomposition on the electrode surface after electrolysis. All electrodes tested by SEM-EDS (JEOL-7800FLV FE) were <u>not</u> rinsed post electrolysis as per established best practices.[44-46] SEM images showing the morphology of the electrode surface were recorded with a field emission gun scanning electron microscope at 20 kV acceleration voltage equipped with an energy dispersive X-ray (EDS) detector. For each electrode, SEM-EDS measurements were conducted at 9 random sites on the electrode surface, and the values were then averaged to give the Co weight % for that specific electrode. Each electrolysis measurement was reproduced after 3 independent electrolysis experiments. Therefore, each EDS measurement reported is an average of at least 27 measurements: 9 measurement spots on 3 electrodes after independent electrolysis. Reported errors are standard deviations of all 27 EDS measurements for each electrolysis condition.

4.5 Results and Discussion

4.5.1 Electrochemical Characterization of [Co(PDI-R)] under Non-Catalytic Conditions

The non-catalytic cyclic voltammograms (CVs) of the [Co(PDI-R)] complexes in N_2-saturated MeCN with 0.1 M tetrabutylammonium hexafluorophosphate (*n*BuNPF$_6$) as supporting electrolyte are shown in Figure 4.2. Note that all Co complexes investigated begin in the Co^{3+} oxidation state and are named without Br counter anions for clarity unless otherwise noted. The CVs of [Co(PDI)], [Co(PDI-Ph)] and [Co(PDI-Py)] all display three reversible redox features in the potential range from +0.30 to −2.30 V (Figure 4.2a-c) which are assigned to $Co^{3+/2+}$, $Co^{2+/+}$ and PDI/PDI$^{\bullet-}$ couples,[40, 47-48] and the $E_{1/2}$ values of these redox processes are summarized in Table 4.1. In addition, the Hammett constants (σ_p) for the electron withdrawing/donating ability of H-, Ph-, and Py-substituents para to the metal coordination site are listed in Table 4.1 as a qualitative metric of the comparative electron-withdrawing ability of the R substituents.[49] Note that the σ_p values are listed only as qualitative comparisons of the electronic effects of the substituents, and we do not attempt to distinguish between the field effects and resonance effects when adding conjugated substituents.
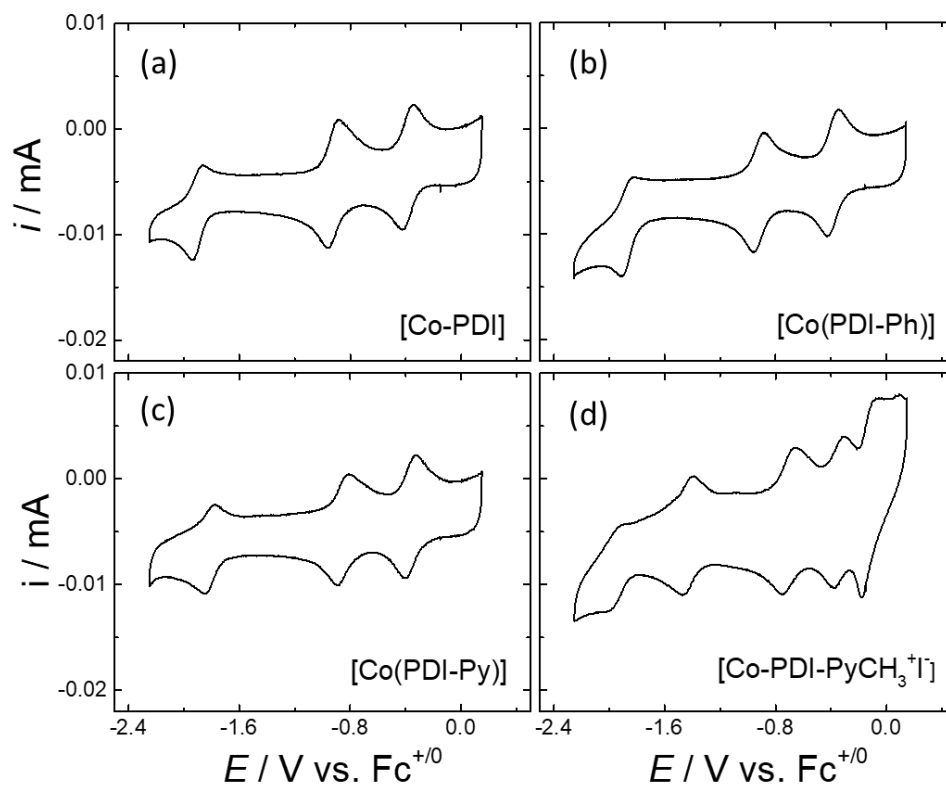
Figure 4.2 CVs of 0.3 mM (a) [Co(PDI)], (b) [Co(PDI-Ph)], (c) [Co(PDI-Py)] and (d) [Co(PDI-PyCH$_3^+$I$^-$)] in N$_2$-saturated MeCN with 0.1 M nBuNPF$_6$, with scan rate 0.05 V/s.

Table 4.1 $E_{1/2}$ values for the Redox Processes and the Hammett constants (σ_p) for substituents for the [Co(PDI-R)] Catalysts.

Catalyst	$\sigma_p{}^a$	$E_{1/2}$ / V vs Fc$^{+/0}$				
		Co$^{3+/2+}$	Co$^{2+/+}$	PDI-R$^+$/PDI-R	PDI-R/PDI-R$^{\cdot-}$	PDI-R$^{\cdot-}$/PDI-R^{2-}
[Co(PDI)]	0	−0.38	−0.92	-	−1.88	≤−2.3^b
[Co(PDI-Ph)]	−0.01	−0.37	−0.91	-	−1.86	−2.43 (red)^c
[Co(PDI-Py)]	0.44	−0.35	−0.85	-	−1.80	−2.37
[Co(PDI-PyCH$_3^+$I$^-$)]	-	−0.34	−0.70	−1.43	−1.95	−2.27 (red)

^{a} Hammett constants for substituents on the PDI ligand scaffold para to the metal-coordination site (H, Ph, or Py) from Ref [49].

^{b}The PDI-R$^{\cdot-}$/PDI-R^{2-} potential for [Co(PDI)] cannot be determined because it coincides with catalytic H$_2$ evolution from residual H$_2$O at −2.3 V (Figure A.94). ^{c} The PDI-R$^{\cdot-}$/PDI-R^{2-} couple for [Co(PDI-Ph)] is irreversible, and the potential of the reduction peak is reported (Figure A.95).

For [Co(PDI-Ph)], there is a very modest positive shift in potential for each redox couple compared to those of the parent [Co(PDI)]. This shift is attributed to the increased delocalization and resonance stabilization of added electrons in the extended π-conjugated structure.[16-17, 19-20] For [Co(PDI-Py)], there is an additional positive shift in the redox potentials compared to [Co(PDI-Ph)] that is ascribed to the added electron-withdrawing effect from the pyridyl group in the ligand.[24-26, 50] An additional redox feature is present in the CVs for [Co(PDI)], [Co(PDI-Ph)] and [Co(PDI-Py)] at potentials more negative than -2.30 V (Figure A.94-A.96), although it is partially obscured due to overlap with the onset of the hydrogen evolution reaction (HER). This additional redox feature is assigned to the ligand-based PDI-R$^{\bullet-}$/PDI-R^{2-} redox couple, although we note that we cannot definitively rule out an alternative assignment of a Co$^{+/0}$ redox couple.

For [Co(PDI-PyCH$_3$$^+I^-$)], a total of five redox features are observed in the same potential window (Figure 4.2d). The most positive redox feature at -0.13 V is associated with the I$_2$/I$^-$ redox process of the I$^-$ counterion, and this assignment is consistent with the CV of KI in MeCN under N$_2$ (Figure A.93). The other four redox features are assigned (from positive to negative) to the Co$^{3+/2+}$, Co$^{2+/+}$, PDI-R$^+$/PDI-R, and PDI-R/PDI-R$^{\bullet-}$ redox couples (Table 4.1). The Co$^{3+/2+}$ and Co$^{2+/+}$ couples are all shifted more positive for [Co(PDI-PyCH$_3$$^+I^-$)] compared to the other [Co(PDI-R)] (Table 4.1), suggesting that the addition of the cationic N-methylpyridinium group to the ligand facilitates reduction of the complex. In the first ligand-based reduction at -1.43 V vs. Fc$^{+/0}$ (PDI-R$^+$/PDI-R), we postulate that the ligand radical is likely mostly localized on the pyridine substituent consistent with the assignment of structurally-similar metalloviologen-like complexes.[51-53] The electron from the second ligand-based reduction at -1.95 V vs. Fc$^{+/0}$ (PDI-R/PDI-R$^{\bullet-}$) is likely delocalized throughout the structure with increased residence time on the imine carbons moieties similar to what is expected for metal complexes with PDI-R and similar

176

ligands.[40, 44-45, 48, 54-63] Note that the more negative potentials of the PDI-R/PDI-R$^{\bullet-}$ redox couple in [Co(PDI-PyCH$_3^+$I$^-$)] compared to the other three [Co(PDI-R)] complexes may be due to the increased electron density on the ligand from the preceding PDI-R$^+$/PDI-R ligand reduction. For [Co(PDI-PyCH$_3^+$I$^-$)], an additional irreversible reduction is observed in the voltammograms at −2.27 V vs Fc$^{+/0}$ consistent with either another ligand reduction (PDI-R$^{\bullet-}$/PDI-R^{2-}) or a Co$^{+/0}$ redox event (Figure A.97, Table 4.1).

4.5.2 Ligand-Based Redox Features in [Zn(PDI-R)] and DAP-R

To check the validity of our assignment of the voltammetric features for the [Co(PDI-R)] complexes, we also measured CVs under identical conditions of the analogous Zn complexes, [Zn(PDI-R)] (Figures A.98-A.101). Because the Zn metal center should be redox inactive in the potential range of interest, these measurements allow us to assess independently the ligand-based redox events. A summary of selected redox potentials from the CVs of the [Zn(PDI-R)] complexes is shown in Table 4.2 (the full table is in Table A.21).

The CVs of the [Zn(PDI)], [Zn(PDI-Ph)] and [Zn(PDI-Py)] complexes (Figure A.98-A.100) all display two stepwise irreversible redox features in the potential range from −2.00 to −1.40 V vs. $Fc^{+/0}$ which are assigned to the redox features of the PDI ligand based on previous reports of similar Zn complexes.[54, 64] In particular, these redox features are consistent with the PDI/PDI$^{\bullet-}$, and PDI-R$^{\bullet-}$/PDI-R^{2-} couples assigned in the analogous [Co(PDI-R)] complexes (Table 4.1 and A.21). The more positive potentials of these ligand reductions in the Zn complexes is attributed to the fact that the ligand is coordinated to a redox-inactive Zn^{2+} (M^{2+} cation), whereas the coordinated Co in [Co(PDI-R)] exists as a less-electron withdrawing Co^+ (M^+ cation) during the ligand reduction events. Importantly, the potential of the PDI/PDI$^{\bullet-}$ becomes more positive as sequential substituent effects are incorporated into the ligand scaffold consistent with the observed behavior of the [Co(PDI-R)] systems. Interestingly, for the [Zn(PDI)], [Zn(PDI-Ph)] and [Zn(PDI-Py)] complexes, the PDI-R$^{\bullet-}$/PDI-R^{2-} potentials become more negative as the sequential substituent effects are added, although it is difficult to ascertain whether this trend is consistent with what is seen in the analogous [Co(PDI-R)] system because accurate assignments of the PDI-R$^{\bullet-}$/PDI-R^{2-} redox potentials in the Co system are complicated by the overlapping onset of the HER.

178

Table 4.2 $E_{1/2}$ values for the Redox Processes for the [Zn(PDI-R)] and DAP-R compounds.

Compound	$E_{1/2}$ / V vs Fc$^{+/0}$		
	PDI-R$^+$/PDI-R	PDI-R/PDI-R$^{\bullet-}$	PDI-R$^{\bullet-}$/PDI-R^{2-}
[Zn(PDI)]	-	−1.65 (red)[a]	−1.84 (red)[a]
[Zn(PDI-Ph)]	-	−1.64 (red)[a]	−1.96 (red)[a]
[Zn(PDI-Py)]	-	−1.49 (red)[a]	−1.98 (red)[a]
[Zn(PDI-PyCH$_3^+$I$^-$)]	−0.98	−1.41	-1.96 (red)[a]
DAP	-	−2.08 (red)[a]	-
DAP-Ph	-	−2.04 (red)[a]	-
DAP-Py	-	−1.92 (red)[a]	-
DAP-PyCH$_3^+$I$^-$	−1.22	−1.76 (red)[a]	-

[a] These redox features are irreversible, and only the potential of the reduction peak is reported.

The CV of Zn(PDI-PyCH$_3$$^+I^-$)] shows four redox processes (Figure A.101): an I$_2$/I$^-$ couple at -0.13 V associated with the I$^-$ counterion, two quasi-reversible ligand-based redox events at -0.98 V and -1.41 V, and a third irreversible ligand-based redox event at -1.96 V (Table 4.2 and A.21). These redox features are consistent with the I$^-$/I$_2$, PDI-R$^+$/PDI-R, and PDI-R/PDI-R$^{\bullet-}$, and PDI-R$^{\bullet-}$/PDI-R^{2-} couples assigned in the analogous [Co(PDI-PyCH$_3$$^+I^-$)] complex (Tables 4.1 and A.21). As with the other [Zn(PDI-R)] complexes, the potentials for these redox events are more positive compared to those of [Co(PDI-PyCH$_3$$^+I^-$)] due to the dicationic nature of the coordinated Zn^{2+} in the complex. Moreover, the PDI-R/PDI-R$^{\bullet-}$ redox potential for [Zn(PDI-PyCH$_3$$^+I^-$)] is shifted significantly positive compared to that of the other [Zn(PDI-R)] complexes, similar to the trend observed for [Co(PDI-PyCH$_3$$^+I^-$)] compared to the other [Co(PDI-R)] complexes. In general, the ligand-based redox features in the [Zn(PDI-R)] complexes are consistent with our assignments in the analogous [Co(PDI-R)] complexes of interest, and provide an important secondary confirmation of our peak assignments.

For a tertiary confirmation, we also measured the CVs of the diacetylpyridine ligand precursors, DAP-R (Figures A.102-A.105). A summary of selected redox potential from the CVs of the DAP-R compounds is shown in Table 4.2 (the full table is in Table A.21). Because the metal PDI-R complexes are synthesized through a template-synthesis, we were unable to isolate the PDI-R ligands. However, we expect the DAP-R ligand precursors to have similar redox features to the PDI-R ligands based on their similar structures. The CVs of ligands DAP, DAP-Ph and DAP-Py (Figure A.102-A.104) all display an electrochemically-irreversible reduction peak at potentials more negative than -1.90 V vs. Fc$^{+/0}$ assigned to the reduction of the DAP-R ligand (DAP-R/DAP-R$^{\bullet-}$). There is a smaller oxidative feature in the anodic scan positive of -1.54 V vs. Fc$^{+/0}$ for these complexes which may be from partial reoxidation of the reduced DAP-R. Overall,

180

the DAP-R/DAP-R$^{\bullet-}$ reduction potential shifts positive as sequential substituent effects are incorporated into the ligand precursor consistent with the observed trend in [Co(PDI-R)] complexes.

For DAP-PyCH$_3$$^+I^-$, three reversible redox features are observed in the CV (Figure A.105): an I$_2$/I$^-$ couple at −0.13 V associated with the I$^-$ counterion, a reversible redox feature at −1.22 V (DAP-R$^+$/DAP-R), and an irreversible redox feature at −1.76 V assigned to a second ligand reduction (DAP-R/DAP-R$^{\bullet-}$). These redox features are qualitatively consistent with the I$^-$/I$_2$, PDI$^+$/PDI, and PDI-R/PDI-R$^{\bullet-}$ couples assigned in the analogous [Co(PDI-PyCH$_3$$^+I^-$)] complex (Table 4.1 and A.21). Moreover, the redox processes for DAP-PyCH$_3$$^+I^-$ are shifted significantly positive compared to the analogous redox processes of the other DAP-R complexes, similar to the trend observed for [Co(PDI-PyCH$_3$$^+I^-$)] compared to the other [Co(PDI-R)] complexes. In general, the redox features in the DAP-R ligand precursors are consistent with our assignments in the analogous [Co(PDI-R)] complexes of interest, and provide an important tertiary confirmation of our peak assignments.

4.5.3 Electrocatalytic Activity of [Co(PDI-R)] for the CO$_2$RR

The CVs of the [Co(PDI-R)] complexes in CO$_2$-saturated MeCN with no added proton source all exhibit a catalytic reduction current near the PDI-R/PDI-R$^{\bullet-}$ redox features (Figure 4.3). This suggests that [Co$^+$(PDI-R)$^{\bullet-}$] is the active species for electrocatalytic CO$_2$ activation and reduction consistent with previous studies of Co complexes with similar tetraazamacrocyclic and related ligands.[40, 44-45, 47-48] A zoomed in region of the CVs near the catalytic onset is shown in Figures A.111-A.114, and the onset potentials are summarized in Table 4.3. Note that although no proton source was added, an estimated ~0.04 M H$_2$O is assumed present in our system based on previously-reported Karl-Fisher titrations of similar electrolyte solutions in MeCN.[39] Under these conditions, [Co(PDI-Ph)] catalyzes the reduction of CO$_2$ at roughly the same onset potential, E_{onset}, compared to [Co(PDI)] but with slightly increased catalytic current as illustrated by the i_c/i_p measurements (i_c = catalytic current under CO$_2$; i_p = redox current of active species under N$_2$). [Co(PDI-Py)], which has the same extent of ligand conjugation as [Co(PDI-Ph)] but with the more electron-withdrawing pyridyl moiety, operates with higher catalytic current and 0.05 V more positive E_{onset} for the CO$_2$RR than [Co(PDI-Ph)]. [Co(PDI-PyCH$_3$$^+I^-$)], which has an additional positive charge on the ligand scaffold compared to [Co(PDI-Py)], operates with even higher catalytic activity and 0.05 V more positive E_{onset} for the CO$_2$RR.

Figure 4.3 CVs of 0.3 mM (a) [Co(PDI)], (b) [Co(PDI-Ph)], (c) [Co(PDI-Py)] and (d) [Co(PDI-PyCH$_3{}^+$I$^-$)] in CO$_2$-saturated MeCN with 0.1 M nBuNPF$_6$, with scan rate 0.05 V/s.

Table 4.3 i_c/i_p and E_{onset} values for the CO$_2$RR by Co(PDI) complexes based on catalytic CVs

Catalysts	No H$_2$O added		11.0 M H$_2$O	
	i_c/i_p	E_{onset} / V vs. Fc$^{+/0}$	i_c/i_p	E_{onset} / V vs. Fc$^{+/0}$
[Co(PDI)]	5.82	−1.75	13.2	−1.70
[Co(PDI-Ph)]	6.07	−1.75	18.7	−1.68
[Co(PDI-Py)]	8.11	−1.70	37.9	−1.60
[Co(PDI-Py-CH$_3{}^+$I$^-$)]	10.5	−1.65	106	−1.52

Adding H_2O as a proton source into the CO_2-saturated solutions leads to dramatically increased catalytic activity for all Co catalysts which is attributed to increased CO_2 reduction activity (Figure 4.4 for 11.0 M H_2O, other concentrations shown in Figure A.107-A.110). We observe the same qualitative increases in activity (i_c/i_p) and positive shifts in catalytic onset potential (E_{onset}) in the presence of 11.0 M H_2O compared to the system with no H_2O added as substituent effects are sequentially incorporated into the [Co(PDI-R)] system, but the magnitude of the changes are much larger in the presence of 11.0 M H_2O (Table 4.3). In particular, the [Co(PDI-PyCH$_3^+$I$^-$)] complex catalyzes the reduction of CO_2 with ~8 × higher i_c/i_p and 0.18 V more positive E_{onset} compared to the [Co(PDI)] parent complex in the presence of 11.0 M H_2O, and ~10 × higher i_c/i_p and 0.13 V more positive E_{onset} compared to [Co(PDI-PyCH$_3^+$I$^-$)] in the solution with no water added (Table 4.3). Note that the catalytic peak shape for the most active catalysts [Co(PDI-Py)] and [Co(PDI-Py-CH$_3^+$I$^-$)] resembles an inverted peak.[65] We attribute this peak shape to the overlap of the catalytic current response with a more negative redox event, presumably (PDI-R$^{•-}$/PDI-R^{2-}), resulting in an electrocatalytically-inactive complex at more negative potentials that regains activity upon reoxidation. A similar behavior has been observed in the case of CO_2 reduction by Co-[44-45], Mn-[66] and Re-based[26, 67] catalysts.
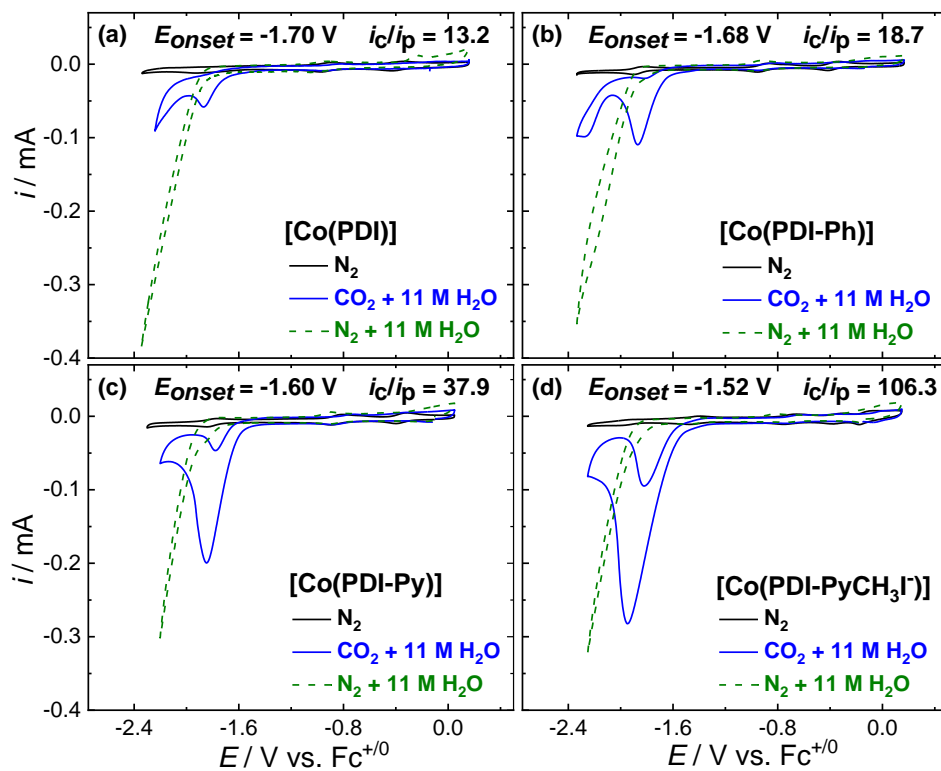
Figure 4.4 CVs of 0.3 mM [Co(PDI-R)] complexes in N_2-saturated MeCN (black solid line), CO_2-saturated MeCN with 11 M H_2O (blue solid line) and N_2 with 11 M H_2O (green dashed line). The supporting electrolyte is 0.1 M nBuNPF$_6$ and the scan rate is 0.05 V/s.

For [Co(PDI-Py-CH$_3^+$I$^-$)], the catalytic onset for the CO$_2$RR in the presence of 11 M H$_2$O is shifted significantly positive such that the catalytic onset coincides with the [(PDI-R$^+$/PDI-R)] redox couple as shown in the zoomed in region of the CV near the catalytic onset in Figure A.114. This suggests that there is a change in catalytically-active species upon addition of H$_2$O, from the quadruply reduced [Co^I(PDI-Py-CH$_3$)$^{\bullet-}$] species in solutions with no added H$_2$O, to the triply reduced [Co^I(PDI-Py-CH$_3$)]$^+$ in the solutions with 11 M H$_2$O. We postulate that this change in the catalytically-active species is due to the reducing power of these charge equivalents relative to the thermodynamic potential for the CO$_2$RR, $E_{CO_2}^0$. When considering the CO$_2$RR in acetonitrile with water as a proton source, $E_{CO_2}^0$ is often estimated as -1.36 V vs Fc$^{+/0}$ (-0.72 V vs SHE) which takes into account the fact that the true proton donor is dissolved CO$_2$ (i.e. carbonic acid, H$_2$CO$_3$).[27, 31] More recently, it has been shown that the apparent acidity of the CO$_2$-saturated acetonitrile/water system is dependent on the concentration of H$_2$O, and the result is that $E_{CO_2}^0$ can vary substantially: from -1.25 V vs Fc$^{+/0}$ in the presence of 11 M H$_2$O to -1.63 V vs Fc$^{+/0}$ in 0.01 M H$_2$O.[41-42] In the case of the CO$_2$RR by [Co(PDI-Py-CH$_3^+$I$^-$)] with no water added (~0.04 M H$_2$O),[39] the expected $E_{CO_2}^0 < -1.57$ V is negative of the (PDI-R$^+$/PDI-R) redox couple, suggesting that [Co^I(PDI-Py-CH$_3$)]$^+$ does not have the reducing power to activate and reduce CO$_2$. Thus, in the system with no water added, further reduction of the catalyst to [Co^I(PDI-Py-CH$_3$)$^{\bullet-}$] is necessary to activate and reduce CO$_2$. However, when 11 M H$_2$O is added to the system, $E_{CO_2}^0$ becomes 0.3 V more positive compared to the system with no added H$_2$O, and [Co^I(PDI-Py-CH$_3$)]$^+$ has sufficient reducing power to activate and reduce CO$_2$. Thus, for the CO$_2$RR by [Co(PDI-Py-CH$_3^+$I$^-$)] in the presence of 11 M H$_2$O, the catalytic onset is near that of the (PDI-R$^+$/PDI-R) couple.

As a control experiment, CVs of the [Co(PDI-R)] in N_2-saturated solution under otherwise equivalent conditions show catalytic activity for the competitive HER at much more negative potential, supporting our assertion that the catalytic currents measured in the CO_2-saturated solutions are due to the CO_2RR (Figure 4.4). However, it is important to note that the solution acidity in CO_2-saturated solutions in the presence of H_2O will be much more acidic than analogous N_2-saturated solutions,[27, 31, 41-42, 68] and so the comparison of CVs under N_2 and CO_2 in Figure 4.4 are not solely sufficient to substantiate that the observed catalytic activity in the CO_2-saturated solution is due to the CO_2RR. To further confirm that the catalytic activity in CO_2-saturated solutions with 11 M H_2O is due to CO_2 reduction, we conducted 30-min controlled-potential electrolysis (CPE) experiments with 0.3 mM solutions of each [Co(PDI-R)] catalyst at $E_{app} = -1.95$ V (without iR-compensation), which is the peak potential of [Co(PDI)] for the CO_2RR. Representative CPE current traces are shown in Figure A.119, and the results of the CPE experiments are summarized in Table 4.4. Gas phase products were analyzed by gas chromatography and the Faradaic efficiency of each product, FE(product), was determined. Turnover numbers, TON_{CPE}, and turnover frequencies, TOF_{CPE}, from the electrolyses were calculated from the CPE data using the equations described by Savéant *et al.* (see SI for further discussion of TOF_{CPE}).[69-70] SEM-EDS measurements on un-rinsed glassy carbon working electrodes post-electrolysis were used to assess the extent of metal deposition from catalyst decomposition during the electrolysis (Figure A.115-A.118).[44-46]

Table 4.4 Summary of CPE Results for the [Co(PDI-R)] Catalysts.

Catalyst	CPE under CO_2 with 11 M H_2O @ -1.95 V					
	Charge/ C	FE(CO) / %	FE(H_2) / %	TOF_{CPE} / s^{-1} [a]	TON_{CPE}[a]	Co weight%
[Co(PDI)]	6.2 ± 1.0	43 ± 12	11 ± 7	9.8 ± 6.6	$1.8 \pm 1.2 \times 10^4$	0.56 ± 0.18
[Co(PDI-Ph)]	8.8 ± 1.4	59 ± 4	1.5 ± 0.4	$3.1 \pm 1.3 \times 10^1$	$5.5 \pm 2.4 \times 10^4$	0.24 ± 0.11
[Co(PDI-Py)]	9.8 ± 1.2	97 ± 5	0.4 ± 0.1	$1.0 \pm 0.3 \times 10^2$	$1.9 \pm 0.5 \times 10^5$	0.11 ± 0.05
[CoPDI-PyCH$_3^+$I$^-$]	16.7 ± 1.8	96 ± 3	0.6 ± 0.6	$8.0 \pm 1.6 \times 10^2$	$1.4 \pm 0.3 \times 10^6$	0.06 ± 0.05

Reported values are averages from three or more independent measurements with reported standard deviations. [a] TOF_{CPE} and TON_{CPE} values were determined from each independent CPE measurement, and the reported values are averages of these individual TOF_{CPE} and TON_{CPE} values with reported standard deviations.

The CPE results show increasing activity, reflected by increased charged passed and TOF$_{CPE}$, in the order of [Co(PDI)] < [Co(PDI-Ph)] < [Co(PDI-Py)] < [Co(PDI-PyCH$_3^+$I$^-$)] (Table 4.4). This general activity trend is analogous to that seen from the electrocatalytic CVs in Figure 4.4. The FE(CO) also increases according to the same trend, and the Co weight% of deposited metal measured post-electrolysis decreases in the same catalyst order. These results suggest that the activity and selectivity for the CO$_2$RR and stability of the [Co(PDI-R)] catalysts increase as the substituent effects are sequentially incorporated into the structure. In particular, [Co(PDI-PyCH$_3^+$I$^-$)] reduces CO$_2$ with ~82 × higher TOF$_{CPE}$ compared to [Co(PDI)] and > 95% FE for CO production with very little Co weight% from catalyst deposition or decomposition during the electrolysis.

Other control experiments were conducted to further confirm the catalytic ability of [Co(PDI-R)] complexes for the CO$_2$RR. The CVs of the bare glassy carbon electrode in the CO$_2$-saturated solution in the presence of 11.0 M H$_2$O (Figure A.120) show negligible catalytic current increase at < −2.20 V vs. Fc$^{+/0}$, and we have previously reported that no CO product is detected in the 30-min CPE experiment at bare glassy carbon electrodes under equivalent conditions (Table A.23).[44] This supports our assertion that the observed catalytic activity for the CO$_2$RR in CVs and CPE experiments with [Co(PDI-R)] catalysts requires the presence of the dissolved Co complexes and is not due to background activity from the glassy carbon electrodes. In addition, CVs of [Zn(PDI-R)] analogues in CO$_2$-saturated solutions under the equivalent conditions also exhibit negligible activity for the CO$_2$RR (Figure A.121-A.124), indicating that the presence of the Co center in the structure is essential to achieve the catalytic ability for the CO$_2$RR. Finally, the CVs of [Co(PDI-Py)] in CO$_2$-saturated MeCN solutions in the presence of 11.0 M H$_2$O displayed no change in catalytic activity with changing concentration of KI (Figure A.125), suggesting that the

I$^-$ counterion of the pyridinium counterion likely plays no role in catalytic activity of the [Co(PDI-R)] catalysts for the CO$_2$RR.

4.5.4 Kinetic Analysis of Voltammetric Data

To better quantify the relative catalytic activity of the [Co(PDI-R)] complexes in comparison to each other and other reported systems, we have conducted kinetic analyses to extract the intrinsic catalytic rate and maximum turnover frequency for these catalysts from the catalytic CVs in Figure 6. Based on previous mechanistic studies of [Co(PDI)],[40, 48] we propose a general *ECEC* mechanism for the CO_2RR by the [Co(PDI-R)] complexes (Schemes 4.9 and 4.10). For [Co(PDI)], [Co(PDI-Ph)], and [Co(PDI-Py)], the catalytic onset in CO_2-saturated solutions with 11 M H_2O occurs near the (PDI-R/PDI-R$^{\bullet-}$) redox couple (Figure A.111-A.113), indicating that [Co^I(PDI-R$^{\bullet-}$)] (E_1) is the active species to initiate the catalysis (C_1) (Scheme 4.9). For [Co(PDI-PyCH_3$^+$I$^-$)], the catalytic onset under the same conditions occurs near the (PDI-R$^+$/PDI-R) redox couple (Figure A.114), suggesting that [Co^I(PDI-Py-CH_3)]$^+$ (E_1) is the active species to initiate the catalysis (C_1) (Scheme 4.10). The rate constants of the sequential E_1C_1 and E_2C_2 steps are denoted k_1 and k_2, but it is difficult to determine which one is rate determining solely based on the catalytic CVs in Figure 4.4.

$$[Co^I(PDI\text{-}R)] \ + \ e^- \ \rightleftharpoons \ [Co^I(PDI\text{-}R^{\bullet-})] \qquad E_1$$

$$[Co^I(PDI\text{-}R^{\bullet-})] \ + \ CO_2 \ \rightleftharpoons \ [Co^I(PDI\text{-}R^{\bullet-})CO_2] \qquad C_1$$

$$k_1$$

$$[Co^I(PDI\text{-}R^{\bullet-})CO_2] \ + \ e^- \ \rightleftharpoons \ [Co(PDI\text{-}R)CO_2]^- \qquad E_2$$

$$[Co(PDI\text{-}R)CO_2]^- \ \xrightarrow{[H^+]} \ [Co^I(PDI\text{-}R)] \ + \ CO \ + \ H_2O \qquad C_2$$

$$k_2$$
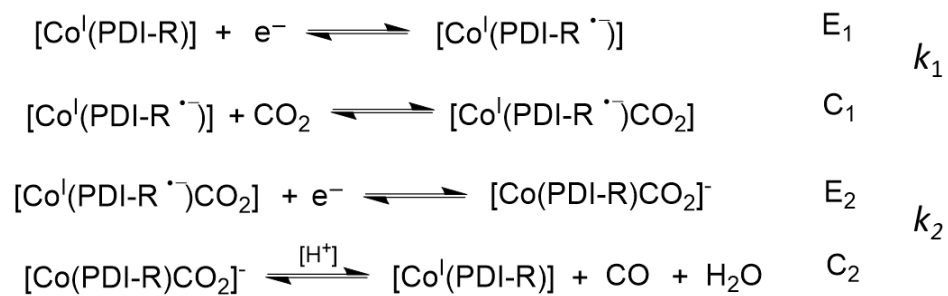
Scheme 4.9 Proposed ECEC mechanism for the CO₂RR by [Co(PDI)], [Co(PDI-Ph)], and [Co(PDI-Py)] in MeCN with 11 M H₂O

$$[Co^I(PDI\text{-}PyCH_3^+)] \ + \ e^- \ \rightleftharpoons \ [Co^I(PDI\text{-}PyCH_3)] \qquad E_1$$

$$k_1$$

$$[Co^I(PDI\text{-}PyCH_3)] \ + \ CO_2 \ \rightleftharpoons \ [Co^I(PDI\text{-}PyCH_3)CO_2] \qquad C_1$$

$$[Co^I(PDI\text{-}PyCH_3)CO_2] \ + \ e^- \ \rightleftharpoons \ [Co^I(PDI\text{-}PyCH_3^{\bullet-})CO_2] \qquad E_2$$

$$k_2$$

$$[Co^I(PDI\text{-}PyCH_3^{\bullet-})CO_2] \ \xrightarrow{[H^+]} \ [Co^I(PDI\text{-}PyCH_3^+)] \ + \ CO \ + \ H_2O \qquad C_2$$
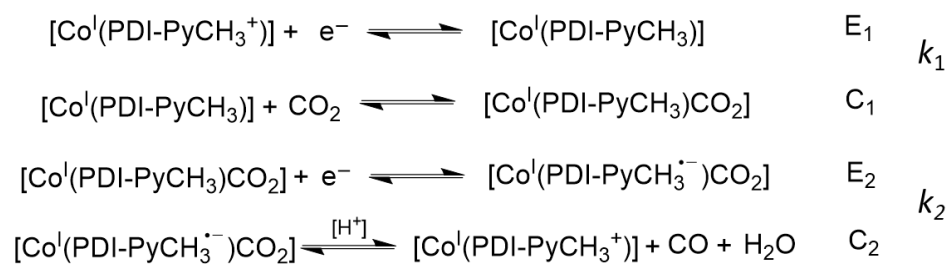
Scheme 4.10 Proposed ECEC mechanism for the CO₂RR by [Co(PDI-PyCH₃⁺I⁻)] in MeCN with 11 M H₂O.

192

In the cases of [Co(PDI)], [Co(PDI-Ph)], and [Co(PDI-Py)], we expect that E_2 is more positive than E_1 ($E_1 < E_2$) (Scheme 4.9) due to the absence of a redox feature for the CO_2-adduct intermediate (E_2) in the catalytic CVs in Figure 4.4. However, for [Co(PDI-PyCH$_3^+$I$^-$)], a prewave feature observed near the (PDI-R$^+$/PDI-R) redox couple prior to the catalytic current increase (Figure A.114) indicates the slow formation of CO_2 adduct intermediate [Co^I(PDI-PyCH$_3$)CO$_2$] (C_1) before the reduction of the intermediate (E_2C_2) to the final produce CO.[71] This observation suggests that E_2 is likely more negative than E_1 ($E_1 > E_2$) for [Co(PDI-PyCH$_3^+$I$^-$)] (Scheme 4.10),[71] which is consistent with the lower nucleophilicity of the Co center in [Co(PDI-PyCH$_3^+$I$^-$)] compared to the other [Co(PDI-R)] complexes as evidenced by the much more positive Co$^{2+/+}$ couple of [Co(PDI-PyCH$_3^+$I$^-$)]. In order to determine the catalytic rates constants for the [Co(PDI-R)] complexes, we first conducted foot-of-the-wave analysis (FOWA) on the catalytic CVs in Figure 4.4. For internal consistency, a standard potential window of (E_{onset} + 0.03 V) to (E_{onset} − 0.03 V) was used in the FOWA to extract kinetic parameters. A rigorous explanation of our FOWA procedure and calculations can be found in the SI. Note that for the purpose of comparison with known systems, we use $E^0_{CO_2} = -1.36$ V vs Fc$^{+/0}$ as the thermodynamic potential for CO_2 reduction in our calculations.[27, 31] This thermodynamic potential takes into consideration that in CO_2-saturated mixed acetonitrile/aqueous solutions, the proton donor is dissolved CO_2 (i.e. carbonic acid, H_2CO_3).[27, 31]

For [Co(PDI)], [Co(PDI-Ph)], and [Co(PDI-Py)], the FOWA plots in Figures A.136-A.138 showed significant curvature which may indicate that $k_1 > k_2$.[72] Under such conditions, the FOWA only estimates the k_1 value[72] rather than the rate-determining k_2, and therefore will not result in an accurate estimate of the overall catalytic rate. In contrast, in the case of [Co(PDI-PyCH$_3^+$I$^-$)] where E_2 is more negative than E_1 ($E_1 > E_2$) (Scheme 4.10), the curvature of the FOWA

plot for [Co(PDI-PyCH$_3^+$I$^-$)] in Figure A.135 indicates $k_1 < k_2$,[72] and the FOWA only estimates the k_2 value rather than the rate-determining k_1.[72] Nevertheless, we estimated the maximum turnover frequency from the FOWA, labeled TOF$_{FOWA}$, according to the procedures outline the SI, and we report the resulting k_{FOWA} = TOF$_{FOWA}$ (=k_1 for [Co(PDI)], [Co(PDI-Ph)], and [Co(PDI-Py)]; =k_2 for [Co(PDI-PyCH$_3^+$I$^-$)]) and log(TOF$_{FOWA}$) values in Table 4.5.   We observe increasing TOF$_{FOWA}$ in the order of [Co(PDI)] < [Co(PDI-Ph)] < [Co(PDI-Py)] < [Co(PDI-PyCH$_3^+$I$^-$)], analogous to the trend in catalytic CVs (Figure 4.4) and CPE experiments (Table 4.4).

Table 4.5 Kinetic parameters for the CO$_2$RR by [Co(PDI-R)] in the presence of 11.0 M H$_2$O

	[Co(PDI)]	[Co(PDI-Ph)]	[Co(PDI-Py)]	[Co(PDI-PyCH$_3^+$I$^-$)]
E_{onset}/ V vs.Fc$^{+/0}$	−1.70	−1.68	−1.60	−1.52
Foot-of-wave analysis (FOWA)				
k_{FOWA} = TOF$_{FOWA}$/ s^{-1}	1.6×10^5	4.2×10^5	2.8×10^6	3.6×10^7
log(TOF$_{FOWA}$/ s^{-1})	5.2	5.6	6.4	7.6
Variable Scan Rate Parameters				
$i_{plateau}$ / mA	1.5×10^{-1}	2.8×10^{-1}	3.8×10^{-1}	5.3×10^{-1}
k_{cat} = TOF$_{cat}$ / s^{-1}	1.5×10^3	4.0×10^3	7.6×10^3	4.1×10^4
log(TOF$_{cat}$/ s^{-1})	3.2	3.6	3.9	4.6
log(TOF$_0$/ s^{-1})	−5.7	−4.9	−3.6	−2.2

In an ideal system, the rate-determining k_{cat} would be determined from the plateau current of an ideal S-shaped current response in pure kinetic zone with no substrate depletion.[70-73] Such an ideal current response is not achievable for the [Co(PDI-R)] system due to the inverted peak shape of the catalytic current response, but can be approximated at fast scan rate where the effects of mass-transport and substrate depletion are minimized.[74] CVs of the [Co(PDI-R)] complexes at variable scan rates from 0.05 V/s to 8.0 V/s are shown in Figure 4.5. A plot of peak current, i_c, as a function of the scan rate, v, asymptotically approaches a limiting current denoted $i_{plateau}$ at fast scan rates ($v \geqslant 4.0$ V/s, Figure 4.6). This limiting current $i_{plateau}$ at fast scan rates is used to calculate the pseudo-first order catalytic rate constant k_{cat} according to Equation 4.1: [70, 75]

$$k_{cat} = \left(\frac{i_{plateau}}{i_p}\right)^2 \frac{(0.466)^2 \cdot nFv}{n'RT} \qquad (4.1)$$

Here, i_p is the peak current associated with the active species under non-catalytic conditions measured at scan rate v, $n = 2$ is the number of electrons transferred per CO_2 per catalyst, $n' = 1$ is the number of catalyst equivalents per turnover, $R = 8.31415$ J mol^{-1} K^{-1} is the ideal gas constant, and $T = 298$ K is room temperature. The resulting $k_{cat} = TOF_{cat}$ values calculated using the corresponding i_p values measured at 0.05 V/s are shown in Table 4.5. As a confidence check, k_{cat} values calculated based on i_p values from all measured scan rates (Figures A.139 – A.142) are shown in Table A.28, and all are equivalent within +/− 20 %. In the case of [Co(PDI)], [Co(PDI-Ph)], and [Co(PDI-Py)] where $E_2 > E_1$ and the curvature of the FOWA plots in Figures A.136-A.138 suggest that $k_1 > k_2$, then k_{cat} is dictated by k_2.[72] In the case of [Co(PDI-PyCH$_3^+$I$^-$)] where $E_1 > E_2$ and the curvature of the FOWA plots in Figure A.135 suggests that $k_1 < k_2$, then k_{cat} is dictated by k_1.[72] Again, we observe increasing k_{cat} in the order of [Co(PDI)] < [Co(PDI-Ph)] < [Co(PDI-Py)] < [Co(PDI-PyCH$_3^+$I$^-$)], analogous to the trend in our other activity metrics.
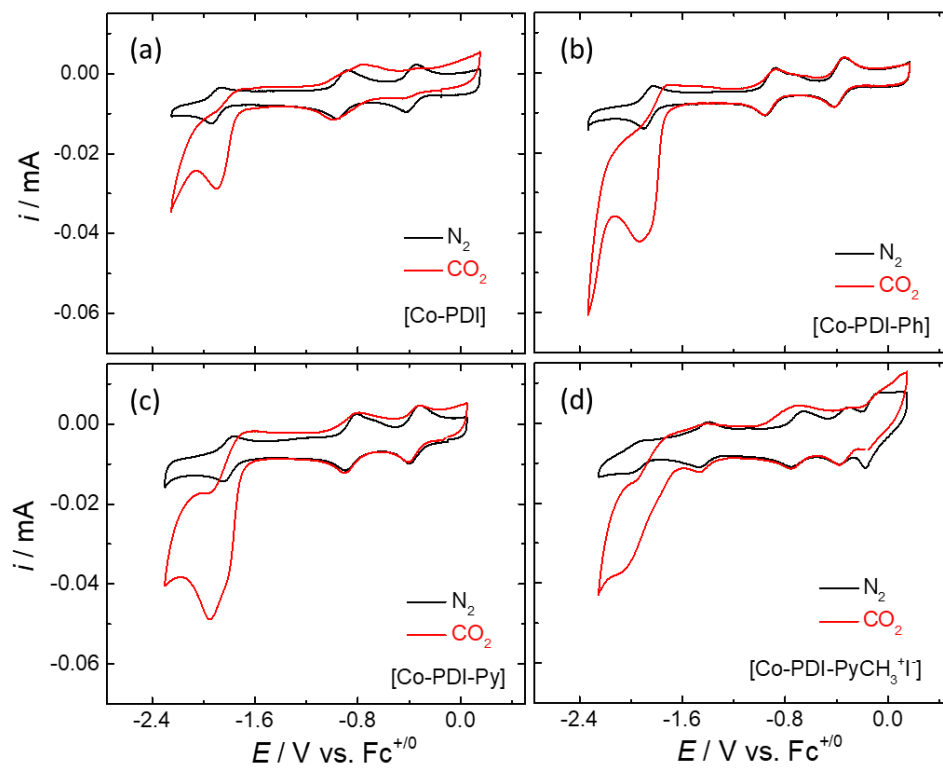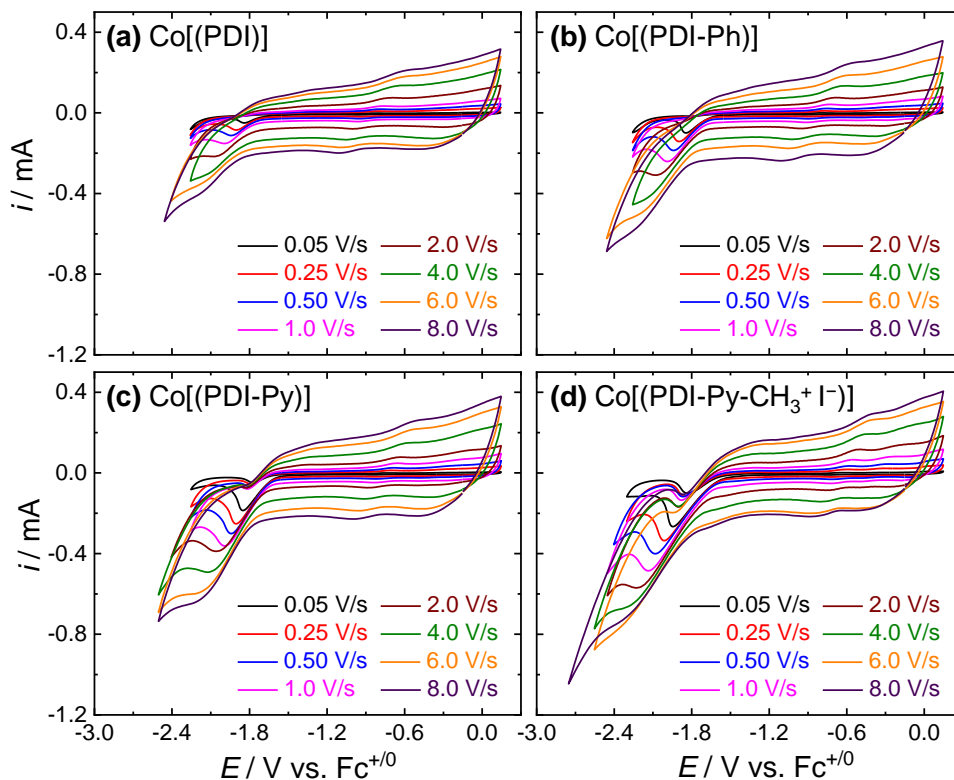
Figure 4.5 CVs of 0.3 mM (a) [Co(PDI)], (b) [Co(PDI-Ph)], (c) [Co(PDI-Py)] and (d) [Co(PDI-PyCH$_3$$^+I^-$)] in CO$_2$-saturated MeCN with 0.1 M nBuNPF$_6$ and 11.0 M H$_2$O, with varying scan rates from 0.05 V/s to 8.0 V/s.
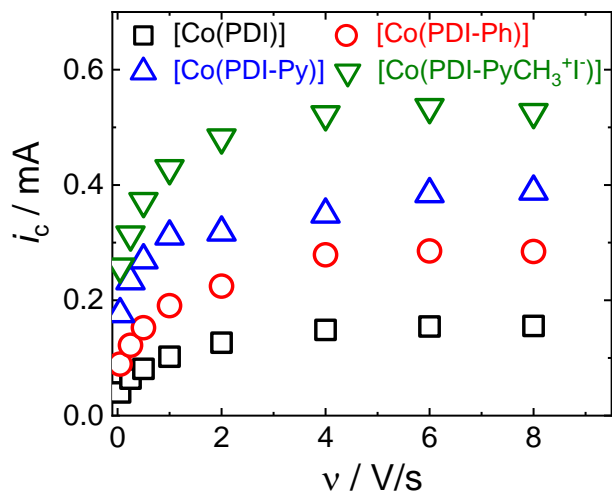
Figure 4.6 Plots of the catalytic current, i_c, as a function of the scan rate, ν, for the CO$_2$RR by [Co(PDI-R)] complexes in CO$_2$-saturated MeCN with 11 M H$_2$O. At sufficiently fast scan rates $\nu \geqslant 4.0$ V/s, we observe scan-rate independent catalytic peak currents for each [Co(PDI-R)] which we denote as the plateau current, $i_{plateau}$.

Using the k_{cat} values calculated from the variable scan rate measurements, we constructed plots of log(TOF) as a function of overpotential η for the CO_2RR by the [Co(PDI-R)] complexes as shown in Figure 4.7 (detailed calculations can be found in the SI).[70, 75] Note that for the purpose of comparison with known systems, we use $E^0_{CO_2} = -1.36$ V vs $Fc^{+/0}$ as the thermodynamic potential for CO_2 reduction in our calculations.[27, 31] For [Co(PDI)], [Co(PDI-Ph)] and [Co(PDI-Py)] where $E_1 < E_2$ in the proposed *ECEC* mechanism, the redox potential of catalytic active species $E^0_{cat} = E_1 = E_{1/2}(PDI-R/PDI-R^{\cdot-})$.[72] In contrast, for [Co(PDI-PyCH$_3^+$I$^-$)] where $E_1 > E_2$, the redox potential of catalytic active species $E^0_{cat} = E_2$ is the redox potential of CO_2 adduct intermediate [Co^I(PDI-PyCH$_3$)CO$_2$] which is not easy to estimate directly from the CVs. Therefore, $E_{cat/2} = -1.76$ V vs $Fc^{+/0}$ (the potential corresponding to the half of the catalytic peak current) is used as an approximation for E^0_{cat}.[72] The intrinsic catalytic activity term TOF_0 is accessed by extrapolating the log(TOF) curve to $\eta = 0$, and the log(TOF_0) values are reported in Table 4.5 (detailed calculations can be found in SI). TOF_0 increases in same the order of [Co(PDI)] < [Co(PDI-Ph)] < [Co(PDI-Py)] < [Co(PDI-PyCH$_3^+$I$^-$)] as seen for the other activity metrics. Overall, the [Co(PDI-PyCH$_3^+$I$^-$)] reduces CO_2 with comparable or higher activity than most other molecular catalysts for the CO_2RR (Table A.30), including systems with incorporated intramolecular electrostatic substituents,[29-35, 76] excepting Fe-*o*-TMA[31] and [Fe(tpyPY2Me)]$^{2+}$.[76]
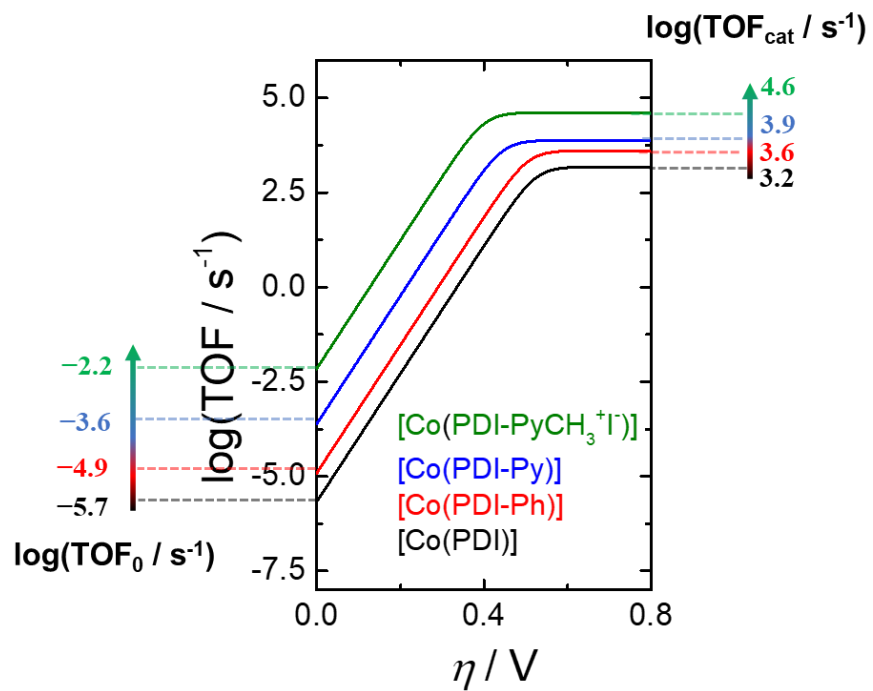
Figure 4.7 The plots of log(TOF) vs. overpotential η for the CO_2RR by the [Co(PDI-R)] catalysts in CO_2-saturated MeCN with 11 M H_2O as proton source.

Typical molecular catalyst scaling relationships show decreased catalytic activity with decreased effective overpotential for the CO_2RR (dashed gray line in Figure 4.8).[13, 27, 32, 38] This trend is often attributed to the correlation between the effective overpotential to a catalyst's metal site nucleophlicity,[24-26, 36-37] an important factor in the ability of molecular catalysts to coordinate and activate CO_2. However, for the [Co(PDI-R)] systems, we observe the opposite behavior, an *inverse scaling relationship* in which every metric of catalytic activity for the CO_2RR increases (TOF_{cat}, TOF_{FOWA} and TOF_{CPE}) as E_{onset} shifts more positive, decreasing the effective overpotential (Figure 4.8).

We postulate that this observed inverse scaling relationship may be because E_{onset} is dictated by a ligand reduction event and thus may not be directly correlated to the nucleophilicity of the catalyst metal site. Consequently, decreasing the effective overpotential of these [CoPDI-R] catalysts does not lead to decreased ability to coordinate and activate CO_2. Instead, introduction of the sequential conjugated, electron withdrawing, and positively charged substituents into the ligand scaffold facilitates the storage of charge equivalents in the ligand, both shifting the potential of the complex more positive and increasing the overall activity for the CO_2RR. In the case of [Co(PDI-PyCH$_3^+$I$^-$)], the increase in activity may also be due to intramolecular electrostatic stabilization of reduced CO_2 intermediates by the *N*-methylpyridinium moiety.[31, 33-34, 77] Note that inverse scaling relationships for the CO_2RR have been observed before for catalysts with incorporated intramolecular electrostatic effects,[31, 38, 78-79] but rarely for systems incorporating extended ligand conjugation or electron-withdrawing effects.
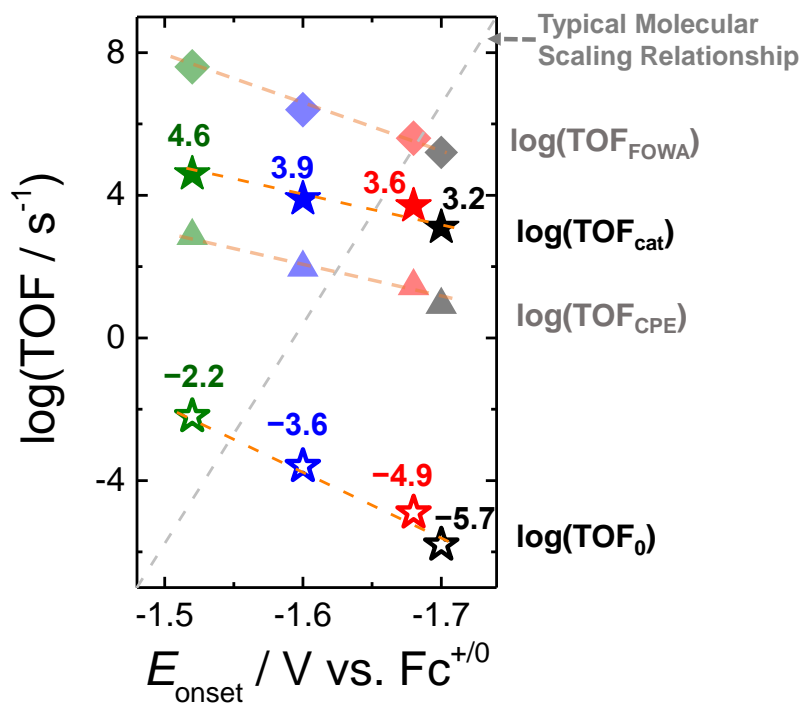
Figure 4.8 The atypical inverse scaling relationship (orange dashed lines) for the CO_2RR by [Co(PDI)] (black), [Co(PDI-Ph)] (red), [Co(PDI-Py)] (blue) and [Co(PDI-PyCH$_3^+$I$^-$)] (green) in CO_2-saturated MeCN with 11 M H_2O as proton source using various activity metrics: TOF$_{cat}$ (solid star), TOF$_0$ (hollow star), TOF$_{FOWA}$ (solid diamond), and TOF$_{CPE}$ (solid triangle). The TOF$_{cat}$ and TOF$_0$ metrics are the primary metrics for comparison, and are bolded compared to the TOF$_{CPE}$ and TOF$_{FOWA}$ data. The gray dashed line depicts a typical scaling relationship trend with increasing log(TOF / s^{-1}) with decreasing E_{onset}. Note that all dashed lines are included as guides to the eye and not necessarily indicative of fits to the data.

4.6 Conclusion

We have introduced a new three-in-one catalyst design strategy of progressively integrating extended π-conjugation, electron withdrawing effects, and intramolecular electrostatic effects into a single Co-PDI complex structure, which greatly improves the intrinsic activity while decreasing the overpotential of these molecular catalysts for CO_2RR. This *inverse* molecular scaling relationship is unusual in CO_2RR electrocatalysts, and is attributed to the fact that a ligand-based redox event directly precedes electrochemical CO_2 activation and reduction rather than a metal-based redox event. The catalytic onset potential, and therefore effective overpotential, is dictated by the redox potential of the ligand, not that of the metal. This suggests that the ability of the ligand to store charge equivalents, which is facilitated by our three-in-one catalyst design strategy, likely plays a large role in defining catalytic activity for these systems.

The combination of the three ligand effects in $[Co(PDI-PyCH_3^+I^-)]$ leads to a catalyst with substantially enhanced activity and more positive catalytic onset compared to the parent complex $[Co(PDI)]$: ~4 orders of magnitude larger TOF_0, > 1 order of magnitude higher TOF_{cat}, and 0.18 V more positive E_{onset}. The outstanding catalytic activity of the $[Co(PDI-PyCH_3^+I^-)]$ makes it among the most active molecular catalysts reported for the CO_2RR. We believe that application of the three-in-one catalyst design strategy highlighted here to other molecular catalyst systems in which a ligand redox event directly precedes catalytic onset may result in similar inverse molecular scaling relationships and high catalytic activity as those observed with the $[Co(PDI-R)]$ system.

4.7 Reference

1.   De Luna, P.; Hahn, C.; Higgins, D.; Jaffer, S. A.; Jaramillo, T. F.; Sargent, E. H. "What would it take for renewably powered electrosynthesis to displace petrochemical processes?," *Science* **2019**, *364*, eaav3506. http://dx.doi.org/10.1126/science.aav3506

2.   Dalle, K. E.; Warnan, J.; Leung, J. J.; Reuillard, B.; Karmel, I. S.; Reisner, E. "Electro- and Solar-Driven Fuel Synthesis with First Row Transition Metal Complexes," *Chemical Reviews* **2019**, *119*, 2752-2875. http://dx.doi.org/10.1021/acs.chemrev.8b00392

3.   Birdja, Y. Y.; Pérez-Gallent, E.; Figueiredo, M. C.; Göttle, A. J.; Calle-Vallejo, F.; Koper, M. T. M. "Advances and challenges in understanding the electrocatalytic conversion of carbon dioxide to fuels," *Nature Energy* **2019**, *4*, 732-745. http://dx.doi.org/10.1038/s41560-019-0450-y

4.   Nielsen, D. U.; Hu, X.-M.; Daasbjerg, K.; Skrydstrup, T. "Chemically and electrochemically catalysed conversion of CO2 to CO with follow-up utilization to value-added chemicals," *Nature Catalysis* **2018**, *1*, 244-254. http://dx.doi.org/10.1038/s41929-018-0051-3

5.   Chen, C.; Khosrowabadi Kotyk, J. F.; Sheehan, S. W. "Progress toward Commercial Application of Electrochemical Carbon Dioxide Reduction," *Chem* **2018**, *4*, 2571-2586. http://dx.doi.org/https://doi.org/10.1016/j.chempr.2018.08.019

6.   Appel, A. M.; Bercaw, J. E.; Bocarsly, A. B.; Dobbek, H.; DuBois, D. L.; Dupuis, M.; Ferry, J. G.; Fujita, E.; Hille, R.; Kenis, P. J. A.; Kerfeld, C. A.; Morris, R. H.; Peden, C. H. F.; Portis, A. R.; Ragsdale, S. W.; Rauchfuss, T. B.; Reek, J. N. H.; Seefeldt, L. C.; Thauer, R. K.; Waldrop, G. L. "Frontiers, Opportunities, and Challenges in Biochemical and Chemical Catalysis of CO2 Fixation," *Chemical Reviews* **2013**, *113*, 6621-6658. http://dx.doi.org/10.1021/cr300463y

7.   Benson, E. E.; Kubiak, C. P.; Sathrum, A. J.; Smieja, J. M. "Electrocatalytic and homogeneous approaches to conversion of CO2 to liquid fuels," *Chem. Soc. Rev.* **2009**, *38*, 89-99. http://dx.doi.org/10.1039/b804323j

8.   Elgrishi, N.; Chambers, M. B.; Wang, X.; Fontecave, M. "Molecular polypyridine-based metal complexes as catalysts for the reduction of CO2," *Chemical Society Reviews* **2017**, *46*, 761-796. http://dx.doi.org/10.1039/c5cs00391a

9.   Bonin, J.; Maurin, A.; Robert, M. "Molecular catalysis of the electrochemical and photochemical reduction of CO2 with Fe and Co metal based complexes. Recent advances," *Coordination Chemistry Reviews* **2017**, *334*, 184-198. http://dx.doi.org/http://dx.doi.org/10.1016/j.ccr.2016.09.005

10.   Grills, D. C.; Ertem, M. Z.; McKinnon, M.; Ngo, K. T.; Rochford, J. "Mechanistic aspects of CO2 reduction catalysis with manganese-based molecular catalysts," *Coord. Chem. Rev.* **2018**, *374*, 173-217. http://dx.doi.org/https://doi.org/10.1016/j.ccr.2018.05.022

11.   Jiang, C.; Nichols, A. W.; Machan, C. W. "A look at periodic trends in d-block molecular electrocatalysts for CO2 reduction," *Dalton Trans.* **2019**, *48*, 9454-9468. http://dx.doi.org/10.1039/C9DT00491B

12.   Wang, J.-W.; Liu, W.-J.; Zhong, D.-C.; Lu, T.-B. "Nickel complexes as molecular catalysts for water splitting and CO2 reduction," *Coordination Chemistry Reviews* **2019**, *378*, 237-261. http://dx.doi.org/https://doi.org/10.1016/j.ccr.2017.12.009

13.   Barlow, J. M.; Yang, J. Y. "Thermodynamic Considerations for Optimizing Selective CO_2 Reduction by Molecular Catalysts," *ACS Cent. Sci.* **2019**. http://dx.doi.org/10.1021/acscentsci.9b00095

14.   Portenkirchner, E.; Oppelt, K.; Ulbricht, C.; Egbe, D. A. M.; Neugebauer, H.; Knör, G.; Sariciftci, N. S. "Electrocatalytic and photocatalytic reduction of carbon dioxide to carbon monoxide using the alkynyl-substituted rhenium(I) complex (5,5′-bisphenylethynyl-2,2′-bipyridyl)Re(CO)3Cl," *J. Organomet. Chem.* **2012**, *716*, 19-25. http://dx.doi.org/10.1016/j.jorganchem.2012.05.021

15.   Thoi, V. S.; Kornienko, N.; Margarit, C. G.; Yang, P.; Chang, C. J. "Visible-Light Photoredox Catalysis: Selective Reduction of Carbon Dioxide to Carbon Monoxide by a Nickel N-Heterocyclic Carbene–Isoquinoline Complex," *Journal of the American Chemical Society* **2013**, *135*, 14413-14424. http://dx.doi.org/10.1021/ja4074003

16.   Qiao, X.; Li, Q.; Schaugaard, R. N.; Noffke, B. W.; Liu, Y.; Li, D.; Liu, L.; Raghavachari, K.; Li, L.-s. "Well-Defined Nanographene–Rhenium Complex as an Efficient Electrocatalyst and Photocatalyst for Selective CO2 Reduction," *J. Am. Chem. Soc.* **2017**, *139*, 3934-3937. http://dx.doi.org/10.1021/jacs.6b12530

17.   Garrido-Barros, P.; Gimbert-Suriñach, C.; Moonshiram, D.; Picón, A.; Monge, P.; Batista, V. S.; Llobet, A. "Electronic π-Delocalization Boosts Catalytic Water Oxidation by Cu(II) Molecular Catalysts Heterogenized on Graphene Sheets," *J. Am. Chem. Soc.* **2017**, *139*, 12907-12910. http://dx.doi.org/10.1021/jacs.7b06828

18.   Abul-Futouh, H.; Skabeev, A.; Botteri, D.; Zagranyarski, Y.; Görls, H.; Weigand, W.; Peneva, K. "Toward a Tunable Synthetic [FeFe]-Hydrogenase H-Cluster Mimic Mediated by Perylene Monoimide Model Complexes: Insight into Molecular Structures and Electrochemical Characteristics," *Organometallics* **2018**, *37*, 3278-3285. http://dx.doi.org/10.1021/acs.organomet.8b00450

19.   Whang, D. R.; Apaydin, D. H.; Park, S. Y.; Sariciftci, N. S. "An electron-reservoir Re(I) complex for enhanced efficiency for reduction of CO2 to CO," *J. Catal.* **2018**, *363*, 191-196. http://dx.doi.org/10.1016/j.jcat.2018.04.028

20.   Schaugaard, R. N.; Raghavachari, K.; Li, L.-s. "Redox "Innocence" of Re(I) in Electrochemical CO2 Reduction Catalyzed by Nanographene–Re Complexes," *Inorg. Chem.* **2018**, *57*, 10548-10556. http://dx.doi.org/10.1021/acs.inorgchem.8b01092

21.   Liu, D.-C.; Wang, H.-J.; Ouyang, T.; Wang, J.-W.; Jiang, L.; Zhong, D.-C.; Lu, T.-B. "Conjugation Effect Contributes to the CO2-to-CO Conversion Driven by Visible-Light," *ACS Appl. Energy Mater.* **2018**, *1*, 2452-2459. http://dx.doi.org/10.1021/acsaem.8b00673

22.   Koenig, J. D. B.; Willkomm, J.; Roesler, R.; Piers, W. E.; Welch, G. C. "Electrocatalytic CO2 Reduction at Lower Overpotentials Using Iron(III) Tetra(meso-thienyl)porphyrins," *ACS Appl. Energy Mater.* **2019**, *2*, 4022-4026. http://dx.doi.org/10.1021/acsaem.9b00761

23.   Oh, S.; Gallagher, J. R.; Miller, J. T.; Surendranath, Y. "Graphite-Conjugated Rhenium Catalysts for Carbon Dioxide Reduction," *J. Am. Chem. Soc.* **2016**, *138*, 1820-1823. http://dx.doi.org/10.1021/jacs.5b13080

24.   Todorova, T. K.; Huan, T. N.; Wang, X.; Agarwala, H.; Fontecave, M. "Controlling Hydrogen Evolution during Photoreduction of CO2 to Formic Acid Using [Rh(R-bpy)(Cp*)Cl]+ Catalysts: A Structure–Activity Study," *Inorg. Chem.* **2019**, *58*, 6893-6903. http://dx.doi.org/10.1021/acs.inorgchem.9b00371

25.   Tignor, S. E.; Kuo, H.-Y.; Lee, T. S.; Scholes, G. D.; Bocarsly, A. B. "Manganese-Based Catalysts with Varying Ligand Substituents for the Electrochemical Reduction of CO2 to CO," *Organometallics* **2019**, *38*, 1292-1299. http://dx.doi.org/10.1021/acs.organomet.8b00554

26.   Clark, M. L.; Cheung, P. L.; Lessio, M.; Carter, E. A.; Kubiak, C. P. "Kinetic and Mechanistic Effects of Bipyridine (bpy) Substituent, Labile Ligand, and Brønsted Acid on Electrocatalytic CO2 Reduction by Re(bpy) Complexes," *ACS Catal.* **2018**, *8*, 2021-2029. http://dx.doi.org/10.1021/acscatal.7b03971

27.   Azcarate, I.; Costentin, C.; Robert, M.; Savéant, J.-M. "Dissection of Electronic Substituent Effects in Multielectron–Multistep Molecular Catalysis. Electrochemical CO2-to-CO Conversion Catalyzed by Iron Porphyrins," *The Journal of Physical Chemistry C* **2016**, *120*, 28951-28960. http://dx.doi.org/10.1021/acs.jpcc.6b09947

28.   Elgrishi, N.; Chambers, M. B.; Fontecave, M. "Turning it off! Disfavouring hydrogen evolution to enhance selectivity for CO production during homogeneous CO2 reduction by cobalt-terpyridine complexes," *Chemical Science* **2015**, *6*, 2522-2531. http://dx.doi.org/10.1039/c4sc03766a

29.   Wang, M.; Torbensen, K.; Salvatore, D.; Ren, S.; Joulié, D.; Dumoulin, F.; Mendoza, D.; Lassalle-Kaiser, B.; Işci, U.; Berlinguette, C. P.; Robert, M. "CO2 electrochemical catalytic reduction with a highly active cobalt phthalocyanine," *Nature Communications* **2019**, *10*, 3602. http://dx.doi.org/10.1038/s41467-019-11542-w

30.   Rao, H.; Schmidt, L. C.; Bonin, J.; Robert, M. "Visible-light-driven methane formation from CO2 with a molecular iron catalyst," *Nature* **2017**, *advance online publication*. http://dx.doi.org/10.1038/nature23016

31.   Azcarate, I.; Costentin, C.; Robert, M.; Savéant, J.-M. "Through-Space Charge Interaction Substituent Effects in Molecular Catalysis Leading to the Design of the Most Efficient Catalyst of CO2-to-CO Electrochemical Conversion," *Journal of the American Chemical Society* **2016**, *138*, 16639-16644. http://dx.doi.org/10.1021/jacs.6b07014

32.   Zhu, M.; Yang, D.-T.; Ye, R.; Zeng, J.; Corbin, N.; Manthiram, K. "Inductive and electrostatic effects on cobalt porphyrins for heterogeneous electrocatalytic carbon dioxide reduction," *Catalysis Science & Technology* **2019**, *9*, 974-980. http://dx.doi.org/10.1039/C9CY00102F

33.   Sahu, S.; Cheung, P. L.; Machan, C. W.; Chabolla, S. A.; Kubiak, C. P.; Gianneschi, N. C. "Charged Macromolecular Rhenium Bipyridine Catalysts with Tunable CO_2 Reduction Potentials," *Chemistry – A European Journal* **2017**, *23*, 8619-8622. http://dx.doi.org/https://doi.org/10.1002/chem.201701901

34.   Sung, S.; Li, X.; Wolf, L. M.; Meeder, J. R.; Bhuvanesh, N. S.; Grice, K. A.; Panetier, J. A.; Nippe, M. "Synergistic Effects of Imidazolium-Functionalization on fac-Mn(CO)3 Bipyridine Catalyst Platforms for Electrocatalytic Carbon Dioxide Reduction," *J. Am. Chem. Soc.* **2019**, *141*, 6569-6582. http://dx.doi.org/10.1021/jacs.8b13657

35.   Sung, S.; Kumar, D.; Gil-Sepulcre, M.; Nippe, M. "Electrocatalytic CO_2 Reduction by Imidazolium-Functionalized Molecular Catalysts," *J. Am. Chem. Soc.* **2017**, *139*, 13993-13996. http://dx.doi.org/10.1021/jacs.7b07709

36.   Martin, D. J.; Wise, C. F.; Pegis, M. L.; Mayer, J. M. "Developing Scaling Relationships for Molecular Electrocatalysis through Studies of Fe-Porphyrin-Catalyzed O2 Reduction," *Accounts of Chemical Research* **2020**, *53*, 1056-1065. http://dx.doi.org/10.1021/acs.accounts.0c00044

37.   Ceballos, B. M.; Yang, J. Y. "Directing the reactivity of metal hydrides for selective CO_2 reduction," *Proceedings of the National Academy of Sciences* **2018**, *115*, 12686-12691. http://dx.doi.org/10.1073/pnas.1811396115

38.   Costentin, C.; Robert, M.; Savéant, J.-M. "Molecular catalysis of electrochemical reactions," *Current Opinion in Electrochemistry* **2017**, *2*, 26-31. http://dx.doi.org/https://doi.org/10.1016/j.coelec.2017.02.006

39.   McCrory, C. C. L.; Szymczak, N. K.; Peters, J. C. "Evaluating Activity for Hydrogen-Evolving Cobalt and Nickel Complexes at Elevated Pressures of Hydrogen and Carbon Monoxide," *Electrocatalysis* **2016**, *7*, 87-96. http://dx.doi.org/10.1007/s12678-015-0281-y

40.   Lacy, D. C.; McCrory, C. C. L.; Peters, J. C. "Studies of Cobalt-Mediated Electrocatalytic CO2 Reduction Using a Redox-Active Ligand," *Inorganic Chemistry* **2014**, *53*, 4980-4988. http://dx.doi.org/10.1021/ic403122j

41.   Matsubara, Y. "Standard Electrode Potentials for the Reduction of CO2 to CO in Acetonitrile–Water Mixtures Determined Using a Generalized Method for Proton-Coupled Electron-Transfer Reactions," *ACS Energy Lett.* **2017**, *2*, 1886-1891. http://dx.doi.org/10.1021/acsenergylett.7b00548

42.   Matsubara, Y. "Unified Benchmarking of Electrocatalysts in Noninnocent Second Coordination Spheres for CO2 Reduction," *ACS Energy Lett.* **2019**, *4*, 1999-2004. http://dx.doi.org/10.1021/acsenergylett.9b01180

43.   Nie, W.; Wang, Y.; Zheng, T.; Ibrahim, A.; Xu, Z.; McCrory, C. C. L. "Electrocatalytic CO2 Reduction by Cobalt Bis(pyridylmonoimine) Complexes: Effect of Ligand Flexibility on Catalytic Activity," *ACS Catalysis* **2020**, 4942-4959. http://dx.doi.org/10.1021/acscatal.9b05513

44.   Nie, W.; Wang, Y.; Zheng, T.; Ibrahim, A.; Xu, Z.; McCrory, C. C. L. "Electrocatalytic CO2 Reduction by Cobalt Bis(pyridylmonoimine) Complexes: Effect of Ligand Flexibility on Catalytic Activity," *ACS Catal.* **2020**, *10*, 4942-4959. http://dx.doi.org/10.1021/acscatal.9b05513

45.   Nie, W.; McCrory, C. C. L. "Electrocatalytic CO_2 reduction by a cobalt bis(pyridylmonoimine) complex: effect of acid concentration on catalyst activity and stability," *Chemical Communications* **2018**, *54*, 1579-1582. http://dx.doi.org/10.1039/C7CC08546J

46.   Kaeffer, N.; Morozan, A.; Fize, J.; Martinez, E.; Guetaz, L.; Artero, V. "The Dark Side of Molecular Catalysis: Diimine–Dioxime Cobalt Complexes Are Not the Actual Hydrogen Evolution Electrocatalyst in Acidic Aqueous Solutions," *ACS Catalysis* **2016**, *6*, 3727-3737. http://dx.doi.org/10.1021/acscatal.6b00378

47.   Garza, A. J.; Pakhira, S.; Bell, A. T.; Mendoza-Cortes, J. L.; Head-Gordon, M. "Reaction mechanism of the selective reduction of CO_2 to CO by a tetraaza $[CoIIN4H]2+$ complex in the presence of protons," *Physical Chemistry Chemical Physics* **2018**, *20*, 24058-24064. http://dx.doi.org/10.1039/C8CP01963K

48.   Zhang, M.; El-Roz, M.; Frei, H.; Mendoza-Cortes, J. L.; Head-Gordon, M.; Lacy, D. C.; Peters, J. C. "Visible Light Sensitized CO_2 Activation by the Tetraaza $[CoIIN4H(MeCN)]2+$ Complex Investigated by FT-IR Spectroscopy and DFT Calculations," *The Journal of Physical Chemistry C* **2015**, *119*, 4645-4654. http://dx.doi.org/10.1021/jp5127738

49.   Hansch, C.; Leo, A.; Taft, R. W. "A survey of Hammett substituent constants and resonance and field parameters," *Chem. Rev.* **1991**, *91*, 165-195. http://dx.doi.org/10.1021/cr00002a004

50.   Gonell, S.; Massey, M. D.; Moseley, I. P.; Schauer, C. K.; Muckerman, J. T.; Miller, A. J. M. "The Trans Effect in Electrocatalytic CO_2 Reduction: Mechanistic Studies of Asymmetric Ruthenium Pyridyl-Carbene Catalysts," *Journal of the American Chemical Society* **2019**, *141*, 6658-6671. http://dx.doi.org/10.1021/jacs.9b01735

51.   Kamatsuka, T.; Shinokubo, H.; Miyake, Y. "Design and Synthesis of Tunable Ligands with 4,4′-Bipyridyl as an Electron-Accepting Unit and Their Rhenium Complexes," *Organometallics* **2017**, *36*, 3429-3434. http://dx.doi.org/10.1021/acs.organomet.7b00611

52.   Miyake, Y.; Nakajima, K.; Higuchi, Y.; Nishibayashi, Y. "Synthesis and Redox Properties of PNP Pincer Complexes Based on N-Methyl-4,4′-bipyridinium," *European Journal of Inorganic Chemistry* **2014**, *2014*, 4273-4280. http://dx.doi.org/10.1002/ejic.201402349

53.   Kobayashi, M.; Masaoka, S.; Sakai, K. "Synthesis, crystal structure, spectroscopic and electrochemical properties, and H2-evolving activity of a new [PtCl(terpyridine)]+ derivative with viologen-like redox properties," *Dalton Transactions* **2012**, *41*, 4903-4911. http://dx.doi.org/10.1039/C2DT12209J

54.   de Bruin, B.; Bill, E.; Bothe, E.; Weyhermüller, T.; Wieghardt, K. "Molecular and Electronic Structures of Bis(pyridine-2,6-diimine)metal Complexes [ML2](PF6)n (n = 0, 1, 2, 3; M = Mn, Fe, Co, Ni, Cu, Zn)," *Inorganic Chemistry* **2000**, *39*, 2936-2947. http://dx.doi.org/10.1021/ic000113j

55.   Budzelaar, P. H. M.; de Bruin, B.; Gal, A. W.; Wieghardt, K.; van Lenthe, J. H. "Metal-to-Ligand Electron Transfer in Diiminopyridine Complexes of Mn−Zn. A Theoretical Study," *Inorg. Chem.* **2001**, *40*, 4649-4655. http://dx.doi.org/10.1021/ic001457c

56.   Butin, K. P.; Beloglazkina, E. K.; Zyk, N. V. "Metal complexes with non-innocent ligands," *Russ. Chem. Rev.* **2005**, *74*, 531-553. http://dx.doi.org/10.1070/rc2005v074n06abeh000977

57.   Archer, A. M.; Bouwkamp, M. W.; Cortez, M.-P.; Lobkovsky, E.; Chirik, P. J. "Arene Coordination in Bis(imino)pyridine Iron Complexes: Identification of Catalyst Deactivation

Pathways in Iron-Catalyzed Hydrogenation and Hydrosilation," *Organometallics* **2006**, *25*, 4269-4278. http://dx.doi.org/10.1021/om060441c

58.   Bart, S. C.; Chłopek, K.; Bill, E.; Bouwkamp, M. W.; Lobkovsky, E.; Neese, F.; Wieghardt, K.; Chirik, P. J. "Electronic Structure of Bis(imino)pyridine Iron Dichloride, Monochloride, and Neutral Ligand Complexes: A Combined Structural, Spectroscopic, and Computational Study," *J. Am. Chem. Soc.* **2006**, *128*, 13901-13912. http://dx.doi.org/10.1021/ja064557b

59.   Knijnenburg, Q.; Gambarotta, S.; Budzelaar, P. H. M. "Ligand-centred reactivity in diiminepyridine complexes," *Dalton Trans.* **2006**, 5442-5448. http://dx.doi.org/10.1039/B612251E

60.   Bowman, A. C.; Milsmann, C.; Hojilla Atienza, C. C.; Lobkovsky, E.; Wieghardt, K.; Chirik, P. J. "Synthesis and Molecular and Electronic Structures of Reduced Bis(imino)pyridine Cobalt Dinitrogen Complexes: Ligand versus Metal Reduction," *J. Am. Chem. Soc.* **2010**, *132*, 1676-1684. http://dx.doi.org/10.1021/ja908955t

61.   Zhu, D.; Thapa, I.; Korobkov, I.; Gambarotta, S.; Budzelaar, P. H. M. "Redox-Active Ligands and Organic Radical Chemistry," *Inorg. Chem.* **2011**, *50*, 9879-9887. http://dx.doi.org/10.1021/ic2002145

62.   Stieber, S. C. E.; Milsmann, C.; Hoyt, J. M.; Turner, Z. R.; Finkelstein, K. D.; Wieghardt, K.; DeBeer, S.; Chirik, P. J. "Bis(imino)pyridine Iron Dinitrogen Compounds Revisited: Differences in Electronic Structure Between Four- and Five-Coordinate Derivatives," *Inorg. Chem.* **2012**, *51*, 3770-3785. http://dx.doi.org/10.1021/ic202750n

63.   Bowman, A. C.; Tondreau, A. M.; Lobkovsky, E.; Margulieux, G. W.; Chirik, P. J. "Synthesis and Electronic Structure Diversity of Pyridine(diimine)iron Tetrazene Complexes," *Inorg. Chem.* **2018**, *57*, 9634-9643. http://dx.doi.org/10.1021/acs.inorgchem.8b00140

64.   Myers, T. W.; Sherbow, T. J.; Fettinger, J. C.; Berben, L. A. "Synthesis and characterization of bis(imino)pyridine complexes of divalent Mg and Zn," *Dalton Transactions* **2016**, *45*, 5989-5998. http://dx.doi.org/10.1039/C5DT01541C

65.   Limoges, B. t.; Savéant, J.-M. "Catalysis by immobilized redox enzymes. Diagnosis of inactivation and reactivation effects through odd cyclic voltammetric responses," *J. Electroanal. Chem.* **2004**, *562*, 43-52. http://dx.doi.org/10.1016/j.jelechem.2003.07.035

66.   Sampson, M. D.; Nguyen, A. D.; Grice, K. A.; Moore, C. E.; Rheingold, A. L.; Kubiak, C. P. "Manganese Catalysts with Bulky Bipyridine Ligands for the Electrocatalytic Reduction of Carbon Dioxide: Eliminating Dimerization and Altering Catalysis," *J. Am. Chem. Soc.* **2014**, *136*, 5460-5471. http://dx.doi.org/10.1021/ja501252f

67.   Machan, C. W.; Yin, J.; Chabolla, S. A.; Gilson, M. K.; Kubiak, C. P. "Improving the Efficiency and Activity of Electrocatalysts for the Reduction of CO2 through Supramolecular Assembly with Amino Acid-Modified Ligands," *Journal of the American Chemical Society* **2016**, *138*, 8184-8193. http://dx.doi.org/10.1021/jacs.6b03774

68.   Chen, L.; Guo, Z.; Wei, X.-G.; Gallenkamp, C.; Bonin, J.; Anxolabéhère-Mallart, E.; Lau, K.-C.; Lau, T.-C.; Robert, M. "Molecular Catalysis of the Electrochemical and Photochemical Reduction of CO2 with Earth-Abundant Metal Complexes. Selective Production of CO vs HCOOH by Switching of the Metal Center," *J. Am. Chem. Soc.* **2015**, *137*, 10918-10921. http://dx.doi.org/10.1021/jacs.5b06535

69.   Costentin, C.; Robert, M.; Saveant, J.-M. "Catalysis of the electrochemical reduction of carbon dioxide," *Chemical Society Reviews* **2013**, *42*, 2423-2436. http://dx.doi.org/10.1039/c2cs35360a

70.   Costentin, C.; Drouet, S.; Robert, M.; Savéant, J.-M. "Turnover Numbers, Turnover Frequencies, and Overpotential in Molecular Catalysis of Electrochemical Reactions. Cyclic Voltammetry and Preparative-Scale Electrolysis," *Journal of the American Chemical Society* **2012**, *134*, 11235-11242. http://dx.doi.org/10.1021/ja303560c

71.   Lee, K. J.; McCarthy, B. D.; Dempsey, J. L. "On decomposition, degradation, and voltammetric deviation: the electrochemist's field guide to identifying precatalyst transformation," *Chemical Society Reviews* **2019**, *48*, 2927-2945. http://dx.doi.org/10.1039/C8CS00851E

72.   Wang, V. C. C.; Johnson, B. A. "Interpreting the Electrocatalytic Voltammetry of Homogeneous Catalysts by the Foot of the Wave Analysis and Its Wider Implications," *ACS Catalysis* **2019**, 7109-7123. http://dx.doi.org/10.1021/acscatal.9b00850

73.   Savéant, J. M. *Elements of Molecular and Biomolecular Electrochemistry*; John Wiley & Sons, Inc.: Hoboken, NJ, 2006, p 111-119.

74.   Cometto, C.; Chen, L.; Anxolabéhère-Mallart, E.; Fave, C.; Lau, T.-C.; Robert, M. "Molecular Electrochemical Catalysis of the CO2-to-CO Conversion with a Co Complex: A Cyclic Voltammetry Mechanistic Investigation," *Organometallics* **2019**, *38*, 1280-1285. http://dx.doi.org/10.1021/acs.organomet.8b00555

75.   Rountree, E. S.; McCarthy, B. D.; Eisenhart, T. T.; Dempsey, J. L. "Evaluation of Homogeneous Electrocatalysts by Cyclic Voltammetry," *Inorg. Chem.* **2014**, *53*, 9983-10002. http://dx.doi.org/10.1021/ic500658x

76.   Derrick, J. S.; Loipersberger, M.; Chatterjee, R.; Iovan, D. A.; Smith, P. T.; Chakarawet, K.; Yano, J.; Long, J. R.; Head-Gordon, M.; Chang, C. J. "Metal–Ligand Cooperativity via Exchange Coupling Promotes Iron- Catalyzed Electrochemical CO2 Reduction at Low

Overpotentials," *Journal of the American Chemical Society* **2020**. http://dx.doi.org/10.1021/jacs.0c10664

77.   Li, F.; Thevenon, A.; Rosas-Hernández, A.; Wang, Z.; Li, Y.; Gabardo, C. M.; Ozden, A.; Dinh, C. T.; Li, J.; Wang, Y.; Edwards, J. P.; Xu, Y.; McCallum, C.; Tao, L.; Liang, Z.-Q.; Luo, M.; Wang, X.; Li, H.; O'Brien, C. P.; Tan, C.-S.; Nam, D.-H.; Quintero-Bermudez, R.; Zhuang, T.-T.; Li, Y. C.; Han, Z.; Britt, R. D.; Sinton, D.; Agapie, T.; Peters, J. C.; Sargent, E. H. "Molecular tuning of CO2-to-ethylene conversion," *Nature* **2020**, *577*, 509-513. http://dx.doi.org/10.1038/s41586-019-1782-2

78.   Chantarojsiri, T.; Ziller, J. W.; Yang, J. Y. "Incorporation of redox-inactive cations promotes iron catalyzed aerobic C–H oxidation at mild potentials," *Chemical Science* **2018**, *9*, 2567-2574. http://dx.doi.org/10.1039/C7SC04486K

79.   Chantarojsiri, T.; Reath, A. H.; Yang, J. Y. "Cationic Charges Leading to an Inverse Free-Energy Relationship for N−N Bond Formation by MnVI Nitrides," *Angewandte Chemie International Edition* **2018**, *57*, 14037-14042. http://dx.doi.org/10.1002/anie.201805832

Chapter 5 Multitasking Active Moieties in Binuclear Co-Co and Co-Zn Pyridyldiimine Complexes Boost the Activity for Electrocatalytic CO$_2$ Reduction

5.1 Preface

This chapter presents the design and electrocatalytic study of binuclear metal pyridyldiimine complexes bi-[M(PDI)], where two metal pyridyldiimine ([M(PDI)]) moieties are connected by an electron-conjugated ligand scaffold. Compared to the mononuclear [(Co(PDI)] complex, bi-[Co(PDI)] displays dramatically increased activity and excellent selectivity (~94% Faradaic efficiency) for the reduction of CO$_2$ to CO, with more positive catalytic onset in acetonitrile with 11 M water. Kinetic studies show that the two Co(PDI) moieties in bi-[Co(PDI)] bind CO$_2$ individually as active catalytic sites, as evidenced by the CO$_2$RR activity being half order in bi-[Co(PDI)]. In addition, both Co(PDI) moieties of bi-[Co(PDI)] serve as electronic substituents that modulate redox features and catalytic ability of one another. In non-catalytic CVs, bi-[Co(PDI)] shows a positive shift of redox couples compared to the mononuclear [Co(PDI)] along with splitting of redox peaks at Co$^{2+/+}$ and ligand-based redox potentials. These redox features result from the intramolecular electrostatic effect exerted by each Co(PDI) moiety on the other and the electronic coupling between two Co(PDI) moieties through the conjugated ligand, both of which are proposed to correlate with the improved catalytic ability of bi-[Co(PDI)] for the CO$_2$RR compared to [(Co(PDI)].

To further assess and elucidate these two effects on the enhanced activity of bi-[Co(PDI)], another binuclear compound bi-[ZnCo(PDI)] with one Co center replaced by redox-inert Zn was prepared and studied for the CO$_2$RR as well. Compared to the mononuclear [Co(PDI)], bi-

[ZnCo(PDI)] shows similar positive shift of Co-based redox couples as bi-[Co(PDI)] does, but no peak splitting is observed for the redox processes. These redox features of bi-[ZnCo(PDI)] indicate that although an intramolecular electrostatic effect is exerted by Zn^{2+} on the Co(PDI) moiety, there is no evidence of electronic coupling between two M(PDI) moieties in this heterobimetallic structure. However, bi-[ZnCo(PDI)] shows even higher activity for the CO_2RR compared to bi-[Co(PDI)], implying that the intramolecular electrostatic effect in the binuclear structures of bi-[ZnCo(PDI)] and bi-[Co(PDI)] is more influential than the electronic coupling as the main effect resulting in the improved catalytic ability of these binuclear systems. The intramolecular electrostatic effect on the activity of binuclear catalysts is further confirmed by the study of another binuclear analog, bi-ex-[Co(PDI)], with an extended ligand structure and longer Co-Co distance. Although there is negligible electronic coupling between further separated Co(PDI) moieties, bi-ex-[Co(PDI)] still shows much higher activity for the CO_2RR compared to mononuclear [Co(PDI)], but lower activity than those of bi-[Co(PDI)] and bi-[ZnCo(PDI)]. This lower activity for bi-ex-[Co(PDI)] is due to the longer Co-Co distance and thus weaker electrostatic effect, which confirms the beneficial impact of electrostatic effect on the activity of binuclear molecular catalysts.

The work in this chapter highlights a novel molecular catalyst design for highly active and efficient binuclear metal complexes with "multitasking" moieties for the CO_2RR, where each active moiety not only plays a catalytic role of binding and reducing CO_2 but also serves to modulate the catalytic ability of the other. This chapter of my dissertation is derived from the uncompleted work in preparation for submission. I am the first author of the work and I am responsible for all the compound synthesis and characterization, electrochemical experiment measurements and data analysis, as well as the manuscript writing and revision. Drew E. Tarnopol

provided help with sample synthesis and manuscript proofreading. Dr. Charles C. L. McCrory provided significant insight and expertise in electroanalytic instruction and discussion and helped with writing and revising the manuscript.

5.2 Introduction

The electrochemical CO_2 reduction reaction (CO_2RR) is a promising strategy of storing renewable electricity generated from intermittent energy sources (e.g. solar and wind power) via converting CO_2, an industrial waste product and environmental contaminant, into value-added products.[1-4] Compared to state-of-the-art solid-state catalysts such as Cu, which reduce CO_2 with high activity but suffer from poor selectivity,[5-6] molecular catalysts—in particular transition metal complexes—show promise for the selective conversion of CO_2 to single products with intrinsic catalytic ability that can be tuned through synthetic structure modifications.[7-11]

Despite many structural modification strategies have been developed to optimize the catalytic ability of molecular catalysts for the CO_2RR, most of them are confined to mononuclear systems, where "decorating" ligand frameworks is the only way to modulate electronic features and thus catalytic ability of the complex.[12-24] In the last few years, some bio-inspired binuclear molecular catalysts have been designed and reported to show better CO_2RR performance compared to their mononuclear analogs, due to the synergistic coordination and activation of the substrate by two metal sites in the structure.[25-28] These binuclear molecular catalysts provide a different strategy of optimizing the catalytic ability of the catalyst by introducing the synergistic cooperation between two metal sites in a single ligand scaffold. However, two metal sites in such binuclear structures are single-tasking in the catalytic process—one metal center functions as a reducing site transferring electrons to the substrate and the other serves as an assistant coordination site "decorating" the secondary coordination sphere,[25-28] both of which are exclusively single-tasking in the mechanism.

In this work, we designed and prepared a binuclear cobalt pyridyldiimine complex bi-[Co(PDI)] where two Co pyridyldiimine (Co(PDI)) moieties are connected by an electron-

conjugated redox-active ligand linker (Figure 5.1a). Compared to its mononuclear analog [Co(PDI)] studied previously,[29] bi-[Co(PDI)] shows dramatically higher activity and excellent selectivity (~94% Faradaic efficiency) for the reduction of CO_2 to CO, operating with over 4 orders of magnitude higher intrinsic activity ($\log(TOF_0/s^{-1}) = -1.3$), ~2 orders of magnitude higher maximum kinetic activity ($\log(TOF_{cat}/s^{-1}) = 5.0$) and 0.15 V more positive catalytic onset ($E_{onset} = -1.55$ V vs $Fc^{+/0}$), in acetonitrile with 11 M water. In contrast to the bio-inspired binuclear catalysts discussed above, both Co(PDI) moieties in bi-[Co(PDI)] are active sites for binding and reducing CO_2 individually, which is supported by the half reaction order of bi-[Co(PDI)] for the CO_2RR based on the kinetic studies. In addition, each Co(PDI) moiety of bi-[Co(PDI)] also plays another role as an electronic modulator to tune redox features and thus catalytic ability of each other. Compared to the mononuclear [Co(PDI)], bi-[Co(PDI)] shows positive shift of redox couples with peak splitting feature at $Co^{2+/+}$ and ligand-based potentials, suggesting the intramolecular static effect exerted by one Co(PDI) moiety on the other and the electronic coupling interaction between two Co(PDI) moieties through the conjugated redox-active ligand. These two electronic effects of "multi-tasking" Co(PDI) moieties in the structure are proposed to correlate with the improved catalytic ability of bi-[Co(PDI)] for the CO_2RR.

To further elucidate these effects of "multitasking" Co(PDI) moieties on the improved catalytic ability of bi-[Co(PDI)], heterobimetallic compound bi-[ZnCo(PDI)], where one Co center was replaced by a redox-inert Zn center to cut off the electronic coupling between two metal moieties, was prepared and studied for the CO_2RR as well (Figure 5.1b). Compared to the mononuclear [Co(PDI)], bi-[ZnCo(PDI)] shows similar positive shift of Co-based redox couples observed for bi-[Co(PDI)], but no peak splitting at Co-based redox process. These redox features of bi-[ZnCo(PDI)] support that only intramolecular electrostatic effect exerted by Zn^{2+} on the

Co(PDI) moiety but no electronic coupling between two M(PDI) moieties exists in this heterobimetallic structure. However, bi-[ZnCo(PDI)] shows even higher activity for the CO_2RR compared to bi-[Co(PDI)], making itself among the most active molecular catalysts for the CO_2RR reported so far, which suggests that the intramolecular static effect rather than the electronic coupling in binuclear structures is the main factor leading to the boosted activity of binuclear bi-[Co(PDI)] and bi-[ZnCo(PDI)]. The beneficial impact of electrostatic effect on the activity of binuclear systems is also confirmed by another binuclear analog bi-ex-[Co(PDI)] with negligible electronic coupling but weak electrostatic effect between further separated Co sites in the extended structure (Figure 5.1b), which still shows increased activity for the CO_2RR compared to the mononuclear [Co(PDI)], despite lower activity that that of bi-[Co(PDI)] and bi-[ZnCo(PDI)].

In this report, our work highlights a novel design of highly active and efficient binuclear metal complexes with "multitasking" moieties for the CO_2RR, and also provides a new insight in the design of multinuclear molecular assemblies and molecule-based extended frameworks as the next generation of efficient catalytic systems in the future.
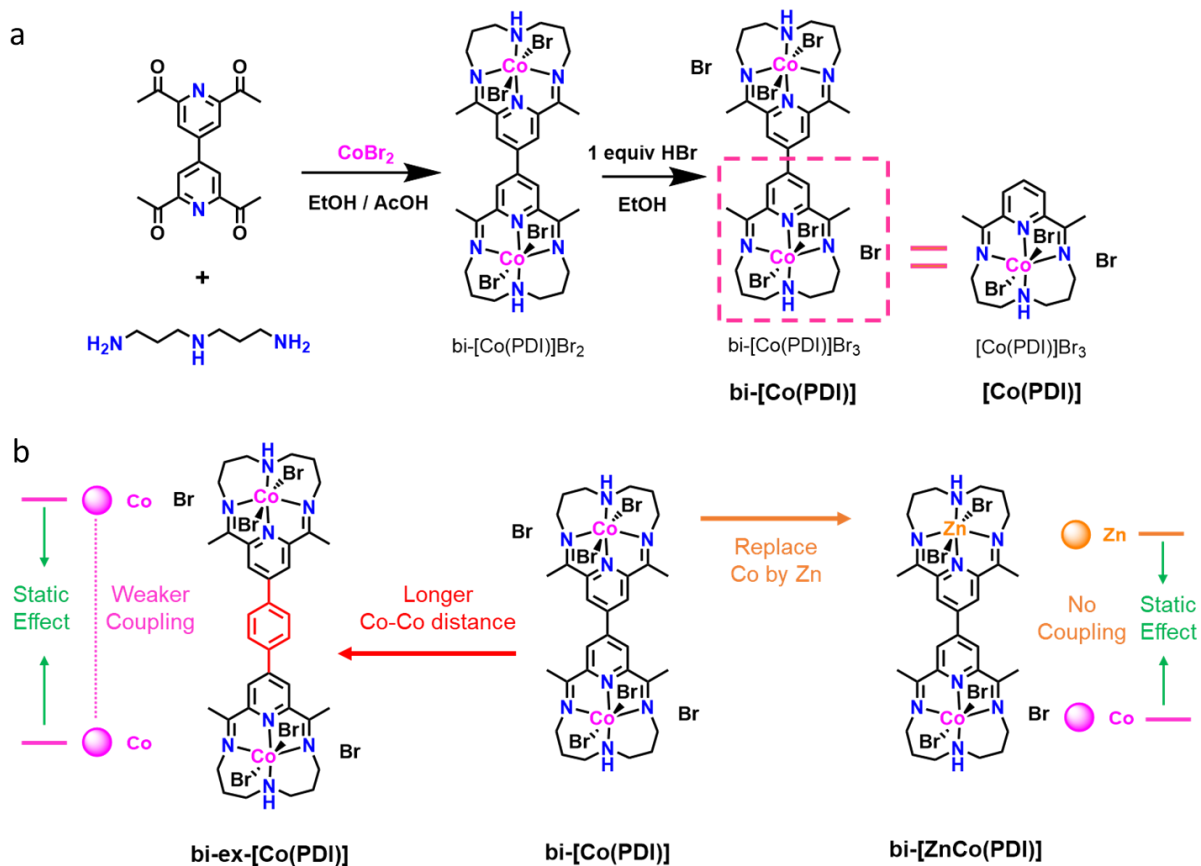
Figure 5.1 (a) Design and synthesis of the binuclear cobalt pyridyldiimine complex bi-[Co(PDI)] (named without counter Br anions for clarity unless otherwise noted); (b) Control binuclear compounds bi-ex-[Co(PDI)] with longer Co-Co distance and hetero-bimetallic bi-[ZnCo(PDI)] with one Co center replaced by redox-inert Zn showing weaker and negligible electronic coupling between metal sites but maintaining intramolecular static effect on metal moieties exerted by each other.

5.3 Experimental Section

5.3.1 Chemicals, Materials and General Methods

Tetrabutylammonium hexafluorophosphate (nBu$_4$NPF$_6$, >98.0%) was purchased from Oakwood Chemical and recrystallized from Ethanol/H$_2$O (v/v = 8/1) before use. Acetonitrile (MeCN, HPLC plus, ≥ 99.9%), and methanol (HPLC grade, ≥ 99.9%) were purchased from Sigma Aldrich and used without further purification. The typical water concentration in MeCN as received has been previously measured to be [H$_2$O] ≈ 0.04 M.[30] Ethanol (EtOH, 200 proof, anhydrous) was purchased from Decon Labs, Inc., and used without further purification. Dichloromethane (DCM, Certified ACS) and Ethyl acetate (Certified ACS) were purchased from Fisher Chemical and used without further purification. Anhydrous dimethylformamide (DMF, 99.8%) was purchased from Sigma Aldrich and used without further purification. p-Dioxane, 1,4-Phenylenediboronic acid, Bis(pinacolato)diboron, Potassium acetate, Pd(dppf)Cl$_2$, Zinc bromide (ZnBr2, 98%) and CsF were purchased from Oakwood Chemical and used without further purification. Cobalt bromide (CoBr$_2$, 99%), hydrogen bromide aqueous solutions (HBr(aq), ACS reagent, 48%) and p-toluenesulfonic acid monohydrate (p-TsOH) were purchased from Sigma Aldrich and used without further purification. AgNO$_3$ (99.7%) was purchased from Sigma and used without further purification. Anhydrous MgSO$_4$, Silica gel 60 (0.032-0.063mm, 230-450 mesh) and NH$_4$Cl (98+%) were purchased from Alfa Aesar and used without further purification. 3,3'-Diaminodipropylamine (>98%) was purchased from TCI America and used without further purification. Glacial acetic acid (HPLC grade, 99.7%) was purchased from Fisher scientific and used without further purification. Trimethyl orthoformate was purchased from Alfa Aesar and used without further purification. 4-Bromo-2,6-diacetylpyridine and [Co(PDI)] were synthesized according to methods reported in the chapter 4. All water used in this study was purified to 18.2

MΩ cm resistivity using a Thermo Scientific Barnstead^{TM} GenPure^{TM} UV-TOC/UF xCAD-plus water purification system. Nitrogen (N_2) was boil-off gas from a liquid nitrogen source. Carbon dioxide (CO_2, medical grade, $> 99.0\%$) was purchased from Cryogenic Gases. All other chemicals were purchased from commercial sources, and all chemicals were used as received unless otherwise noted.

NMR spectra were recorded on Varian MR-400 (400 MHz) spectrometers, and chemical shifts are reported in ppm relative to TMS standards. Elemental analyses were performed by Midwest Microlab, Inc. SEM-EDS tests were conducted in JEOL-7800FLV FE.

5.3.2 Synthesis

Preparation of 4,4'-bi(2,6-diacetylpyridine). Synthesis of 4,4'-bi(2,6-diacetylpyridine) is shown in Scheme 5.1. 4-Bromo-2,6-diacetylpyridine (484 mg, 2.0 mmol) and bis(pinacolato)diboron (609 mg, 2.4 mmol) were dissolved in anhydrous DMF (8.0 mL) under N_2. Potassium acetate KOAc (392 mg, 4.0 mmol) and Pd(dppf)Cl$_2$ (20 mg, 0.026 mmol) were quickly added into the solution. The mixture was stirred at 90 ℃ for 24 hours. After cooling down to the room temperature, 50 mL water was added. The mixture was extracted by ethyl acetate (EtOAc, 3 × 40 mL). The combined EtOAc fractions were dried by anhydrous MgSO$_4$. After removing the solvent, crude compound **1** was obtained as dark oil and used without purification for the next step. 4-Bromo-2,6-diacetylpyridine (448 mg, 1.85 mmol) and crude compound **1** were dissolved in 20 mL mixed solvent of *p*-dioxane/H$_2$O (16 mL/4 mL), which was deoxygenated by three freeze-pump-thaw cycles and protected by N_2. After adding CsF (701 mg, 4.63 mmol) and Pd(dppf)Cl$_2$ (33.8 mg, 0.046 mmol), the suspension was stirred and heated at 90 ℃ for 24 hours. After cooling down to the room temperature, 100 mL of 20 wt.% NH$_4$Cl aqueous solution was added. The mixture was extracted by DCM (3 × 50 mL). The organic fractions were combined and washed with saturated brine, dried with anhydrous MgSO$_4$. After removing the solvent, 4,4'-bi(2,6-diacetylpyridine) (245 mg, yield: 54.7%) was obtained by column chromatography (silica gel, DCM/EtOAc, 4/1). ^{1}H NMR (CD$_3$Cl-d_3, 400 MHz, Figure A.143): δ 8.56 (4H, s, *Py*-H), δ 2.85 (12H, s, CH$_3$). ^{13}C NMR (CD$_3$Cl-d_3, 100 MHz, Figure A.144): δ 198.92, δ 154.14, δ 164.84, δ 122.41, δ 25.84.
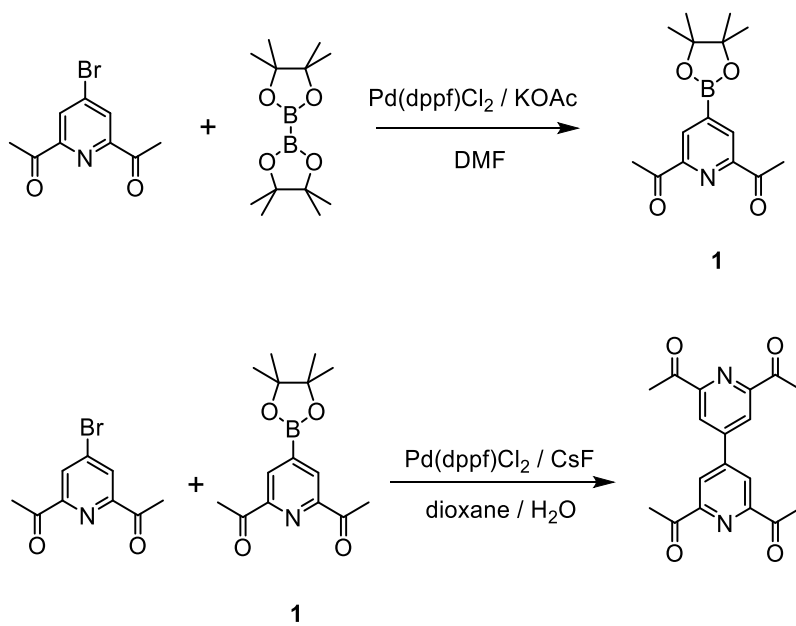
Scheme 5.1 Synthetic route for 4,4'-bi(2,6-diacetylpyridine).

Preparation of 4,4'-(1,4-Phenylene)-bi(2,6-diacetylpyridine). Synthesis of 4,4'-(1,4-Phenylene)-bi(2,6-diacetylpyridine) is shown in Scheme 5.2. 4-Bromo-2,6-diacetylpyridine (960.0 mg, 4.00 mmol) and 1,4-phenylenediboronic acid (331.5 mg, 2.00 mmol) were dissolved in 20 mL mixed solvent of *p*-dioxane/H_2O (16 mL/4 mL), which was deoxygenated by three freeze-pump-thaw cycles and protected by N_2. After adding CsF (757.8 mg, 5.00 mmol) and Pd(dppf)Cl_2 (73.0 mg, 0.10 mmol), the suspension was stirred and heated at 90 ℃ for 24 hours. After cooling down to the room temperature, 100 mL of 20 wt.% NH_4Cl aqueous solution was added. The mixture was extracted by DCM (3 × 50 mL). The organic fractions were combined and dried with anhydrous $MgSO_4$. After removing the solvent, 4,4'-(1,4-Phenylene)-bi(2,6-diacetylpyridine) (100 mg, yield: 12.5%) was obtained by column chromatography (silica gel, DCM/EtOAc, 20/1). ^{1}H NMR (CD_3Cl-d_3, 400 MHz, Figure A.145): δ 8.51 (4H, s, *Py*-H), δ 7.91 (4H, s, *Ar*-H), δ 2.85 (12H, s, CH_3).
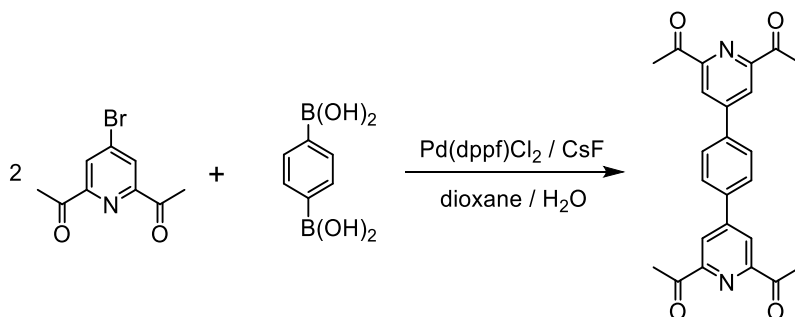
Scheme 5.2 Synthetic route for 4,4'-(1,4-Phenylene)-bi(2,6-diacetyl-pyridine).

Preparation of 4-Bromo-2,6-bis(1,1-dimethoxyethyl)-pyridine. Synthesis of 4-Bromo-2,6-bis(1,1-dimethoxyethyl)-pyridine is shown in Scheme 5.3. 4-Bromo-2,6-diacetylpyridine (361.0 mg, 1.50 mmol) and trimethyl orthoformate (849.0 mg, 875 uL, 8.0mmol) were dissolved and stirred in 8.0 mL MeOH in the air with *p*-toluenesulfonic acid monohydrate (*p*-TsOH, 57.0 mg, 0.3 mmol). After 24 hours, the solution was poured into the aqueous $NaHCO_3$ solution (5.0 mL saturated aqueous $NaHCO_3$ + 5.0 mL H_2O). The mixture was extracted with 10.0 mL EtOAc three times. The combined organic fractions were washed with saturated brine and dried with anhydrous $MgSO_4$. 4-Bromo-2,6-bis(1,1-dimethoxyethyl)-pyridine (473 mg, yield: 94.0%) was obtained as white solid after the solvent was removed. ^{1}H NMR (CD_3Cl-d_3, 400 MHz, Figure A.147): δ 7.79 (4H, s, *Py*-H), δ 3.18 (12H, s, OCH_3), δ 1.63 (6H, s, CH_3). ^{13}C NMR (CD_3Cl-d_3, 100 MHz, Figure A.148): δ 161.58, δ 133.75, δ 124.21, δ 101.55, δ 49.33, δ 23.69.
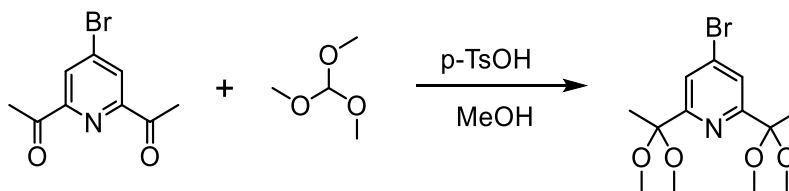
Scheme 5.3 Synthetic route for 4-Bromo-2,6-bis(1,1-dimethoxyethyl)-pyridine.

Preparation of (2,6-bis(1,1-dimethoxyethyl))-(2',6'-diacetyl)-4,4'-dipyridine. Synthesis of (2,6-bis(1,1-dimethoxyethyl))-(2',6'-diacetyl)-4,4'-dipyridine is shown in Scheme 5.4. 4-bromo-2,6-diacetylpyridine (433.6 mg, 1.8 mmol) and bis(pinacolato)diboron (558.3 mg, 2.2 mmol) were dissolved in anhydrous DMF (8.0 mL) under N_2. Potassium acetate KOAc (392 mg, 4.0 mmol) and Pd(dppf)Cl_2 (20 mg, 0.026 mmol) were quickly added into the solution. The mixture was stirred at 90 ℃ for 24 hours. After cooling down to the room temperature, 50 mL water was added. The mixture was extracted by ethyl acetate (EtOAc, 3×40 mL). The combined EtOAc fractions were dried by anhydrous $MgSO_4$. After removing the solvent, crude compound **1** was obtained as dark oil and used without purification for the next step.

4-Bromo-2,6-bis(1,1-dimethoxyethyl)-pyridine (473 mg, 1.41 mmol) and crude compound **1** were dissolved in 20 mL mixed solvent of *p*-dioxane/H_2O (16 mL/4 mL), which was deoxygenated by three freeze-pump-thaw cycles and protected by N_2. After adding CsF (701 mg, 4.63 mmol) and Pd(dppf)Cl_2 (33.8 mg, 0.046 mmol), the suspension was stirred and heated at 90 ℃ for 24 hours. After cooling down to the room temperature, 100 mL of 20 wt.% NH_4Cl aqueous solution was added. The mixture was extracted by DCM (3×50 mL). The organic fractions were combined and washed with saturated brine, dried with anhydrous $MgSO_4$. After removing the solvent, (2,6-bis(1,1-dimethoxyethyl))-(2',6'-diacetyl)-4,4'-dipyridine (366.3 mg, yield: 62.4%) was obtained by column chromatography (silica gel, DCM/EtOAc, 3/1). ^{1}H NMR (CD$_3$Cl-d_3, 400 MHz, Figure A.149): δ 7.79 (4H, s, Py-H), δ 3.18 (12H, s, OCH_3), δ 1.63 (6H, s, CH_3).. ^{13}C NMR (CD$_3$Cl-d_3, 100 MHz, Figure A.150): δ 199.56, δ 161.77, δ 153.77, δ 149.00, δ 144.73, δ 122.73, δ 118.49, δ 49.35, δ 25.92, δ 23.86.
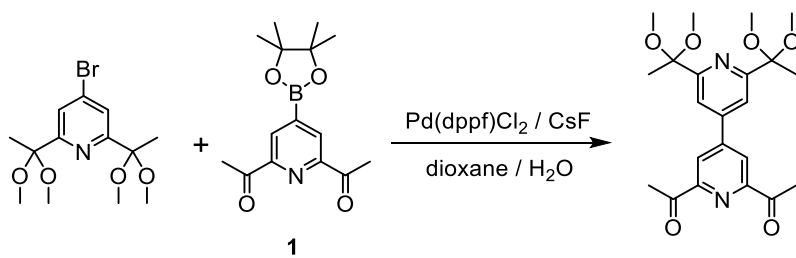
Scheme 5.4 Synthetic route for (2,6-bis(1,1-dimethoxyethyl))-(2',6'-diacetyl)-4,4'-dipyridine.

Preparation of bi-[Co(PDI)]Br₃. The synthesis of bi-[Co(PDI)]Br$_3$ is shown in Scheme 5.5. 4,4'-bi(2,6-diacetylpyridine) (121.6 mg, 0.375 mmol) was suspended in 10 mL ethanol. A 2.00 mL ethanol solution of CoBr$_2$ (164.7 mg, 0.75 mmol) was added into this mixture with stirring. The slurry was heated under N$_2$ at 60°C for 30 min. Then 3,3'-diaminodipropylamine (98.5 mg, 105.0 µL, 0.75 mmol) was slowly dropped in. The mixture was stirred and refluxed at 78°C for 24 hours. After the mixture was cooled to room temperature, the dark purple precipitate bi-[Co(PDI)]Br$_2$ was collected by filtration and then washed with cold ethanol three times. bi-[Co(PDI)]Br$_2$ was aerobically oxidized by suspending and stirring in ethanol with 2 equiv HBr(aq) overnight (18 h) in the air, resulting in the green solid product bi-[Co(PDI)]Br$_3$ (314 mg, 75.3 % yield). ^{1}H NMR (DMSO-d_6, 400 MHz, Figure A.151): δ 9.44 (4H, s, *Py*-H), δ 6.78 (2H, t, -CH$_2$*NH*CH$_2$-), δ 4.28~4.24 (4H, d, -*CH$_2$*NHCH$_2$-), δ 3.58~3.62 (4H, t, -C=N-*CH$_2$*-), δ 3.23~3.30 (8H, m, -CH$_2$*CH$_2$*CH$_2$- and -CH$_2$NH*CH$_2$*-), δ 3.13 (12H, s, CH$_3$), δ 2.29~2.33 (4H, m, -CH$_2$*CH$_2$*CH$_2$-), δ 2.08~2.17 (4H, m, -C=N-*CH$_2$*-). Anal. Calcd (found) for bi-[Co(PDI)]Br$_3$ (C$_{30}$H$_{42}$N$_8$Co$_2$Br$_6$): %C 32.40, (31.92); %H 3.81, (3.69); %N 10.08, (9.81).
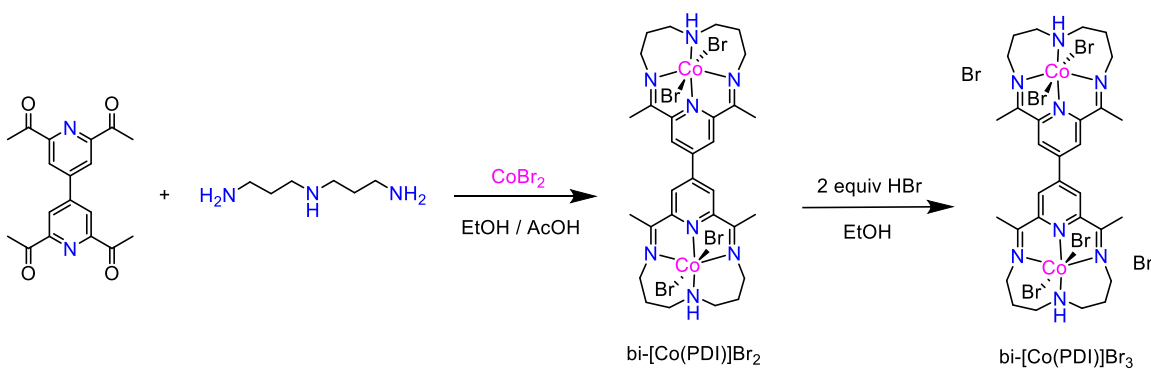
Scheme 5.5 Synthetic route for bi-[Co(PDI)]Br$_3$

Preparation of bi-ex-[Co(PDI)]Br₃. The synthesis of bi-ex-[Co(PDI)]Br$_3$ is shown in Scheme 5.6. 4,4'-(1,4-Phenylene)-bi(2,6-diacetylpyridine) (96.7 mg, 0.242 mmol) was suspended in 12 mL DCM. A 6.00 mL ethanol/DCM (V/V = 1/1) solution of CoBr$_2$ (105.65 mg, 0.483 mmol) was added into the mixture with stirring. Then 3,3'-diaminodipropylamine (94.7 µL, 0.483 mmol) was slowly dropped in. The mixture was stirred and refluxed at 50°C for 24 hours. After the mixture was cooled to room temperature, the dark precipitate bi-ex-[Co(PDI)]Br$_2$ was collected by filtration and then washed with cold ethanol three times. bi-ex-[Co(PDI)]Br$_2$ was aerobically oxidized by suspending and stirring in ethanol with 2 equiv HBr(aq) overnight (18 h) in the air, resulting in the dark green solid product bi-ex-[Co(PDI)]Br$_3$ (105.3 mg, 36.7 % yield). ^{1}H NMR (DMSO-d_6, 400 MHz, Figure A.152): δ 9.13 (4H, s, *Py*-H), δ 8.60 (4H, s, *Ar*-H), δ 6.72 (2H, t, -CH$_2$*NH*CH$_2$-), δ 4.23~4.27 (4H, d, -*CH$_2$*NHCH$_2$-), δ 3.56~3.60 (4H, t, -C=N-*CH$_2$*-), δ 3.20~3.30 (8H, m, -CH$_2$*CH$_2$*CH$_2$- and -CH$_2$NH*CH$_2$*-), δ 3.10 (12H, s, CH$_3$), δ 2.28~2.32 (4H, m, -CH$_2$*CH$_2$*CH$_2$-), δ 2.10~2.13 (4H, m, -C=N-*CH$_2$*-).
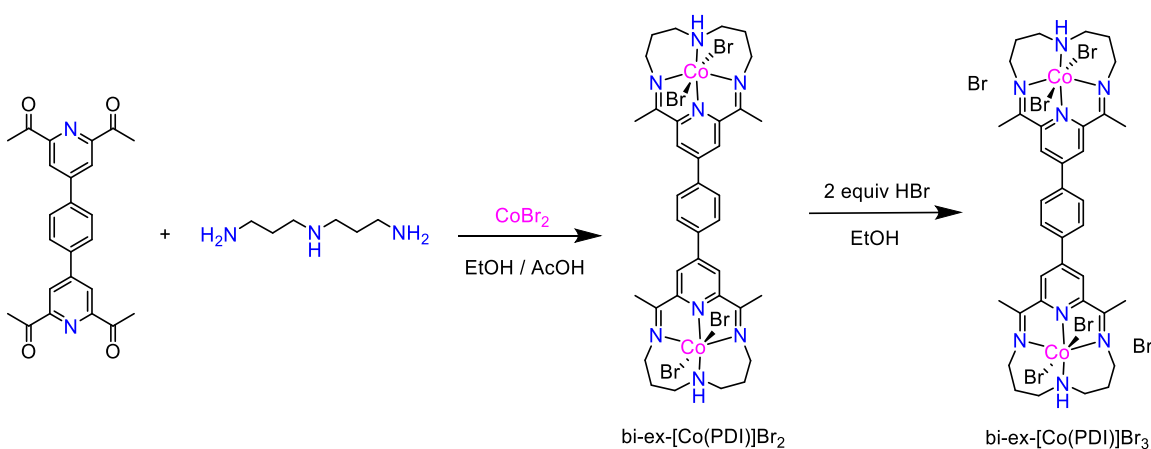
Scheme 5.6 Synthetic route for bi-ex-[Co(PDI)]Br$_3$.

Preparation of bi-[ZnCo(PDI)]. The synthesis of bi-[ZnCo(PDI)] is shown in Scheme 5.7. (2,6-bis(1,1-dimethoxyethyl))-(2',6'-diacetyl)-4,4'-dipyridine (390.0 mg, 0.84 mmol) was suspended in 10 mL ethanol. A 4.00 mL ethanol solution of $ZnBr_2$ (191.41 mg, 0.85 mmol) was added into the mixture with stirring. Then 3,3'-diaminodipropylamine (117.4 µL, 0.84 mmol) was slowly dropped in. The mixture was stirred and refluxed at 78°C for 24 hours. After the mixture was cooled to room temperature, the volume of the solution was reduced to 5mL under N_2 and diethyl ether was added to obtain white precipitate mono-Zn-precusor-1. Then the precipitate mono-Zn-precusor-1 was collected by filtration and then washed with cold ethanol three times (220 mg, yield: 35.7%). Then mono-Zn-precusor-1 (220 mg, 0.3 mmol) was suspended and stirred in 8 mL MeOH/EtOH (V/V = 1/3) mixed solvent with 1 equiv HBr(aq). After stirring 18 hours, the precipitate mono-Zn-precusor-2 was filtered out and washed with cold ethanol three times and used without further purification for the next step.

Mono-Zn-precusor-2 from the last step was suspended in 10 mL MeOH/EtOH (V/V = 2/3) mixed solvent. A 3.00 mL EtOH solution of $CoBr_2$ (65.6 mg, 0.3 mmol) was added into the mixture with stirring. Then 3,3'-diaminodipropylamine (41.8 µL, 0.3 mmol) was slowly dropped in. The mixture was stirred and refluxed at 78°C under N_2 for 24 hours. After 24 hours, extra $CoBr_2$ (16.4 mg, 0.075 mmol) and 3,3'-diaminodipropylamine (20.94 µL, 0.15 mmol) was added into the reaction mixture for extra 5 hours reaction. After the mixture was cooled to room temperature, the solvent was evaporated under N_2 to obtain the dark precipitate. Then the precipitate was aerobically oxidized by suspending and stirring in 5 mL ethanol with 1 equiv HBr(aq) overnight (18 h) in the air, resulting in the dark green solid product bi-[ZnCo(PDI)] (257 mg, 82.5 % yield). ^{1}H NMR (DMSO-d_6, 400 MHz, Figure A.153): δ 9.32 (2H, s, *Py*-H, @Co(PDI)), δ 9.21 (2H, s, *Py*-H, @Zn(PDI)), δ 6.77 (H, t, -CH$_2$*NH*CH$_2$-, @Co(PDI)), δ 4.62~4.65 (H, t, -CH$_2$*NH*CH$_2$-,

@Zn(PDI)), δ 4.24~4.34 (4H, m, -*CH₂*NHCH₂-, @Co(PDI) and Zn(PDI)), δ 3.83 (2H, t, -C=N-*CH₂*-, @Zn(PDI)), δ 3.61 (2H, t, -C=N-*CH₂*-, @Co(PDI)), δ 3.42~3.45 (4H, m, -CH₂*CH₂*CH₂- and -CH₂NH*CH₂*-, @Co(PDI)), δ 3.17~3.20 (2H, m, -CH₂*CH₂*CH₂-, @Zn(PDI)), δ 2.98~3.01 (2H, d, -CH₂NH*CH₂*-, @Zn(PDI)), *δ* 3.13 (6H, s, CH₃, @Co(PDI)), *δ* 2.77 (6H, s, CH₃, @Zn(PDI)), δ 2.29~2.33 (2H, m, -CH₂*CH₂*CH₂-, @Co(PDI)), δ 2.17~2.21 (2H, d, -CH₂*CH₂*CH₂-, @Zn(PDI)), δ 2.08 (2H, m, -C=N-*CH₂*-, @Co(PDI)), δ 1.72~1.76 (2H, m, -C=N-*CH₂*-, @Zn(PDI)).
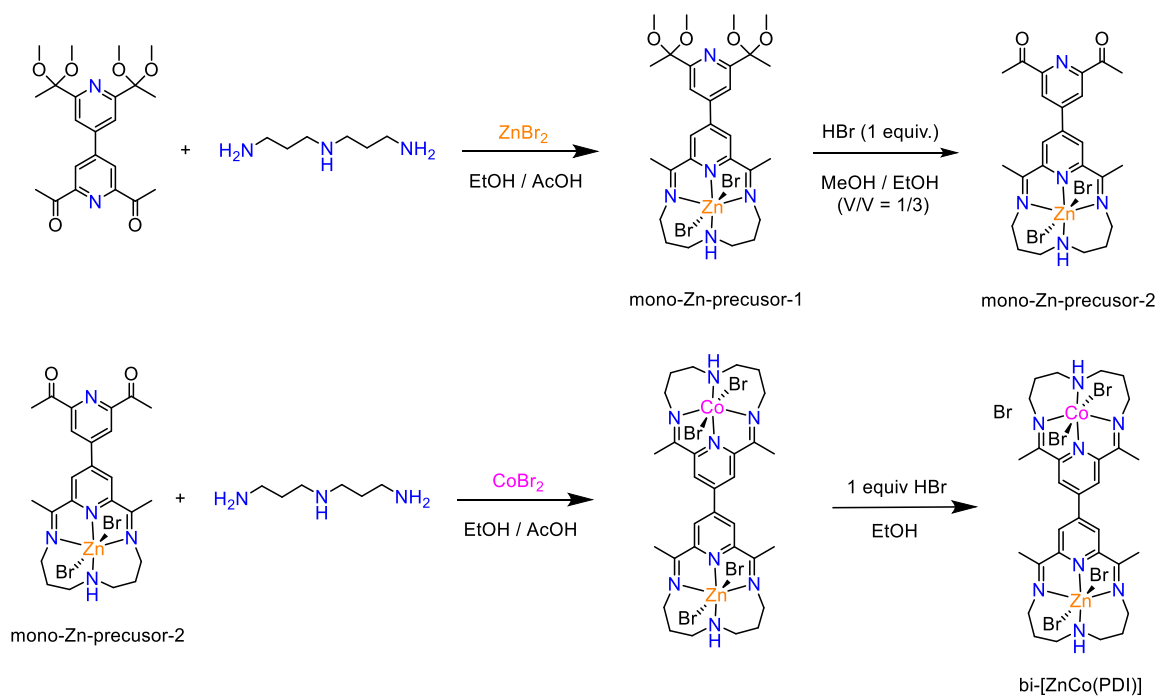
Scheme 5.7 Synthetic route for bi-[ZnCo(PDI)].

Preparation of bi-[Zn(PDI)]Br₂. The synthesis of bi-[Zn(PDI)]Br$_2$ is shown in Scheme 5.8. 4,4'-bi(2,6-diacetylpyridine) (65.5 mg, 0.2 mmol) was suspended in 5.00 mL ethanol. A 2.00 mL ethanol solution of ZnBr$_2$ (90.1 mg, 0.4 mmol) was added into this mixture with stirring. The slurry was heated under N$_2$ at 60°C for 30 min. Then 3,3'-diaminodipropylamine (78.4 µL, 0.4 mmol) was slowly dropped in. The mixture was stirred and refluxed at 78°C for 24 hours. After the mixture was cooled to room temperature, the white precipitate was collected by filtration and then washed with cold ethanol three times, resulting in the white solid product bi-[Zn(PDI)]Br$_2$ (120.0 mg, 62.1 % yield). ^{1}H NMR (DMSO-d_6, 400 MHz, Figure A.154): δ 9.09 (4H, s, *Py*-H), δ 4.61~4.67 (2H, t, -CH$_2$*NH*CH$_2$-), δ 4.20~4.24 (4H, d, -*CH$_2$*NHCH$_2$-), δ 3.79~3.85 (4H, t, -C=N-*CH$_2$*-), δ 3.13~3.22 (4H, m, -CH$_2$*CH$_2$*CH$_2$-), δ 2.97~3.01 (4H, d, -CH$_2$NH*CH$_2$*-), δ 2.76 (12H, s, CH$_3$), δ 2.16~2.20 (4H, d, -CH$_2$*CH$_2$*CH$_2$-), δ 1.68~1.78 (4H, m, -C=N-*CH$_2$*-). Anal. Calcd (found) for bi-[Zn(PDI)]Br$_2$ (C$_{30}$H$_{42}$N$_8$Zn$_2$Br$_4$): %C 37.34, (37.36); %H 4.39, (4.34); %N 11.61, (11.55).
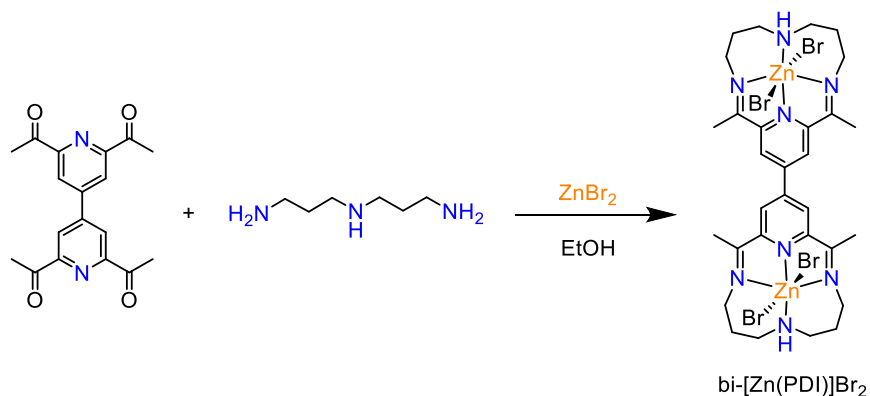
Scheme 5.8 Synthetic route for bi-[ZnCo(PDI)].

5.3.3 Electrochemical Methods and Product Analysis

Electrochemical experiments were conducted using a Bio-Logic SP-200 potentiostat/galvanostat with data recorded using the Bio-Logic EC-Lab V10.44 software package. In all measurements, the reference electrode was a Ag/AgNO₃ (1.0 mM in MeCN with 0.1 M nBu₄NPF₆) nonaqueous reference electrode separated from the solution by a CoralPor® glass frit (Bioanalytical Systems, Inc.) and externally referenced to the ferrocenium/ferrocene redox couple (Fc$^{+/0}$).

Cyclic Voltammetry (CV) under N₂ and CO₂. Cyclic voltammograms were conducted in quiescent solution, using a 0.071 cm^2 glassy carbon disk working electrode (CH instruments), a Ag/AgNO₃ (1.0 mM in MeCN with 0.1 M nBu₄NPF₆) nonaqueous reference electrode and a carbon rod auxiliary electrode (99.999%, Strem Chemicals). Electrolyte solutions contained 0.1 M nBu₄NPF₆ in MeCN with reported concentrations of H₂O. The typical scan rate for reported CVs was 0.050 V/s unless otherwise noted. Prior to each measurement, the electrolyte solution was sparged with either N₂ or CO₂ as indicated for at least 10 min, and the headspace was then blanketed with the same gas during the measurement. To avoid electrolyte evaporation, all gases were saturated with MeCN before use by first bubbling them through a gas-washing bottle filled with MeCN. The uncompensated solution resistance ($R_u \approx 120$ Ω) in the cell was measured using a single-point impedance measurement at 100 kH$_z$ with a 20 mV amplitude about the open-circuit potential before each set of measurements. CVs were automatically corrected for iR drop at 85% through positive feedback using the Bio-Logic EC-Lab software.

For all the calculations of kinetic parameters in our study, $E^0_{CO_2} = -1.36$ V vs Fc$^{+/0}$ (-0.72 V vs SHE) is used as the thermodynamic potential for the CO₂ reduction in MeCN in the presence of H₂O. This thermodynamic potential takes into consideration that the true proton source is

dissolved CO_2 (i.e. carbonic acid, H_2CO_3) instead of H_2O.[31-32] More recently, some reports have shown that apparent acidity of the CO_2-saturated acetonitrile/water system is also dependent on the concentration of H_2O, and that $E^0_{CO_2}$ can vary greatly from -1.63 V vs $Fc^{+/0}$ in 0.01 M H_2O to -1.25 V vs $Fc^{+/0}$ in the presence of 11 M H_2O.[33-34]

Controlled-Potential Electrolysis (CPE). All controlled-potential electrolysis experiments in this study were conducted in the H-cell. We have previously shown this electrolysis cell design is gas-tight through electrolysis experiments in N_2-sparged MeCN solutions with 1 M acetic acid for the hydrogen evolution reaction (HER) at Pt foil (0.1 mm thick, Premion™, 99.99% metals basis) and glassy carbon plate (HTW Hochtemperatur-Werkstoff GmbH) working electrodes in chapter 4. The Faradaic Efficiency for H_2 production as measured from the post-electrolysis headspace was ~100% in these previous studies of chapter 4, confirming that the electrolysis cell is gastight.

The left chamber held the glassy carbon working electrode and $Ag/AgNO_3$ reference electrode, and was filled with 20 mL MeCN solution of 0.3 mM catalyst with 0.1 M nBu$_4$NPF$_6$ and the reported concentrations of H_2O in the manuscript. The right chamber held the Nichrome wire counter electrode, filled with 15 mL MeCN solution of 5 mM Fc with 0.1 M nBu$_4$NPF$_6$ and the same concentration of H_2O as the left chamber. The two chambers were separated by a fine-porosity glass frit. The total volume of cell (149.56 mL) was determined by measuring the mass of H_2O necessary to fill the cell completely when the cell was fully assembled with the working and reference electrode, and the headspace volume of 114.56 mL for the CPE was calculated by subtracting the electrolyte solution volume 35.00 mL from the total cell volume.

The working electrode was a glassy carbon plate (3.2 cm × 1.6 cm × 0.1 cm, HTW Hochtemperatur-Werkstoff GmbH) with half immersed in the electrolyte solution. Before each experiment, the working electrode was manually polished on 600-grit SiC polishing paper (Buehler, Ltd) and sonicated for 5 min in i-PrOH. The counter electrode was Nichrome wire (0.2595 Ω ft^{-1}, Arcor Electronics). Prior to each CPE experiment, the electrolyte solution was purged with CO_2 or N_2 for 30 minutes and then sealed under an atmosphere of CO_2 or N_2. To prevent electrolyte evaporation, all gases were saturated with MeCN before use by first bubbling them through a gas-washing bottle filled with MeCN.

The CPE experiments were conducted without iR compensation for solution resistance (Ru ≈ 60 Ω), and the reported electrolysis potentials are the actual applied potentials. After each electrolysis, 5 mL aliquots of the headspace of the electrolysis cell was collected by a Pressure-Lok gas-tight syringe (10 mL, Valco VICI Precision Sampling, Inc.), and injected into a 3 mL sample loop on a gas chromatography system to determine CO and H_2 concentrations. The post-electrolysis solution was analyzed using high performance liquid chromatography to determine the concentrations of other possible liquid products including HCOOH. The Faradaic efficiency of every product was calculated by dividing the measured product amount by the amount expected on the basis of charge passed during the CPE measurement. In general, the only products observed in measurable quantities (> 0.02 % v/v for GC and > 0.025 mM for HPLC) from our experiments were CO and H_2.

Product Analysis. Gaseous products (*i.e.* CO and H_2) in the headspace after electrolysis were tested by a Thermo Scientific Trace 1310 Gas Chromatograph (GC) with a single 3 mL sample loop leading to two analyzer channels. Using a valve system, column configuration, and method developed by Thermo Scientific and Custom Solutions Group LLC., gases were separated

so that H_2 was detected on one channel using an Argon carrier gas, and all other gases were detected on a second channel using a Helium carrier gas. Gases were detected on both channels using thermal conductivity detectors (TCDs), and chromatographs were analyzed using Thermo Scientific Dionex Chromeleon^{TM} 7.2.2.6686 Chromatography Data System software.

Liquid samples were analyzed for possible dissolved products such as formic acid using a Thermo Scientific Dionex Ultimate 3000 series HPLC equipped with a 5 cm Thermo Scientific HyperREZ XP Carbohydrate H^+ LC guard column and a 30 cm Thermo Scientific HyperREZ XP Carbohydrate H^+ 8µm LC analytical column in series. ~1 mL liquid samples were collected from the working-electrode chamber post electrolysis and placed in an autosampler from which 10 µL aliquots of each liquid sample were injected into the columns. The eluent was 0.005 M H_2SO_4 aqueous solution with a flow rate of 0.6 mL·min^{-1}. The temperature of the column was maintained at 50 ℃. Products were detected using a UV-Vis detector, and chromatographs were analyzed using Thermo Scientific Dionex Chromeleon^{TM} 7.2.2.6686 Chromatography Data System software.

5.5.4 Scanning Electron Microscopy/Energy Dispersive X-Ray Spectroscopy (SEM-EDS)

SEM-EDS measurements were used to detect metal deposits associated with catalyst decomposition on the electrode surface after electrolysis. All electrodes tested by SEM-EDS (JEOL-7800FLV FE) were <u>not</u> rinsed post electrolysis as per established best practices.[13, 35] SEM images showing the morphology of the electrode surface were recorded with a field emission gun scanning electron microscope at 20 kV acceleration voltage equipped with an energy dispersive X-ray (EDS) detector. For each electrode, SEM-EDS measurements were conducted at 9 random sites on the electrode surface, and the values were then averaged to give the Co weight % for that specific electrode. Each electrolysis measurement was reproduced after 3 independent electrolysis

experiments. Therefore, each EDS measurement reported is an average of at least 27 measurements: 9 measurement spots on 3 electrodes after independent electrolysis. Reported errors are standard deviations of all 27 EDS measurements for each electrolysis condition.

5.4 Results and Discussion

5.4.1 Electrochemical Characterization of bi-[Co(PDI)] under Non-Catalytic Conditions.

The non-catalytic cyclic voltammograms (CVs) of mononuclear [Co(PDI)] and binuclear bi-[Co(PDI)] in N_2-saturated MeCN solutions with 0.1 M tetrabutylammonium hexafluorophosphate (nBuNPF$_6$) as supporting electrolyte are shown in Figure 5.2a and 5.2b. Note that all CVs are iR-compensated, and potentials are referenced versus Fc$^{+/0}$ in this report. According to the previous study of [Co(PDI)],[29, 36] three reversible redox features at -0.38 V, -0.92 V and -1.88 V (Figure 5.2a and Table 5.1) of [Co(PDI)] are assigned to Co$^{3+/2+}$, Co$^{2+/+}$ and PDI/PDI$^{\bullet-}$ redox processes. In the CV of bi-[Co(PDI)], these three redox processes are also observed but with notable peak splitting feature at Co$^{2+/+}$ and PDI/PDI$^{\bullet-}$ couples (Figure 5.2b). Based on the scan-rate dependent CVs of bi-[Co(PDI)] under N_2 (Figure A.155~A.158), the diffusion coefficient D values calculated at the stepwise redox features of Co$^{2+/+}$ show negligible change compared to that at Co$^{3+/2+}$ couple (Table A.31), indicating no dimerization of species occurred in the solution.[13] Therefore, the stepwise redox features at Co$^{2+/+}$ and PDI/PDI$^{\bullet-}$ couples of bi-[Co(PDI)] represent the sequential formation of [Co^{2+}(PDI)/Co$^+$(PDI)], [Co$^+$(PDI)/Co$^+$(PDI)], [Co$^+$(PDI$^{\bullet-}$)/Co$^+$(PDI)] and [Co$^+$(PDI$^{\bullet-}$)/Co$^+$(PDI$^{\bullet-}$)], which suggests the electronic coupling between two Co(PDI) moieties in the binuclear structure. In addition, the $E_{1/2}$ of Co^{3+}/Co^{2+}, Co^{2+}Co^{2+}/Co^{2+}Co$^+$ and PDI-PDI/PDI-PDI$^{\bullet-}$ couples of bi-[Co(PDI)] are more positive than those of Co$^{3+/2+}$, Co$^{2+/+}$ and PDI/PDI$^{\bullet-}$ couples of [Co(PDI)] (Table 5.1), which indicates that both Co-based and ligand-based reductions are more favorable in the binuclear structure. This is probably due to the electrostatic effect on the redox property of the Co(PDI) moiety exerted by a proximate cationic group, which is the other Co(PDI) moiety in bi-[Co(PDI)].
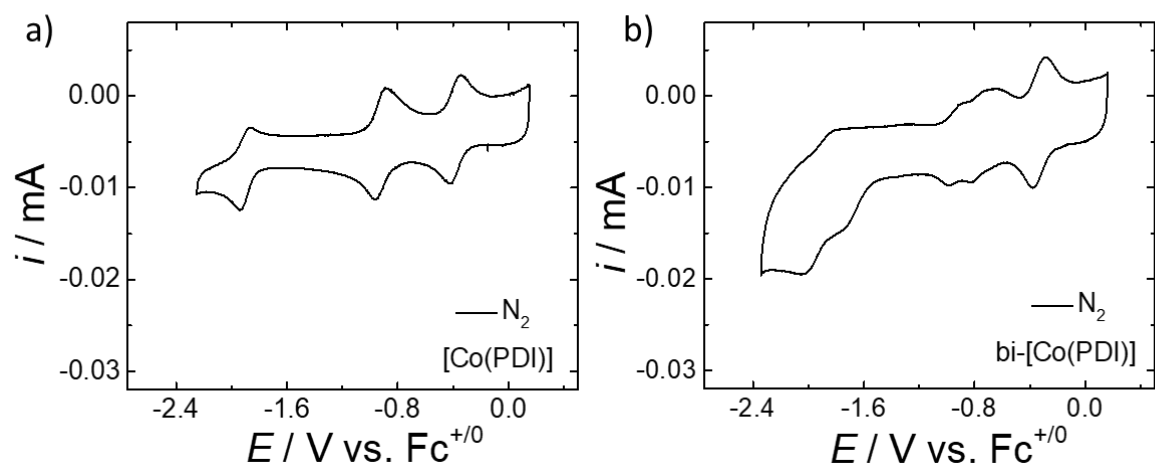
Figure 5.2 Non-catalytic CVs of (a) 0.3mM [Co(PDI)] and (b) 0.15 mM bi-[Co(PDI)] in N_2-saturated MeCN with 0.1 M nBuNPF$_6$, with scan rate 0.05 V/s.

Table 5.1 $E_{1/2}$ of redox processes and catalytic parameters of Co complexes in this report.

Catalysts	$E_{1/2}$ / V vs Fc$^{+/0}$ in non-catalytic CVs under N_2				
	PDI/PDI$^{\bullet-}$		Co$^{2+/+}$		Co$^{3+/2+}$
[Co(PDI)]	−1.88		−0.92		−0.38
bi-[Co(PDI)]	−2.02 (red)^a	−1.73 (red)^a	−0.95^b	−0.75^b	−0.33
bi-[ZnCo(PDI)]	−1.90 (red)^a	−1.58 (red)^a	−0.76		−0.33
bi-ex-[Co(PDI)]	−1.86		−0.90		−0.35

^{a}These redox features are irreversible, and only the potential of the reduction peak is reported for PDI/PDI-PDI$^{\bullet-}$ and PDI-PDI$^{\bullet-}$/PDI$^{\bullet-}$-PDI$^{\bullet-}$ process. ^{b}These are Co^{2+}Co^{2+}/Co^{2+}Co^{+} (−0.75 V) and Co^{2+}Co^{+}/Co^{+}Co^{+} (−0.95 V) processes at Co$^{2+/+}$ couple.

5.4.2 Electrocatalytic Activity of bi-[Co(PDI] for the CO$_2$RR.

The catalytic CVs of mononuclear [Co(PDI)] and binuclear bi-[Co(PDI)] complexes in CO$_2$-saturated MeCN with no added proton source are shown in Figure 5.3a and 5.3b. Note that estimated ~0.04 M H$_2$O is assumed present in MeCN without proton sources added based on previously-reported Karl-Fisher titrations of similar electrolyte solutions.[30] For rational comparison, the concentration of Co sites in both solutions remains the same (0.3 mM Co site = 0.3 mM [Co(PDI)] = 0.15 mM bi-[Co(PDI)]). Both [Co(PDI)] and bi-[Co(PDI)] exhibit a catalytic reduction current near the PDI/PDI$^{\bullet-}$ redox couple (Figure 5.3a and 5.3b), which suggests that the CO$_2$ reduction is initiated by the formation of active species with the ligand radical, consistent with the previous studies of [Co(PDI)][29, 36]. Compared to [Co(PDI)], bi-[Co(PDI)] shows 0.1 V more positive E_{onset} but with roughly 4 $\times$ higher catalytic current as illustrated by the i_c/i_p measurements (i_c = catalytic current under CO$_2$; i_p = redox current of active species under N$_2$; Figure 5.3a and 5.3b, Table 5.2).

Adding H$_2$O as a proton source into the CO$_2$-saturated solutions leads to increased catalytic current and positive shift of E_{onset} for both [Co(PDI)] and bi-[Co(PDI)] complexes (Figure 5.3c and 5.3d for 11.0 M H$_2$O, other concentrations shown in Figure A.165~A.166). In particular, bi-[Co(PDI)] shows dramatically higher activity for the CO$_2$RR, with ~9 $\times$ larger i_c/i_p ratio and 0.15 V more positive E_{onset} compared to the mononuclear [Co(PDI)] (Table 5.2). In contrast to most binuclear catalysts reported, two Co sites in bi-[Co(PDI)] are not possible to bind and activate CO$_2$ via synergistic coordination to facilitate the reaction, due to the rigid and planar structure. Instead, we postulate that the remarkable improvement in the activity of bi-[Co(PDI)] might correlate with the electronic coupling between Co(PDI) moieties and/or the electrostatic effect exerted by each Co(PDI) moiety on the other in the binuclear structure, despite we are not able to distinguish these

two effects merely based on the catalytic CVs. The control CVs of both [Co(PDI)] and bi-[Co(PDI)] in N_2-saturated solutions with 11.0 M H_2O show the current increase for the HER at much more negative potential (green dashed curve in Figure 5.3c and 5.3d), supporting our assertion that the catalytic current peaks measured in the CO_2-saturated solutions are due to the CO_2RR.
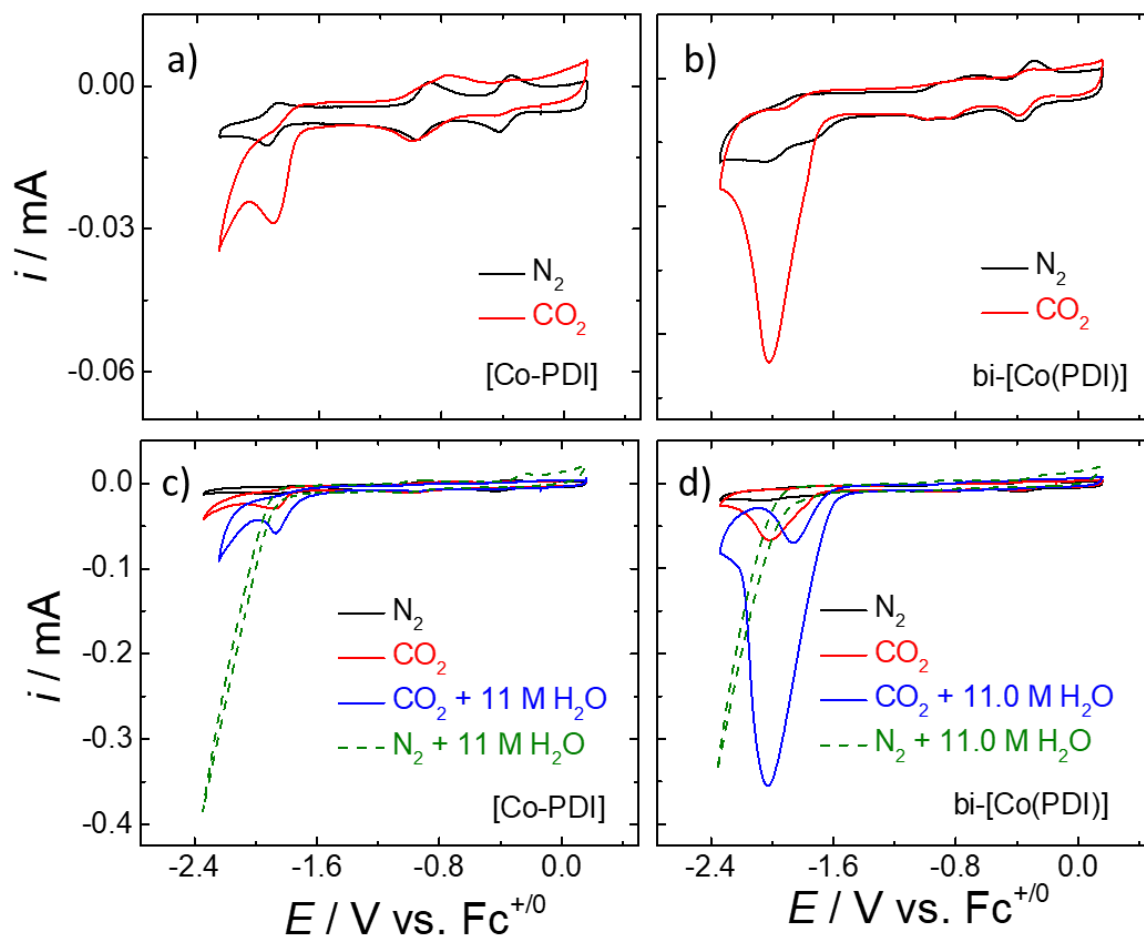
Figure 5.3 Catalytic CVs of (a) 0.3mM [Co(PDI)] and (b) 0.15 mM bi-[Co(PDI)] in MeCN with 0.1 M nBuNPF$_6$, under N_2 (black solid curve), CO_2 (red solid curve) with scan rate 0.05 V/s; Catalytic CVs of (c) 0.3mM [Co(PDI)] and (d) 0.15 mM bi-[Co(PDI)] in MeCN solution with 0.1 M nBuNPF$_6$ under N_2 (black solid curve), CO_2 (red solid curve), CO_2 with 11.0 M H_2O (blue solid curve) and N_2 with 11.0 M H_2O (green dashed curve), with scan rate 0.05 V/s.

Table 5.2 i_c/i_p and E_{onset} values for the CO$_2$RR by the Co complexes based on catalytic CVs

Catalysts	No H$_2$O added		11.0 M H$_2$O	
	i_c/i_p	E_{onset} / V vs. Fc$^{+/0}$	i_c/i_p	E_{onset} / V vs. Fc$^{+/0}$
[Co(PDI)]	5.8	−1.75	13.2	−1.70
bi-[Co(PDI)]	19.4	−1.65	115.5	−1.55
bi-[ZnCo(PDI)]	-	-	207.9	−1.51
bi-ex-[Co(PDI)]	-	-	78.7	−1.59

To further confirm the excellent activity of bi-[Co(PDI)] for the CO$_2$RR, 30-min controlled-potential electrolysis (CPE) experiments were conducted in MeCN solutions of 0.15 mM bi-[Co(PDI)] (= 0.3 mM Co sites) with 11.0 M H$_2$O at E_{app} = −1.95 V (without *iR*-compensation), which is the catalytic peak potential of [Co(PDI)] for the CO$_2$RR (Figure 5.3c). The Faradaic efficiency (FE) of each gas product analyzed by gas chromatography was determined and summarized in Table 5.3. The turnover frequency, TOF$_{CPE}$, were calculated based on the CPE data using the method developed by Savéant *et al.* (see SI for further discussion of TOF$_{CPE}$).[37-38] In addition, the stability of the catalyst was also investigated by SEM-EDS measurements on un-rinsed post-electrolysis working electrode surface, assessing the extent of Co deposition from catalyst decomposition (Figure A.167). The CPE results show the greatly improved activity of bi-[Co(PDI)] for the CO$_2$RR, reflected by ~1.8 × more charge passed and ~14 × larger TOF$_{CPE}$ for CO production compared to [Co(PDI)] (Table 5.3), which is consistent with the larger catalytic current of bi-[Co(PDI)] observed in the electrocatalytic CVs in Figure 5.3d. The bi-[Co(PDI)] also displays an excellent selectivity of reducing CO$_2$ to CO (FE = 93.8 %) with only trace amount of H$_2$ (FE = 0.2 %) generated, while [Co(PDI)] shows 43.0% FE for CO and 11.1% FE for H$_2$. Moreover, the much lower Co weight% on the post-electrolysis electrode surface suggests less catalyst decomposition and thus improved stability of bi-[Co(PDI)] during electrolysis compared to [Co(PDI)].

Table 5.3 Summary of CPE results for Co catalysts in the report.

Catalysts	CPE under CO_2 with 11 M H_2O @ −1.95 V				
	Charge/ C	FE(CO) / %	FE(H_2) / %	TOF_{CPE} / s^{-1} [a]	Co weight%
[Co(PDI)][b]	6.2 ± 1.0	43.0 ± 11.6	11.1 ± 7.4	9.8 ± 6.6	0.56 ± 0.18
bi-[Co(PDI)]	10.8 ± 1.9	93.8 ± 6.4	0.2 ± 0.2	$1.4 \pm 0.6 \times 10^2$	0.24 ± 0.19
bi-[ZnCo(PDI)]	12.5 ± 0.7	95.2 ± 3.0	0	$5.4 \pm 0.7 \times 10^2$	0.12 ± 0.05
bi-ex-[Co(PDI)]	8.9 ± 0.3	75.5 ± 1.7	0.5 ± 0.1	$4.8 \pm 0.5 \times 10^1$	0.29 ± 0.11

Reported values are averages from three or more independent measurements with reported standard deviations. [a] TOF_{CPE} values were determined from each independent CPE measurement, and the reported values are averages of these individual TOF_{CPE} values with reported standard deviations. [b]The data of [Co(PDI)] is from chapter 4.

5.4.3 Kinetic Study of bi-[Co(PDI)] for the CO₂RR

To quantify the activity of bi-[Co(PDI)] for the CO₂RR, kinetic studies have been conducted to extract the intrinsic catalytic rate k_{cat} and catalytic turnover frequency TOF$_{cat}$ of bi-[Co(PDI)] for the comparison with [Co(PDI)] discussed in our chapter 4. Ideally under pure kinetic conditions with no substrate depletion, the rate-determining k_{cat} can be estimated from the plateau current of an S-shaped CV response. Based on our previous study in chapter 4, such an ideal S-shaped response can not be achieved for [Co(PDI)] based systems, but can be approximated at fast scan rates, minimizing mass-transport and substrate depletion. Scan-rate dependent catalytic CVs of the bi-[Co(PDI)] catalyst for the CO₂RR in MeCN with 11.0 M H₂O are shown in Figure 5.4a. The peak current i_c was plotted in the function of the scan rate v, asymptotically approaching a limiting plateau current $i_{plateau}$ when the scan rate is larger than 12.0 V/s (Figure 5.4b). The limiting plateau current $i_{plateau}$ of bi-[Co(PDI)] (= 1.06 mA, Figure 5.4b) at fast scan rate, which is ~7 × larger than that of [Co(PDI)] (0.15 mA, gray curve in Figure 5.4b from our previous study in chapter 4), is applied to calculate the rate constant k_{cat} based on the equation below[38-39]:

$$k_{cat} = \left(\frac{i_{plateau}}{i_p}\right)^2 \frac{(0.466)^2 \cdot nFv}{n'RT} \qquad \text{Eq. 5.1}$$

Here, i_p is the peak current associated with the active species in non-catalytic CVs measured at scan rate v, $n = 2$ is the number of electrons transferred per CO₂, $n' = 1$ is the number of Co site equivalents per turnover, $R = 8.31415$ J mol^{-1} K^{-1} is the ideal gas constant, and $T = 298$ K is room temperature. The resulting $k_{cat} = $ TOF$_{cat} = 6.2 \times 10^4$ s^{-1} of bi-[Co(PDI)] calculated using the corresponding i_p values measured at 0.05 V/s is ~40 × higher than that of [Co(PDI)] (Table 5.4, see Appendices A.4 for detailed calculation of TOF$_{cat}$). With the k_{cat} above, we were be able to construct plots of log(TOF) *vs*. overpotential η for the CO₂RR by the [Co(PDI)] and bi-[Co(PDI)] complexes as shown in Figure 5.5 (detailed calculations can be found in Appendices

A.4). The intrinsic catalytic activity term TOF_0 is accessed by extrapolating the log(TOF) curve to $\eta = 0$ (Table 5.4). The bi-[Co(PDI)] catalyst shows more than 3 orders of magnitude higher TOF_0 than [Co(PDI)] (Table 5.4), consistent with the same trend of TOF_{cat} (Table 5.4) and TOF_{CPE} from CPE experiments (Table 5.3).
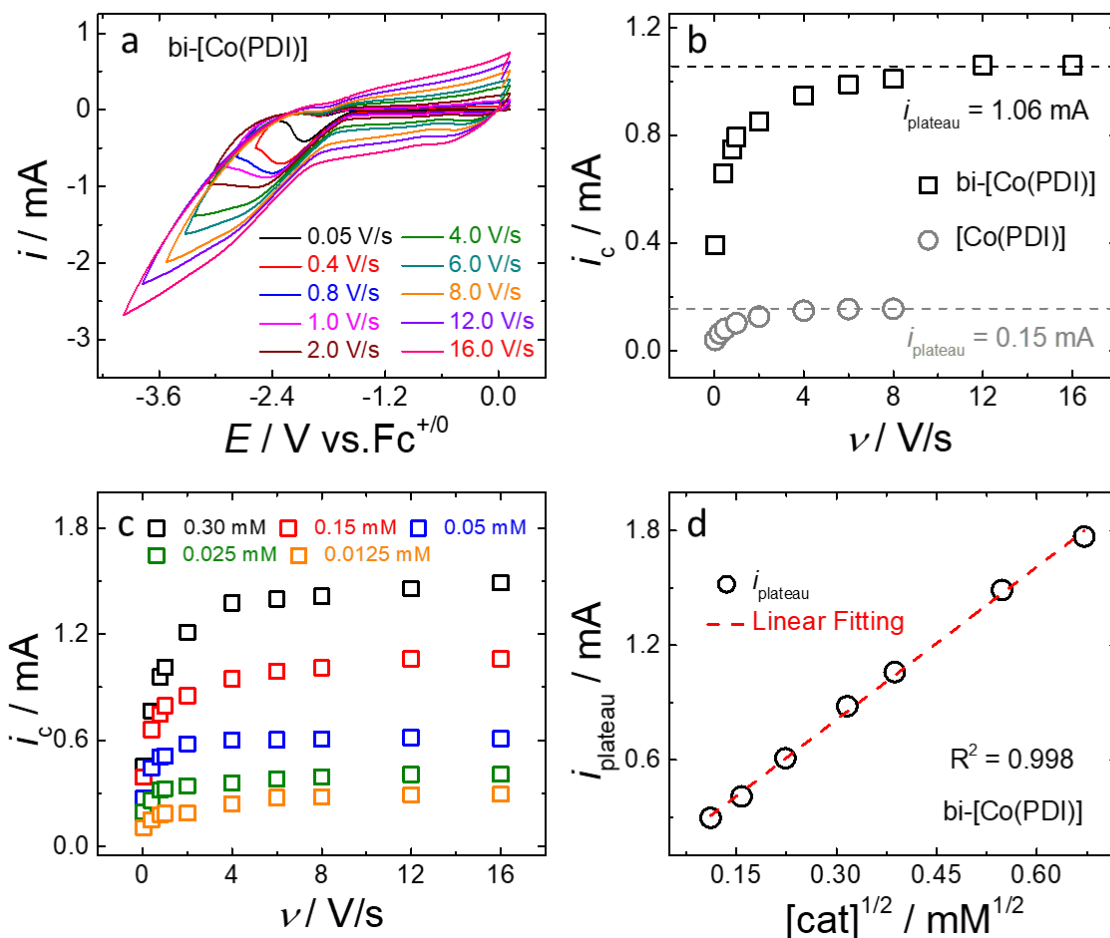
Figure 5.4 (a) Scan rate dependent CVs of 0.15 mM bi-[Co(PDI)] catalyst for the CO_2RR in MeCN with 11.0 M H_2O; (b) Plots of the catalytic current, i_c, as a function of the scan rate, v, for the CO_2RR by 0.15 mM bi-[Co(PDI)] (black square) and 0.3 mM [Co(PDI)] (gray circle) in CO_2-saturated MeCN with 11 M H_2O; (c) Plots of the catalytic current, i_c, as a function of the scan rate, v, for the CO_2RR by different concentrations of bi-[Co(PDI)] in CO_2-saturated MeCN with 11 M H_2O; (d) The plot of the limiting plateau current, $i_{plateau}$, for the CO_2RR in MeCN with 11.0 M H_2O as a function of the square root of concentrations of bi-[Co(PDI)] with a linear fitting line, showing the a half-order dependence on the concentration of bi-[Co(PDI)] for the CO_2RR.

Table 5.4 Kinetic parameters for the CO$_2$RR by Co complexes in the presence of 11.0 M H$_2$O

	[Co(PDI)][a]	bi-[Co(PDI)]	bi-[ZnCo(PDI)]	bi-ex-[Co(PDI)]
E_{onset}/ V vs.Fc$^{+/0}$	−1.70	−1.55	−1.51	−1.59
Variable Scan Rate Parameters				
$k_{cat} = TOF_{cat}$ / s^{-1}	1.5 ×10^3	9.6 × 10^4	2.4 × 10^5	5.6 × 10^4
log(TOF$_{cat}$/ s^{-1})	3.2	5.0	5.4	4.8
log(TOF$_0$/ s^{-1})	−5.7	−1.3	1.7	−3.7

[a]The data of [Co(PDI)] is from our previous study in Chapter 4
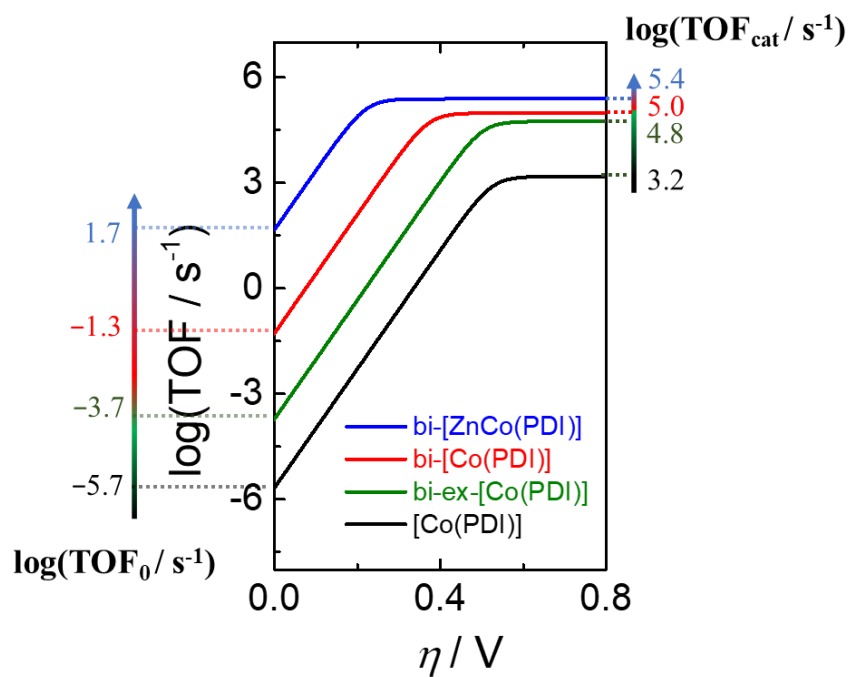
Figure 5.5 The plots of log(TOF) vs. overpotential η for the CO$_2$RR by the Co catalysts in CO$_2$-saturated MeCN with 11 M H$_2$O as proton source.

To further elucidate mechanism of bi-[Co(PDI)] for the CO_2RR, scan-rate dependent catalytic CV measurements with varying concentrations of bi-[Co(PDI)] in the CO_2-saturated MeCN with 11.0 M H_2O were conducted and the plots of catalytic current, i_c, vs. scan rate, v, for five catalyst concentrations are shown in Figure 5.4c (plots for other concentrations seen in Figure A.171). The $i_{plateau}$ of these i_c vs. v plots shows a square root dependence on the catalyst concentration (Figure 5.4d) suggesting a half reaction order of bi-[Co(PDI)] for the CO_2RR, which is different from the first reaction order for the CO_2RR in the cases of those binuclear molecular catalysts with synergistic effect reported in literature[25-26, 28] and the mononuclear [Co(PDI)] (Figure A.173 and A.174). The half reaction order of bi-[Co(PDI)] for the CO_2RR suggests that each Co(PDI) moiety in the structure (half of the complex structure) binds and reduces CO_2 individually as an active catalytic site, providing one of rare examples of binuclear complexes containing two catalytic active sites without synergistic effect but showing boosted activity for the CO_2RR so far.

5.4.4 "Multitasking" Co(PDI) Moieties in the Binuclear Structure for the Boosted Activity: Intramolecular Electrostatic Effect on the Catalytic Ability

According to the kinetic study of bi-[Co(PDI)] for the CO_2RR above, both Co(PDI) moieties in the structure bind and reduce CO_2 individually as active catalytic sites. In addition, bi-[Co(PDI)] shows >2× higher catalytic activity than that of the mononuclear [Co(PDI)], which suggests improved catalytic ability of each Co(PDI) moiety in bi-[Co(PDI)] compared to the Co site in the mononuclear analog. Based on the analysis of redox features of bi-[Co(PDI)] in non-catalytic CVs, we postulate that the boosted catalytic ability of bi-[Co(PDI)] for the CO_2RR is probably due to the electronic coupling and/or electrostatic effect between two Co(PDI) moieties in the binuclear structure. Compared to its mononuclear [Co(PDI)], Co(PDI) moieties in bi-[Co(PDI)] play multitasking roles in the CO_2RR process, acting not only as catalytic sites of binding and reducing CO_2 but also as redox modulators to manipulate the electronic structure and catalytic ability of each other. To elucidate which factor, the electronic coupling or the electrostatic effect in the structure, is the main contributor to the increased activity of bi-[Co(PDI)], two control binuclear compounds— hetero-bimetallic bi-[ZnCo(PDI)] with one Co center replaced by a redox-inert Zn and bi-ex-[Co(PDI)] with a longer Co-Co distance (Scheme 5.1b)—have been prepared and studied for the CO_2RR.

For bi-[ZnCo(PDI)], the electronic coupling between Co and Zn moieties should be cut off due to the redox-inactive property of the Zn center. However, charged Zn^{2+} should remain the electrostatic effect on the Co(PDI) moiety in the structure (Scheme 5.1b). In the non-catalytic CV of bi-[ZnCo(PDI)] (Figure 5.6a), $Co^{3+/2+}$ and $Co^{2+/+}$ redox couples are observed at −0.33 V and −0.76 V (Table 5.1) with no peak splitting features as observed for bi-[Co(PDI)], confirming the redox-inactive property of the Zn center and no electronic coupling between Zn and Co sites in the

structure. In addition, two stepwise ligand-based redox features at -1.58 V and -1.90 V (Figure 5.6a and Table 5.1) are assigned to the corresponding PDI/PDI$^{\bullet-}$ couple of Zn(PDI) and Co(PDI) moieties respectively in bi-[ZnCo(PDI)]. Compared to the mononuclear [Co(PDI)], bi-[ZnCo(PDI)] shows more positive $E_{1/2}$ of Co$^{3+/2+}$ and Co$^{2+/+}$ couples (Table 5.1), which are almost the same as those of Co^{3+}/Co^{2+} and Co^{2+}Co^{2+}/Co^{2+}Co$^+$ couples of bi-[Co(PDI)] (Table 5.1), suggesting the similar electrostatic effect on the redox property of Co(PDI) moiety in both bi-[ZnCo(PDI)] and bi-[Co(PDI)] binuclear structures.

Under CO_2 atmosphere, bi-[ZnCo(PDI)] displays even higher activity and more positive onset potential for the CO_2RR compared to bi-[Co(PDI)] (Figure 5.6b, Table 5.2). In particular, in the presence of 11.0 M H_2O, bi-[ZnCo(PDI)] shows ~2 × higher catalytic current increase (i_c/i_p) with 40 mV more positive E_{onset} (-1.51 V) compared to bi-[Co(PDI)] based on the catalytic CVs. The improved catalytic ability of bi-[ZnCo(PDI)] compared to bi-[Co(PDI)] is also confirmed by its higher TOF$_{CPE}$, TOF$_0$ and TOF$_{cat}$ from electrolysis experiments (Table 5.3) and kinetic studies (Table 5.3). All these results make bi-[ZnCo(PDI)] among the most efficient molecular catalysts reported for the CO_2RR so far, which also supports that the boosted activity of bi-[ZnCo(PDI)] and bi-[Co(PDI)] compared to the mononuclear [Co(PDI)] mainly results from the electrostatic effect rather than the electronic coupling between two metal moieties in binuclear structures. The extra increased activity of bi-[ZnCo(PDI)] compared to bi-[Co(PDI)] is probably due to the more influential electrostatic effect exerted by Zn^{2+} (M^{2+} cation with two positive charge) than a less-charged Co$^+$ (M$^+$ cation with only one positive charge) in the binuclear structure of catalytic active species during the CO_2RR.

The intramolecular electrostatic effect on the activity of binuclear catalysts is also supported by the study of bi-ex-[Co(PDI)], where both the electrostatic effect exerted by one

Co(PDI) moiety on the other and the electronic coupling between Co(PDI) moieties in the structure are supposed to be weaker due to the longer Co-Co distance (Figure 5.1b). The non-catalytic CV of bi-ex-[Co(PDI)] shows very similar redox features compared to that of [Co(PDI)]. No peak splitting features are observed at $Co^{3+/2+}$, $Co^{2+/+}$ and $PDI/PDI^{\bullet-}$ redox couples at -0.35 V, -0.90 V and -1.86 V (Figure 5.6c and Table 5.1), confirming negligible electronic coupling between Co(PDI) moieties through the longer Co-Co distance. Despite the $E_{1/2}$ of redox couples of bi-ex-[Co(PDI)] are more negative than those of bi-[Co(PDI)] (Table 5.1), the slight positive shift of $E_{1/2}$ compared to [Co(PDI)] (Table 5.1) indicates a weak but not negligible electrostatic effect of distant Co(PDI) moieties on each other in bi-ex-[Co(PDI)]. In CO_2-saturated MeCN with 11.0 M H_2O, bi-ex-[Co(PDI)] shows $6 \times$ higher i_c/i_p with 0.11 V more positive E_{onset} for the CO_2RR compared to [Co(PDI)] (Figure 5.6d and Table 5.2), despite the activity is much lower and onset potential is less positive compared to both bi-[Co(PDI)] and bi-[ZnCo(PDI)] (Table 5.2) due to the weaker electrostatic effect in bi-ex-[Co(PDI)], which is consistent with the order of TOF_{CPE}, TOF_0 and TOF_{cat} from CPE experiments and kinetic study among [Co(PDI)], bi-[Co(PDI)] and bi-[ZnCo(PDI)] (Table 5.3 and Table 5.4 and Figure 5.5). These catalytic metrics of bi-ex-[Co(PDI)] suggest again that the electrostatic effect rather than the electronic coupling between Co(PDI) moieties in the binuclear structure is the main factor influencing the catalytic ability of the system.

Figure 5.6 (a) Non-catalytic CV of 0.3mM bi-[ZnCo(PDI)] in MeCN with 0.1 M nBuNPF$_6$, under N$_2$ with scan rate 0.05 V/s; (b) Catalytic CVs of 0.15mM [ZnCo(PDI)] in MeCN with 0.1 M nBuNPF$_6$ under N$_2$ (black solid curve), CO$_2$ (red solid curve), CO$_2$ with 11.0 M H$_2$O (blue solid curve) and N$_2$ wi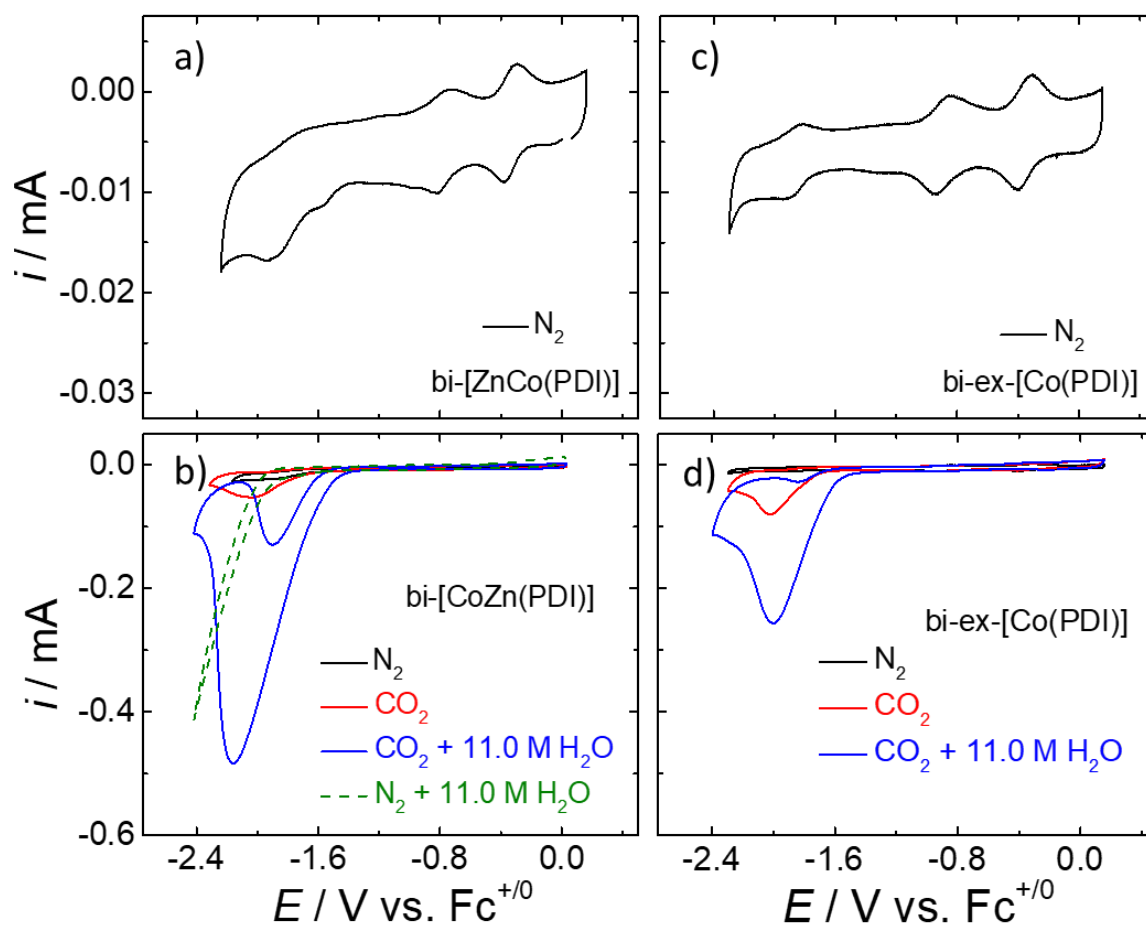th 11.0 M H$_2$O (green dashed curve), with scan rate 0.05 V/s; (c) Non-catalytic CV of 0.15mM bi-ex-[Co(PDI)] in MeCN with 0.1 M nBuNPF$_6$, under N$_2$ with scan rate 0.05 V/s; (b) Catalytic CVs of 0.15mM bi-ex-[Co(PDI)] in MeCN with 0.1 M nBuNPF$_6$ under N$_2$ (black solid curve), CO$_2$ (red solid curve) and CO$_2$ with 11.0 M H$_2$O (blue solid curve) with scan rate 0.05 V/s.

5.5 Conclusion

In this work, we designed and prepared a binuclear cobalt pyridyldiimine complex bi-[Co(PDI)] where two Co(PDI) moieties are connected through an electronic conjugated redox-active ligand linker. Compared to the mononuclear [Co(PDI)], bi-[Co(PDI)] shows dramatically boosted catalytic ability for reducing CO_2 to CO selectively (~94% Faradaic efficiency), operating with over 4 orders of magnitude higher intrinsic activity ($\log(TOF_0/s^{-1}) = -1.3$), ~2 orders of magnitude higher maximum kinetic activity ($\log(TOF_{cat}/s^{-1}) = 5.0$) and 0.15 V more positive catalytic onset ($E_{onset} = -1.55$ V vs $Fc^{+/0}$), in acetonitrile with 11 M water. The kinetic study also shows that each Co(PDI) moiety in bi-[Co(PDI)] plays a multitasking role in the CO_2RR process, acting not only as a catalytic site of binding and reducing CO_2 but also as a redox modulator to manipulate the electronic structure and catalytic ability of each other. The catalysis study of the hetero-bimetallic bi-[ZnCo(PDI)] complex with one Co center replaced by a redox-inert Zn and the bi-ex-[Co(PDI)] complex with a longer Co-Co distance reveals that the intramolecular electrostatic effect rather than the electronic coupling between M(PDI) moieties in the binuclear structure is the main factor leading to the greatly enhanced activity and more positive catalytic onset for the CO_2RR. Both bi-[Co(PDI)] and bi-[ZnCo(PDI)] are among the most efficient molecular catalysts for the CO_2RR reported so far. Moreover, our study not only highlights a few of rare examples of binuclear molecular catalysts with "multitasking" moieties in the structure boosting the catalytic activity for the CO_2RR, but also provides a new insight in the design of multinuclear molecular assemblies and molecule-based extended frameworks as the next generation of efficient catalytic systems in the future.

5.6 Reference

1.   De Luna, P.; Hahn, C.; Higgins, D.; Jaffer, S. A.; Jaramillo, T. F.; Sargent, E. H. "What would it take for renewably powered electrosynthesis to displace petrochemical processes?," *Science* **2019**, *364*, eaav3506. http://dx.doi.org/10.1126/science.aav3506

2.   Dalle, K. E.; Warnan, J.; Leung, J. J.; Reuillard, B.; Karmel, I. S.; Reisner, E. "Electro- and Solar-Driven Fuel Synthesis with First Row Transition Metal Complexes," *Chemical Reviews* **2019**, *119*, 2752-2875. http://dx.doi.org/10.1021/acs.chemrev.8b00392

3.   Birdja, Y. Y.; Pérez-Gallent, E.; Figueiredo, M. C.; Göttle, A. J.; Calle-Vallejo, F.; Koper, M. T. M. "Advances and challenges in understanding the electrocatalytic conversion of carbon dioxide to fuels," *Nature Energy* **2019**, *4*, 732-745. http://dx.doi.org/10.1038/s41560-019-0450-y

4.   Nielsen, D. U.; Hu, X.-M.; Daasbjerg, K.; Skrydstrup, T. "Chemically and electrochemically catalysed conversion of CO2 to CO with follow-up utilization to value-added chemicals," *Nature Catalysis* **2018**, *1*, 244-254. http://dx.doi.org/10.1038/s41929-018-0051-3

5.   Kuhl, K. P.; Cave, E. R.; Abram, D. N.; Jaramillo, T. F. "New insights into the electrochemical reduction of carbon dioxide on metallic copper surfaces," *Energy & Environmental Science* **2012**, *5*, 7050-7059. http://dx.doi.org/10.1039/C2EE21234J

6.   Hori, Y. "Electrochemical CO2 Reduction on Metal Electrodes," In *Modern Aspects of Electrochemistry*; Vayenas, C. G.; White, R. E.; Gamboa-Aldeco, M. E., Eds.; Springer New York: New York, NY, 2008, p 89-189.

7.   Wang, J.-W.; Liu, W.-J.; Zhong, D.-C.; Lu, T.-B. "Nickel complexes as molecular catalysts for water splitting and CO2 reduction," *Coordination Chemistry Reviews* **2019**, *378*, 237-261. http://dx.doi.org/https://doi.org/10.1016/j.ccr.2017.12.009

8.   Jiang, C.; Nichols, A. W.; Machan, C. W. "A look at periodic trends in d-block molecular electrocatalysts for CO2 reduction," *Dalton Transactions* **2019**, *48*, 9454-9468. http://dx.doi.org/10.1039/C9DT00491B

9.   Barlow, J. M.; Yang, J. Y. "Thermodynamic Considerations for Optimizing Selective CO2 Reduction by Molecular Catalysts," *ACS Central Science* **2019**, *5*, 580-588. http://dx.doi.org/10.1021/acscentsci.9b00095

10.   Elgrishi, N.; Chambers, M. B.; Wang, X.; Fontecave, M. "Molecular polypyridine-based metal complexes as catalysts for the reduction of CO2," *Chemical Society Reviews* **2017**, *46*, 761-796. http://dx.doi.org/10.1039/c5cs00391a

11.   Benson, E. E.; Kubiak, C. P.; Sathrum, A. J.; Smieja, J. M. "Electrocatalytic and homogeneous approaches to conversion of CO2 to liquid fuels," *Chemical Society Reviews* **2009**, *38*, 89-99. http://dx.doi.org/10.1039/b804323j

12.   Rønne, M. H.; Cho, D.; Madsen, M. R.; Jakobsen, J. B.; Eom, S.; Escoudé, É.; Hammershøj, H. C. D.; Nielsen, D. U.; Pedersen, S. U.; Baik, M.-H.; Skrydstrup, T.; Daasbjerg, K. "Ligand-Controlled Product Selectivity in Electrochemical Carbon Dioxide Reduction Using Manganese Bipyridine Catalysts," *Journal of the American Chemical Society* **2020**, *142*, 4265-4275. http://dx.doi.org/10.1021/jacs.9b11806

13.   Nie, W.; Wang, Y.; Zheng, T.; Ibrahim, A.; Xu, Z.; McCrory, C. C. L. "Electrocatalytic CO2 Reduction by Cobalt Bis(pyridylmonoimine) Complexes: Effect of Ligand Flexibility on Catalytic Activity," *ACS Catalysis* **2020**, 4942-4959. http://dx.doi.org/10.1021/acscatal.9b05513

14.   Hooe, S. L.; Dressel, J. M.; Dickie, D. A.; Machan, C. W. "Highly Efficient Electrocatalytic Reduction of CO2 to CO by a Molecular Chromium Complex," *ACS Catalysis* **2020**, *10*, 1146-1151. http://dx.doi.org/10.1021/acscatal.9b04687

15.   Derrick, J. S.; Loipersberger, M.; Chatterjee, R.; Iovan, D. A.; Smith, P. T.; Chakarawet, K.; Yano, J.; Long, J. R.; Head-Gordon, M.; Chang, C. J. "Metal–Ligand Cooperativity via Exchange Coupling Promotes Iron- Catalyzed Electrochemical CO_2 Reduction at Low Overpotentials," *Journal of the American Chemical Society* **2020**, *142*, 20489-20501. http://dx.doi.org/10.1021/jacs.0c10664

16.   Sung, S.; Li, X.; Wolf, L. M.; Meeder, J. R.; Bhuvanesh, N. S.; Grice, K. A.; Panetier, J. A.; Nippe, M. "Synergistic Effects of Imidazolium-Functionalization on fac-Mn(CO)3 Bipyridine Catalyst Platforms for Electrocatalytic Carbon Dioxide Reduction," *Journal of the American Chemical Society* **2019**, *141*, 6569-6582. http://dx.doi.org/10.1021/jacs.8b13657

17.   Steinlechner, C.; Roesel, A. F.; Oberem, E.; Päpcke, A.; Rockstroh, N.; Gloaguen, F.; Lochbrunner, S.; Ludwig, R.; Spannenberg, A.; Junge, H.; Francke, R.; Beller, M. "Selective Earth-Abundant System for CO_2 Reduction: Comparing Photo- and Electrocatalytic Processes," *ACS Catalysis* **2019**, *9*, 2091-2100. http://dx.doi.org/10.1021/acscatal.8b03548

18.   Gonell, S.; Massey, M. D.; Moseley, I. P.; Schauer, C. K.; Muckerman, J. T.; Miller, A. J. M. "The Trans Effect in Electrocatalytic CO_2 Reduction: Mechanistic Studies of Asymmetric Ruthenium Pyridyl-Carbene Catalysts," *Journal of the American Chemical Society* **2019**, *141*, 6658-6671. http://dx.doi.org/10.1021/jacs.9b01735

19.   Schaugaard, R. N.; Raghavachari, K.; Li, L.-s. "Redox "Innocence" of Re(I) in Electrochemical CO_2 Reduction Catalyzed by Nanographene–Re Complexes," *Inorganic Chemistry* **2018**, *57*, 10548-10556. http://dx.doi.org/10.1021/acs.inorgchem.8b01092

20.   Nie, W.; McCrory, C. C. L. "Electrocatalytic CO_2 reduction by a cobalt bis(pyridylmonoimine) complex: effect of acid concentration on catalyst activity and stability," *Chemical Communications* **2018**, *54*, 1579-1582. http://dx.doi.org/10.1039/C7CC08546J

21.   Haviv, E.; Azaiza-Dabbah, D.; Carmieli, R.; Avram, L.; Martin, J. M. L.; Neumann, R. "A Thiourea Tether in the Second Coordination Sphere as a Binding Site for CO2 and a Proton Donor Promotes the Electrochemical Reduction of CO2 to CO Catalyzed by a Rhenium Bipyridine-Type Complex," *Journal of the American Chemical Society* **2018**, *140*, 12451-12456. http://dx.doi.org/10.1021/jacs.8b05658

22.   Clark, M. L.; Cheung, P. L.; Lessio, M.; Carter, E. A.; Kubiak, C. P. "Kinetic and Mechanistic Effects of Bipyridine (bpy) Substituent, Labile Ligand, and Brønsted Acid on Electrocatalytic CO2 Reduction by Re(bpy) Complexes," *ACS Catalysis* **2018**, *8*, 2021-2029. http://dx.doi.org/10.1021/acscatal.7b03971

23.   Qiao, X.; Li, Q.; Schaugaard, R. N.; Noffke, B. W.; Liu, Y.; Li, D.; Liu, L.; Raghavachari, K.; Li, L.-s. "Well-Defined Nanographene–Rhenium Complex as an Efficient Electrocatalyst and Photocatalyst for Selective CO2 Reduction," *Journal of the American Chemical Society* **2017**, *139*, 3934-3937. http://dx.doi.org/10.1021/jacs.6b12530

24.   Thoi, V. S.; Kornienko, N.; Margarit, C. G.; Yang, P.; Chang, C. J. "Visible-Light Photoredox Catalysis: Selective Reduction of Carbon Dioxide to Carbon Monoxide by a Nickel N-Heterocyclic Carbene–Isoquinoline Complex," *Journal of the American Chemical Society* **2013**, *135*, 14413-14424. http://dx.doi.org/10.1021/ja4074003

25.   Ouyang, T.; Huang, H.-H.; Wang, J.-W.; Zhong, D.-C.; Lu, T.-B. "A Dinuclear Cobalt Cryptate as a Homogeneous Photocatalyst for Highly Selective and Efficient Visible-Light Driven CO2 Reduction to CO in CH3CN/H2O Solution," *Angewandte Chemie International Edition* **2017**, *56*, 738-743. http://dx.doi.org/10.1002/anie.201610607

26.   Guo, Z.; Chen, G.; Cometto, C.; Ma, B.; Zhao, H.; Groizard, T.; Chen, L.; Fan, H.; Man, W.-L.; Yiu, S.-M.; Lau, K.-C.; Lau, T.-C.; Robert, M. "Selectivity control of CO versus HCOO−

production in the visible-light-driven catalytic reduction of CO2 with two cooperative metal sites," *Nature Catalysis* **2019**, *2*, 801-808. http://dx.doi.org/10.1038/s41929-019-0331-6

27.   Cao, L.-M.; Huang, H.-H.; Wang, J.-W.; Zhong, D.-C.; Lu, T.-B. "The synergistic catalysis effect within a dinuclear nickel complex for efficient and selective electrocatalytic reduction of CO2 to CO," *Green Chemistry* **2018**, *20*, 798-803. http://dx.doi.org/10.1039/C7GC03451B

28.   Ouyang, T.; Wang, H.-J.; Huang, H.-H.; Wang, J.-W.; Guo, S.; Liu, W.-J.; Zhong, D.-C.; Lu, T.-B. "Dinuclear Metal Synergistic Catalysis Boosts Photochemical CO2-to-CO Conversion," *Angewandte Chemie International Edition* **2018**, *57*, 16480-16485. http://dx.doi.org/10.1002/anie.201811010

29.   Lacy, D. C.; McCrory, C. C. L.; Peters, J. C. "Studies of Cobalt-Mediated Electrocatalytic CO2 Reduction Using a Redox-Active Ligand," *Inorganic Chemistry* **2014**, *53*, 4980-4988. http://dx.doi.org/10.1021/ic403122j

30.   McCrory, C. C. L.; Szymczak, N. K.; Peters, J. C. "Evaluating Activity for Hydrogen-Evolving Cobalt and Nickel Complexes at Elevated Pressures of Hydrogen and Carbon Monoxide," *Electrocatalysis* **2016**, *7*, 87-96. http://dx.doi.org/10.1007/s12678-015-0281-y

31.   Azcarate, I.; Costentin, C.; Robert, M.; Savéant, J.-M. "Dissection of Electronic Substituent Effects in Multielectron–Multistep Molecular Catalysis. Electrochemical CO2-to-CO Conversion Catalyzed by Iron Porphyrins," *The Journal of Physical Chemistry C* **2016**, *120*, 28951-28960. http://dx.doi.org/10.1021/acs.jpcc.6b09947

32.   Azcarate, I.; Costentin, C.; Robert, M.; Savéant, J.-M. "Through-Space Charge Interaction Substituent Effects in Molecular Catalysis Leading to the Design of the Most Efficient Catalyst of CO2-to-CO Electrochemical Conversion," *Journal of the American Chemical Society* **2016**, *138*, 16639-16644. http://dx.doi.org/10.1021/jacs.6b07014

33.   Matsubara, Y. "Standard Electrode Potentials for the Reduction of CO_2 to CO in Acetonitrile–Water Mixtures Determined Using a Generalized Method for Proton-Coupled Electron-Transfer Reactions," *ACS Energy Letters* **2017**, *2*, 1886-1891. http://dx.doi.org/10.1021/acsenergylett.7b00548

34.   Matsubara, Y. "Unified Benchmarking of Electrocatalysts in Noninnocent Second Coordination Spheres for CO_2 Reduction," *ACS Energy Letters* **2019**, *4*, 1999-2004. http://dx.doi.org/10.1021/acsenergylett.9b01180

35.   Kaeffer, N.; Morozan, A.; Fize, J.; Martinez, E.; Guetaz, L.; Artero, V. "The Dark Side of Molecular Catalysis: Diimine–Dioxime Cobalt Complexes Are Not the Actual Hydrogen Evolution Electrocatalyst in Acidic Aqueous Solutions," *ACS Catalysis* **2016**, *6*, 3727-3737. http://dx.doi.org/10.1021/acscatal.6b00378

36.   Zhang, M.; El-Roz, M.; Frei, H.; Mendoza-Cortes, J. L.; Head-Gordon, M.; Lacy, D. C.; Peters, J. C. "Visible Light Sensitized CO_2 Activation by the Tetraaza $[CoIIN4H(MeCN)]2+$ Complex Investigated by FT-IR Spectroscopy and DFT Calculations," *The Journal of Physical Chemistry C* **2015**, *119*, 4645-4654. http://dx.doi.org/10.1021/jp5127738

37.   Costentin, C.; Robert, M.; Saveant, J.-M. "Catalysis of the electrochemical reduction of carbon dioxide," *Chemical Society Reviews* **2013**, *42*, 2423-2436. http://dx.doi.org/10.1039/c2cs35360a

38.   Costentin, C.; Drouet, S.; Robert, M.; Savéant, J.-M. "Turnover Numbers, Turnover Frequencies, and Overpotential in Molecular Catalysis of Electrochemical Reactions. Cyclic Voltammetry and Preparative-Scale Electrolysis," *Journal of the American Chemical Society* **2012**, *134*, 11235-11242. http://dx.doi.org/10.1021/ja303560c

39.   Rountree, E. S.; McCarthy, B. D.; Eisenhart, T. T.; Dempsey, J. L. "Evaluation of Homogeneous Electrocatalysts by Cyclic Voltammetry," *Inorganic Chemistry* **2014**, *53*, 9983-10002. http://dx.doi.org/10.1021/ic500658x

Chapter 6 Conclusions and Future Research

6.1 Conclusions

The work in this thesis mainly focuses on designing and studying novel and efficient molecular catalyst systems showing high activity at low effective overpotentials for the electrocatalytic CO_2 reduction, which break the typical "*molecular scaling relationship*" observed in most traditional molecular catalyst designs.

Chapter 1 presents the background information and fundamental concepts necessary to understand the electrochemical CO_2 reduction (CO_2RR) by molecular catalysts. Molecular catalysts, in particular transition metal complexes, show promise for selectively reducing CO_2 to single products compared to the solid-state catalysts. However beneficial decreases in overpotentials for molecular catalysts are usually correlated with detrimental decreases in catalytic activity, which is referred to as the "*molecular scaling relationship*." An overview of "*molecular scaling relationship*" and reported strategies for breaking it are also discussed. Almost all reported strategies have a similar approach of stabilizing CO_2-adduct intermediates to lower the activation energy of converting reduced CO_2 intermediates to the final product, resulting in increased overall activity for the CO_2RR and a deviation from the typical scaling relationship. In contrast, there are almost no examples of breaking the "*molecular scaling relationship*" through modulating the redox potential of molecular catalysts. This is because for most molecular catalysts, the catalytic reaction is initiated by the redox activation of the metal center in the complex, the site at which the substrate is coordinated and electrons are transferred. Shifting the redox potential of the metal

263

center positive leads to the lower nucleophilicity of the metal site and weaker bonding affinity to the substrate, which results in decreased overall activity.

All these scaling correlations between the catalytic activity and the effective overpotential of a molecular catalyst are based on a prerequisite that the catalytic onset for the CO_2RR is preceded by a metal-based redox process. In this thesis, the strategies proposed and applied for making efficient molecular catalysts for the CO_2RR aim at breaking this prerequisite by designing molecular catalysts with redox active ligands, in which the catalytic onset is preceded by the formation of ligand radical structure—a ligand-based redox process rather than a metal-based redox event. In this scenario, the affinity of CO_2 bonding correlates to neither $E_{cat/2}$ nor nucleophilicity of the metal center, instead the initial catalytic onset can be modulated by the redox potential of ligand/ligand-radical couple. In addition, modulating redox-active ligand structures to increase their ability to store charge equivalents can not only result in a more positive ligand-based redox potential to initiate the catalytic onset, but also have a beneficial influence on catalytic activity of molecular catalysts. This provides an effective approach to break the "*molecular scaling relationship*" through both thermodynamic and kinetic modifications.

In the initial work of Chapter 2, a Co complex with a redox-active bis(pyridylmonoimine) ligand [Co(L-L)] is designed and prepared, which shows activity for the CO_2 reduction to CO in acetonitrile with the catalytic onset preceded by the formation of $[Co^I(L\text{-}L^{\bullet-})]$ as the active species at the ligand-based redox couple. Addition of a proton source such as water or trifluoroethanol dramatically improves the activity and stability of [Co(L-L)] for the CO_2RR. However, further electrochemical kinetic studies of [Co(L-L)] in Chapter 3 show that it undergoes a reductive dimerization at the ligand-based redox couple before the formation of the active species $[Co^I(L\text{-}L^{\bullet-})]$, which thus delays the catalytic onset for the CO_2RR. To prevent catalyst dimerization and

facilitate the catalytic onset, a series of [Co(L-R-L)] complexes with distorted square planarity geometry were prepared by modulating the flexibility of L-R-L ligand scaffolds but without changing the redox-active property of pyridylmonoimine moieties. Compared to the rigid and planar [Co(L-L)], these more flexible, less planar [Co(L-R-L)] complexes operate with more positive catalytic onset potentials for the CO_2 reduction due to the successful prevention of reductive catalyst dimerization, and even show slightly increased initial activity for the CO_2RR in the absence of added proton source H_2O, which is opposed to the typical "*molecular scaling relationship*". However, in the presence of a proton source, these [Co(L-R-L)] complexes display unexpected lower overall activity, despite greatly more positive onset potentials, for the CO_2RR compared to the [Co(L-L)]. The following CO-binding and inhibition studies in Chapter 3 reveal that the diminished overall activity of the [Co(L-R-L)] complexes for the CO_2 reduction in the presence of a proton source is due to CO poisoning because of the stronger bonding affinity of the CO product to the more nucleophilic Co^+ center in the less planar coordination geometry. Although the inverse "*molecular scaling relationship*" of the [Co(L-R-L)] complexes for the CO_2RR in the absence of a proton source is not maintained due to the CO poisoning when H_2O is added, the work in Chapter 2 and 3 supports the validity of our strategy applied in this thesis—breaking the "*molecular scaling relationship*" by modulating the molecular catalyst systems where the catalytic onset is preceded by a ligand-based redox event.

Consistent with the design strategy applied in the previous chapters of this thesis, a series of cobalt pyridyldiimine complexes ([Co(PDI-R)]) was prepared and studied in Chapter 4, where the activity for the CO_2RR is initiated by the formation of [Co(PDI-R$^{\bullet-}$)] via a ligand-based redox event. Instead of changing the structural geometry of the complex to tune the catalytic pathway, the redox features and catalytic ability of [Co(PDI-R)] complexes are modulated by sequentially

integrating extended π-conjugation effects, electron withdrawing effects, and intramolecular electrostatic effects into a single PDI ligand scaffold with phenyl, pyridyl, and *N*-methylpyridinium groups respectively, to form [Co(PDI-Ph)], [Co(PDI-Py)] and [Co(PDI-PyCH$_3$$^+I^-$)]. These substituent effects improve the ability of the ligand PDI-R to store charge equivalents and stabilize CO$_2$-adducte intermediate. When each substituent effect is sequentially introduced into the system, there is a corresponding positive shift in the catalytic onset potential and an increase in the catalyst's intrinsic activity parameter (TOF$_0$) for CO$_2$ reduction to CO in acetonitrile (MeCN) with 11 M H$_2$O as the proton source, which breaks the typical "*molecular scaling relationship*". Moreover, the [Co(PDI-PyCH$_3$$^+I^-$)] complex with all three substituent effects simultaneously incorporated in the structure operates with a 0.18 V more positive onset potential and nearly 4 orders of magnitude higher TOF$_0$ for the CO$_2$RR compared to the parent [Co(PDI)] and > 95% FE for CO, outstanding among the most active molecular catalysts reported for the CO$_2$ reduction reaction so far. Combined with Chapter 2 and 3, the work in Chapter 4 again supports the validity of our strategy of breaking the "*molecular scaling relationship*" by modulating the catalytic systems where a ligand redox event directly precedes catalytic onset, and also suggests that this catalyst design strategy may result in similar inverse molecular scaling relationships and high catalytic activity for other molecular catalyst systems.

In Chapter 5, the successful design strategy for mononuclear metal complex systems was applied to binuclear metal pyridyldiimine complexes bi-[M(PDI)], where two metal pyridyldiimine ([M(PDI)]) moieties are connected by an electron-conjugated ligand scaffold. Compared to the mononuclear [Co(PDI)] studied in Chapter 4, bi-[Co(PDI)] shows dramatically higher activity and excellent selectivity (~94% Faradaic efficiency) for the reduction of CO$_2$ to CO, operating with over 4 orders of magnitude higher intrinsic activity (log(TOF$_0$/s^{-1}) = −1.3), ~2

orders of magnitude higher maximum kinetic activity ($\log(\text{TOF}_{\text{cat}}/\text{s}^{-1}) = 5.0$) and 0.15 V more positive catalytic onset ($E_{\text{onset}} = -1.55$ V vs $\text{Fc}^{+/0}$), in acetonitrile with 11 M water. Different from the reported bio-inspired binuclear catalysts where the improved catalytic ability arises from the synergistic coordination of a substrate between two metal sites in the structure, the kinetic studies in Chapter 5 show that two Co(PDI) moieties in bi-[Co(PDI)] bind CO_2 independently and concurrently as active catalytic sites. Therefore, the improved catalytic ability of this binuclear system is proposed to correlate with the second role of each Co(PDI) moiety as an electronic modulator to adjust redox features and catalytic ability of each other.

To elucidate these two electronic effects of Co(PDI) moieties on the improved catalytic ability of bi-[Co(PDI)], a heterobimetallic compound bi-[ZnCo(PDI)] with one Co center replaced by a redox-inert Zn center and an extended binuclear Co complex bi-ex-[Co(PDI)] with longer distance between two Co sites were prepared and studied for the CO_2RR as controls in Chapter 5 as well. Compared to the mononuclear [Co(PDI)], bi-[ZnCo(PDI)] shows no peak splitting features at Co-based redox couples but positive shift of each redox couple observed for bi-[Co(PDI)]. These redox features of the bi-[ZnCo(PDI)] suggest that the electronic coupling between metal sites is cut off due to the redox-inert Zn^{2+} center but the intramolecular electrostatic effect exerted by Zn^{2+} on the Co(PDI) moiety remains in this heterobimetallic structure. For the CO_2RR, the bi-[ZnCo(PDI)] shows boosted activity even higher than that of the bi-[Co(PDI)] under the same catalytic condition. This result suggests that the intramolecular electrostatic effect rather than the electronic coupling is the main factor leading to the improved catalytic ability of the binuclear bi-[Co(PDI)] and bi-[ZnCo(PDI)]. This is further supported by another control study of the bi-ex-[Co(PDI)] with negligible electronic coupling but weaker electrostatic effect between further separated Co sites in the extended structure. Despite showing higher activity than the mononuclear

267

[Co(PDI)] due to the electrostatic effect in the binuclear structure, the bi-ex-[Co(PDI)] shows much lower activity for the CO_2RR compared to the bi-[Co(PDI)] and bi-[ZnCo(PDI)], due to the weaker electrostatic effect due to the longer Co-Co distance in the bi-ex-[Co(PDI)]. Although more detailed mechanistic study in the future work is quite necessary for better understanding the boosted activity of such binuclear metal pyridyldiimine complexes for the CO_2RR, the work conducted in Chapter 5 highlights one more valid application of our catalyst design strategy even in multinuclear systems for successfully breaking "*molecular scaling relationship*" by modulating catalytic systems where a ligand redox event initiates the catalytic onset.

The work in this thesis mainly focuses on two series of Co molecular catalysts with redox-active ligands, cobalt bis(pyridylmonoimine) complexes ([Co(L-R-L)]) and cobalt pyridyldiimine complexes ([Co(PDI-R)] and bi-[Co(PDI)]), both of which show inverse "*molecular scaling relationship*" for the CO_2RR under certain catalytic conditions. Especially for cobalt pyridyldiimine complexes, the optimized mononuclear [Co(PDI-PyCH$_3^+$I$^-$)] complex and binuclear bi-[Co(PDI)] and bi-[ZnCo(PDI)] complexes show several orders of magnitude higher activity and 0.15 ~ 0.18 V lower overpotential for the CO_2RR compared to the parent [Co(PDI)] complex, which are outstanding among the most efficient molecular catalysts reported so far. The strategy applied in these molecular catalyst designs is to create molecular catalytic systems where the catalytic onset is preceded by a ligand-based redox process rather than a metal-based redox event. In doing so, both the effective overpotential and catalytic activity of the complex can be decoupled from the nucleophilicity of the metal center and metal based redox potentials, which is in fact the key of breaking the typical molecular scaling relationship in this thesis. It is believed that the work in this thesis provides a new and inspiring insight in the design of more efficient molecular catalyst systems with higher activity but at lower effective overpotentials for the

CO$_2$RR, which might be also applicable for other small molecular activation reactions interested by the electrocatalytic community.

6.2 Future Research

Based on the work and results discussed in this thesis, there are several interesting directions and topics that are worth investigating in the future research. For Co bis(pyridylmonoimine) complexes [Co(L-R-L)] with more flexible ligand scaffolds, CO poisoning is the main problem for them to reach high overall activity for the CO_2RR in the presence of a proton source despite they display more positive catalytic onset compared to the rigid [Co(L-L)] analog. Questions about how to dissociate the CO from the [Co(L-R-L)CO] adduct to reactivate these catalysts and how to decrease the CO bonding affinity of [Co(L-R-L)] complexes to maintain their activity for the CO_2RR are very urgent to answer and investigate in the future research work. Integrating electron withdrawing substituent groups into bis(pyridylmonoimine) L-R-L ligands is a promising strategy to decrease the electron density at Co site and thus weaken the Co-CO bond to dissociate CO to reactivate the catalyst for the CO_2RR (Scheme 6.1a), despite such a ligand modification might lead to lower activity of the complex due to the decreased electron density at the Co site.

For cobalt pyridyldiimine complexes ([Co(PDI-R)]), simultaneously incorporating extended conjugation, electron-withdrawing ability, and intramolecular electrostatic effects into a single [Co(PDI-R)] structure results in the [Co(PDI-PyCH$_3^+$I$^-$)] displaying dramatically enhanced activity at lower effective overpotential for CO_2 reduction. Among these three substituent effects, the intramolecular electrostatic effect of the positive charge in the ligand structure is the most influential on the improved catalytic ability of the catalyst for the CO_2RR. Based on these results and understanding from Chapter 4, further modulating the distance between the positive charge in the ligand structure and the Co site or the position of the positive charge in the ligand is worth

investigating in order to obtain a more optimized [Co(PDI-R)] catalyst for the CO_2RR (Scheme 6.1b).

For binuclear metal pyridyldiimine complexes bi-[M(PDI)], the work in Chapter 5 has already shown that binuclear bi-[Co(PDI)], bi-ex-[Co(PDI)] and bi-[ZnCo(PDI)] complexes display dramatically higher activity and much lower effective overpotentials for the CO_2RR compared to the mononuclear [Co(PDI)] complex, which is mainly due to the intramolecular electrostatic effect in these binuclear systems. In addition, bi-[ZnCo(PDI)] shows even higher activity than bi-[Co(PDI)], which is likely explained by the more influential electrostatic effect exerted by the di-cationic Zn^{2+} than the mono-cationic Co^+ in the active species of these binuclear catalysts for the CO_2RR. In the future work, people can take one more step forward to incorporate M^{3+} metal cation into the bi-[MCo(PDI)] structure (Scheme 6.1c), which is expected to result in a more efficient binuclear molecular catalyst for the CO_2RR than both bi-[Co(PDI)] and bi-[ZnCo(PDI)] complexes. Moreover, more detailed mechanistic study of these binuclear bi-[M(PDI)] catalysts combined with spectroscopical investigations such as in situ XANES and in situ EPR is quite necessary and very significant in the future work for better understanding the electronic features of the active intermediates and elucidating the catalytic pathway for the CO_2RR by these binuclear complexes.
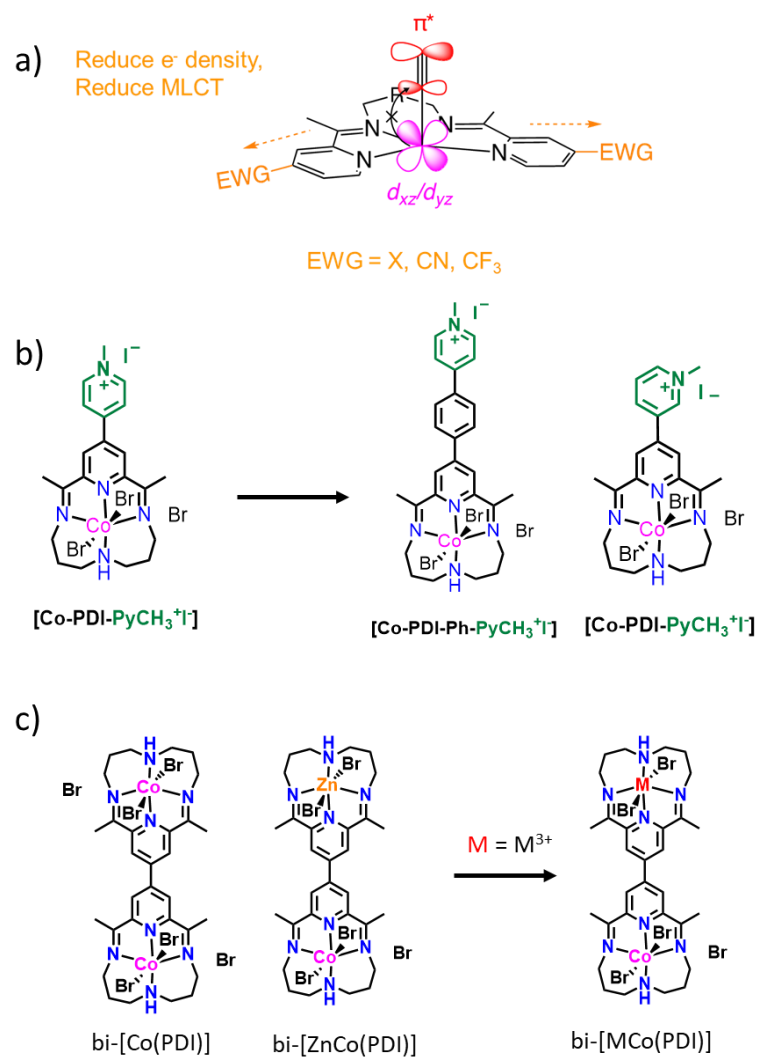
Scheme 6.1 a) Integrating electron withdrawing substituent groups into bis(pyridylmonoimine) L-R-L ligands weakens the Co-CO bond to dissociate CO to reactivate the catalyst; b) Modulating the distance between the positive charge in the ligand structure and the Co site or the position of the positive charge in the ligand optimizes the [Co(PDI-R)] catalyst; c) Incorporating M^{3+} metal cation into the bi-[MCo(PDI)] structure results in a more efficient binuclear molecular catalyst for the CO_2RR.

272

Appendices A: Supporting Information

A.1 Supporting Information for Chapter 2

A.1.1 Supporting Figures
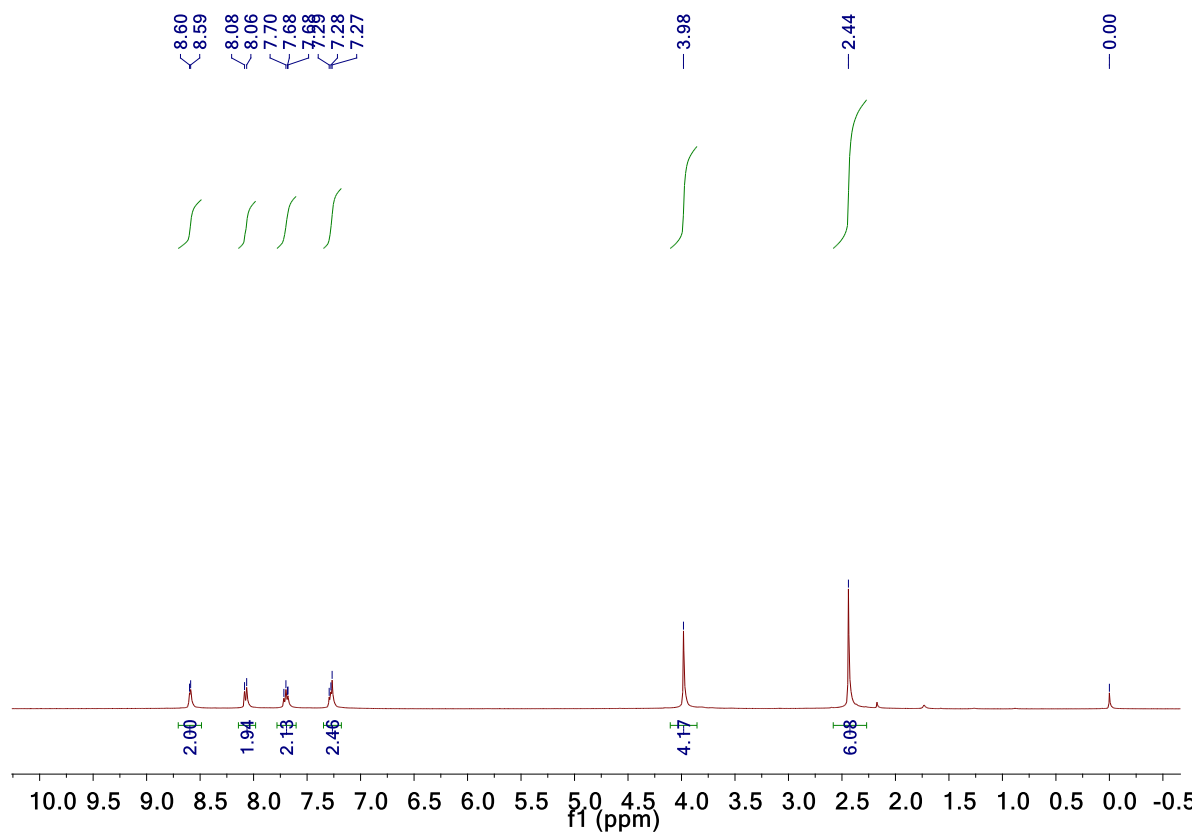
Figure A.1 ^{1}H-NMR Spectrum of Ligand **L-L** in CD$_3$Cl-d_3 (δ 7.69 solvent residual peak).
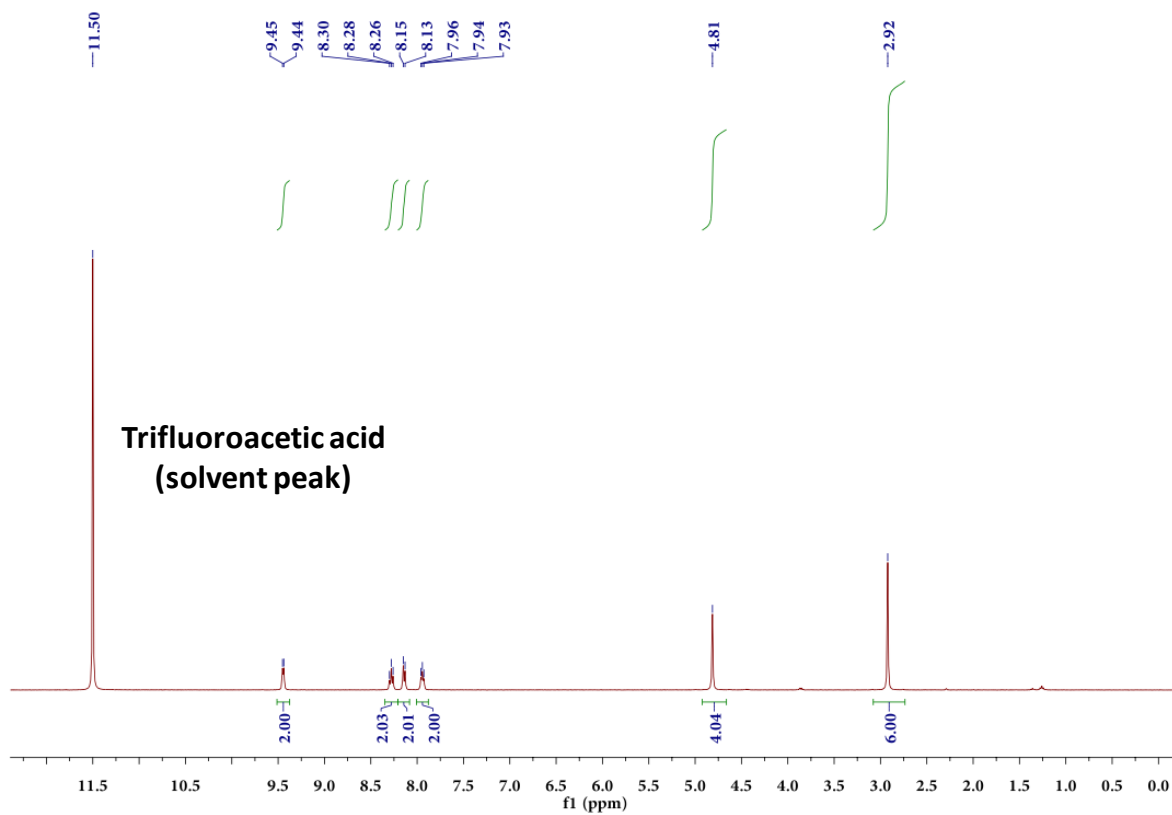
Figure A.2 ^{1}H-NMR Spectrum of **[Co(L-L)Br₂]Br** in Trifluoroacetic acid-d_1 (δ=11.5 solvent residual peak)
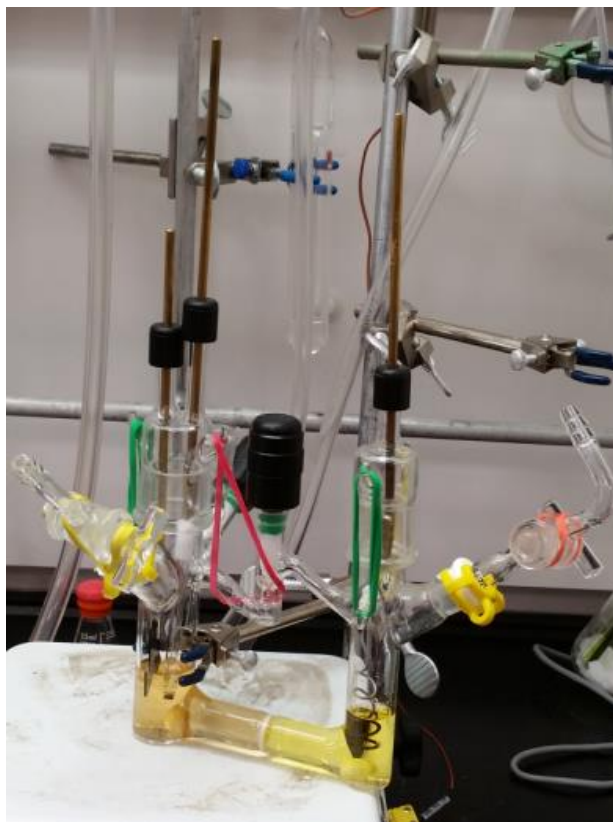
Figure A.3 The Controlled-Potential Electrolysis cell setup in Chapter 2. The left chamber held the working and reference electrodes and was filled with 20 mL of 0.3 mM catalyst solution in MeCN with 0.1 M nBu$_4$NPF$_6$. The right chamber held the counter electrode in 15 mL of a 5 mM ferrocene solution in MeCN. These two chambers were separated by a fine-porosity glass frit. The working electrode was a 3.2 cm × 1.6 cm × 0.1 cm glassy carbon plate (HTW Hochtemperatur-Werkstoff GmbH) which was half immersed in the solution. The reference electrode was a Ag/AgNO$_3$ (1.0 mM)/MeCN nonaqueous reference electrode (also containing 0.1 M nBu$_4$NPF$_6$) separated from the solution by a Vycor frit (Bioanalytical Systems, Inc.). The counter electrode was nichrome wire (ARCOR).

Figure A.4 IR Spectra of **[Co(L-L)Br₂]** and **[Co(L-L)Br₂]Br.**
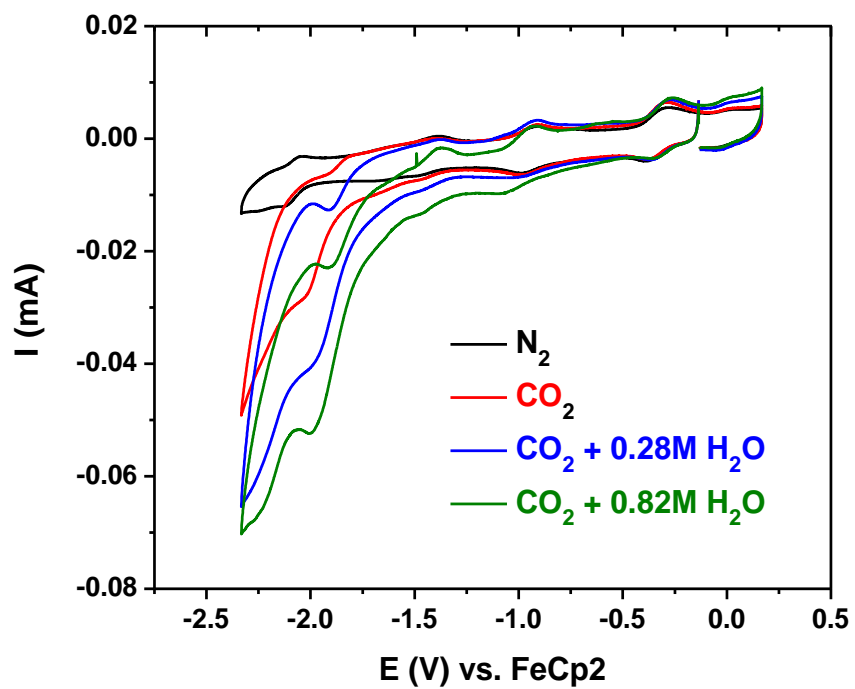
Figure A.5 CVs of 0.3 mM **[Co(L-L)Br₂]** in acetonitrile with 0.1 M nBu₄NPF₆ under N_2, CO_2, CO_2 with 0.28 M H_2O and CO_2 with 0.82 M H_2O.
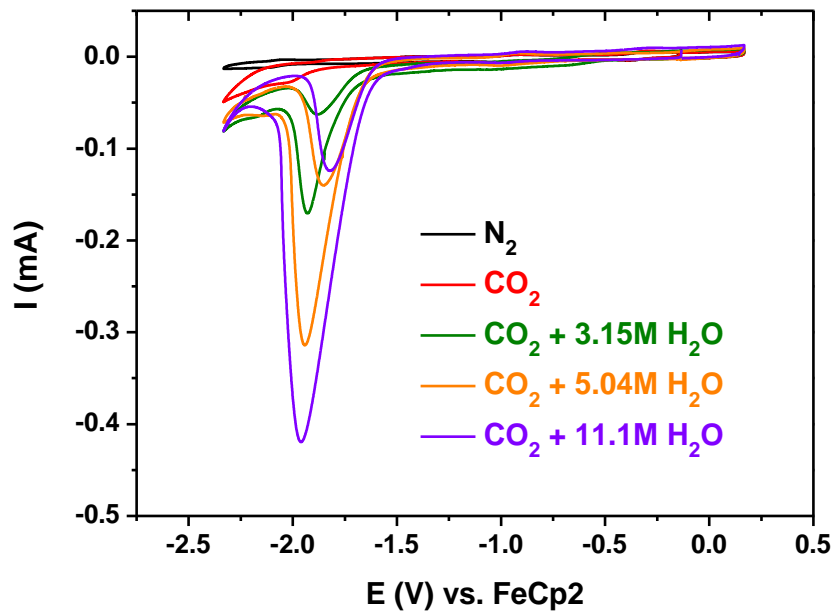
Figure A.6 CVs of 0.3 mM **[Co(L-L)Br₂]** in acetonitrile with 0.1 M *n*Bu₄NPF₆ under N₂, CO₂, CO₂ with 3.15 M H₂O, CO₂ with 5.04 M H₂O and CO₂ with 11.1 M H₂O.
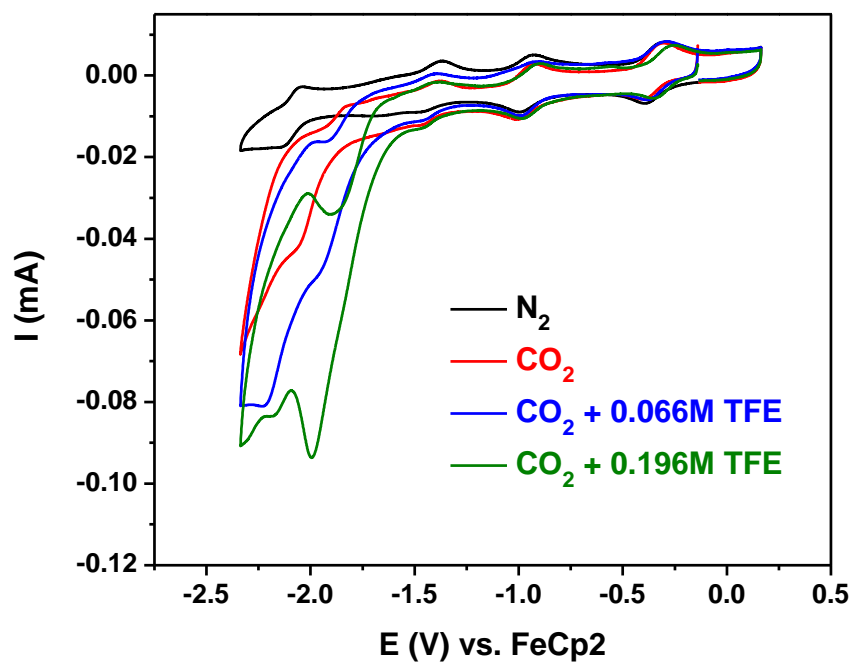
Figure A.7 CVs of 0.3 mM **[Co(L-L)Br₂]** in acetonitrile with 0.1 M nBu₄NPF₆ under N₂, CO₂, CO₂ with 0.066 M THF and CO₂ with 0.196 M THF.
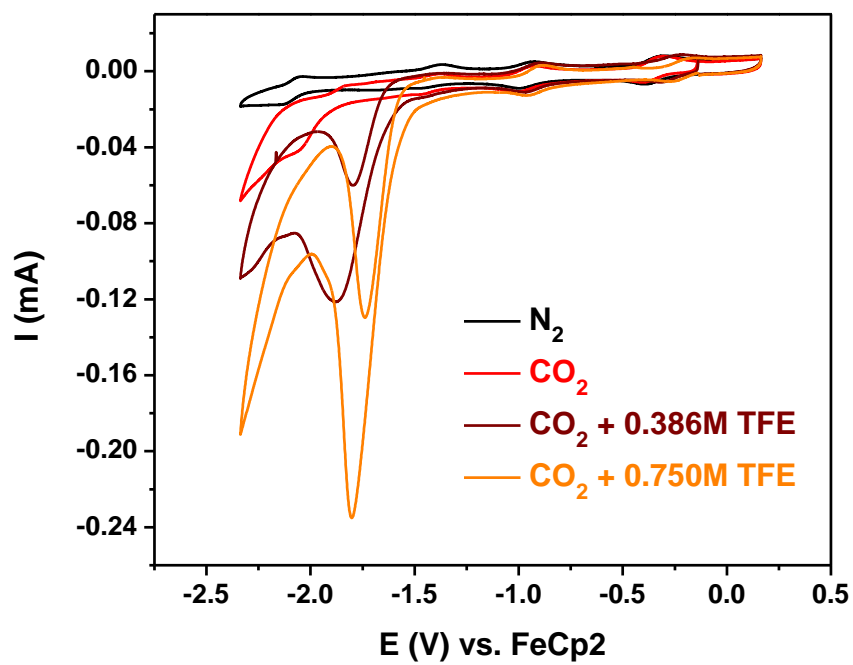
Figure A.8 CVs of 0.3 mM **[Co(L-L)Br₂]** in acetonitrile with 0.1 M *n*Bu₄NPF₆ under N₂, CO₂, CO₂ with 0.386 M THF and CO₂ with 0.750 M THF.
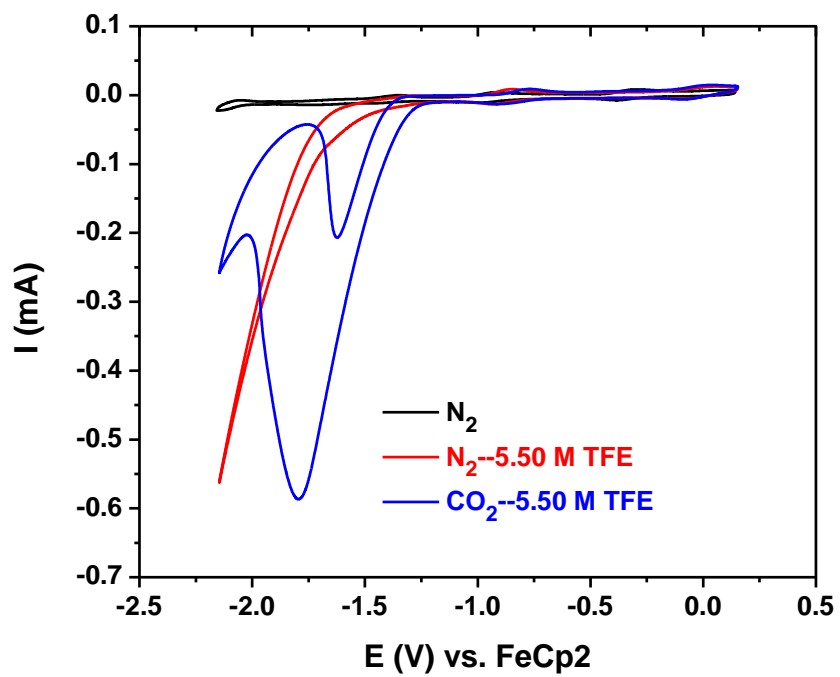
Figure A.9 CVs of 0.3 mM **[Co(L-L)Br$_2$]** in acetonitrile with 0.1 M nBu$_4$NPF$_6$ under N$_2$, N$_2$ with 5.50 M THF and CO$_2$ with 5.50 M TFE.
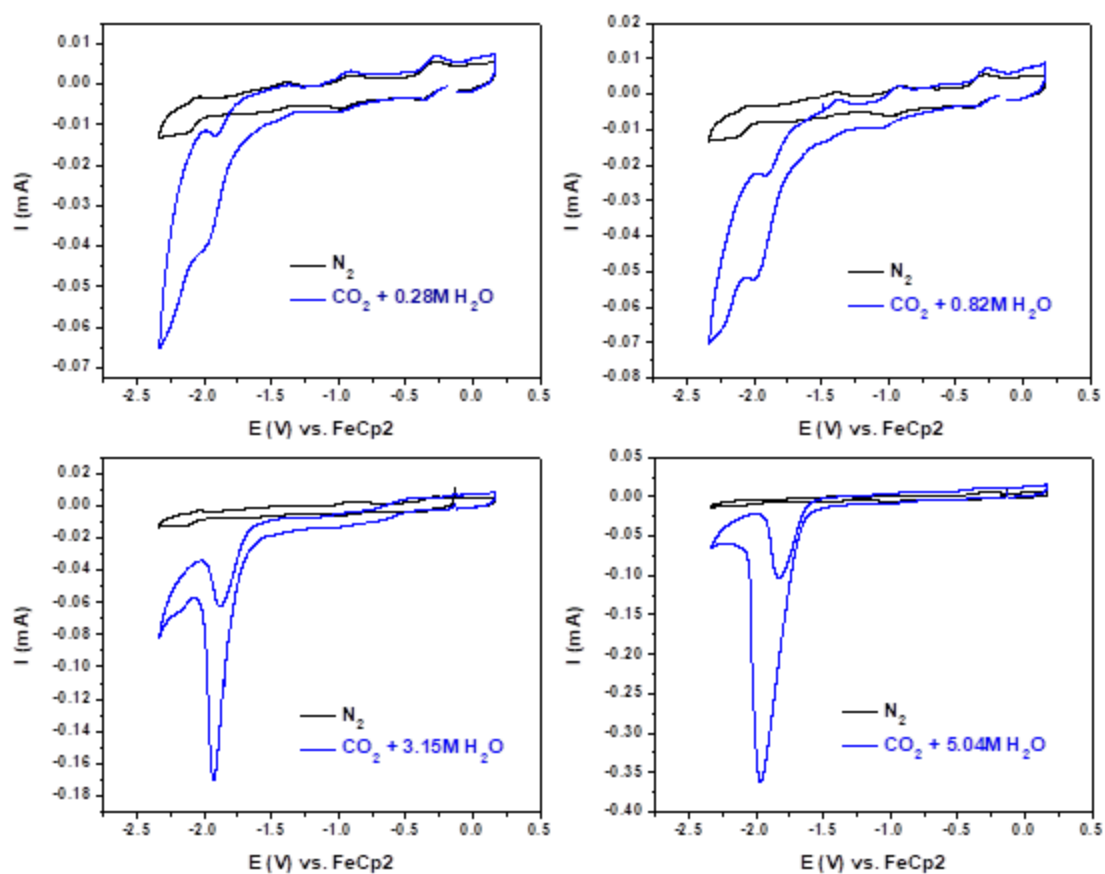
Figure A.10 CVs of 0.3 mM **[Co(L-L)Br₂]** in acetonitrile with 0.1 M *n*Bu₄NPF₆ under N₂ and CO₂ with different H₂O concentrations to show that the inverted peak shape is attributed to the overlap of the catalytic current response for CO₂ reduction with the more negative, reversible $Co^{1+/0}$ redox feature.
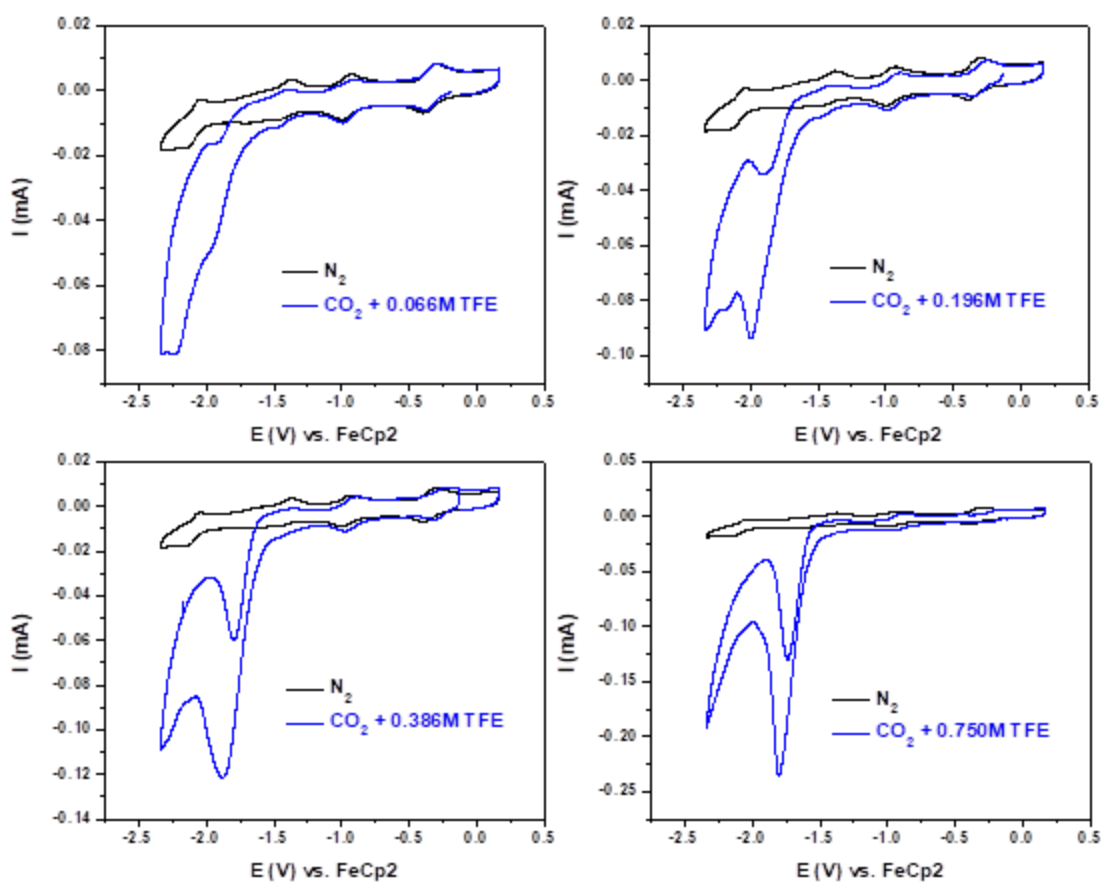
Figure A.11 CVs of 0.3 mM **[Co(L-L)Br₂]** in acetonitrile with 0.1 M *n*Bu₄NPF₆ under N_2 and CO_2 with different THF concentrations to show that the inverted peak shape is attributed to the overlap of the catalytic current response for CO_2 reduction with the more negative, reversible $Co^{1+/0}$ redox feature.

Spectrum 10	Wt%	σ
C	69.9	0.5
N	13.5	0.6
O	7.3	0.2
F	7.3	0.2
Co	1.4	0.1
P	0.5	0.0
Ni	0.1	0.0
Ag	0.0	0.0
Cr	0.0	0.0

Spectrum 11	Wt%	σ
C	69.3	0.5
N	13.0	0.6
O	8.3	0.2
F	7.0	0.2
Co	1.8	0.1
P	0.6	0.0
Cr	0.0	0.0
Ni	0.0	0.0
Ag	0.0	0.0

| Spectrum 12	Wt%	σ
C	71.0	0.5
N	12.2	0.6
O	7.6	0.2
F	7.1	0.2
Co	1.6	0.1
P	0.5	0.0
Cr	0.0	0.0
Ni	0.0	0.0
Ag	0.0	0.0
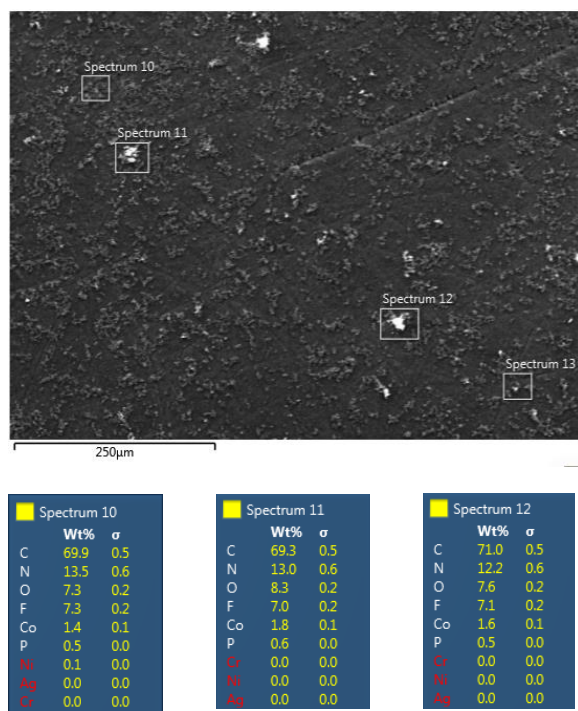
Figure A.12 SEM-EDS analysis of a representative working electrode surface after a 30-minute CO_2RR electrolysis using 0.3 mM [Co(L-L)Br$_2$] with 0.1 M nBu$_4$PF$_6$ in acetonitrile at -1.95 V vs. Fc$^{+/0}$

Spectrum 1	At%
C	90.0
F	6.3
O	2.5
N	0.9
P	0.3

Spectrum 2	At%
C	84.2
F	11.2
O	2.1
N	1.6
P	0.8

Spectrum 3	At%
C	79.6
F	14.8
N	2.5
O	2.1
P	1.0
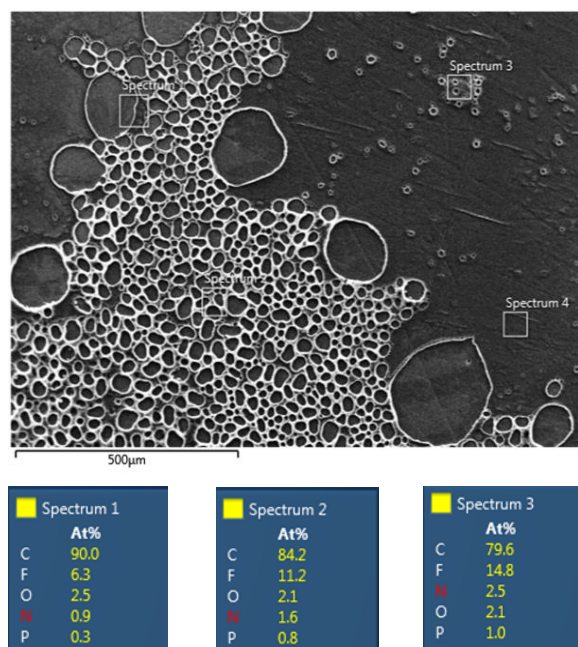
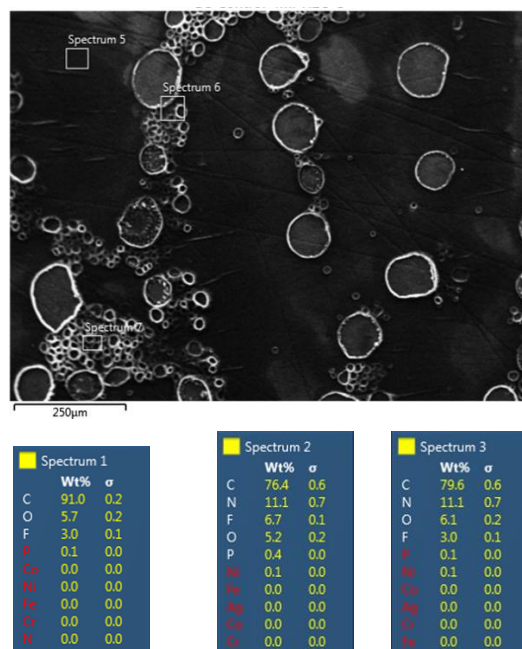**Figure A.13** SEM-EDS analysis of a representative working electrode surface after a 30-minute CO_2RR electrolysis using 0.3 mM Ligand L-L in acetonitrile with 11.00 M H$_2$O and 0.1 M nBu$_4$PF$_6$ in acetonitrile at -1.95 V vs. Fc$^{+/0}$
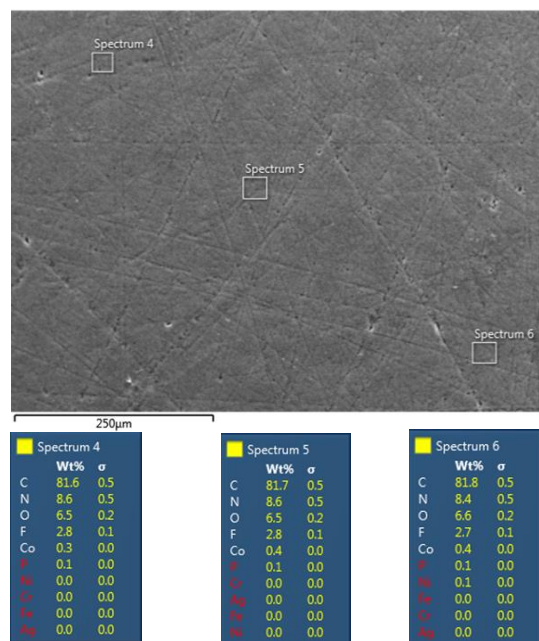
Figure A.14 SEM-EDS analysis of a representative working electrode surface after a 30-minute CO_2RR electrolysis using 0.3 mM [Co(L-L)Br$_2$] with 11.00 M H_2O and 0.1 M nBu$_4$PF$_6$ in acetonitrile at -1.95 V vs. Fc$^{+/0}$
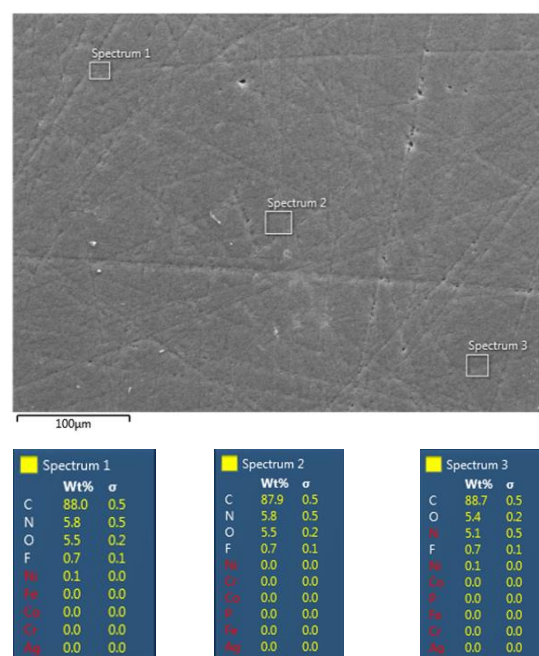
Figure A.15 SEM-EDS analysis of a representative working electrode surface after a 30-minute CO_2RR electrolysis using 0.3 mM [Co(L-L)Br$_2$] with 5.50 M TFE and 0.1 M nBu$_4$PF$_6$ in acetonitrile at -1.85 V vs. Fc$^{+/0}$

285
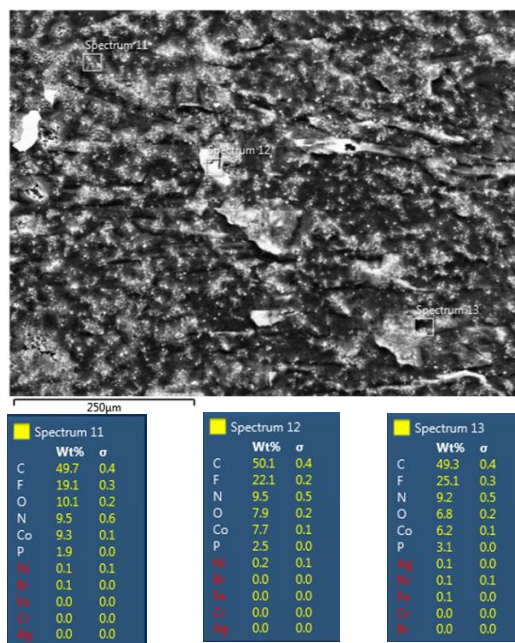
Figure A.16 SEM-EDS analysis of a representative working electrode surface after a 30-minute CO_2RR electrolysis using 0.3 mM $CoBr_2$ with 11.00 M H_2O and 0.1 M $n\text{Bu}_4\text{PF}_6$ in acetonitrile at -1.95 V vs. $Fc^{+/0}$
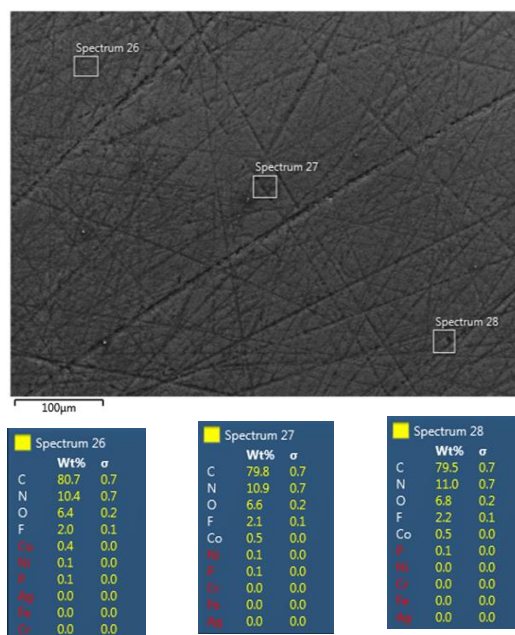
Figure A.17 SEM-EDS analysis of a representative working electrode surface after a 30-minute CO_2RR electrolysis using 0.3 mM $CoBr_2$ with 5.50 M TFE and 0.1 M $n\text{Bu}_4\text{PF}_6$ in acetonitrile at -1.85 V vs. $Fc^{+/0}$

Spectrum 1

	Wt%	σ
C	91.0	0.2
O	5.7	0.2
F	3.0	0.1
P	0.1	0.0
Cu	0.0	0.0
Ni	0.0	0.0
Fe	0.0	0.0
Cr	0.0	0.0
Ni	0.0	0.0

Spectrum 2

	Wt%	σ
C	76.4	0.6
N	11.1	0.7
F	6.7	0.1
O	5.2	0.2
P	0.4	0.0
Ni	0.1	0.0
Fe	0.0	0.0
Ag	0.0	0.0
Cu	0.0	0.0
Cr	0.0	0.0

Spectrum 3

	Wt%	σ
C	79.6	0.6
N	11.1	0.7
O	6.1	0.2
F	3.0	0.1
P	0.1	0.0
Ni	0.1	0.0
Cu	0.0	0.0
Ag	0.0	0.0
Cr	0.0	0.0
Fe	0.0	0.0

Figure A.18 SEM-EDS analysis of a representative working electrode surface after a 30-minute CO_2RR electrolysis using bare glassy carbon electrode with 11.00 M H_2O and 0.1 M nBu$_4$PF$_6$ in acetonitrile at -1.95 V vs. Fc$^{+/0}$

Spectrum 17

	Wt%	σ
C	82.4	0.7
N	9.6	0.7
O	6.8	0.2
F	1.1	0.1
Ni	0.0	0.0
Fe	0.0	0.0
Cr	0.0	0.0
P	0.0	0.0
Cu	0.0	0.0
Ag	0.0	0.0

Spectrum 18

	Wt%	σ
C	81.8	0.7
N	9.8	0.7
O	6.3	0.2
F	1.8	0.1
Ni	0.1	0.0
P	0.1	0.0
Ag	0.0	0.0
Cr	0.0	0.0
Cu	0.0	0.0
Fe	0.0	0.0

Spectrum 19

	Wt%	σ
C	82.0	0.7
N	9.7	0.7
O	6.7	0.2
F	1.6	0.1
P	0.1	0.0
Ag	0.0	0.0
Cr	0.0	0.0
Cu	0.0	0.0
Ni	0.0	0.0
Fe	0.0	0.0
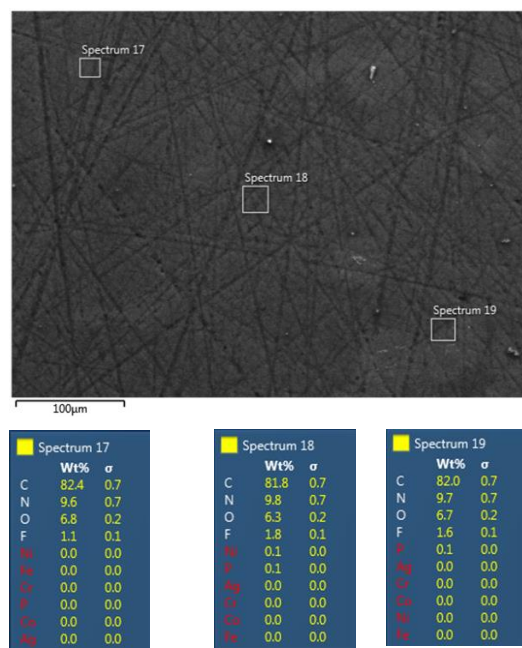
Figure.A.19 SEM-EDS analysis of a representative working electrode surface after a 30-minute CO_2RR electrolysis using bare glassy carbon electrode with 5.50 M TFE and 0.1 M nBu$_4$PF$_6$ in acetonitrile at -1.85 V vs. Fc$^{+/0}$
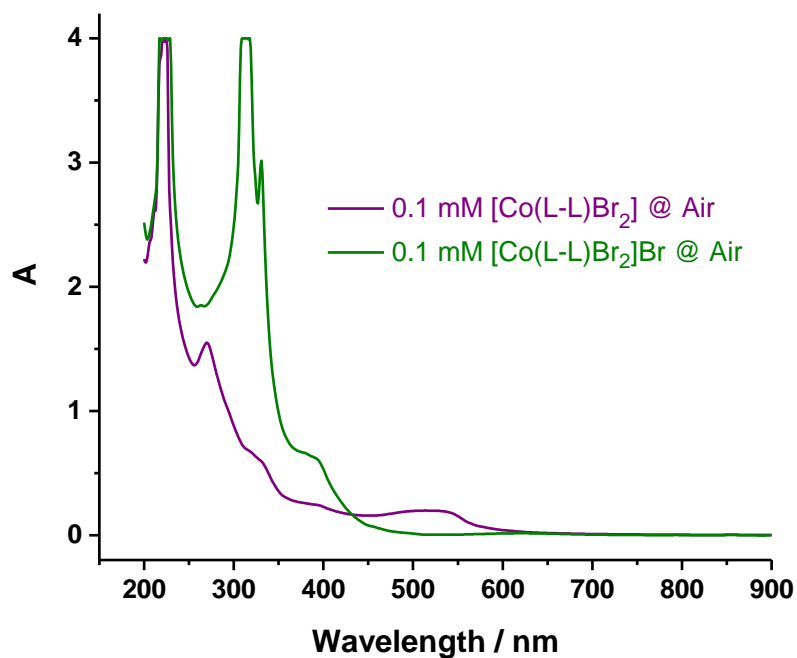
Figure A.20 UV-vis spectrum of 0.1 mM **[Co(L-L)Br₂]** and **[Co(L-L)Br₂]Br** in MeCN in air. Based on UV-vis spectra of Co complexes adopting similar structures reported in literatures[S3, S18, S19], the intense peaks at 221 nm and 270 nm (for **[Co(L-L)Br₂]**), 221 nm and 313 nm (for **[Co(L-L)Br₂]Br**) were assigned to ligand $\pi \rightarrow \pi^*$ transition. The peak at 528 nm in **[Co(L-L)Br₂]** spectrum was assigned to Co^{2+} *d-d* transition ($^4T_{1g}(F) \rightarrow {}^4T_{1g}(P)$), which is not observed in **[Co(L-L)Br₂]Br** spectrum.
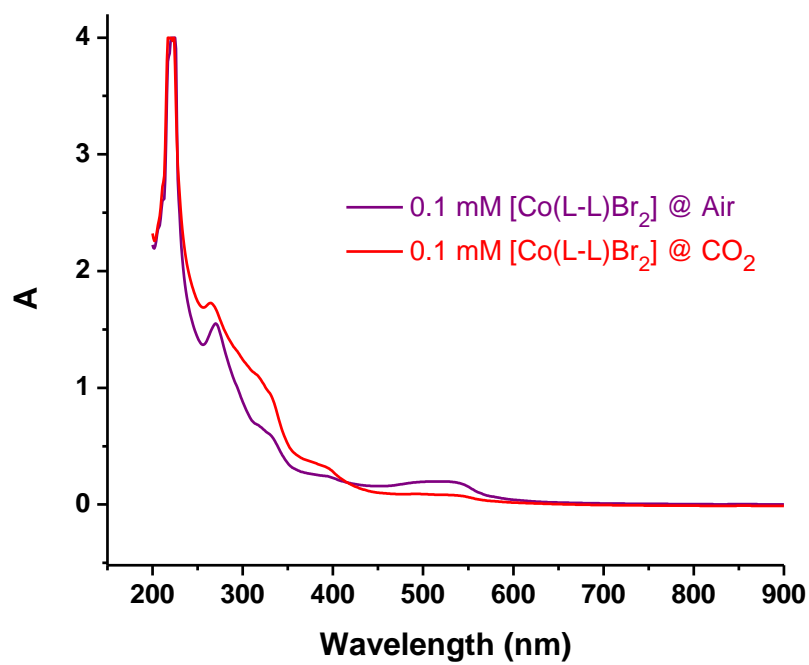
Figure A.21 UV-vis spectrum of 0.1 mM **[Co(L-L)Br$_2$]** in MeCN in air and under CO$_2$. CO$_2$ has little influence on UV-vis spectrum of 0.1mM **[Co(L-L)Br$_2$]** in MeCN.
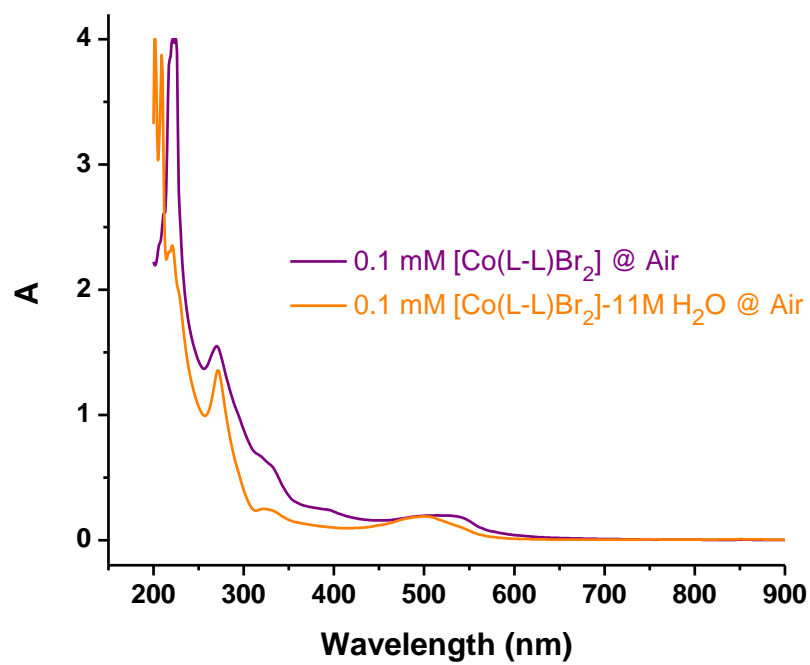
Figure A.22 UV-vis spectrum of 0.1 mM **[Co(L-L)Br$_2$]** in MeCN in air and with 11 M H$_2$O in air. Proton source H$_2$O has little influence on UV-vis spectrum of 0.1 mM **[Co(L-L)Br$_2$]** in MeCN.
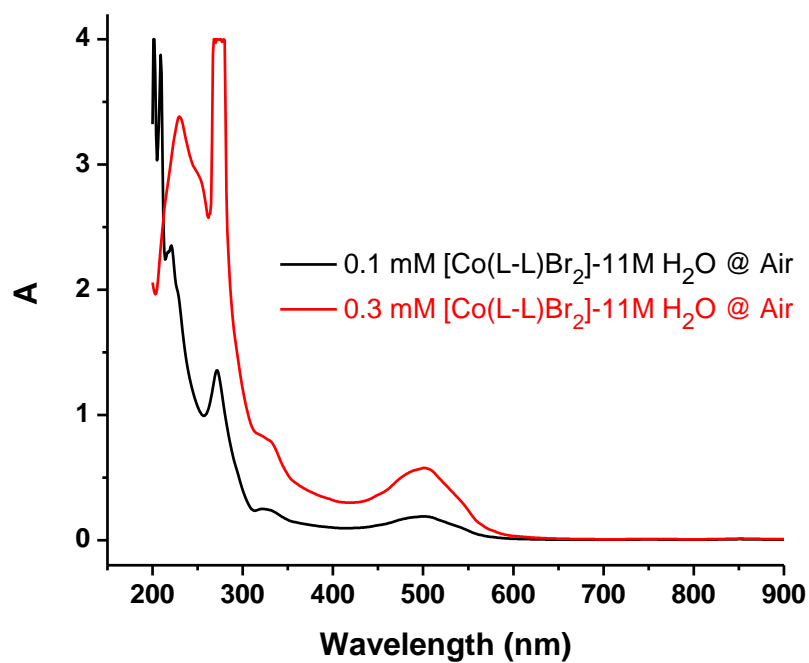
Figure A.23 UV-vis spectrum of 0.1 mM (black curve) and 0.3 mM (red curve) **[Co(L-L)Br₂]** in MeCN in air. The concentration of **[Co(L-L)Br₂]** affects absorption features of ligand $\pi \rightarrow \pi^*$ transition but has little influence on Co^{2+} *d-d* transition. The concentration 0.3 mM was used consistently in the following electrolysis experiments.
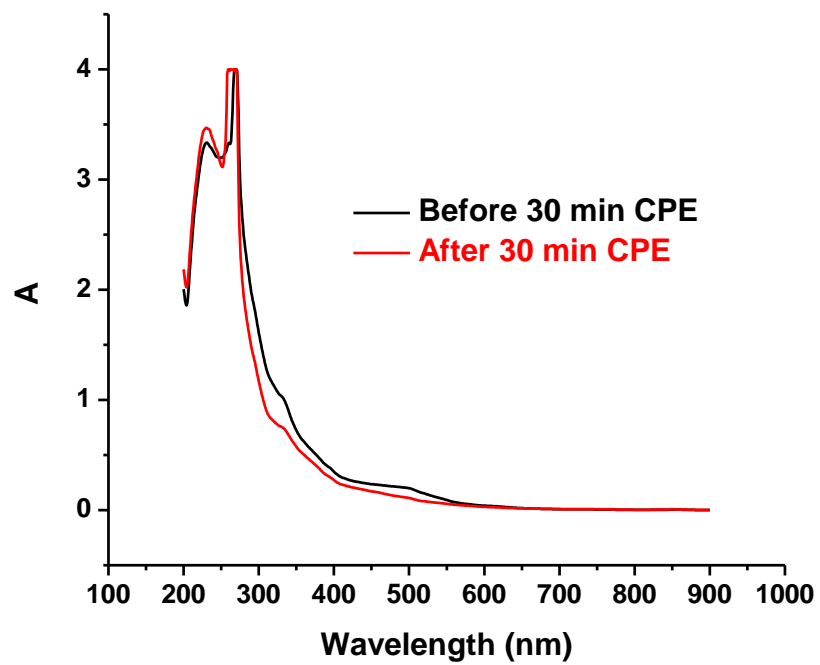
Figure A.24 The UV-vis spectra of the acetonitrile solution of 0.3 mM [Co(L-L)Br$_2$] with 11.00 M H$_2$O at -1.95 V vs. Fc$^{+/0}$ before and after 30-minute CPE for CO$_2$RR
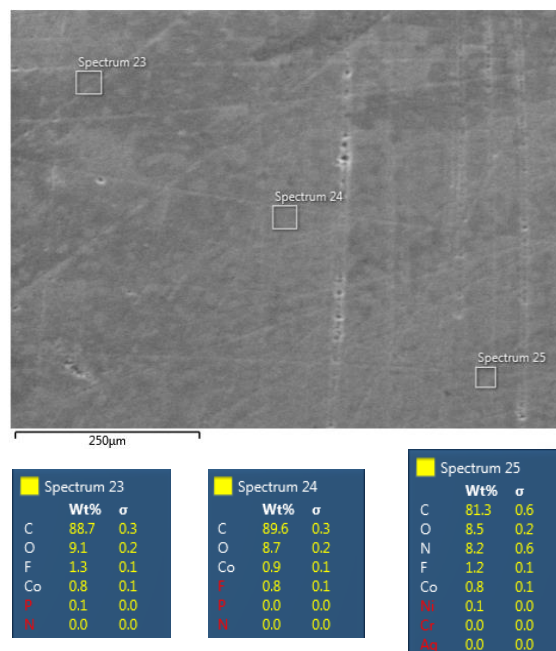
Figure A.25 SEM-EDS analysis of the working electrode surface after a 60-minute CO$_2$RR electrolysis using 0.3 mM [Co(L-L)Br$_2$] with 11.00 M H$_2$O in acetonitrile at -1.95 V vs. Fc$^{+/0}$
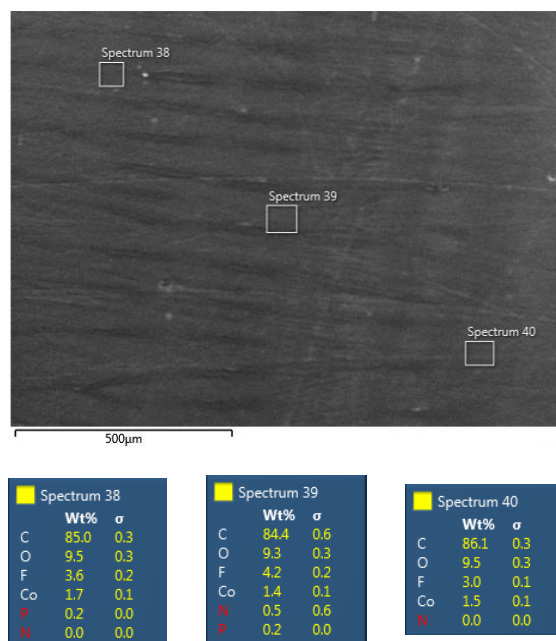
Figure A.26 SEM-EDS analysis of the working electrode surface after a 90-minute CO$_2$RR electrolysis using 0.3 mM [Co(L-L)Br$_2$] with 11.00 M H$_2$O in acetonitrile at -1.95 V vs. Fc$^{+/0}$
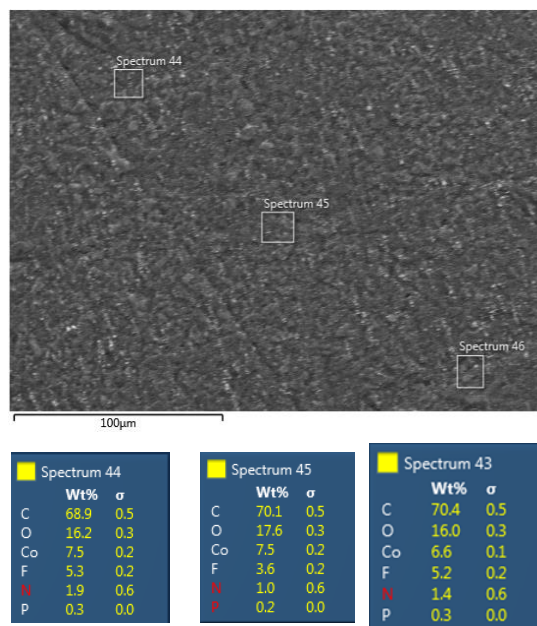
Figure A.27 SEM-EDS analysis of the working electrode surface after a 120-minute CO_2RR electrolysis using 0.3 mM [Co(L-L)Br$_2$] with 11.00 M H_2O in acetonitrile at -1.95 V vs. Fc$^{+/0}$
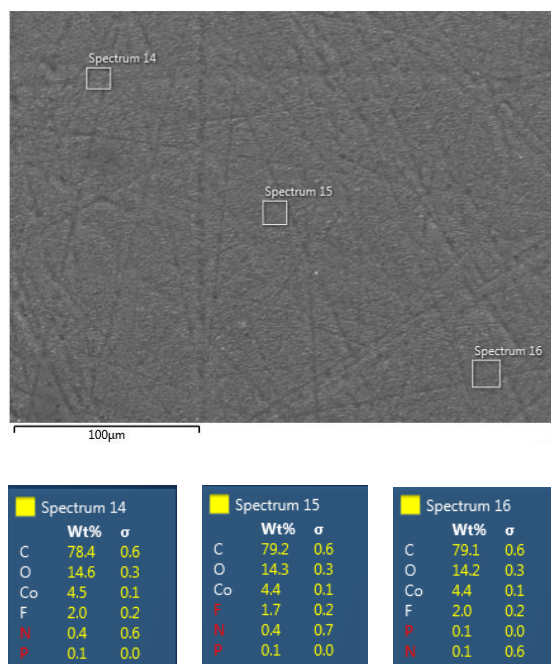
Figure A.28 SEM-EDS analysis of the working electrode surface after a 120-minute CO_2RR electrolysis using 0.3 mM [Co(L-L)Br$_2$] with 5.50 M TFE in acetonitrile at -1.85 V vs. Fc$^{+/0}$

A.1.2 Supporting Tables

Table A.1 Crystal data and structure refinement for the cobalt complex catalyst.[2]

Formula	**[Co(L-L)Br$_2$]Br** (C$_{16}$H$_{18}$Br$_3$CoN$_4$)
FW	565.00
Crystal system	triclinic
Space group	P $_{-1}$
a (Å)	8.2736(4)
b (Å)	10.7007(5)
c (Å)	11.1674(4)
α (deg)	85.313(4)
β (deg)	71.078(4)
γ (deg)	86.856(4)
Z	2
Volume (Å^3)	931.71(7)
Temperature (K)	293(2)
Density (g/mL)	2.014
Reflections collected / unique	13611 / 3345 [R(int) = 0.0293]
Final R indices [I>2sigma(I)]	R1 = 0.0252, wR2 = 0.0637
R indices (all data)	R1 = 0.0254, wR2 = 0.0638
Goodness-of-fit on F^2	1.005

Table A.2 Related bond lengths and bond angles of the cobalt complex **[Co(L-L]Br$_2$]Br**

Bonds	/ Å
Co(1)-N(3)	1.865(2)
Co(1)-N(2)	1.868(2)
Co(1)-N(4)	1.961(2)
Co(1)-N(1)	1.971(2)
Co(1)-Br(2)	2.3906(4)
Co(1)-Br(1)	2.4047(4)

Bond angles	/ deg
N(3)-Co(1)-N(2)	85.81(9)
N(3)-Co(1)-N(4)	82.78(9)
N(2)-Co(1)-N(4)	167.50(9)
N(3)-Co(1)-N(1)	167.50(9)
N(2)-Co(1)-N(1)	82.52(9)
N(4)-Co(1)-N(1)	109.22(9)
N(3)-Co(1)-Br(2)	91.40(6)
N(2)-Co(1)-Br(2)	88.44(6)
N(4)-Co(1)-Br(2)	86.76(6)
N(1)-Co(1)-Br(2)	92.75(6)
N(3)-Co(1)-Br(1)	87.00(6)
N(2)-Co(1)-Br(1)	92.69(6)
N(4)-Co(1)-Br(1)	91.79(6)
N(1)-Co(1)-Br(1)	89.08(6)
Br(2)-Co(1)-Br(1)	177.965(19)

Table A.3 Conditions and Product Analysis of the Controlled Potential Electrolysis for CO_2 reduction with 0.3 mM [Co(L-L)Br$_2$]

Entry	E / V vs. Fc$^{+/0}$	[Proton source] / M	Charge / C	Faradaic Efficiency / % CO	H$_2$	HCOOH	Co / wt%^{a}
0	-1.95	-	2.2 ± 0.3	2.8 ± 2.7	0	6.3 ± 2.6	0.52
1-a	-1.95	[H$_2$O] 0.55 M	2.2 ± 0.5	7.0 ± 2.9	0	7.5 ± 3.8	_^{b}
1-b	-1.95	[H$_2$O] 1.10 M	3.4 ± 0.4	16.3 ± 5.1	0	4.5 ± 1.1	_^{b}
1-c	-1.95	[H$_2$O] 2.75 M	5.2 ± 0.3	56.5 ± 11.5	0	3.4 ± 0.8	_^{b}
1-d	-1.95	[H$_2$O] 5.50 M	7.1 ± 0.7	67.4 ± 11.0	0.3 ± 0.1	1.9 ± 0.5	_^{b}
1	-1.95	[H$_2$O] 11.00 M	8.3 ± 0.9	80.5 ± 4.7	1.1 ± 0.5	0.7 ± 0.3	0.3
2-a	-1.85	[TFE] 0.275 M	3.4 ± 0.6	13.6 ± 1.7	0	5.6 ± 2.4	_^{b}
2-b	-1.85	[TFE] 0.55 M	4.0 ± 0.4	34.7 ± 1.4	0	4.0 ± 0.3	_^{b}
2-c	-1.85	[TFE] 1.10 M	6.2 ± 1.1	65.8 ± 5.2	0	2.2 ± 1.1	0.13
2-d	-1.85	[TFE] 2.75 M	11.2 ± 3.0	75.4 ± 1.0	1.3 ± 1.2	0.7 ± 0.6	0.01
2	-1.85	[TFE] 5.50 M	10.1 ± 2.3	87.7 ± 8.2	1.7 ± 0.7	0	0.01

^{a}Weight percent of Co deposited onto the electrode post-electrolysis as measured by SEM-EDS. ^{b}Not measured.

Table A.4 Conditions and Product Analysis of the CPE control groups for CO_2 reduction

Entry	Catalyst / 0.3 mM	E/V vs. Fc$^{+/0}$	[Proton source] / M	Charge / C	Faradaic Efficiency / %^{a}		Co / wt%^{b}
					CO	H$_2$	
1-A	CoBr$_2$	-1.95	[H$_2$O] 11.00 M	2.0 ± 0.1	0	24.5 ± 13.6	7.2
2-A	CoBr$_2$	-1.85	[TFE] 5.5 M	6.2 ± 1.3	0	21.5 ± 13.0	0.45
1-B	Glassy Carbon	-1.95	[H$_2$O] 11.00 M	2.0 ± 0.1	0	20.2 ± 4.1	-^{c}
2-B	Glassy Carbon	-1.85	[TFE] 5.5 M	3.8 ± 1.2	0	20.1 ± 12.0	-^{c}
1-C	Ligand	-1.95	[H$_2$O] 11.00 M	2.9 ± 0.3	3.5 ± 3.2	6.6 ± 3.4	-^{c}

^{a}No HCOOH was detected after electrolysis with control groups. ^{b}Weight percent of Co deposited onto the electrode post-electrolysis as measured by SEM-EDS. ^{c}Not measured.

Table A.5 Conditions and Product Analysis of the CPE control groups for CO_2 reduction at different potentials.

E / V vs. Fc$^{+/0}$	[Proton source] / M	Charge / C	Faradaic Efficiency / %			Co / wt%^{a}
			CO	H$_2$	HCOOH	
No proton source						
-1.95	0	2.2 ± 0.3	2.8 ± 2.7	0	6.3 ± 2.6	0.52%
-2.15	0	4.3 ± 1.4	4.2 ± 1.7	0	2.7 ± 0.9	0.52%
Water						
-1.75	11.00 M	3.1 ± 0.3	30.3 ± 10.8	6.4 ± 1.8	0	0.97%
-1.95	11.00 M	8.3 ± 0.9	80.5 ± 4.7	1.1 ± 0.5	0.7 ± 0.3	0.35%
-2.15	11.00 M	16.2 ± 2.5	104.3 ± 5.5	0.7 ± 0.4	0	0.18%
-2.35	11.00 M	17.0 ± 0.6	44.3 ± 12.2	45.5 ± 2.5	0	0.54%
TFE						
-1.85	5.5 M	10.1 ± 2.3	87.7 ± 8.2	1.7 ± 0.7	0	0.01%
-2.05	5.5 M	16.8 ± 2.5	102.7 ± 3.1	1.0 ± 0.4	0	0.007%

^{a}Weight percent of Co deposited onto the electrode post-electrolysis as measured by SEM-EDS.

Table A.6 ICP-MS results of Co content on the surface of GC electrode after electrolysis

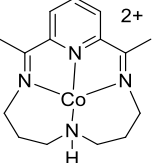| Electrode, [proton source], potential vs. $Fc^{+/0}$	[Co] in ICP-MS test solution / ppb (as measured)	[Co] in ICP-MS test solution / ppb (after background correction)[a]	$n(Co)$ on electrode surface / mol	Calculated fraction of [Co(L-L)Br$_2$] decomposed on the electrode surface
GC1, no H2O, -1.95 V	2.983	2.056	3.48×10^{-7}	5.81 %
GC2, no H2O, -1.95 V	2.953	2.026	3.43×10^{-7}	5.72 %
GC3, no H2O, -1.95 V	3.135	2.208	3.74×10^{-7}	6.24 %
Average				**5.92 ± 0.27 %**
GC4, 11 M H2O, -1.95 V	2.801	1.874	3.18×10^{-7}	5.29 %
GC5, 11 M H2O, -1.95 V	2.424	1.497	2.54×10^{-7}	4.23 %
GC6, 11 M H2O, -1.95 V	1.933	1.006	1.71×10^{-7}	2.84 %
Average				**4.12 ± 1.23 %**
GC7 (5.5M TFE, -1.85V)	1.034	0.107	0.18×10^{-7}	0.30 %
GC8 (5.5M TFE, -1.85V)	1.750	0.823	1.39×10^{-7}	2.32 %
GC9 (5.5M TFE, -1.85V)	1.069	0.142	0.24×10^{-7}	0.40%
Average				**1.01 ± 1.13 %**
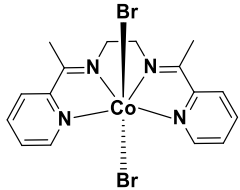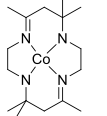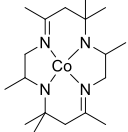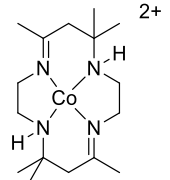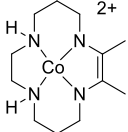
[a][Co] in ICP-MS test solution (after correction) = [Co] in ICP-MS test solution - [Co] background
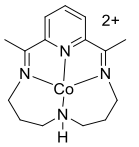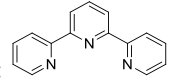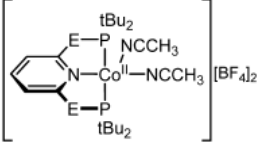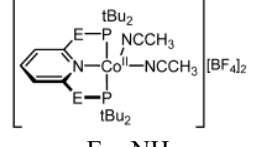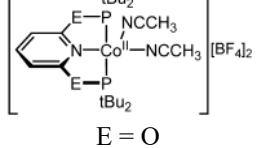
Table A.7 Conditions and product analysis of the long-time CPE control groups for the CO_2 reduction of 0.3 mM [Co(L-L)Br$_2$]
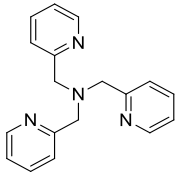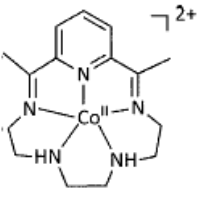
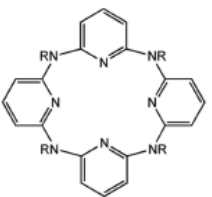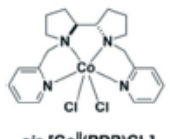| T/min	E /V vs. Fc$^{+/0}$	[Proton source]	Charge /C	TOF^a/s^{-1}	TOF^b/s^{-1}	Faradaic Efficiency /%		Co / wt%^{c}
						CO	H$_2$	
60	-1.95	[H$_2$O] 11.00 M	14.4	3.0×10^{-3}	560	88.2	1.6	0.83 %
90	-1.95	[H$_2$O] 11.00 M	21.6	2.7×10^{-3}	448	78.9	3.5	1.53 %
120	-1.95	[H$_2$O] 11.00 M	28.5	1.0×10^{-3}	61.3	29.5	18.7	7.20 %
120	-1.85	[TFE] 5.5 M	31.4	0.8×10^{-3}	34.9	20.2	7.9	4.43 %

^{a}TOF is the turnover frequency for CO calculated based on total concentration of catalyst in solution, and therefore is a significant underestimate of catalytic activity (see Section A.1.3). ^{b}TOF is the turnover frequency for CO generation, derived from CPE data using the equations described by Savéant et al (See Section A.1.3). ^{c}Weight percent of Co deposited onto the electrode post-electrolysis as measured by SEM-EDS.
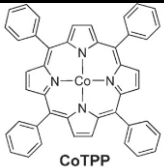
Table A.8 A summary of Co-molecular catalysts for the electrochemical CO_2RR in the recent literature

Catalyst	CO_2RR E_{onset} /V vs. Fc^+/Fc	CPE condition	CO_2RR $E_{applied}$ /V vs. Fc^+/Fc	TOF /s^{-1} [a]	TOF /s^{-1} [b]	TOF /s^{-1} [c]	Product selectivity	Ref.
	-1.65	0.3 mM Cat in MeCN(0.1 M nBu₄NPF₆) CO_2 with 11M H_2O	-1.95	$(3.2 \pm 0.4) \times 10^{-3}$	620	-[d]	CO (80.5%) : H₂ (1.1%) : HCOOH (0.7%)	This work
			-2.15	$(8.1 \pm 1.3) \times 10^{-3}$	3961	-	CO (104.3%) : H₂ (0.6%)	
		0.3 mM Cat in MeCN(0.1 M nBu₄NPF₆) CO_2 with 5.5M TFE	-1.85	$(4.2 \pm 0.5) \times 10^{-3}$	1089	-	CO (87.7%) : H₂ (1.7%)	
			-2.05	$(8.2 \pm 0.9) \times 10^{-3}$	4131	-	CO (102.7%) : H₂(1.0%)	
	-	1.2 mM Cat 0.1 M KNO, in H₂O/CH,CN 2: 1 (v/v) or H₂O only	-2.00	2.2×10^{-3}	-	-	CO (46.5%) : H₂(46.5%)	Ref[6]
	-		-1.90	2.5×10^{-3}	-	-	CO (45.0%) : H₂(45.0%)	
	~-1.8	0.18-0.21 mM Cat mercury electrode DMF/H₂O (95/5 v/v) 0.1 M Et₄NCl. H₂O	-1.70	-	-	-	CO (7.9%) : H₂(13.1%)	Ref[7]
			-2.0		-	-	CO (56.2%) : H₂(25.0%)	
	~-1.8	0.18-0.21 mM Cat mercury electrode DMF/H₂O (95/5 v/v) 0.1 M Et₄NCl. H₂O	-2.0	-	-	-	CO (13.3%) : H₂(58.8%)	Ref[7]

Catalyst	E (V)	Conditions					Products	Ref
	~-1.8		-1.7	-	-	-	CO (66.4%) : H$_2$(5.3%)	
			-2.0	-	-	-	CO (41.5%) : H$_2$(10.9%)	
[Co(tpy)$_2$]$^{2+}$ tpy:	~-2.03	2 mM Cat CO2-saturated DMF/ H2O (95 : 5, v : v) with 0.1 M TBAP	-1.93	-	-	-	CO (20.0%) : H$_2$(1.0%)	Ref[8]
			-2.03	-	-	-	CO (12.0%) : H$_2$(5.0%)	
	~-1.55	0.3 mM Cat MeCN(0.1 M nBu$_4$NPF$_6$) CO$_2$ with 10M H$_2$O	-2.13	1.7× 10^{-3}	-	-	CO (45.0%) : H$_2$(30.0%)	Ref[9]
  E = CH$_2$	~-2.1	1.0 mM Cat in CH$_3$CN with 0.20 M Bu$_4$NBF$_4$	-	-	-	-	-	Ref[10]
  E = NH	~-2.5		-	-	-	-	-	
  E = O	~-2.2	1.0 mM Cat in CH$_3$CN with 0.20 M Bu$_4$NBF$_4$	-	-	-	-	-	Ref[10]

Structure								
[Co^{II}(TPA)Cl][Cl] TPA:	~-1.94	MeCN(0.1 M nBu$_4$NPF$_6$)	-	-	-	-	-	Ref[11]
	~-1.7	1.0 mM Cat in DMF, 0.1M nBu$_4$NPF$_6$	-1.9	-	-	-	CO (82.0%)	Ref[12]
[Co^{II}(L-R)(solv1)(solv2)] L-R: R = H; solv1 = solv 2 = acetone	-2.36	0.5 mM Cat in DMF, 0.1M nBu$_4$NPF$_6$ CO$_2$ with 1.2M TFE	-2.8	0.86× 10^{-3}	170	360	CO (98.0%)	Ref[13]
[Co^{II}(L-R)(solv1)(solv2)] R = Me; solv1 = MeCN solv 2 = none	-2.58	0.5 mM Cat in DMF, 0.1M nBu$_4$NPF$_6$ CO$_2$ with 1.2M TFE	-2.8	0.04× 10^{-3}	0.5	78	CO (23.0%)	Ref[13]
cis-[Co^{II}(PDP)Cl$_2$]	-1.95	1 mM Cat in MeCN, 0.1M nBu$_4$NPF$_6$ CO$_2$	-2.1	-	-	-	30min: CO (96.0%) 4 hours: CO (85.0%)	Ref[14]

Catalyst		Conditions						Ref
cis-[Co^{II}(DMPDP)Cl$_2$]	-1.93	1 mM Cat in MeCN, 0.1M nBu$_4$NPF$_6$ CO$_2$	-2.1	low	low	-	-	
cis-[Co^{II}(PDMBP)Cl$_2$]	-1.97	1 mM Cat in MeCN, 0.1M nBu$_4$NPF$_6$ CO$_2$	-2.1	low	low	-	-	
cis-[Co^{II}(BQCN)Cl$_2$]	-1.87	1 mM Cat in MeCN, 0.1M nBu$_4$NPF$_6$ CO$_2$	-2.1	low	low	-	-	
[Co(TPA)X]$^+$ TPA: X = Cl	-1.96	in MeCN, 0.1M nBu$_4$NPF$_6$ CO$_2$	-	-	-	-	-	Ref[15]
[Co(TPA)X]$^+$ X = Br	-1.83		-	-	-	-	-	
[Co(TPA)X]$^+$ X = I	-1.72	in MeCN, 0.1M nBu$_4$NPF$_6$ CO$_2$	-	-	-	-	-	
[Co(TPA)X]$^+$ X = NCS	-1.76		-	-	-	-	-	
1(R'= Cy; R=Bn)	-2.08	0.5 mM Cat in DMF, 0.1M nBu$_4$NPF$_6$ CO$_2$ with 1.1M H$_2$O	-2.10	2.2× 10^{-3}	70	-	HCOOH(92%): CO (<1%) : H$_2$(5%)	Ref[16]
			-2.25	7.2× 10^{-3}	650	-	HCOOH(98%): CO (<1%) : H$_2$(5%)	
2(R'= Cy; R=Ph)	-2.0	0.5 mM Cat in DMF, 0.1M nBu$_4$NPF$_6$ CO$_2$ with 1.1M H$_2$O	-2.05	1.4× 10^{-3}	60	-	HCOOH(94%): CO (1%) : H$_2$(3%)	

			-2.20	2.5×10^{-3}	180	-	HCOOH(98%): CO (<1%) : H$_2$(4%)	
3(R'= Ph; R=Bn)	-1.93	0.5 mM Cat in DMF, 0.1M nBu$_4$NPF$_6$ CO$_2$ with 1.1M H$_2$O	-2.00	0.5×10^{-3}	20	-	HCOOH(88%): CO (<1%) : H$_2$(8%)	
			-2.05	1.0×10^{-3}	40	-	HCOOH(86%): CO (<1%) : H$_2$(6%)	
CoTPP	-2.20	1 mm CoTPP in DMF, 0.1M nBu$_4$NPF$_6$ CO$_2$ with	-2.35	2.6×10^{-4}	-	-	CO (50.0%) : H$_2$(2.0%): HCOOH(4%):	Ref[17]

[a]TOF is the turnover frequency for CO calculated based on total concentration of catalyst in solution, and therefore is a significant underestimate of catalytic activity (See Section A.1.3). Included for comparison purposes only. [b]TOF is the turnover frequency for CO generation, derived from CPE data using the equations described by Savéant et al. (See Section A.1.3). [c]TOF is the turnover frequency derived from CV experiments. [d]Not measured

A.1.3 Supporting Methods

A.1.3.1 Paramagnetic Susceptibility Measurements (Evans Method)

The measurement of paramagnetic susceptibility

The paramagnetic susceptibility of [Co(L-L)]Br$_2$ was studied by Evans method which was established in 1959 for paramagnetic susceptibility measurement by using NMR.[20] The most commonly used equation is

$$\chi_{mass} = \frac{3\Delta f}{4\pi f c} + \chi_0 + \frac{\chi_0(d_0 - d_s)}{c}$$

$$\chi_{mol} = M\chi_{mass}$$

Where χ_{mass} is mass susceptibility ($cm^3 \cdot g^{-1}$), χ_{mol} is molar susceptibility ($cm^3 \cdot mol^{-1}$), Δf is observed frequency difference (Hz), f is spectrometer frequency ($400 \times 10^6 Hz$), c is concentration of the sample solution ($g \cdot cm^{-3}$), χ_0 is mass susceptibility of solvent DMSO ($-0.68 \times 10^{-6} cm^3 \cdot g^{-1}$), d_0 is density of solvent ($g \cdot cm^{-3}$), d_s is density of solution ($g \cdot cm^{-3}$), M is molecular weight of [Co(L-L)]Br$_2$ (485.08 $g \cdot mol^{-1}$). In the most cases, the density of the solution is almost the same as the density of the solvent. Therefore, the equation is usually

$$\chi_{mass} = \frac{3\Delta f}{4\pi f c} + \chi_0$$

The Evans ^{1}H-NMR measurement was conducted by using the Evans NMR tube which consists of a regular NMR tube with a thinner tube coaxially inserted. The regular NMR tube was filled with the complex solution in d^6-DMSO and the thinner tube was filled with pure d^6-DMSO. The ^{1}H-NMR of the sample is shown in Figure A.29 and the calculation results of the paramagnetic susceptibility of [Co(L-L)]Br$_2$ is summarized in Table A.9.
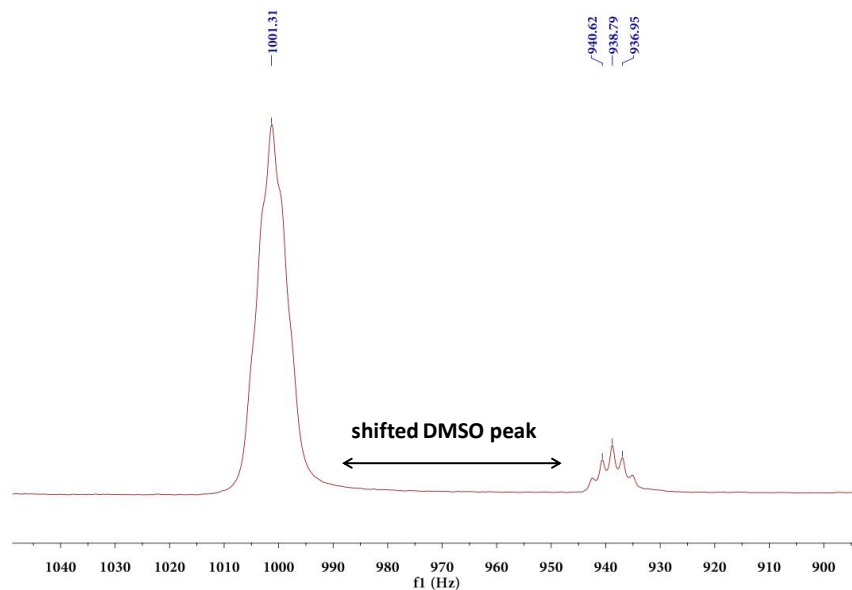
Figure A.29 The shifted DMSO peaks in ^{1}H-NMR spectrum of 2.0 mg **[Co(L-L)Br2]** in 0.55 mL d^6-DMSO

Table A.9 The paramagnetic susceptibility of [Co(L-L)]Br2 calculated based on Evans Method

$m(sample)/g$	$V(d_6 DMSO)/cm^3$	$[sample]/g \cdot ml^{-1}$	$\chi_{mass}/cm^3 \cdot g$	$\chi_{mol}/cm^3 \cdot mol$
0.0028	0.55	0.0051	8.7×10^{-6}	4.2×10^{-3}
0.0022	0.55	0.0040	7.5×10^{-6}	3.6×10^{-3}
0.0020	0.55	0.0036	9.6×10^{-6}	4.7×10^{-3}
Average				4.2×10^{-3}

The number of unpaired electrons

Based on Curie's Law,

$$\chi_{mol}T = constant\ for\ a\ simple\ paramagnet$$

$$\chi_{mol}T = \frac{1}{2}[S(S+1)] = 8n(n+2)$$

$$\mu_{eff} = \sqrt{8(\chi_{mol}T)} = 2\sqrt{S(S+1)} = \sqrt{n(n+2)}$$

Where T is temperature (K), S is total spin quantum number, n is the number of unpaired electrons, μ_{eff} is effective magnetic moment $(Bohr\ magneton, \mu_B)$, which is independent of temperature.

The calculation of the effective magnetic moment for [Co(L-L)]Br$_2$ at the room temperature is summarized in Table A.10.

Table A.10 The calculated μ_{eff} and n for [Co(L-L)]Br$_2$ at 293K based on χ_{mol}

$\chi_{mol}/cm^3 \cdot mol$	$\chi_{mol}T$	μ_{eff}	n	μ_{eff} in literature [3]	n in literature [3]
4.2×10^{-3}	1.22	3.12	2.28	2.85	2.02

The effective magnetic moment μ_{eff} 3.12 matches the value 2.85 reported in the literature.[3] Based on the calculation [Co(L-L)]Br$_2$ shows μ_{eff} between the value ca. 1.73 for a pure octahedral low spin state and 3.87 for a pure octahedral high spin state. This could be explained by the occurrence of a thermal equilibrium between these two spin states at the room temperature.

A.1.3.2 ICP-MS Tests

Deposits on the surface of unrinsed glassy carbon (GC) electrode after electrolysis was digested in 3.0 mL TraceMetal Grade HNO_3. Then the acidic solution was first diluted to a 10.0 mL stock solution with 18 MΩ water, and then a final test solution for ICP-MS measurements was made by diluting 10 uL stock solution into 10.0 mL with water. A [Co] background of 0.927 ppb was measured from the ICP-MS test solution of a bare GC electrode without electrolysis, and this background was subtracted from all ICP-MS measurements.

The fraction of the catalyst [Co(L-L)]Br_2 decomposed on the electrode surface could be calculated based on the following equations:

$$n(Co)_{on\ electrode\ surface} = \frac{[Co]_{ICP-MS} \times 10^{-6} \left(\frac{g}{L}\right) \times 1000 \times 0.01(L)}{59 \left(\frac{g}{mol}\right)}$$

$$Fraction = \frac{n(Co)_{on\ electrode\ surface}}{([Cat] \times V_{solution})}$$

Where $[Co]_{ICP-MS}$ is Co concentration in ICP-MS test solution after correction, $[Cat]$ is [Co(L-L)]Br_2 concentration in the electrolysis solution, $V_{solution}$ is the volume of the electrolysis solution.

ICP-MS results of Co content on the surface of GC electrode after electrolysis are summarized in Table A.6

A.1.3.3 Turnover Frequency (TOF) calculations

The Calculation Method for TOF$_a$

TOFs for CO are calculated based on the total amount of CO generated divided by the total amount of the catalyst in the electrolysis solution and the time of the electrolysis.

$$TOF = \frac{\frac{n(CO)}{n(Cat)}}{t}$$

$n(CO)$ is the total number of moles of CO produced, $n(Cat)$ is the number of moles of the catalyst in the solution, and t is the electrolysis time in seconds.

$n(CO)$ is calculated based on the amount of electrons used specifically for CO generation divided by a factor $2F$ (it is a two-electron reduction reaction from CO_2 to CO):

$$n(CO) = \frac{Q \times FE(CO)}{2F}$$

Q is the charge passed in Coulombs (C); $FE(CO)$ is the Faradaic Efficiency of CO in percentage (%); F is Faraday constant (C/mol)

$n(Cat)$ is calculated based on the following equation:

$$n(Cat) = [Cat] \times V_{sol}$$

$[Cat]$ is the concentration of the catalyst (mol/L); V_{sol} is the volume of the solution (L)

The Calculation Method for TOF$_b$

TOF values for CO are calculated from CPE data with the equations described by Savéant et al. [4,5]

Calculation of diffusion constants D from cyclic voltammograms

For the homogenous system, the relation between the peak current and scan rate in CV is given by the Randles-Sevcik equation:

$$i_p = 0.4463 \left(\frac{F}{RT}\right)^{\frac{1}{2}} n_p^{\frac{3}{2}} FAD^{\frac{1}{2}}[Cat]v^{\frac{1}{2}}$$

i_p is peak current (A), F is Faraday constant ($96500 \ C/mol$), R is the universal gas constant ($8.31 \ J \cdot K^{-1} \cdot mol^{-1}$), T is temperature ($298 \ K$), n_p is the number of electrons transferred (1 for each Co-complex redox process), A is the active surface area of the electrode ($A = 0.071 \ cm^2$), D is the diffusion coefficient for the complex (cm^2/s), $[Cat]$ is the concentration of the catalyst (mol/cm^3), and v is the scan rate (V/s).

The scan rate dependent CVs of [Co(L-L)Br$_2$] are shown in Figure A.30. The diffusion coefficient D of the catalyst [Co(L-L)Br$_2$] could be calculated based on the slopes of the fitted linear curves in Figure A.31 and A.32, concentration of [Co(L-L)Br$_2$] and the working electrode surface area, using the Randles-Sevcik equation mentioned above. The result is shown in Table A.11.
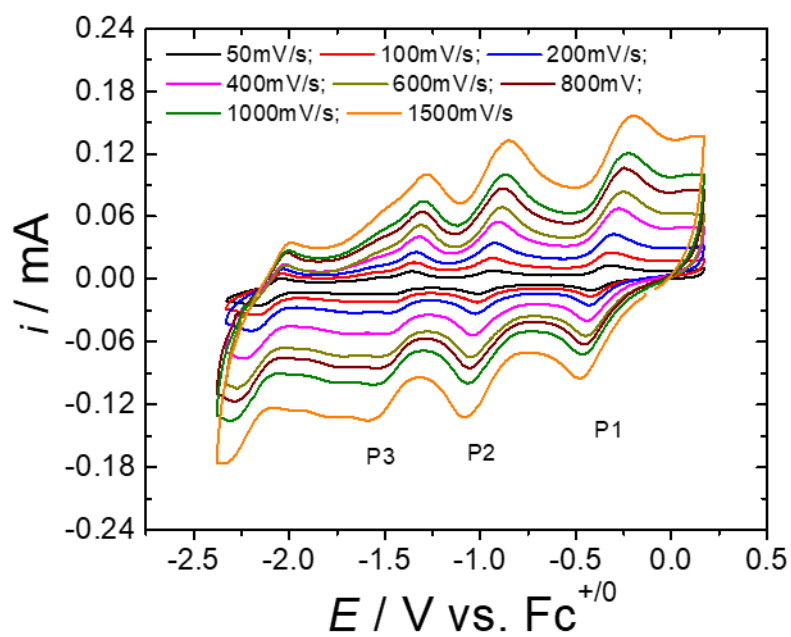
Figure A.30 CVs of the 1.2 mM [Co(L-L)Br$_2$] in MeCN (with 0.1 M nBu$_4$NPF$_6$) recorded at different scan rates. The couples of redox peaks P1, P2 and P3 are corresponded to Co$^{3+/2+}$, Co$^{2+/1+}$ and L-L/L-L$^-$ process.
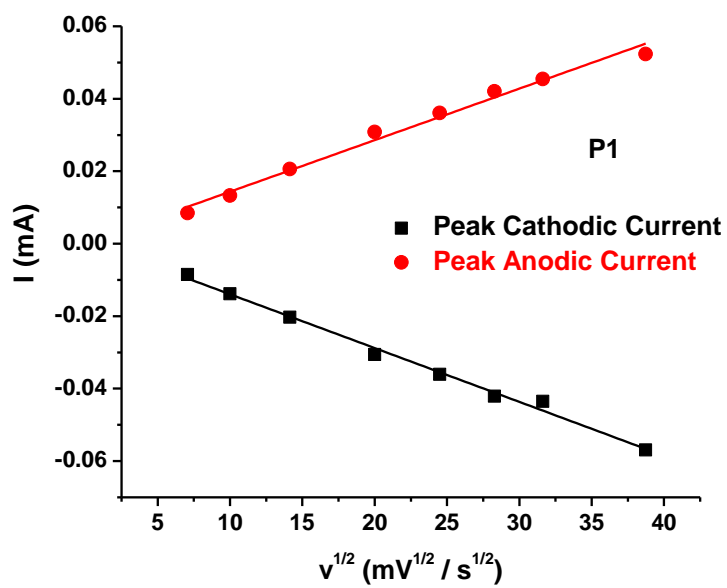
Figure A.31 i_p–$v^{1/2}$ plots of P1 ($Co^{3+/2+}$ redox process)
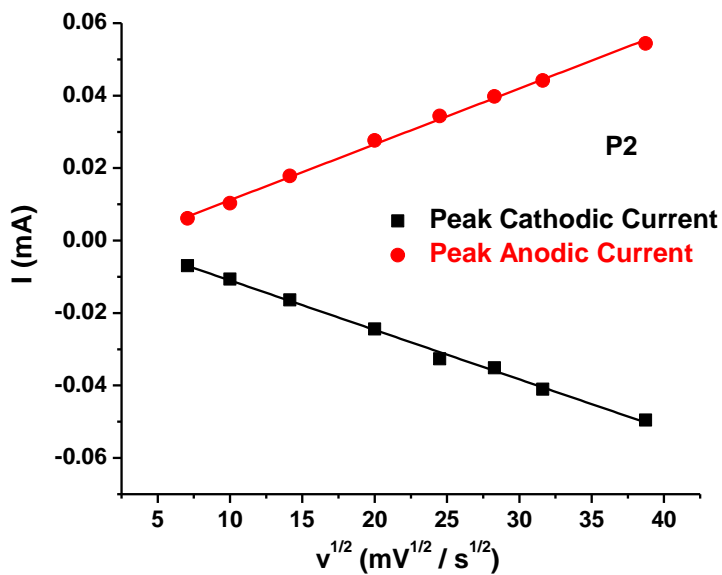
Figure A.32 i_p–$v^{1/2}$ plots of P2 ($Co^{2+/1+}$ redox process)

Table A.11 The calculation of the diffusion coefficient D for [Co(L-L)Br$_2$]

Peak	slope / (mV/s)$^{1/2}$	[Cat] / mM	A /cm^2	D /cm^2/s	D(average)/ cm^2/s
P1cathodic	0.00149	1.2	0.071	4.24×10^{-6}	
P1anodic	0.00142	1.2	0.071	3.85×10^{-6}	4.05×10^{-6}
P2cathodic	0.00137	1.2	0.071	3.58×10^{-6}	
P2anodic	0.00154	1.2	0.071	4.53×10^{-6}	

Calculation of TOF from CPE data using the equations described by Savéant et al. [3,4]

TOF values for CO generation were calculated from the CPE data as reported by Saveant and co-workers.[3,4,15] In the homogeneous case, $n(Cat)$ is obtained by space integration of catalyst amount in the reaction-diffusion layer near the surface of the working electrode. $n(CO)$ is calculated based on the charge specially used for CO generation.

$$TOF = \frac{\frac{n(CO)}{n(Cat)}}{t}$$

$$n(Cat) = A\sqrt{\frac{D}{k_{cat}}}[Cat] = A\sqrt{\frac{D}{TOF_{max}}}[Cat]$$

$$n(CO) = \frac{Q_{el} \times FE}{F}$$

Here, A is the active surface area of the working electrode ($2.56 \; cm^2$), D is the diffusion coefficient for the complex ($4.05 \times 10^{-6} \; cm^2/s$), k_{Cat} is the reaction rate of catalysis process, TOF_{mas} is the maximum turnover frequency obtained from CVs. It is used to replace k_{Cat} in the calculation, $[Cat]$ is the concentration of the catalyst ($0.3 \times 10^{-6} \; mol/cm^3$), F is Faraday constant ($96500 \; C/mol$).

Therefore, the expression of TOF can be written as:

$$TOF = \frac{\frac{n(CO)}{n(Cat)}}{t} = \frac{\frac{\frac{Q_{el} \times FE}{F}}{A\sqrt{\frac{D}{TOF_{max}}}[Cat]}}{t}$$

$$i_{el} = \frac{Q_{el} \times FE}{t}$$

$$TOF = \frac{i_{el}}{FA} \frac{\sqrt{TOF_{max}}}{\sqrt{D}[Cat]}$$

Here, i_{el} is average current of CPE for CO generation (A), Q_{el} is the charge passed in 30-min CPE (C), FE is the faradaic efficiency of CO (%), t is the time of CPE (s).

When the electron transfer process to the catalyst is fast and the Nernst equation is obeyed, TOF values can be calculated based on the equation below:

$$TOF = \frac{TOF_{max}}{1 + exp\left[\frac{F}{RT}\left(E_{app} - E_{1/2}\right)\right]}$$

Here, R is the universal gas constant ($8.31\ J \cdot K^{-1} \cdot mol^{-1}$), T is temperature ($298\ K$), E_{app} is the applied potential during electrolysis (V), $E_{1/2}$ is the redox potential of the ligand ($1.65V$).

Combination of the equations above gives the final expression:

$$TOF = \frac{i_{el}^2\left(1 + exp\left[\frac{F}{RT}\left(E_{app} - E_{1/2}\right)\right]\right)}{F^2A^2D[Cat]^2}$$

A.1.4 References

1. C. C. L. McCrory, N. K. Szymczak, and J. C. Peters, *Electrocatalysis*, 2016, **7**, 87-96.

2. *SHELXTL (version 5.0), Reference Manual*, Siemens Industrial Automation, Analytical Instruments, Madison, WI, 1995.

3. S. Gourbatsis, S. P. Perlepes, N. Hadjiliadis, *Transition Met. Chem.*, 1990, **15**, 300.

4. C. Costentin, M. Robert, J.-M. Saveant, *Chem. Soc. Rev.*, 2013, **42**, 2423.

5. C. Costentin, S. Drouet, M. Robert, J.-M. Savéant, *Science,* 2012, **338**, 90

6. B. J. Fisher, R. Eisenberg, *J. Am. Chem. Soc.*, 1980, **102**, 7361

7. A. H. A. Tinnemans, T. P. M. Koster, D. H. M. W. Thewissen, A. Mackor, *Rec. Trav. Chim. Pays Bas,* 1984, **103**, 288.

8. N. Elgrishi, M. B. Chambers, V. Artero, M. Fontecave, *Phys. Chem. Chem. Phys.* 2014, **16**, 13635

9. D. C. Lacy, C. C. L. McCrory, J. C. Peters*, Inorg. Chem* 2014, **53**, 4980

10. D. W. Shaffer, S. I. Johnson, A. L. Rheingold, J. W. Ziller, W. A. Goddard, R. J. Nielsen, J. Y. Yang, *, Inorg. Chem* 2014, **53**, 13031.

11. S. L.-F. Chan, T. L. Lam, C. Yang, S.-C. Yan, N. M. Cheng, *Chem. Commun.* 2015, **51**, 7799

12. L. Chen, Z. Guo, X.-G. Wei, C. Gallenkamp, J. Bonin, E. Anxolabéhère-Mallart, K.-C. Lau, T.-C. Lau, M. Robert, *J. Am. Chem. Soc.*, 2015, **137**, 10918.

13. A. Chapovetsky, T. H. Do, R. Haiges, M. K. Takase, S. C. Marinescu, *J. Am. Chem. Soc.*, 2016, **138**, 5765.

14. F. Wang, B. Cao, W.-P. To, C.-W. Tse, K. Li, X.-Y. Chang, C. Zang, S. L.-F. Chan, C.-M. Che, *Catal. Sci. Technol.,* 2016, **6**, 7408

15. S. L.-F. Chan, T. L. Lam, C. Yang, J. Lai, B. Cao, Z. Zhou, Q. Zhu, *Polyhedron* 2017, **125,** 156.

16. S. Roy, B. Sharma, J. Pécaut, P. Simon, M. Fontecave, P. D. Tran, E. Derat, V. Artero, *J. Am. Chem. Soc.*, 2017, **139**, 3685.

17. X-M. Hu, M. H. Rønne, S. U. Pedersen, T. Skrydstrup, K. Daasbjerg. *Angew. Chem. Int. Ed.* 2017, *56*, 6468.

18. M. Popescu, P. Rotaru, M-V. Bubulica, A. Kriza, *J. Therm. Anal. Calorim.*, 2015, *120*, 641.

19. B. D. Stubbert, J. C. Peters, H. B. Gray*, J. Am. Chem. Soc.* 2011*, 133,* 18070.

20. D.F. Evans, *J. Chem. Soc.,* 1959, **0**, 2003.

A.2 Supporting Information for Chapter 3

A.2.1 Supporting Figures
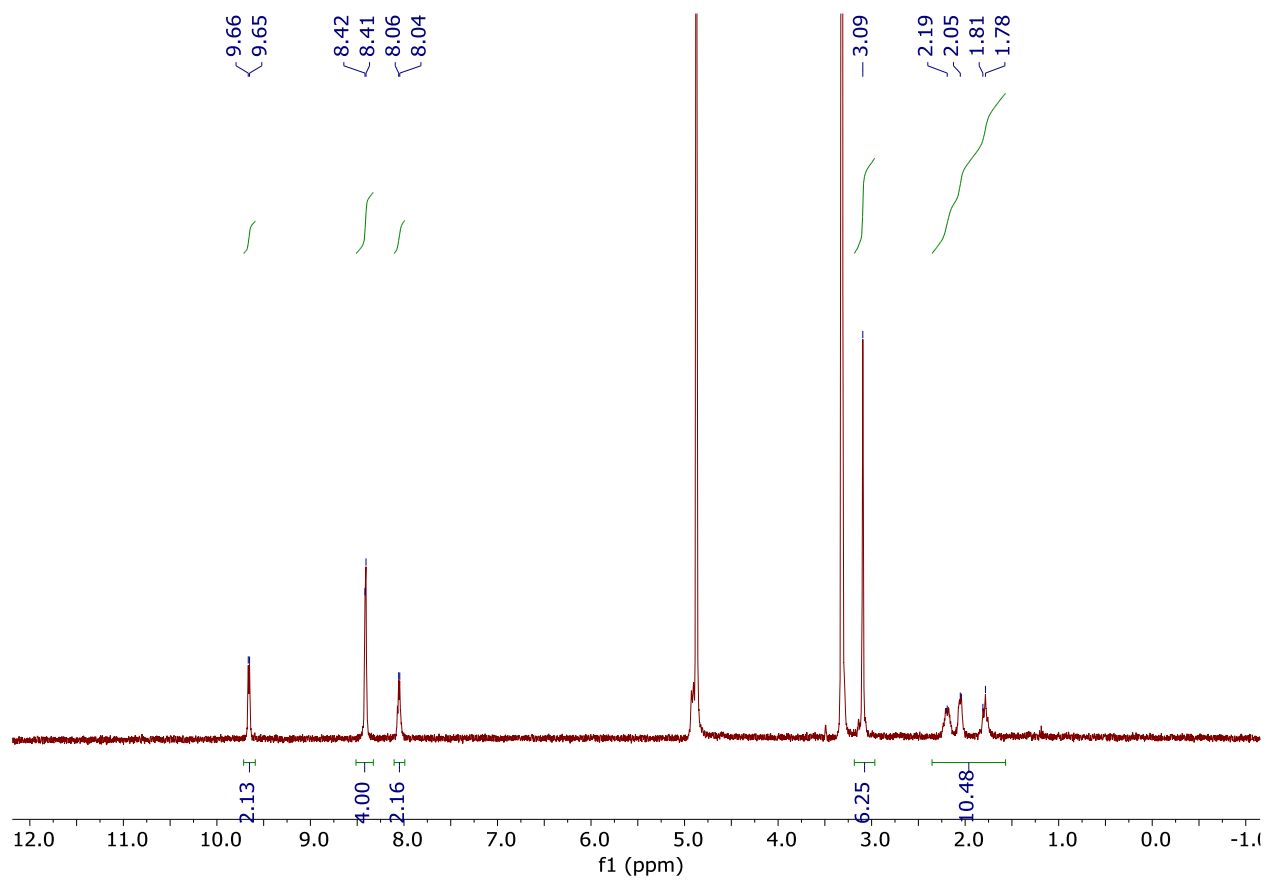
Figure A.33 ^{1}H-NMR Spectrum of [Co(L-cyc-L)Br$_2$]Br in CD$_3$OD-d_4 (δ 3.31 solvent residual peak, δ 4.87 water peak).
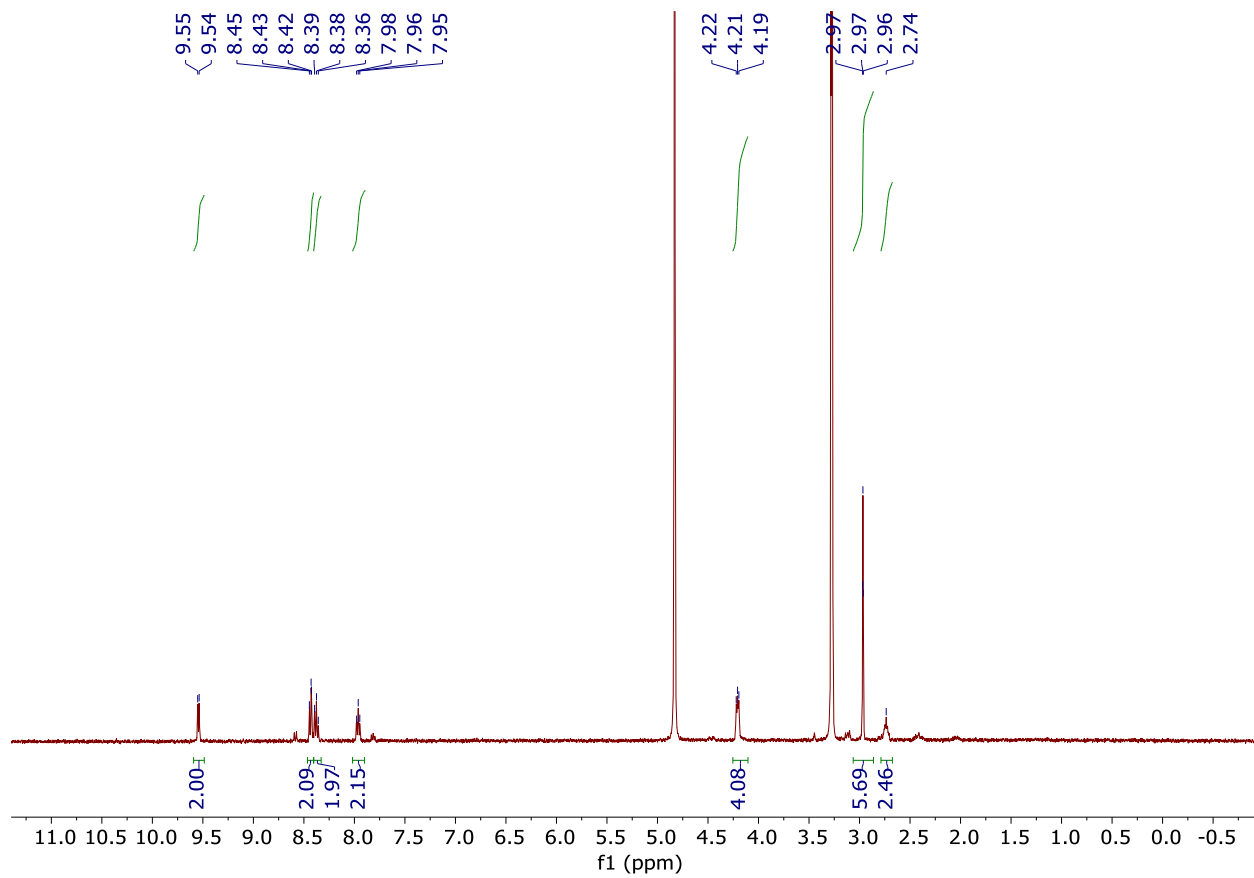
Figure A.34 ^{1}H-NMR Spectrum of [Co(L-CH$_2$-L)Br$_2$]Br in CD$_3$OD-d_4 (δ 3.31 solvent residual peak, δ 4.87 water peak)
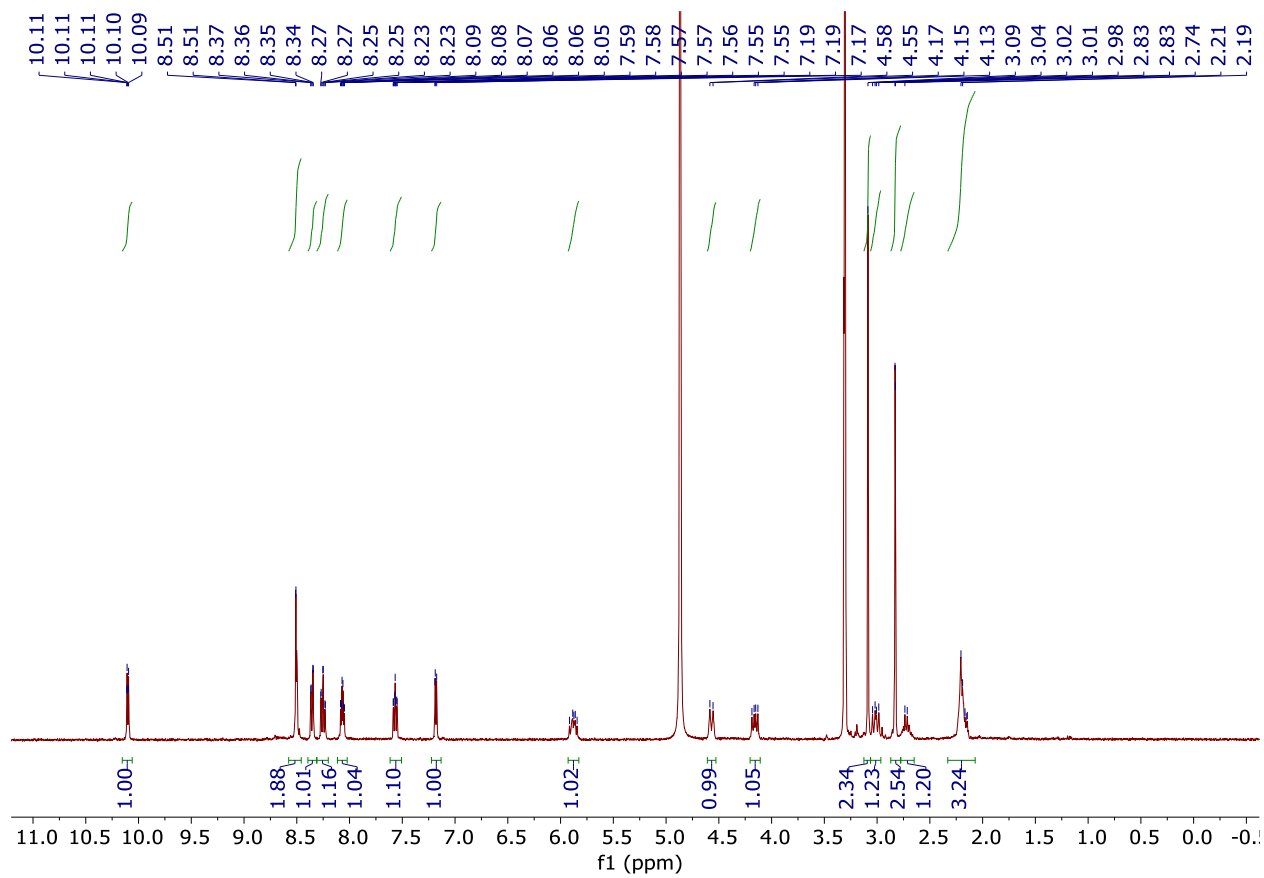
Figure A.35 ^{1}H-NMR Spectrum of [Co(L-CH$_2$CH$_2$-L)Br$_2$]Br in CD$_3$OD-d_4 (δ 3.31 solvent residual peak, δ 4.87 water peak)
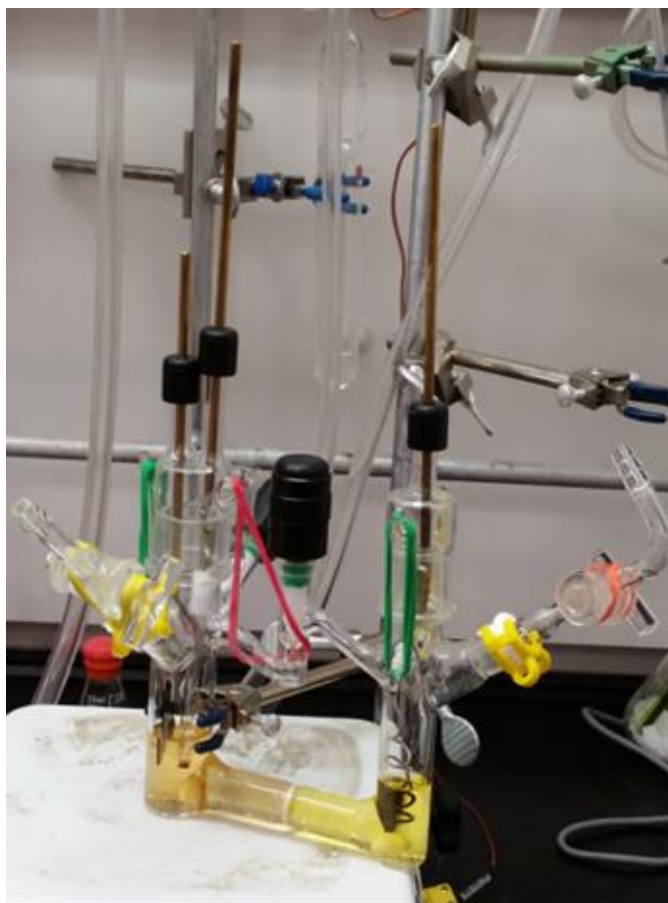
Figure A.36 The two-chamber H-cell used for controlled-potential electrolysis experiments. The first chamber (left) holds the glassy carbon working electrode and Ag/AgNO$_3$ (1.0 mM)/MeCN(0.1 M nBu$_4$NPF$_6$) reference electrode, and is filled with 20 mL solution of MeCN containing 0.3 mM catalyst, 0.1 M nBu$_4$NPF$_6$, and the reported concentrations of H$_2$O. The second chamber (right) holds the Nichrome wire counter electrode in a 15 mL solution of MeCN containing 0.1 M nBu$_4$NPF$_6$, 5 mM Fc, and the same concentration of H$_2$O as the first chamber. The two chambers as separated by a fine-porosity glass frit.
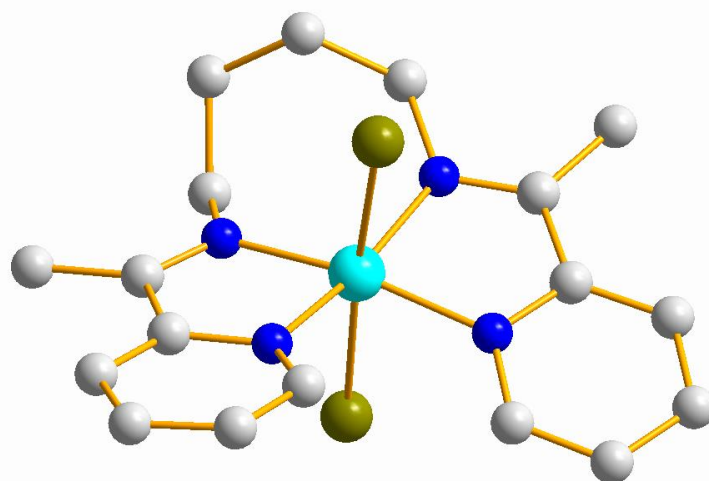
Figure A.37 The optimized structure of $[Co^{3+}(L\text{-}CH_2CH_2\text{-}L)Br_2]$ from the DFT calculation. Hydrogen atoms are omitted for clarity. Color code: Co (pink); N (blue) and C (gray).
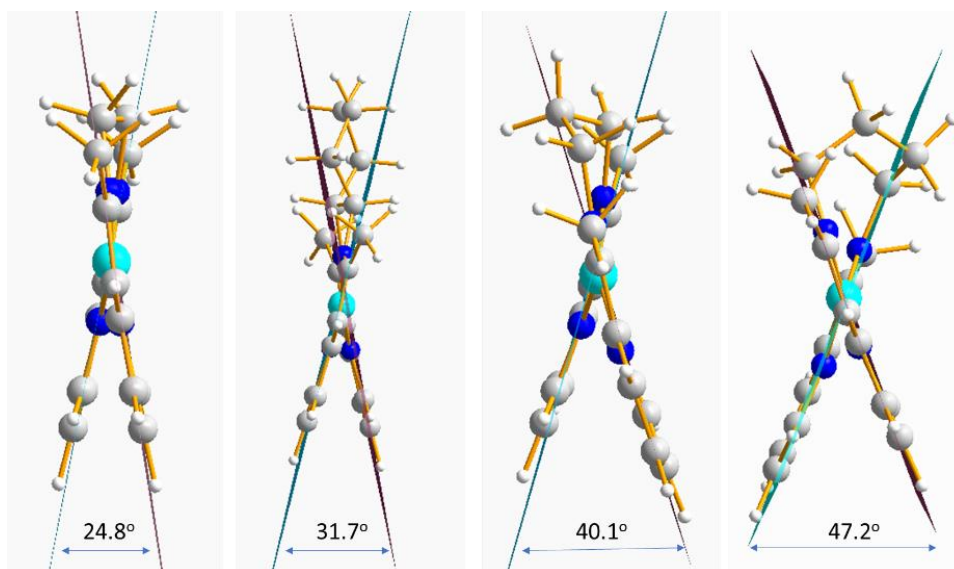
Figure A.38 The twist angle between pyridyl planes in the structure of $[Co^+(L\text{-}L^{\bullet-})]$, $[Co^+(L\text{-}cyc\text{-}L^{\bullet-})]$, $[Co^+(L\text{-}CH_2\text{-}L^{\bullet-})]$ and $[Co^+(L\text{-}CH_2CH_2\text{-}L^{\bullet-})]$ (from left to right) based on DFT calculations.
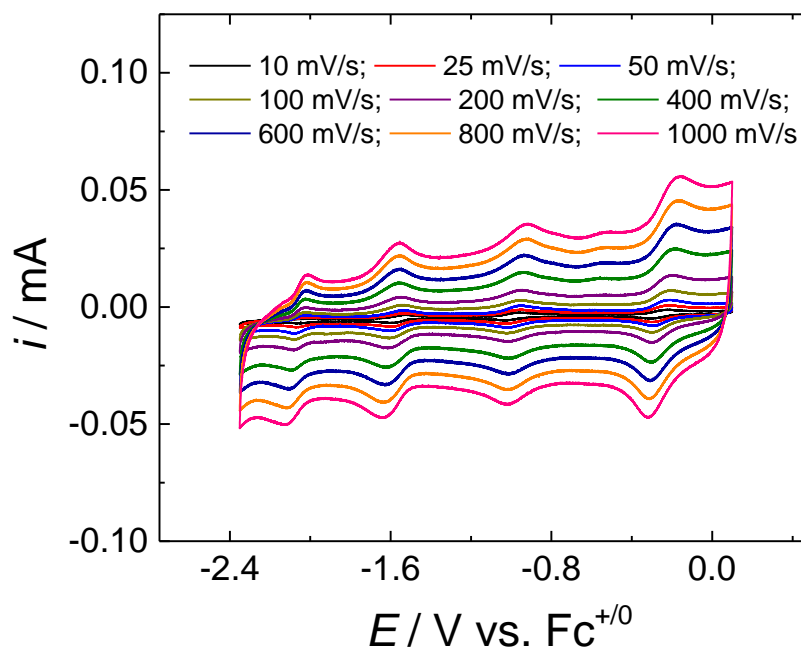
Figure A.39 CVs of 0.3 mM [Co(L-cyc-L)Br₂]Br at different scan rates in MeCN with 0.1 M nBu₄NPF₆ under N₂.
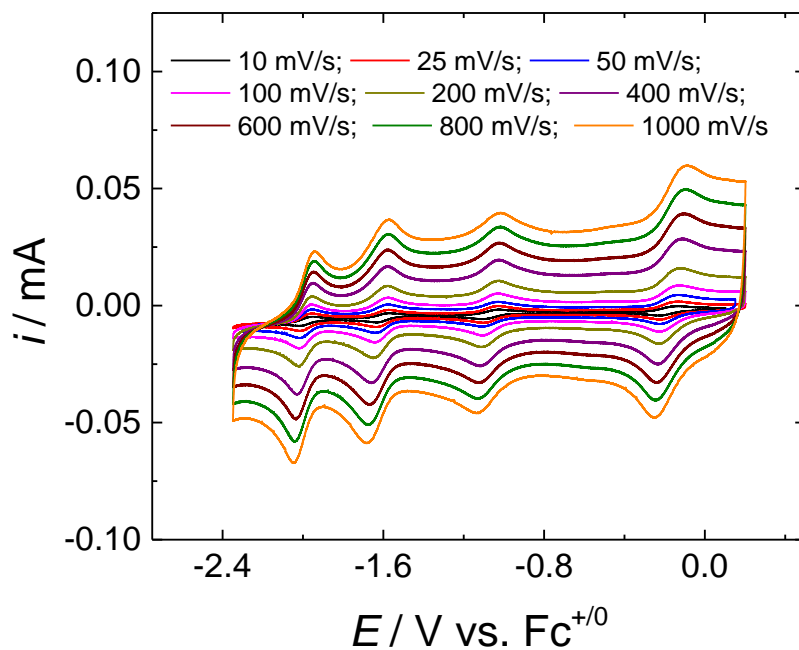
Figure A.40 CVs of 0.3 mM [Co(L-CH₂-L)Br₂]Br at different scan rates in MeCN with 0.1 M nBu₄NPF₆ under N₂.
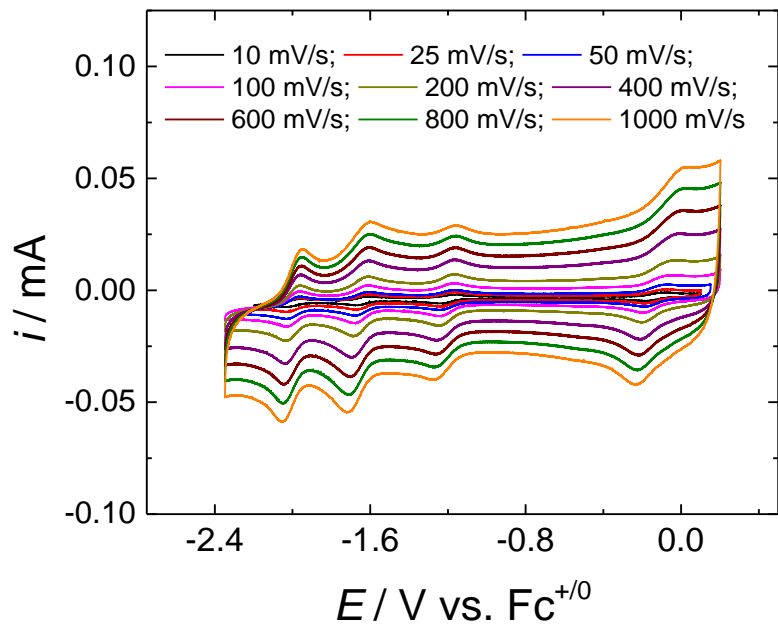
Figure A.41 CVs of 0.3 mM [Co(L-CH$_2$CH$_2$-L)Br$_2$]Br at different scan rates in MeCN with 0.1 M nBu$_4$NPF$_6$ under N$_2$.
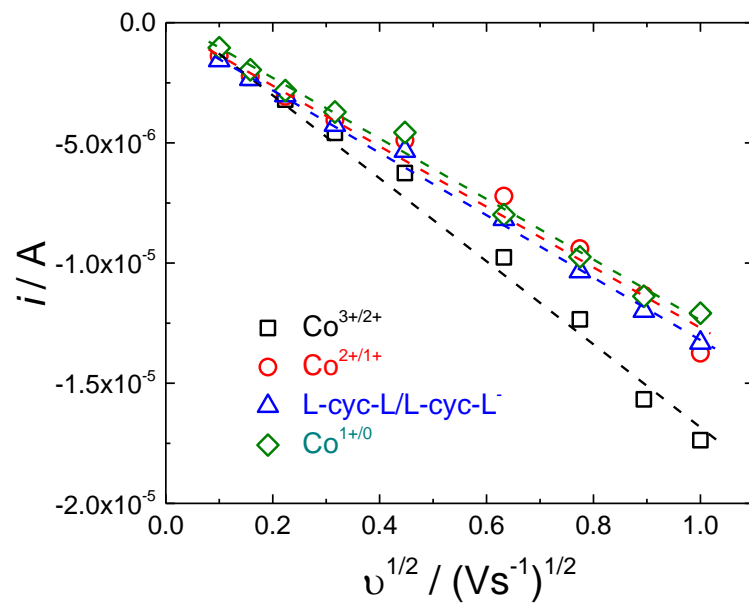
Figure A.42 Representative plots of i_p as a function of $v^{1/2}$ for the Co$^{3+/2+}$, Co$^{2+/+}$, L-cyc-L$^{0/-}$, and Co$^{+/0}$ couples for [Co(L-cyc-L)Br$_2$]Br based on the Randles-Sevcik equation.
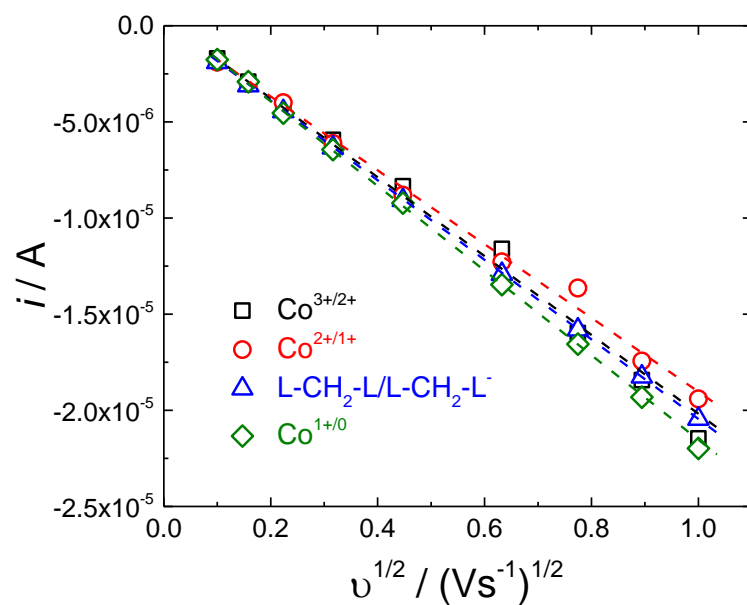
Figure A.43 Representative plots of i_p as a function of $v^{1/2}$ for the $Co^{3+/2+}$, $Co^{2+/+}$, L-CH2-L$^{0/-}$, and $Co^{+/0}$ couples for [Co(L-CH2-L)Br2]Br based on the Randles-Sevcik equation.
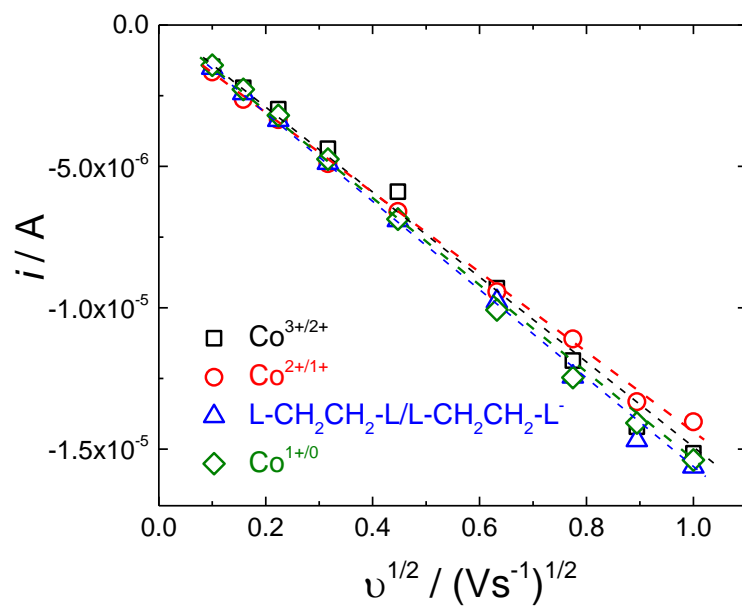
Figure A.44 Representative plots of i_p as a function of $v^{1/2}$ for the $Co^{3+/2+}$, $Co^{2+/+}$, L-CH2CH2-L$^{0/-}$, and $Co^{+/0}$ couples for [Co(L-CH2CH2-L)Br2]Br based on the Randles-Sevcik equation.
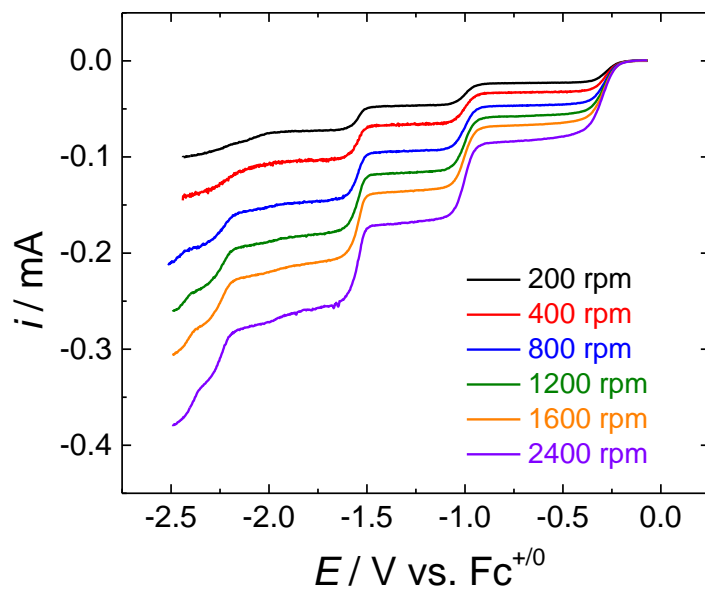
Figure A.45 Rotating disk voltammograms (RDVs) 0.3 mM [Co(L-cyc-L)Br$_2$]Br at different rotation rates in MeCN with 0.1 M nBu$_4$NPF$_6$ under N$_2$.
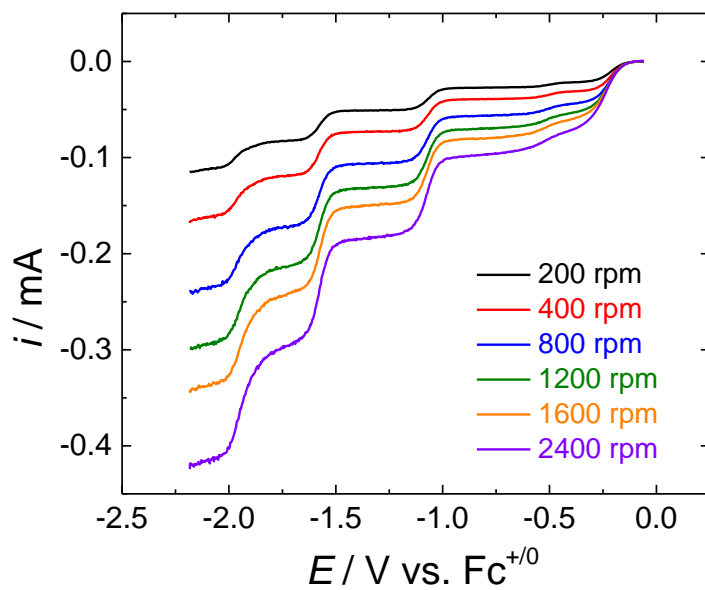
Figure A.46 Rotating disk voltammograms (RDVs) 0.3 mM [Co(L-CH$_2$-L)Br$_2$]Br at different rotation rates in MeCN with 0.1 M nBu$_4$NPF$_6$ under N$_2$.
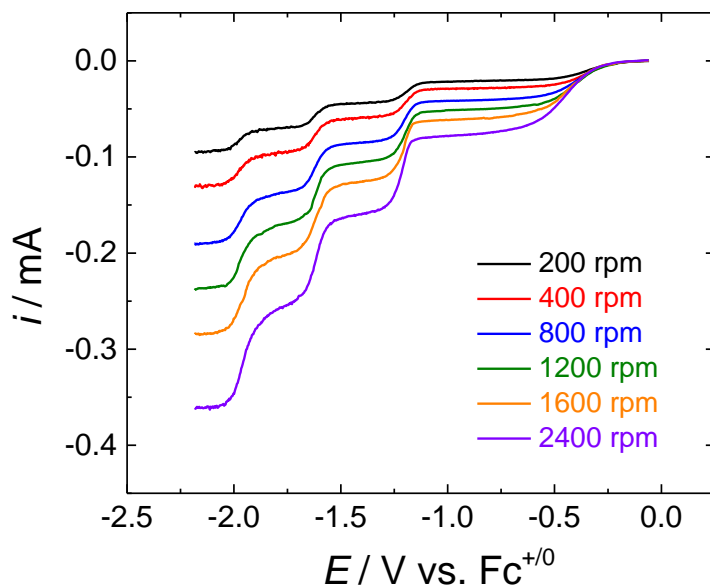
Figure A.47 Rotating disk voltammograms (RDVs) 0.3 mM [Co(L-CH$_2$CH$_2$-L)Br$_2$]Br at different rotation rates in MeCN with 0.1 M nBu$_4$NPF$_6$ under N$_2$.
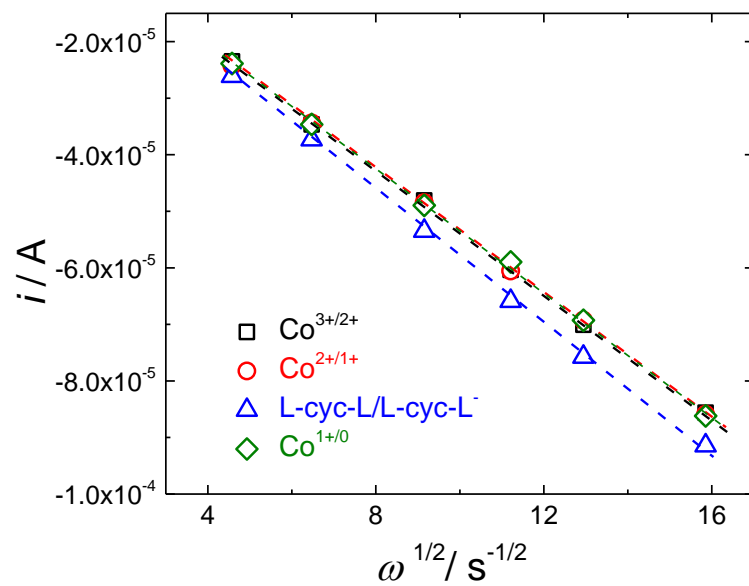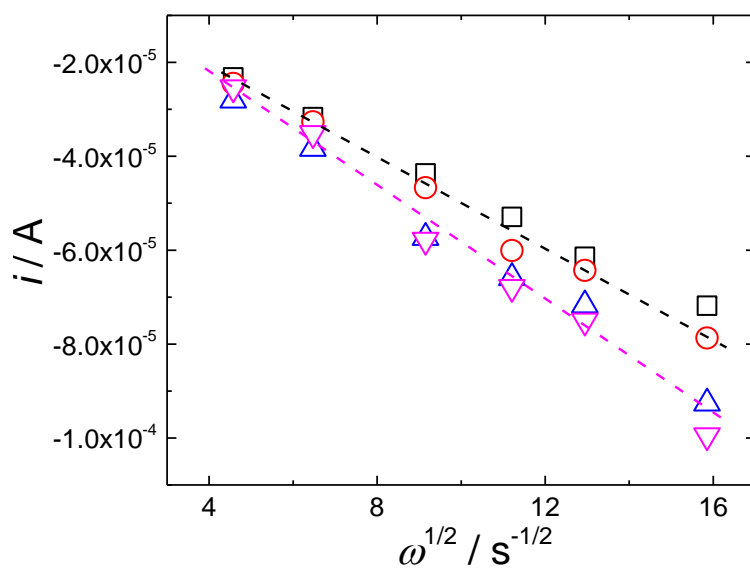

Figure A.48 Representative plots of i_L as a function of $\omega^{1/2}$ at potentials just negative of the Co$^{3+/2+}$, Co$^{2+/+}$, L-cyc-L$^{0/-}$, and Co$^{+/0}$ couple for [Co(L-cyc-L)Br$_2$]Br based on the Levich equation.
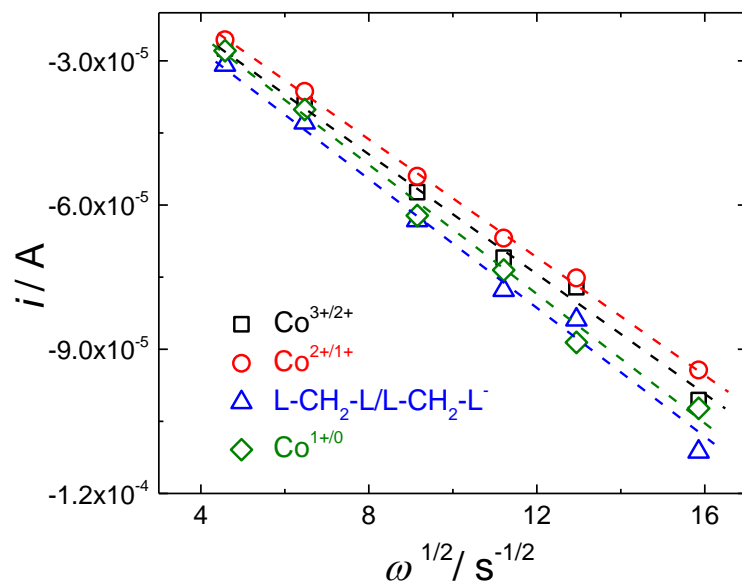
Figure A.49 Representative plots of i_L as a function of $\omega^{1/2}$ at potentials just negative of the $Co^{3+/2+}$, $Co^{2+/+}$, L-CH_2-$L^{0/-}$, and $Co^{+/0}$ couple for $[Co(L$-CH_2-$L)Br_2]Br$ based on the Levich equation.
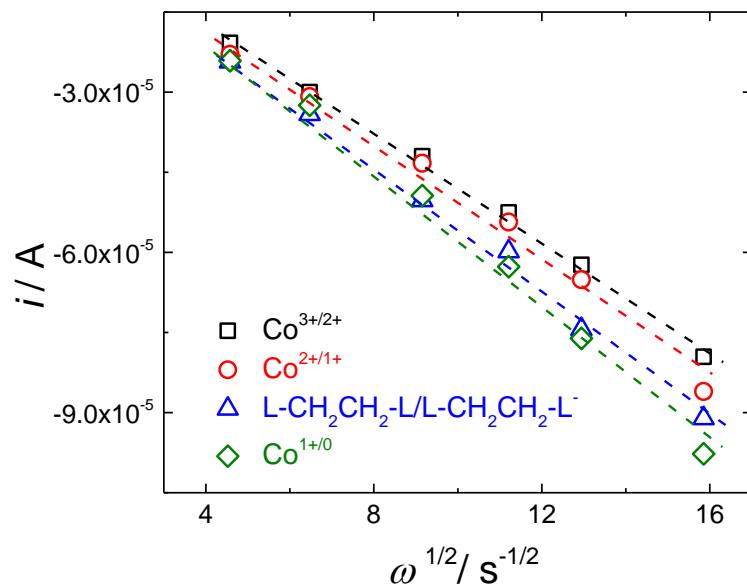
Figure A.50 Representative plots of i_L as a function of $\omega^{1/2}$ at potentials just negative of the $Co^{3+/2+}$, $Co^{2+/+}$, L-CH_2CH_2-$L^{0/-}$, and $Co^{+/0}$ couple for $[Co(L$-CH_2CH_2-$L)Br_2]Br$ based on the Levich equation.
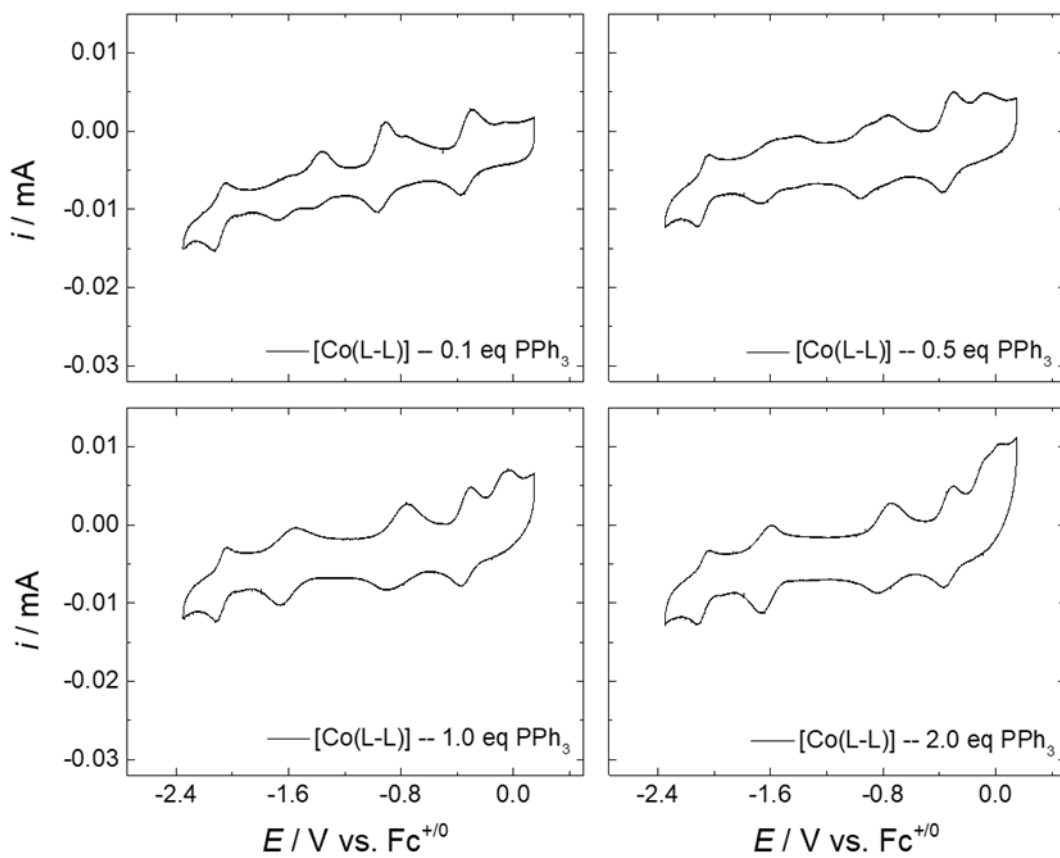
Figure A.51 CVs of 0.3 mM [Co(L-L)Br₂]Br with different equivalent of added PPh₃ in MeCN with 0.1 M nBu₄NPF₆ under N₂.
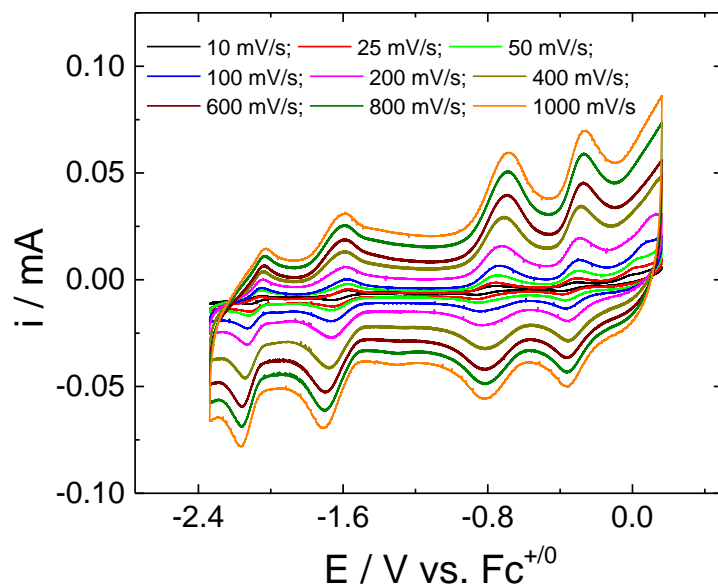
Figure A.52 CVs of 0.3 mM [Co(L-L)Br₂]Br with 2 equivalent of PPh₃ at different scan rates in MeCN with 0.1 M *n*Bu₄NPF₆ under N₂.
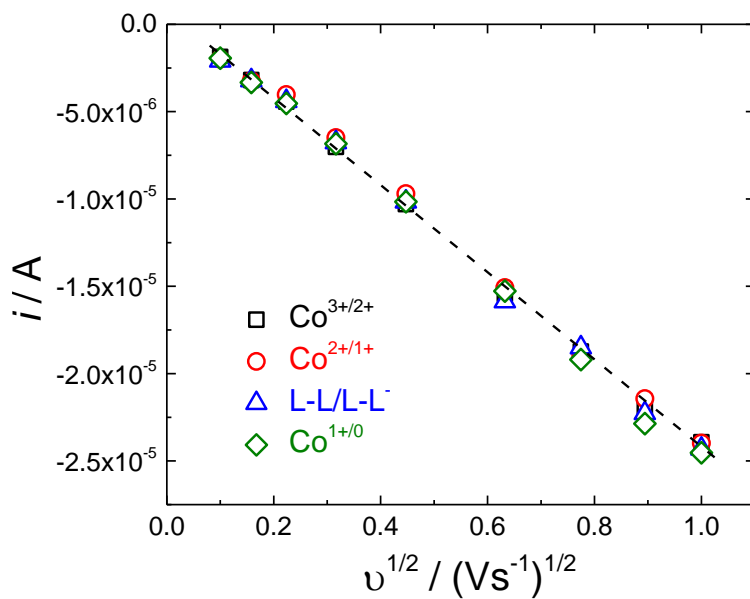
Figure A.53 Representative plots of i_p as a function of $v^{1/2}$ for the $Co^{3+/2+}$, $Co^{2+/+}$, L-L$^{0/-}$, and $Co^{+/0}$ couples for [Co(L-L)Br₂]Br with 2 equivalent of PPh₃ based on the Randles-Sevcik equation.
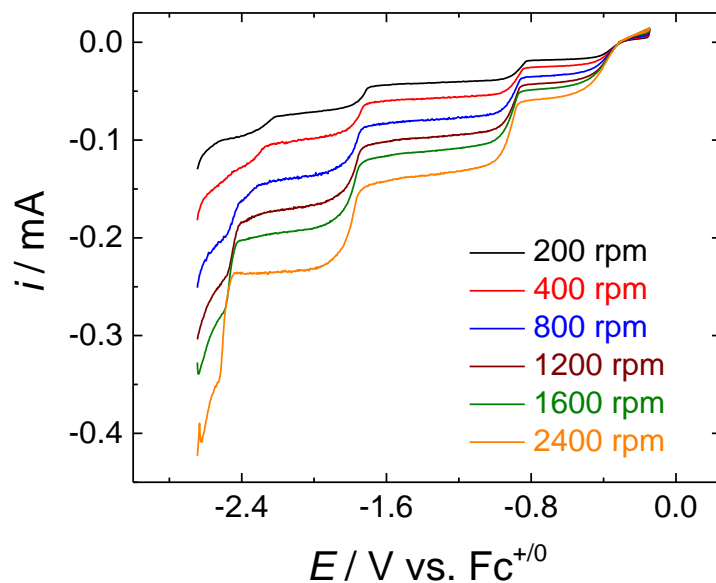
Figure A.54 Rotating disk voltammograms (RDVs) 0.3 mM [Co(L-L)Br$_2$]Br with 2 equivalent of PPh$_3$ based at different rotation rates in MeCN with 0.1 M nBu$_4$NPF$_6$ under N$_2$.

Figure A.55 Representative plots of i_L as a function of $\omega^{1/2}$ at potentials just negative of the Co$^{3+/2+}$, Co$^{2+/+}$, L-L$^{0/-}$, and Co$^{+/0}$ couple for [Co(L-L)Br$_2$]Br with 2 equivalent of PPh$_3$ based on the Levich equation.
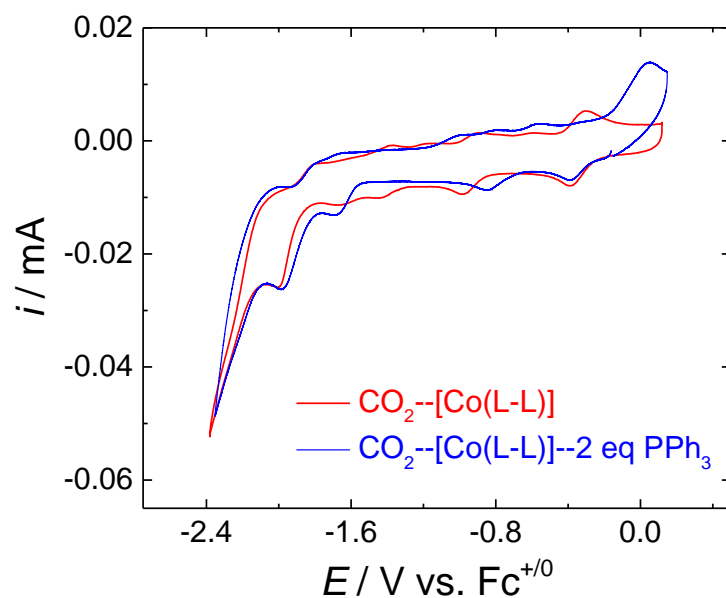
Figure A.56 The CV of [Co(L-L)] complex with 2 equivalents of PPh3 in MeCN solutions with 0.1 M nBu$_4$NPF$_6$ under N$_2$ and CO$_2$.
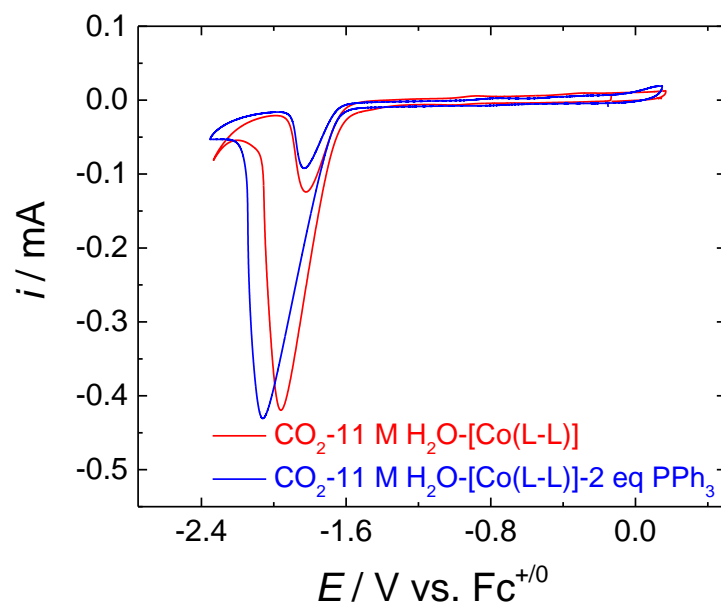
Figure A.57 The CV of [Co(L-L)] complex with 2 equivalents of PPh3 in MeCN solutions with 11 M H$_2$O and 0.1 M nBu$_4$NPF$_6$ under N$_2$ and CO$_2$.
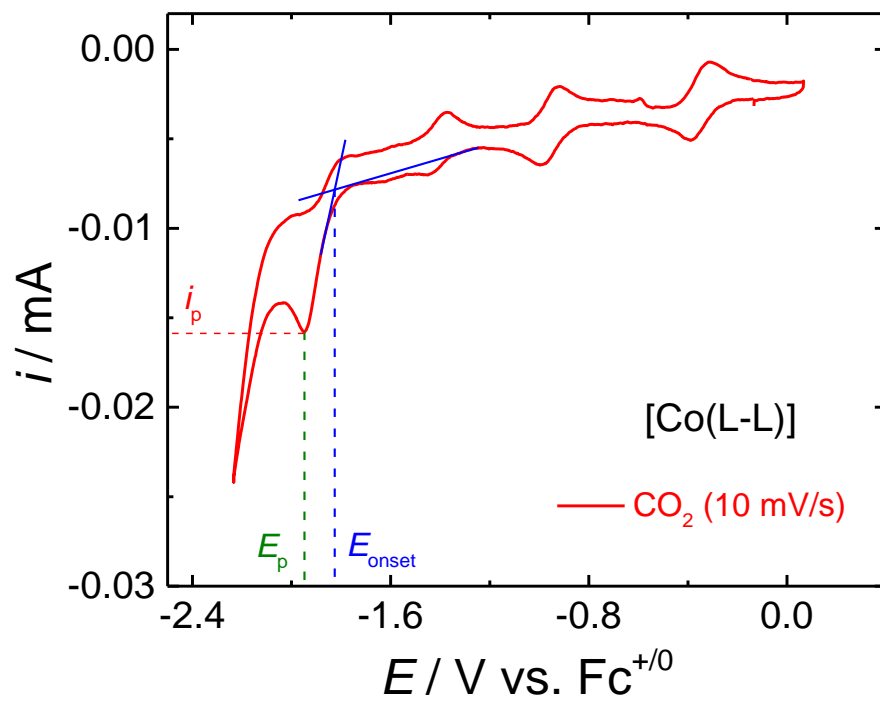
Figure A.58 Cyclic voltammograms of [Co(L-L)] complex under CO_2 (scan rate: 10 mV/s) with i_p, E_p and E_{onset} denoted. In our study, the catalytic peak current, i_p is the maximum current intensity of the catalytic peak at the peak potentials, E_p; the onset potential, E_{onset} is measured by linearly extrapolating the rising current portion of the current wave to the linear extrapolation of the baseline current, and the intercept potential is regarded as E_{onset}.
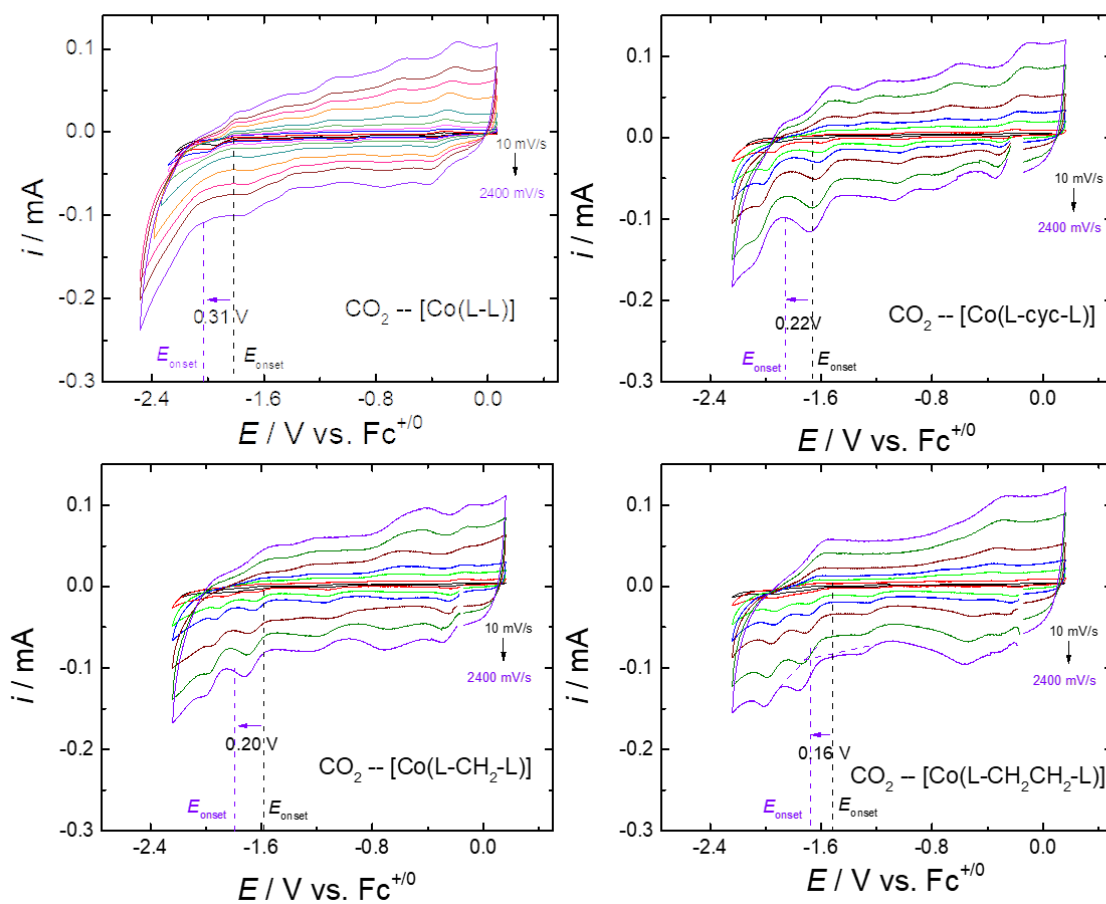
Figure A.59 Cyclic voltammograms of [Co(L-R-L)] complexes under CO_2 (scan rate:10, 25, 50, 100, 200, 400, 800, 1200, 1600, 2400 mV/s) with E_{onset} denoted.
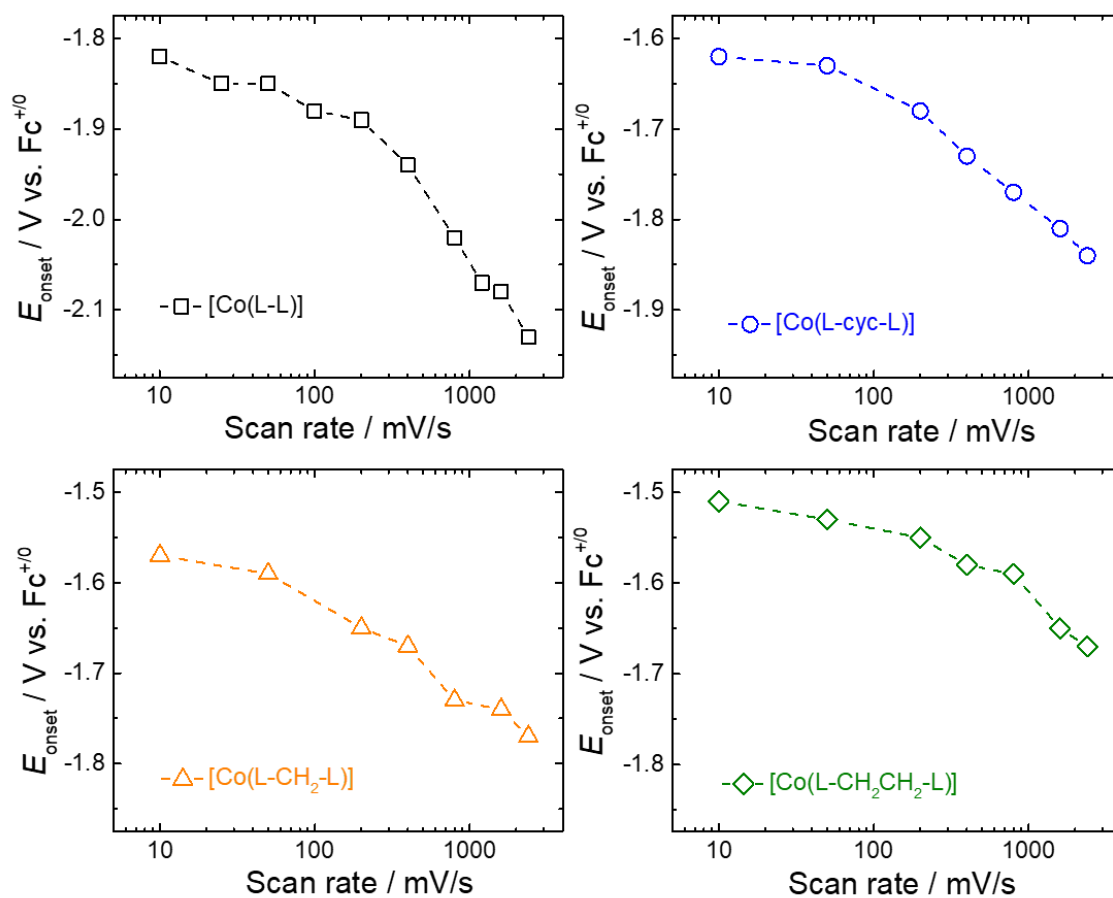
Figure A.60 The plots of E_{onset} of [Co(L-R-L)] for CO_2RR in the function of different scan rates of CV measurements (scan rate:10, 25, 50, 100, 200, 400, 800, 1200, 1600, 2400 mV/s).
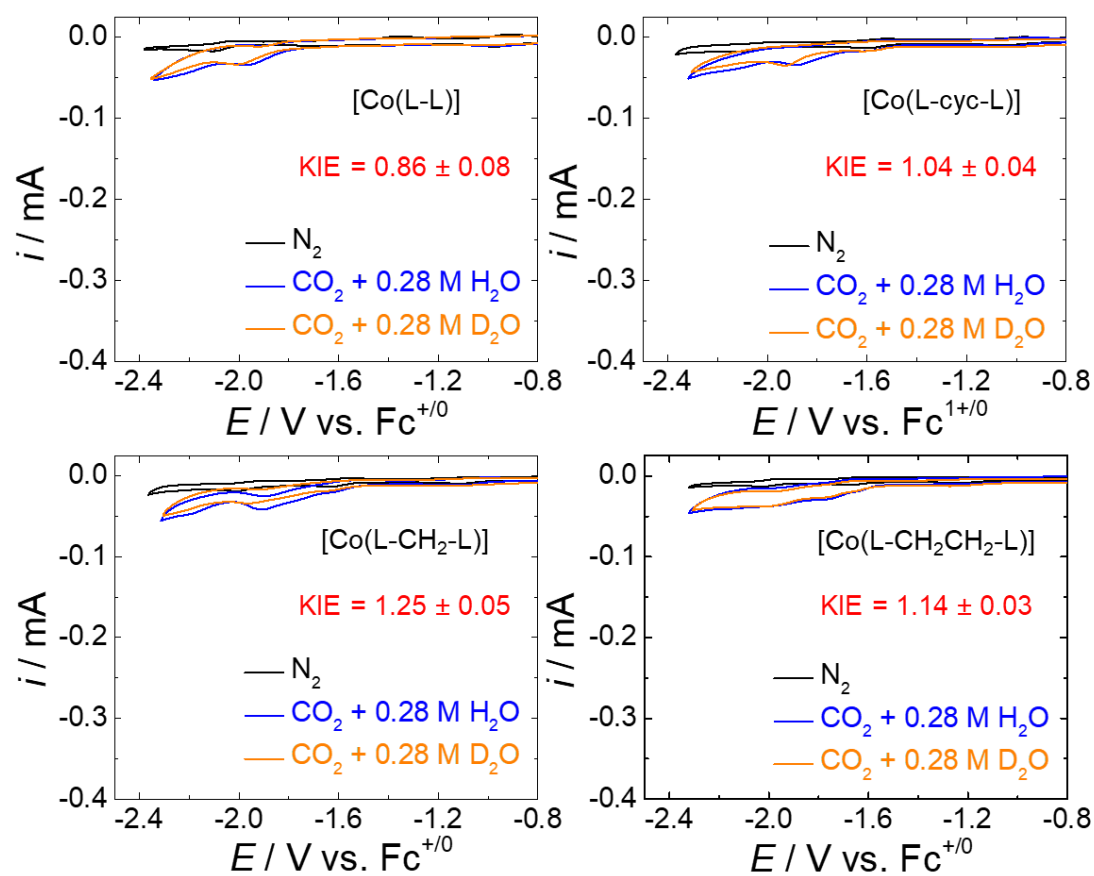
Figure A.61 CVs and KIE studies of all [Co(L-R-L)] complexes in MeCN solutions (with 0.1 M nBu$_4$NPF$_6$) in the presence of 0.28 M H$_2$O and D$_2$O under CO$_2$.
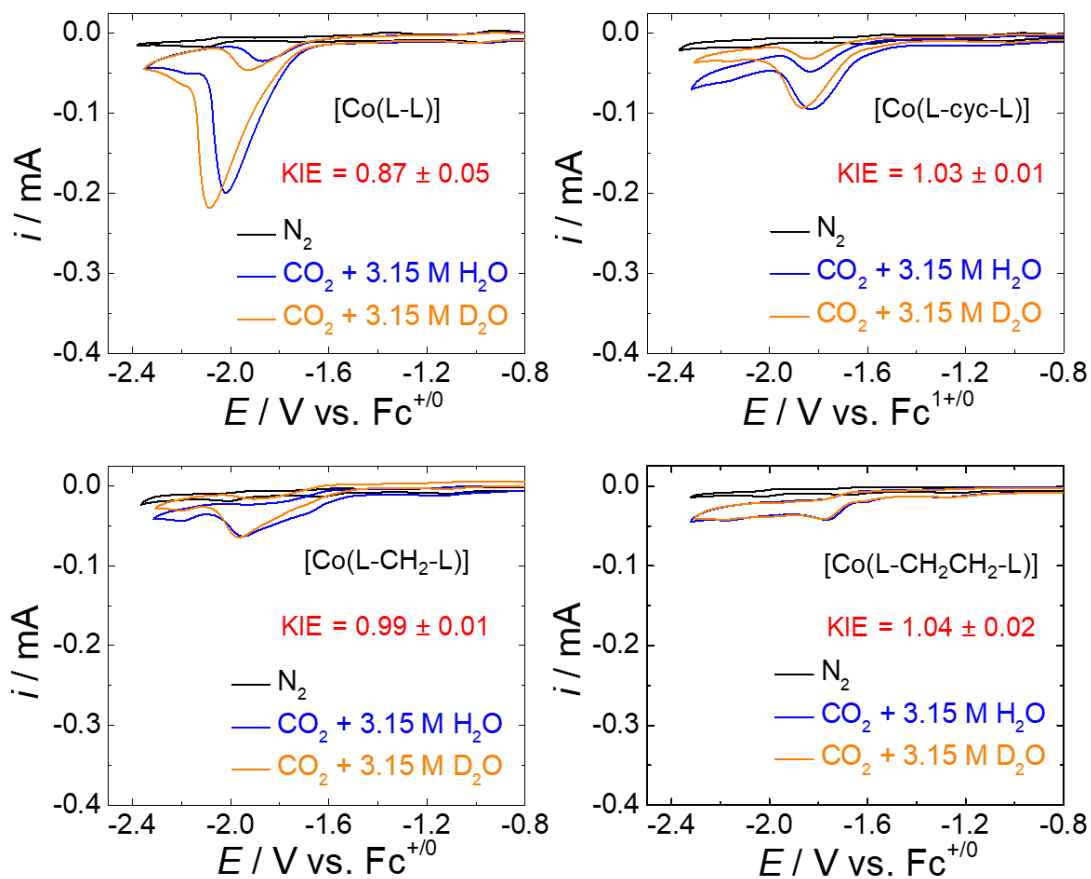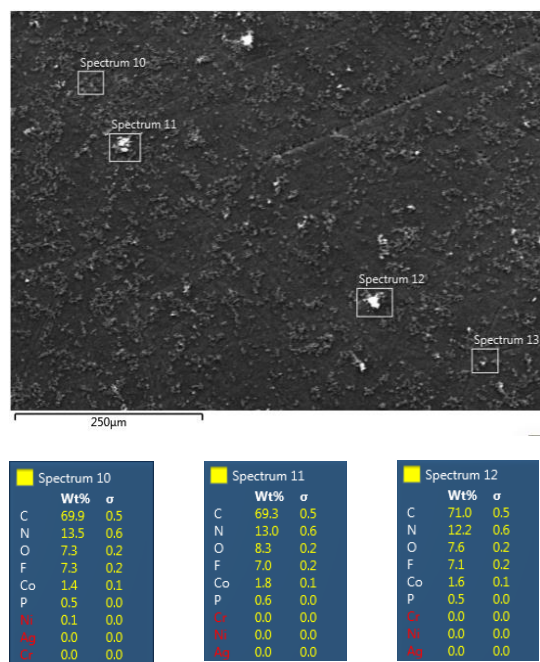
Figure A.62 CVs and KIE studies of all [Co(L-R-L)] complexes in MeCN solutions (with 0.1 M nBu$_4$NPF$_6$) in the presence of 3.15 M H$_2$O and D$_2$O under CO$_2$.
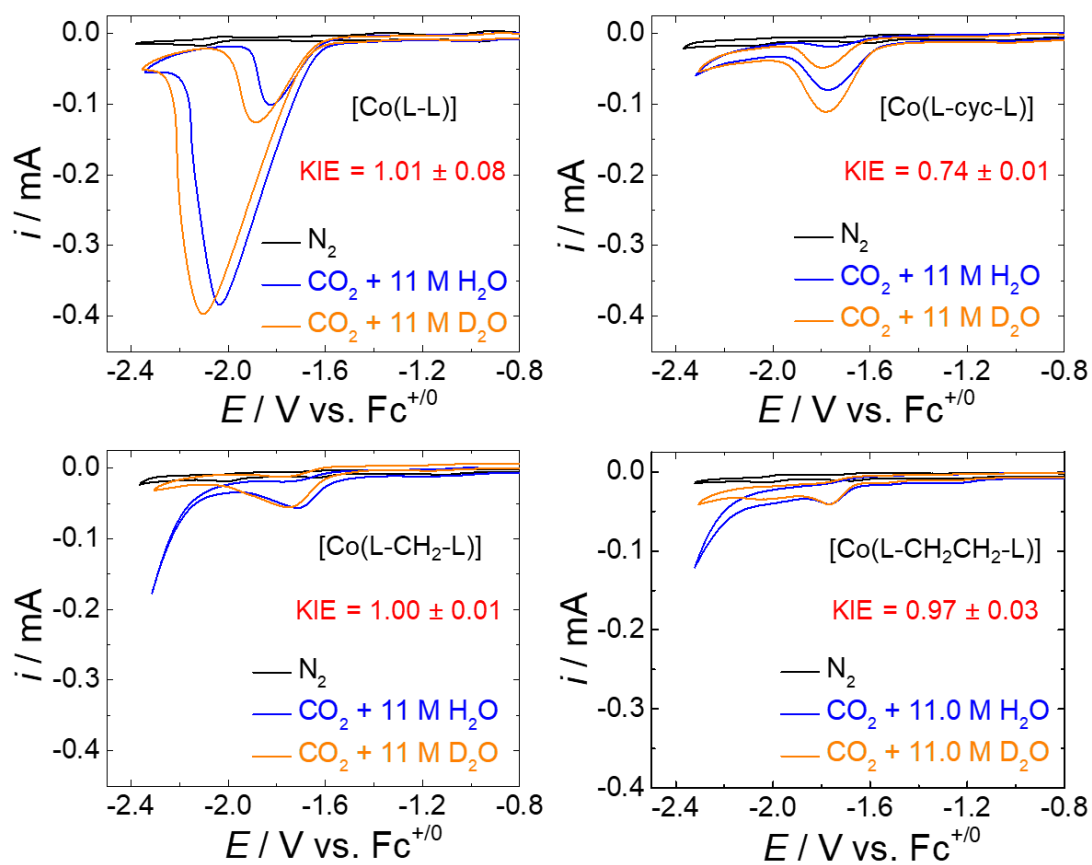
Figure A.63 CVs and KIE studies of all [Co(L-R-L)] complexes in MeCN solutions (with 0.1 M nBu$_4$NPF$_6$) in the presence of 11.0 M H$_2$O and D$_2$O under CO$_2$
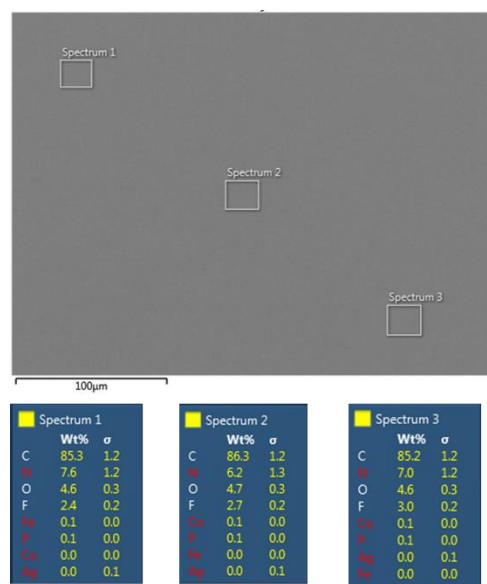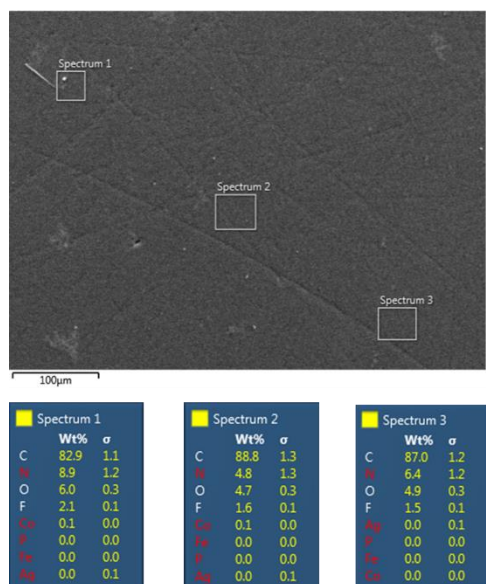
Figure A.64 SEM-EDS analysis of a working electrode surface after a 30-minute CO_2RR electrolysis of 0.3 mM [Co(L-L)] in acetonitrile with 0.1 M nBu_4PF_6 at -1.95V vs. $Fc^{+/0}$

Figure A.65 SEM-EDS analysis of a working electrode surface after a 30-minute CO_2RR electrolysis of 0.3 mM [Co(L-cyc-L)] in acetonitrile with 0.1 M nBu_4PF_6 at -1.95V vs. $Fc^{+/0}$
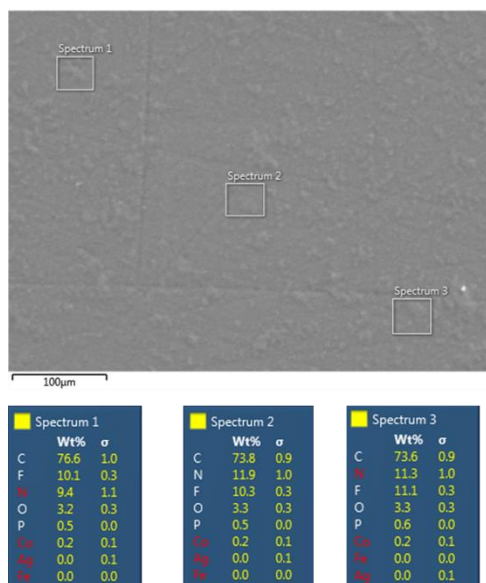
Figure A.66 SEM-EDS analysis of a working electrode surface after a 30-minute CO_2RR electrolysis of 0.3 mM [Co(L-CH$_2$-L)] in acetonitrile with 0.1 M nBu$_4$PF$_6$ at -1.95V vs. Fc$^{+/0}$

Figure A.67 SEM-EDS analysis of a working electrode surface after a 30-minute CO_2RR electrolysis of 0.3 mM [Co(L-CH$_2$CH$_2$-L)] in acetonitrile with 0.1 M nBu$_4$PF$_6$ at -1.95V vs. Fc$^{+/0}$
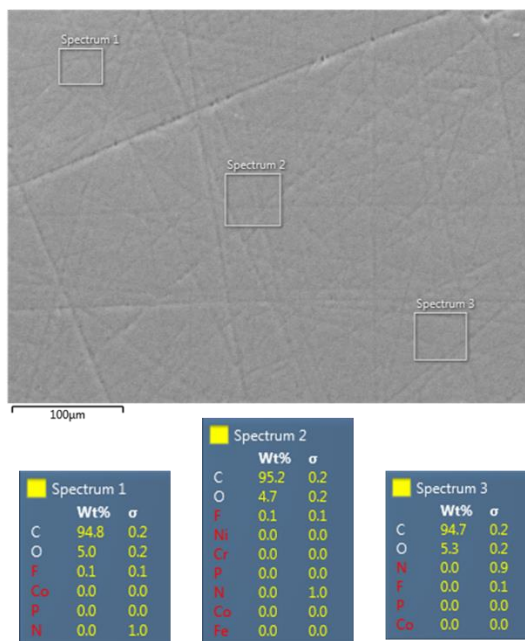
Figure A.68 SEM-EDS analysis of a working electrode surface at open circuit potential for 30 minutes in acetonitrile with 0.3 mM [Co(L-L)], 0.1 M nBu$_4$PF$_6$ and 11.0 M H$_2$O.
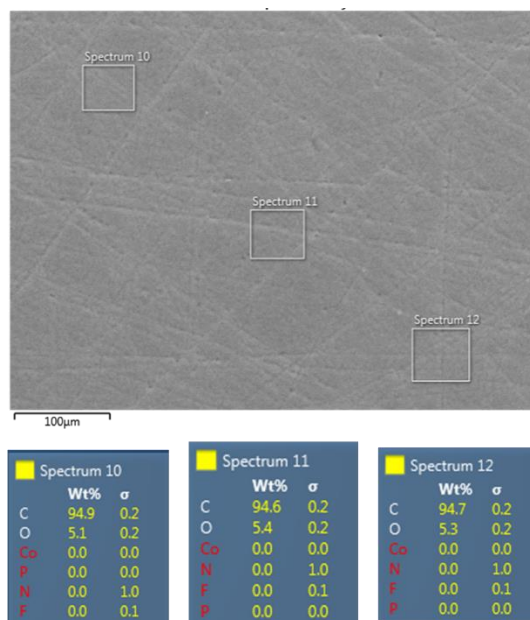

Figure A.69 SEM-EDS analysis of a working electrode surface at open circuit potential for 30 minutes in acetonitrile with 0.3 mM [Co(L-cyc-L)], 0.1 M nBu$_4$PF$_6$ and 11.0 M H$_2$O.

Figure A.70 SEM-EDS analysis of a working electrode surface at open circuit potential for 30 minutes in acetonitrile with 0.3 mM [Co(L-CH$_2$-L)], 0.1 M nBu$_4$PF$_6$ and 11.0 M H$_2$O.

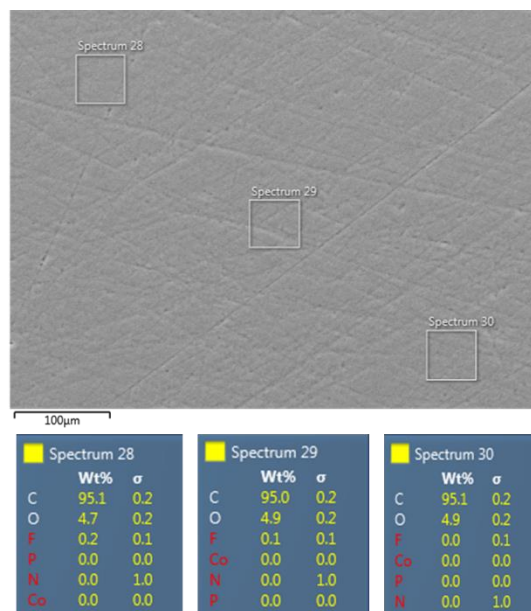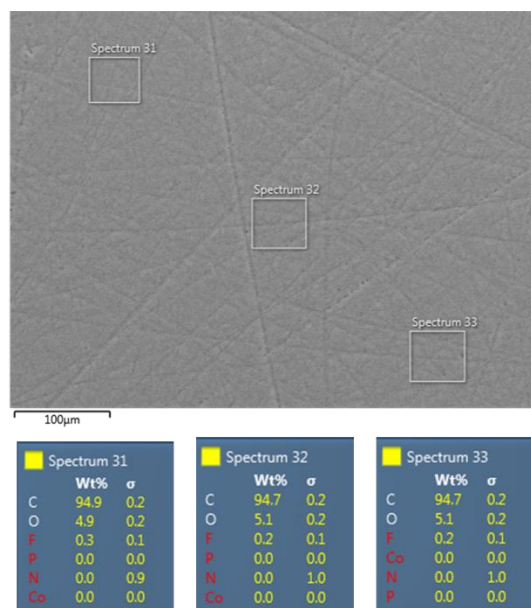**Figure A.71** SEM-EDS analysis of a working electrode surface at open circuit potential for 30 minutes in acetonitrile with 0.3 mM [Co(L-CH$_2$CH$_2$-L)], 0.1 M nBu$_4$PF$_6$ and 11.0 M H$_2$O.

Figure A.72 SEM-EDS analysis of a working electrode surface after a 30-minute CO_2RR electrolysis of 0.3 mM [Co(L-L)] in acetonitrile with 0.1 M nBu$_4$PF$_6$ and 11.0 M H_2O at -1.95V vs. Fc$^{+/0}$

Figure A.73 SEM-EDS analysis of a working electrode surface after a 30-minute CO_2RR electrolysis of 0.3 mM [Co(L-cyc-L)] in acetonitrile with 0.1 M nBu$_4$PF$_6$ and 11.0 M H_2O at -1.95V vs. Fc$^{+/0}$
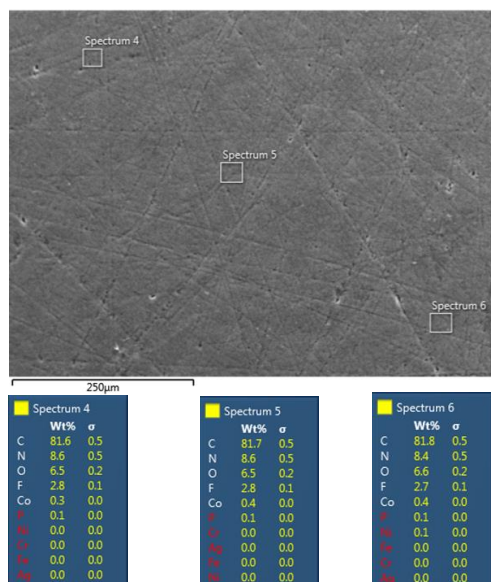
Figure A.74 SEM-EDS analysis of a working electrode surface after a 30-minute CO₂RR electrolysis of 0.3 mM [Co(L-CH₂-L)] in acetonitrile with 0.1 M nBu₄PF₆ and 11.0 M H₂O at -1.95V vs. Fc$^{+/0}$
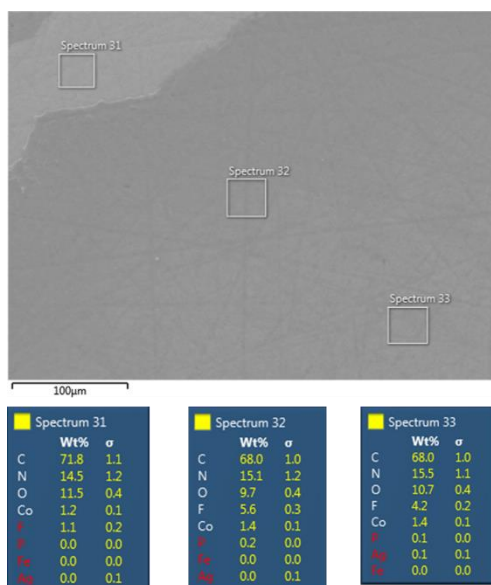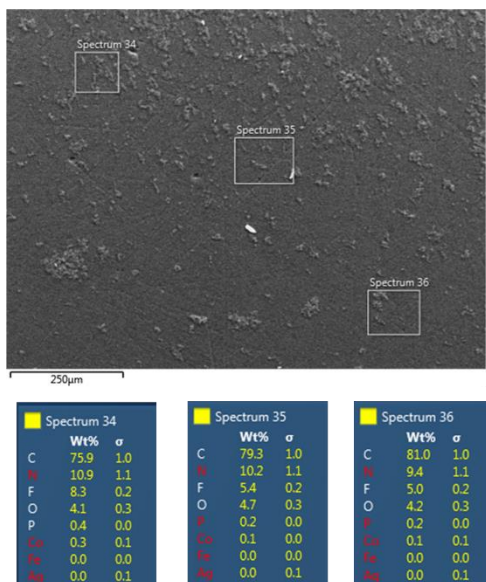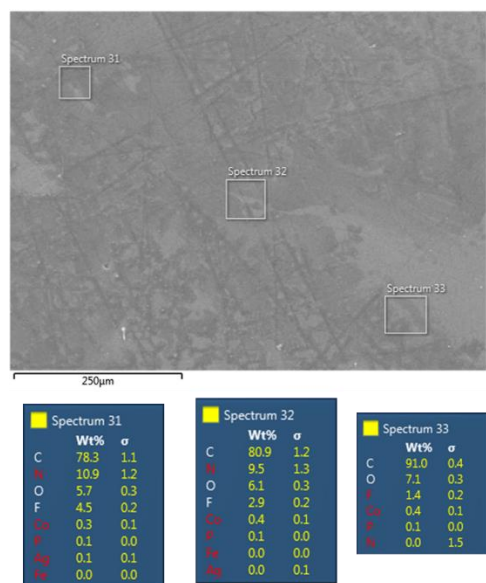

Figure A.75 SEM-EDS analysis of a working electrode surface after a 30-minute CO₂RR electrolysis of 0.3 mM [Co(L-CH₂CH₂-L)] in acetonitrile with 0.1 M nBu₄PF₆ and 11.0 M H₂O at -1.95V vs. Fc$^{+/0}$

Figure A.76 Cyclic voltammograms of [Co(L-L)] complex measured in each CO/N$_2$ mixture

Figure A.77 Cyclic voltammograms of [Co(L-cyc-L)] complex measured in each CO/N$_2$ mixture

Figure A.78 Cyclic voltammograms of [Co(L-CH2-L)] complex measured in each CO/N2 mixture

Figure A.79 Cyclic voltammograms of [Co(L-CH2CH2-L)] complex measured in each CO/N2 mixture

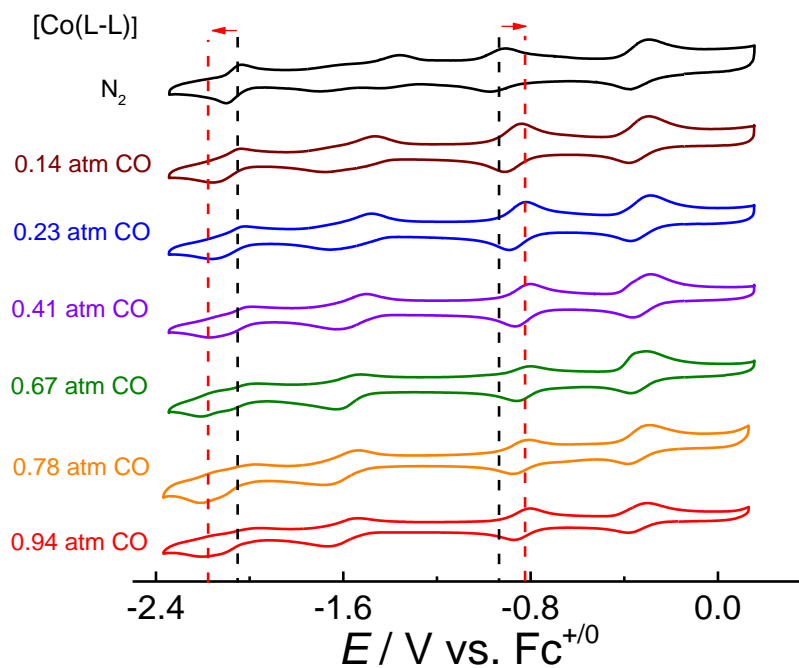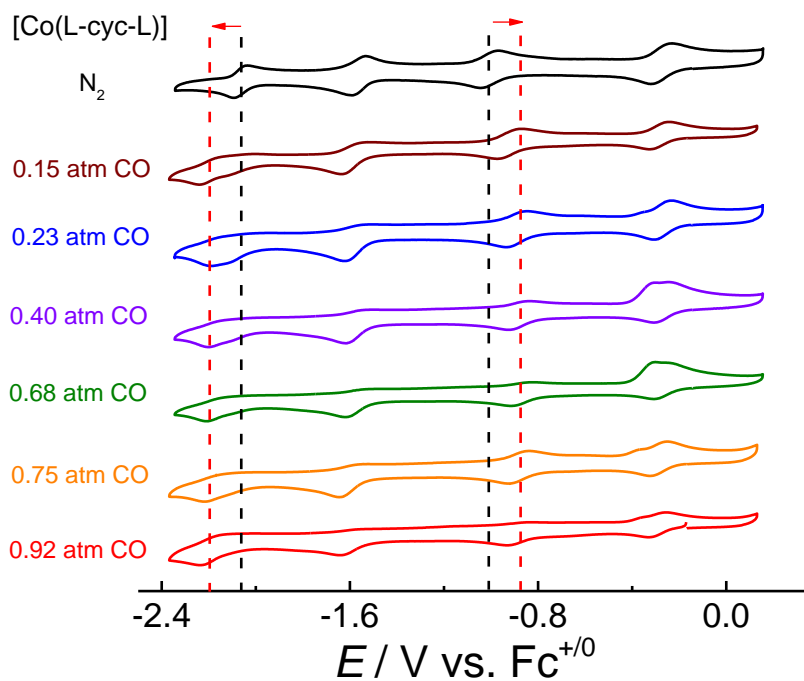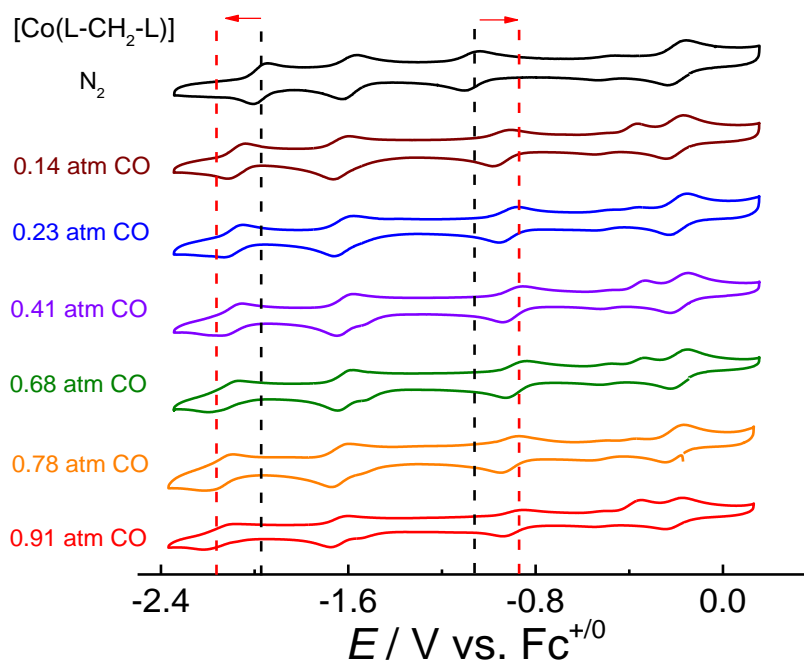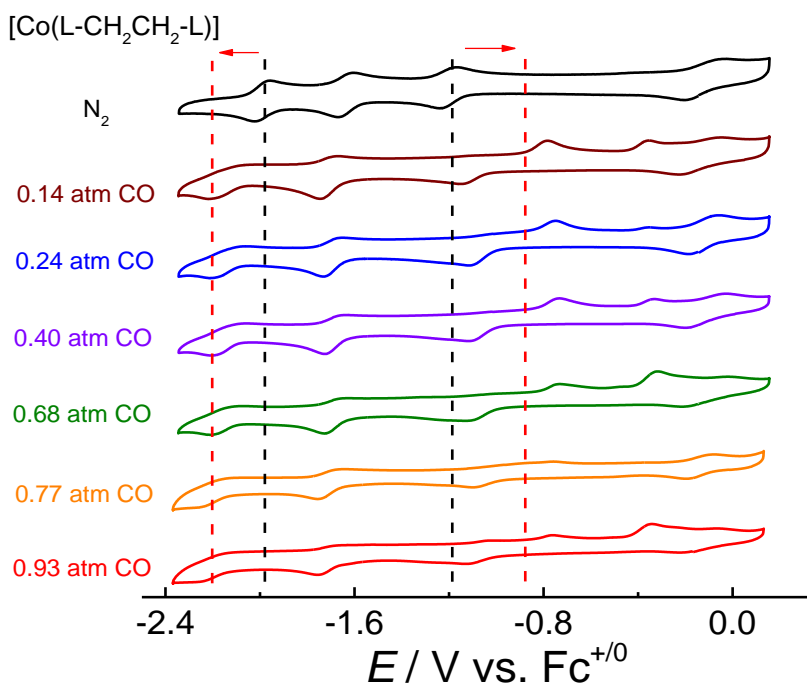## A.2.2 Supporting Tables

Table A.12 Control CPE experiments with Pt and bare GC working electrodes in MeCN solution with 1 M acetic acid under N_2 to show the cell is gastight.

Electrode	Electrolysis Time	Q / C	FE(H2) / %
Pt	60 min	31.8	102.2
GC	60 min	41.5	99.5

Table A.13 Crystal data and structure refinement for [Co(L-R-L)Br$_2$]Br catalysts

Formula	**[Co(L-L)Br$_2$]Br** ($C_{16}H_{18}Br_3CoN_4$)	**[Co(L-cyc-L)Br$_2$]Br** ($C_{20}H_{24}Br_3CoN_4$)	**[Co(L-CH$_2$-L)Br$_2$]Br** ($C_{17}H_{20}Br_3CoN_4$)
FW	565.00	655.07	579.03
Crystal system	triclinic	monoclinic	monoclinic
Space group	P$_{-1}$	P$_{21}$	C$_{12/c1}$
a (Å)	8.2736(4)	8.61750(10)	8.1492(3)
b (Å)	10.7007(5)	38.5636(5)	21.7174(9)
c (Å)	11.1674(4)	14.6145(2)	10.8432(3)
α (deg)	85.313(4)	90	90
β (deg)	71.078(4)	95.2430(10)	94.498(3)
γ (deg)	86.856(4)	90	90
Z	2	4	4
Volume (Å^3)	931.71(7)	4836.40(11)	1913.11(12)
Temperature (K)	293(2)	85(2)	85(2)
Density (g/mL)	2.014	1.7992	2.01022
Reflections collected / unique	13611 / 3345 [R(int) = 0.0293]	74825 / 15418 [R(int) = 0.0696]	14137 / 1748 [R(int) = 0.0704]
Final R indices [I>2sigma(I)]	R1 = 0.0253 wR2 = 0.0654	R1 = 0.0422 wR2 = 0.1105	R1 = 0.0344 wR2 = 0.1032
R indices (all data)	R1 = 0.0254 wR2 = 0.0655	R1 = 0.1169 wR2 = 0.0655	R1 = 0.0346 wR2 = 0.1035
Goodness-of-fit on F^2	1.137	1.000	1.132

Table A.14 The comparison of structural parameters of [Co(L-R-L)Br$_2$]Br complexes from DFT calculations and X-ray diffraction experimental data. [Co(L-CH$_2$CH$_3$-L)Br$_2$]Br has no X-ray diffraction experimental data.

Structure parameters	[Co(L-L)Br$_2$]Br		[Co(L-cyc-L)Br$_2$]Br		[Co(L-CH$_2$-L)Br$_2$]Br		Co(L-CH$_2$CH$_3$-L)
	X-ray	DFT	X-ray	DFT	X-ray	DFT	DFT
Co-N1 / Å	1.971(2)	1.996	1.959(2)	1.961	1.973(3)	1.958	1.946
Co-N2 / Å	1.868(2)	1.868	1.890(2)	1.887	1.933(3)	1.872	1.938
Co-N3 / Å	1.865(2)	1.874	1.893(2)	1.870	1.933(3)	1.919	1.902
Co-N4 / Å	1.961(2)	1.996	1.942(2)	1.975	1.973(3)	1.951	1.942
N1-Co-N2 / ⁰	82.52(8)	82.63	82.62(30)	83.63	81.33(10)	82.72	82.89
N2-Co-N3 / ⁰	85.80(9)	86.28	86.33(30)	87.66	96.56(11)	98.12	102.70
N3-Co-N4 / ⁰	82.78(8)	82.58	82.88(30)	83.68	81.33(10)	83.03	82.81
N4-Co-N1 / ⁰	109.23(8)	110.97	108.17(30)	108.14	101.01(10)	99.91	100.84

Table A.15 ($n^{3/2}CD_{obs}^{1/2}$) and ($nCD_{obs}^{2/3}$) of [Co(L-L)] at each redox couple calculated based on Randles-Sevcik equation and Levich equation.

	Co$^{3+/2+}$	Co$^{2+/+}$	L-L/L-L$^{\bullet-}$		Co$^{+/0}$
($n^{3/2} \cdot C \cdot D^{1/2}_{obs}$) / mol·cm^{-2}·s$^{-1/2}$ from Randles-Sevcik equation	(13.3 ± 2.0) $\times 10^{-10}$	(13.6 ± 3.1) $\times 10^{-10}$	(5.4 ± 1.2) $\times 10^{-10}$	(4.4 ± 0.6) $\times 10^{-10}$	(12.5 ± 2.9) $\times 10^{-10}$
($n \cdot C \cdot D^{2/3}_{obs}$) / mol·cm$^{-5/3}$·s$^{-2/3}$ from Levich equation	(18.9 ± 4.3) $\times 10^{-11}$	(20.0 ± 4.0) $\times 10^{-11}$	(13.7 ± 2.7) $\times 10^{-11}$	(11.1 ± 2.1) $\times 10^{-11}$	(17.9 ± 4.4) $\times 10^{-11}$

Table A.16 The onset potentials of [Co(L-R-L)] for CO$_2$RR at different scan rates in CV measurements

[Co(L-L)]							
Scan rate / mV/s	10	25	50	100	200	400	800
E_{onset} / V vs.Fc$^{+/0}$	-1.82	-1.85	-1.86	-1.88	-1.89	-1.94	-2.02
Scan rate / mV/s	1200	1600	2400				
E_{onset} / V vs.Fc$^{+/0}$	-2.07	-2.08	-2.13				
[Co(L-cyc-L)]							
Scan rate / mV/s	10	50	200	400	800	1600	2400
E_{onset} / V vs.Fc$^{+/0}$	-1.62	-1.63	-1.68	-1.73	-1.77	-1.81	1.84
[Co(L-CH$_2$-L)]							
Scan rate / mV/s	10	50	200	400	800	1600	2400
E_{onset} / V vs.Fc$^{+/0}$	-1.57	-1.59	-1.65	1.67	-1.73	-1.74	-1.77
[Co(L-CH$_2$CH$_2$-L)]							
Scan rate / mV/s	10	50	200	400	800	1600	2400
E_{onset} / V vs.Fc$^{+/0}$	-1.51	-1.53	-1.55	-1.58	-1.59	-1.65	-1.67

Table A.17 SEM-EDS results for working electrode surface at open circuit potential for 30 minutes in the electrolyte solution with 0.03 M Co catalysts to show no decomposition.

catalyst	Co weight% on electrode from EDS
[Co(L-L)]	0
[Co(L-cyc-L)]	0
[Co(L-CH$_2$-L)]	0
[Co(L-CH$_2$CH$_2$-L)]	0

Table A.18 Control CPEs conducted with the post-electrolysis electrodes and the bare glassy carbon electrode in fresh CO_2-saturated electrolyte in the presence of 11.0 M H_2O with no Co complex.

Electrode	Q / C	$FE(H_2)$ / %	$FE(CO)$ / %	$FE(HCOOH)$ / %
Post-electrolysis electrode from CPE of [Co(L-cyc-L)]	4.1 ± 1.5	24.0 ± 15.4	0	0
Post-electrolysis electrode from CPE of [Co(L-CH₂-L)]	2.9 ± 0.2	29.6 ± 5.4	0	0
Post-electrolysis electrode from CPE of [Co(L- CH₂CH₂-L)]	4.0 ± 0.7	28.6 ± 6.1	0	0
Bare Glassy Carbon	2.0 ± 0.1	20.2 ± 4.1	0	0

Table A.19 Results of CPE experiments of [Co(L-L)] and [Co(L-R-L)] for CO_2RR with 11.0 M H_2O for 15 min, 30 min and 90 min.

Catalyst	$(E_p - iR)$ / V vs Fc$^{+/0}$	Time / min	Q / C	Faradaic efficiency / %			Co weight% on electrode from EDS
				CO	H_2	HCOOH	
[Co(L-L)]	-2.15	15	7.5 ± 1.5	96.8 ± 1.6	0.3 ± 0.2	0.1 ± 0.08	0
		30	16.2 ± 2.5	104.3 ± 5.5	0.6 ± 0.4	0	0.18%
		90	35.0 ± 3.3	50.9 ± 10.2	15.3 ± 8.6	0.7 ± 0.4	1.05%
[Co(L-cyc-L)]	-1.93	15	3.1 ± 0.2	6.4 ± 2.1	17.9 ± 5.4	0.1 ± 0.09	0.69%
		30	6.4 ± 0.4	5.6 ± 1.0	19.6 ± 3.6	0.4 ± 0.3	0.99%
		90	17.5 ± 1.2	2.2 ± 0.4	26.1 ± 6.3	0.1 ± 0.1	8.53%
[Co(L-CH₂-L)]	-1.93	15	3.1 ± 0.1	50.0 ± 1.7	0.3 ± 0.5	0	0.06%
		30	5.5 ± 0.2	51.2 ± 8.6	1.0 ± 0.7	1.1 ± 1.0	0.05%
		90	16.1 ± 1.4	42.3 ± 12.5	5.0 ± 1.3	0.4 ± 0.3	0.42%
[Co(L-CH₂CH₂-L)]	-1.89	15	2.5 ± 0.1	31.9 ± 9.0	5.7 ± 2.3	0	0
		30	5.6 ± 0.6	28.6 ± 9.2	9.1 ± 4.6	1.1 ± 0.9	0.31%
		90	16.4 ± 0.4	12.1 ± 1.7	13.0 ± 2.9	0.1 ± 0.07	2.73%

A.2.3 Supporting Methods

A.2.3.1 Diffusion Coefficients Calculations

Method 1: Randles-Sevcik Method

In CV measurements of homogenous molecular catalysts, the peak current in the absence of substrate is related to the diffusion coefficient of the species at the peak potential based on the Randles-Sevcik equation:

$$i_p = 0.446 n^{3/2} AC \left(\frac{\nu F^3 D_{obs}}{RT} \right)^{1/2}$$

Here, diffusion coefficient is expressed as D_{obs} based on the assumption that the effective concentration of electroactive species at each redox potential, C, is equal to the bulk concentration of [Co(L-R-L)Br$_2$]Br in solution. $n = 1$ is the number of electrons transferred for each redox event, $A = 0.0707$ cm^2 is the surface area of the electrode, $C = 3 \times 10^{-7}$ mol/cm^3 is the bulk concentration of [Co(L-R-L)Br$_2$]Br in solution, $T = 298$ K is the temperature, R is the ideal gas constant, F is Faraday's constant, and υ is the scan rate in units of V·s^{-1}.

Method 2: Rotating disk voltammetry (RDV)

Diffusion coefficients are also determined by using rotating disk voltammetry (RDV) of measuring the rotation-rate dependence of the plateau currents near each potential of interest. Representative RDVs at different rotation rates for [Co(L-cyc-L)Br$_2$]Br, [Co(L-CH$_2$-L)Br$_2$]Br and [Co(L-CH$_2$CH$_2$-L)Br$_2$]Br are shown in Figure S13-S15. The plateau currents, i_L, are related to the diffusion coefficient, D, by the Levich equation:

$$i_L = 0.62 n F A D^{2/3} v^{-1/6} C \omega^{1/2}$$

Here, $n = 1$ is the number of electrons transferred for each redox event, $A = 0.1963$ cm^2 is the surface area of the electrode, F is Faraday's constant, $v = 0.00448$ cm^2/s is the kinematic viscosity

of the electrolyte solution, $C = 3 \times 10^{-7}$ mol/cm^3 is the bulk concentration of [Co(BPMI)]Br$_3$ in solution, and ω is the angular momentum in units of s^{-1} calculated from the rotation rate (in rotations per minute, rpm) according to:

$$\omega = \frac{2\pi \times rpm}{60}$$

A.2.3.2 Turnover Frequency (TOF) calculations

Method 1 (TOF-A):

TOFs for CO_2RR products are calculated based on the total amount of the products (CO and HCOOH) generated divided by the total amount of the catalyst [Co(BPMI)] in the electrolyte solution and the time of the electrolysis:

$$TOF = \frac{\frac{n(CO) + n(HCOOH)}{n(Cat)}}{t}$$

$$n(CO) + n(HCOOH) = \frac{Q \times (FE(CO) + FE(HCOOH))}{2F}$$

$$n(Cat) = [Cat] \times V_{sol}$$

Here, n(CO) and n(HCOOH) are the total number of moles of CO and HCOOH produced, n(Cat) is the number of moles of the catalyst in the solution, and $t = 30$ s is the electrolysis time in seconds. Q is the amount of charge passed in Coulombs (C); FE(CO) and FE(HCOOH) are the Faradaic Efficiency of CO and HCOOH in percentage (%); $F = 96485$ C/mol is Faraday constant. $[Cat] = 3 \times 10^{-7}$ mol/cm^3 is the concentration of the catalyst; $V_{sol} = 20$ cm^3 is the volume of the solution.

Method 2 (TOF-B):

TOF values for CO are calculated from CPE data with the equations described by Savéant et al.

$$TOF = \frac{\frac{n(CO) + n(HCOOH)}{n(Cat)}}{t}$$

$$n(Cat) = A \sqrt{\frac{D}{k_{cat}}} [Cat] = A \sqrt{\frac{D}{TOF_{max}}} [Cat]$$

$$n(CO) + n(HCOOH) = \frac{Q \times (FE(CO) + FE(HCOOH))}{2F}$$

In the homogeneous case, n(Cat) is obtained by space integration of catalyst amount in the reaction-diffusion layer near the surface of the working electrode. $A = 2.56$ cm^2 is the active surface area of the working electrode, $t = 30$ s is the electrolysis time. D is the diffusion coefficient for the complex, k_{cat} is the reaction rate of catalysis process, TOF_{max} is the maximum turnover frequency obtained from CVs. It is used to replace k_{cat} in the calculation, $[Cat] = 3 \times 10^{-7}$ mol/cm^3 is the concentration of the catalyst, $F = 96485$ C/mol is Faraday constant.

The expression of TOF would be:

$$TOF = \frac{\dfrac{n(CO) + n(HCOOH)}{n(Cat)}}{t} = \frac{\dfrac{\frac{Q \times (FE(CO) + FE(HCOOH))}{F}}{A\sqrt{\dfrac{D}{TOF_{max}}}[Cat]}}{t}$$

$$i = \frac{Q \times (FE(CO) + FE(HCOOH))}{t}$$

$$TOF = \frac{i}{FA} \times \frac{\sqrt{TOF_{max}}}{\sqrt{D}[Cat]}$$

Assumption that the electron transfer process to the catalyst is fast and the Nernst equation is obeyed, the expression of TOF can be also expressed as:

$$TOF = \frac{TOF_{max}}{1 + exp\left[\frac{F}{RT}\left(E_{app} - E_{1/2}\right)\right]}$$

R is the universal gas constant, $T = 298.15$ K is temperature of the solution, E_{app} is the applied potential during electrolysis, $E_{1/2}$ is the ligand-based redox potential. Combination of the equations above gives:

$$TOF = \frac{i^2\left(1 + exp\left[\frac{F}{RT}\left(E_{app} - E_{1/2}\right)\right]\right)}{F^2 A^2 D[Cat]^2}$$

A.2.3.3 Optimized structures information

Cartesian coordinates (Å) of optimized structures using DFT/BP86 method.

Co(L-CH$_2$CH$_2$-L)]Br$_2$ (charge = +1)

C	-3.937588	-2.594671	0.518014
C	-3.949244	-1.262977	0.086493
C	-2.733641	-0.572779	-0.051721
N	-1.528934	-1.178260	0.189721
Co	0.015766	0.050687	0.014323
N	-1.409628	1.316616	-0.402962
C	-2.628155	0.841383	-0.431796
C	-3.856685	1.601763	-0.840401
C	-1.104383	2.645072	-0.967802
C	1.400961	2.805702	0.594024
N	1.488082	1.349327	0.270555
C	2.686745	0.814770	0.313626
C	3.939923	1.608512	0.559727
C	2.737371	-0.640207	0.117329
N	1.510243	-1.225505	-0.043024
C	1.453855	-2.527819	-0.391756
C	2.594830	-3.336040	-0.478191
C	3.848661	-2.767398	-0.230058
C	3.920164	-1.396736	0.046780
C	-1.532493	-2.435698	0.682692
C	-2.708486	-3.180556	0.842611
H	-4.872890	-3.150812	0.626418
H	-4.890573	-0.753074	-0.128985
H	-4.235347	1.219035	-1.805437
H	-4.652059	1.449160	-0.092180
H	-3.679767	2.680365	-0.928615

H	-0.156816	2.525967	-1.516154
H	-1.866431	2.922859	-1.711976
H	1.668489	3.364700	-0.324529
H	2.187923	3.016543	1.333845
H	3.996916	1.913725	1.621570
H	4.842792	1.029606	0.330308
H	3.953495	2.524393	-0.051767
H	0.475143	-2.936043	-0.638885
H	2.481296	-4.388723	-0.748931
H	4.760459	-3.368933	-0.280198
H	4.889894	-0.918236	0.193290
H	-0.574994	-2.857067	0.986260
H	-2.640844	-4.200730	1.228638
C	-0.960671	3.718553	0.111316
H	-0.649681	4.648917	-0.398749
H	-1.937284	3.917164	0.587478
C	0.072422	3.317771	1.169758
H	0.315113	4.198137	1.790624
H	-0.338461	2.555544	1.851892
Br	-0.063296	0.002713	2.544682
Br	0.172746	-0.142197	-2.502177

[Co(L-CH$_2$CH$_2$-L)] (charge = 0)

C	-3.833282	-2.531020	0.799347
C	-3.873356	-1.303995	0.137614
C	-2.685152	-0.560210	-0.059390
N	-1.442896	-1.070886	0.350859
Co	0.026685	0.091656	0.065613
N	-1.310109	1.240684	-0.538310
C	-2.568323	0.760317	-0.614244

C	-3.720207	1.509499	-1.232685
C	-1.010067	2.586130	-1.038871
C	1.349038	2.705980	0.859577
N	1.446893	1.297134	0.410028
C	2.693453	0.776015	0.369704
C	3.934268	1.566904	0.691914
C	2.723900	-0.617816	0.021204
N	1.437879	-1.162391	-0.116354
C	1.342346	-2.448044	-0.571644
C	2.445343	-3.257166	-0.832655
C	3.747027	-2.732969	-0.631434
C	3.874757	-1.409333	-0.212950
C	-1.438830	-2.251147	1.038794
C	-2.586698	-3.003293	1.281016
H	-4.750520	-3.105853	0.959850
H	-4.826048	-0.898448	-0.215920
H	-3.572636	1.661030	-2.318849
H	-4.664613	0.959859	-1.106160
H	-3.854196	2.508601	-0.781170
H	-0.024835	2.543075	-1.533963
H	-1.742477	2.910192	-1.799298
H	1.729080	3.373644	0.057260
H	2.028530	2.847082	1.720068
H	3.985551	1.830621	1.766270
H	4.846749	1.002104	0.452290
H	3.970382	2.516523	0.128894
H	0.327619	-2.825732	-0.720787
H	2.289055	-4.280526	-1.185671
H	4.634464	-3.345752	-0.816868
H	4.867269	-0.969624	-0.078954

H	-0.461868	-2.589972	1.394707
H	-2.506384	-3.943382	1.834107
C	-0.957324	3.607284	0.113670
H	-0.583259	4.563455	-0.299728
H	-1.979705	3.797988	0.489695
C	-0.058470	3.156665	1.276956
H	0.052179	3.999203	1.983857
H	-0.538601	2.333409	1.836941

[Co(L-CH$_2$-L)]Br$_2$ (charge = +1)

C	-1.698787	3.584269	3.051208
C	-2.073238	2.237061	3.145984
C	-1.419478	1.283105	2.349422
N	-0.385004	1.635772	1.522317
Co	0.421088	0.105329	0.594469
N	-1.141848	-0.787241	1.306866
C	-1.835553	-0.118679	2.194181
C	-3.017362	-0.686769	2.929172
C	-1.535179	-2.153128	0.940420
C	-0.348631	-3.056211	0.616253
C	0.396128	-2.644360	-0.648417
N	1.071800	-1.348244	-0.509845
C	2.072145	-1.056639	-1.303110
C	2.557815	-1.969114	-2.391643
C	2.726816	0.222051	-0.997096
N	2.125304	0.908088	0.024740
C	2.777127	1.952214	0.576335
C	3.990002	2.434762	0.064393
C	4.562178	1.798971	-1.043279
C	3.932490	0.661510	-1.566416

C	-0.090581	2.942589	1.369441
C	-0.717045	3.945851	2.122277
H	-2.193562	4.338878	3.669020
H	-2.877895	1.936512	3.819576
H	-2.721162	-1.586130	3.496736
H	-3.445293	0.034045	3.636325
H	-3.808550	-0.985252	2.220189
H	-2.121200	-2.601199	1.757770
H	-2.200350	-2.072319	0.058353
H	0.345084	-3.096479	1.473068
H	-0.741890	-4.074438	0.455277
H	1.146746	-3.412944	-0.897909
H	-0.307846	-2.574517	-1.501323
H	1.707805	-2.353112	-2.978971
H	3.245396	-1.454374	-3.075537
H	3.087518	-2.839409	-1.962705
H	2.332220	2.402910	1.463839
H	4.466827	3.292143	0.545795
H	5.500307	2.158397	-1.475232
H	4.385409	0.105990	-2.389908
H	0.648416	3.200970	0.611205
H	-0.429072	4.988177	1.964339
Br	-0.846430	0.883138	-1.428856
Br	1.669938	-0.662135	2.637327

[Co(L-CH$_2$-L)] (charge = 0)

C	-1.837422	3.650026	2.752135
C	-2.178629	2.311879	2.942041
C	-1.471865	1.290534	2.260720
N	-0.367543	1.598801	1.451352

Co	0.436134	0.086734	0.616168
N	-0.998585	-0.822359	1.405769
C	-1.795784	-0.107160	2.230389
C	-2.932060	-0.713436	3.010293
C	-1.336510	-2.244277	1.231630
C	-0.247390	-3.055231	0.533454
C	0.177659	-2.462586	-0.812793
N	0.938813	-1.227131	-0.600188
C	2.002853	-0.962439	-1.385490
C	2.421109	-1.813429	-2.556542
C	2.730295	0.199943	-0.955291
N	2.120821	0.830582	0.139363
C	2.832039	1.802164	0.783510
C	4.074627	2.260889	0.349760
C	4.645850	1.698092	-0.818571
C	3.970541	0.659444	-1.459400
C	-0.098020	2.920323	1.233680
C	-0.788568	3.960960	1.850913
H	-2.384728	4.442478	3.271801
H	-3.008189	2.044538	3.602742
H	-2.572430	-1.463890	3.739867
H	-3.489605	0.049654	3.572196
H	-3.650601	-1.231809	2.349025
H	-1.556229	-2.705336	2.212676
H	-2.270791	-2.314732	0.634488
H	0.643381	-3.143866	1.183091
H	-0.637775	-4.076275	0.371062
H	0.783264	-3.203288	-1.362495
H	-0.719798	-2.250598	-1.430183
H	1.569180	-2.028477	-3.225244

H	3.191337	-1.307107	-3.157367
H	2.839311	-2.787698	-2.238553
H	2.365200	2.219885	1.679397
H	4.584365	3.046851	0.914041
H	5.608781	2.052773	-1.198702
H	4.405444	0.176484	-2.339355
H	0.715017	3.133049	0.535333
H	-0.508592	4.995452	1.633069

[Co(L-L)]Br$_2$ (charge = +1)

C	0.973352	-0.716693	6.068215
C	1.644453	-1.230462	4.950278
C	1.075917	-1.075016	3.677743
N	-0.116562	-0.416903	3.488133
Co	-0.642418	-0.398802	1.560105
N	0.957752	-1.369605	1.385951
C	1.685330	-1.595554	2.442279
C	3.019827	-2.273670	2.450241
C	1.342441	-1.644294	-0.007432
C	0.062490	-1.688644	-0.845843
N	-0.880687	-0.712966	-0.277759
C	-1.914104	-0.202141	-0.883940
C	-2.284281	-0.434009	-2.315593
C	-2.743581	0.630047	0.003640
C	-3.888888	1.317975	-0.422618
C	-4.598057	2.103826	0.495813
C	-4.126919	2.184558	1.810477
C	-2.977219	1.465577	2.170794
N	-2.301358	0.686879	1.304599
C	-0.763567	0.049666	4.573054

C	-0.254207	-0.074506	5.874496
H	1.399365	-0.826376	7.069432
H	2.598300	-1.752063	5.058237
H	3.017926	-3.105827	3.174927
H	3.294762	-2.663527	1.461602
H	3.796261	-1.557357	2.773542
H	1.990277	-0.811812	-0.335453
H	1.903875	-2.587148	-0.099892
H	0.281241	-1.479431	-1.904681
H	-0.414434	-2.682214	-0.771597
H	-1.520735	-1.008992	-2.855315
H	-3.239608	-0.986800	-2.364761
H	-2.435504	0.530333	-2.829939
H	-4.213754	1.238328	-1.462577
H	-5.494237	2.647830	0.184473
H	-4.629170	2.795081	2.565108
H	-2.589472	1.535941	3.186410
H	-1.728134	0.529703	4.410693
H	-0.829430	0.330893	6.710685
Br	0.667202	1.702566	1.173182
Br	-1.999665	-2.454090	2.020954

[Co(L-L)] (charge = 0)

C	0.806636	-0.774689	6.066770
C	1.585511	-1.148917	4.972824
C	1.077960	-1.023566	3.657246
N	-0.198204	-0.468384	3.424292
Co	-0.639537	-0.411303	1.551400
N	0.931432	-1.300313	1.379545
C	1.722644	-1.470778	2.451107

C	3.096287	-2.077758	2.373684
C	1.338958	-1.650279	0.010213
C	0.062945	-1.660493	-0.850531
N	-0.893078	-0.741855	-0.213430
C	-1.989764	-0.273133	-0.830637
C	-2.338798	-0.605608	-2.255313
C	-2.752413	0.588036	0.034054
C	-3.906402	1.324970	-0.325447
C	-4.487660	2.210429	0.580846
C	-3.888496	2.368942	1.855140
C	-2.767195	1.604569	2.172445
N	-2.201616	0.693805	1.328964
C	-0.950531	-0.159224	4.519326
C	-0.503590	-0.288107	5.833121
H	1.194886	-0.873533	7.085238
H	2.589281	-1.558859	5.120365
H	3.057054	-3.147636	2.093392
H	3.715492	-1.568404	1.612727
H	3.625108	-2.005913	3.335804
H	2.050019	-0.888366	-0.365165
H	1.853737	-2.628050	-0.026737
H	0.282288	-1.365301	-1.893141
H	-0.373010	-2.678356	-0.880344
H	-2.345848	-1.698705	-2.420222
H	-3.332621	-0.221816	-2.530183
H	-1.607268	-0.177800	-2.967031
H	-4.326206	1.203513	-1.328465
H	-5.378060	2.783633	0.304371
H	-4.285491	3.073934	2.590859
H	-2.281104	1.717990	3.144929

H	-1.961283	0.202983	4.314538
H	-1.167348	-0.012429	6.657326

[Co(L-cyc-L)]Br$_2$ (charge = +1)

C	-4.394410	-1.221744	-0.233723
C	-4.439212	-0.357251	0.865848
C	-3.239303	0.158152	1.377684
N	-2.039997	-0.135148	0.839280
Co	-0.242752	0.423938	1.406760
N	-0.464951	1.949715	2.623154
C	-1.533917	2.747815	2.806435
C	-1.521263	3.826450	3.702763
C	-0.351921	4.099659	4.421695
C	0.777688	3.298233	4.204590
C	0.699315	2.235210	3.291805
C	1.841005	1.383489	2.903061
C	3.128886	1.418499	3.673970
N	1.575273	0.615326	1.879297
C	2.446728	-0.426839	1.293544
C	3.900733	-0.057220	0.925941
C	4.637815	-1.352423	0.515202
C	3.910636	-2.123667	-0.601165
C	2.412179	-2.350894	-0.295589
C	1.769921	-0.980117	0.011945
N	0.301901	-0.902808	0.178658
C	-0.612199	-1.370017	-0.630198
C	-0.368068	-2.156394	-1.885535
C	-1.983089	-1.013755	-0.214038
C	-3.146757	-1.561519	-0.775076
H	-5.311598	-1.641613	-0.656019

H	-5.383521	-0.081137	1.341793
H	-3.247030	0.803263	2.256821
H	-2.419253	2.536485	2.205982
H	-2.420976	4.436562	3.815380
H	-0.309433	4.933515	5.128081
H	1.715645	3.506525	4.724258
H	2.938550	1.725218	4.713244
H	3.604377	0.427200	3.693538
H	3.839107	2.140612	3.233893
H	2.462722	-1.237364	2.051490
H	3.887396	0.669763	0.092747
H	4.431165	0.413300	1.764551
H	5.664888	-1.101966	0.196178
H	4.730723	-1.999540	1.408529
H	3.991449	-1.559456	-1.550176
H	4.400252	-3.099108	-0.769037
H	1.938100	-2.845377	-1.153792
H	2.284822	-3.012930	0.580954
H	1.993375	-0.283799	-0.822977
H	0.561756	-1.835143	-2.377137
H	-0.297519	-3.237662	-1.672609
H	-1.197329	-2.006148	-2.592391
H	-3.075130	-2.260993	-1.610980
Br	-0.094523	2.114560	-0.446573
Br	-0.486887	-1.224104	3.288133

[Co(L-cyc-L)] (charge = 0)
C	-4.381127	-1.236919	-0.109874
C	-4.377055	-0.432830	1.057137
C	-3.165629	0.076128	1.521242

N	-1.966656	-0.147176	0.909120
Co	-0.211693	0.413392	1.400016
N	-0.452144	1.923765	2.539175
C	-1.506871	2.782280	2.651928
C	-1.522778	3.878145	3.512612
C	-0.384653	4.135207	4.317092
C	0.729457	3.306778	4.185219
C	0.708525	2.221503	3.276074
C	1.825324	1.372957	2.940903
C	3.111557	1.390264	3.726770
N	1.542907	0.573789	1.893583
C	2.433707	-0.454445	1.315915
C	3.908247	-0.105055	1.013304
C	4.631469	-1.389408	0.545579
C	3.920926	-2.082270	-0.632237
C	2.409643	-2.294829	-0.383332
C	1.776985	-0.936125	-0.007494
N	0.313418	-0.837729	0.172884
C	-0.626020	-1.329283	-0.658321
C	-0.376563	-2.088617	-1.936407
C	-1.956227	-1.008255	-0.203281
C	-3.164921	-1.526841	-0.727728
H	-5.316581	-1.641882	-0.508179
H	-5.300016	-0.203420	1.597098
H	-3.131988	0.696051	2.421195
H	-2.368677	2.563002	2.015871
H	-2.408728	4.518014	3.553569
H	-0.369376	4.980038	5.012671
H	1.637554	3.504277	4.762639
H	2.942908	1.814331	4.729424

H	3.506670	0.370061	3.867004
H	3.905147	1.992477	3.246181
H	2.431772	-1.312654	2.022870
H	3.945984	0.673423	0.226903
H	4.425287	0.297648	1.895627
H	5.675153	-1.151416	0.271041
H	4.683536	-2.090076	1.402009
H	4.039215	-1.463358	-1.543330
H	4.403811	-3.052731	-0.847527
H	1.954307	-2.724974	-1.286442
H	2.246634	-3.015151	0.441564
H	2.050486	-0.208017	-0.802130
H	0.487410	-1.675834	-2.483610
H	-0.183919	-3.165139	-1.770636
H	-1.250044	-2.013022	-2.603359
H	-3.132819	-2.178243	-1.606202

A.3 Supporting Information for Chapter 4

A.3.1 Supporting Figures
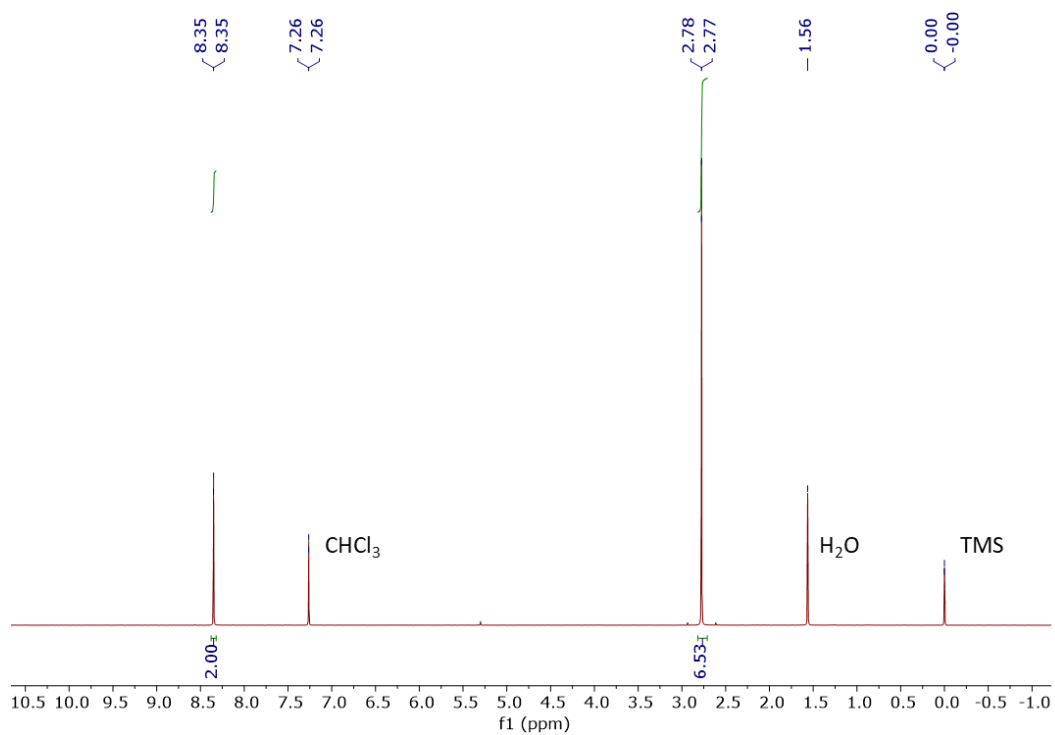
Figure A.80 ^{1}H-NMR Spectrum of 4-Bromo-2,6-diacetylpyridine in CDCl$_3$-d (δ 7.26 solvent residual peak, δ 1.56 water peak).
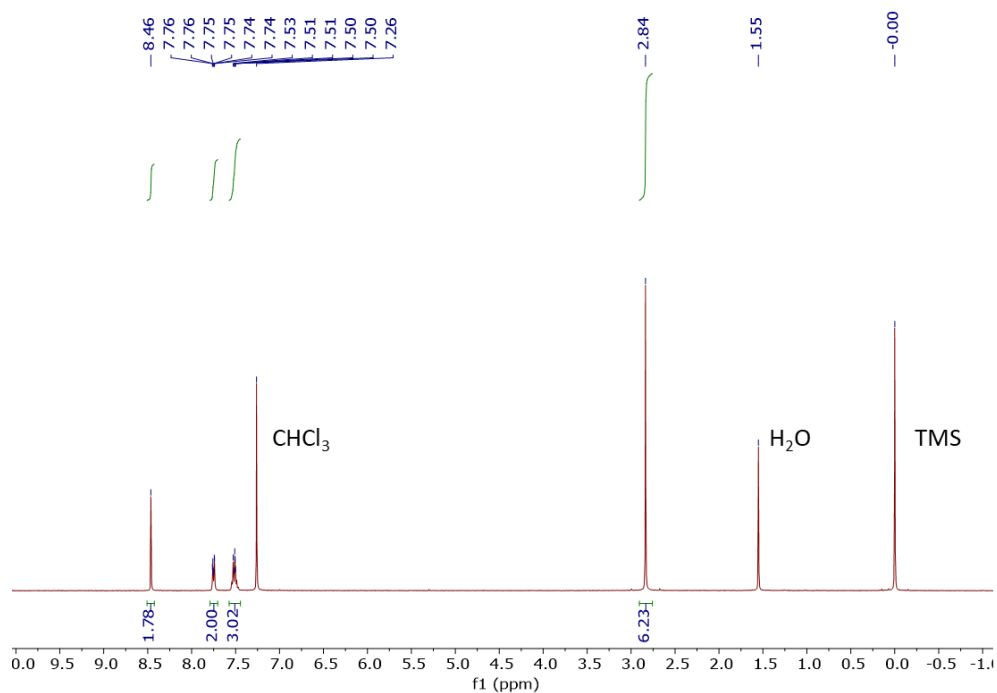
Figure A.81 ^{1}H-NMR Spectrum of 4-Phenyl-2,6-diacetylpyridine in CDCl$_3$-d (δ 7.26 solvent residual peak, δ 1.56 water peak).
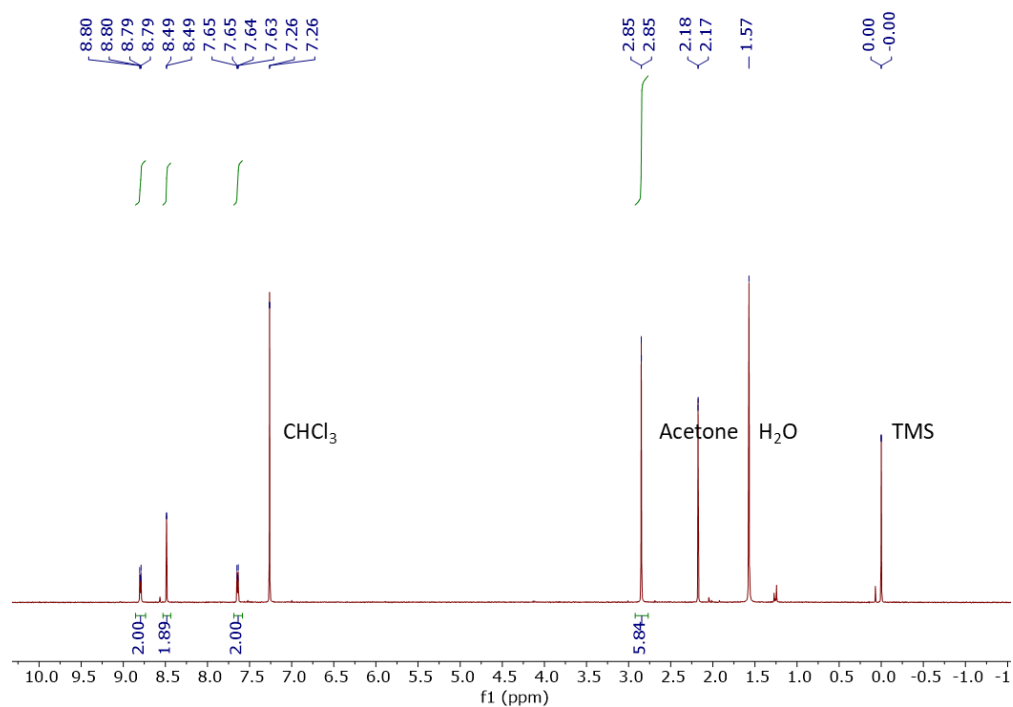
Figure A.82 ^{1}H-NMR Spectrum of 4-4-Pyridyl-2,6-diacetylpyridine in CDCl$_3$-d (δ 7.26 solvent residual peak, δ 2.18 acetone peak, δ 1.56 water peak).
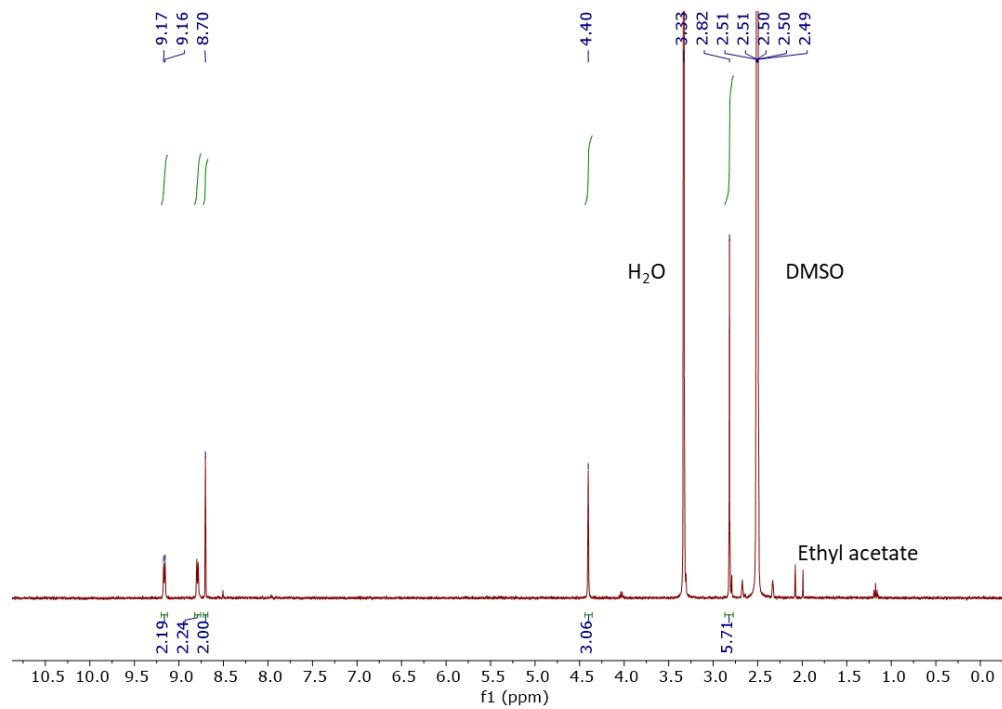
Figure A.83 ^{1}H-NMR Spectrum of 4-(N-methyl-4-Pyridyl)-2,6-diacetylpyridine in DMSO-d_6 (δ 2.50 solvent residual peak, δ 3.33 water peak, δ 1.26~2.05 ethyl acetate peak).
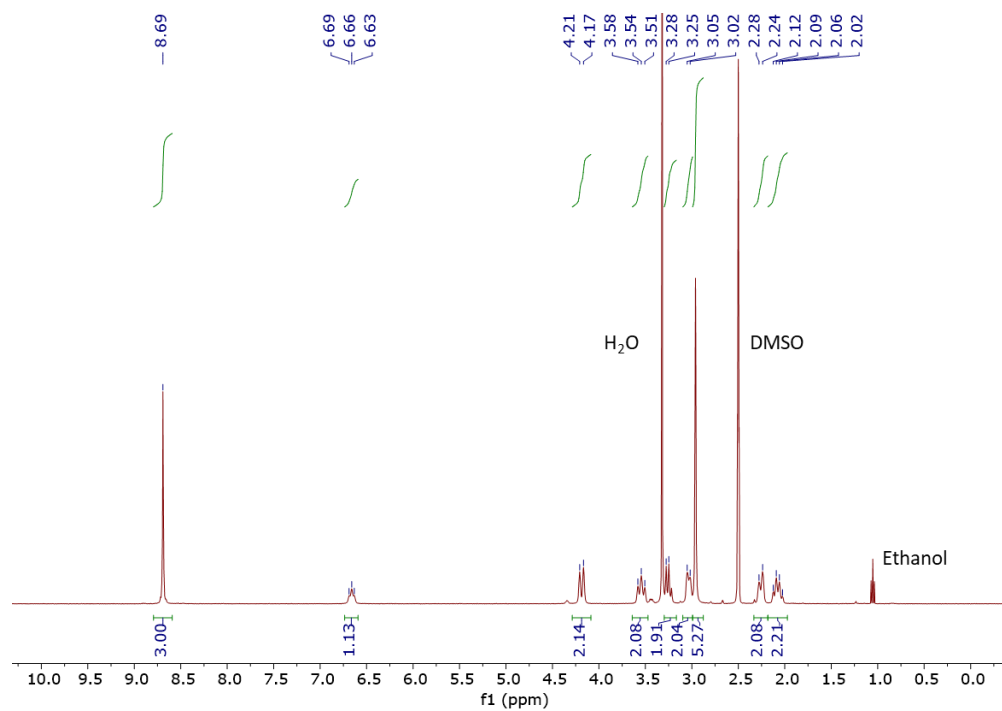
Figure A.84 ^{1}H-NMR Spectrum of [Co(PDI)]Br$_3$ in DMSO-d_6 (δ 2.50 solvent residual peak, δ 3.33 water peak, δ 1.06 ethanol peak).
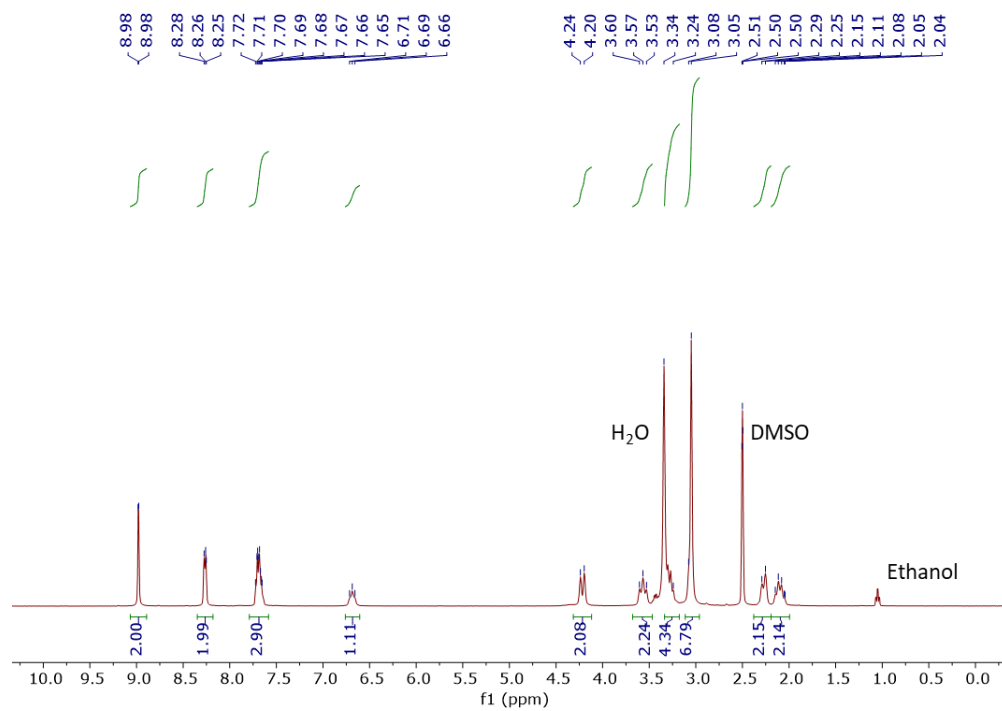
Figure A.85 ^{1}H-NMR Spectrum of [Co(PDI-Ph)]Br$_3$ in DMSO-d_6 (δ 2.50 solvent residual peak, δ 3.33 water peak, δ 1.06 ethanol peak).
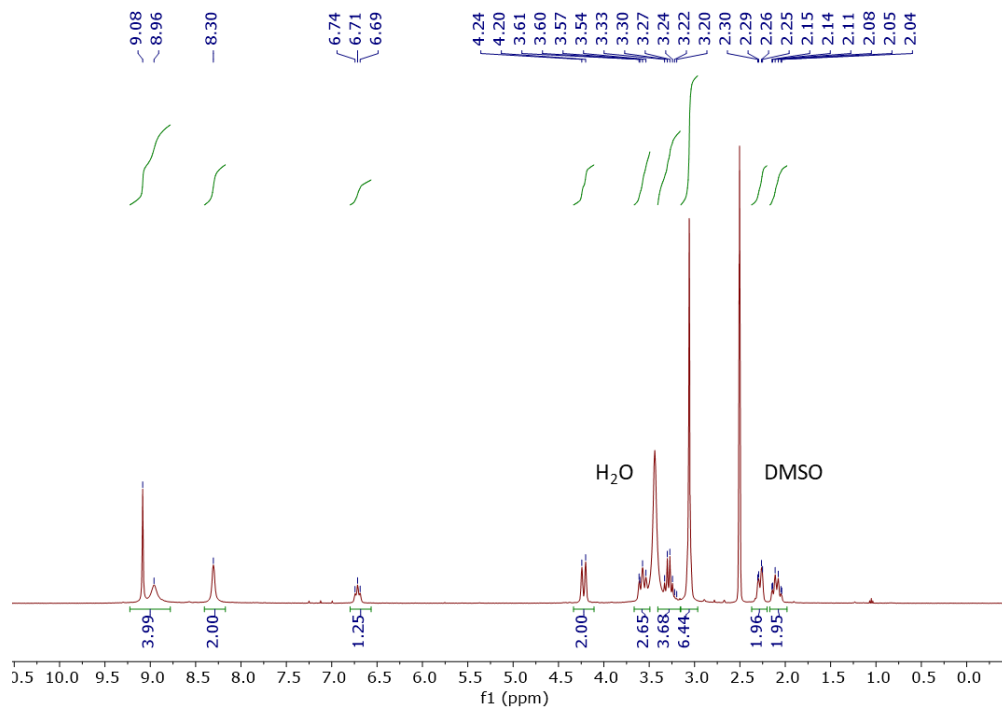
Figure A.86 ^{1}H-NMR Spectrum of [Co(PDI-Py)]Br$_3$ in DMSO-d_6 (δ 2.50 solvent residual peak, δ 3.33 water peak, δ 1.06 ethanol peak).

372
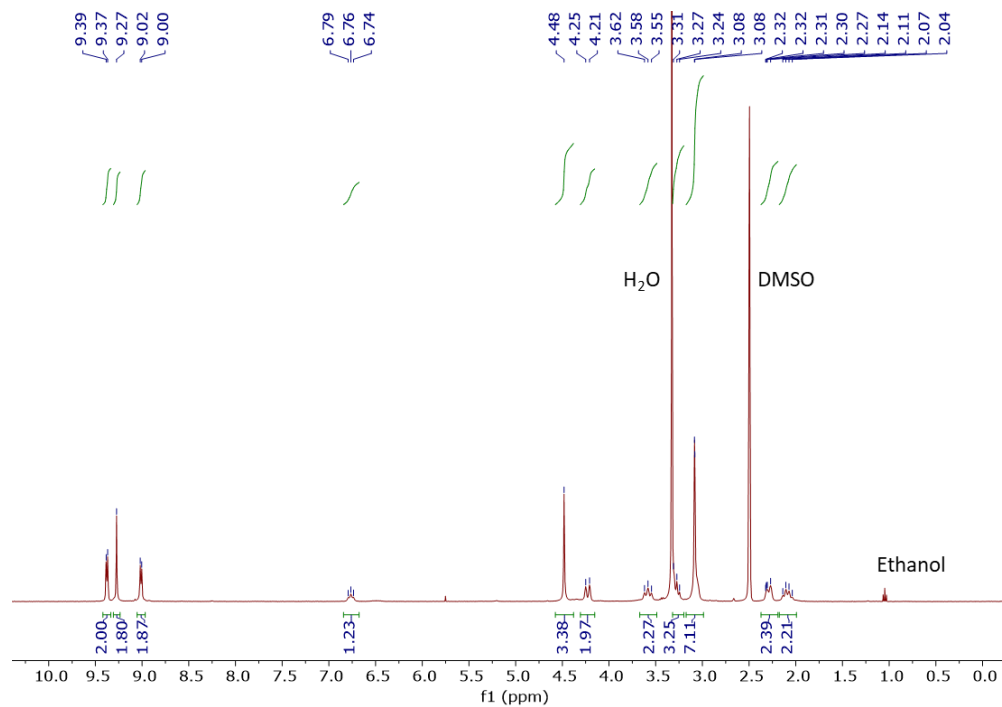
Figure A.87 ^{1}H-NMR Spectrum of [Co(PDI-Py-CH$_3^+$I$^-$)]Br$_3$ in DMSO-d_6 (δ 2.50 solvent residual peak, δ 3.33 water peak, δ 1.06 ethanol peak).'
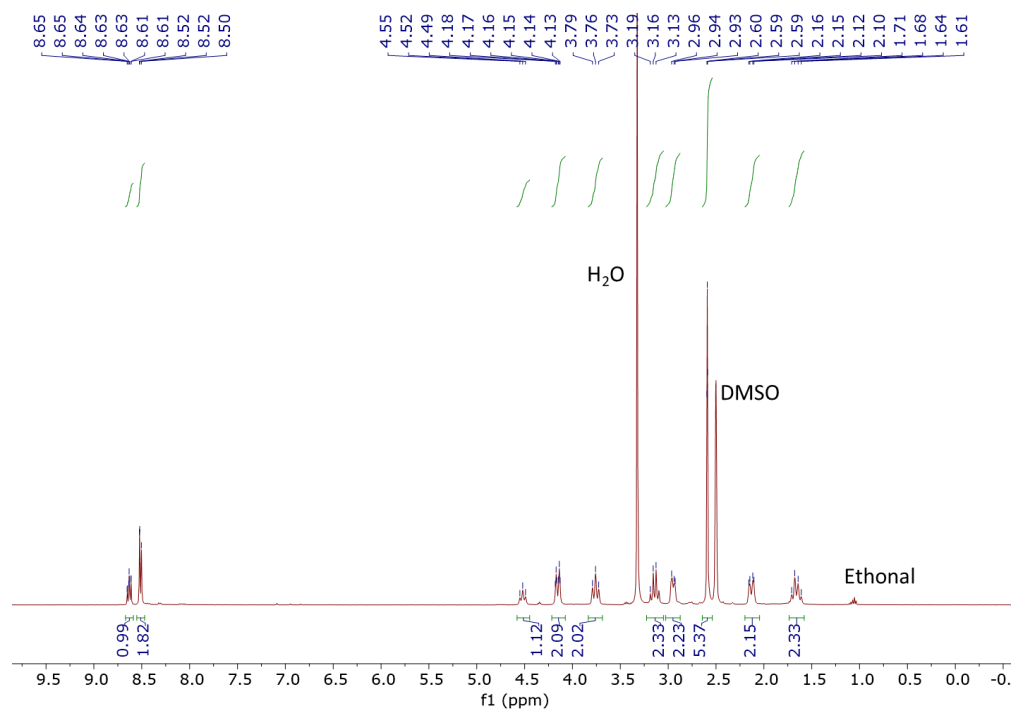
Figure A.88 ^{1}H-NMR Spectrum of [Zn(PDI)]Br$_2$ in DMSO-d_6 (δ 2.50 solvent residual peak, δ 3.33 water peak, δ 1.06 ethanol peak).
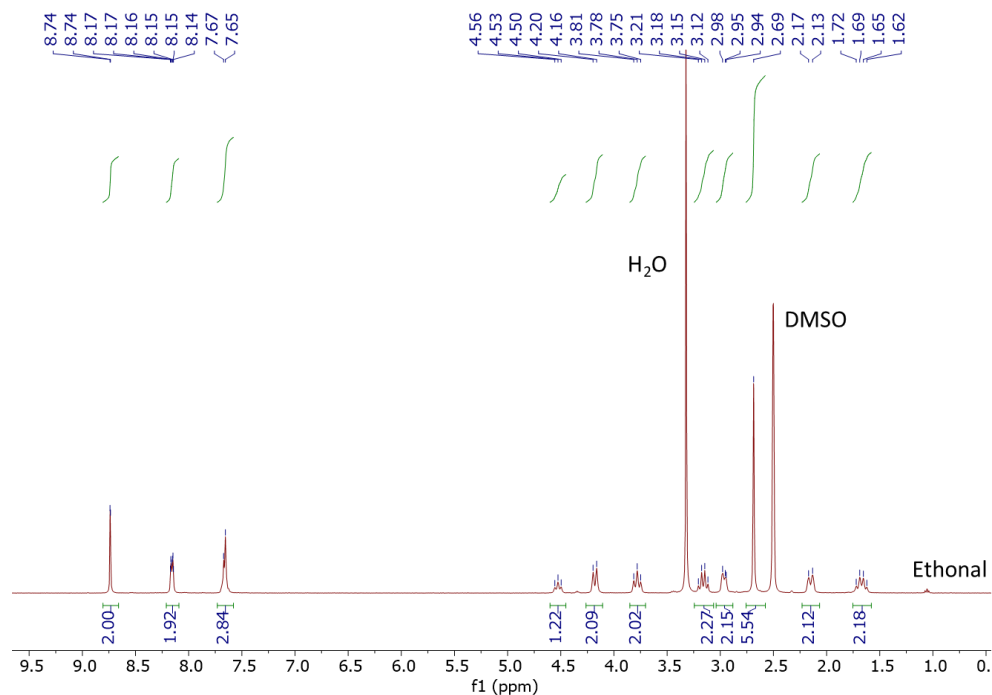
Figure A.89 ^{1}H-NMR Spectrum of [Zn(PDI-Ph)]Br$_2$ in DMSO-d_6 (δ 2.50 solvent residual peak, δ 3.33 water peak, δ 1.06 ethanol peak).
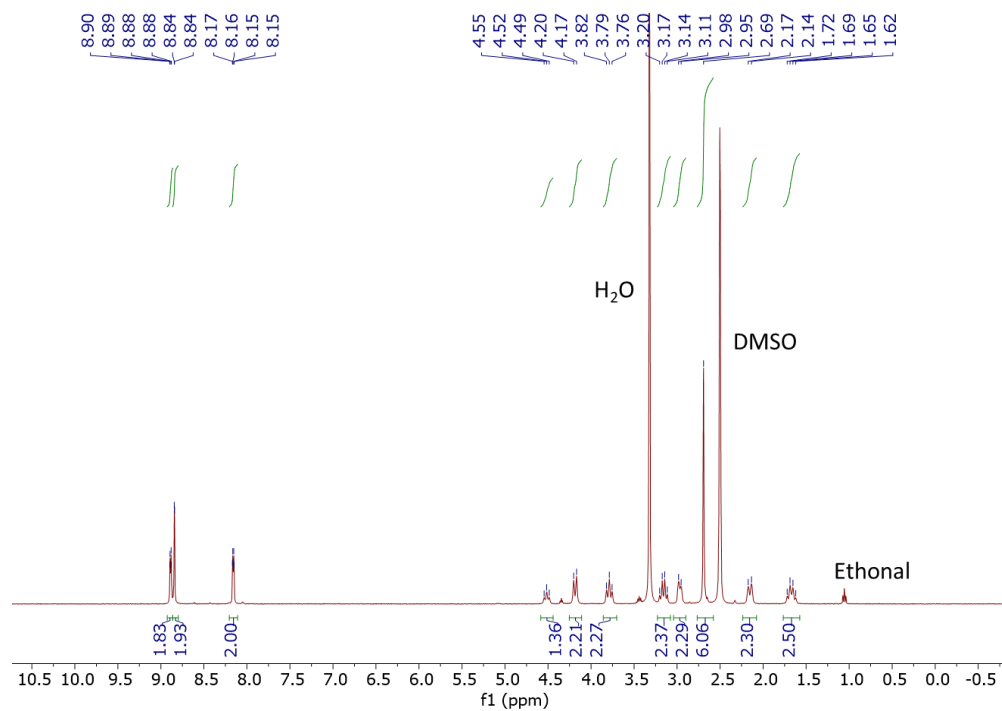
Figure A.90 ^{1}H-NMR Spectrum of [Zn(PDI-Py)]Br$_2$ in DMSO-d_6 (δ 2.50 solvent residual peak, δ 3.33 water peak, δ 1.06 ethanol peak).
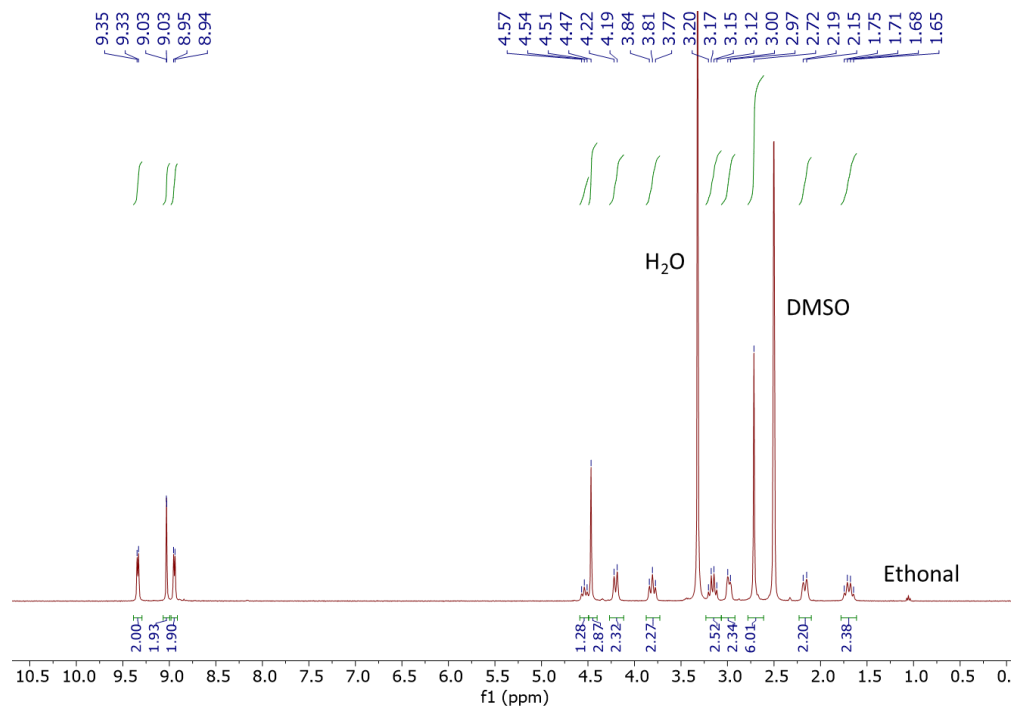
Figure A.91 ^{1}H-NMR Spectrum of [Zn(PDI-Py-CH$_3$$^+I^-$)]Br$_2$ in DMSO-d_6 (δ 2.50 solvent residual peak, δ 3.33 water peak, δ 1.06 ethanol peak).

Figure A.92 The H-cell is used for controlled-potential electrolysis experiments in this study. The left chamber is filled with 20 mL MeCN solution of 0.3 mM [Co(PDI-R)] catalyst with 0.1 M nBu$_4$NPF$_6$, and the reported concentrations of H$_2$O. The glassy carbon plate working electrode and Ag/AgNO$_3$ (1.0 mM in MeCN with 0.1 M nBu$_4$NPF$_6$) reference electrode are inserted into the solution. The right chamber is filled with 15 mL MeCN solution of 5 mM Fc with 0.1 M nBu$_4$NPF$_6$, and the same concentrations of H$_2$O as the left chamber. Nichrome wire is used as a counter electrode. Two chamber solutions are isolated by a fine-porosity glass frit.

Figure A.93 The CV of KI N_2-saturated MeCN with 0.1 M nBuNPF$_6$.

Figure A.94 The CV of 0.3 mM [Co(PDI)] in N_2-saturated MeCN with 0.1 M nBuNPF$_6$ showing formal PDI-R$^{\bullet-}$/PDI-R^{2-} couple in the potential window of +0.30 ~ −2.60 V.

Figure A.95 The CV of 0.3 mM [Co(PDI-Ph)] in N_2-saturated MeCN with 0.1 M nBuNPF$_6$ showing formal PDI-R$^{\bullet-}$/PDI-R^{2-} couple in the potential window of +0.30 ~ −2.60 V.

Figure A.96 The CV of 0.3 mM [Co(PDI-Py)] in N_2-saturated MeCN with 0.1 M nBuNPF$_6$ showing formal PDI-R$^{\bullet-}$/PDI-R^{2-} couple in the potential window of +0.30 ~ −2.60 V.

Figure A.97 The CV of 0.3 mM [Co(PDI-Py-CH$_3^+$I$^-$)] in N$_2$-saturated MeCN with 0.1 M nBuNPF$_6$ showing formal PDI-R$^{\bullet-}$/PDI-R^{2-} couple in the potential window of +0.30 ~ −2.60 V.

Figure A.98 The CV of 0.3 mM [Zn(PDI)] in N_2-saturated MeCN with 0.1 M nBuNPF$_6$.

Figure A.99 The CV of 0.3 mM [Zn(PDI-Ph)] in N_2-saturated MeCN with 0.1 M nBuNPF$_6$.

Figure A.100 The CV of 0.3 mM [Zn(PDI-Py)] in N$_2$-saturated MeCN with 0.1 M nBuNPF$_6$

Figure A.101 The CV of 0.3 mM [Zn(PDI-Py-CH$_3^+$I$^-$)] in N$_2$-saturated MeCN with 0.1 M nBuNPF$_6$.

Figure A.102 The CV of 0.3 mM DPA in N$_2$-saturated MeCN with 0.1 M *n*BuNPF$_6$.

Figure A.103 The CV of 0.3 mM DPA-Ph in N$_2$-saturated MeCN with 0.1 M *n*BuNPF$_6$.

Figure A.104 The CV of 0.3 mM DPA-Py in N_2-saturated MeCN with 0.1 M nBuNPF$_6$.

Figure A.105 The CV of 0.3 mM DPA-PyCH$_3^+$I$^-$ in N_2-saturated MeCN with 0.1 M nBuNPF$_6$.

Figure A.106 Cyclic voltammograms of [Co(PDI)] complex under CO_2 with i_p, E_p and E_{onset} denoted. In this study, the catalytic peak current, i_p is the maximum current intensity of the catalytic peak at the peak potentials, E_p; the onset potential, E_{onset} is measured by linearly extrapolating the rising current portion of the current wave to the linear extrapolation of the baseline current, and the intercept potential is regarded as E_{onset}.

Figure A.107 CVs of 0.3 mM [Co(PDI)] in MeCN with 0.1 M nBuNPF$_6$ under CO$_2$ with different concentrations of H$_2$O.

Figure A.108 CVs of 0.3 mM [Co(PDI-Ph)] in MeCN with 0.1 M nBuNPF$_6$ under CO$_2$ with different concentrations of H$_2$O.

Figure A.109 CVs of 0.3 mM [Co(PDI-Py)] in MeCN with 0.1 M nBuNPF$_6$ under CO$_2$ with different concentrations of H$_2$O.

Figure A.110 CVs of 0.3 mM [Co(PDI-PyCH$_3$$^+I^-$)] in MeCN with 0.1 M nBuNPF$_6$ under CO$_2$ with different concentrations of H$_2$O.
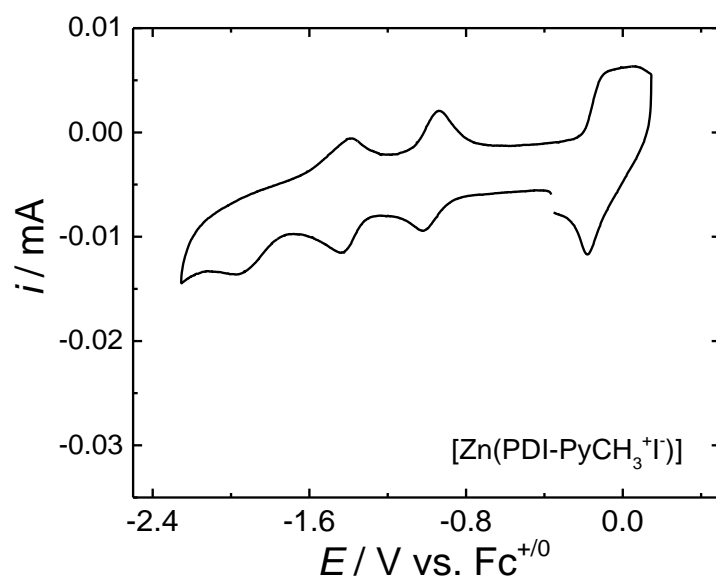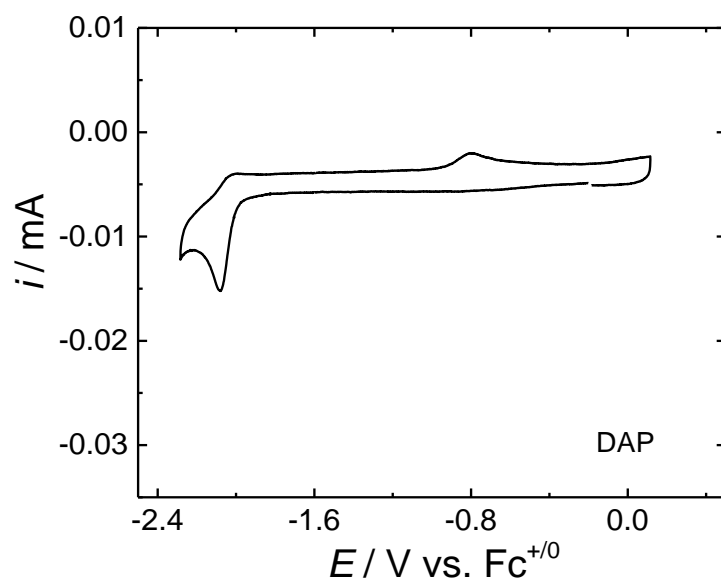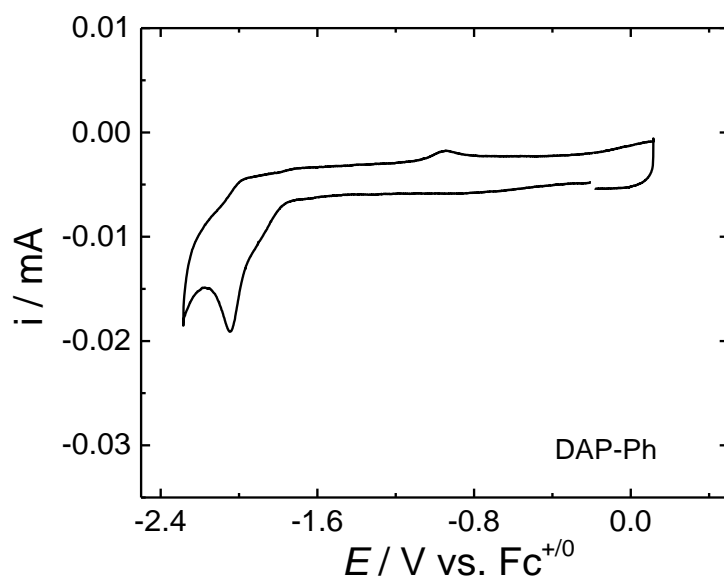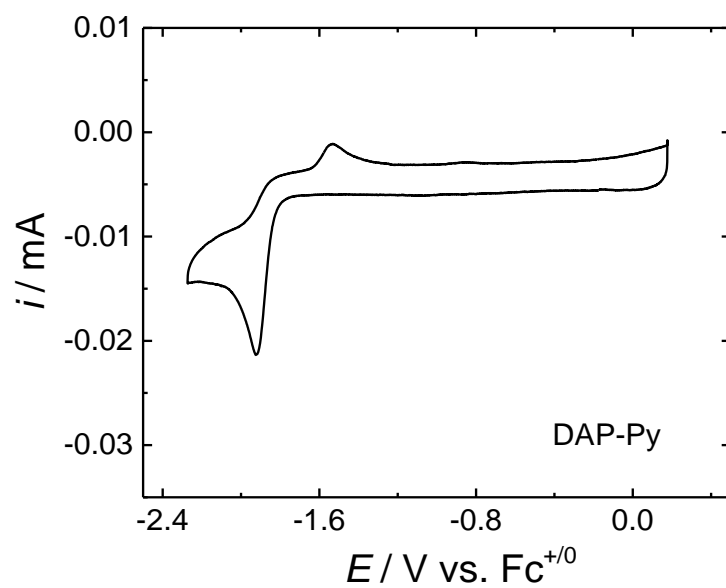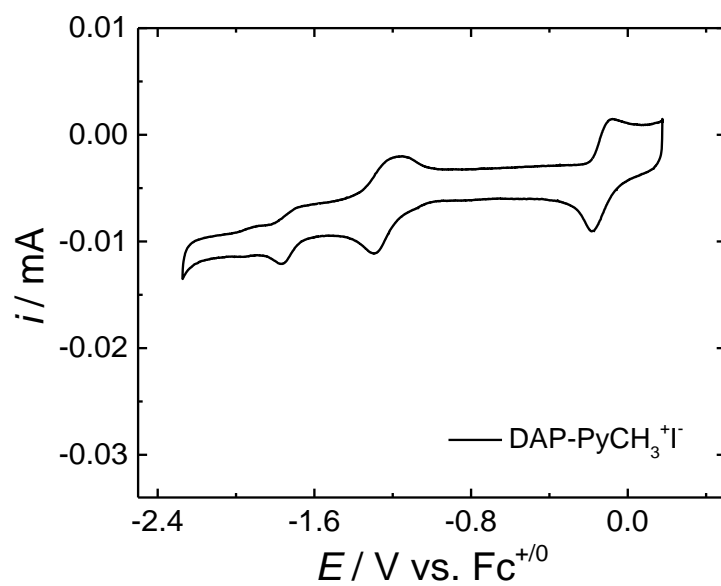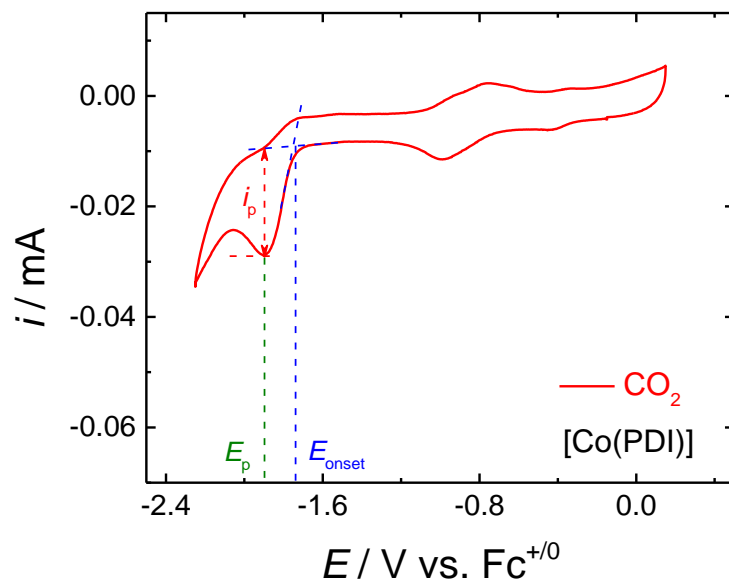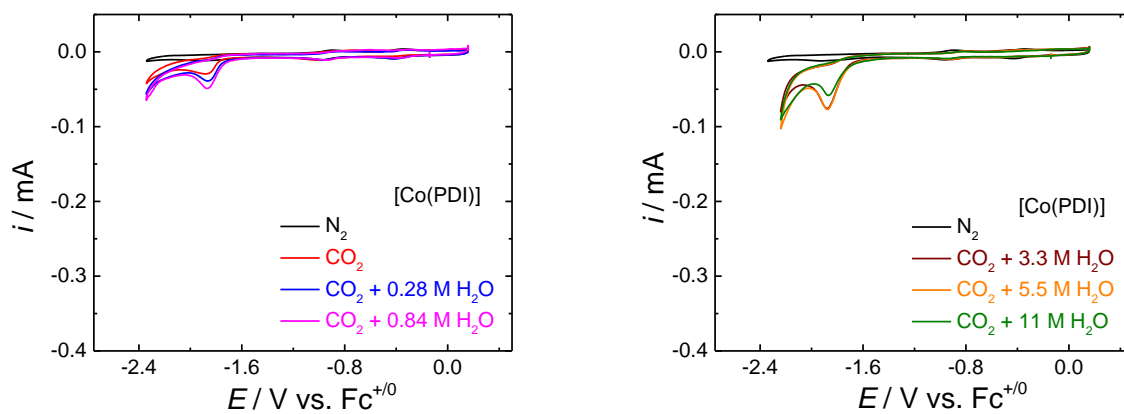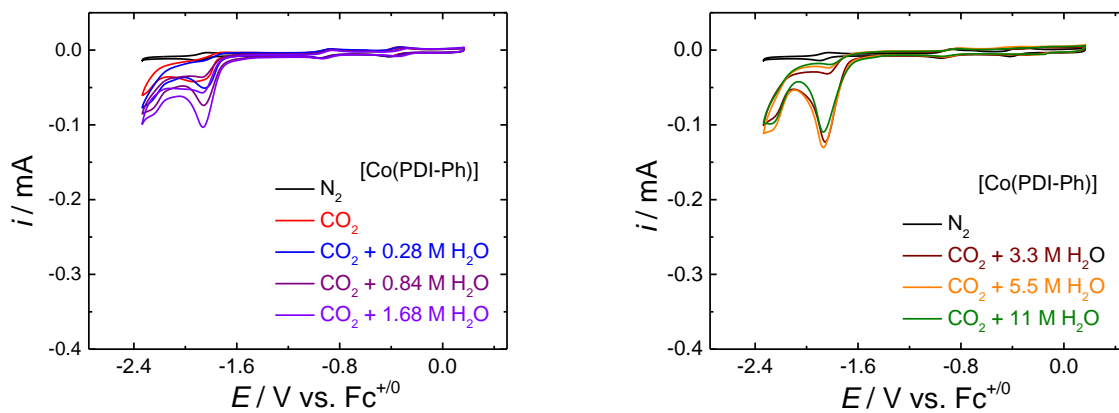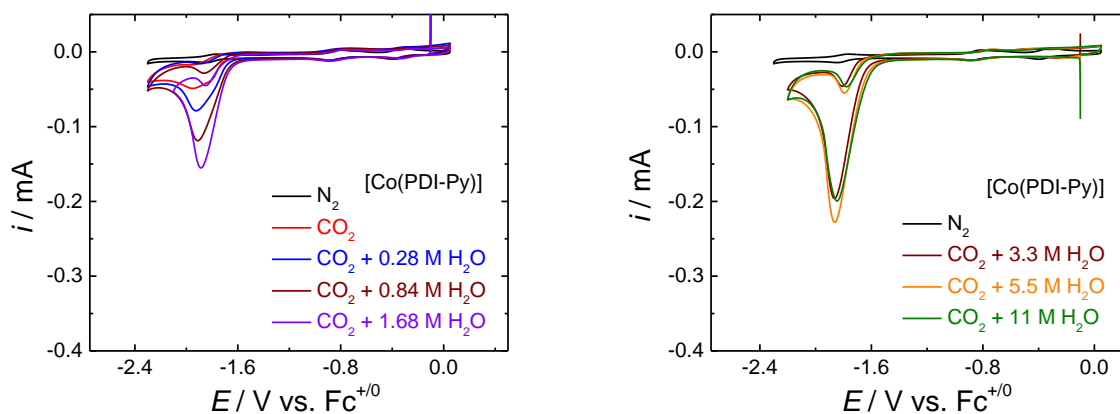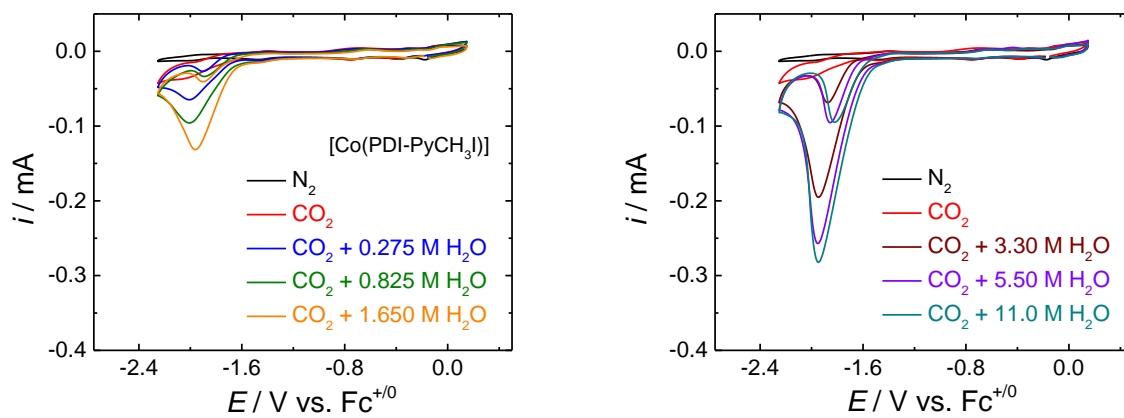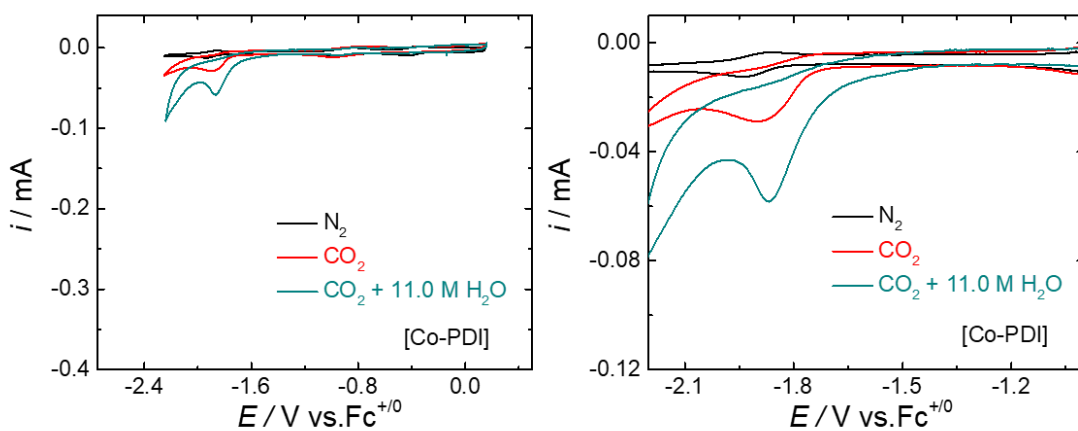
Figure A.111 Left: CVs of 0.3 mM [Co(PDI)] in MeCN with 0.1 M nBuNPF$_6$ under N$_2$ (black curve), CO$_2$ (red curve) and CO$_2$ with 11.0 M H$_2$O (green curve); Right: the zoomed-in view of the catalytic onset potential window of the CVs in the left.
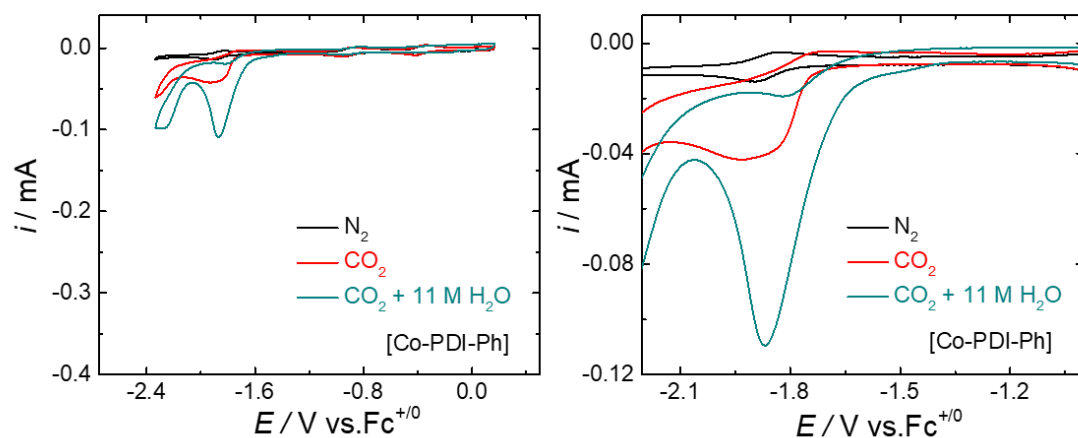
Figure A.112 Left: CVs of 0.3 mM [Co(PDI-Ph)] in MeCN with 0.1 M nBuNPF$_6$ under N$_2$ (black curve), CO$_2$ (red curve) and CO$_2$ with 11.0 M H$_2$O (green curve); Right: the zoomed-in view of the catalytic onset potential window of the CVs in the left.
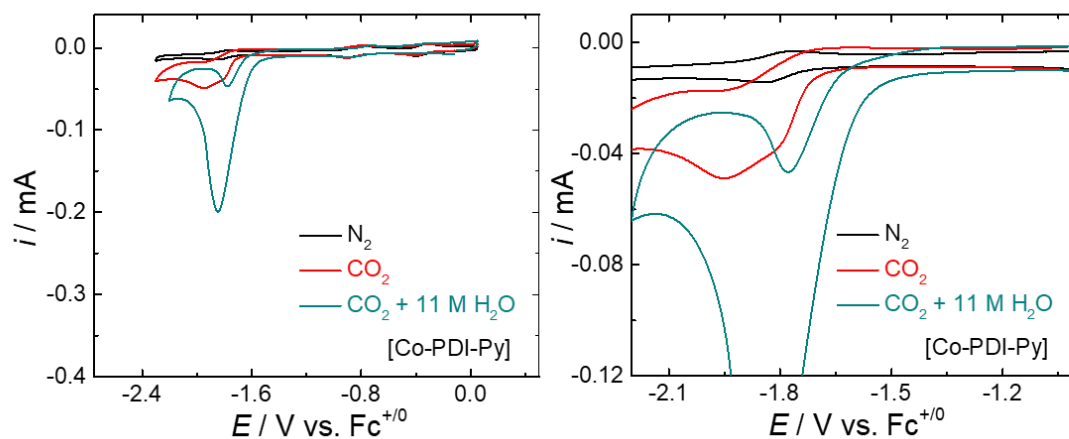
Figure A.113 Left: CVs of 0.3 mM [Co(PDI-Py)] in MeCN with 0.1 M nBuNPF$_6$ under N$_2$ (black curve), CO$_2$ (red curve) and CO$_2$ with 11.0 M H$_2$O (green curve); Right: the zoomed-in view of the catalytic onset potential window of the CVs in the left.
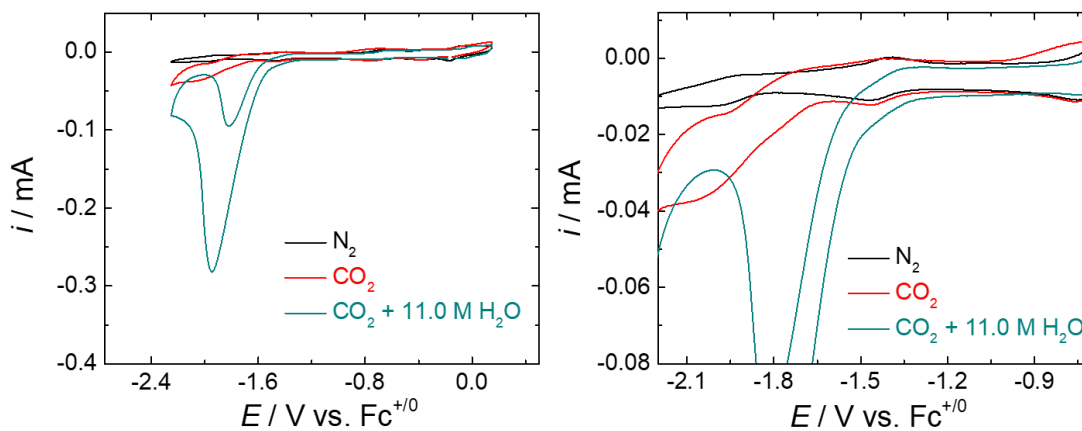
Figure A.114 Left: CVs of 0.3 mM [Co(PDI-PyCH$_3^+$I$^-$)] in MeCN with 0.1 M nBuNPF$_6$ under N$_2$ (black curve), CO$_2$ (red curve) and CO$_2$ with 11.0 M H$_2$O (green curve); Right: the zoomed-in view of the catalytic onset potential window of the CVs in the left.
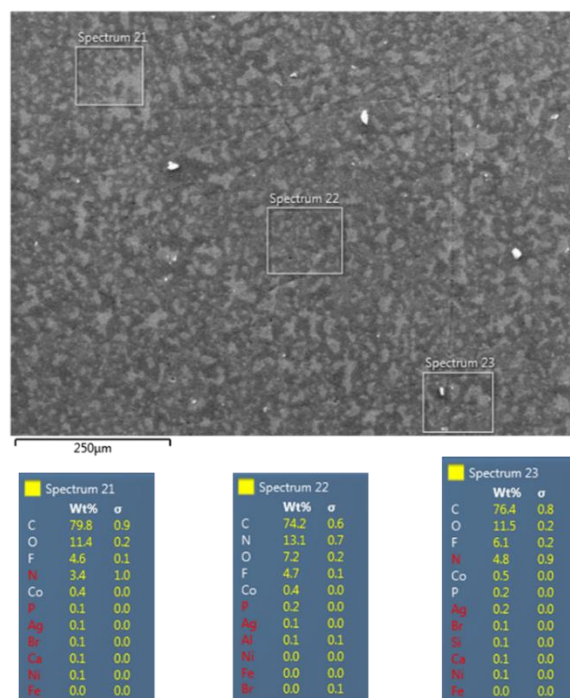
Figure A.115 SEM-EDS analysis of a working electrode surface after a 30-minute CO_2RR electrolysis of 0.30 mM [Co(PDI)] in acetonitrile with 0.1 M nBu$_4$PF$_6$ at −1.95 V vs. Fc$^{+/0}$
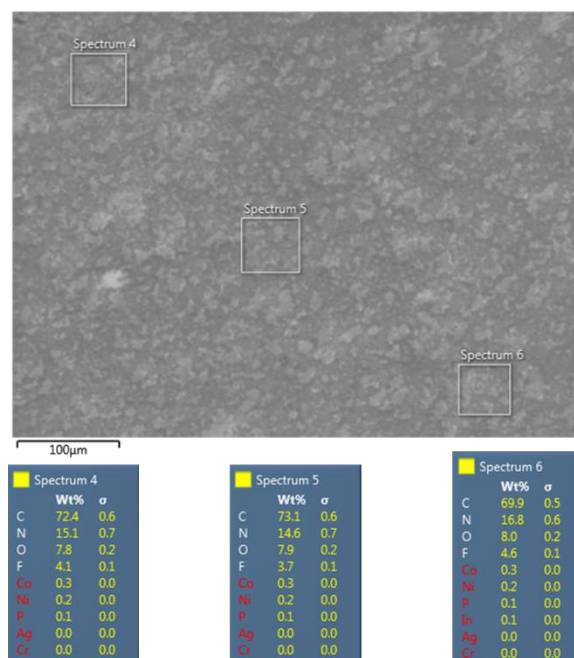
Figure A.116 SEM-EDS analysis of a working electrode surface after a 30-minute CO_2RR electrolysis of 0.30 mM [Co(PDI-Ph)] in acetonitrile with 0.1 M nBu$_4$PF$_6$ at −1.95 V vs. Fc$^{+/0}$
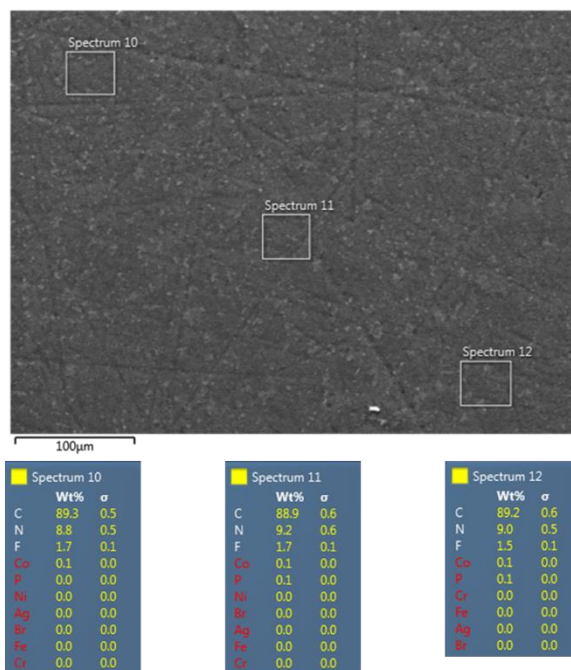
Figure A.117 SEM-EDS analysis of a working electrode surface after a 30-minute CO$_2$RR electrolysis of 0.30 mM [Co(PDI-Py)] in acetonitrile with 0.1 M nBu$_4$PF$_6$ at −1.95 V vs. Fc$^{+/0}$
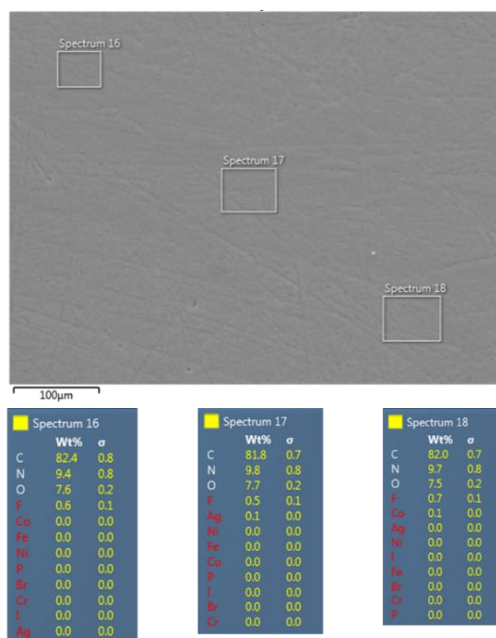
Figure A.118 SEM-EDS analysis of a working electrode surface after a 30-minute CO$_2$RR electrolysis of 0.30 mM [Co(PDI-PyCH$_3^+$I$^-$)] in acetonitrile with 0.1 M nBu$_4$PF$_6$ at −1.95 V vs. Fc$^{+/0}$
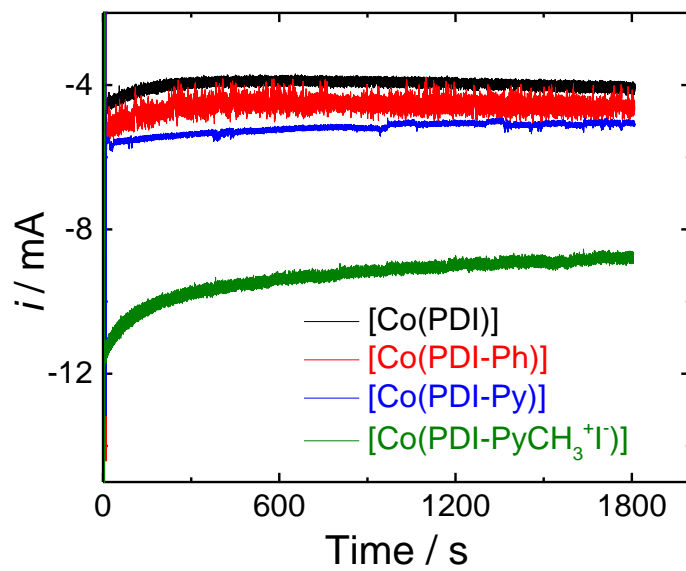
Figure A.119 Representative 30-min CPE current trace of [Co(PDI-R)] complexes for the CO_2RR with 11.0 M H_2O.
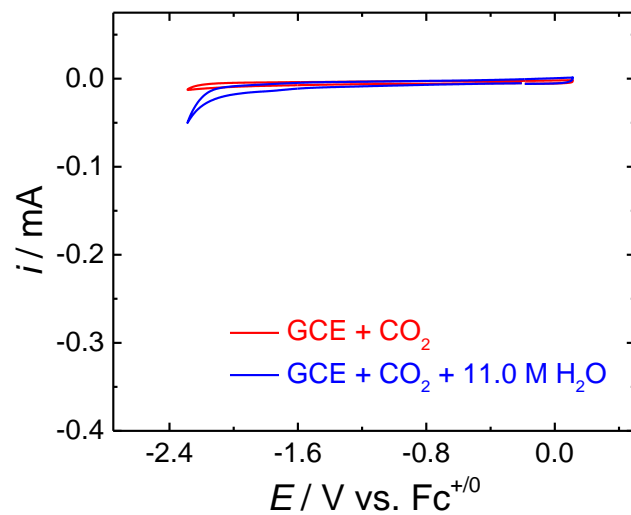
Figure A.120 CVs of the bare glassy carbon electrode in MeCN with 0.1 M nBuNPF$_6$ under CO_2 with no added H_2O (red) and 11.0 M H_2O (blue), indicating the negligible activity of glassy carbon electrode for the CO_2RR compared to those of [Co(PDI-R)] complexes.
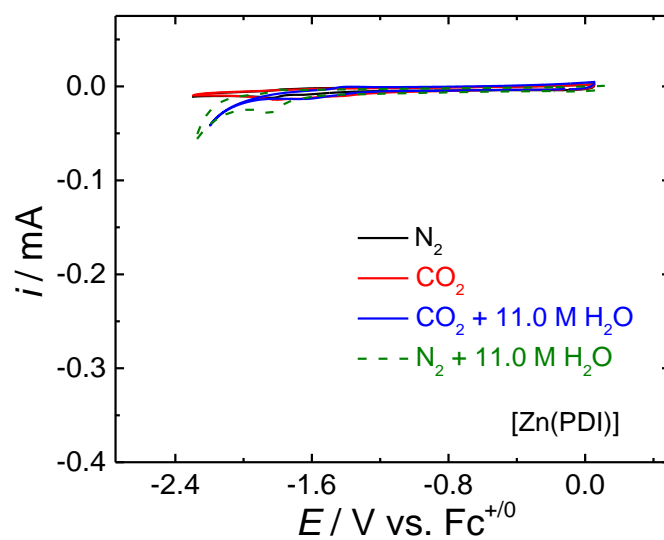
Figure A.121 CVs of 0.3 mM [Zn(PDI)] in MeCN with 0.1 M nBuNPF$_6$ under N_2, CO_2, CO_2 with 11.0 M H_2O and N_2 with 11.0 M H_2O.
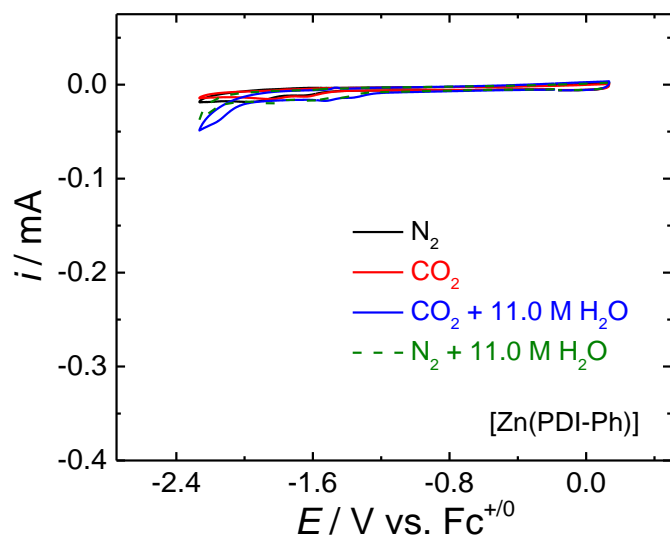
Figure A.122 CVs of 0.3 mM [Zn(PDI-Ph)] in MeCN with 0.1 M nBuNPF$_6$ under N$_2$, CO$_2$, CO$_2$ with 11.0 M H$_2$O and N$_2$ with 11.0 M H$_2$O.
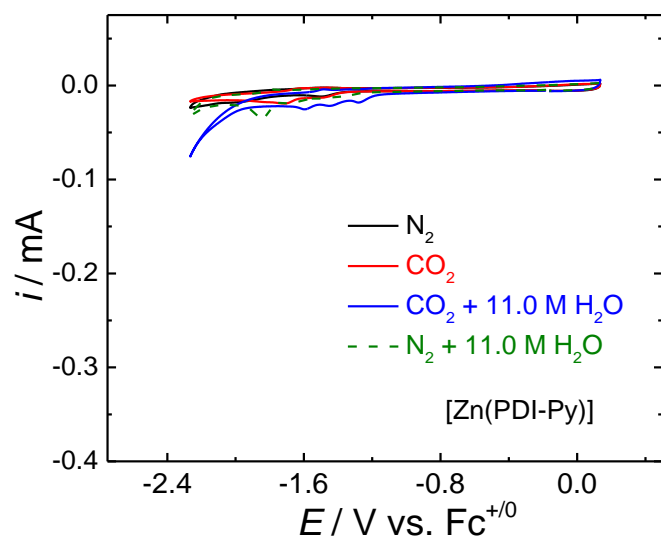
Figure A.123 CVs of 0.3 mM [Zn(PDI-Py)] in MeCN with 0.1 M nBuNPF$_6$ under N$_2$, CO$_2$, CO$_2$ with 11.0 M H$_2$O and N$_2$ with 11.0 M H$_2$O.
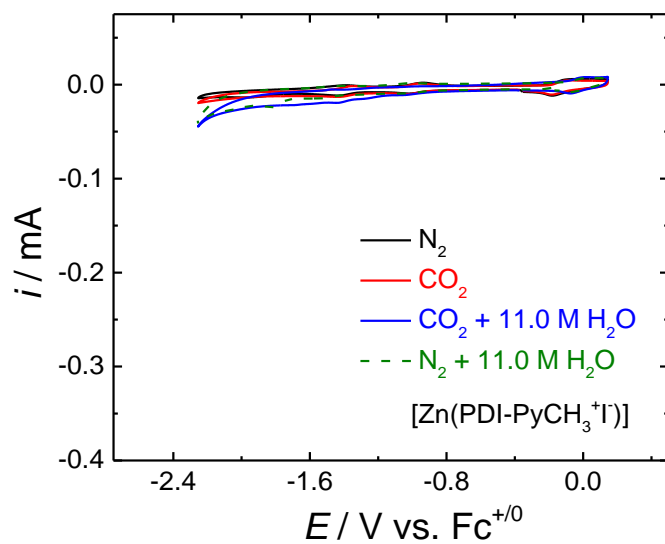
Figure A.124 CVs of 0.3 mM [Zn(PDI-PyCH$_3$$^+I^-$)] in MeCN with 0.1 M nBuNPF$_6$ under N$_2$, CO$_2$, CO$_2$ with 11.0 M H$_2$O and N$_2$ with 11.0 M H$_2$O.

Figure A.125 CVs of 0.3 mM [Co(PDI-Py)] in MeCN with 0.1 M nBuNPF$_6$ and 11.0 M H$_2$O under CO$_2$ in the presence of KI. As the concentration of KI increases, there is no change in catalytic current for the CO$_2$RR, suggesting there is no effect of I$^-$ on the catalytic activity of the catalyst for the CO$_2$ reduction.

Figure A.126 CVs of 0.3 mM [Co(PDI)] at different scan rates in MeCN with 0.1 M *n*Bu4NPF6 under N2.

Figure A.127 CVs of 0.3 mM [Co(PDI-Ph)] at different scan rates in MeCN with 0.1 M *n*Bu4NPF6 under N2.

Figure A.128 CVs of 0.3 mM [Co(PDI-Py)] at different scan rates in MeCN with 0.1 M nBu$_4$NPF$_6$ under N$_2$.

Figure A.129 CVs of 0.3 mM [Co(PDI-Py-CH$_3^+$I$^-$)] at different scan rates in MeCN with 0.1 M nBu$_4$NPF$_6$ under N$_2$.

Figure A.130 The representative plot of i_{redox} as a function of $\upsilon^{1/2}$ for 0.3 mM [Co(PDI)] in MeCN with 0.1 M nBu$_4$NPF$_6$ under N$_2$.
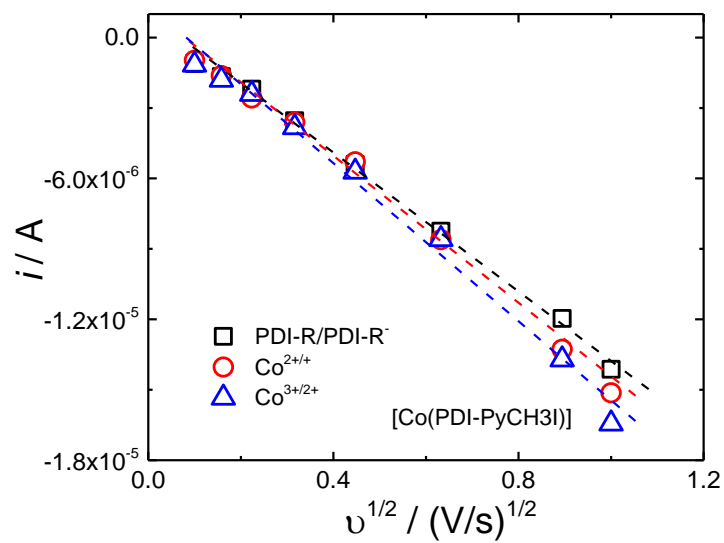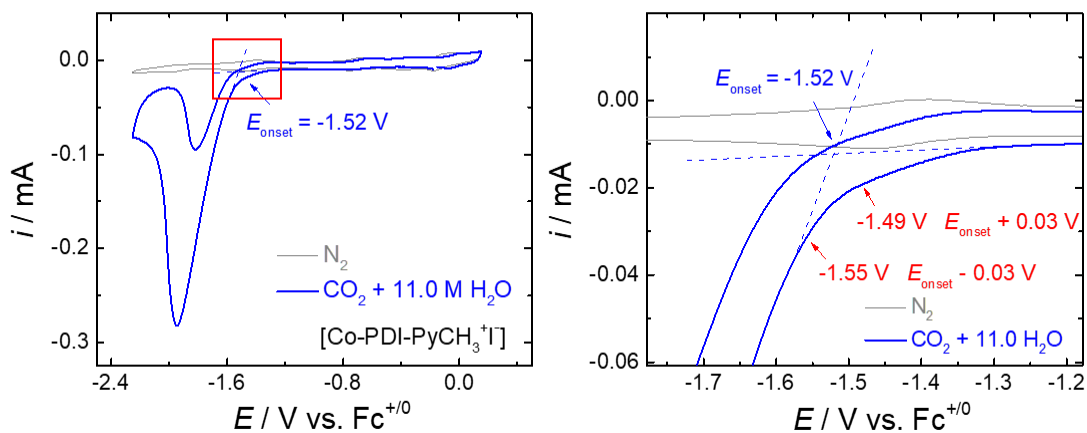

Figure A.131 The representative plot of i_{redox} as a function of $\upsilon^{1/2}$ for 0.3 mM [Co(PDI-Ph)] in MeCN with 0.1 M nBu$_4$NPF$_6$ under N$_2$.

Figure A.132 The representative plot of i_{redox} as a function of $\upsilon^{1/2}$ for 0.3 mM [Co(PDI-Py)] in MeCN with 0.1 M nBu$_4$NPF$_6$ under N$_2$.

Figure A.133 The representative plot of i_{redox} as a function of $\upsilon^{1/2}$ for 0.3 mM [Co(PDI-PyCH$_3$$^+I^-$)] in MeCN with 0.1 M nBu$_4$NPF$_6$ under N$_2$.
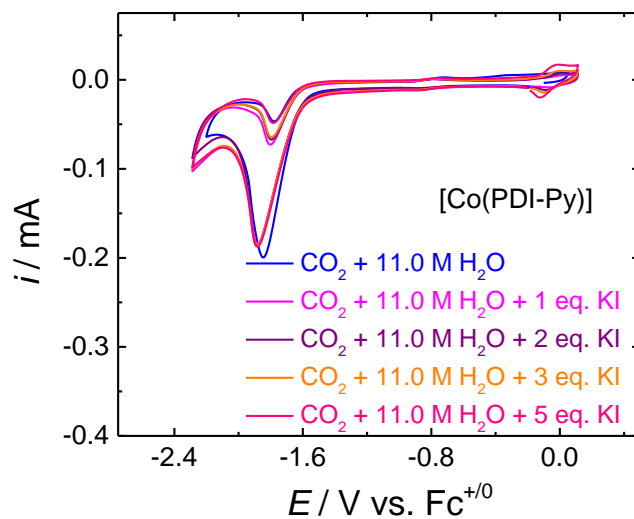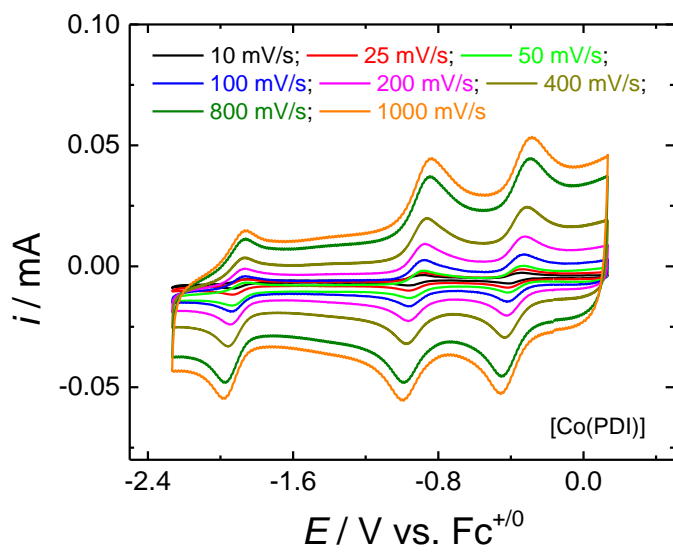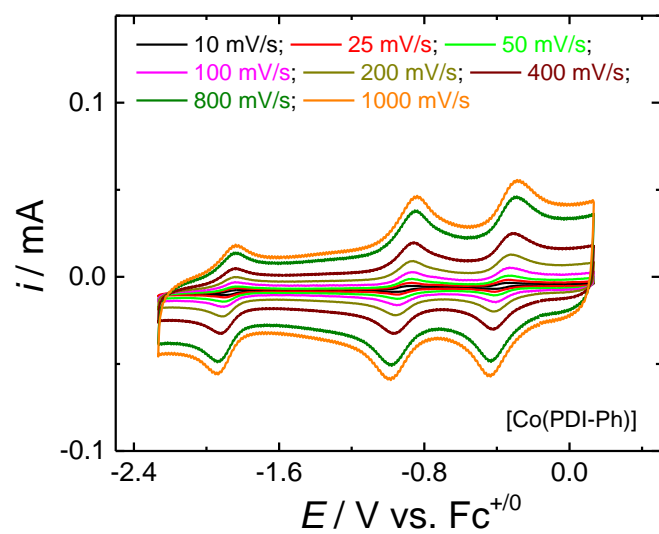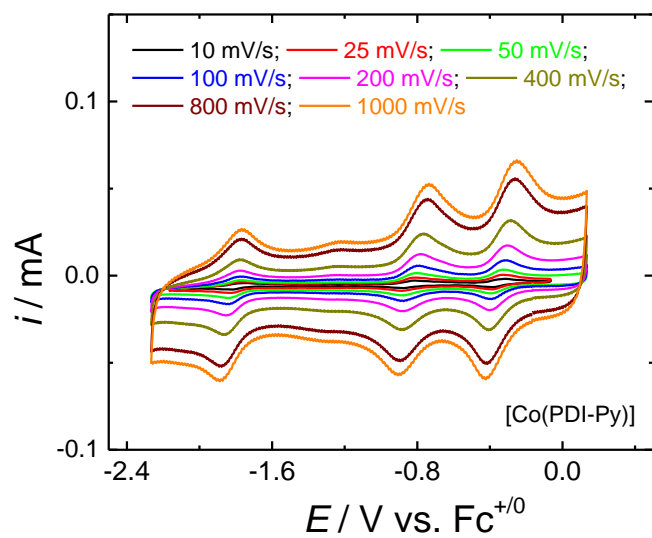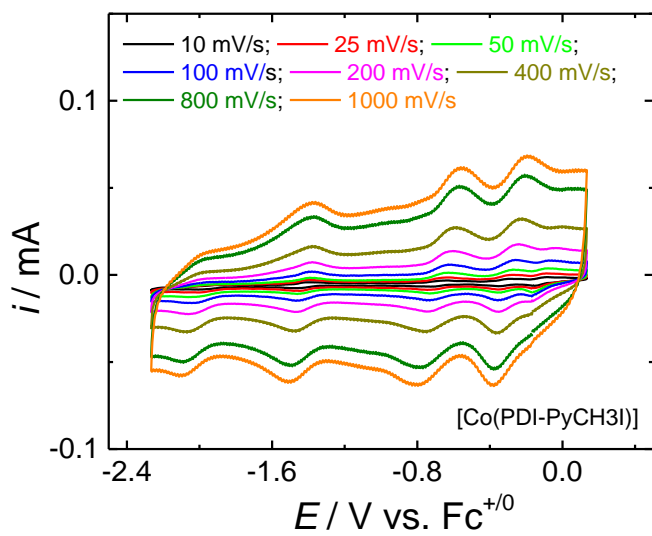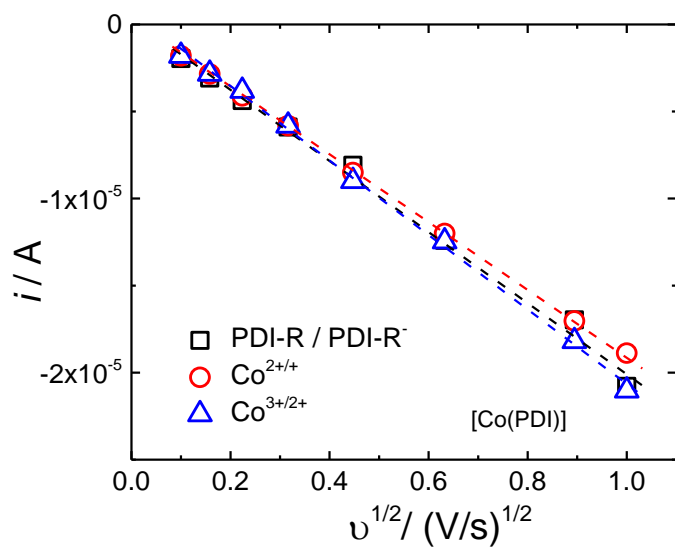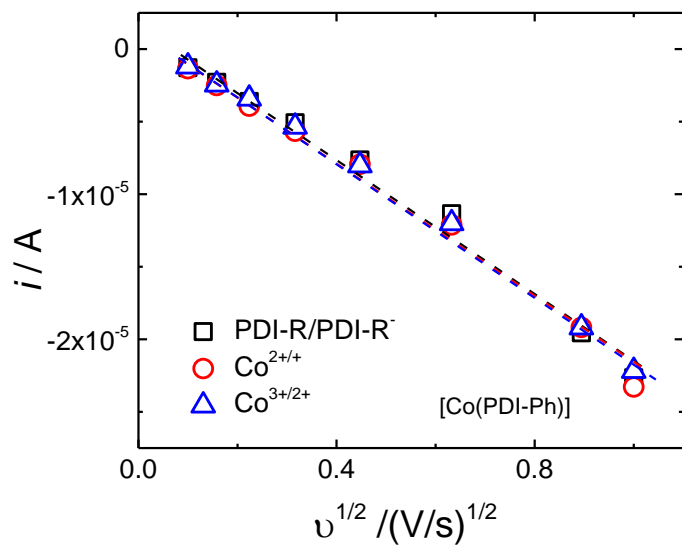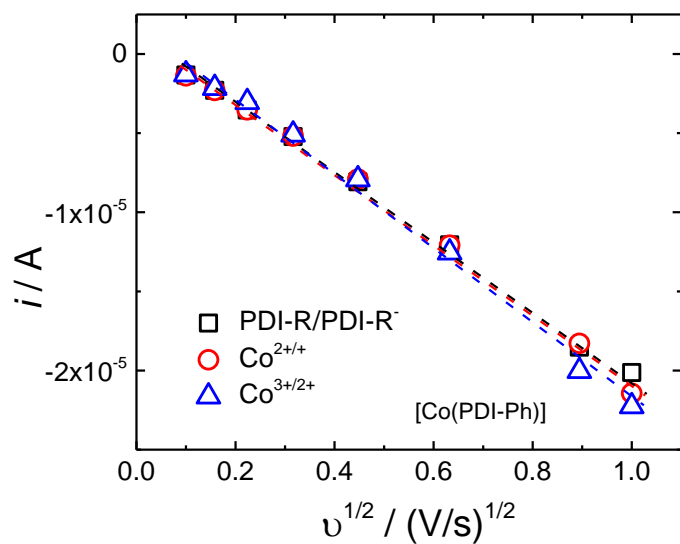
Figure A.134 Left: the CV of 0.30 mM [Co(PDI-Py-CH$_3$$^+I^-$)] in MeCN with 0.1 M nBu$_4$NPF$_6$ under N$_2$ and CO$_2$ in the presence of 11.0 M H$_2$O; Right: the definition of the potential range (E_{onset} + 30 mV) ~ (E_{onset} − 30 mV) in the zoom-in square of the left figure.

Figure A.135 Left: the plot of i/i^0 vs. $1/1+\exp[(F/RT)\times(E−E^0)]$ in the "foot-of-the-wave" potential window with the selected potential range highlighted for [Co(PDI-Py-CH$_3$$^+I^-$)] (red); Right: The slope obtained by the linear fitting of the selected data points.
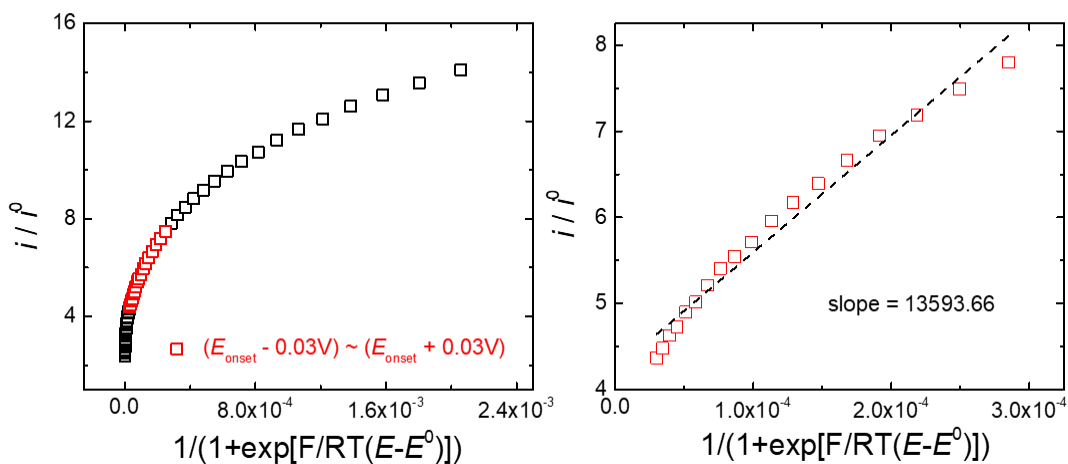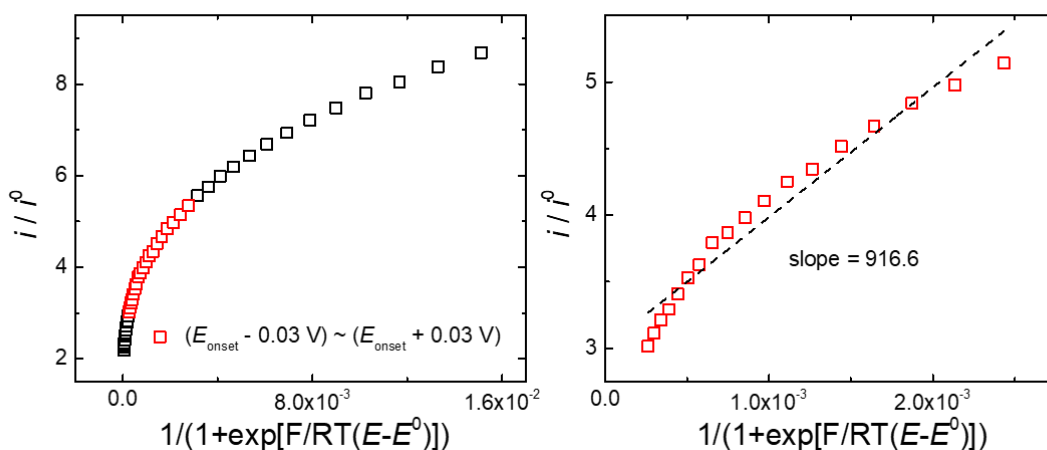
Figure A.136 Left: the plot of i/i^0 vs. $1/1+\exp[(F/RT)\times(E-E^0)]$ in the "foot-of-the-wave" potential window for [Co(PDI)] with the selected potential range highlighted (red); Right: The slope obtained by the linear fitting of the selected data pointes.
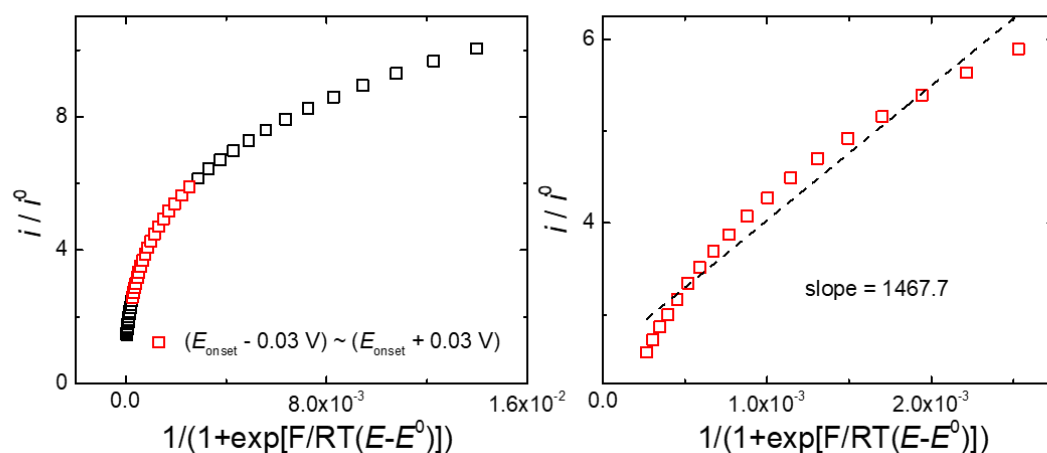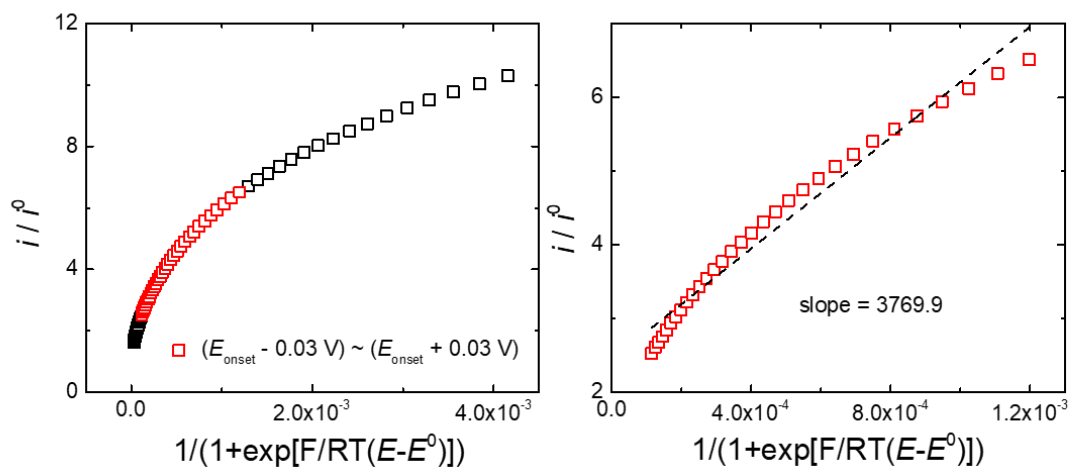

Figure A.137 Left: the plot of i/i^0 vs. $1/1+\exp[(F/RT)\times(E-E^0)]$ in the "foot-of-the-wave" potential window for [Co(PDI-Ph)] with the selected potential range highlighted (red); Right: The slope obtained by the linear fitting of the selected data pointes.

Figure A.138 Left: the plot of i/i^0 vs. $1/1+\exp[(F/RT)\times(E-E^0)]$ in the "foot-of-the-wave" potential window for [Co(PDI-Py)] with the selected potential range highlighted (red); Right: The slope obtained by the linear fitting of the selected data pointes.
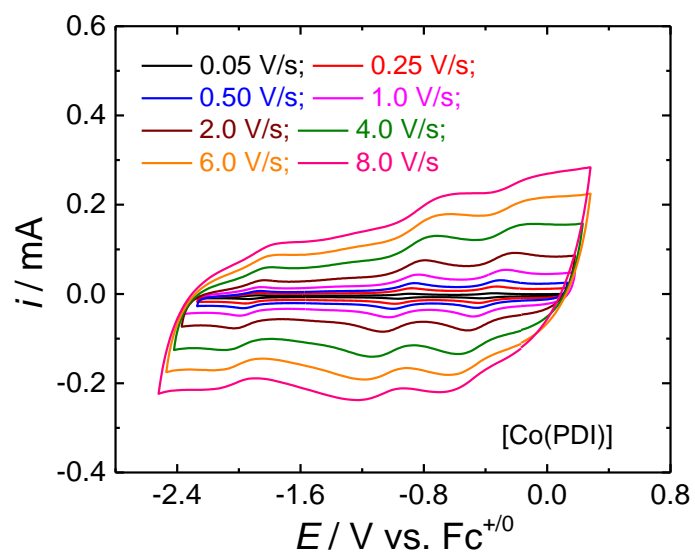
Figure A.139 CVs of 0.3 mM [Co(PDI)] in N$_2$-saturated MeCN with 0.1 M nBuNPF$_6$ with varying scan rates from 0.05 V/s to 8.0 V/s.
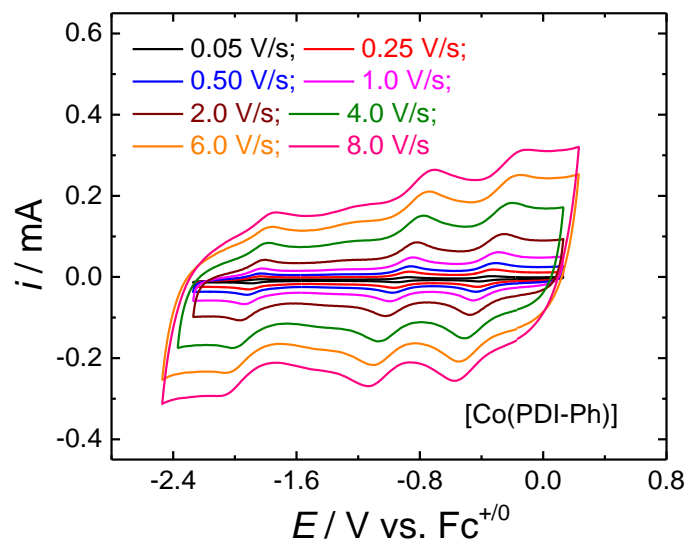

Figure A.140 CVs of 0.3 mM [Co(PDI-Ph)] in N$_2$-saturated MeCN with 0.1 M nBuNPF$_6$ with varying scan rates from 0.05 V/s to 8.0 V/s.
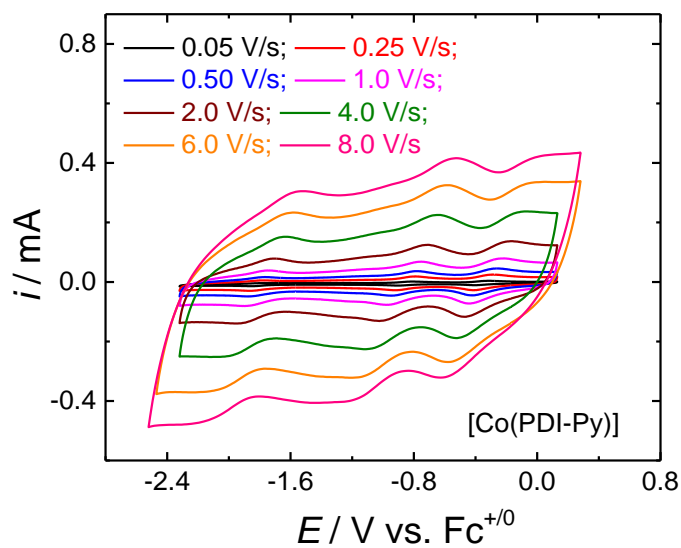
Figure A.141 CVs of 0.3 mM [Co(PDI-Py)] in N$_2$-saturated MeCN with 0.1 M nBuNPF$_6$ with varying scan rates from 0.05 V/s to 8.0 V/s
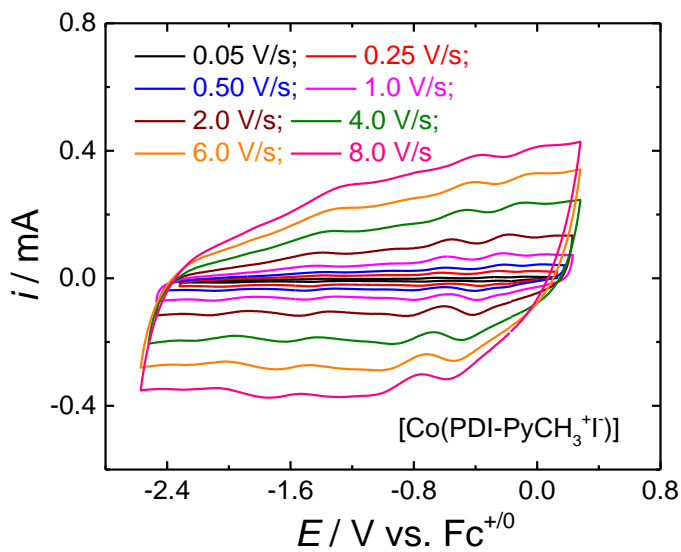

Figure A.142 CVs of 0.3 mM [Co(PDI-PyCH$_3$$^+I^-$)] in N$_2$-saturated MeCN with 0.1 M nBuNPF$_6$ with varying scan rates from 0.05 V/s to 8.0 V/s.

A.3.2 Supporting Tables

Table A.20 Control CPE experiments with Pt and bare GC working electrodes in MeCN solution with 1 M acetic acid under N_2 to show the cell is gastight.

Electrode	Electrolysis Time	Q / C	FE(H2) / %
Pt	60 min	31.8	102.2
GC	60 min	41.5	99.5

Table A.21 $E_{1/2}$ values for the Redox Processes of the [Co(PDI-R)], [Zn(PDI-R)] and DAP-R.

Catalyst	$E_{1/2}$ / V vs Fc$^{+/0}$					
	I$^-$/I$_2$	Co$^{3+/2+}$	Co$^{2+/+}$	PDI-R$^+$/PDI-R	PDI-R/PDI-R$^{\bullet-}$	PDI-R$^{\bullet-}$/PDI-R^{2-}
[Co(PDI)]	-	−0.38	−0.92	-	−1.88	⩽ −2.3[a]
[Co(PDI-Ph)]	-	−0.37	−0.91	-	−1.86	−2.43 (red)[b]
[Co(PDI-Py)]	-	−0.35	−0.85	-	−1.80	−2.37
[Co(PDI-PyCH$_3^+$I$^-$)]	−0.13	−0.34	−0.70	−1.43	−1.95	−2.27 (red)[b]
[Zn(PDI)]	-	-	-	-	−1.65 (red)[b]	−1.84 (red)[b]
[Zn(PDI-Ph)]	-	-	-	-	−1.64 (red)[b]	−1.96 (red)[b]
[Zn(PDI-Py)]	-	-	-	-	−1.49 (red)[b]	−1.98 (red)[b]
[Zn(PDI-PyCH3+I−)]	−0.13	-	-	−0.98	−1.41	-1.96 (red)[b]
DAP	-	-	-	-	−2.08 (red)[b]	-
DAP-Ph	-	-	-	-	−2.04 (red)[b]	-
DAP-Py	-	-	-	-	−1.92 (red)[b]	-
DAP-PyCH$_3^+$I$^-$	−0.13	-	-	−1.22	−1.76 (red)[b]	-

[a]The PDI-R$^{\bullet-}$/PDI-R^{2-} potential for [Co(PDI)] cannot be determined because it coincides with catalytic H_2 evolution from residual H_2O at −2.3 V (Figure A.94). [b] The redox couple is irreversible, and the potential of the reduction peak is reported.

Table A.22 i_c/i_p and E_{onset} values of four Co complexes for CO$_2$RR based on their catalytic CVs

Catalysts	No H$_2$O added		11.0 M H$_2$O added	
	i_c/i_p	E_{onset} / V vs. Fc$^{+/0}$	i_c/i_p	E_{onset} / V vs. Fc$^{+/0}$
[Co(PDI)]	5.8	−1.75	13.2	−1.70
[Co(PDI-Ph)]	6.1	−1.75	18.7	−1.68
[Co(PDI-Py)]	8.1	−1.70	37.9	−1.60
[Co(PDI-Py-CH$_3^+$I$^-$)]	10.5	−1.65	106.3	−1.52

Table A.23 Control CPEs conducted with the bare glassy carbon electrode in fresh CO$_2$-saturated electrolyte in the presence of 11.0 M H$_2$O with no Co complex, and with 0.3 mM [Co(PDI-Py)] and 5 eq. KI added.

	Q / C	FE(H$_2$) / %	FE(CO) / %
Bare Glassy Carbon	2.0 ± 0.1	20.2 ± 4.1	0
0.3 mM [Co(PDI-Py)] with 5eq. KI	9.6 ± 1.7	0.7 ± 0.2	93 ± 6

All reported values are averages from independent sets of measurements in at least three independently prepared electrolyte solutions and are reported with standard deviations.

Table A.24 D_{obs} Values Measured at Different Redox Peak Potentials of [Co(PDI-R)] Catalysts

Catalyst	$D_{obs}(Co^{3+/2+})$ / 10^{-6} cm^{2}s^{-1}	$D_{obs}(Co^{2+/+})$ / 10^{-6} cm^{2}s^{-1}	$D_{obs}(PDI\text{-}R/PDI\text{-}R^{\bullet-})$ / 10^{-6} cm^{2}s^{-1}
[Co(PDI)]	17.9 ± 3.1	14.5 ± 2.4	13.2 ± 4.0
[Co(PDI-Ph)]	15.3 ± 1.0	15.5 ± 1.7	13.3 ± 2.9
[Co(PDI-Py)]	18.3 ± 1.9	13.5 ± 1.7	12.6 ± 3.4
Catalyst	$D_{obs}(Co^{3+/2+})$ / 10^{-6} cm^{2}s^{-1}	$D_{obs}(Co^{2+/+})$ / 10^{-6} cm^{2}s^{-1}	$D_{obs}(PDI\text{-}R^+/PDI\text{-}R)$ / 10^{-6} cm^{2}s^{-1}
[Co(PDI-Py-CH$_3^+$I$^-$)]	8.2 ± 0.4	7.1 ± 0.4	4.9 ± 1.0

D_{obs} values are averages from independent sets of measurements in at least three independently-prepared electrolyte solutions and are reported with standard deviations.

Table A.25 TOF_{CPE} values of four Co catalysts

Catalyst	E_{app} / V	E^0 / V	Q / C	FE$_{CO}$ / %	TOF_{CPE} / s^{-1}
[Co(PDI)]		-1.88[a]	6.2 ± 1.0	43 ± 12	9.8 ± 6.6
[Co(PDI-Ph)]	-1.95	-1.86[a]	8.8 ± 1.4	59 ± 4	$3.1 \pm 1.3 \times 10^1$
[Co(PDI-Py)]		-1.80[a]	9.8 ± 1.2	97 ± 5	$1.0 \pm 0.3 \times 10^2$
[Co(PDI-Py-CH$_3^+$I$^-$)]		-1.76[b]	16.7 ± 1.8	96 ± 3	$8.0 \pm 1.6 \times 10^2$

Reported values are averages from three or more independent measurements with reported standard deviations. [a]For [Co(PDI)], [Co(PDI-Ph)] and [Co(PDI-Py)], $E^0 = E_1 = E_{1/2}(PDI\text{-}R/PDI\text{-}R^{\bullet-})$. [b]For [Co(PDI-Py-CH$_3^+I^-$)], $E^0 = E_2 = E_{cat/2}$.

Table A.26 k_{FOWA} and corresponding $\log TOF_{FOWA}$ values of four Co catalysts studied in the report

Catalysts	k_{FOWA} / s^{-1}	$\log(TOF_{FOWA}/$ s$^{-1})$
[Co(PDI)]	1.6×10^5	5.2
[Co(PDI-Ph)]	4.2×10^5	5.6
[Co(PDI-Py)]	2.8×10^6	6.4
[Co(PDI-Py-CH$_3^+$I$^-$)]	3.6×10^7	7.6

Table A.27 i_c and corresponding k_{cat} of four [Co(PDI-R)] complexes

Catalyst	F / C·mol^{-1}	υ / V·s^{-1}	R / J·mol^{-1}·K^{-1}	T / K	i_c / mA	i_p/ mA	k_{cat} / s^{-1}
[Co(PDI)]					-1.5×10^{-1}	-3.4×10^{-3}	1.5×10^3
[Co(PDI-Ph)]					-2.8×10^{-1}	-3.9×10^{-3}	4.0×10^3
[Co(PDI-Py)]	96485	0.050	8.314	298	-3.8×10^{-1}	-3.9×10^{-3}	7.6×10^3
[Co(PDI-PyCH$_3^+$I$^-$)]					-5.3×10^{-1}	-2.3×10^{-3}	4.1×10^4

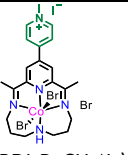**Table A.28** k_{cat} calculated based on i_p at different scan rates.

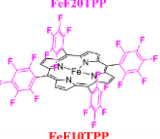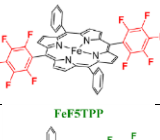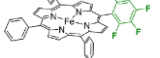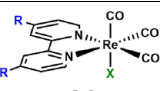| Scan Rate of Non-catalytic CVs (for i_p)		[Co(PDI)]	[Co(PDI-Ph)]	[Co(PDI-Py)]	[Co(PDI-PyCH$_3$$^+I^-$)]
0.05 V	i_p / mA	3.4×10^{-3}	3.9×10^{-3}	3.9×10^{-3}	2.3×10^{-3}
	k_{cat} / s^{-1}	1.5×10^{3}	4.0×10^{3}	7.6×10^{3}	4.1×10^{4}
0.25 V/s	i_p / mA	7.8×10^{-3}	9.0×10^{-3}	8.5×10^{-3}	5.1×10^{-3}
	k_{cat} / s^{-1}	1.4×10^{3}	3.8×10^{3}	7.7×10^{3}	4.2×10^{4}
0.50 V/s	i_p / mA	1.1×10^{-2}	1.3×10^{-2}	1.3×10^{-2}	7.1×10^{-3}
	k_{cat} / s^{-1}	1.5×10^{3}	3.7×10^{3}	6.9×10^{3}	4.4×10^{4}
1.0 V/s	i_p / mA	1.6×10^{-2}	1.7×10^{-2}	1.8×10^{-2}	1.0×10^{-2}
	k_{cat} / s^{-1}	1.4×10^{3}	4.1×10^{3}	6.8×10^{3}	4.1×10^{4}
2.0 V/s	i_p / mA	2.0×10^{-2}	2.4×10^{-2}	2.5×10^{-2}	1.4×10^{-2}
	k_{cat} / s^{-1}	1.7×10^{3}	4.3×10^{3}	7.0×10^{3}	4.2×10^{4}
4.0 V/s	i_p / mA	3.1×10^{-2}	3.4×10^{-2}	3.4×10^{-2}	2.0×10^{-2}
	k_{cat} / s^{-1}	1.4×10^{3}	4.2×10^{3}	7.6×10^{3}	4.5×10^{4}
6.0 V/s	i_p / mA	3.7×10^{-2}	4.3×10^{-2}	4.3×10^{-2}	2.6×10^{-2}
	k_{cat} / s^{-1}	1.5×10^{3}	3.9×10^{3}	7.4×10^{3}	3.9×10^{4}
8.0 V/s	i_p / mA	4.3×10^{-2}	5.0×10^{-2}	5.0×10^{-2}	2.9×10^{-2}
	k_{cat} / s^{-1}	1.5×10^{3}	3.9×10^{3}	7.4×10^{3}	4.1×10^{4}
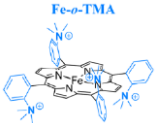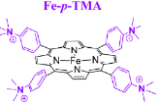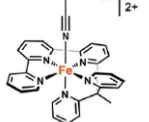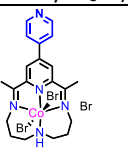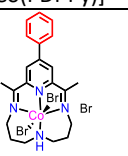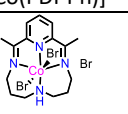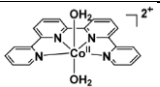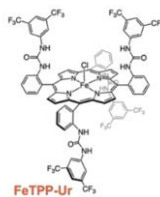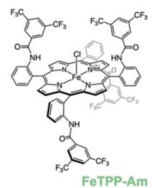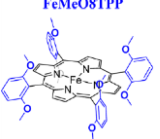
$i_{plateau}$ for these calculations are summarized in Table 4.5, and are 1.5×10^{-1} mA for [Co(PDI)], 2.8×10^{-1} mA for [Co(PDI-Ph)], 3.8×10^{-1} mA for [Co(PDI-Py)], and 5.3×10^{-1} mA for [Co(PDI-PyCH$_3$$^+I^-$)].

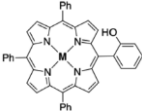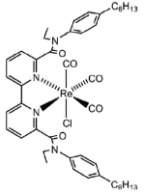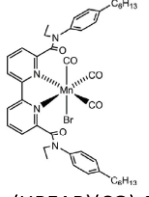**Table A.29** k_{cat} and corresponding logTOF_{cat} and logTOF_0 of four [Co(PDI-R)] complexes

Catalysts	k_{cat} / s^{-1}	log(TOF_{cat} / s^{-1})	log(TOF_0 / s^{-1})
[Co(PDI)]	1.5×10^{3}	3.2	-5.7
[Co(PDI-Ph)]	4.0×10^{3}	3.6	-4.9
[Co(PDI-Py)]	7.6×10^{3}	3.9	-3.6
[Co(PDI-Py-CH$_3$$^+I^-$)]	4.1×10^{4}	4.6	-2.2
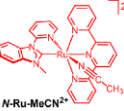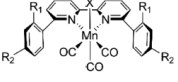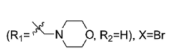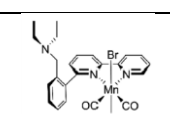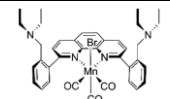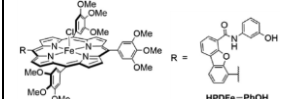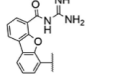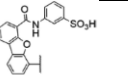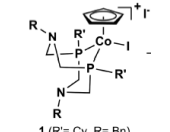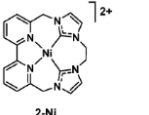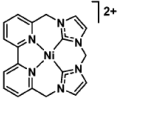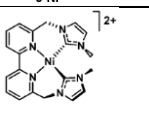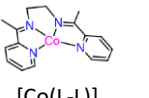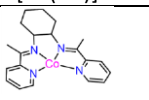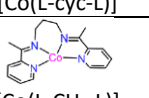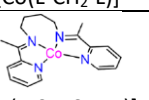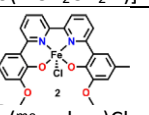
Table A.30 Selected reported molecular catalysts for electrochemical CO2RR in the last few years

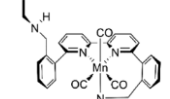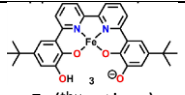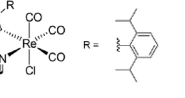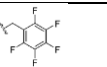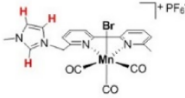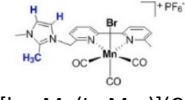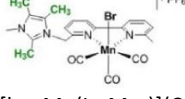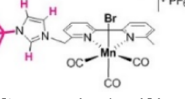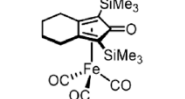| Catalyts	Solvent condition	E_{onset} / V vs.Fc$^{+/0}$	$E_{applied}$ / V vs.Fc$^{+/0}$	log(TOF_{cat}/ s^{-1})	log(TOF_0/s^{-1})	log(TOF_{CPE}/s^{-1})	Products	Ref
Fe-*o*-TMA	1 mM [cat] DMF 0.1 M H2O 3 M PhOH	~−1.44	−1.60	6.0	2.5	-	CO (93%)	Ref 1
Fe-*p*-TMA		~−1.64	−1.83	4.5	−4.4	-	CO (92%) H$_2$ (7%)	
[Fe(tpyPY2Me)(CH3CN)]	1 mM [cat] MeCN 3.5 M PhOH	> −1.50	−1.60 ~ −1.98	~ 5.2	~ 1.0	>5.7 (@−1.98)	CO (~94%) H$_2$ (<5.0%)	Ref 2
[Co(PDI-PyCH$_3$$^+I^-$)]	0.3 mM [cat] MeCN 11.0 M H$_2$O	−1.52	−1.95	4.6	−2.2	2.9	CO (96%) H$_2$ (0.6%)	This work
[Co(PDI-Py)]		−1.60		3.9	−3.6	2.0	CO (97%) H$_2$ (0.4%)	
[Co(PDI-Ph)]		−1.68		3.6	−4.9	1.5	CO (59%) H$_2$ (1.5%)	
[Co(PDI)]		−1.70		3.2	−5.7	1.0	CO (43%) H$_2$ (11%)	

Catalyst	Conditions						Product	Ref
Co complex (OH₂)₂ ²⁺	1 mM [cat] MeCN 3M PhOH	~−1.3	~−1.50	4.5	-	2.7	CO (94%)	Ref [3]
FeTPP-Ur	1 mM [cat] DMF 5.5 M H2O	~−1.54	−1.72	3.83	2.66	-	CO (91%)	Ref [4]
FeTPP-Am		~−1.74	-	3.85	-	-	-	
FeMeO8TPP	1 mM [cat] DMF 0.1 M H2O 1 M PhOH	~−2.14	−2.30	3.8	<−12	-	CO (86%)	Ref [5]
FeF20TPP		~−1.60	-	−0.2	−7.4	-	-	
FeF10TPP		~−1.74	−1.90	1.1	−8.5	-	CO (91%)	
FeF5TPP		~−1.79	-	2.5	−8.7	-	-	
Re complex R= OCH₃	1 mM [cat] MeCN 1 M PhOH	~−1.80	-	3.7	-	-	CO (70%)	Ref [6]
R= ᵗBu		~−1.75		3.8			CO (96%)	
R= CH₃		~−1.75		3.8			CO (100%)	
R= H		~−1.70		3.6			CO (100%)	
R= CF₃		~−2.15		4.0			CO (3%)	

Catalyst	Conditions						Products	Ref
R= CN		~−1.85		3.8			CO (3%)	
C-Ru-MeCN²⁺	1 mM [cat] MeCN 5% H₂O	~−1.85	~−2.15	3.4	-	-	CO (87%)	Ref [7]
N-Ru-MeCN²⁺		~−2.00		3.3			CO (91%)	
M=Fe	1 mM [cat] MeCN 1M H₂O	~−1.85	−2.3	3.7	-	−0.25	-	Ref [8]
[Re(HPEAB)(CO)₃Cl]	2 mM [cat] MeCN 2% H2O	-	−2.45	2.8	−8.0	−3.3	-	Ref [9]
[Mn(HPEAB)(CO)₃Br]	2 mM [cat] MeCN 5% H2O	-	−2.45	3.5	−4.9	−2.3	-	
R1=CH₂NEt₂ R2=H X=Br	1 mM [cat] MeCN 2 M TFE	-	−2.17	2.3 (LO:low overpotential) 3.7 (HO:high overpotential)	-	-	CO (4.8%) HCOOH(71%) H₂ (6.4%)	Ref [10]
R1=H R2= CH₂NEt₂ X=Br				2.9 (HO)	-	-	CO (83%) HCOOH(5%) H₂ (2.1%)	
R1= CH₂OH R2=H X=Br				1.6(LO) 2.9(HO)	-	-	CO (92%) HCOOH(0%) H₂ (1.9%)	

Catalyst	Conditions						Products	Ref
R1= Et R2=H X=Br				2.8 (HO)	-	-	CO (94%) HCOOH(0%) H_2 (0.1%)	
(R1= [morpholinium structure], R2=H), X=Br				1.6(LO) 2.9(HO)	-	-	CO (68%) HCOOH(23%) H_2 (0.5%)	
[Mn complex structure: OC, CO, Br, N, N]				1.9(LO) 3.7(HO)	-	-	CO (12.5%) HCOOH(63%) H_2 (5.5%)	
[Mn complex structure]				2.0(LO) 3.6(HO)	-	-	CO (5.6%) HCOOH(70%) H_2 (5.9%)	
[Mn complex structure with NH]				2.1(LO) 3.9(HO)	-	-	CO (35%) HCOOH(25%) H_2 (31%)	
HPDFe−PhOH	1 mM [cat] DMF 0.4 M PhOH	~−2.1	-	2.71		-	-	Ref [11]
HPDFe−Gnd			-	2.47		-	-	
HPDFe−3SA			-	2.18		-	-	
1 (R'= Cy, R= Bn) [Co complex]	1 mM [cat] DMF 1.1M H_2O	~−2.0	−2.25	2.6	-	2.8	CO (<1%) HCOOH(98%) H_2 (5%)	Ref [12]
[(bpy^{R}PY2Me)Fe] R = H, L1 = L2 = MeCN, n = 2	1 mM [cat] MeCN 11.0 M H_2O	~−1.60	−1.91	1.7	-	-	CO (22%) H_2 (0%)	Ref [13]
[(bpy^{R}PY2Me)Fe]				1.2	-	-	CO (24%) H_2 (53%)	

Catalyst	Conditions							Products	Ref
R = OH, L1 = L2 = MeCN, n = 2									
[(bpy^{R}PY2Me)Fe] R = OMe, L1 = L2 = MeCN, n = 2				1.4	-	-		CO (38%) H$_2$ (0%)	
[(bpy^{R}PY2Me)Fe] R = NHEt, L1 = L2 = CF$_3$SO$_3^-$, n = 2				3.3	-	-		CO (81%) H$_2$ (10%)	
2-Ni	1 mM [cat] MeCN 2% H$_2$O		−2.42	1.3	-	-		CO (56%) H$_2$ (43%)	Ref [14]
3-Ni			−2.44	1.7	-	-		CO (87%) H$_2$ (11%)	
1-Ni		-	−2.25	-	-	-		CO (5%) H$_2$ (93%)	Ref [14]
[Co(L-L)]	0.3 mM [cat] MeCN 11.0 M H$_2$O	−1.86	−1.95		-	-	2.1	CO (80.5%) HCOOH(0.7%) H$_2$ (1.1%)	Ref [15]
[Co(L-cyc-L)]		−1.63			-	-	0.7	CO (11.1%) H$_2$ (34.3%)	
[Co(L-CH$_2$-L)]		−1.59			-	-	1.6	CO (51.5%) HCOOH(1.8%) H$_2$ (1.6%)	
[Co(L-CH$_2$CH$_2$-L)]		−1.53			-	-	1.4	CO (31.2%) HCOOH(1.8%) H$_2$ (27.9%)	
Fe(^{me}crebpy)Cl	0.5 mM [cat] DMF 0.9 M PhOH	−2.2	−2.5		-	-	−3.3	CO (5%) HCOOH(84%) H$_2$ (12%)	Ref [16]

	Conditions						Products	Ref
Fe(tbucatbpy)	0.5 mM [cat] DMF 0.5 M PhOH			-	-	−3.5	CO (0.8%) HCOOH(71%) H$_2$ (23%)	
Cr(tbudhbpy)Cl(H$_2$O)	1 mM [cat] DMF 0.62 M PhOH	−1.9	−2.1	-	-	0.8	CO (96%)	Ref [17]
R = (2,6-diisopropylphenyl)	1 mM [cat] DMF 0.1 M MeOH	~ −2.0	−2.30	-	-	−1.1	CO (99%) H$_2$ (<1.0%)	Ref [18]
R = (pentafluorophenyl)			−2.30	-	-	−1.5	CO (64%) H$_2$ (<1.0%)	
[Mn[bpyMe(ImMe)](CO)$_3$Br]PF$_6$	1 mM [cat] MeCN 9.25 M H$_2$O	~−1.25 (1st) ~−1.40 (2nd)	−1.56 −1.82	-	-	-	CO (77.7%) @−1.56 V CO (70.3%) @−1.82 V	Ref [19]
[Mn[bpyMe(ImMe$_2$)](CO)$_3$Br]PF$_6$				-	-	-	CO (77.6%) @−1.56 V CO (72.6%) @−1.82 V	
[Mn[bpyMe(ImMe$_4$)](CO)$_3$Br]PF$_6$				-	-	-	CO (77.7%) @−1.56 V CO (70.3%) @−1.82 V	
[Mn[bpyMe(Im^{t}Bu)](CO)$_3$Br]PF$_6$				-	-	-	CO (72.2%) @−1.56 V	
(Fe SiMe$_3$ complex)	1 mM [cat] MeCN	−2.14	−2.29	-	-	−2.0	CO (99%)	Ref [20]

	THF/ Methanol (95/5)	~−1.12	~−1.50	-	-	-	CO (96%)	Ref [21]

A.3.3. Supporting Methods

A.3.3.1 Diffusion Coefficient Calculations

Diffusion coefficients, D, for each complex were determined from the redox peaks in the non-catalytic CVs of the [Co(PDI-R)] systems based on the Randles–Sevcik equation:[15]

$$i_{redox} = 0.446 n^{3/2} A C_{cat} \left(\frac{\upsilon F^3 D_{obs}}{RT} \right)^{1/2} \qquad \text{Eq. S1}$$

The diffusion coefficient, expressed here as D_{obs}, is based on the assumption that the effective concentration of the electroactive species at each redox potential is equal to the bulk concentration of [Co(PDI)-R] in solution. i_{redox} is the reduction peak current of the redox couple of the catalyst in the non-catalytic CV under N_2; $n = 1$ is the number of electrons transferred in the redox process; $C_{cat} = 3 \times 10^{-7}$ mol/cm^3 is the concentration of the catalyst dissolved in the solution; $F = 96485$ C/mol is Faraday's constant; $A = 0.0707$ cm^2 is the surface area of the glassy carbon working electrode in CV measurements; $T = 298$ K is the temperature; $R = 8.314$ J·K^{-1}·mol^{-1} is the ideal gas constant; and υ is the scan rate in units of V·s^{-1}.

Values of D_{obs} were determined at the Co$^{3+/2+}$, Co$^{2+/+}$, and PDI-R/PDI-R$^{\bullet-}$ couple for each complex by measuring i_{redox} as a function of scan rate. Representative voltammograms of each complex at different scan rates are shown in Figures A.126-A.129, and representative plots of i_{redox} as a function of $\upsilon^{1/2}$ for each complex are shown in Figures A.130-A.133. D_{obs} was calculated at each redox couples from the slopes of the best-fit lines according to Eq S1, and the results are summarized in Table A.24. The D_{obs} value calculated at every redox potential are equivalents suggesting there is no potential-dependent change in mass transport (e.g. as might be expected for a reductive dimerization event).[15] For calculations of TOF$_{CPE}$, the D_{obs} for the PDI-R/PDI-R$^{\bullet-}$

couples was used as the diffusion coefficient of the complex.

A.3.3.2 TOF calculations

A.3.3.2.1 TOF$_{CPE}$ calculations based on the CPE data

Turnover frequencies for CO production by [Co(PDI-R)] catalysts calculated from CPE data, TOF_{CPE}, are determined according to the procedure described by Savéant et al.[22-23] TOF$_{CPE}$ at a given potential is defined by equation S2.

$$\text{TOF}_{\text{CPE}} = \frac{n(\text{CO})}{n(\text{Cat}) \times t} \qquad \text{Eq. S2}$$

Here, $n(\text{CO})$ is the number of moles of CO produced during the electrolysis, and $n(\text{Cat})$ is the number of moles of [Co(PDI-R)] estimated in the reaction-diffusion layer during the electrolysis,[22-23] and t is the time of electrolysis in the unit of s. $n(\text{CO})$ is given by equation S3:

$$n(CO) = \frac{Q \times \text{FE(CO)}}{2F} \qquad \text{Eq. S3}$$

Here, Q is the charged passed during the CPE, FE(CO) is the measured Faradaic efficiency for CO production, and $F = 96485$ C/mol is the Faraday constant.

For a homogeneous molecular electrocatalyst, $n(Cat)$ is estimated from the space integration of the estimated catalyst amount in the reaction-diffusion layer near the surface of the working electrode as determined by equation S4.[15, 22-23]

$$n(\text{Cat}) = A \sqrt{\frac{D_{obs}}{TOF}} [\text{Cat}] \qquad \text{Eq. S4}$$

Here, $A = 2.56$ cm^2 is the active surface area of the working electrode, $t = 30$ min $= 1800$ s is the electrolysis time, D_{obs} is the diffusion coefficient for the complex determined at the PDI-R/PDI-R$^{\bullet-}$ couple in Table A.24, [Cat] $= 3 \times 10^{-7}$ mol/cm^3 is the concentration of the catalyst, and TOF is the maximum turnover frequency as determined from catalytic CVs at large overpotential. Combining Eq. S2, S3, and S4 leads to the expression for TOF$_{CPE}$ shown in Equation S5.

$$\text{TOF}_{CPE} = \frac{n(\text{CO})}{n(\text{Cat}) \times t} = \frac{\frac{Q \times FE(CO)}{2F}}{A \sqrt{\frac{D_{obs}}{TOF}}[Cat] \times t} \qquad \text{Eq. S5}$$

If we define the fractional current going to CO production as i according to Eq. S6:

$$i = \frac{Q \times FE(CO)}{t} \qquad \text{Eq. S6}$$

Then we can substitute this into Equation S5 to yield Equation S7 below:

$$\text{TOF}_{CPE} = \frac{i \times}{2FA} \frac{\sqrt{TOF}}{\sqrt{D_{obs}}[Cat]} \qquad \text{Eq. S7}$$

Alternatively, if we assume that the electron transfer to the catalyst is fast and that the redox process is Nernstian, then we can derive an alternate expression for the potential-dependent TOF$_{CPE}$ according to equation S8:[22-23]
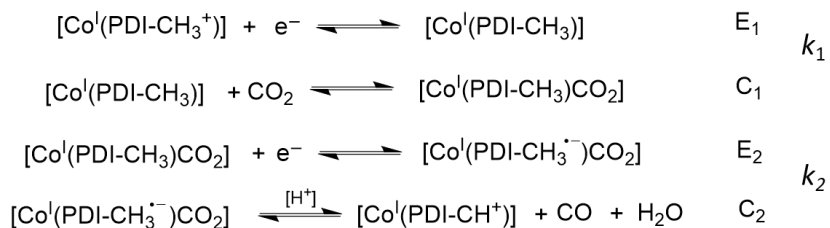
$$\text{TOF}_{CPE} = \frac{TOF}{1 + exp\left[\frac{F}{RT}(E_{app} - E^0)\right]} \qquad \text{Eq. S8}$$

Here, $R = 8.314$ J·K^{-1}·mol^{-1} is the universal gas constant, $T = 298.15$ K is temperature of the solution, E_{app} is the applied potential during electrolysis, E^0 is the redox potential of active species for the catalyst.

Previous studies and our own work suggest that Co(PDI)-based catalysts reduce CO_2 through an ECEC mechanism:[24-25]

$$[Co^I(PDI\text{-}R)] + e^- \rightleftharpoons [Co^I(PDI\text{-}R^{\bullet-})] \qquad E_1$$
$$\qquad\qquad\qquad\qquad\qquad\qquad\qquad\qquad\qquad k_1$$
$$[Co^I(PDI\text{-}R^{\bullet-})] + CO_2 \rightleftharpoons [Co^I(PDI\text{-}R^{\bullet-})CO_2] \qquad C_1$$
$$[Co^I(PDI\text{-}R^{\bullet-})CO_2] + e^- \rightleftharpoons [Co(PDI\text{-}R)CO_2]^- \qquad E_2$$
$$\qquad\qquad\qquad\qquad\qquad\qquad\qquad\qquad\qquad k_2$$
$$[Co(PDI\text{-}R)CO_2]^- \xrightarrow{[H^+]} [Co^I(PDI\text{-}R)] + CO + H_2O \qquad C_2$$

Scheme 0.1 Proposed ECEC mechanism for the CO_2RR by [Co(PDI)], [Co(PDI-Ph)], and [Co(PDI-Py)] in MeCN with 11 M H_2O.

$$[Co^I(PDI\text{-}CH_3^+)] + e^- \rightleftharpoons [Co^I(PDI\text{-}CH_3)] \qquad E_1$$
$$\qquad\qquad\qquad\qquad\qquad\qquad\qquad\qquad\qquad k_1$$
$$[Co^I(PDI\text{-}CH_3)] + CO_2 \rightleftharpoons [Co^I(PDI\text{-}CH_3)CO_2] \qquad C_1$$
$$[Co^I(PDI\text{-}CH_3)CO_2] + e^- \rightleftharpoons [Co^I(PDI\text{-}CH_3^{\bullet-})CO_2] \qquad E_2$$
$$\qquad\qquad\qquad\qquad\qquad\qquad\qquad\qquad\qquad k_2$$
$$[Co^I(PDI\text{-}CH_3^{\bullet-})CO_2] \xrightarrow{[H^+]} [Co^I(PDI\text{-}CH^+)] + CO + H_2O \qquad C_2$$

Scheme 0.2 Proposed ECEC mechanism for the CO_2RR by [Co(PDI-PyCH$_3^+$I$^-$)] in MeCN with 11 M H_2O.

For [Co(PDI)], [Co(PDI-Ph)], and [Co(PDI-Py)], the catalytic onset in CO_2-saturated solutions with 11 M H_2O occurs near the (PDI-R/PDI-R$^{\bullet-}$) redox couple (Figure A.111-A.113), indicating that [Co^I(PDI-R$^{\bullet-}$)] (E_1) is the active species to initiate the catalysis (C_1) (Scheme A.1). We expect that E_2 is more positive than E_1 ($E_1 < E_2$) (Scheme S1) due to the absence of the redox feature of CO_2 adduct intermediate (E_2) in the catalytic CVs in Figure A.111-A.113. Thus, the redox potential of the active species $E^0 = E_1 = E_{1/2}$(PDI-R/PDI-R$^{\bullet-}$).[22-23, 26] For [Co(PDI-PyCH$_3^+$I$^-$)], the catalytic onset under the same conditions occurs near the (PDI-R$^+$/PDI-R) redox

couple (Figure A.114), suggesting that $[Co^I(PDI-Py-CH_3)]^+$ (E_1) is the active species to initiate the catalysis (C_1) (Scheme A.2). However, for $[Co(PDI-PyCH_3{}^+I^-)]$, a prewave feature observed near the ($PDI-R^+/PDI-R$) redox couple prior to the catalytic current increase (Figure A.114) indicates the slow formation of CO_2 adduct intermediate $[Co^I(PDI-PyCH_3)CO_2]$ (C_1) before the reduction of the intermediate (E_2C_2) to the final produce CO.[26-27] This suggests $E_1 > E_2$ (Scheme A.2), which may be due to the lower nucleophilicity of the Co center of $[Co(PDI-PyCH_3{}^+I^-)]$ to bond CO_2 to form the adduct or the weaker catalytic driving force to efficiently conduct the further reduction of the CO_2 adduct intermediate $[Co^I(PDI-PyCH_3)CO_2]$ to the final product at the more positive onset potential compared to the other $[Co(PDI-R)]$ analogs. So the redox potential of the active species $E^0 = E_2$ is the redox potential of CO_2 adduct intermediate $[Co^I(PDI-PyCH_3)CO_2]$, which is not easy to estimate directly from the CVs. Therefore, in the most cases, $E_{cat/2}$ ($= -1.76$ V vs $Fc^{+/0}$, the potential corresponding to the half of the catalytic peak current) is used instead of E_2 as E_{cat}^0 for the analysis.[27]

Combining Equation S7 and S8 yields the following expression for TOF_{CPE}:

$$TOF_{CPE} = \frac{i^2\left(1 + exp\left[\frac{F}{RT}(E_{app} - E^0)\right]\right)}{4F^2 A^2 D_{obs}[Cat]^2} \qquad \text{Eq. S9}$$

In the final expression of TOF_{CPE} in Equation S9, all parameters are known constants for measurable values. TOF_{CPE} values for the four Co catalyst are summarized in Table A.25.

A.3.3.2.2. TOF$_{FOWA}$ calculation based on the Foot-of-Wave-Analysis of CVs

Our foot-of-wave-analysis and corresponding TOF$_{FOWA}$ calculations are based on reported procedures.[22-23, 26, 28-30] Note that these calculations are based on an ECEC mechanism for the CO$_2$RR by the [Co(PDI-R)] catalysts as discussed in last section of TOF$_{CPE}$ calculations.[24-26]

In an ideal system where no side-phenomenon perturbs the catalytic reaction, one obtains the classical S-shaped catalytic wave and the catalytic current in the CV response is given by equation S10:

$$\frac{i}{FS} = \frac{C_{cat}\sqrt{D}\sqrt{2k \cdot C_{CO2}}}{1 + exp\left[\frac{F}{RT}(E - E^0)\right]} \qquad \text{Eq. S10}$$

Here, i is the current of catalytic wave; F = 96485 C/mol is Faraday constant; S is the electrode surface area; C_{cat} is the concentration of the catalyst dissolved in the solution; D is the diffusion coefficient of the catalyst; k is the kinetic rate constant; C_{CO2} = 0.28 M is the concentration of CO$_2$ dissolved in MeCN solution; T = 298 K is the temperature of the electrolyte solution; R = 8.314 J·K^{-1}·mol^{-1} is the ideal gas constant; E is the scanned potential in CV measurements; E^0 is the redox potential of active species of the active species of the catalyst.

The redox peak current of the catalyst under N$_2$ is defined by the Randles–Sevcik equation, given by equation S11:

$$\frac{i^0}{FS} = 0.446 \times C_{cat}\sqrt{D}\sqrt{\frac{F\upsilon}{RT}} \qquad \text{Eq. S11}$$

Here, i^0 is the redox peak current of the catalyst in non-catalytic CVs under N$_2$; υ is the scan rate

of CV measurements; other parameters in the equation have been defied above.

Combining Equation S10 and S11 gives the following expression for i/i^0 in the function of $1/1+\exp[(F/RT)\times(E-E^0)]$, shown by equation S12

$$\frac{i}{i^0} = \frac{2.24\sqrt{\frac{RT}{F\upsilon}2k\cdot C_{CO2}}}{1+exp\left[\frac{F}{RT}(E-E^0)\right]} \quad \text{Eq. S12}$$

Note that equations S10 and S12 are based on the assumption that no side-phenomenon perturbs the catalytic reaction. Without side phenomenon, plotting i/i^0 vs $1/1+\exp[(F/RT)\times(E-E^0)]$ gives rise to a straight line, the slope of which gives the access to the kinetic rate constant k.

However, in real experimental scenarios, several possible side-phenomena (such as consumption of the substrate, deactivation of the catalyst and inhibition by product) occur, causing the predicted linear plot of of i/i^0 vs $1/1+\exp[(F/RT)\times(E-E^0)]$ in equation S12 to deviate from linearity. In order to solve this realistic problem, a foot-of-the-wave-analysis (FOWA) method has been developed to extract the kinetic rate constant k from CVs in experimental scenarios, based on the idea that electrocatalysis follows pure kinetic conditions within Nernstian behavior in the region of low overpotential (the foot of the catalytic wave region) before side-phenomena take place.[7-8] Application of the FOWA method allows the observation of a linear plot i/i^0 vs $1/1+\exp[(F/RT)\times(E-E^0)]$ at the "foot of the catalytic wave", devoid of distortion resulting from the interference of side-phenomena.

In this report, for internal consistency, $(E_{onset} + 30 \text{ mV}) \sim (E_{onset} - 30 \text{ mV})$ is selected as the standard FOWA potential window to extract kinetic parameters for all catalysts in this study.[9] Note that we use the CV of [Co-PDI-Py-CH$_3^+$I$^-$] under CO_2 with 11.0 M H_2O as an example of the FOWA approach we used, and this approach was used for all catalysts in this study. Figure

A.134 shows where the $(E_{onset} + 30\ mV) \sim (E_{onset} - 30\ mV)$ falls on the catalytic CV for [Co-PDI-Py-CH$_3^+$I$^-$], and Figure A.135 shows a plot of i/i^0 vs. $1/1+\exp[(F/RT)\times(E-E^0)]$ for the full potential window and in the $(E_{onset} + 30\ mV) \sim (E_{onset} - 30\ mV)$ potential range.

Based on the equation S12, the slope of the plot of i/i^0 vs. $1/1+\exp[(F/RT)\times(E-E^0)]$ in the "foot-of-the-wave" potential window $(E_{onset} + 30\ mV) \sim (E_{onset} - 30\ mV)$ is related to k as follows:

$$slope = 2.24\sqrt{\frac{RT}{F\upsilon}2kC_{CO2}} \qquad \text{Eq. S13}$$

Using equation S13, k can be calculated:

slope	F / C·mol^{-1}	υ / V·s^{-1}	R / J·mol^{-1}·K^{-1}	T / K	C_{CO2} / M	k / M^{-1}·s^{-1}	k_{obs} / M^{-1}·s^{-1}
13593.66	96485	0.050	8.314	298	0.28	1.3×10^8	3.6×10^7

Here, $k_{obs} = k \cdot C_{CO2}$ is defined as the observed kinetic rate constant. According to the previous study about FOWA application, the characteristic feature of FOWA plots can be used to diagnose kinetic profiles of a catalytic mechanism.[26] In our study, for [Co(PDI)], [Co(PDI-Ph)], and [Co(PDI-Py)], the curvature shape of FOWA plots of the [Co(PDI-R)] catalysts (Figure A.136-A.138) indicates that k_1 is $> k_2$ based on ECEC mechanism discussed in last section of TOF$_{CPE}$ calculations.[26] The k_{obs} estimated from the FOWA can only accurately represent the rate constant for the faster step,[26] which is k_1 in the cases of [Co(PDI)], [Co(PDI-Ph)], and [Co(PDI-Py)] complexes. For [Co(PDI-PyCH$_3^+$I$^-$)], E_2 is more negative than E_1 ($E_1 > E_2$) (Figure A.144), the curvature of the FOWA plot for [Co(PDI-PyCH$_3^+$I$^-$)] in Figure A.135 indicates $k_1 < k_2$,[27] and the FOWA only estimates the k_2 value rather than the rate-determining k_1.[27] Nevertheless, we estimated the maximum turnover frequency from the FOWA, labeled TOF$_{FOWA}$ (TOF_{k1}, Eq. 14) defined as k_{obs}

here:[5-6]

$$TOF_{FOWA} = k_{obs} = k_{FOWA} = k_{1 \text{ or } 2} \qquad \text{Eq. S14}$$

k_{FOWA} and corresponding $\log TOF_{FOWA}$ of all [Co(PDI-R)] catalysts are calculated using the same method described above and summarized in Table A.26.

A.3.3.2.3. TOF_{cat} and TOF_0 calculations based on the scan rate independent plateau current

For the CO_2RR, the catalytic reaction rate k_{cat} can be calculated from the plateau current independent of scan rates based on the following equation:[23, 28]

$$\frac{i_{plateau}}{i_p} = \frac{1}{0.446}\sqrt{\frac{RT}{nFv}}n'\,k_{cat} \qquad \text{Eq. S15}$$

Here, $i_{plateau}$ is the catalytic plateau current under CO_2 independent of scan rates, i_p is the redox current of active species under N_2 measured with the scan rate v, R is the gas constant, T is the temperature, F is Faraday's constant, n is the number of unique electron transfer processes for CO_2RR per catalyst ($n = 2$), n' is the catalyst equivalents needed per turnover ($n' = 1$), and k_{cat} is the intrinsic catalytic rate constant.

To determine $i_{plateau}$, catalytic CVs of four [Co(PDI-R)] complexes under CO_2 in the presence of 11.0 M H_2O are collected with varying scan rates (Figure 4.5 in Chapter 4). Although we cannot really reach a true "plateau current" with a perfect S shape, which is probably due to the inverted peak shape of the catalytic current response in CVs, however, a plot of peak current vs scan rate asymptotically approaches a limit at fast scan rates ($v > 4$ V/s, Figure 4.6 in Chapter 4), and this limiting current $i_{plateau}$ is used to estimate the rate k_{cat} based on Eq. S15. $i_{plateau}$ and corresponding k_{cat} of four [Co(PDI-R)] complexes were calculated and summarized in Table A.27. The same k_{cat} values calculated based on i_p values from all measured scan rates (Figures A.139 – A.142) are shown in Table A.28 and are equivalent within +/− 20 %.

Based on the definition and mathematic derivation of TOF[23, 30], the expression of TOF is shown in equation S16:

$$TOF = \frac{k_{cat}}{1+exp\left[\frac{F}{RT}\left(E^0_{CO2}-E^0_{cat}-\eta\right)\right]} \qquad \text{Eq. S16}$$

Here E^0_{CO2} ($= -1.36$ V vs. Fc$^{+/0}$) is the thermodynamic potential for the CO$_2$RR in MeCN with 11.0 M H$_2$O as the proton source calculated and applied in the previous literature, which takes into account the fact that the true proton donor is dissolved CO$_2$ (i.e. carbonic acid, H$_2$CO$_3$).[1, 5-6, 31] E^0_{cat} is the estimated redox potential of the active species of the catalyst. As discussed in the calculation of TOF$_{CPE}$, for [Co(PDI)], [Co(PDI-Ph)] and [Co(PDI-Py)], the redox potential of catalytic active species $E^0_{cat} = E_{1/2}$(PDI-R/PDI-R$^{\bullet-}$), while for [Co(PDI-PyCH$_3$$^+I^-$)], E_2 is more negative than E_1 ($E_1 > E_2$) (Figure A.144) due to the presence of the prewave prior to the catalytic current increase and E_2 is the redox potential of CO$_2$ adduct intermediate [Co^I(PDI-PyCH$_3$)CO$_2$], which is not easy to estimate directly from the CVs. So the redox potential of catalytic active species $E^0_{cat} = E_{cat/2}$ ($= -1.76$ V vs Fc$^{+/0}$, the potential corresponding to the half of the catalytic peak current) is used instead of E_2 for the analysis.[26] Plotting logTOF vs. η gives Figure 4.7 in Chapter 4. logTOF when $\eta = 0$, logTOF_0, is a measure of the intrinsic catalytic ability of a catalyst. logTOF_{cat} is the maximum catalytic ability of a catalyst at the high overpotential. k_{cat} and corresponding logTOF_{cat} and logTOF_0 are summarized in Table A.29.

A.3.4 Supporting References

1.   Azcarate, I.; Costentin, C.; Robert, M.; Savéant, J.-M. "Through-Space Charge Interaction Substituent Effects in Molecular Catalysis Leading to the Design of the Most Efficient Catalyst of CO2-to-CO Electrochemical Conversion," *Journal of the American Chemical Society* **2016**, *138*, 16639-16644. http://dx.doi.org/10.1021/jacs.6b07014

2.   Derrick, J. S.; Loipersberger, M.; Chatterjee, R.; Iovan, D. A.; Smith, P. T.; Chakarawet, K.; Yano, J.; Long, J. R.; Head-Gordon, M.; Chang, C. J. "Metal–Ligand Cooperativity via Exchange Coupling Promotes Iron- Catalyzed Electrochemical CO2 Reduction at Low Overpotentials," *Journal   of   the   American   Chemical   Society* **2020**. http://dx.doi.org/10.1021/jacs.0c10664

3.   Cometto, C.; Chen, L.; Lo, P.-K.; Guo, Z.; Lau, K.-C.; Anxolabéhère-Mallart, E.; Fave, C.; Lau, T.-C.; Robert, M. "Highly Selective Molecular Catalysts for the CO2-to-CO Electrochemical Conversion at Very Low Overpotential. Contrasting Fe vs Co Quaterpyridine Complexes upon Mechanistic   Studies," *ACS   Catalysis* **2018**,   *8*,   3411-3417. http://dx.doi.org/10.1021/acscatal.7b04412

4.   Gotico, P.; Boitrel, B.; Guillot, R.; Sircoglou, M.; Quaranta, A.; Halime, Z.; Leibl, W.; Aukauloo, A. "Second-Sphere Biomimetic Multipoint Hydrogen-Bonding Patterns to Boost CO2 Reduction of Iron Porphyrins," *Angewandte Chemie International Edition* **2019**, *58*, 4504-4509. http://dx.doi.org/https://doi.org/10.1002/anie.201814339

5.   Azcarate, I.; Costentin, C.; Robert, M.; Savéant, J.-M. "Dissection of Electronic Substituent Effects in Multielectron–Multistep Molecular Catalysis. Electrochemical CO_2-to-CO Conversion Catalyzed by Iron Porphyrins," *The Journal of Physical Chemistry C* **2016**, *120*, 28951-28960. http://dx.doi.org/10.1021/acs.jpcc.6b09947

6. Clark, M. L.; Cheung, P. L.; Lessio, M.; Carter, E. A.; Kubiak, C. P. "Kinetic and Mechanistic Effects of Bipyridine (bpy) Substituent, Labile Ligand, and Brønsted Acid on Electrocatalytic CO_2 Reduction by Re(bpy) Complexes," *ACS Catalysis* **2018**, *8*, 2021-2029. http://dx.doi.org/10.1021/acscatal.7b03971

7. Gonell, S.; Massey, M. D.; Moseley, I. P.; Schauer, C. K.; Muckerman, J. T.; Miller, A. J. M. "The Trans Effect in Electrocatalytic CO_2 Reduction: Mechanistic Studies of Asymmetric Ruthenium Pyridyl-Carbene Catalysts," *Journal of the American Chemical Society* **2019**, *141*, 6658-6671. http://dx.doi.org/10.1021/jacs.9b01735

8. Sinha, S.; Warren, J. J. "Unexpected Solvent Effect in Electrocatalytic CO_2 to CO Conversion Revealed Using Asymmetric Metalloporphyrins," *Inorganic Chemistry* **2018**, *57*, 12650-12656. http://dx.doi.org/10.1021/acs.inorgchem.8b01814

9. Shipp, J. D.; Carson, H.; Spall, S. J. P.; Parker, S. C.; Chekulaev, D.; Jones, N.; Mel'nikov, M. Y.; Robertson, C. C.; Meijer, A. J. H. M.; Weinstein, J. A. "Sterically hindered Re- and Mn-CO_2 reduction catalysts for solar energy conversion," *Dalton Transactions* **2020**, *49*, 4230-4243. http://dx.doi.org/10.1039/D0DT00252F

10. Rønne, M. H.; Cho, D.; Madsen, M. R.; Jakobsen, J. B.; Eom, S.; Escoudé, É.; Hammershøj, H. C. D.; Nielsen, D. U.; Pedersen, S. U.; Baik, M.-H.; Skrydstrup, T.; Daasbjerg, K. "Ligand-Controlled Product Selectivity in Electrochemical Carbon Dioxide Reduction Using Manganese Bipyridine Catalysts," *Journal of the American Chemical Society* **2020**, *142*, 4265-4275. http://dx.doi.org/10.1021/jacs.9b11806

11. Margarit, C. G.; Schnedermann, C.; Asimow, N. G.; Nocera, D. G. "Carbon Dioxide Reduction by Iron Hangman Porphyrins," *Organometallics* **2019**, *38*, 1219-1223. http://dx.doi.org/10.1021/acs.organomet.8b00334

12.   Roy, S.; Sharma, B.; Pécaut, J.; Simon, P.; Fontecave, M.; Tran, P. D.; Derat, E.; Artero, V. "Molecular Cobalt Complexes with Pendant Amines for Selective Electrocatalytic Reduction of Carbon Dioxide to Formic Acid," *Journal of the American Chemical Society* **2017**, *139*, 3685-3696. http://dx.doi.org/10.1021/jacs.6b11474

13.   Zee, D. Z.; Nippe, M.; King, A. E.; Chang, C. J.; Long, J. R. "Tuning Second Coordination Sphere Interactions in Polypyridyl–Iron Complexes to Achieve Selective Electrocatalytic Reduction of Carbon Dioxide to Carbon Monoxide," *Inorganic Chemistry* **2020**, *59*, 5206-5217. http://dx.doi.org/10.1021/acs.inorgchem.0c00455

14.   Su, X.; McCardle, K. M.; Panetier, J. A.; Jurss, J. W. "Electrocatalytic CO_2 reduction with nickel complexes supported by tunable bipyridyl-N-heterocyclic carbene donors: understanding redox-active macrocycles," *Chem. Commun.* **2018**, *54*, 3351-3354. http://dx.doi.org/10.1039/C8CC00266E

15.   Nie, W.; Wang, Y.; Zheng, T.; Ibrahim, A.; Xu, Z.; McCrory, C. C. L. "Electrocatalytic CO_2 Reduction by Cobalt Bis(pyridylmonoimine) Complexes: Effect of Ligand Flexibility on Catalytic Activity," *ACS Catalysis* **2020**, *10*, 4942-4959. http://dx.doi.org/10.1021/acscatal.9b05513

16.   Nichols, A. W.; Hooe, S. L.; Kuehner, J. S.; Dickie, D. A.; Machan, C. W. "Electrocatalytic CO_2 Reduction to Formate with Molecular Fe(III) Complexes Containing Pendent Proton Relays," *Inorganic Chemistry* **2020**, *59*, 5854-5864. http://dx.doi.org/10.1021/acs.inorgchem.9b03341

17.   Hooe, S. L.; Dressel, J. M.; Dickie, D. A.; Machan, C. W. "Highly Efficient Electrocatalytic Reduction of CO_2 to CO by a Molecular Chromium Complex," *ACS Catalysis* **2020**, *10*, 1146-1151. http://dx.doi.org/10.1021/acscatal.9b04687

18.   Suntrup, L.; Stein, F.; Klein, J.; Wilting, A.; Parlane, F. G. L.; Brown, C. M.; Fiedler, J.; Berlinguette, C. P.; Siewert, I.; Sarkar, B. "Rhenium Complexes of Pyridyl-Mesoionic Carbenes: Photochemical Properties and Electrocatalytic CO2 Reduction," *Inorganic Chemistry* **2020**, *59*, 4215-4227. http://dx.doi.org/10.1021/acs.inorgchem.9b02591

19.   Sung, S.; Li, X.; Wolf, L. M.; Meeder, J. R.; Bhuvanesh, N. S.; Grice, K. A.; Panetier, J. A.; Nippe, M. "Synergistic Effects of Imidazolium-Functionalization on fac-Mn(CO)3 Bipyridine Catalyst Platforms for Electrocatalytic Carbon Dioxide Reduction," *Journal of the American Chemical Society* **2019**, *141*, 6569-6582. http://dx.doi.org/10.1021/jacs.8b13657

20.   Oberem, E.; Roesel, A. F.; Rosas-Hernández, A.; Kull, T.; Fischer, S.; Spannenberg, A.; Junge, H.; Beller, M.; Ludwig, R.; Roemelt, M.; Francke, R. "Mechanistic Insights into the Electrochemical Reduction of CO2 Catalyzed by Iron Cyclopentadienone Complexes," *Organometallics* **2019**, *38*, 1236-1247. http://dx.doi.org/10.1021/acs.organomet.8b00517

21.   Qiao, X.; Li, Q.; Schaugaard, R. N.; Noffke, B. W.; Liu, Y.; Li, D.; Liu, L.; Raghavachari, K.; Li, L.-s. "Well-Defined Nanographene–Rhenium Complex as an Efficient Electrocatalyst and Photocatalyst for Selective CO2 Reduction," *Journal of the American Chemical Society* **2017**, *139*, 3934-3937. http://dx.doi.org/10.1021/jacs.6b12530

22.   Costentin, C.; Robert, M.; Saveant, J.-M. "Catalysis of the electrochemical reduction of carbon dioxide," *Chemical Society Reviews* **2013**, *42*, 2423-2436. http://dx.doi.org/10.1039/c2cs35360a

23.   Costentin, C.; Drouet, S.; Robert, M.; Savéant, J.-M. "Turnover Numbers, Turnover Frequencies, and Overpotential in Molecular Catalysis of Electrochemical Reactions. Cyclic Voltammetry and Preparative-Scale Electrolysis," *Journal of the American Chemical Society* **2012**, *134*, 11235-11242. http://dx.doi.org/10.1021/ja303560c

24.   Lacy, D. C.; McCrory, C. C. L.; Peters, J. C. "Studies of Cobalt-Mediated Electrocatalytic CO_2 Reduction Using a Redox-Active Ligand," *Inorganic Chemistry* **2014**, *53*, 4980-4988. http://dx.doi.org/10.1021/ic403122j

25.   Zhang, M.; El-Roz, M.; Frei, H.; Mendoza-Cortes, J. L.; Head-Gordon, M.; Lacy, D. C.; Peters, J. C. "Visible Light Sensitized CO2 Activation by the Tetraaza [CoIIN4H(MeCN)]2+ Complex Investigated by FT-IR Spectroscopy and DFT Calculations," *The Journal of Physical Chemistry C* **2015**, *119*, 4645-4654. http://dx.doi.org/10.1021/jp5127738

26.   Wang, V. C. C.; Johnson, B. A. "Interpreting the Electrocatalytic Voltammetry of Homogeneous Catalysts by the Foot of the Wave Analysis and Its Wider Implications," *ACS Catalysis* **2019**, 7109-7123. http://dx.doi.org/10.1021/acscatal.9b00850

27.   Lee, K. J.; McCarthy, B. D.; Dempsey, J. L. "On decomposition, degradation, and voltammetric deviation: the electrochemist's field guide to identifying precatalyst transformation," *Chemical Society Reviews* **2019**, *48*, 2927-2945. http://dx.doi.org/10.1039/C8CS00851E

28.   Rountree, E. S.; McCarthy, B. D.; Eisenhart, T. T.; Dempsey, J. L. "Evaluation of Homogeneous Electrocatalysts by Cyclic Voltammetry," *Inorganic Chemistry* **2014**, *53*, 9983-10002. http://dx.doi.org/10.1021/ic500658x

29.   Costentin, C.; Savéant, J.-M. "Multielectron, Multistep Molecular Catalysis of Electrochemical Reactions: Benchmarking of Homogeneous Catalysts," *ChemElectroChem* **2014**, *1*, 1226-1236. http://dx.doi.org/10.1002/celc.201300263

30.   Costentin, C.; Passard, G.; Savéant, J.-M. "Benchmarking of Homogeneous Electrocatalysts: Overpotential, Turnover Frequency, Limiting Turnover Number," *Journal of the American Chemical Society* **2015**, *137*, 5461-5467. http://dx.doi.org/10.1021/jacs.5b00914

31.   Pegis, M. L.; Roberts, J. A. S.; Wasylenko, D. J.; Mader, E. A.; Appel, A. M.; Mayer, J. M. "Standard Reduction Potentials for Oxygen and Carbon Dioxide Couples in Acetonitrile and N,N-Dimethylformamide," *Inorganic Chemistry* **2015**, *54*, 11883-11888. http://dx.doi.org/10.1021/acs.inorgchem.5b02136

A.4 Supporting Information for Chapter 5

A.4.1 Supporting Figures
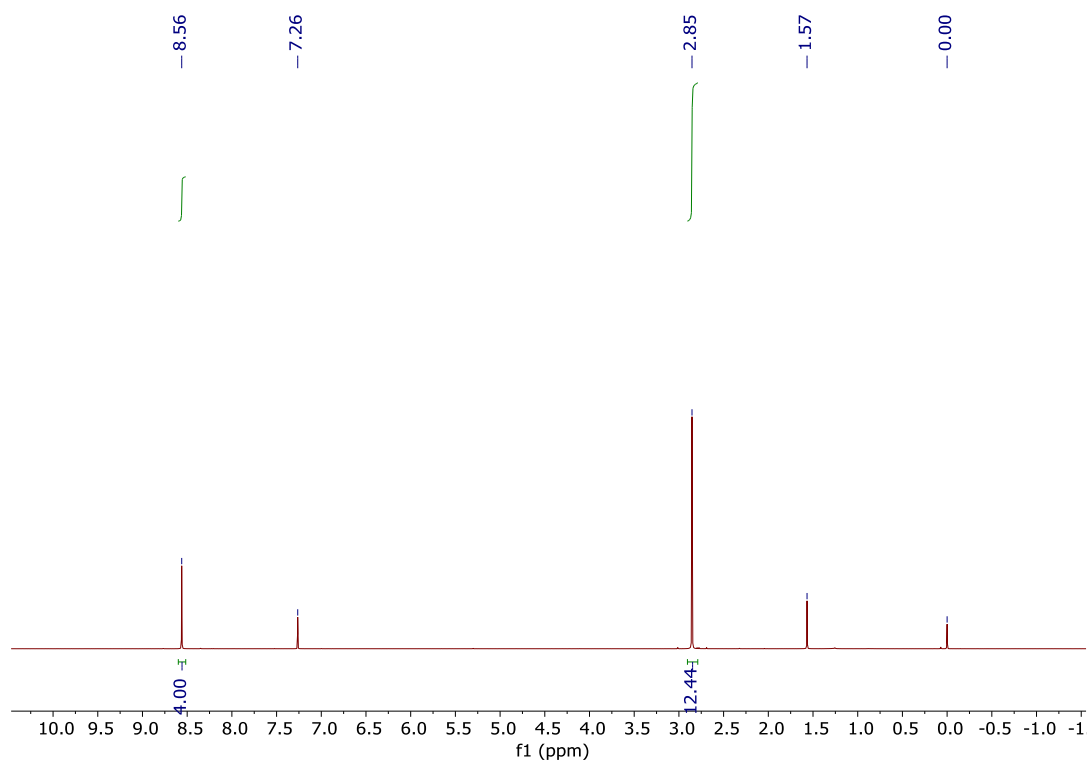
Figure A.143 ^{1}H-NMR Spectrum of 4,4'-bi(2,6-diacetylpyridine) in CD$_3$Cl-d_3 (δ 7.26 solvent residual peak, δ 1.57 water peak, δ 0.00 TMS standard peak).
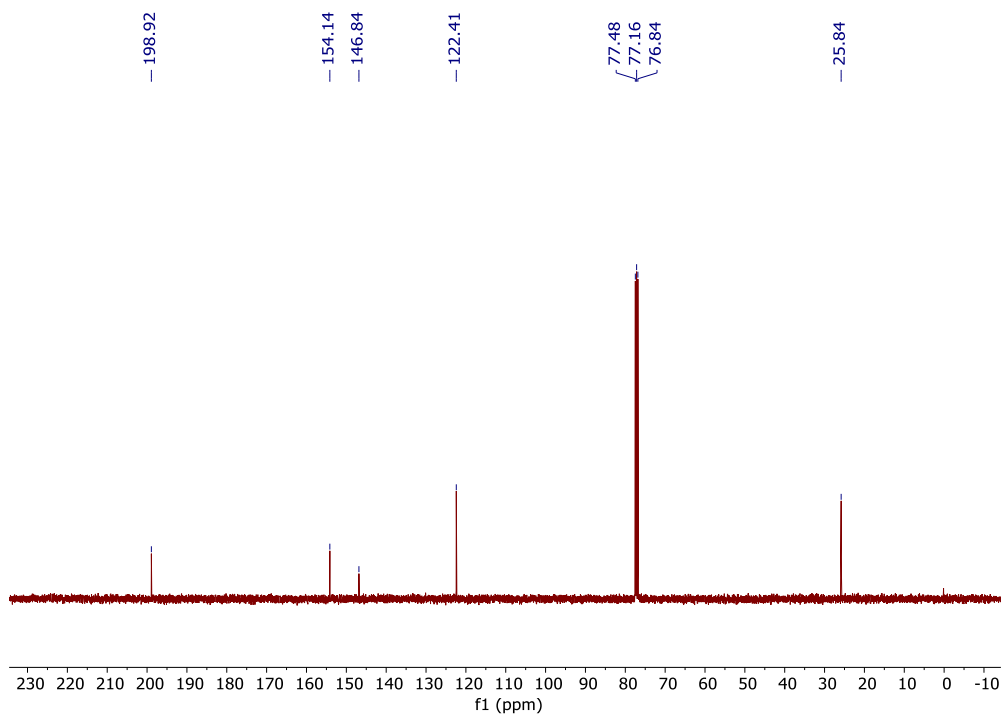
Figure A.144 ^{13}C-NMR Spectrum of 4,4'-bi(2,6-diacetylpyridine) in CD₃Cl-d_3 (δ 77.16 solvent residual peak).
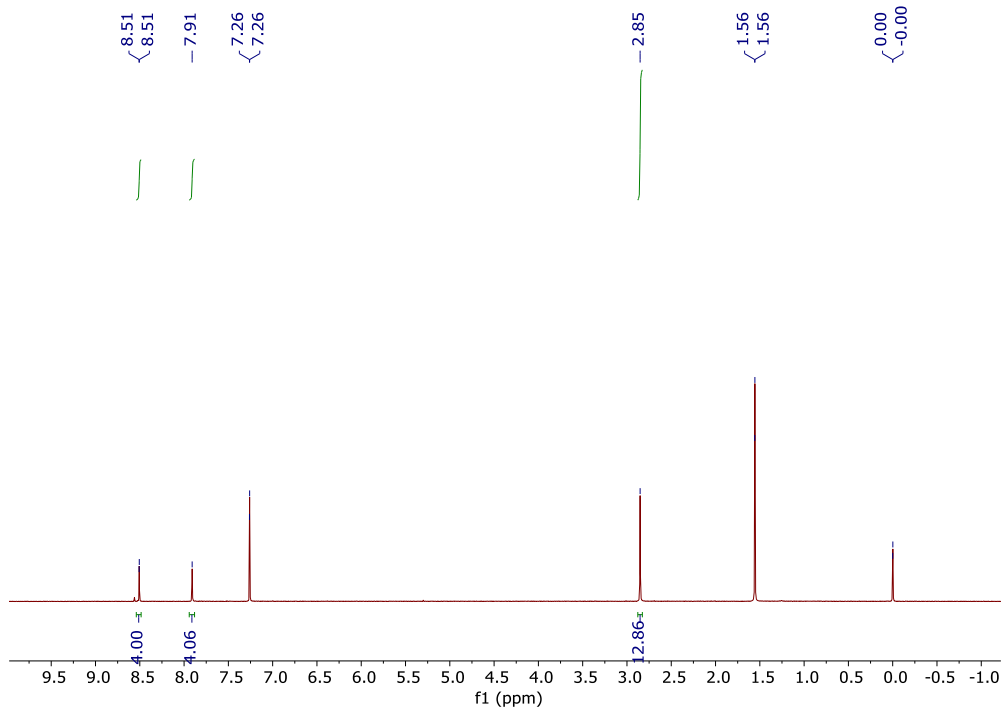
Figure A.145 ^{1}H-NMR Spectrum of 4,4'-(1,4-Phenylene)-bi(2,6-diacetylpyridine) in CD₃Cl-d_3 (δ 7.26 solvent residual peak, δ 1.56 water peak, δ 0.00 TMS standard peak).
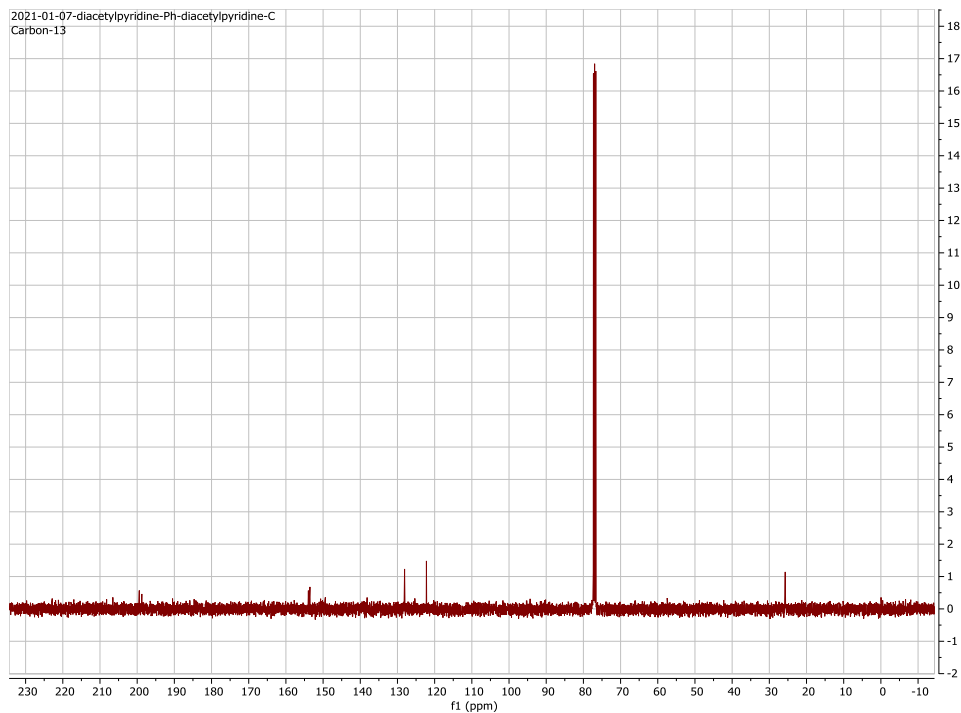
Figure A.146 ^{13}C-NMR Spectrum of 4,4'-(1,4-Phenylene)-bi(2,6-diacetylpyridine) in CD$_3$Cl-d_3 (δ 77.16 solvent residual peak).
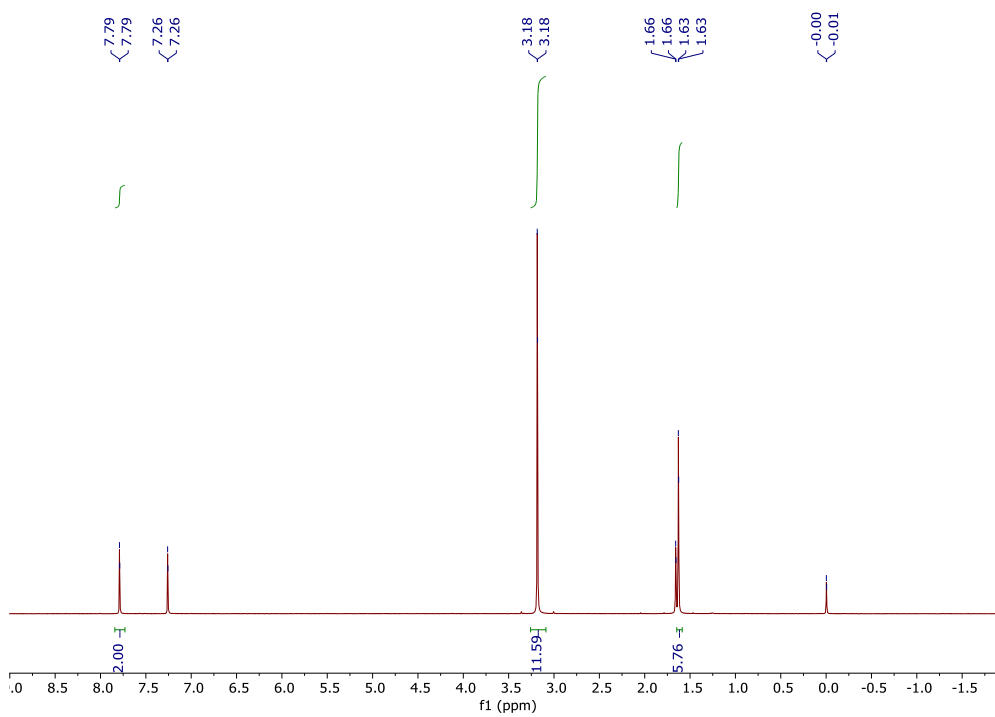
Figure A.147 ^{1}H-NMR Spectrum of 4-bromo-2,6-bis(1,1-dimethoxyethyl)-pyridine in CD$_3$Cl-d_3 (δ 7.26 solvent residual peak, δ 1.66 water peak, δ 0.00 TMS standard peak).
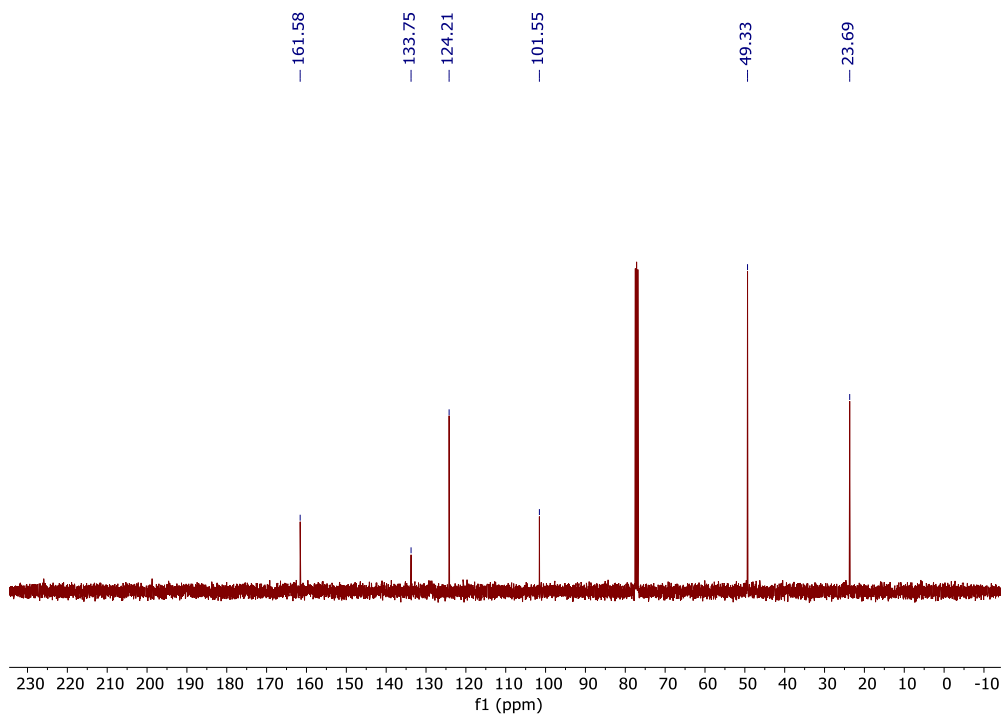
Figure A.148 ^{13}C-NMR Spectrum of 4-Bromo-2,6-bis(1,1-dimethoxyethyl)-pyridine in CD$_3$Cl-d_3 (δ 77.16 solvent residual peak).
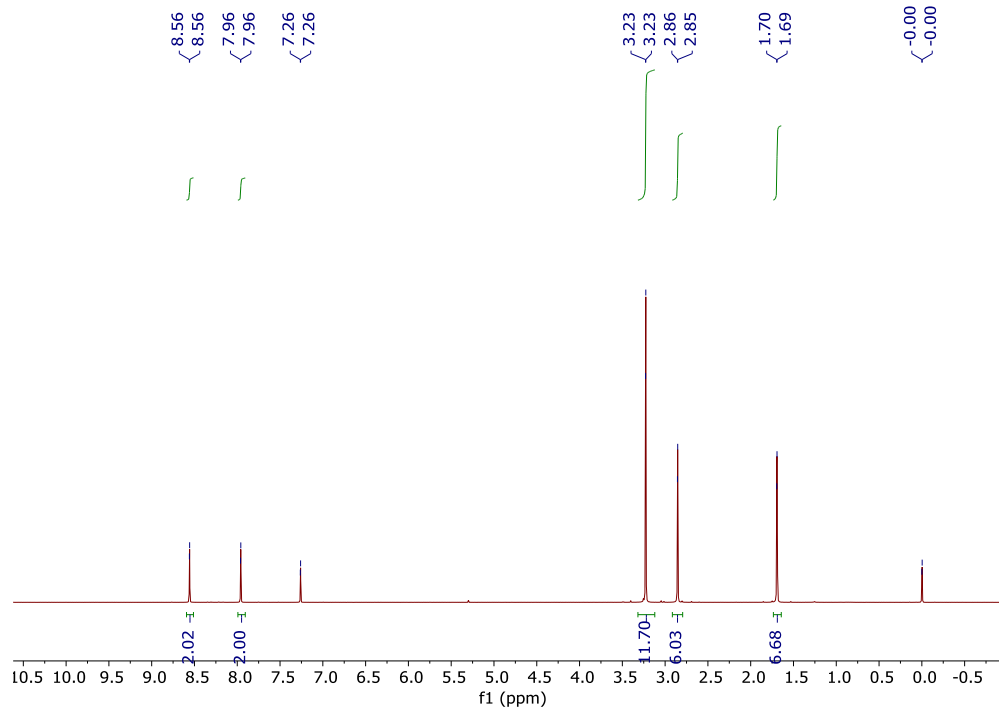
Figure A.149 ^{1}H-NMR Spectrum of (2,6-bis(1,1-dimethoxyethyl))-(2',6'-diacetyl)-4,4'-dipyridine in CD$_3$Cl-d_3 (δ 7.26 solvent residual peak, δ 0.00 TMS standard peak).
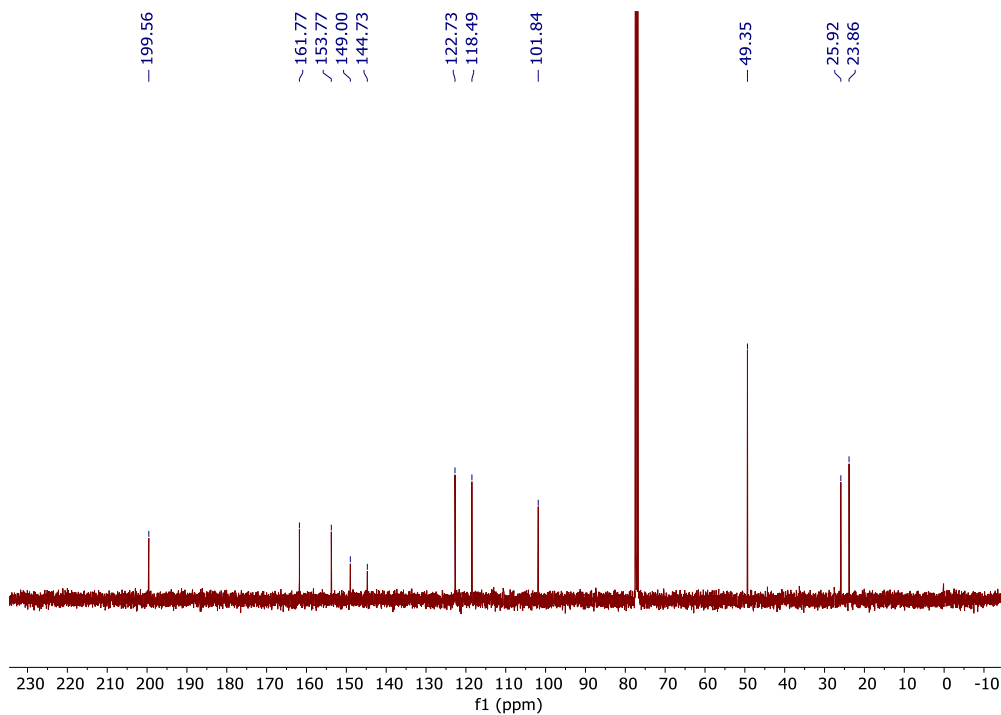
Figure A.150 ^{13}C-NMR Spectrum of (2,6-bis(1,1-dimethoxyethyl))-(2',6'-diacetyl)-4,4'-dipyridine in CD$_3$Cl-d_3 (δ 77.16 solvent residual peak).
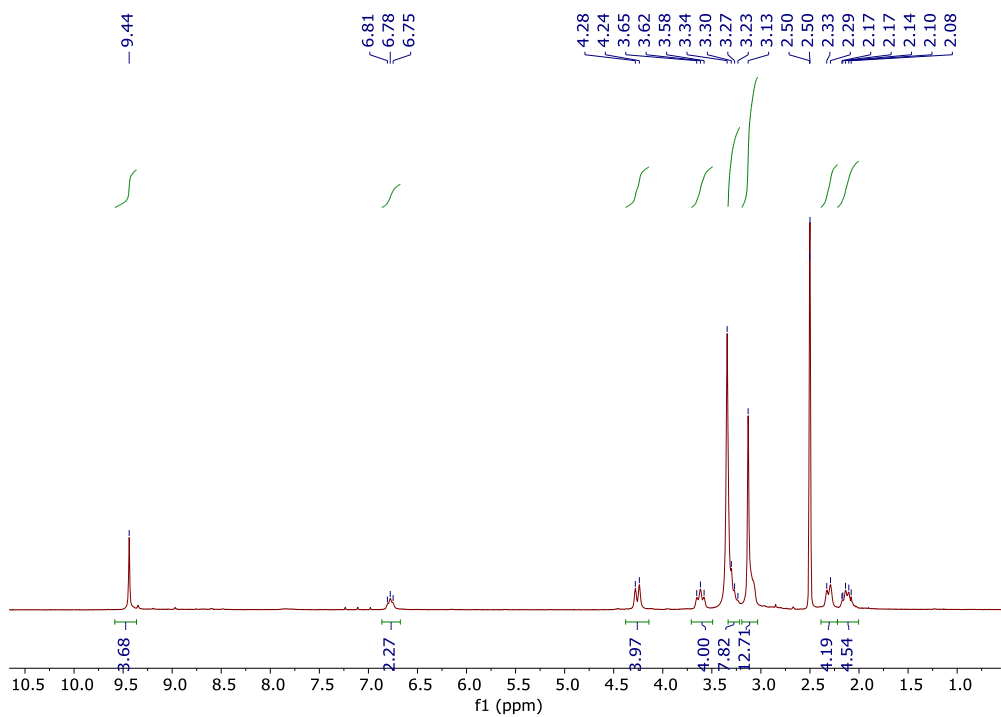
Figure A.151 ^{1}H-NMR Spectrum of bi-[Co(PDI)] in DMSO-d_6 (δ 2.50 solvent residual peak, δ 3.34 water peak).
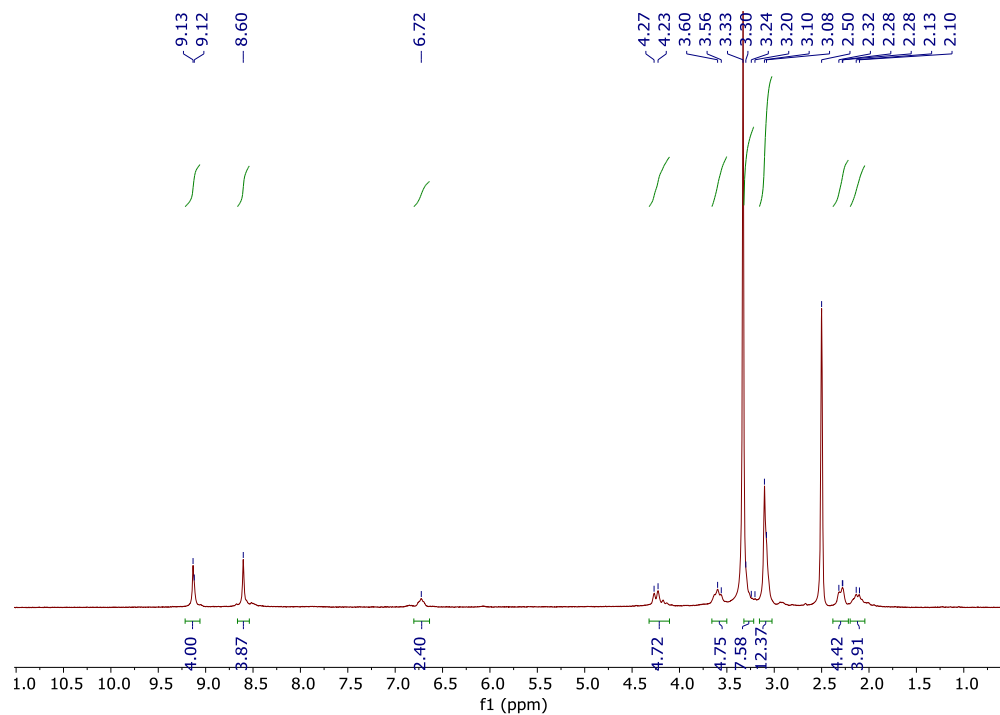
Figure A.152 ^{1}H-NMR Spectrum of bi-ex-[Co(PDI)] in DMSO-d_6 (δ 2.50 solvent residual peak, δ 3.34 water peak).
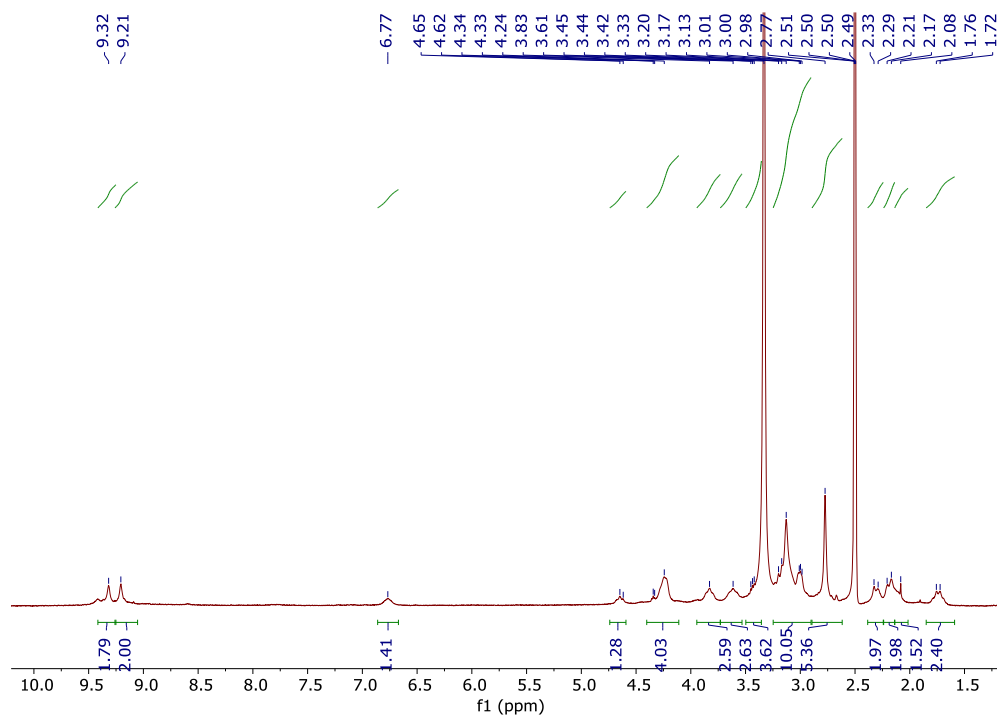
Figure A.153 ^{1}H-NMR Spectrum of bi-[ZnCo(PDI)] in DMSO-d_6 (δ 2.50 solvent residual peak, δ 3.34 water peak).
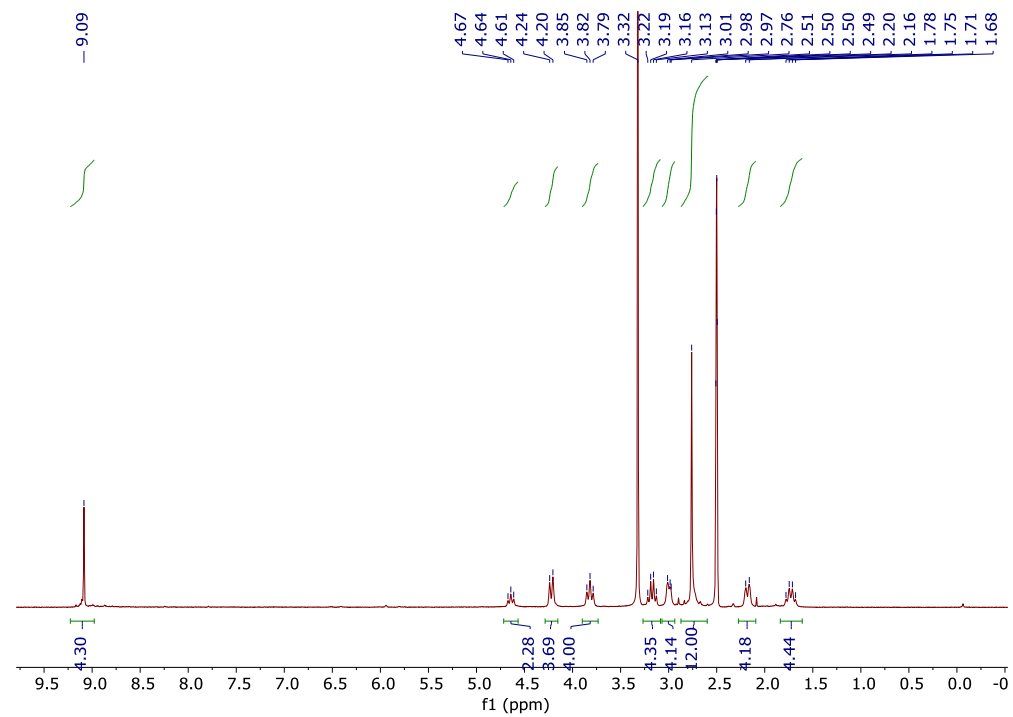
Figure A.154 ¹H-NMR Spectrum of bi-[Zn(PDI)] in DMSO-*d₆* (*δ* 2.50 solvent residual peak, *δ* 3.34 water peak).
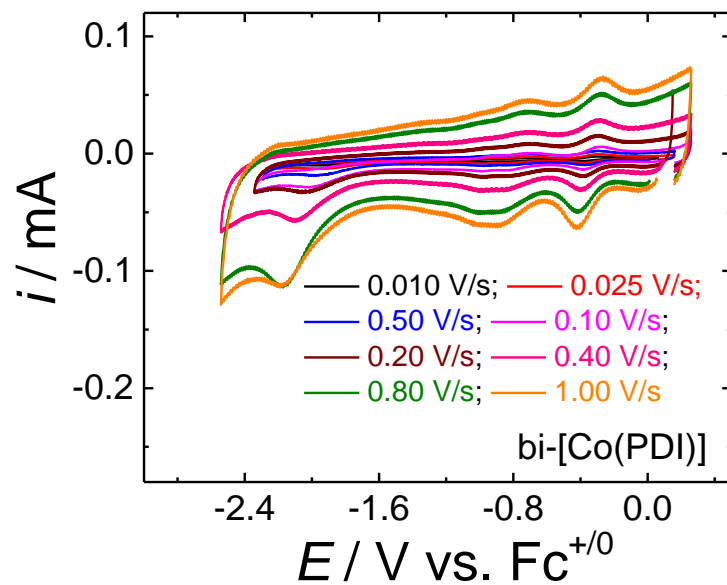
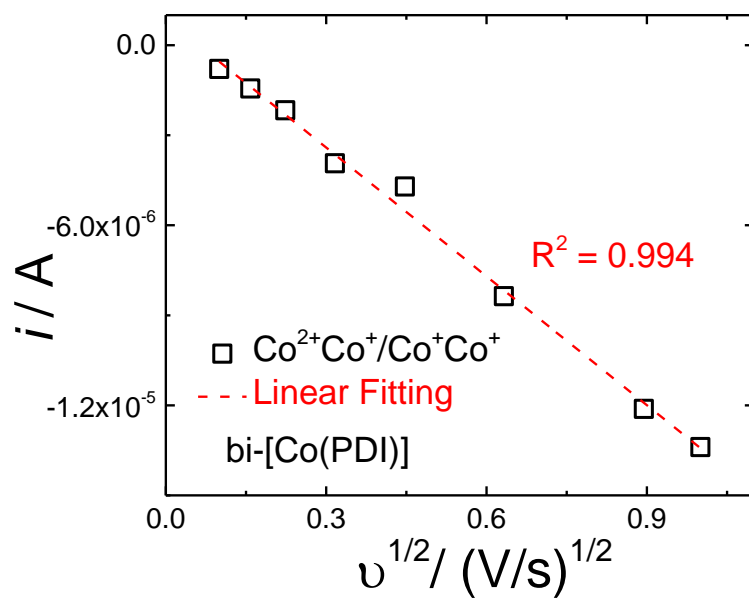**Figure A.155** Scan-rate dependent CVs of 0.15 mM bi-[Co(PDI)] in MeCN with 0.1 M nBuNPF$_6$ under N$_2$
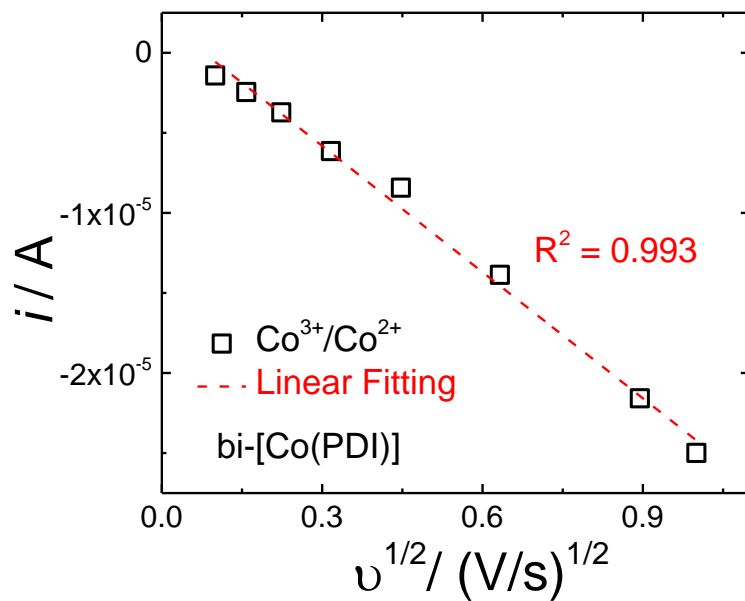
Figure A.156 The representative plot of $i_{reduction}$ at Co^{3+}/Co^{2+} couple as a function of $\upsilon^{1/2}$ for 0.15 mM bi-[Co(PDI)] in MeCN with 0.1 M nBu$_4$NPF$_6$ under N$_2$.

Figure A.157 The representative plot of $i_{reduction}$ at $Co^{2+}Co^{2+}/Co^{2+}Co^{+}$ couple as a function of $\upsilon^{1/2}$ for 0.15 mM bi-[Co(PDI)] in MeCN with 0.1 M nBu$_4$NPF$_6$ under N$_2$.
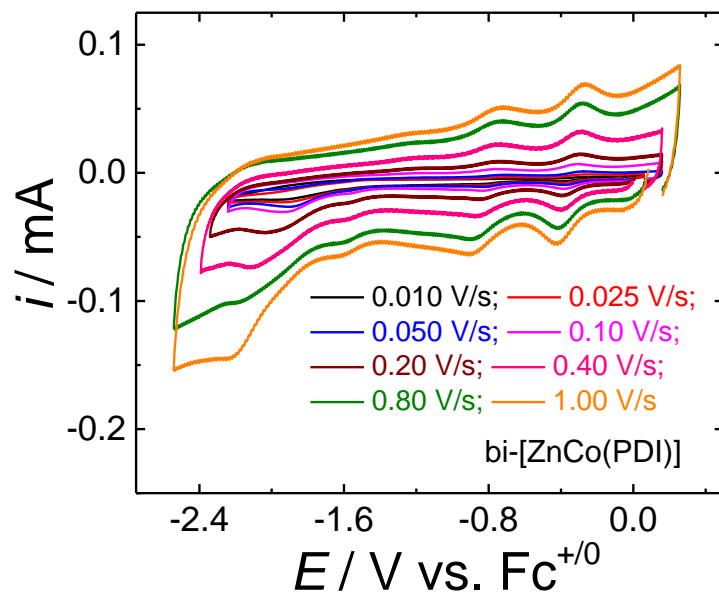

Figure A.158 The representative plot of $i_{reduction}$ at $Co^{2+}Co^{+}/Co^{+}Co^{+}$ couple as a function of $\upsilon^{1/2}$ for 0.15 mM bi-[Co(PDI)] in MeCN with 0.1 M nBu$_4$NPF$_6$ under N$_2$.

Figure A.159 Scan-rate dependent CVs of 0.30 mM bi-[ZnCo(PDI)] in MeCN with 0.1 M nBuNPF$_6$ under N$_2$

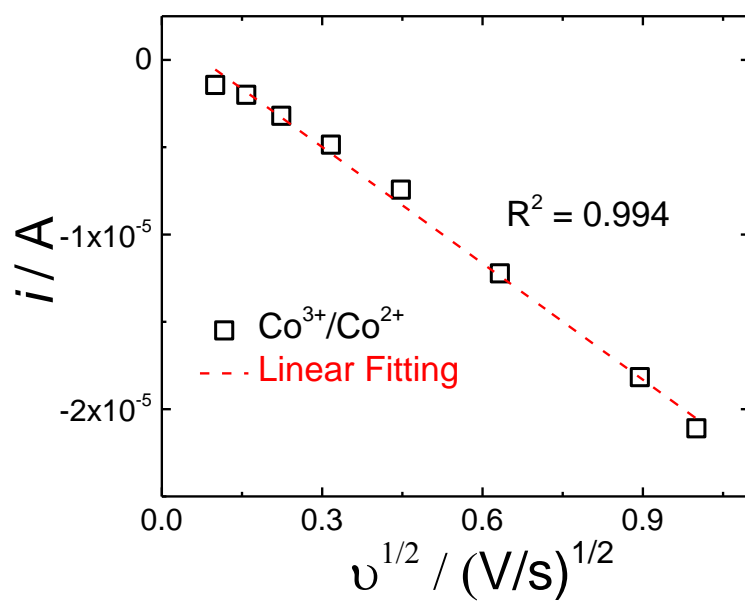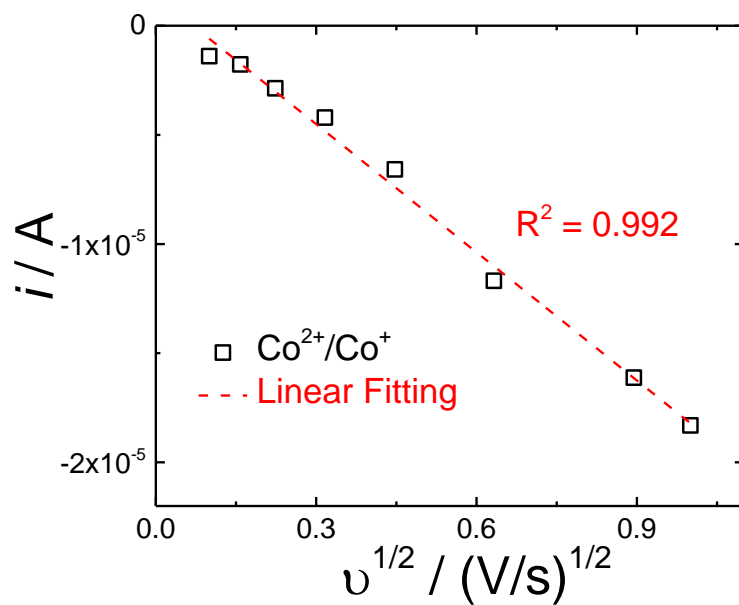**Figure A.160** The representative plot of $i_{\text{reduction}}$ at Co^{3+}/Co^{2+} couple as a function of $\upsilon^{1/2}$ for 0.30 mM bi-[ZnCo(PDI)] in MeCN with 0.1 M nBu$_4$NPF$_6$ under N$_2$.

Figure A.161 The representative plot of $i_{reduction}$ at Co^{2+}/Co$^+$ couple as a function of $\upsilon^{1/2}$ for 0.30 mM bi-[ZnCo(PDI)] in MeCN with 0.1 M nBu$_4$NPF$_6$ under N$_2$.
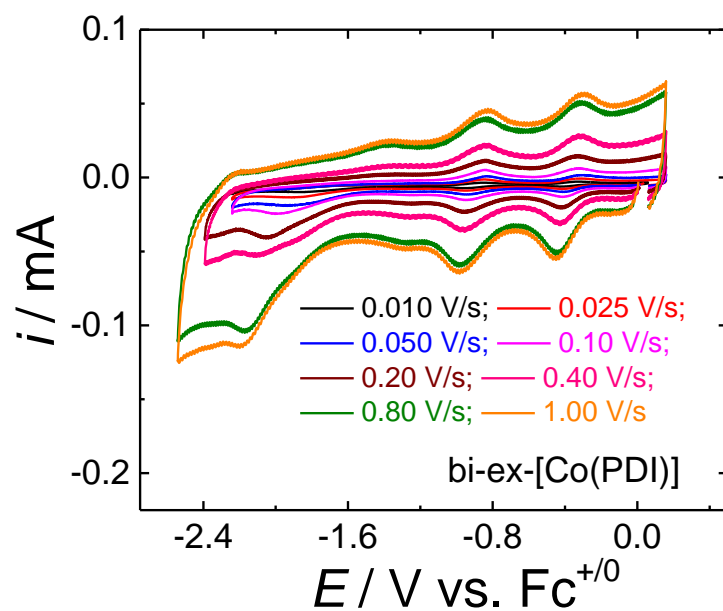
Figure A.162 Scan-rate dependent CVs of 0.15 mM bi-ex-[Co(PDI)] in MeCN with 0.1 M nBuNPF$_6$ under N$_2$
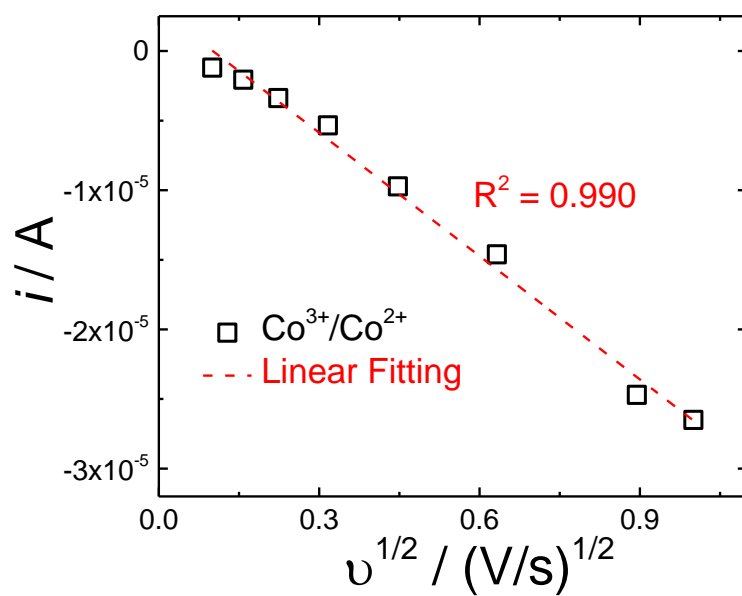

Figure A.163 The representative plot of $i_{reduction}$ at Co^{3+}/Co^{2+} couple as a function of $\upsilon^{1/2}$ for 0.15 mM bi-ex-[Co(PDI)] in MeCN with 0.1 M nBu$_4$NPF$_6$ under N$_2$.
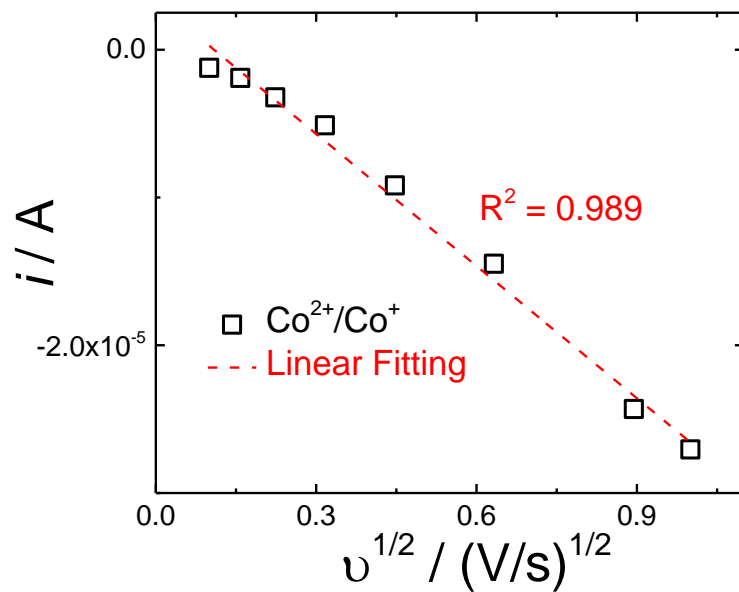
Figure A.164 The representative plot of $i_{reduction}$ at Co^{2+}/Co^+ couple as a function of $v^{1/2}$ for 0.15 mM bi-ex-[Co(PDI)] in MeCN with 0.1 M nBu$_4$NPF$_6$ under N$_2$.
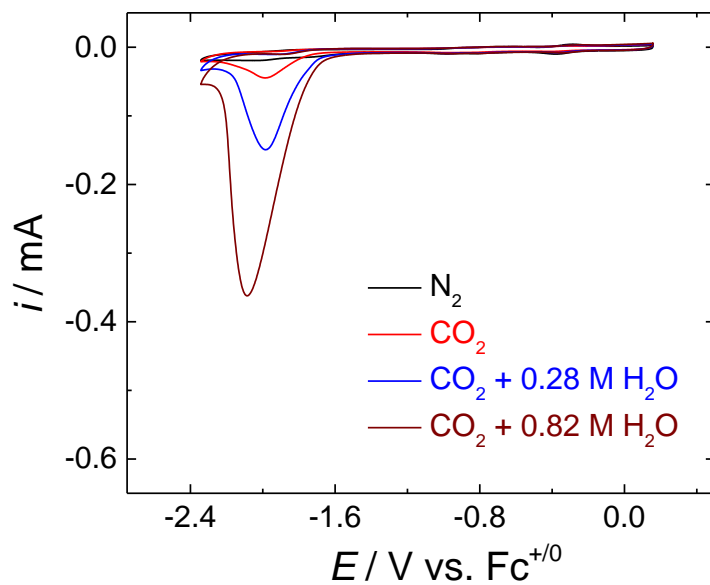
Figure A.165 CVs of 0.15 mM bi-[Co(PDI)] in MeCN with 0.1 M nBuNPF$_6$ under CO$_2$ with different concentrations of H$_2$O.
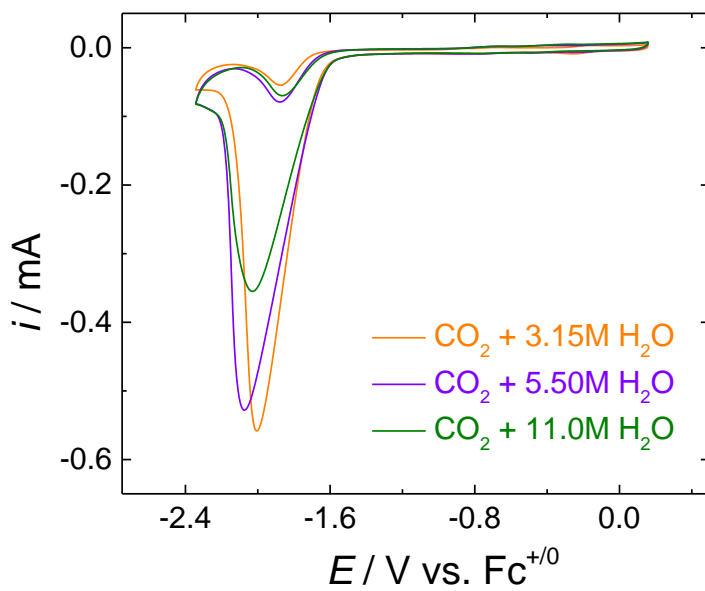

Figure A.166 CVs of 0.15 mM bi-[Co(PDI)] in MeCN with 0.1 M nBuNPF$_6$ under CO$_2$ with different concentrations of H$_2$O.

Figure A.167 SEM-EDS analysis of a working electrode surface after a 30-minute CO$_2$RR electrolysis of 0.15 mM bi-[Co(PDI)] in acetonitrile with 11.0 M H$_2$O with 0.1 M nBu$_4$PF$_6$ at −1.95 V vs. Fc$^{+/0}$

Figure A.168 SEM-EDS analysis of a working electrode surface after a 30-minute CO_2RR electrolysis of 0.15 mM bi-ex-[Co(PDI)] in acetonitrile with 11.0 M H_2O with 0.1 M nBu$_4$PF$_6$ at -1.95 V vs. Fc$^{+/0}$
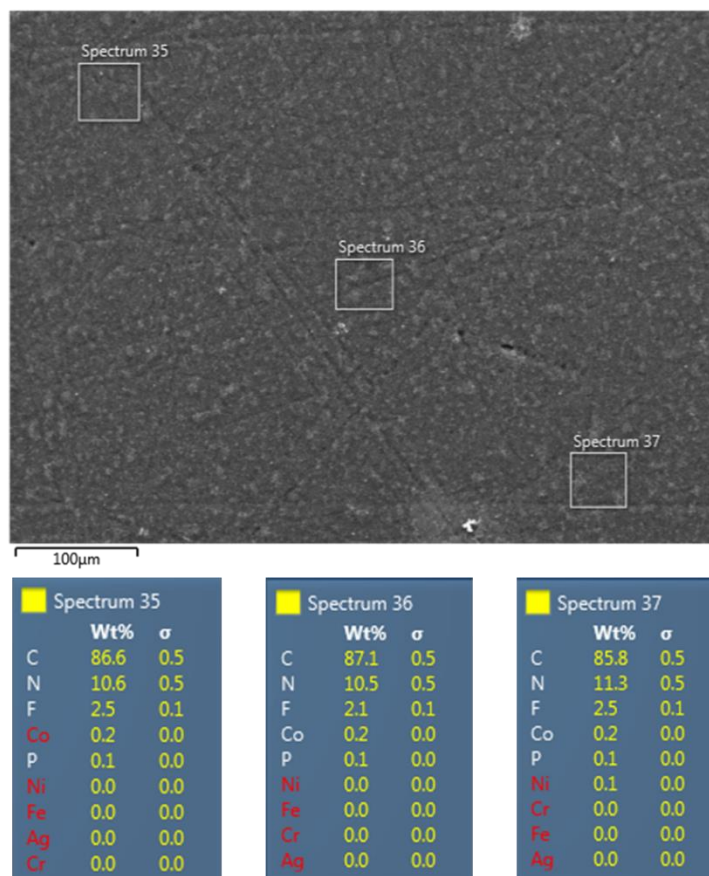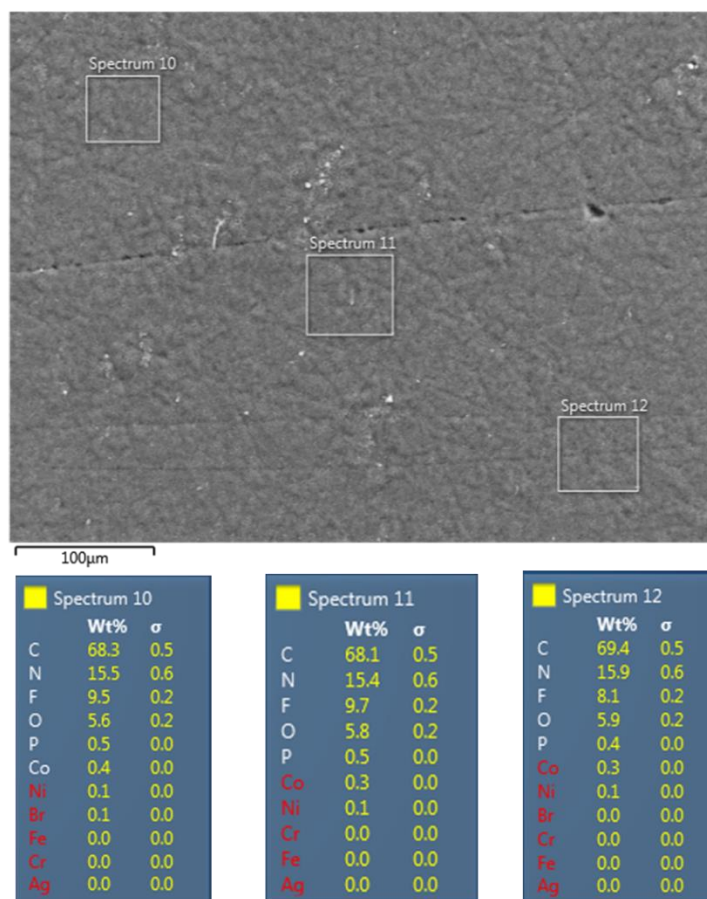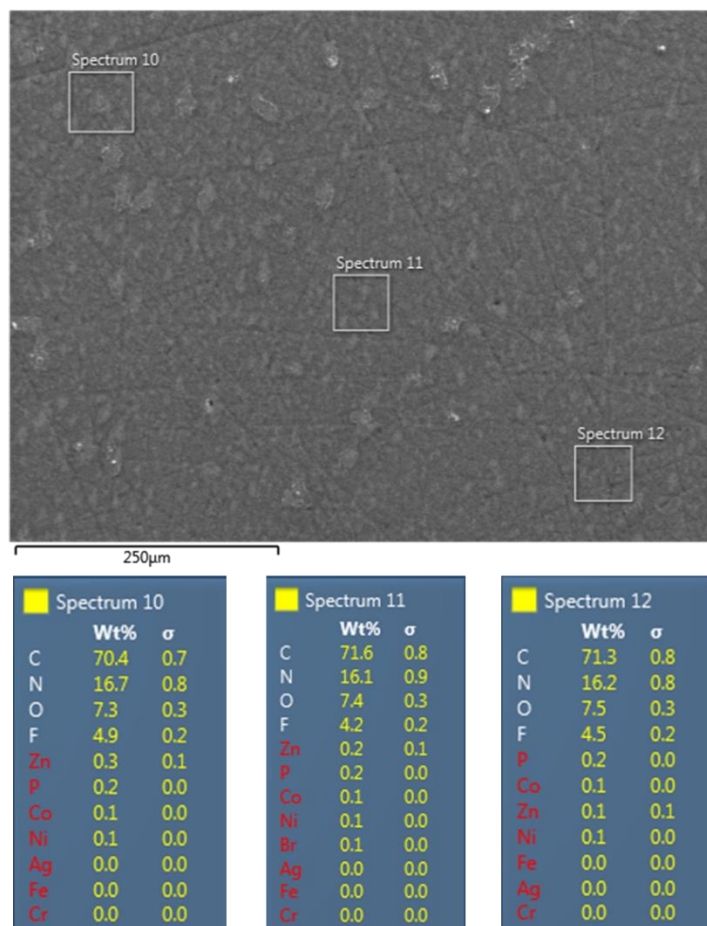
Figure A.169 SEM-EDS analysis of a working electrode surface after a 30-minute CO_2RR electrolysis of 0.15 mM bi-[ZnCo(PDI)] in acetonitrile with 11.0 M H_2O with 0.1 M nBu$_4$PF$_6$ at −1.95 V vs. Fc$^{+/0}$
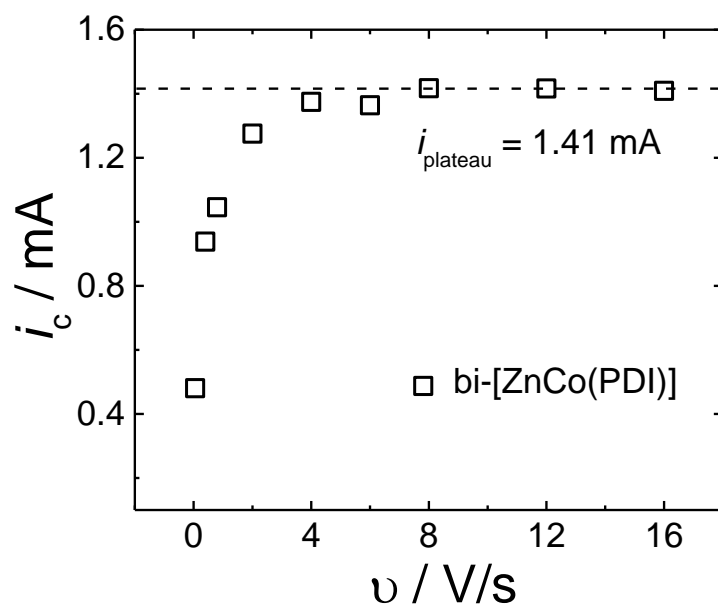
Figure A.170 Plots of the catalytic current, i_c, as a function of the scan rate, v, for the CO_2RR by 0.30 mM bi-[ZnCo(PDI)] (black square) in CO_2-saturated MeCN with 11 M H_2O.
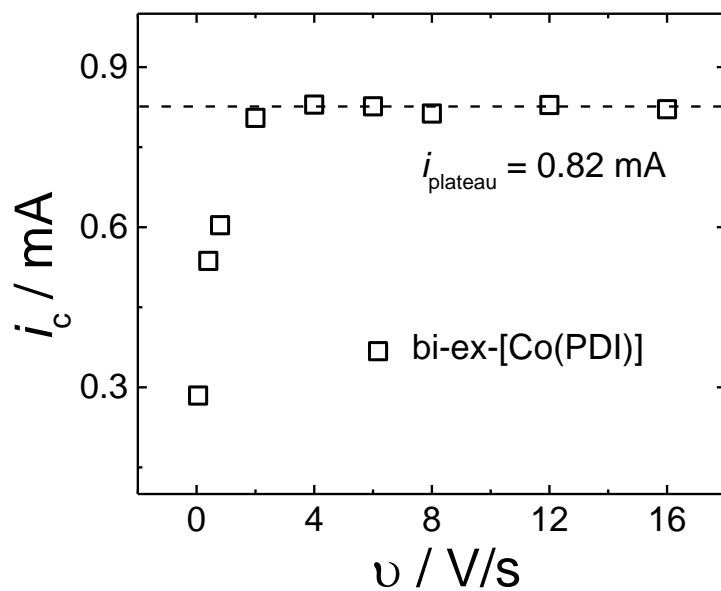
Figure A.171 Plots of the catalytic current, i_c, as a function of the scan rate, v, for the CO_2RR by 0.15 mM bi-ex-[Co(PDI)] (black square) in CO_2-saturated MeCN with 11 M H_2O.
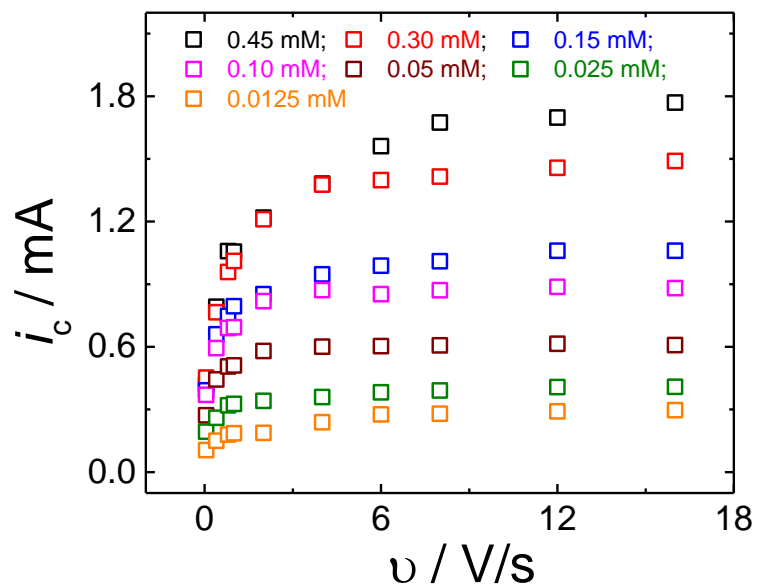
Figure A.172 Plots of the catalytic current, i_c, as a function of the scan rate, v, for the CO$_2$RR by different concentrations of bi-[Co(PDI)] in CO$_2$-saturated MeCN with 11 M H$_2$O;
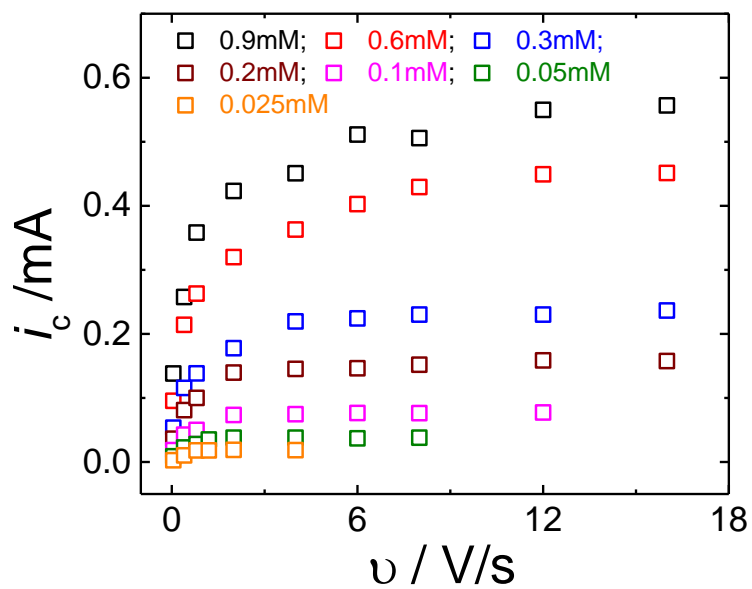
Figure A.173 Plots of the catalytic current, i_c, as a function of the scan rate, v, for the CO$_2$RR by different concentrations of [Co(PDI)] in CO$_2$-saturated MeCN with 11 M H$_2$O
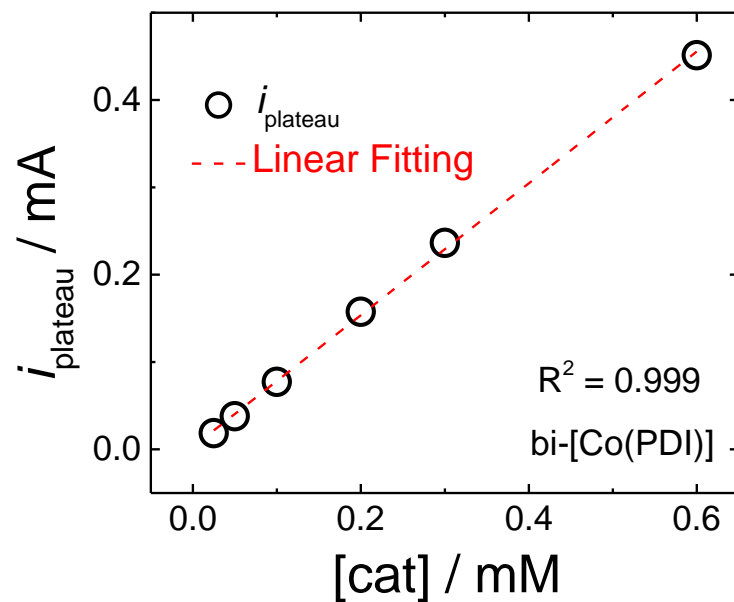
Figure A.174 The plot of the limiting plateau current, $i_{plateau}$, for the CO_2RR in MeCN with 11.0 M H_2O as a function of the concentrations of [Co(PDI)] with a linear fitting line, showing the a first-order dependence on the concentration of [Co(PDI)] for the CO_2RR.

A.4.2 Supporting Tables

Table A.31 *D* values calculated at each redox process for Co complexes in this report.

Catalysts	*D* values calculated at Co-based redox process / cm^2/s		
	Co$^{2+/+}$		Co$^{3+/2+}$
[Co(PDI)][a]	1.45×10^{-5}		1.79×10^{-5}
bi-[Co(PDI)]	2.52×10^{-5}	3.16×10^{-5}	1.10×10^{-5}
bi-ex-[Co(PDI)]	1.34×10^{-5}		1.37×10^{-5}
bi-[ZnCo(PDI)]	1.18×10^{-5}		1.52×10^{-5}

[a]The data of [Co(PDI)] is from chapter 4.

A.4.3 Supporting Methods

A.4.3.1 Diffusion Coefficient Calculations

Diffusion coefficients, D, for each complex were determined from the redox peaks in the non-catalytic CVs based on the Randles–Sevcik equation:

$$i_{\text{redox}} = 0.446 n^{3/2} A C_{cat} \left(\frac{\upsilon F^3 D_{\text{obs}}}{RT}\right)^{1/2} \qquad \text{Eq. S1}$$

The diffusion coefficient, expressed here as D_{obs}, is based on the assumption that the effective concentration of the electroactive species at each redox potential is equal to the bulk concentration of the catalyst molecule in solution. i_{redox} is the reduction peak current of the redox couple of the catalyst in the non-catalytic CV under N_2; n is the number of electrons transferred in the redox process; C_{cat} is the concentration of the catalyst dissolved in the solution; $F = 96485$ C/mol is Faraday's constant; A = 0.0707 cm^2 is the surface area of the glassy carbon working electrode in CV measurements; $T = 298$ K is the temperature; $R = 8.314$ J·K^{-1}·mol^{-1} is the ideal gas constant; and υ is the scan rate in units of V·s^{-1}.

As PDI-R/PDI-R$^{\bullet-}$ couple is not reversible for all binuclear molecular catalysts, values of D_{obs} are determined only at the Co$^{3+/2+}$ and Co$^{2+/+}$ (including Co^{2+}Co^{2+}/Co^{2+}Co$^+$, Co^{2+}Co$^+$/Co$^+$Co$^+$) couples for each complex by measuring i_{redox} as a function of scan rate. Representative voltammograms of each complex at different scan rates are shown in Figures A.155, A.159 and A.162, and representative plots of i_{redox} as a function of $\upsilon^{1/2}$ for each complex are shown in Figures A.156-A.158, A.160-A.161 and A.163-A.164. D_{obs} was calculated at each redox couple from the slopes of the best-fit lines according to Eq S1, and the results are summarized in Table A.31. The D_{obs} value calculated at every redox potential are equivalents suggesting there is no potential-

dependent change in mass transport (e.g. as might be expected for a reductive dimerization event). For calculations of TOF_{CPE}, the D_{obs} for the $Co^{3+/2+}$ couple was used as the diffusion coefficient of the complex for consistence.

A.4.3.2 TOF calculations

A.4.3.2.1 TOF$_{CPE}$ calculations based on the CPE data

Turnover frequencies for CO production by binuclear molecular catalysts calculated from CPE data, TOF_{CPE}, are determined according to the procedure described by Savéant et al,[1-2] which was discussed in chapter 4. TOF$_{CPE}$ at a given potential is defined by equation S2.

$$\text{TOF}_{\text{CPE}} = \frac{n(\text{CO})}{n(\text{Cat}) \times t} \qquad \text{Eq. S2}$$

Here, n(CO) is the number of moles of CO produced during the electrolysis, and n(Cat) is the number of moles of [Co(PDI-R)] estimated in the reaction-diffusion layer during the electrolysis, and t is the time of electrolysis in the unit of s. n(CO) is given by equation S3:

$$n(CO) = \frac{Q \times \text{FE(CO)}}{2F} \qquad \text{Eq. S3}$$

Here, Q is the charged passed during the CPE, FE(CO) is the measured Faradaic efficiency for CO production, and $F = 96485$ C/mol is the Faraday constant.

For a homogeneous molecular electrocatalyst, $n(Cat)$ is estimated from the space integration of the estimated catalyst amount in the reaction-diffusion layer near the surface of the working electrode as determined by equation S4.[1-3]

$$n(\text{Cat}) = A \sqrt{\frac{D_{obs}}{TOF}} [\text{Cat}] \qquad \text{Eq. S4}$$

Here, $A = 2.56$ cm^2 is the active surface area of the working electrode, $t = 30$ min $= 1800$ s is the electrolysis time, D_{obs} is the diffusion coefficient for the complex determined at the Co$^{3+/2+}$ couple in Table A.31, [Cat] $= 1.5 \times 10^{-7}$ mol/cm^3 is the concentration of the catalyst, and TOF is the maximum turnover frequency as determined from catalytic CVs at large overpotential. Combining Eq. S2, S3, and S4 leads to the expression for TOF$_{CPE}$ shown in Equation S5.

$$\text{TOF}_{CPE} = \frac{n(CO)}{n(Cat) \times t} = \frac{\frac{Q \times FE(CO)}{2F}}{A \sqrt{\frac{D_{obs}}{TOF}}[Cat] \times t} \qquad \text{Eq. S5}$$

If we define the fractional current going to CO production as i according to Eq. S6:

$$i = \frac{Q \times FE(CO)}{t} \qquad \text{Eq. S6}$$

Then we can substitute this into Equation S5 to yield Equation S7 below:

$$\text{TOF}_{CPE} = \frac{i \times}{2FA} \frac{\sqrt{TOF}}{\sqrt{D_{obs}}[Cat]} \qquad \text{Eq. S7}$$

Alternatively, if we assume that the electron transfer to the catalyst is fast and that the redox process is Nernstian, then we can derive an alternate expression for the potential-dependent TOF$_{CPE}$ according to equation S8:[1-2]

$$\text{TOF}_{CPE} = \frac{TOF}{1 + exp\left[\frac{F}{RT}(E_{app} - E^0)\right]} \qquad \text{Eq. S8}$$

458

Here, $R = 8.314$ J·K^{-1}·mol^{-1} is the universal gas constant, $T = 298.15$ K is temperature of the solution, E_{app} is the applied potential during electrolysis, E^0 is the redox potential of active species for the catalyst. For all binuclear bi-[Co(PDI)], bi-[ZnCo(PDI)] and bi-ex-[Co(PDI)] complexes, the catalytic onset in CO_2-saturated solutions with 11 M H_2O occurs near the (PDI/PDI$^{\cdot-}$) redox couple (Figure 5.2 and 5.6 in chapter 5), indicating that Co^{I}(PDI$^{\cdot-}$) is the active species to initiate the catalysis. Thus, the redox potential of the active species $E^0 = E_{1/2}$(PDI-PDI/PDI-PDI$^{\cdot-}$) for bi-[Co(PDI)] and bi-[ZnCo(PDI)] and $E_{1/2}$(PDI/PDI$^{\cdot-}$) for bi-ex-[Co(PDI)].

Combining Equation S7 and S8 yields the following expression for TOF$_{CPE}$:

$$\text{TOF}_{CPE} = \frac{i^2\left(1+exp\left[\frac{F}{RT}(E_{app}-E^0)\right]\right)}{4F^2A^2D_{obs}[Cat]^2} \qquad \text{Eq. S9}$$

In the final expression of TOF$_{CPE}$ in Equation S9, all parameters are known constants for measurable values. TOF$_{CPE}$ values for the binuclear catalysts are summarized in Table 5.2 in the chapter 5.

A.4.3.2.2. TOF_{cat} and TOF_0 calculations based on the scan rate independent plateau current

For the CO_2RR, the catalytic reaction rate k_{cat} can be calculated from the plateau current independent of scan rates based on the following equation:[2, 4]

$$\frac{i_{plateau}}{i_p} = \frac{1}{0.446}\sqrt{\frac{RT}{nFv}}\, n'\, k_{cat} \qquad \text{Eq. S15}$$

Here, $i_{plateau}$ is the catalytic plateau current under CO_2 independent of scan rates, i_p is the redox current of active species under N_2 measured with the scan rate v, R is the gas constant, T is the temperature, F is Faraday's constant, n is the number of unique electron transfer processes for CO_2RR per catalyst ($n = 2$), n' is the catalyst equivalents needed per turnover ($n' = 2$ for binuclear), and k_{cat} is the intrinsic catalytic rate constant.

To determine $i_{plateau}$, catalytic CVs of binuclear complexes under CO_2 in the presence of 11.0 M H_2O are collected with varying scan rates. Although we cannot really reach a true "plateau current" with a perfect S shape, however, a plot of peak current vs scan rate asymptotically approaches a limit at fast scan rates ($v > 4$ V/s, Figure 5.4b in Chapter 5 and Figure A.170 and A.171), and this limiting current $i_{plateau}$ is used to estimate the rate k_{cat} based on Eq. S15. k_{cat} of binuclear complexes were calculated and summarized in Table 5.4 in Chapter 5.

Based on the definition and mathematic derivation of TOF,[2, 4] the expression of TOF is shown in equation S16:

$$TOF = \frac{k_{cat}}{1+exp\left[\frac{F}{RT}\left(E^0_{CO2}-E^0_{cat}-\eta\right)\right]} \qquad \text{Eq. S16}$$

Here E^0_{CO2} (= −1.36 V vs. Fc$^{+/0}$) is the thermodynamic potential for the CO$_2$RR in MeCN with 11.0 M H$_2$O as the proton source calculated and applied in the previous literature, which takes into account the fact that the true proton donor is dissolved CO$_2$ (i.e. carbonic acid, H$_2$CO$_3$).[2] E_{cat}^0 is the redox potential of the active species of the catalyst. As discussed in the calculation of TOF$_{CPE}$, the redox potential of the active species $E_{cat}^0 = E_{1/2}$(PDI-PDI/PDI-PDI$^{\bullet-}$) for bi-[Co(PDI)] and bi-[ZnCo(PDI)] and $E_{1/2}$(PDI/PDI$^{\bullet-}$) for bi-ex-[Co(PDI)]. Plotting logTOF vs. η gives Figure 5.5 in Chapter 5. When $\eta = 0$, logTOF = logTOF_0, is a measure of the intrinsic catalytic ability of a catalyst. logTOF_{cat} is the maximum catalytic ability of a catalyst at the high overpotential. k_{cat} and corresponding logTOF_{cat} and logTOF_0 are summarized in Table 5.4 in Chapter 5.

A.4.4 Supporting References

1.   Costentin, C.; Robert, M.; Saveant, J.-M. "Catalysis of the electrochemical reduction of carbon dioxide," *Chemical Society Reviews* **2013**, *42*, 2423-2436. http://dx.doi.org/10.1039/c2cs35360a

2.   Costentin, C.; Drouet, S.; Robert, M.; Savéant, J.-M. "Turnover Numbers, Turnover Frequencies, and Overpotential in Molecular Catalysis of Electrochemical Reactions. Cyclic Voltammetry and Preparative-Scale Electrolysis," *Journal of the American Chemical Society* **2012**, *134*, 11235-11242. http://dx.doi.org/10.1021/ja303560c

3.   Nie, W.; Wang, Y.; Zheng, T.; Ibrahim, A.; Xu, Z.; McCrory, C. C. L. "Electrocatalytic CO2 Reduction by Cobalt Bis(pyridylmonoimine) Complexes: Effect of Ligand Flexibility on Catalytic Activity," *ACS Catalysis* **2020**, 4942-4959. http://dx.doi.org/10.1021/acscatal.9b05513

4.   Rountree, E. S.; McCarthy, B. D.; Eisenhart, T. T.; Dempsey, J. L. "Evaluation of Homogeneous Electrocatalysts by Cyclic Voltammetry," *Inorganic Chemistry* **2014**, *53*, 9983-10002. http://dx.doi.org/10.1021/ic50065